

Peter C. Chu

P-Vector Inverse Method



Springer

Extra
Materials
extras.springer.com

Peter C. Chu

P-Vector Inverse Method

with 271 Figures and 2 DVDs

 Springer

Prof.Dr. Peter C. Chu
Naval Postgraduate School
Department of Oceanography
Naval Ocean-Atmospheric
Prediction (NOAP) Laboratory
Monterey CA 93943
USA

Email: pcchu@nps.edu

Library of Congress Control Number: 2006926222

ISBN-10 3-540-33384-3 Springer Berlin Heidelberg New York
ISBN-13 978-3-540-35338-5 Springer Berlin Heidelberg New York

This work is subject to copyright. All rights are reserved, whether the whole or part of the material is concerned, specifically the rights of translation, reprinting, reuse of illustrations, recitation, broadcasting, reproduction on microfilm or in any other way, and storage in data banks. Duplication of this publication or parts thereof is permitted only under the provisions of the German Copyright Law of September 9, 1965, in its current version, and permission for use must always be obtained from Springer-Verlag. Violations are liable to prosecution under the German Copyright Law.

Springer is a part of Springer Science+Business Media
springer.com
© Springer-Verlag Berlin Heidelberg 2006

The use of general descriptive names, registered names, trademarks, etc. in this publication does not imply, even in the absence of a specific statement, that such names are exempt from the relevant protective laws and regulations and therefore free for general use.

Cover design: E. Kirchner, Heidelberg
Production: Almas Schimmel
Typesetting: SPi
Printing: Krips bv, Meppel
Binding: Stürtz AG, Würzburg

Printed on acid-free paper 30/3141/as 5 4 3 2 1 0

Preface

The demand for oceanic information is increasing rapidly. Physical oceanographers measure the temperature and salinity quite often, but not the velocity. The inverse problem of ocean circulation is to infer from temperature and salinity data, the velocity fields in global oceans and regional seas. The observational temperature and salinity profiles are usually sparse and irregularly distributed. Analysis of the profile data is necessary before using an inverse method. After analyzing (T, S) profile data, an inverse model on the base of the geostrophic and hydrostatic balances and mass conservation can be used to calculate the absolute velocity (u, v, w) . The inferred (u, v, w) data, along with the (T, S) , provide complete information of physical oceanography for observational study and modeling application.

P-vector inverse method covers the complete procedures from the (T, S) profile data analysis, a simple inverse method (i.e., the P-vector method), including the physical principles and detailed practicing, to wide application of the P-vector inverse method to observational and modeling studies. The emphasis is on the practical application of the subject with many examples. However, the theoretical foundations for various topics are also introduced. The book is intended for graduate or advanced undergraduate students with some basic physical oceanographic knowledge.

The physical oceanographic curricula could use this book for a self-contained course or could be included in courses on ocean data analysis, inverse modeling, ocean analysis and prediction, or ocean circulation. The material is also applicable in marine ecology and related disciplines.

The book is divided into four parts besides the introduction. The first part (Chaps. 2–4) presents the (T, S) profile data analysis, including the representation of profile data, thermal-haline parametric models, decorrelation scales, establishment of gridded (T, S) data using the optimal interpolation and optimal spectral decomposition, and various coordinate (z -, isopycnal, and semi-isopycnal) systems. The second part (Chaps. 5–9) describes theoretical base and technical details of the P-vector inverse method in the z -, isopycnal-, and semi-isopycnal-coordinate systems. The material covers the

necessary conditions for the velocity inversion, P-vector spiral, evaluation of the P-vector method, variational P-vector method, and global volume transport stream function. In addition, a new unit vector (C-vector) representing the secondary circulation is also included. The third part (Chaps. 10–14) presents the basin/regional scale ocean circulations calculated using the P-vector method. Starting from data format description (NetCDF format) in Chap. 10, circulation in the Atlantic, Pacific, Southern, and Arctic Oceans, and selected regional seas is presented. The fourth part (Chaps. 15, 16) shows the application of the P-vector method in numerical modeling and data assimilation. Use of the calculated absolute velocity along with (T, S) fields provides the balanced data assimilation and initial condition. When presenting these materials, physical phenomenon and processes (such as barrier layer, seasonal and interannual variability of mixed layer depth, multieddy structures in the regional seas, Kuroshio intrusion into the South China Sea, thermohaline fronts, etc.) and mechanisms are also discussed. In addition, the software for the P-vector inverse method is given in the appendix. The relevant global datasets (NetCDF format) are provided in DVD-ROMs, including (T, S) atlas in the isopycnal coordinate, heat storage, global, absolute velocity in z - and isopycnal coordinates, and volume transport streamfunction.

I am grateful to Henry Stommel, Carl Wunsch, Russ Davis, Andrew Bennett, and Peter Killworth for their inspiration on ocean inverse problems. The book could not have been written without the support and cooperation of a number of people. My colleagues, students, and visiting professors/scientists at the Naval Ocean Analysis and Prediction (NOAP) Laboratory at the Naval Postgraduate School helped me in developing the new methods and techniques for observational (T, S) data analysis and the P-vector concept for ocean circulation inverse: Wenju Cai, Edmo Campos, Michael Carron, Kuofeng Cheng, Jeng-Ming Chen, Yuchun Chen, Nath Edmons, Laura Ehret, Chenwu Fan, Chin-Lung Fang, Charles Fralick, Jose E. Goncalves, Steven D. Heager, Leonid M. Ivanov, Jeffery L. Kerling, Simon Konstantinidis, Kleantith Kyriakidis, Akira Kuninaka, Jian Lan, Ching-Chung Li, Rongfeng Li, W. Timothy Liu, Carlos Lozano, Shihua Lu, Binbing Ma, Tatanya Margolina, Oleg Melnichenko, Gonzalo Montenegro, Rodrigo Obino, Ahchuang Ong, Patrice Pauly, Michael Roth, Carl Szczechowski, Robert Steadley, Hilbert Strauls, Carl Szczechowski, Hsing-Chia Tseng, Joe Veneziano, Guihua Wang, Qianqian Wang, and Susan Wells. Among them, Chenwu Fan's effort is highly appreciated.

It is my pleasure to acknowledge the contributions of many colleagues and anonymous reviewers whose comments have greatly improved this book. At various stages of this effort I have been fortunately supported by the Naval Oceanographic Office, Office of Naval Research, and National Aeronautics and Space Administration.

Contents

1	Introduction	1
1.1	Basic Physics of the Inverse Problem	1
1.1.1	Basic Equations	1
1.1.2	Ekman Number	2
1.1.3	Thermal Wind Relation	3
1.2	Reference Velocity	4
1.2.1	Level-of-no-Motion	4
1.2.2	Determination of Reference-Level Velocity	4
1.3	Necessary Conditions for Inversion	8
2	Analysis of Observational (T, S) Profiles	11
2.1	Historical (T, S) Profiles	11
2.2	Synoptic (T, S) Profiles	13
2.3	Representation of (T, S) Profiles	15
2.4	Non-Polar Parametric Model	16
2.4.1	Seasonal Variability	16
2.4.2	Model Description	19
2.4.3	Iteration Method	21
2.5	Polar Parametric Model	23
2.5.1	Seasonal Variability	23
2.5.2	Multiple Thermohaline Structures	26
2.5.3	Characteristics from Profiles	29
2.5.4	Vertical Gradients	31
2.5.5	Thermohaline Parametric Description	32
2.5.6	Statistical Tests	32
2.6	Curve-Fitting Model	33
2.6.1	Top Shallow Sub-Model (0–400 m)	34
2.6.2	Mid-Depth Sub-Model (200–2,450 m)	34
2.6.3	Deep Sub-Model (2,000 m to Bottom)	35
2.7	Mixed Layer Depth	35
2.7.1	Simple Criteria	35

VIII Contents

2.7.2	MLD _T	36
2.8	Barrier Layer	40
2.8.1	Two Mechanisms for the Occurrence of Barrier Layer	43
2.8.2	Sulu and Celebes Seas	44
2.8.3	Barrier Layer in the Sulu Sea	45
2.8.4	Barrier Layer in the Celebes Sea	49
2.9	Determination of Vertical Temperature Structure from SST ..	52
2.9.1	Methodology	53
2.9.2	Example – South China Sea	54
2.9.3	Regression Method	58
2.9.4	Multi-Time-Scale Method	59
2.9.5	Verification	60
2.9.6	Limitation of the Multi-Time Scale Hypothesis	62
2.10	Autocorrelation Functions	63
2.10.1	Bin Method	63
2.10.2	Autocorrelation Function in Deep and Shallow Water	65
2.10.3	Shallow Water – Yellow Sea Temperature Field	66
2.11	Temporal and Spatial Decorrelation Scales	71
2.11.1	Gaussian Model	72
2.11.2	<i>F</i> -Test for the Gaussian Model	73
2.11.3	Seasonal Variability of the Decorrelation Scales	73
2.11.4	Usefulness of the Decorrelation Scales	75
3	Establishment of Gridded (<i>T</i>, <i>S</i>) Fields	77
3.1	Two Types of Climatological Data Sets	77
3.1.1	<i>z</i> -Level Analysis	77
3.1.2	Parametric Analysis	80
3.2	Optimal Interpolation	81
3.2.1	Modular Ocean Data Assimilation System	81
3.2.2	MODAS Evaluation	82
3.2.3	Future MODAS Improvement	85
3.3	Optimal Spectral Decomposition	87
3.3.1	Spectral Decomposition	87
3.3.2	Optimal Mode Truncation	88
3.3.3	Rotation Matrix Method for Regularization	89
3.3.4	Accuracy of the Rotation Matrix Method	91
3.3.5	Rotation Matrix Method for Linear Scalar Process ..	91
3.3.6	Rotation Matrix Method for Two-Dimensional Field ..	92
3.3.7	Rotation Matrix Method for Perturbed Lorenz Attractor	94
3.3.8	Bimodality of Temperature Field at Mid-Depth of North Atlantic	99
3.4	Global Heat Storage	102

4	Coordinate Systems	109
4.1	Isopycnal Coordinate System	109
4.2	Semi-Isopycnal Coordinate System.....	110
4.3	Isopycnal Surfaces Determined from Data	112
4.4	Data Transformation.....	113
5	P-Vector	115
5.1	z -Coordinate System.....	115
5.1.1	Definition	115
5.1.2	Horizontal P-Vector Field	116
5.1.3	P-Spiral	117
5.2	Isopycnal Coordinate System	119
5.2.1	P-vector	119
5.2.2	Absolute Velocity Formula.....	120
5.2.3	P-Vector Spiral	120
5.3	Semi-Isopycnal Coordinate	121
5.3.1	P-Vector	121
5.3.2	P-Spiral	123
6	Determination of Speed Parameter	127
6.1	Algebraic Equations	127
6.2	Necessary Conditions	128
6.3	Optimization Scheme	129
6.4	Evaluation Using the Modular Ocean Model (MOM)	131
6.4.1	MOM Implementation	131
6.4.2	MOM Generated Steady-State (ρ, q) Data	133
6.4.3	MOM Generated Statistically Steady-State Velocity Field	133
6.4.4	Necessary Condition Check-up	135
6.4.5	Absolute Velocities Obtained from the P-Vector Inverse Method Using MOM T, S Output	137
6.4.6	Comparison between Nondivergent Portions of Two Flow Fields.....	138
6.5	z -Coordinate System.....	140
6.5.1	Japan/East Sea	141
6.5.2	GDEM for the Japan/East Sea.....	144
6.5.3	Temperature.....	144
6.5.4	Salinity	153
6.5.5	Absolute Velocity	160
6.6	Isopycnal Coordinate System	165
6.6.1	South China Sea	165
6.6.2	Oceanic Conditions	166
6.6.3	Monthly Mean Temperature Field	167
6.6.4	Monthly Mean Salinity Field.....	169
6.6.5	Monthly Mean Pressure Field	171

6.6.6	Monthly Mean Potential Vorticity Field	173
6.6.7	Monthly Mean Circulations	175
6.6.8	Kuroshio Intrusion Through Luzon Strait	178
7	Variational P-Vector Method	185
7.1	Weakness of the P-Vector Method	185
7.2	Variational Algorithm	185
7.3	Combined Local-Global Determination	186
7.4	Annual Mean Velocity	189
7.4.1	Upper Layer	189
7.4.2	Intermediate Layer	191
7.5	Seasonal Variability	191
7.5.1	Surface Circulation	191
7.5.2	Out-of-Phase Variation	193
7.5.3	Ulleung/Tsushima Basin Anticyclonic Eddy	193
7.5.4	Flow through Tsushima/Korea Strait	193
7.6	Volume Transport Through Tsushima/Korea, Tsugaru, and Soya Straits	197
8	Determination of Volume Transport Stream Function	201
8.1	Vertically Integrated Velocity	201
8.2	Volume Transport Stream Function	203
8.3	Volume Transport Vorticity	204
8.3.1	Extra-Equatorial Region	204
8.3.2	Equatorial Region (between 8°S and 8°N)	204
8.4	Boundary Conditions for Poisson Ψ -Equation	206
8.5	Determination of Ψ -Values at Islands	207
8.5.1	Stokes Theorem	208
8.5.2	Algebraic Equation for Ψ -Value at Island- Ω_j	210
8.5.3	Iteration Process	211
8.6	Verification of Island Algorithm	212
8.6.1	A Channel with Two Islands	212
8.6.2	Twin Experiments	213
8.6.3	Sensitivity to $\Psi_1^{(1)}$ -Value	215
8.6.4	Sensitivity to Location of Island-1	216
8.6.5	Sensitivity to Noise	217
8.7	Global Volume Transport Stream Function	221
8.7.1	Ψ -Values for Global Islands	221
8.7.2	Ψ -Values for Global Oceans	221
8.8	Sensitivity to Observational Errors	223
9	C-Vector for Identifying Oceanic Secondary Circulations	229
9.1	C-Vector	229
9.2	Secondary Circulations Across Arctic Fronts in the Fram Strait	232

9.3	Hydrographic Data Collection	233
9.4	Potential Density	233
9.5	Horizontal Pseudovorticity	235
9.6	Two Scalar Functions	236
9.7	Three Types of Forcing Terms for Ageostrophic Circulation ..	237
10	Datasets	241
10.1	General Description	241
10.2	NetCDF Data Model	242
10.2.1	General Structure	242
10.2.2	Dimension	243
10.2.3	Variable	243
10.2.4	Attributes	244
10.3	Data Extraction	245
10.4	Datasets	246
10.4.1	Heat Storage	246
10.4.2	Depth of Isopycnal Surface	246
10.4.3	Potential Vorticity at Isopycnal Surface	247
10.4.4	Absolute Velocity in z -Coordinate	247
10.4.5	Absolute Velocity in Isopycnal Coordinate	247
10.4.6	Volume Transport Stream Function and Vertically Integrated Velocity	247
11	Inverted Circulations in the Pacific Basin	249
11.1	General Features	249
11.2	Water Mass Crossroads	253
11.2.1	General Description	253
11.2.1	(T, S) Fields	256
11.2.2	Velocity Field	257
11.2.3	Seasonal Variability of Major Currents	261
11.2.5	Vertically Integrated Velocity	267
11.2.6	Volume Transport	267
11.3	Indonesia Throughflow	271
11.4	Kuroshio Transport and its Intrusion into the South China Sea	274
11.5	Northwest Pacific Subtropical Counter Current on Isopycnal Surface	276
11.5.1	General Features	276
11.5.2	Circulations	277
11.5.3	Spatial Variability of the Subtropical Counter Current	279
11.5.4	Potential Vorticity	280
11.5.5	Major Features	280
11.6	Seasonal Variability of the South China Sea Thermohaline Structure	281
11.6.1	General Thermal Characteristics	281

XII Contents

11.6.2	Establishment of Monthly Gridded Data from the MOODS	282
11.6.3	Composite Analysis	284
11.7	Seasonal Variability of the South China Sea Circulation	291
11.7.1	General Description	291
11.7.2	Surface Circulation	292
11.7.3	Subsurface (75 m)	293
11.7.4	Intermediate Level (150 m)	294
11.8	South China Sea Thermohaline Front	296
11.8.1	Thermohaline Front Identified Using GDEM	296
11.8.2	Forcing Mechanism	301
11.8.3	Cross-Basin Current	301
11.8.4	Water Mass Characteristics across the Front	305
11.9	MultiEddy Structure Detected from AXBT Data	316
11.9.1	General Description	316
11.9.2	AXBT Measurements	318
11.9.3	Temperature	320
11.9.4	Circulations	323
11.9.5	Mechanisms	329
11.10	Low Salinity Cold-Core Cyclonic Eddy Northwest of Luzon ..	330
11.10.1	Two Regimes	331
11.10.2	Observations	333
11.10.3	Temperature	335
11.10.4	Salinity	337
11.10.5	Velocity	343
11.10.6	Energy Budget of the Northwestern Luzon Eddy	345
11.11	Japan/East Sea MultiEddy Structure Detected from AXBT Data	348
11.11.1	Background	348
11.11.2	AXBT Data	349
11.11.3	Temperature	350
11.11.4	$T-S$ and $T-\bar{S}$ Relations	355
11.11.5	Velocity	355
11.12	Australian Mediterranean and South Australian Gyres	359
12	Inverted Circulations in the Atlantic Basin	365
12.1	North Atlantic Ocean Circulation	365
12.1.1	General Description	365
12.1.2	Circulation at Different Depths	369
12.1.3	Vertical Cross Sections	370
12.1.4	Gulf Stream Volume Transport	372
12.2	South Atlantic Ocean Circulation	373
12.3	Brazil–Malvinas Confluence	375

13 Inverted Circulations for the Southern Ocean 379

13.1 Antarctic Circumpolar and Coastal Currents 379

13.2 Cyclonic (Clockwise) Weddell Double Gyres 383

13.3 Anticyclonic Ross Gyre 385

14 Inverted Circulations in the Arctic Mediterranean Seas 389

14.1 Geographic Features 389

14.2 Thermohaline Features 391

14.2.1 Subsurface Level (50 m Depth) 391

14.2.2 Intermediate Level (500 m Depth) 393

14.2.3 Deep Level (2,000 m Depth) 394

14.3 Inverted Circulation in the Greenland–Iceland–Norwegian Sea . 395

14.3.1 Circulation Patterns 397

14.3.2 Fram Strait Exchange 401

14.4 Inverted Circulation in the Arctic Ocean 401

15 Applications to Data Assimilation 407

15.1 Data Nudging 407

15.2 Linear Shallow Water Model 408

15.3 Balanced Data Assimilation 410

15.4 Unbalanced Data Assimilation 412

16 Applications in Numerical Modeling and Simulation 415

16.1 Velocity Initialization 415

16.1.1 Initial Condition for Velocity in Ocean Models 416

16.1.2 Weakness of the Diagnostic Initialization 416

16.1.3 Measures of “Source/Sink” Strength 417

16.1.4 POM for the Japan/East Sea 418

16.1.5 Extremely Strong Source/Sink Terms 421

16.2 Uncertain Open Boundary Conditions 424

16.2.1 Model Implementation 424

16.2.2 Two-Step Initialization 426

16.2.3 Volume Transport at Open Boundaries 426

16.2.4 Experimental Design 427

16.2.5 Model Uncertainty 428

Appendices

A: P-Vector Module for z-Coordinate 431

A.1 Makefile 431

A.2 Main Subdirectories 432

A.2.1 Subdirectory (pvector) 432

A.2.2 Subdirectory (pvector_nc) 433

A.2.3 Subdirectory (pvector_rotation) 433

A.3 Major FORTRAN Programs 434

A.3.1 ASCII Format (pv.f) 434

XIV Contents

A.3.2	NetCDF Format (pvnc.f)	440
A.3.3	Non-(Lat, Lon) Horizontal Coordinates (pvxync.f) . . .	457
A.4	Include File (pstate.h)	471
A.5	Data Input	471
A.6	Equation of State (whoif)	474
A.7	P-Vector Calculation	485
A.8	Avoiding P-Vector Calculation	494
A.9	Data Output	495
B:	P-Vector Module for Isopycnal-Coordinate	501
B.1	Main Program	501
B.2	Graphic Interface	512
B.3	Transformation of (T , S) Data from z - to Isopycnal-Coordinate	514
B.4	Calculation of Level Depth, Layer Thickness, and Potential Vorticity	518
B.5	Calculation of Absolute Velocity	520
B.6	Functions	523
B.7	Avoiding P-Vector Calculation	525
C:	Thermohaline Parametric Model	527
C.1	Makefile	527
C.2	Gradient Calculated from (T , S) Profiles	527
C.3	Main Program	531
C.4	Subroutines	538
C.4.1	Interpolation	538
C.4.2	Iteration	539
C.4.3	Mixed Layer Depth	544
C.4.4	Depth at the Top of Thermocline/Halocline	547
C.4.5	Depth at the Bottom of Thermocline/Halocline	549
C.4.6	Depth at Top of Near-Zero Gradient Below Thermocline	551
C.4.7	Depth between Two Last Legs of Profile	557
C.4.8	Adjustment of Bottom Gradient	559
C.4.9	Data Input/Output	564
D:	Autocorrelation Matrix Calculated from (T, S) Profile Data	565
	References	577
	Index	599

Introduction

A major task of physical oceanographers is to determine the ocean circulation from real data. Due to the cost and time-consuming factors of current meter measurement, physical oceanographers usually have a relatively frequent hydrographic observation. For example, the US Navy's Master Oceanographic Observational Data Set (MOODS) contains more than six million temperature profiles and nearly one million salinity profiles for the global ocean. How to use the hydrographic data becomes important in inferring the state of the ocean circulation, understanding it dynamically, and even perhaps forecasting it, through a quantitative combination of theory and observations (Wunsch 1996).

1.1 Basic Physics of the Inverse Problem

1.1.1 Basic Equations

Let (x, y, z) be the coordinates with x -axis in the zonal direction (eastward positive), y -axis in the latitudinal direction (northward positive), and z -axis in the vertical direction (upward positive). The unit vectors along the three axes are represented by $(\mathbf{i}, \mathbf{j}, \mathbf{k})$. The linear steady state is reached with the hydrostatic balance in vertical; and the balance among the Coriolis force, pressure gradient force, and gradient of Reynolds stress in horizontal. With the Boussinesq approximation, the basic equations are given by

$$-f(\tilde{v} - v) = A_z \frac{\partial^2 \tilde{u}}{\partial z^2} + A_h \nabla_h^2 \tilde{u}, \quad (1.1a)$$

$$f(\tilde{u} - u) = A_z \frac{\partial^2 \tilde{v}}{\partial z^2} + A_h \nabla_h^2 \tilde{v}, \quad (1.1b)$$

$$\frac{\partial p}{\partial z} = -\rho g, \quad (1.1c)$$

$$\nabla_h \bullet \tilde{\mathbf{V}}_2 + \frac{\partial \tilde{w}}{\partial z} = 0, \quad (1.1d)$$

where ρ is the in situ density; $f = 2\Omega \sin \varphi$, is the Coriolis parameter, Ω the Earth rotation rate, and φ the latitude. $\tilde{\mathbf{V}}_2 = (\tilde{u}, \tilde{v})$, is the horizontal velocity; \tilde{w} is the vertical velocity; $\nabla_h = \mathbf{i}\partial/\partial x + \mathbf{j}\partial/\partial y$ is the horizontal gradient operator; $\mathbf{V}_2 = (u, v)$ is the geostrophic velocity representing the balance between the Coriolis force and the horizontal pressure (p) gradient force,

$$u = -\frac{1}{f\rho_0} \frac{\partial p}{\partial y}, \quad v = \frac{1}{f\rho_0} \frac{\partial p}{\partial x}, \quad (1.2)$$

where ρ_0 is the characteristic value ($1,025 \text{ kg m}^{-3}$) of the sea water density. The two coefficients (A_z, A_h) are the vertical and horizontal eddy diffusivities. The horizontal diffusivity A_h is usually estimated by Smagrinisky parameterization,

$$A_h = \frac{D}{2} \Delta x \Delta y \left[\left(\frac{\partial \tilde{u}}{\partial x} \right)^2 + \frac{1}{2} \left(\frac{\partial \tilde{v}}{\partial x} + \frac{\partial \tilde{u}}{\partial y} \right)^2 + \left(\frac{\partial \tilde{v}}{\partial y} \right)^2 \right]^{1/2}.$$

Here, the nondimensional parameter D varies from 0.1 to 0.2 (Mellor 2003). For horizontal grid of $1^\circ \times 1^\circ$ as in many climatological temperature and salinity datasets, and for spatial variability of the velocity of 0.1 m s^{-1} , the horizontal diffusivity is estimated as

$$A_h = 1.5 \times 10^3 \text{ m}^2 \text{ s}^{-1}.$$

1.1.2 Ekman Number

The Ekman number can identify the relative importance of the horizontal gradient of the Reynolds stress ($A_h \nabla_h^2 \tilde{\mathbf{V}}_2$) versus the Coriolis force ($f \mathbf{V}_h$),

$$E = \frac{O(|A_h \nabla_h^2 \tilde{\mathbf{V}}_2|)}{O(|f \tilde{\mathbf{V}}_2|)} = \frac{A_h}{|f| L^2}.$$

Here, L is the characteristic horizontal length scale. For extra-equatorial regions (north of 8°N and south of 8°S), $|f| > 0.2 \times 10^{-4} \text{ s}^{-1}$ and for length scale of motion L being larger than 200 km, the Ekman number is estimated by

$$E < \frac{1.5 \times 10^3 \text{ m}^2 \text{ s}^{-1}}{(0.2 \times 10^{-4} \text{ s}^{-1}) \times (2 \times 10^5 \text{ m})^2} = 1.875 \times 10^{-3}.$$

The horizontal gradient of the Reynolds stress can be neglected against the Coriolis force. For the equatorial regions especially near the equator, $|f|$ is very small. The Ekman number is not a small parameter. The horizontal gradient of the Reynolds stress, ($A_h \nabla_h^2 \tilde{u}, A_h \nabla_h^2 \tilde{v}$), cannot be neglected against the Coriolis force in the equatorial region.

1.1.3 Thermal Wind Relation

For large-scale motion in extra-equatorial regions, the geostrophic (1.2) and hydrostatic (1.1c) balances are usually satisfied. Differentiating the two equations in (1.2) with respect to z and utilizing (1.1c) yield the thermal wind relation,

$$\frac{\partial u}{\partial z} = \frac{g}{f\rho_0} \frac{\partial \rho}{\partial y}, \quad \frac{\partial v}{\partial z} = -\frac{g}{f\rho_0} \frac{\partial \rho}{\partial x}. \quad (1.3)$$

Vertical integration of the two equations in (1.3) with respect to z leads to the thermal wind relation,

$$u = u_0 + \frac{g}{f\rho_0} \int_{z_0}^z \frac{\partial \rho}{\partial y} dz', \quad (1.4)$$

$$v = v_0 - \frac{g}{f\rho_0} \int_{z_0}^z \frac{\partial \rho}{\partial x} dz', \quad (1.5)$$

which is the linkage between the geostrophic velocity and the in situ density. Here, (u, v) , (u_0, v_0) are the geostrophic velocities at any depth z and at a reference depth z_0 , respectively. It is noticed that only the density data determine the geostrophic shear. The reference-level velocity (u_0, v_0) needs to be determined. The continuity equation is given by

$$\nabla \cdot \mathbf{V} = 0. \quad (1.6)$$

where $\mathbf{V} = (u, v, w)$ is the three-dimensional velocity vector and w is the vertical velocity; and

$$\nabla \equiv \mathbf{i}\partial/\partial x + \mathbf{j}\partial/\partial y + \mathbf{k}\partial/\partial z,$$

is the three-dimensional gradient operator. The density equation (or thermodynamic equation) is generally written by

$$\frac{\partial \rho}{\partial t} + \mathbf{V} \cdot \nabla \rho = \text{Source} - \text{Sink},$$

which changes into

$$\mathbf{V} \cdot \nabla \rho = 0, \quad (1.7)$$

for steady-state and no source/sink terms (mass conservation).

The conservation of potential vorticity equation (Pedlosky 1986) can be obtained by differentiating (1.7) with respect to z , using geostrophic and hydrostatic balances (1.1) and (1.2), and including the latitudinal variation of the Coriolis parameter,

$$\mathbf{V} \cdot \nabla q = 0, \quad (1.8)$$

where q is the potential vorticity

$$q = f \frac{\partial \rho}{\partial z}. \quad (1.9)$$

It is noted that neglect of relative vorticity may induce a small but systematic error into the estimation of potential vorticity.

1.2 Reference Velocity

Determination of the reference-level velocity (u_0, v_0) needs the density conservation (1.7) and potential vorticity conservation (1.8). If the two conservation laws are not used, determination of the reference-level velocity becomes quite subjective. The simplest technique is the level-of-no-motion assumption.

1.2.1 Level-of-no-Motion

Inability to determine the reference-level velocity distorted and stymied the study of oceanography for many decades. Therefore, to avoid complete paralysis, oceanographers made the assumption that if one went deeply enough into the sea, the fluid movement would become as weak as to be negligible (Wunsch 1996). The “level-of-no-motion” assumption,

$$u_0 = 0, \quad v_0 = 0,$$

has been used widely by the oceanographic community with various levels (z_0) ranging from 500 to 4,000 decibars. Defant (1941) proposed to use the level of minimum geostrophic shear representing the level-of-no-motion. Thus, the level was permitted to slope across the ocean. Obviously, the two levels are not the same. However, Defant’s method is a rational one in the absence of any other criterion – the depth of minimum geostrophic shear is the depth for which the resulting velocities and transports are least sensitive to perturbation in the level-of-no-motion (Wunsch 1996).

1.2.2 Determination of Reference-Level Velocity

Several inverse methods have been developed to determine the reference-level velocity (u_0, v_0) using the conservation of mass and density (1.6), (1.7) and to avoid the ambiguity caused by the level-of-no-motion assumption. Those inverse methods are classified into two major categories: area determination, such as the box model (Hidaka 1940a,b; Wunsch 1978), and local determination, such as the β -spiral method (Stommel and Scott 1977; Schott and Stommel 1978; Behringer and Stommel 1980) and the Bernoulli method (Killworth 1986).

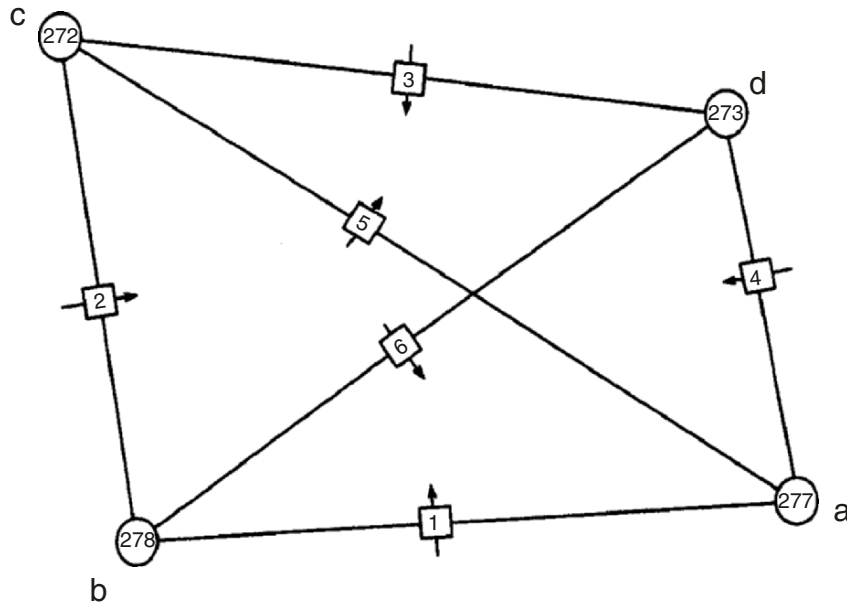


Fig. 1.1. Mass and salt conservation in defined triangular volumes used by Hidaka (1940b) in estimating reference-level velocities $v_0^{(i)}$ ($i = 1, 2, \dots, 6$). Here, the *circled numbers* are station identifiers, and *boxed integers* are interface labels used to identify the flows between volumes

(a) Hidaka's Attempt. Hidaka (1940a,b) made the first attempt to use the mass and salt conservation for determining the reference-level velocity from hydrographic data. He constructed triangles from the hydrographic stations with the side connecting pair of stations. For four hydrographic stations, there are six straight lines (Fig. 1.1). Let the reference-level velocity in each station pair along each line be denoted $v_0^{(i)}$ ($i = 1, 2, \dots, 6$), which are unknowns. The conservation requires that the product of net mass and salt flux with volumes (three triangles) must be zero. Thus, Hidaka obtained six algebraic equations with six unknowns. Hidaka (1940b) solved this system and obtained numerical values of the reference-level velocities. However, Defant (1961) demonstrated that such a system of equations was ill-conditioned and numerical values of the reference-level velocities produced by Hidaka (1940b) were meaningless.

(b) Box model. Following Hidaka's (1940a,b) lead on the conservation of mass and salt with the flow into and out of a volume of ocean (Fig. 1.2), Wunsch (1978) constructed an inverse method (or called the box model) to determine the reference-level velocity. In the recent book, Wunsch (1996) described his method as follows. Consider a closed volume depicted in Fig. 1.2, the flow into and out of the volume should conserve the mass. Make the convention that velocities and transports are positive to the north and/or east and that the sign of the unit normal for a closed volume is positive inward.

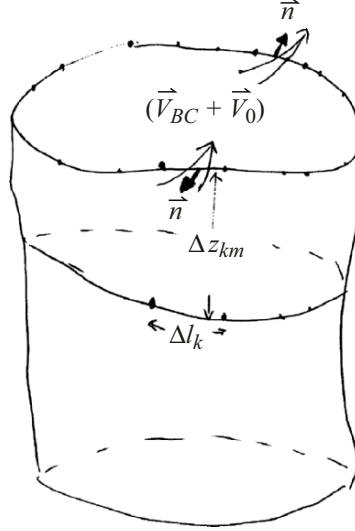


Fig. 1.2. Mass conservation for each layer of the volume

Choose a reference depth $z_0(s_j)$ where s is an arc length along the volume periphery and j denotes the station pair number, and compute the thermal wind relation to this reference-level for each station-pair. If the Ekman flow is assumed negligible, consider first the total amount of fluid moving geostrophically into and out of the closed volume shown in Fig. 1.2,

$$\sum_j^J \sum_k^K \rho_j(k) [v_{Rj}(k) + v_{0j}] \delta_j \Delta a_j(k) \simeq 0, \quad (1.10)$$

where $v_{Rj}(k)$ and $\Delta a_j(k)$ are the thermal wind (relative velocity) and the differential area for the station pair j at the depth interval k ; v_{0j} is the reference-level velocity, and δ_j is the unit normal (± 1) for the volume with the pair j . Equation (1.10) is a discrete approximation to the area integrals over the boundary section and can be carried out in a variety of different approximations. Everything is known in (1.10) except for the reference-level velocities. Equation (1.10) has been written as approximately equal to zero, rather than precisely so, in anticipation of the need to grapple with errors in the various terms of the sum.

Equation (1.10) is one equation with J unknowns, v_{0j} ($j = 1, 2, \dots, J$), and addition of some further constraints would be helpful. It is assumed that the volume of water in the ocean lying in fixed density intervals does not change significantly. Define the depth of fluid of density ρ_i as

$$z(\rho_i, x, y) = k_i(x, y).$$

Then mass conservation in the density interval $\rho_i < \rho < \rho_{i+1}$ is

$$\sum_j^J \sum_{k_i(j)}^{k_{i+1}(j)} \rho_j(k) [v_{Rj}(k) + v_{0j}] \delta_j \Delta a_j(k) \simeq 0. \quad (1.11)$$

Since $v_{Rj}(k)$ is assumed as known, (1.11) can be written as

$$\sum_j^J \sum_{k_i(j)}^{k_{i+1}(j)} \rho_j(k) v_{0j} \delta_j \Delta a_j(k) \simeq - \sum_j^J \sum_{k_i(j)}^{k_{i+1}(j)} \rho_j(k) v_{Rj}(k) \delta_j \Delta a_j(k). \quad (1.12)$$

Usually, the number of unknowns ($v_{01}, v_{02}, \dots, v_{0J}$) is larger than the number of the constraints in the box model (under-determined system). Obviously, if the velocity does not have vertical turning, $v_{Rj}(k) = 0$, the reference-level velocities cannot be obtained by the box model.

(c) β -Spiral method. On the basis of geostrophic balance (1.1), hydrostatic balance (1.2), conservation of mass (1.6), and conservation of potential vorticity (1.8), the β -spiral method was developed (Stommel and Scott 1977; Olbers et al. 1985) to determine the reference-level velocity locally. Solving the density conservation (1.7) for w leads to

$$\begin{aligned} \left(\frac{\partial \rho}{\partial z}\right)^2 \frac{\partial w}{\partial z} = & - \left(\frac{\partial \rho}{\partial z}\right) \left(\frac{\partial u}{\partial z} \frac{\partial \rho}{\partial x} + u \frac{\partial^2 \rho}{\partial x \partial z} + \frac{\partial v}{\partial z} \frac{\partial \rho}{\partial y} + v \frac{\partial^2 \rho}{\partial y \partial z}\right) \\ & + \left(u \frac{\partial \rho}{\partial x} + v \frac{\partial \rho}{\partial y}\right) \frac{\partial^2 \rho}{\partial z^2}. \end{aligned} \quad (1.13)$$

Substitution the equation of the geostrophic balance (1.1) into the mass conservation equation (1.6) leads to the linear vorticity balance,

$$\beta v = f \frac{\partial w}{\partial z}, \quad \beta = \frac{df}{dy}, \quad (1.14)$$

which eliminates w . The thermal wind relations (1.4)–(1.5) are used

$$u_R = \frac{g}{f \rho_0} \int_{z_0}^z \frac{\partial \rho}{\partial y} dz', \quad v_R = -\frac{g}{f \rho_0} \int_{z_0}^z \frac{\partial \rho}{\partial x} dz', \quad (1.15)$$

Substituting (1.4)–(1.5) in (1.13) and using (1.15) yields

$$\begin{aligned} (u_R + u_0) \left[\frac{\partial \rho}{\partial x} - \frac{\partial \rho}{\partial z} \frac{\partial^2 \rho}{\partial x \partial z} \right] \\ + (v_R + v_0) \left[\frac{\partial \rho}{\partial y} - \frac{\partial \rho}{\partial z} \frac{\partial^2 \rho}{\partial y \partial z} - \frac{\beta}{f} \left(\frac{\partial^2 \rho}{\partial z^2} \right)^2 \right] = 0, \end{aligned} \quad (1.16)$$

which is the algebraic equation for determining the reference-level velocity (u_0, v_0) . If the vertical axis is discretized into a series of depths z_i , then $i = 1, 2, \dots, I$. There are I equations in (1.16) and two unknowns u_0, v_0 . Usually I is much larger than two. Thus, the β -spiral method is an over-determined system.

(d) Equivalence between the β -spiral and box models. Davis (1978) pointed out that the β -spiral method (Stommel and Scott 1977) and the box method (Wunsch 1978), no matter how different in appearance, are based on the same order of dynamical sophistication and differ from implicit assumptions about the scales of oceanic variability and different definitions of the smooth field. The physical principle for both methods are the existence of a conservative tracer which allows determination of a family of material (usually the potential vorticity) surfaces $z = h(x, y)$ such as

$$\nabla_h \bullet \int_h^{h+\delta h} [\mathbf{V}_R + \mathbf{V}_0] dz = 0, \quad (1.17)$$

which comes from the box model. Taking the variation of (1.17) with respect to h , Davis (1978) obtained

$$\mathbf{V}_0 \bullet \nabla_h \frac{\partial h}{\partial z} - \frac{\beta}{f} v_0 = -\frac{\partial}{\partial z} (\mathbf{V}_R \bullet \nabla_h h) + \frac{\beta}{f} v_R, \quad (1.18)$$

which differs from the original β -spiral method (Stommel and Scott 1977) by the term, $-(\partial \mathbf{V}_R / \partial z) \bullet \nabla_h h$. Coats (1981) used (1.18) to calculate the absolute velocity in the northeastern Pacific Ocean.

1.3 Necessary Conditions for Inversion

After mathematical manipulation on (1.1), (1.2), (1.6), and (1.7) Needler (1982) obtained the following equation

$$\rho \mathbf{V}(x, y, z) = \frac{g \mathbf{k} \bullet (\nabla \rho \times \nabla q)}{\nabla(f \partial q / \partial z) \bullet (\nabla \rho \times \nabla q)} (\nabla \rho \times \nabla q), \quad (1.19)$$

to determine geostrophic velocity (\mathbf{V}) from density (ρ). Here, \mathbf{k} is the unit vector along the z -axis. As pointed by Needler (1982), direct use of (1.19) for calculating \mathbf{V} is almost impossible. The validity of the Needler's formula (1.19) requires

$$\nabla \rho \times \nabla q \neq 0, \quad (1.20a)$$

$$\nabla(f \partial q / \partial z) \neq 0, \quad (1.20b)$$

$$\nabla(f \partial q / \partial z) \bullet (\nabla \rho \times \nabla q) \neq 0. \quad (1.20c)$$

Vertical derivative of the left-hand side of (1.20a) gives,

$$f \frac{\partial}{\partial z} (\nabla \rho \times \nabla q) = \mathbf{k} \beta \frac{\partial(\rho, q)}{\partial(z, x)} + \nabla \rho \times \nabla \left(f \frac{\partial q}{\partial z} \right). \quad (1.21)$$

The condition of

$$\nabla(f \partial q / \partial z) = 0,$$

is equivalent to the disappearance of vertical turning of the horizontal component of the vector $\nabla \rho \times \nabla q$.

Three necessary conditions can be derived for determination of the absolute velocity \mathbf{V} from the density field ρ using the Needler's formula. Equation (1.20a) implies noncoincidence of the ρ -surface with the q surface (first necessary condition). Equation (1.20b) shows the existence of vertical turning of the horizontal component of the vector $\nabla \rho \times \nabla q$ (second necessary condition). Equation (1.20c) requires that the vector $\nabla \rho \times \nabla q$ should not exist on the iso-surface of $f \partial q / \partial z$ (third necessary condition). If the three necessary conditions are satisfied, the absolute velocity can be determined exclusively from the density field.

Questions and Exercises

- (1) Starting from the mass conservation,

$$\mathbf{V} \cdot \nabla \rho = 0, \quad (E1.1)$$

and using the geostrophic and hydrostatic balances, derive the conservation of potential vorticity,

$$\mathbf{V} \cdot \nabla q = 0, \quad q = f \frac{\partial \rho}{\partial z}, \quad (E1.2)$$

Discuss the physical significance of the potential vorticity conservation.

- (2) Derive the Needler's formula from (1.1), (1.2), (1.6), and (1.7),

$$\rho \mathbf{V}(x, y, z) = \frac{g \mathbf{k} \cdot (\nabla \rho \times \nabla q)}{\nabla(f \partial q / \partial z) \cdot (\nabla \rho \times \nabla q)} (\nabla \rho \times \nabla q), \quad (E1.3)$$

and list all the vectors in the Needler's formula, and find the relationships among these vectors.

- (3) Does the level-of-no-motion exist? Why?
 (4) Derive the formula for the β -spiral method,

$$\mathbf{V}_0 \cdot \nabla_2 \frac{\partial h}{\partial z} - \frac{\beta}{f} v_0 = -\frac{\partial}{\partial z} (\mathbf{V}_R \cdot \nabla_2 h) + \frac{\beta}{f} v_R, \quad (E1.4)$$

from mass conservation of the box model (1.17). Discuss the difference between the β -spiral and box methods.

- (5) What conditions can be drawn from the Needler's formula (E1.3)?
- (6) Since the Needler's formula (E1.3) directly relates the absolute velocity to the density field, can it be used to compute the absolute velocity from density? If not, explain why?

Analysis of Observational (T, S) Profiles

The P-vector method is to invert absolute velocity from hydrographic data and usually requires regularly distributed (T, S) . However, the (T, S) fields are sampled irregularly in space and time. As a first step, the observational (T, S) profiles should be analyzed. This chapter describes basic features of the observational (T, S) -profiles, two-type profile representations, thermal and haline parametric models, and decorrelation scales. There are many hydrographic data sets, however, only those data sets used in this book are described.

2.1 Historical (T, S) Profiles

The MOODS is a compilation of ocean data observed worldwide consisting of (a) temperature-only profiles, (b) both temperature and salinity profiles, (c) sound-speed profiles, and (d) surface temperatures (drifting buoy). It contains the NODC temperature and salinity profiles. The measurements in the MOODS are, in general, irregular in time and space. Due to the sheer size and constant influx of data to the Naval Oceanographic Office from various sources, quality control is very important. The primary editing procedure included removal of profiles with obviously erroneous location, profiles with large spikes (temperature higher than 35°C and lower than -2°C), and profiles displaying features that do not match the characteristics of surrounding profiles, such as profiles showing increase of temperature with depth. The MOODS contains more than six million profiles worldwide.

For example, after quality control the historical MOODS data contains 144,135 temperature and 13,768 salinity profiles for the South China Sea (5°S – 25°N , 105°E – 120°E) during 1930–1997 (Chu et al. 1997c). The main limitation of the MOODS data is its irregular distribution in time and space. Certain periods and areas are over sampled while others lack enough observations to gain any meaningful insights. Vertical resolution and data quality are also highly variable depending much on instrument type and sampling expertise. The monthly distributions of the total temperature (Fig. 2.1)

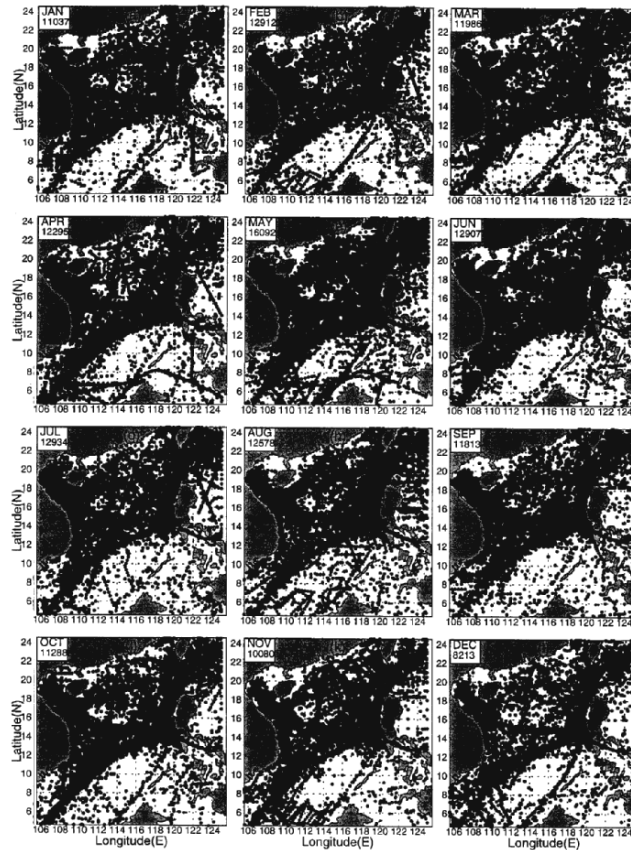


Fig. 2.1. Spatial distribution of the MOODS temperature stations during 1930–1997 (Chu and Li 2000, *Journal of Physical Oceanography*)

and salinity (Fig. 2.2) stations in the South China Sea show that the number of temperature stations is ten times more than the number of salinity stations.

Yearly temperature (Fig. 2.3a) and salinity (Fig. 2.3b) profile numbers show temporally uneven distribution with almost no observations in the whole South China Sea, in certain years (e.g., 1944 for temperature, and 1944–1946, 1952–1954, 1993–1995 for salinity) and many observations in other years (e.g., more than 12,000 temperature profiles in 1966 and 1968, and more than 1,100 salinity profiles in 1981). Spatial and temporal irregularities along with the lack of data in certain regions must be carefully weighted in order to avoid statistically induced variability.

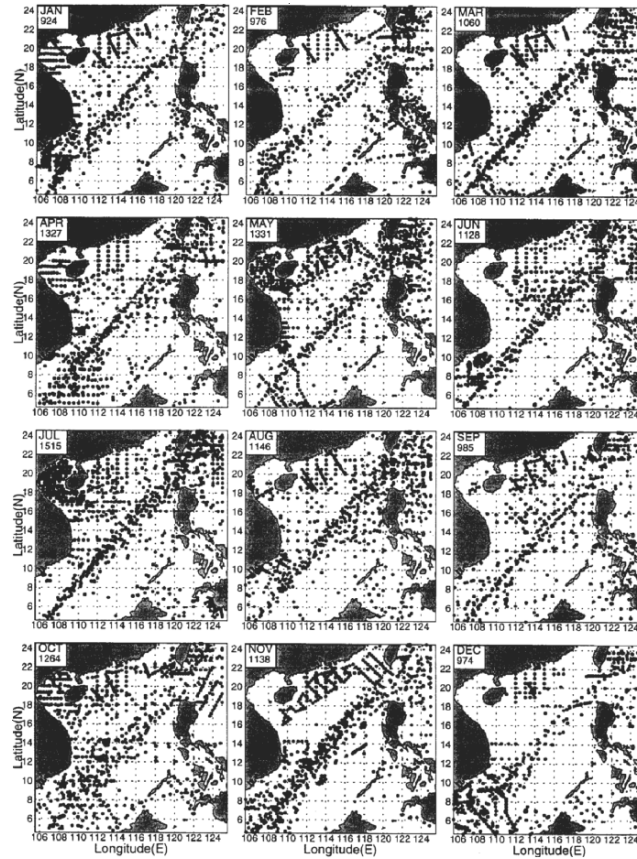


Fig. 2.2. Spatial distribution of MOODS salinity stations during 1930–1997 (Chu and Li 2000, *Journal of Physical Oceanography*)

2.2 Synoptic (T, S) Profiles

Expendable bathythermograph (XBT) and conductivity-temperature-depth (CTD) are commonly used for hydrographic observations. Airborne XBT (AXBT) and CTD (AXCTD) surveys can cover greater geographic extents over shorter periods of time than ship surveys. The AXBT/AXCTD data sets, by virtue of their large spatial extents and the relatively short times required to complete them, essentially provide snapshots of thermal structure (AXBT) and thermohaline structure (AXCTD) over a large portion of water. The AXBT surveys are more frequent than the AXCTD survey.

For example, the Naval Oceanographic Office conducted an intensive AXBT survey between May 14 and May 25, 1995, over the majority of the South China Sea down to about 300 m depth. Figure 2.4 shows the daily AXBT deployment. This data set provides something close to a snapshot of the

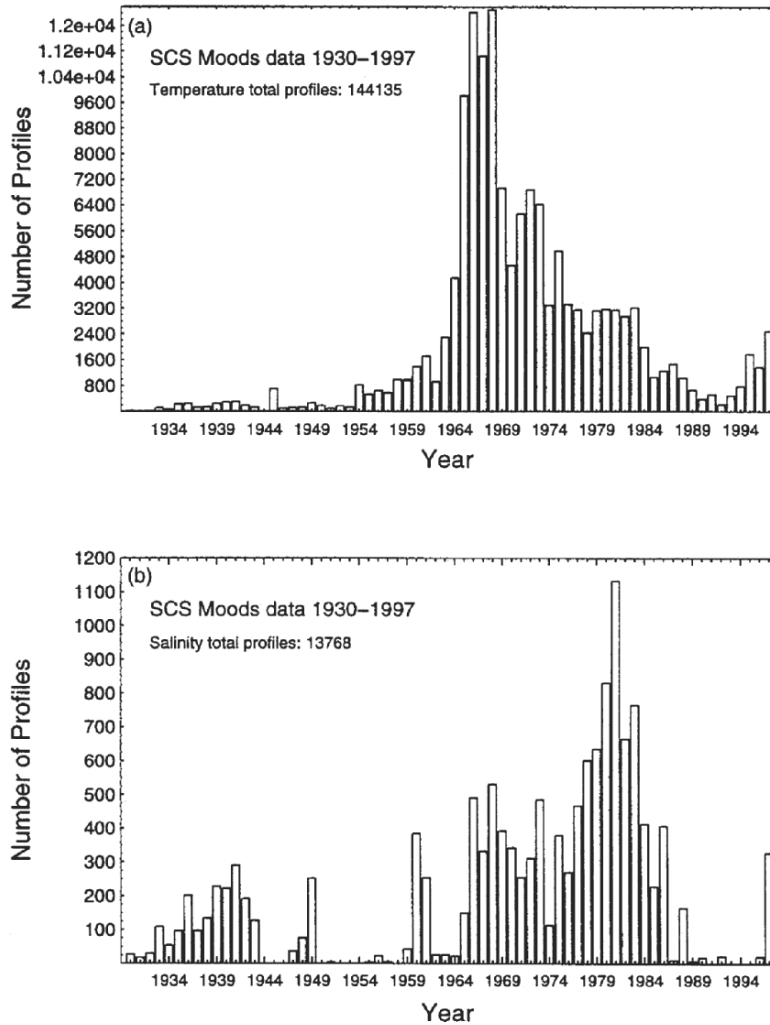


Fig. 2.3. Temporal distribution of the MOODS stations during 1930–1997: (a) temperature, and (b) salinity (Chu and Li 2000, *Journal of Physical Oceanography*)

temperature in the upper ocean in the South China Sea during the transition time before the onset of the monsoon. Most of the 376 AXBTs were deployed at six intervals over a 12-day period from May 14 to May 25, 1995. The majority of the AXBTs were nominally capable of reaching a depth of 360–400 m. The ensemble of temperature profiles (Fig. 2.5a) and the mean profile with an envelope of a standard deviation (Fig. 2.5b) show the existence of a mixed layer with depths ranging from 20 to 60 m and a thermocline with a vertical temperature gradient of 6° – 7° C per 100 m below the mixed layer.

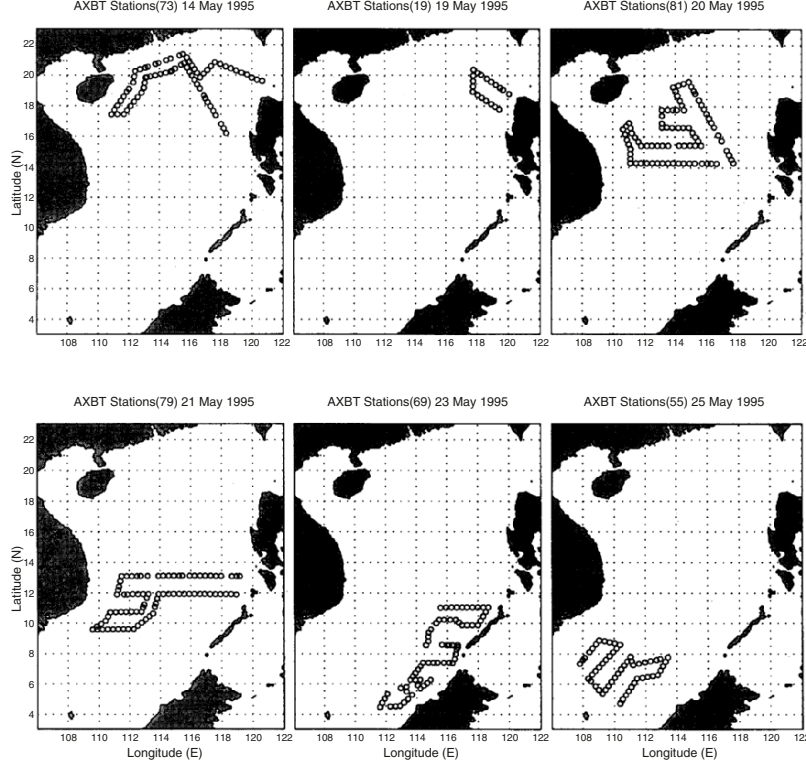


Fig. 2.4. Deployment of the AXBT survey in the South China Sea during 14–25 May 1995 (Chu et al. 1998d, Journal of Geophysical Research)

2.3 Representation of (T, S) Profiles

Usually, the (T, S) profiles for time t are represented by

$$T_{\text{obs}} = T_k(z, t), S_{\text{obs}} = S_k(z, t), \quad (2.1)$$

where the subscript k denotes the horizontal location. Two types are available in profile data analysis. First, the analysis is conducted at the same depth. This is the z -level analysis. Second, the profile data (2.1) can be represented by a set of parameters on the base of the physical characteristics (Chu et al. 1997a,b, 1999a). The analysis is conducted for each parameter. The parameter analysis is conducted as per the process given herewith.

The parameter analysis starts from analytical curve fitting of temperature and salinity profiles. Determination of thermohaline structure (mixed layer, entrainment zone, thermocline, and halocline) from observed temperature and salinity profiles is important for the world oceans for several reasons. First, the heat balance depends on the features of mixed layer, entrainment zone, and thermocline. Mixed layer deepens by entrainment of water from the ocean

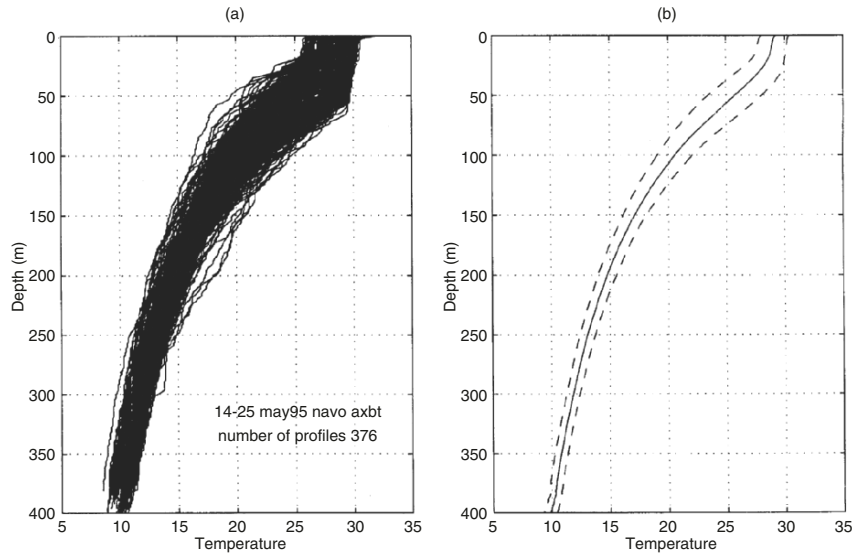


Fig. 2.5. Temperature profiles of the AXBT survey in the South China Sea during 14–25 May 1995 (after Chu et al. 1998d, Journal of Geophysical Research)

below (Chu 1988; Chu et al. 1990; Chu and Garwood 1990, 1991). The mass in the deep water is then transported to surface. Second, for polar oceans the mixed layer acts as a buffer by storing solar heat input during the summer and releasing it back to the ice throughout the fall and early winter (Maykut and McPhee 1995). Non-polar and polar parametric models are available for the analysis. For illustration, the Yellow Sea is taken as an example as the non-polar model, and the Beaufort/Chukchi Seas are taken as examples as the polar model.

2.4 Non-Polar Parametric Model

The Yellow Sea is a semi-enclosed basin covering roughly $295,000 \text{ km}^2$ and is one of the most developed continental shelf areas in the world seas. While the Yellow Sea covers a relatively large area, it is quite shallow reaching a maximum depth of about 140 m (Fig. 2.6). The Yellow Sea temperature profiles are taken as an example as the single-structure pattern for illustration (Chu et al. 1997a,b, 2006c,e).

2.4.1 Seasonal Variability

The water depth over most of the area in the Yellow Sea is less than 50 m. The deepest water is confined to a north–south oriented trench which runs

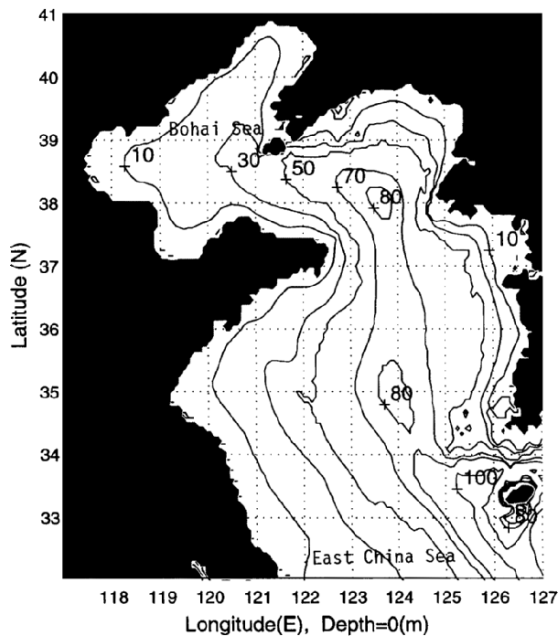


Fig. 2.6. Yellow Sea bathymetry (from Chu et al. 1997b, *Journal of Geophysical Research*)

from the northern boundary south to the 100 m isobaths, where it fans out onto the continental break. The gradients in slope across the bottom are very small. Such a broad and shallow continental shelf leads to the fact that the water is readily affected by seasonally varying atmospheric conditions such as heating, cooling, and wind stress. Therefore, the seasonal variation of the water masses is remarkably large (Chen et al. 1994). Another feature of the depth distribution is the east/west asymmetry. Extensive shoals (<20 m) are located in the western Yellow Sea along the Chinese coast and are not generally found in the South Korea coastal regions. Also, the 50 m isobaths is located more than 100 km from the Chinese coast, but only about 50 km from the South Korean coast. This asymmetry in bottom depth is important for the shoaling mixed layer depth. Furthermore, the hydrographic character of water masses in the Yellow Sea also depends on the degree of mixing of fresh water originating from the China Continent river run-off with the intrusion of East China Sea and Kuroshio waters (Park and Chu 2006b).

The Asian monsoon strongly affects the Yellow Sea thermal structure. During the winter monsoon season, a very cold northwest wind blows over the Yellow Sea as a result of the Siberian High Pressure System. The Jet Stream is positioned to the south of the Yellow Sea and the Polar Front to the north of Philippines. The mean surface wind speed over the Yellow Sea in January is nearly 6 m s^{-1} . The sea surface temperature (SST) is 6°C at

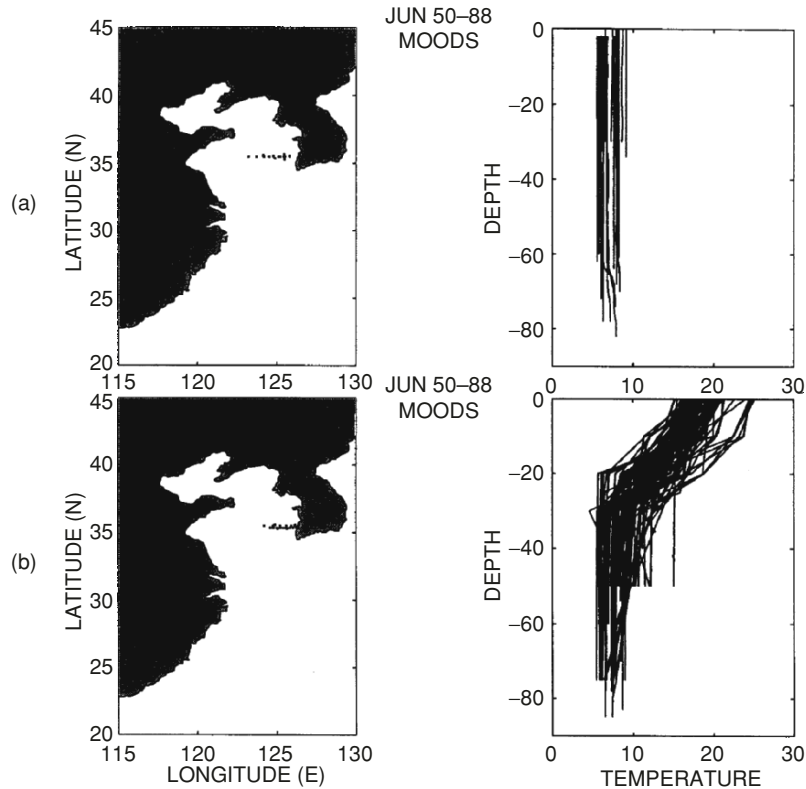


Fig. 2.7. Eastern Yellow Sea (around 36°N) temperature profiles during 1950–1988: (a) January and (b) June. *Solid dots* show the observational stations (from Chu et al. 1997b, *Journal of Geophysical Research*)

the northern extent and 10°C at the southeastern extent. The horizontal SST gradient largely impacts on the atmospheric circulation (Chu 1989).

January surface air temperature varies from 0 to 8°C in the Yellow Sea, roughly 2 to 6°C cooler than SST. The Yellow Sea surface loses heat to the atmosphere. The upward buoyancy flux at the air–ocean interface (thermal forcing), together with the strong wind stress (mechanical forcing), generates turbulence and mixes the surface water with the deeper water. Taking the eastern part of the Yellow Sea around 36°N as an example, the January historical (1950–1988) temperature profiles (Fig. 2.7a) show a single-layer structure (i.e., vertically uniform temperature from surface to the bottom). The different lengths of these profiles in the vertical temperatures are caused by the different water depths where the observations were taken (see Fig. 2.6). This single-layer structure means a very deep mixed-layer extending from the surface to the bottom.

In summer, the wind stress is much weaker than in winter. The monthly mean surface air temperature is quite uniform, around 24–26°C, and is usually 1.5–2°C warmer than the mean SST (Van Loon 1984). The warmer air causes a downward heat flux at the air–ocean interface. This heat flux along with the strong downward net radiation stabilizes the upper layer of the water and causes the surface mixed layer to shoal, creating a multi-layer structure (Fig. 2.7b). Below the thermocline, there is a cold water mass, commonly referred to as Yellow Sea Bottom Cold Water, that remains unchanged and nearly motionless throughout the summer (Li and Zeng 1992).

2.4.2 Model Description

During the summer monsoon season, most profiles in the Yellow Sea exhibit a mixed-layer (for temperature), a thermocline, and a deep layer (Fig. 2.7b), which can be outlined by a “typical” profile. To make the model more general, we assume two deep layers below the thermocline (Fig. 2.8). When the two deep layers have the same vertical gradients, they become one deep layer. If two transition layers are added, the entrainment zone between mixed layer and thermocline and the transition zone between the thermocline and the deep layer, the Yellow Sea thermal structure during summer can be well resolved. We use a parametric model with six layers (Chu 1995b; Chu et al. 1997b) to diagnose shallow-water multi-layer structure from observed Yellow Sea temperature profiles.

Each observed profile is modeled by a set of parameters, most of which have physical meaning, including SST, isothermal layer depth, depth of the base of the thermocline, gradient in the thermocline and deep layers, and additional parameters describing curvature between the mixed-layer and thermocline and curvature below the thermocline. Among them SST is taken as the observed values. The model parameters for each observed profile are computed in gradient space; more specifically, the depths and gradients of the modeled features are fit to the vertical gradient of the observed profile. The parametric model depicts the multi-layer structure. Determination of layer number is based on overall features of the profiles (Fig. 2.7b). The thermal parametric model consists of seven depths (i.e., six layers) and six gradients as shown in Fig. 2.8b. The first and the last depths are assumed to be at the surface and bottom, respectively, and the gradients within the isothermal layer and thermocline are constrained to be constant. The gradients for the four other layers are assumed to vary with depth linearly. The mean gradient is taken as the representative value for these layers. The model parameters are calculated in the gradient space, which will bring larger numerical errors due to the differentiation. We will use the optimization to filter out the noise.

If we consider profiles in the gradient space, i.e., $G_T = \partial T / \partial z$, each profile can be represented by the surface value (SST) along with the gradients,

$$[\text{SST}, G_T(0, z_1), G_T(z_1, z_2), \dots, G_T(z_{n-1}, z_n)],$$

$$\begin{aligned} \hat{T}^{(d1)}(z) &= \hat{T}^{(\text{tr})}(-d_4) + (z + d_4)\bar{G}_T^{(d1)} \\ &+ \frac{(z+d_4)(z+d_5)}{(d_5-d_4)}[G_T^{(\text{tr})}(-d_4) - \bar{G}_T^{(d1)}], \quad z \in [-d_5, -d_4], \end{aligned} \quad (2.2e)$$

$$\begin{aligned} \hat{T}^{(d2)}(z) &= \hat{T}^{(d1)}(-d_5) + (z + d_5)\bar{G}_T^{(d2)} \\ &+ \frac{(z+d_5)(z+H)}{(H-d_5)}[G_T^{(d1)}(-d_5) - \bar{G}_T^{(d2)}], \quad z \in [-H, -d_5], \end{aligned} \quad (2.2f)$$

where $\hat{T}^{(\text{m})}$, $\hat{T}^{(\text{en})}$, $\hat{T}^{(\text{th})}$, $\hat{T}^{(\text{tr})}$, $\hat{T}^{(d1)}$, and $\hat{T}^{(d2)}$ are modeled temperatures in the mixed-layer (or called isothermal layer), entrainment zone, thermocline, transition zone, and first and second deep layers. H is the water depth, d_1 the mixed layer depth for temperature (MLD_T), d_2 the depth of the top of thermocline, d_3 the depth of the bottom of thermocline, d_4 the depth of the top of the first deep layer, and d_5 the bottom of the first deep layer (Fig. 2.8). Here, we assume constant vertical temperature gradients in the ocean mixed-layer (very small, $G_T^{(\text{m})} \simeq 0$) and in the thermocline (very large $G_T^{(\text{th})}$), and linearly varying with z in the entrainment zone, the transition zone, and the two deep layers with average values $\bar{G}_T^{(\text{en})}$, $\bar{G}_T^{(\text{tr})}$, $\bar{G}_T^{(d1)}$, and $\bar{G}_T^{(d2)}$. Here, the mean gradient in the entrainment zone is the average of the isothermal layer and thermocline gradients,

$$\bar{G}^{(\text{en})} = \frac{1}{2}(G_T^{(\text{m})} + G_T^{(\text{th})}).$$

By forcing this parametric model (2.2) to each observed profile, we should have a first-guess of the five depths (d_1, d_2, d_3, d_4, d_5) and a high resolution of temperature/depth points in the vertical gradient in order to obtain the five temperature gradients ($G_T^{(\text{m})}, G_T^{(\text{th})}, \bar{G}_T^{(\text{tr})}, \bar{G}_T^{(d1)}, \bar{G}_T^{(d2)}$). Such a treatment provides the most important features from the observational data.

Each temperature profile is linearly interpolated to $\Delta z = 0.5 \text{ m}$, $T_j = T(z_j)$, where $z_j = z_{j-1} - 0.5 \text{ m}$ ($z_0 = 0$). If the five depths (d_1, d_2, d_3, d_4, d_5) are known, the high resolution profile data set (z_j, T_j) can be divided into six parts (isothermal layer, entrainment zone, thermocline, transition zone, first deep layer, and second deep layer). For each layer the data (z_j, T_j) are fitted to the parametric model (2.2), and a set of temperature gradients ($G_T^{(\text{m})}, G_T^{(\text{th})}, \bar{G}_T^{(\text{tr})}, \bar{G}_T^{(d1)}, \bar{G}_T^{(d2)}$) are obtained.

2.4.3 Iteration Method

A modeled profile with 0.5-m resolution can be established by using the parametric model (2.2) if the five depths (d_1, d_2, d_3, d_4, d_5) are given. In reality, these depths are not known prior to processing the data and vary from one profile to the other. The iteration method is used to obtain the optimal modeled profile.

First, start with a set of first-guess values of the depths and the five gradients (two constants and three mean values),

$$D^{(0)} = [d_1^{(0)}, d_2^{(0)}, d_3^{(0)}, d_4^{(0)}, d_5^{(0)}], \quad (2.3)$$

$$G_T^{(0)} = [G_T^{(m0)}, G_T^{(th0)}, \bar{G}_T^{(tr0)}, \bar{G}_T^{(d10)}, \bar{G}_T^{(d20)}].$$

For example, Chu et al. (1997b) chose,

$$D^{(0)} = [20 \text{ m}, 24 \text{ m}, 32 \text{ m}, 38 \text{ m}, H],$$

$$G_T^{(0)} = [0, 0.5^\circ \text{C m}^{-1}, 0.05^\circ \text{C m}^{-1}, 0, 0],$$

for the Yellow Sea thermal structure. Let $(z_j, \hat{T}_j^{(k)})$ be the k th iterated model profiles. For each high resolution profile, the 0th iterated model profile is easily obtained from the first guess depths and gradients (2.3). The root-mean-square error (rmse) for mismatch of T_j and $\hat{T}_j^{(k)}$ is computed by

$$\text{rmse}^{(k)} = \sqrt{\frac{1}{n} \sum_{j=1}^n (\hat{T}_j^{(k)} - T_j)^2}. \quad (2.4)$$

It is expected that $\text{rmse}^{(0)}$ to be large.

Second, use the iteration method to obtain optimal modeled profile for each observed high resolution profile. Each depth can only be adjusted one vertical grid (Δz or $-\Delta z$) for iteration. From the k th iteration (k starting from 0, the first-guess) set of depths, $D^{(k)}$, we have 242 ($=3^5 - 1$) different combinations of the depth adjustment,

$$D_m^{(k+1)} = D_m^{(k)} + \delta D_m^{(k)}, \quad (2.5)$$

where

$$\delta D_1^{(k)} = (\Delta z, 0, 0, 0, 0),$$

$$\delta D_2^{(k)} = (-\Delta z, 0, 0, 0, 0),$$

$$\dots\dots\dots$$

$$\delta D_{242}^{(k)} = (0, 0, 0, 0, -\Delta z).$$

Equations (2.2a)–(2.2f) are used to obtain 242 modeled profiles, among which we pick a profile with minimum rmse as the $(k + 1)$ th iterated set of depths, $D^{(k+1)}$. This procedure is repeated until the minimum rmse is achieved. We have two check points to terminate the iteration: the maximum number of iterations k_{max} , and the rms error criterion R_c . At each iteration ($k < k_{\text{max}}$), $\text{rmse}^{(k)}$ is compared to a user specified criterion R_c . If $\text{rmse}^{(k)} < R_c$, we terminate the iteration and obtain an optimal set of depths. If $\text{rmse}^{(k)} > R_c$, we continue the iteration until $k = k_{\text{max}}$. If the rmse at the

k_{max} iteration is still greater than R_c , we should reject the parametric model (2.2), i.e., the observed profile cannot be fitted by the parametric model. The rejected profiles are discarded.

Chu et al. (1997b) chose $k_{max} = 400$, and $R_c = 0.4^\circ\text{C}$. This rms criterion (0.4°C) was chosen due to the accuracy of the temperature/depth ($\pm 0.2^\circ\text{C}$, $\pm 2\text{ m}$) measured by the bathythermograph. This criterion can be greatly reduced if the data are obtained by more accurate instruments (e.g., thermometer). The six temperature gradients are updated each iteration. A set of their six optimal gradients is obtained when the rms error of the temperature profile is less than the criterion.

2.5 Polar Parametric Model

2.5.1 Seasonal Variability

The Chukchi Sea is a shallow sea with a mean depth of 40–50 m, having gentle knolls and several troughs which are shallow but with a relief which has a substantial fraction of the mean depth. The Beaufort Sea is a semi-enclosed basin with quite a narrow continental shelf (30–80 km) and a deep submarine canyon, the Mackenzie Canyon. The deepest water is confined to the bowl-shaped Mackenzie Canyon which is enclosed by the 3,000 m isobaths. The gradients in slope across the bottom are very large. The 150 m isobaths approximately characterizes the Beaufort Sea shelf break (Fig. 2.9). The shallow continental shelf waters are affected by seasonally varying atmospheric conditions such as heating, cooling, wind stress, and the formation and melting of ice. The seasonal variation of the water masses is remarkably large. Thus, we have two different types of profiles: (a) shelf profiles (water depth $\leq 150\text{ m}$) and (b) deep water profiles (water depth $> 150\text{ m}$).

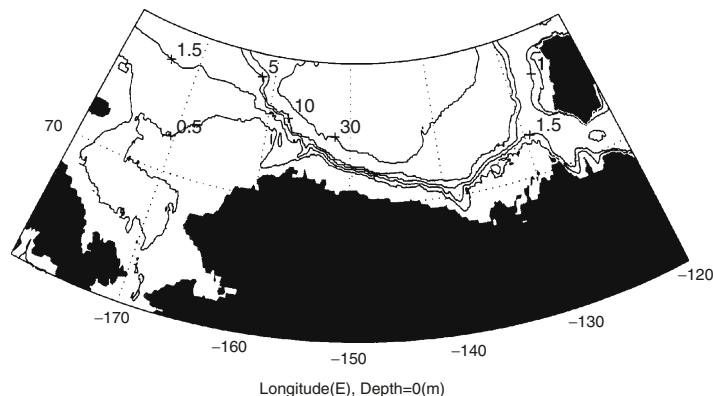


Fig. 2.9. The Beaufort/Chukchi Sea bathymetry. Numbers show the depth in 100 m (from Chu et al. 1999a, *Journal of Atmospheric and Oceanic Technology*)

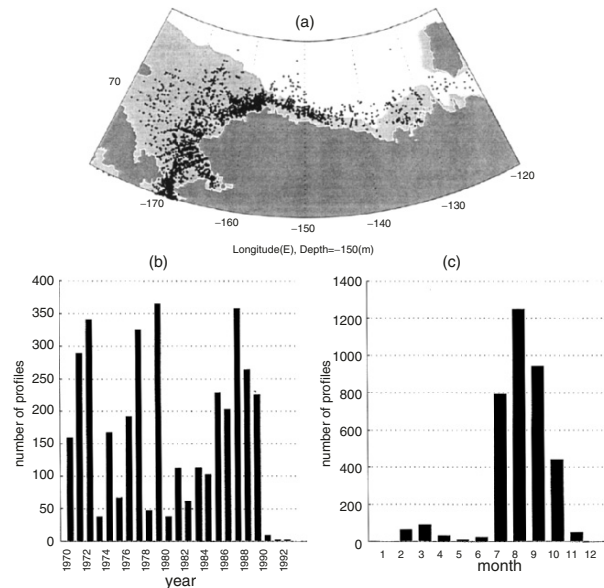


Fig. 2.10. The MOODS data for the Beaufort/Chukchi Sea: (a) station distribution, (b) interannual variation (1970–1993) of number of profiles, and (c) seasonal variation of number of profiles (from Chu et al. 1999a, *Journal of Atmospheric and Oceanic Technology*)

Among the historical (1970–1993) temperature and salinity profiles (3,562) obtained from the Naval Oceanographic Office, 3,384 profiles are shelf profiles, and 178 profiles are deep water profiles. For the area $120\text{--}180^\circ\text{W}$, $65\text{--}75^\circ\text{N}$, the MOODS (CTD and STD) has 3,562 (T, S) profiles during 1970–1993 after rejecting certain data during quality control. These primary editing procedures included removal of profiles with obviously erroneous location, profiles with large spikes, poor vertical resolution, and profiles displaying features that do not match the characteristics of surrounding profiles.

There is a data sparse area north of 73°N (Fig. 2.10a). The periods of 1971–1972, 1977, 1979, and 1985–1989 are found to have a relatively large number of profiles averaging around 200 profiles per year (Fig. 2.10b). Most profiles were observed during the summer season (Fig. 2.10c). August has the most observations (1,253) while no observations have been recorded in the data set in December and January.

The surface radiative flux strongly affects the Beaufort/Chukchi Sea shelf thermohaline structure. During the winter (November–April), long periods of darkness together with low solar elevation give rise to a prolonged period of radiative loss from the surface. The radiative cooling at the surface destabilizes the upper layer through strong upward heat flux and salt rejection by ice freezing, and causes the formation of deep mixed layer, which on the shallow

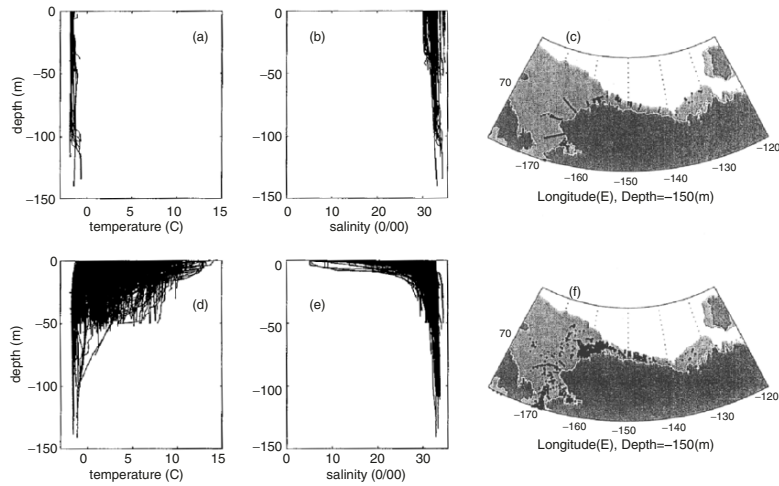


Fig. 2.11. Seasonal variation of T, S profiles over the Beaufort/Chukchi Sea shelf water: (a) winter (November–April) T profiles, (b) winter S profiles, (c) distribution of winter stations, (d) summer (August) T profiles, (e) summer S profiles, and (f) distribution of summer stations. The shaded areas indicate shelf region (water depth ≤ 150 m) (from Chu et al. 1999a, *Journal of Atmospheric and Oceanic Technology*)

shelves might reach the bottom resulting in an isothermal/isohaline structure (Figs. 2.11a,b).

Different lengths of these profiles in the vertical gradients are caused by the different water depths where the observations were taken (Fig. 2.9). During the summer (August), long daylight hours together with relatively high solar elevation give rise to a period of radiative deposition to the surface. The radiative warming at the surface stabilizes the upper layer through downward heat flux and fresh water influx by ice melting, causing the mixed layer to shoal and forming a multi-layered structure (i.e., a mixed-layer, upper and lower thermoclines and haloclines, and a deep layer), as shown in Figs. 2.11d,e. The number and spatial distribution of observations are much greater in summer than in winter (Figs. 2.11c,f).

In the deep water off the shelf the near surface waters of the Beaufort Sea also experience seasonal variations. During the winter (November–April), surface cooling causes the formation of a deep thermal mixed layer (Fig. 2.12a). However, the surface salt flux caused by local ice freezing generates a relatively shallow salinity mixed layer (Fig. 2.12b). Below both the thermal and salinity mixed layers there exists a lower thermocline and halocline, appearing at 160–300 m depth (Figs. 2.12a,b). During summer (August), surface warming and associated ice melting increase the SST (a maximum value near 8°C), decrease the sea surface salinity (a minimum value near 20 ppt), and cause both the thermal and salinity mixed layers to shoal (Figs. 2.12d,e). We also notice that both winter and summer stations (Fig. 2.12c,f) do not extend far from the

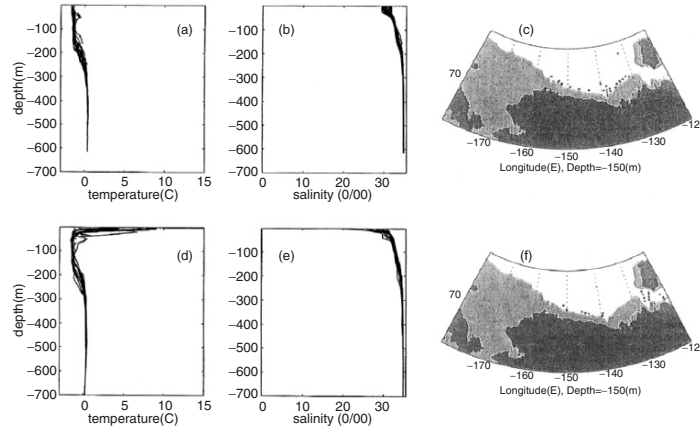


Fig. 2.12. Seasonal variation of T, S profiles over the Beaufort/Chukchi Sea deep water: (a) winter (November–April) T profiles, (b) winter S profiles, (c) distribution of winter stations, (d) summer (August) T profiles, (e) summer S profiles, and (f) distribution of summer stations. The shaded areas indicate shelf region (water depth ≤ 150 m) (from Chu et al. 1999a, *Journal of Atmospheric and Oceanic Technology*)

shelf break, and the intermediate waters (below 150 m depth) do not exhibit a seasonal variation.

2.5.2 Multiple Thermohaline Structures

The historical Beaufort/Chukchi Sea temperature and salinity profiles (Figs. 2.11 and 2.12) demonstrate the existence of several basic profile shapes which are deep mixing, shallow mixing, and advection.

(a) Deep mixing type (T, S) profiles. This type of T, S profiles is characterized by a single well-mixed layer in the shelf region (Fig. 2.13a) and a deep surface isothermal layer (Fig. 2.14a) and a thermocline in the deep water region. This type of T, S profiles are caused by surface destabilization, such as strong wind forcing, surface cooling, and brine rejection due to ice freezing. They are most prevalent during winter.

(b) Shallow mixing type (T, S) profiles. This type of T, S profiles is characterized by a multi-layered structure: shallow isothermal layer, isohaline layer (or called mixed layer for salinity), entrainment zone, thermoclines and haloclines, and a sub-layer in both the shelf region (Figs. 2.13b,d) and the deep water region (Figs. 2.14b,d). This profile type is generally present during the summer and is caused by surface stabilization, such as weak wind forcing, surface warming, and fresh water influx due to ice melting and river run-off, and therefore usually has a warm SST and a low sea surface salinity.

Beneath the mixed layer the thermocline/halocline profile is complex reflecting the seasonal adjustment. Thus, shallow mixing profiles feature a monotonic decrease of temperature with depth in the upper thermocline and a

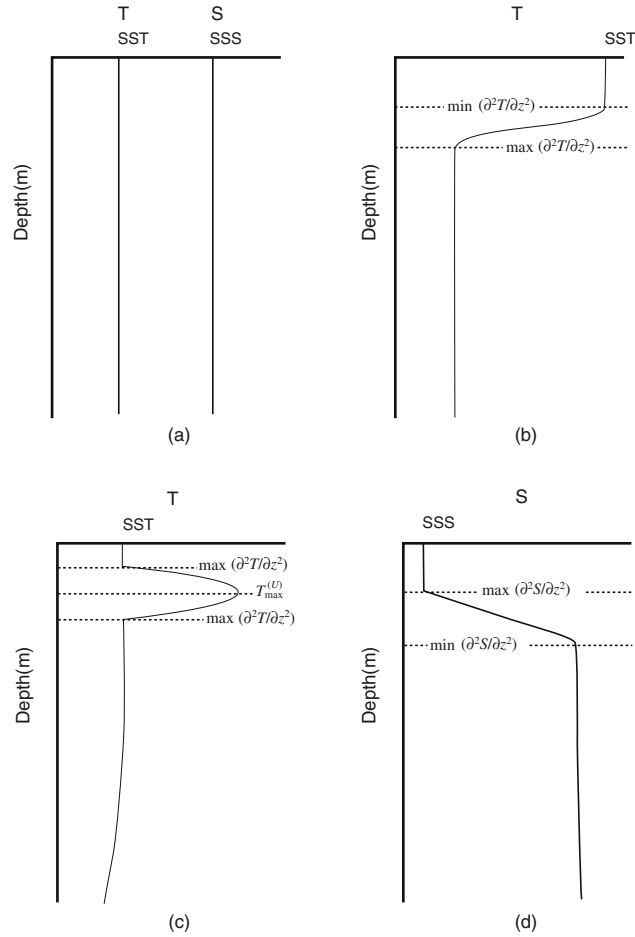


Fig. 2.13. Typical T, S profiles for the shelf water: (a) deep-mixing type, (b) shallow-mixing type T , (c) advection type T , and (d) shallow-mixing type S (from Chu et al. 1999a, Journal of Atmospheric and Oceanic Technology)

monotonic increase of salinity with depth in the upper halocline (Figs. 2.13b,d and 2.14b,d).

(c) Advection type T -profiles. Advection type T profiles also have a multi-layer structure (shallow isothermal and isohaline layers, entrainment zone, upper and lower thermoclines, and a sub-layer) in both the shelf region (Fig. 2.13c) and the deep water region (Fig. 2.14c).

This type of profiles, identified by a nose-shape curve in the upper thermocline (monotonic increasing T with depth to a maximum value T_{\max} and then monotonic decreasing with depth), is generated by a prominent hydrographic feature on the Beaufort Sea shelf: a sub-surface temperature maximum,

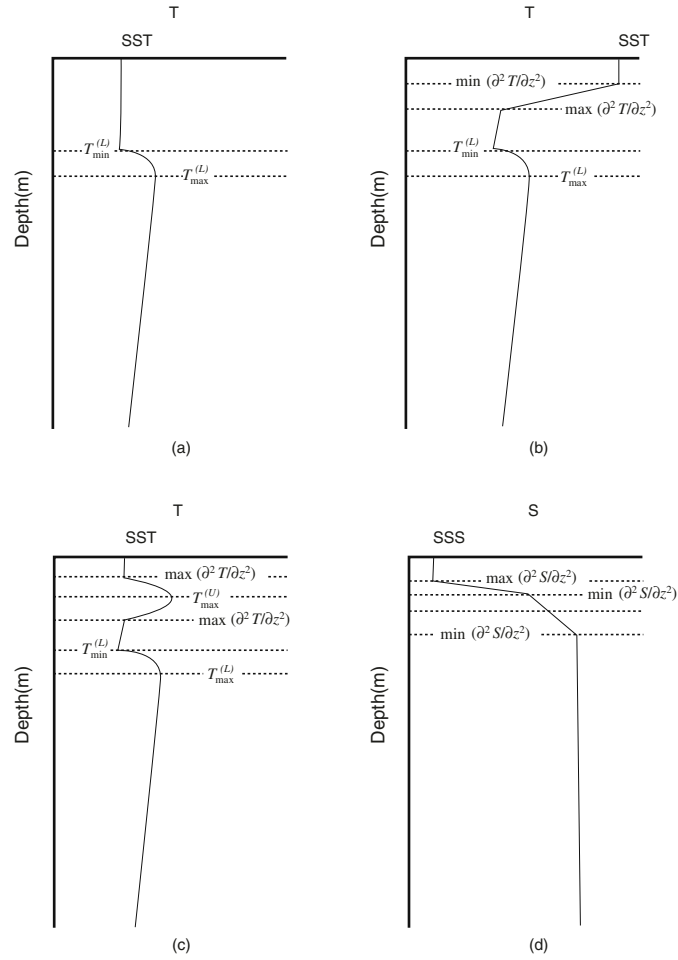


Fig. 2.14. Typical T, S profiles for the deep water: (a) deep-mixing type T, S , (b) shallow-mixing type T , (c) advection-type T , and (d) shallow-mixing type S (from Chu et al. 1999a, *Journal of Atmospheric and Oceanic Technology*)

generally found at about 20–30 m depth in the deep water and at about 10 m depth in the shelf water. This temperature maximum is associated with the eastward flowing Bering Sea water (Coachman and Barnes 1961; Aagaard 1989). The warm water that enters the Beaufort Sea comes through the eastern Bering Strait and follows the Alaskan coast around Point Barrow. Mountain et al. (1976) identified this warm intrusion as the combination of the two water masses: warm (5–10°C) and fresh (salinity below 31.5 ppt) Alaskan Coastal Water, and more saline Bering Sea Water. The two water masses mix rapidly with the ambient surface water as they move eastward. Aagaard (1989) estimated that the Alaskan Coastal Water is not clearly identifiable east of

147–148°W, and the Bering Sea Water east of 143°W. Thus, the longitude of 141°W is chosen as the separation for the western and eastern parts of the Beaufort Sea Shelf Water.

2.5.3 Characteristics from Profiles

(a) Heterogeneous mesh difference scheme. Second derivatives $\partial^2 F(z_j)/\partial z^2$ (F is T or S) are used to describe the features of profiles and to identify various types of T , S profiles in the polar region. For each profile (temperature or salinity), $F(z_j)$, $j = 1, 2, \dots, N$, the following heterogeneous mesh difference scheme is used for the second-order derivatives,

$$\frac{\partial^2 F}{\partial z^2} \Big|_{z_j} \simeq \frac{1}{z_{j+1} - z_{j-1}} \left(\frac{F_{j+1} - F_j}{z_{j+1} - z_j} - \frac{F_j - F_{j-1}}{z_j - z_{j-1}} \right), \quad (2.6)$$

where $j = 1$ refers to the surface, with increasing values indicating downward extension of the measurement. Equation (2.6) shows that two neighboring values, F_{j-1} and F_{j+1} , are needed to compute the second-order derivative at z_j . For $j = 1, N$, the next point value is used, i.e.,

$$\frac{\partial^2 F}{\partial z^2} \Big|_{z_1} = \frac{\partial^2 F}{\partial z^2} \Big|_{z_2}, \quad \frac{\partial^2 F}{\partial z^2} \Big|_{z_N} = \frac{\partial^2 F}{\partial z^2} \Big|_{z_{N-1}}. \quad (2.7)$$

After the second-order difference is computed, we can use the following model to determine the top and bottom of the upper thermocline and halocline.

(b) Features of the shelf water profiles. Three types of profiles (deep-mixing, shallow-mixing, and advection) are found in the shelf water. The deep-mixing T , S profiles reveal a single layer structure (Fig. 2.13a), i.e., the surface mixed layer extends to the bottom of the shelf (vertically uniform). The shallow-mixing T -profiles are characterized by a minimum/maximum of $\partial^2 T/\partial z^2$ at the top/bottom of the thermocline. Thus, the depths of the first minimum and the first maximum of $\partial^2 T/\partial z^2$ are taken as the top, $d_1^{(T)}$, and the bottom, $d_2^{(T)}$, of the thermocline (Fig. 2.13b).

The advection-type T -profiles are depicted by maxima of $\partial^2 T/\partial z^2$ at both top of the upper thermocline and bottom of the lower thermocline and a depth, d_{\max}^T , with the maximum temperature T_{\max}^U . The depths of the first and second maxima of $\partial^2 T/\partial z^2$ are taken as top, d_1^T , and bottom, d_2^T , of the upper/lower thermoclines (Fig. 2.13c).

The shallow-mixing type S -profiles are featured by a maximum/minimum of $\partial^2 S/\partial z^2$ at top/bottom of the halocline. From the ocean surface downward, the depths of the first maximum and the first minimum of $\partial^2 S/\partial z^2$ are taken as top, d_1^T , and bottom, d_2^T , of the halocline (Fig. 2.13d).

(c) Features of the deep water profiles. The deep-mixing type T -profiles reveal a thick surface mixed layer (Fig. 2.14a) above a positive gradient thermocline. The shallow-mixing type T -profiles are characterized by a minimum/maximum of $\partial^2 T/\partial z^2$ at top/bottom of the upper thermocline. Thus,

the depths of the first minimum and the first maximum of $\partial^2 T / \partial z^2$ are taken as top, d_1^T , and bottom, d_2^T , of the upper thermocline (Fig. 2.14b). Below the upper thermocline, a region of cold, nearly isothermal water exists which is a remnant of the previously cooling and convective mixing of water. Beneath this isothermal layer, there is a positive gradient lower thermocline similar to that described by the deep-mixing profiles.

The advection type T -profiles are depicted by maxima of $\partial^2 T / \partial z^2$ at both top and bottom of the upper and lower thermoclines and at a depth, d_{\max}^T , with a maximum temperature T_{\max}^U . The depths of the first and second maxima of $\partial^2 T / \partial z^2$ are taken as top, d_1^T , and bottom, d_2^T , of the upper thermocline (Fig. 2.14c). Below the depth of intrusion of warm Bering Sea water, the temperature profile is similar to that described by the deep-mixing profiles.

The shallow-mixing type S -profiles are characterized by a maximum/minimum of $\partial^2 S / \partial z^2$ at top/bottom of the upper halocline. From the ocean surface downward, the depths of the first maximum and the first minimum of $\partial^2 S / \partial z^2$ are taken as the top, d_1^S , and bottom, d_2^S , of the upper halocline (Fig. 2.14d). A lower halocline, when present, is often concurrent with the positive thermocline of the shallow-mixing type T -profile and is characterized by a minimum of $\partial^2 S / \partial z^2$ at the lower halocline.

(d) Mixed layer depth. MLD for temperature and salinity is usually estimated by d_1^F ,

$$\text{MLD}_F = d_1^F. \quad (2.8)$$

When d_1^F tends to an infinitesimally small depth ($d_1^F \simeq 0$), the upper thermocline (halocline) reaches the surface and the surface mixed layer disappears. Such profiles may be called stratified layers and treated as special case of the ordinary shallow-mixing or advection type profiles.

(e) Lower thermocline. The lower thermocline appears in the Beaufort Sea Deep Water. The major feature of T -profiles is the existence of minimum and maximum temperatures below the upper thermocline for the shallow-mixing and advection type profiles (Figs. 2.14b,c),

$$T_{\min} = \min_{z < -d_2^T} T(z), \quad T_{\max} = \max_{z < -d_2^T} T(z), \quad (2.9)$$

$$d_3^T = -\{z | T(z) = T_{\min}\}, \quad (2.10)$$

$$d_4^T = -\{z | T(z) = T_{\max}\}, \quad (2.11)$$

where d_3^T and d_4^T are the depths of the minimum and maximum temperatures below the upper thermocline, the corresponding data are $T(-d_3^T)$ and $T(-d_4^T)$. The layer between d_3^T and d_4^T may be identified as the lower thermocline. Usually, between the upper and lower thermoclines there exists a transition zone with a very weak vertical gradient.

2.5.4 Vertical Gradients

After the four depths, d_1^F , d_2^F , d_3^F , and d_4^F , are determined (F is T or S), some important physical parameters can be obtained from each T , S profile.

(a) Isothermal and isohaline layers. The water above the depth of d_1^F is taken as the mixed layer. Within the isothermal (isohaline) layer, the temperature (salinity) is assumed to be uniform with depth, i.e., the mixed layer temperature is the same as the SST,

$$\hat{F}(z) = F(0), \quad -d_1^F < z \leq 0. \quad (2.12)$$

(b) Entrainment zone. The entrainment zone below the mixed layer is assumed to be infinitesimally thin near the depth of d_1^F . The temperature (salinity) at the top of the entrainment zone is the same as the mixed layer temperature, and the temperature (salinity) at the bottom of the entrainment zone equals the temperature (salinity) at the top of the thermocline. Therefore, the temperature and salinity jump across the entrainment zone is represented as

$$\Delta F = F(0) - F(-d_1^F). \quad (2.13)$$

(c) Upper thermocline and halocline. The upper thermocline and halocline are located between $z = -d_1^F$ and $z = -d_2^F$. Vertical gradients of the upper thermocline (G_{th}^U) and halocline (G_{ha}^U) for the shallow mixing type T , S profiles are,

$$G_{\text{th}}^U = \frac{T(-d_1^T) - T(-d_2^T)}{d_2^T - d_1^T}, \quad G_{\text{ha}}^U = \frac{S(-d_1^S) - S(-d_2^S)}{d_2^S - d_1^S}. \quad (2.14)$$

The vertical gradient of the upper thermocline (G_{th}^U) for the advection type T -profiles is estimated by

$$G_{\text{th}}^U = \frac{1}{2} \left[\frac{|T(-d_1^T) - T(-d_{\text{max}}^T)|}{d_{\text{max}}^T - d_1^T} + \frac{|T(-d_{\text{max}}^T) - T(-d_2^T)|}{d_2^T - d_{\text{max}}^T} \right]. \quad (2.15)$$

(d) Lower thermocline and halocline. The lower thermocline and halocline are located between $z = -d_3^F$ and $z = -d_4^F$. Vertical gradients of the lower thermocline (G_{th}^L) and halocline (G_{ha}^L) are estimated by

$$G_{\text{th}}^L = \frac{T(-d_3^T) - T(-d_4^T)}{d_4^T - d_3^T}, \quad G_{\text{ha}}^L = \frac{S(-d_3^S) - S(-d_4^S)}{d_4^S - d_3^S}. \quad (2.16)$$

2.5.5 Thermohaline Parametric Description

The thermohaline parametric model turns any profile into physical parameters: four depths ($d_1^F, d_2^F, d_3^F, d_4^F$), temperature or salinity jump ΔF , upper and lower thermocline (halocline) strength. Taking shallow-mixing type (T, S) profiles as an example (remember that the deep-mixing type is a special case of the shallow-mixing type), the thermohaline parametric model is represented by

$$\begin{aligned}\hat{F}(z) &= F(0), & -d_1^F < z \leq 0, \\ \hat{F}(z) &= F(-d_1^F) - \frac{z+d_1^F}{d_2^F-d_1^F} [F(-d_2^F) - F(-d_1^F)], & d_2^F \leq z \leq -d_1^F, \\ \hat{F}(z) &= F(-d_2^F) - \frac{z+d_2^F}{d_3^F-d_2^F} [F(-d_3^F) - F(-d_2^F)], & -d_3^F \leq z \leq -d_2^F, \\ \hat{F}(z) &= F(-d_3^F) - \frac{z+d_3^F}{d_4^F-d_3^F} [F(-d_4^F) - F(-d_3^F)], & -d_4^F \leq z \leq -d_3^F, \\ {}^c\hat{F}(z) &= F(-d_4^F) - \frac{z+d_4^F}{d_N^F-d_4^F} [F(-d_N^F) - F(-d_4^F)], & -d_N^F \leq z \leq -d_4^F,\end{aligned}\quad (2.17)$$

which is vertically uniform in the mixed layer and piecewise linear with depth below the mixed layer to the deepest depth of the observational point, $z = -d_N^F$. Note that the ‘‘model profile’’ takes the value of $F(-d_1^F)$ at the mixed layer base $z = -d_1^F$.

The advection type profiles can also be represented by (2.17) except for the upper thermocline ($-d_2^T \leq z \leq -d_1^T$) which should be parameterized by

$$\begin{aligned}\hat{T}(z) &= T(-d_1^T) - \frac{z+d_1^T}{d_{\max}^T-d_1^T} [T(-d_{\max}^T) - T(-d_1^T)], & -d_{\max}^T \leq z \leq -d_1^T, \\ \hat{T}(z) &= T(-d_{\max}^T) - \frac{z+d_{\max}^T}{d_2^T-d_{\max}^T} [T(-d_2^T) - T(-d_{\max}^T)], & -d_2^T \leq z \leq -d_{\max}^T,\end{aligned}\quad (2.18)$$

where

$$T(-d_{\max}^T) = T_{\max}^U.$$

2.5.6 Statistical Tests

For any profile, $F(z_j)$, $j = 1, 2, \dots, N$, using (2.17) or (2.17) and (2.18), we obtain a corresponding model profile, $\hat{F}(z_j)$. Both $F(z_j)$ and $\hat{F}(z_j)$ have the same values at the depths 0, depths $-d_1^F, -d_2^F, -d_3^F, -d_4^F$, and $-d_N^F$, but do not necessarily have the same values at the other observational depths. If $\hat{F}(z_j)$ fits $F(z_j)$ well, the difference $\delta F(z_j) = F(z_j) - \hat{F}(z_j)$ should be very small at all observational points. We need to test if the difference is small enough to be neglected. The first test (t -test) is used to justify whether the mean value of $\delta F(z_j)$ is taken as zero. The second test (correlation test) is utilized to see if $\hat{F}(z_j)$ correlates well with $F(z_j)$.

After calculating the mean and standard deviation of $\delta F(z_j)$,

$$\overline{\delta F} = \frac{1}{N} \sum_{j=1}^N \delta F(z_j), s_{\delta F}^2 = \frac{1}{(N-1)} \sum_{j=1}^N [\delta F(z_j) - \overline{\delta F}]^2, \quad (2.19)$$

we begin with the null hypothesis that $\overline{\delta F}$ is zero. The significance level (α) is the probability that the given value of

$$t = \frac{\overline{\delta F}}{s_{\delta F}/\sqrt{N}} \quad (2.20)$$

is exceeded purely by chance. This value satisfies the t -distribution with $(N-1)$ degrees of freedom. If $|t| > t_{\alpha, N-1}$, we reject the null hypothesis, the modeled profile $\hat{F}(z_j)$ does not fit the observed profile $F(z_j)$ and should be rejected.

After a modeled profile $\hat{F}(z_j)$ passes the t -test, we start with the null hypothesis that $\hat{F}(z_j)$ does not correlate with the observation $F(z_j)$. The significance level (α) is the probability that the given value of

$$\mu = \frac{\sum_{j=1}^N \left| \hat{F}(z_j) - \bar{F} \right|^2}{\sum_{j=1}^N \left| \hat{F}(z_j) - F(z_j) \right|^2 / (N-2)} \quad (2.21)$$

is not exceeded purely by chance. This value satisfies the F -distribution with $(1, N-2)$ degrees of freedom. If $\mu > F_{\alpha}(1, N-2)$, we reject the null hypothesis and conclude that the modeled profile $\hat{F}(z_j)$ does correlate with the observation $F(z_j)$.

2.6 Curve-Fitting Model

In the thermohaline parametric models described in Sects. 2.3 and 2.4, temperature and salinity are vertically continuous, but their gradients are discontinuous at the layer transition. If the vertical gradients are required continuous, we need to use a curve-fitting model. The basic concept of this model is to determine a set of analytical curves (mathematical expressions with parameters) that represent the vertical distribution of T, S profiles. Different families of representative curves have been chosen for three sub-models, shallow top, mid-depth, and deep ranges, with each chosen such that the number of parameters required would yield a smooth profile. The matching conditions through the depth range transitions are chosen so that no discontinuities in vertical gradients occur. This requires overlapping of the two connected layers. For example, in constructing the US Navy's Generalized Digital Environmental Model (GDEM), Teague et al. (1990) suggested division of three sub-models as follows: shallow top sub-model (0–400 m), mid-depth sub-model (200–2,450 m), and deep sub-model (2,000 m to bottom).

2.6.1 Top Shallow Sub-Model (0–400 m)

The basic functional form used in GDEM to fit the top 400 m of temperature (top most temperature profile) is the squared amplitude response of the Butterworth filter (Oppenheim and Schafer 1975). This expression describes the vertical profile from the surface ($z = 0$) to the base of the seasonal thermocline (i.e., $z = -d$). It is then merged with an exponential tail which extends the fit to 400 m ($z = -H_{\text{top}} = -400$ m). The fitted temperature is given by

$$\hat{T}(z) = \frac{(T_0 - T_{-d}) [1 + (d/A)^{2B}]}{(d/A)^{2B} [1 + (-z/A)^{2B}]} + T_{-d} - \frac{(T_0 - T_{-d})}{(d/A)^{2B}}, \quad 0 \geq z \geq -d, \quad (2.22a)$$

$$\hat{T}(z) = (T_{-H_{\text{TOP}}} T_{-d}) x^{ax+b} + T_{-d}, \quad x \equiv -\frac{z+d}{H_{\text{TOP}} - d}, \quad -d \leq z \leq -H_{\text{TOP}}, \quad (2.22b)$$

where T_0 is SST. T_{-d} is the temperature at the base of the seasonal thermocline $z = -d$. $T_{-H_{\text{TOP}}}$ is the temperature at the depth H_{TOP} (400 m). Each temperature profile in the top layer (0–400 m depths) is represented by a set of eight parameters,

$$(T_0, T_{-d}, T_{-H_{\text{TOP}}}, d, A, B, a, b).$$

2.6.2 Mid-Depth Sub-Model (200–2,450 m)

An orthogonal polynomial expansion,

$$\hat{F}(D) = a_0 + a_1 P_{N1}(D) + \dots + a_M P_{NM}(D) \quad (2.23)$$

is used to fit observed temperature and salinity profiles (F) for the depth range 200–2,450 m and salinity profiles over the range of 0–400 m (top sub-model salinity profile). Here, D represents the depth index; $D = 1, 2, \dots, N$ for evenly spaced data in the layer. The polynomials, $P_{NK}(D)$, $K = 1, 2, \dots, M$, are orthogonal Gram polynomials (Wylie 1975) defined by

$$P_{NK}(D) = \sum_{I=0}^K (-1)^I C_K^I C_{K+I}^I \frac{D^I}{N^I}. \quad (2.24)$$

The benefit of using orthogonal polynomial expansions is that computation of higher-order coefficients does not require re-computation of the lower-order coefficients. Each temperature (or salinity) profile is represented by a set of parameters, (a_0, a_1, \dots, a_M) . In GDEM, $M = 6.0$ the maximum allowed rms error of fit is 0.1 ppt for the top salinity model, 0.05 ppt for the mid-depth salinity model, and 0.25°C for the mid-depth temperature model.

2.6.3 Deep Sub-Model (2,000 m to Bottom)

Deep temperature and salinity profiles are least squares fitted to a simple quadratic polynomial,

$$\hat{F}(z) = b_0 + b_1z + b_2z^2, \quad (2.25)$$

with rms errors less than 0.25°C for temperature and 0.05 ppt for salinity. The thermohaline parametric models (2.2), (2.17), and curve-fitting model (2.22)–(2.25) transform observed profiles with different data points in vertical into a set parameters. For example, the non-polar thermal parametric model (2.2) has 12 parameters with SST, five depths (d_1, d_2, d_3, d_4, d_5), and six gradients ($G_T^{(m)}, G_T^{(th)}, \bar{G}_T^{(en)}, \bar{G}_T^{(tr)}, \bar{G}_T^{(d1)}, \bar{G}_T^{(d2)}$). Since winter (December through April) profiles reveal a single-layer structure (Fig. 2.7a), the set of characteristic parameters reduces to (SST, H). The curve-fitting model has eight parameters in the shallow top sub-model, seven parameters in the mid-depth sub-model, and three parameters in the deep sub-model. The temperature and salinity profiles with irregular vertical sampling space can be represented by parameters with same number of data points. Furthermore, these parameters represent important physical features.

The non-polar parametric model (2.2) is used to process 4.5 million temperature profiles (Levitus and Boyer 1994) from NODC. Here, we present global (60°S – 60°N) MLD (d_1) data for illustration. It is noted that the density depends non-linearly on temperature, salinity, and pressure. The MLD for density (MLD_ρ) might not be the same as the MLD for temperature (MLD_T).

2.7 Mixed Layer Depth

Two kinds of methods are used to determine the MLD: simple criteria and parametric modeling. The former were used by many oceanographers, and the later emerges after the parametric model was proposed (Chu et al. 1997b). Sections 2.4 and 2.5 describe the parametric models to determine the thermohaline parameters including the MLD. Here, we only present the simple criteria.

2.7.1 Simple Criteria

There are two types of criteria, difference and gradient, for determining H_T and H_D in the upper ocean. The difference criterion requires that the value for deviation of temperature (density) from its surface need to be smaller than a certain fixed value. The gradient criterion requires the vertical derivative of temperature (density) to be smaller than a certain fixed value.

The criterion for determining MLD_T varies from 0.5°C (Wyrski 1961a,b; Monterey and Levitus 1997) to 0.8°C (Kara et al. 2000). The criterion for

determining MLD_ρ from potential density (σ_t) profile is given by (Miller 1976; Spall 1991),

$$\Delta\sigma_t = 0.125\sigma_t(0), \quad (2.26a)$$

or by (Sprintall and Tomczak 1992; Ohlmann et al. 1996; Monterey and Levitus 1997),

$$\Delta\sigma_t = 0.5^\circ\text{C} (\partial\sigma_t/\partial T). \quad (2.26b)$$

Here, $\partial\sigma_t/\partial T$ is the thermal expansion coefficient evaluated using the surface values of temperature and salinity. The difference in criterion (2.26b) is based on the assumptions that the salinity effect on the seawater expansion is negligible, and that MLD_ρ is corresponding to the depth with temperature difference of 0.5°C from the surface (Sprintall and Tomczak 1992).

Defant (1961) was among the first to use the gradient method. He used a gradient of $0.015^\circ\text{C m}^{-1}$ to determine H_T of the Atlantic Ocean. Bathen (1972) chose $0.02^\circ\text{C m}^{-1}$, and Lukas and Lindstrom (1991) used $0.025^\circ\text{C m}^{-1}$. The following gradient criterion is widely used (e.g., Lukas and Lindstrom 1991)

$$\partial\sigma_t/\partial z = 0.01 \text{ kg m}^{-4}. \quad (2.26c)$$

2.7.2 MLD_T

MLD_T is obtained from the MOODS data using the parametric model. The global (60°S – 60°N) ocean is divided into 10° latitude by longitude boxes. Means and standard deviations are calculated for each box. Each MLD_T data point in the box is checked against the statistics. Any MLD data whose value exceeds three times the standard deviation is flagged out. Such a check is only performed if there are more than five or more MLD data points in the box. After the first check, means and standard deviations are re-calculated, excluding individual values which failed the first check. Such a procedure is repeated three times.

After the standard deviation check, we built up a raw MLD_T data set which contains 3.5 million data points. The data are unevenly distributed in space and time. Certain periods and areas are over sampled while others lack enough observations to gain any meaningful insights. Both North Pacific Ocean and North Atlantic Ocean, especially the Gulf Stream and Kuroshio, are featured as dense sampled regions. But, the Southern Hemispheric oceans are featured as low sampled regions. Quite a few areas have no MLD_T data both in January (Fig. 2.15a) and July (Fig. 2.15b) especially in the Southern Hemisphere. The temporally uneven distribution can be seen from Fig. 2.16, which indicates yearly number of temperature observations during 1958–1992 for the global oceans (Fig. 2.16). The year of 1966 is found to have the maximum number of profiles (around 120,000 profiles in the global oceans), and the year of 1992 is found to have the minimum number of profiles (near 10,000 profiles in the global oceans).

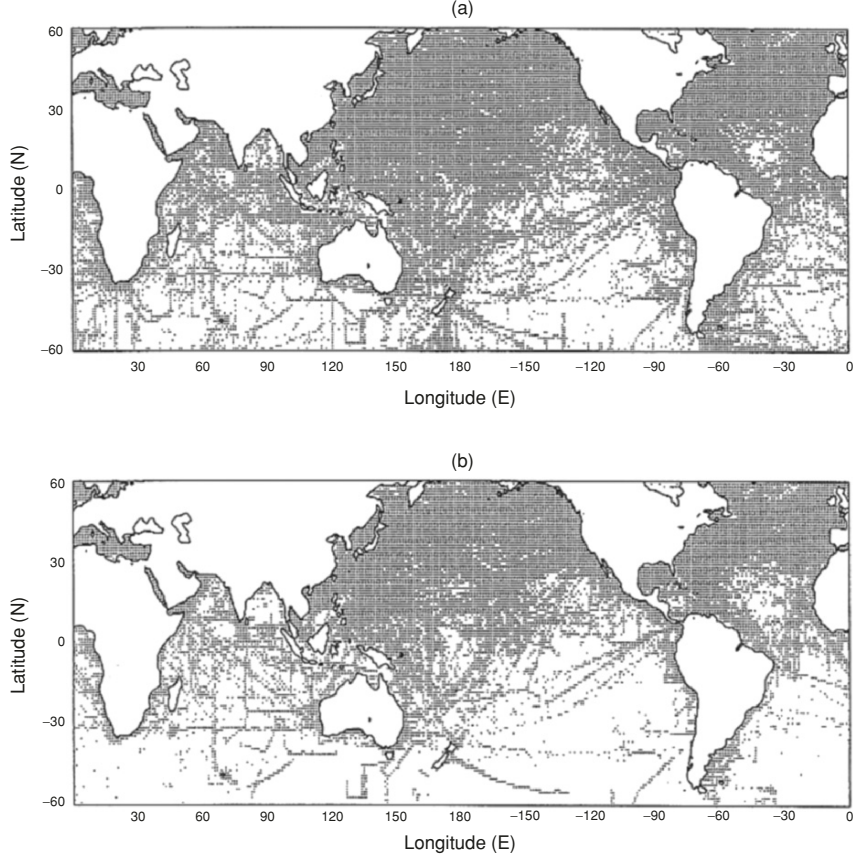


Fig. 2.15. MLD_T data distribution for the world oceans between 60°S and 60°N : (a) January, and (b) July (From Chu and Liu 1999, Proceedings on the 10th Symposium on Global Change Studies, American Meteorological Society)

The monthly mean gridded MLD_T data set is established using the optimal interpolation on $1^\circ \times 1^\circ$ grid points. Let MLD_T data be represented by $H_T(x_i, y_j, \tau_k, t_l)$, where, $\tau_k = 1958, 1959, \dots, 1992$, is the time sequence in years, and $t_l = 1, 2, \dots, 12$, the time sequence of month within a year. Before investigating the monthly variation of MLD_T , two temporally averaging operators are defined,

$$\bar{H}_T(x_i, y_j, t_l) = \frac{1}{\Delta\tau} \sum_{k=1958}^{1992} H_T(x_i, y_j, \tau_k, t_l), \quad \Delta\tau = 35 \text{ yr}, \quad (2.27a)$$

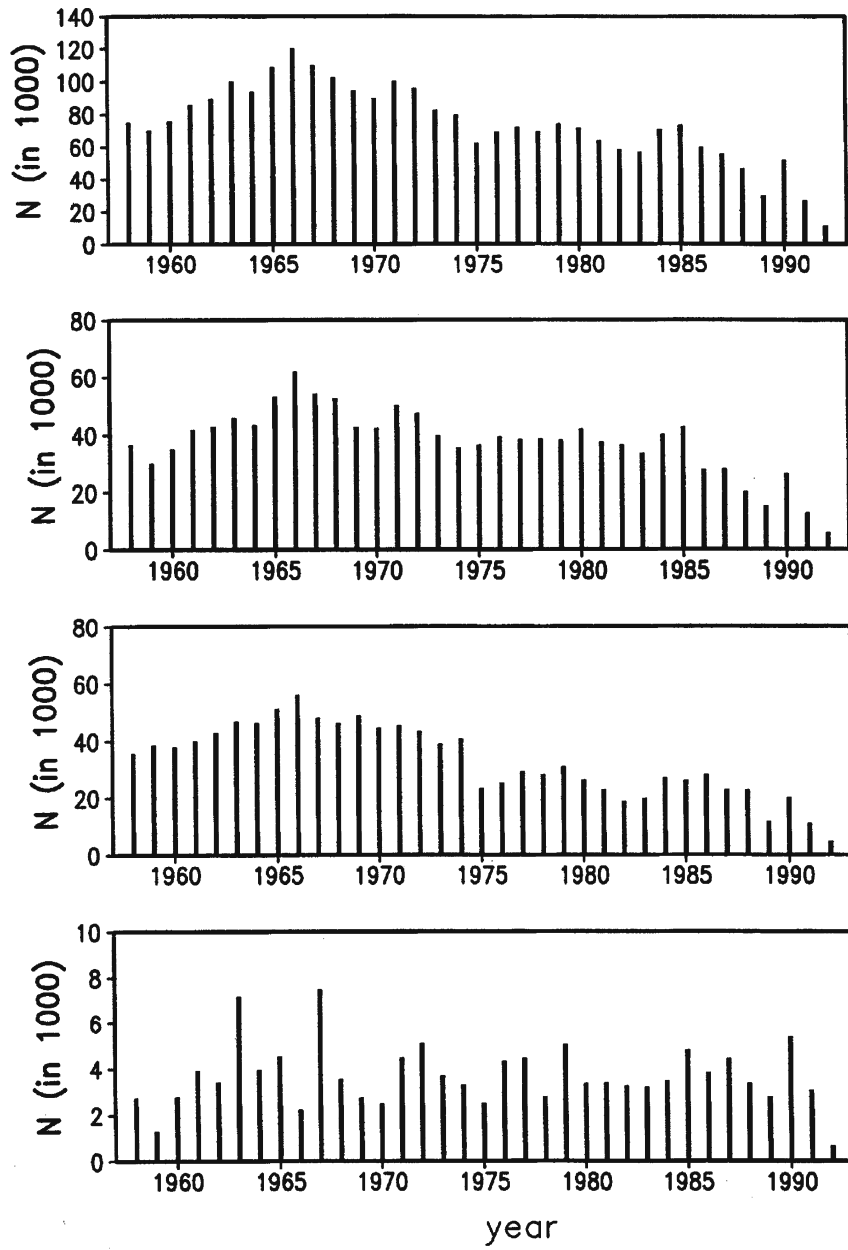


Fig. 2.16. Temporal variability of MLD_T data points of the world oceans (From Chu and Liu 1999, Proceedings on the 10th Symposium on Global Change Studies, American Meteorological Society)

which is the long-term mean value for the month t_l (or called climatological monthly mean) and

$$\bar{\bar{H}}_T(x_i, y_j) = \frac{1}{12} \sum_{l=1}^{12} \bar{H}_T(x_i, y_j), \quad (2.27b)$$

which is the climatological annual mean.

It is noted that the MLD_T climatology (i.e., climatological monthly and/or annual mean) computed here is different from the MLD_T climatology calculated from the monthly mean temperature profiles (Monterey and Levitus 1997). The MLD_T climatology is quite different between the two approaches because the spatial average of MLD_T from observed temperature profiles (first approach) is different from the MLD_T of the spatially averaged temperature profiles over that data set (second approach). Usually, the MLD_T calculated using the second approach is much thicker than the one using the first approach.

Monthly mean MLD_T (Fig. 2.17) show several interesting features: (a) deep mixed layer ($MLD_T \geq 60$ m) in the northeast part of the North Atlantic Ocean, (b) zonally asymmetric pattern in the tropical Pacific with deep MLD_T (≥ 40 m) in the western part, and shallow MLD_T (≤ 20 m) in the eastern part.

Different characteristics of the El Nino-Southern Oscillation (ENSO) between the 1980s duration and the 1960s and 1970s durations lead to the investigation of connection between SST inter-annual and inter-decadal variabilities. The connection should also be identified using the MLD_T data. To do so, the seasonal variability should be filtered out, and the MLD_T anomaly to the climatological monthly mean is calculated

$$\hat{H}_T(x_i, y_j, \tau_k, t_l) = H_T(x_i, y_j, \tau_k, t_l) - \bar{\bar{H}}_T(x_i, y_j, t_l). \quad (2.28)$$

Since the data $\hat{H}_T(x_i, y_j, \tau_k, t_l)$ are not sufficient to obtain statistically significant results on $1^\circ \times 1^\circ$ grid, the latitudinally averaged (10°S – 10°N) anomalies for the Pacific Ocean and zonally averaged anomalies for the Pacific and Atlantic Oceans are calculated. The inter-annual variability can be identified from latitudinally averaged MLD_T anomaly in the equatorial Pacific. Time-longitude plot of MLD_T anomaly from January 1958 to December 1992 (Fig. 2.18) shows westward propagated equatorial Rossby waves and eastward propagated equatorial Kelvin waves. Most negative MLD_T anomalies propagate westward from the eastern Pacific with speeds from 25 to 10 cm s^{-1} . The westward propagating events with maximum negative anomaly (-10 m) are identified during 1959–1960, 1971–1974, 1981–1985, and 1988–1992. It takes 2–5 years across the basin. This indicates that the mixed layer shallows as the equatorial Rossby waves propagate. This confirms the results from earlier numerical mode simulations (McCreary and Anderson 1984). The decadal variability can be identified from zonal averaged MLD anomaly in the Pacific and Atlantic Oceans from time-latitude plot of MLD_T anomaly from January 1958 to December 1992 (Fig. 2.19).

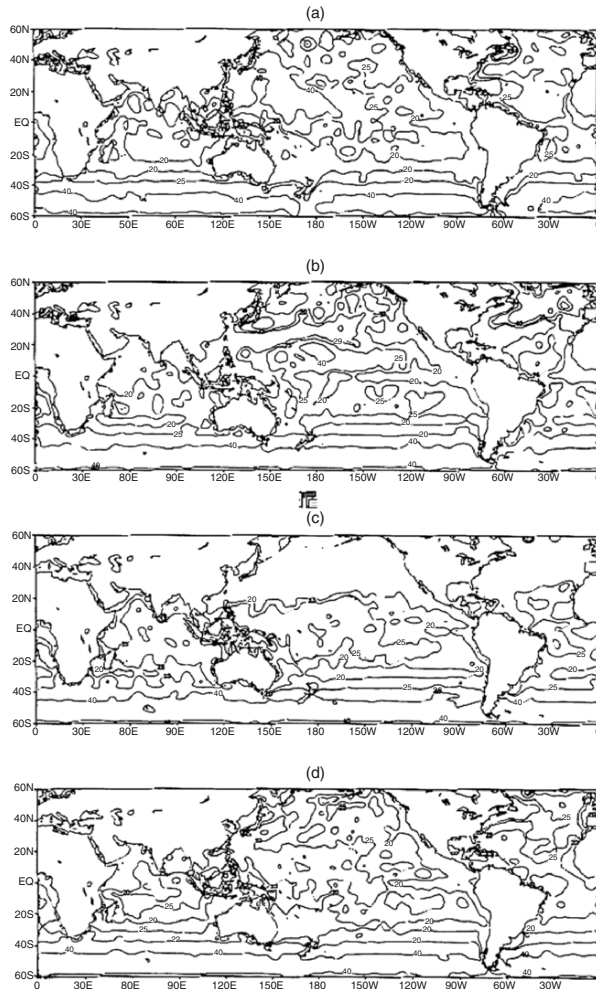


Fig. 2.17. Climatological monthly mean MLD_T : (a) January, (b) April, (c) July, and (d) October (From Chu and Liu 1999, Proceedings on the 10th Symposium on Global Change Studies, American Meteorological Society)

2.8 Barrier Layer

There are areas of the world ocean where MLD_T (represented by H_T) is larger than MLD_ρ (represented by H_D) (Lindstrom et al. 1987; Lukas and Lindstrom 1991; Sprintall and Tomczak 1992; You 1995, 1998; Chu et al. 2001d). When the “barrier layer” occurs ($H_T > H_D$), the barrier layer thickness is defined as the difference, $H_T - H_D$ (Fig. 2.20). There is a little temperature change (near-zero vertical gradient) and a great density change in the barrier layer, which isolates the density mixed layer from the cool water below

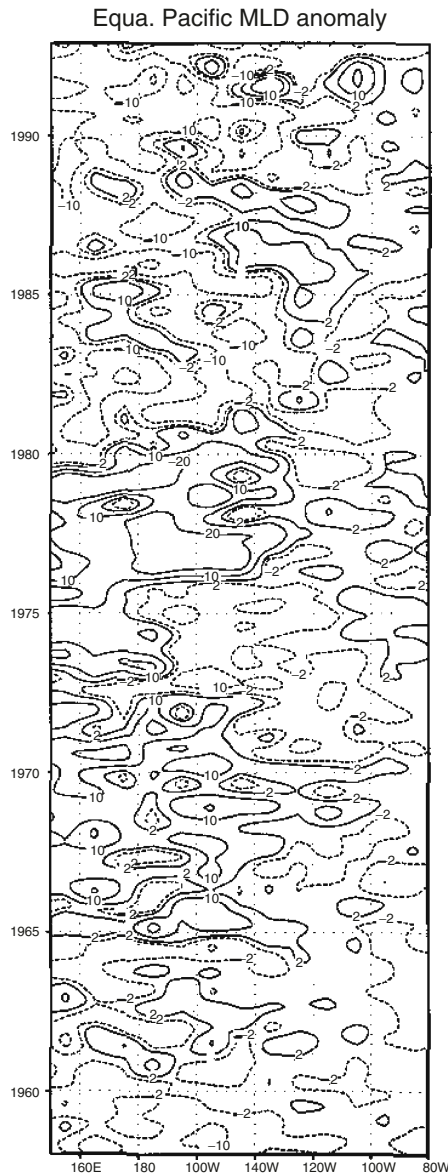


Fig. 2.18. Time-longitude plot of monthly MLD_T anomaly in the equatorial Pacific averaged between $10^\circ S$ and $10^\circ N$ (From Chu and Liu 1999, Proceedings on the 10th Symposium on Global Change Studies, American Meteorological Society)

the thermal mixed layer (i.e., the thermocline). Such insolation makes SST vary in a short period when the net surface heat flux is not negligible, which has impacts on ocean heat budgets (Swenson and Hansen 1999) and affects

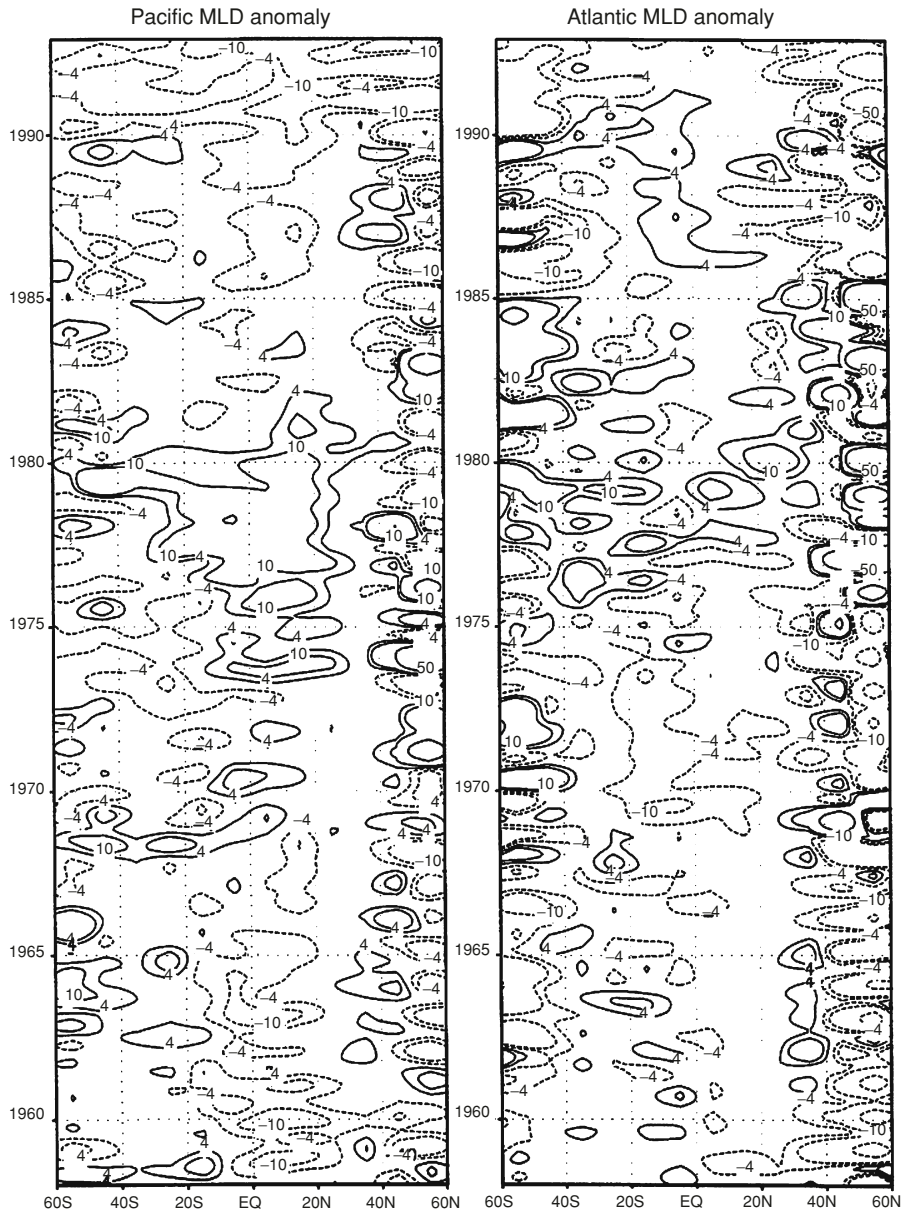


Fig. 2.19. Time-latitude plot of zonally averaged monthly MLD_T anomaly in the (a) Pacific Ocean, and (b) Atlantic Ocean (From Chu and Liu 1999, Proceedings on the 10th Symposium on Global Change Studies, American Meteorological Society)

the heat exchange with the atmosphere. Therefore, understanding spatial and temporal distributions of a barrier layer leads to accurate estimate of upper ocean thermohaline structure and the air–ocean fluxes.

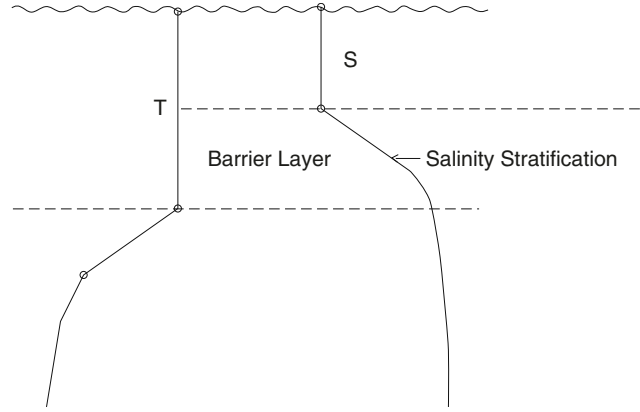


Fig. 2.20. A sketch diagram of isothermal, mixed, and barrier layers (from Chu et al. 2001d, *Journal of Physical Oceanography*)

Barrier layer occurs in open oceans and regional seas. Identification of the barrier layer can be conducted after analyzing the hydrographic data. For example, Chu et al. (2001d) identify the occurrence of barrier layer in the Sulu and Celebes Seas from the CTD data of the MOODS data.

2.8.1 Two Mechanisms for the Occurrence of Barrier Layer

Two major factors determining $H_T(H_D)$ are: (1) surface winds and net heat (buoyancy) flux and (2) thermal (density) stratification underneath the isothermal (mixed) layer. Thus, the condition ($H_T > H_D$) is caused by the surface fresh water flux (precipitation excess evaporation) and strong salinity stratification underneath the mixed layer. Thus, the barrier layer can be classified as (a) rain-formed, and (b) stratification-formed (weaker thermal and strong salinity stratification).

There are two regimes in the ocean mixed layer dynamics (Chu 1988; Chu et al. 1990; Chu and Garwood 1990, 1991; Chu 1993): entrainment and detrainment. The detrainment process occurs with weak winds, and strong surface warming (or excessive precipitation over evaporation). The two depths H_T and H_D are determined by

$$H_T = \frac{C_1 u_*^3}{C_2 \alpha_* g F / \rho_0 c_p}, \quad H_D = \frac{C_1 u_*^3}{C_2 B}, \quad (2.29)$$

where C_1 and C_2 are tuning coefficients, g the gravity, α_* the thermal expansion coefficient, ρ_0 the characteristic density, c_p the specific heat under constant pressure, F the net surface heat flux (downward positive). In detrainment regime, we have $F > 0$. The ratio between the two depths is calculated by

$$\frac{H_T}{H_D} = 1 + \frac{\beta_*(P-E)S}{\alpha_*F/\rho_0c_p}, \quad (2.30)$$

where P and E are the precipitation and surface evaporation rate, and β_* is the salinity contraction coefficient. Thus, the rain-formed mechanism ($P-E > 0$) becomes evident in the detrainment regime with weak winds, weak surface warming (low positive value of F), and strong surface fresh water flux [(large positive value of $(P-E)$].

The stratification-formed mechanism is evident in the entrainment regime. Suppose that the rain-formed mechanism is absent ($P = E$) and that the initial H_T coincides with H_D ,

$$H_T|_{t=0} = H_D|_{t=0}. \quad (2.31)$$

The ratio of the initial entrainment velocities ($w_e = dH/dt$) between isothermal and mixed layers is given by (Chu 1993)

$$\frac{w_e^{(T)}}{w_e^{(D)}} = \frac{[-(\rho - \rho_{-H_D})]}{\alpha_*(T - T_{-H_T})}. \quad (2.32)$$

A larger density jump

$$[-(\rho - \rho_{-H_D})] > \alpha_*(T - T_{-H_T}) \quad (2.33)$$

causes a larger entrainment velocity for the mixed thermal layer than the mixed density layer. Since the density stratification is determined by the temperature and salinity stratifications, the stratification-formed mechanism becomes important when the salinity stratification is strong. Thus, the stratification-formed mechanism becomes evident in the entrainment regime with strong winds, strong surface cooling (negative value of F), and strong salinity stratification. Usually, both rain-formed and stratification-formed mechanisms may take place at the same time; and precipitation may also strengthen the stratification.

2.8.2 Sulu and Celebes Seas

The Sulu and Celebes Seas are the two major marginal seas in the outer southeastern Asia region (Fig. 2.21), which consists of an island arc stretching across some 5,150 km along the equator at about 94°E–14°E and 15°N–11°S, and which has two contrasting zones (Arief 1998). The Sulu Sea belongs to the western zone where approximately 15–20% of the global freshwater discharge enters (Toole 1987) from freshwater influx that is supported by a high annual rainfall, between 2 and 4 m y⁻¹, (ASEAN Subcommittee on Climatology 1982). The Celebes Sea belongs to the eastern zone which is composed of deep-basin chains of 1,000–4,000 m depth and filled mainly by western Pacific water masses. This zone has a low annual rainfall, less than 2 m y⁻¹ (ASEAN Subcommittee on Climatology 1982).

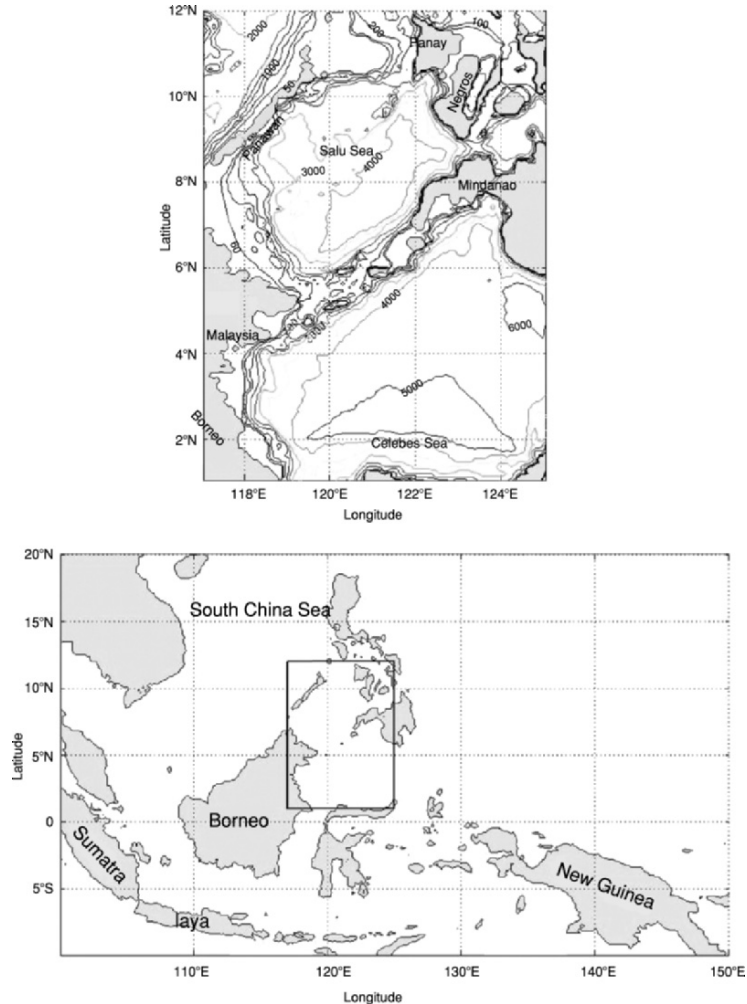


Fig. 2.21. Geography and isobaths showing the bottom topography of the Sulu and Celebes Seas (from Chu et al. 2001d, Journal of Physical Oceanography)

2.8.3 Barrier Layer in the Sulu Sea

The two depths, H_T and H_D , are obtained from 221 CTD profiles. Monthly CTD stations (denoted by the symbol “o”) and the stations with the barrier layer occurrence ($H_T > H_D$, represented by the symbol “+”) in the Sulu Sea (Fig. 2.22) show a rather frequent occurrence of barrier layer. For example, among 16 (6) CTD stations in September (November), there are 15 (6) stations where the barrier layer occurs. The rate of occurrence reaches 94% in September and 100% in November (Table 2.1). When barrier layer occurs, the barrier layer thickness is computed as the difference between H_T and H_D . The

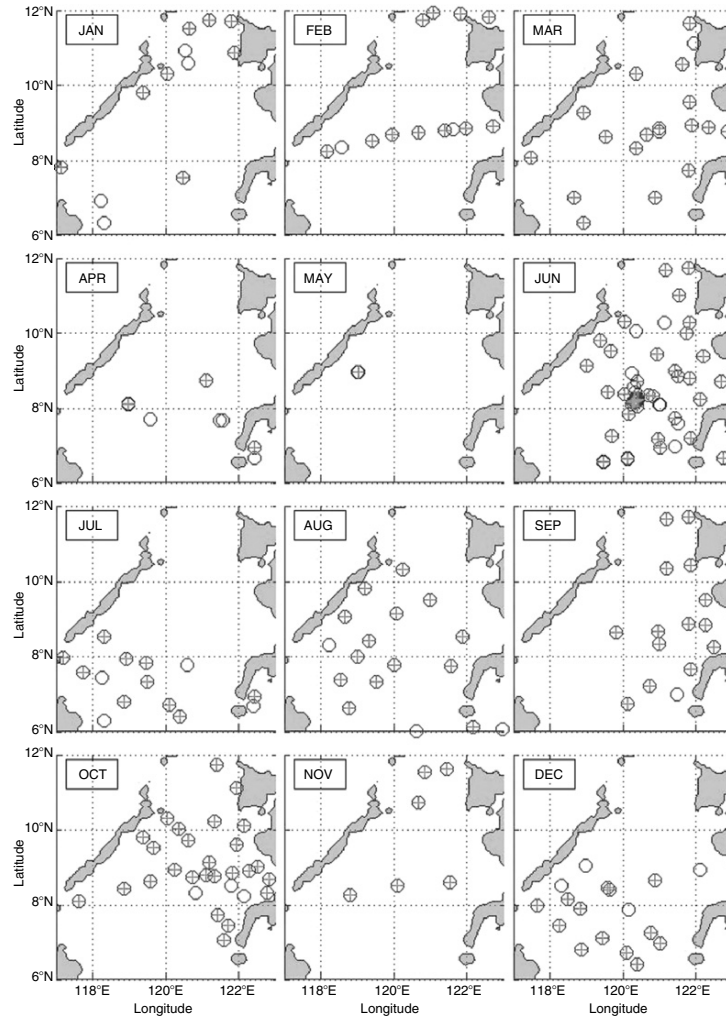


Fig. 2.22. Monthly CTD stations (denoted by the symbol “o”) and the stations with the barrier layer occurrence ($H_T > H_D$, represented by the symbol “+”) in the Sulu Sea (after Chu et al. 2001d, *Journal of Physical Oceanography*)

climatological characteristics are outlined as follows: (a) barrier layer occurs most frequent in September–November (fall) with a frequency of 90–100% and least frequent in April and May (spring) with a frequency of 50%; (b) MLD has a minimum value of 3 m in May and a maximum value of 30.5 m in February; and (c) barrier layer depth has large values (39.7–47.6 m) in September–October and small values (9–11.3 m) in April and May. It is noted that the sample size is not sufficiently large, thus the statistical features mentioned here may have bias values, especially in May.

Table 2.1. Monthly occurrence frequency and climate features of the barrier layer in the Sulu Sea

	Jan	Feb	Mar	Apr	May	Jun	Jul	Aug	Sep	Oct	Nov	Dec
N	12	13	19	8	2	61	16	19	16	31	6	18
B	8	11	17	4	1	48	11	16	15	28	6	14
B/N (%)	67	85	89	50	50	79	69	84	94	90	100	78
mean MLD (m)	29	30.5	19.5	16.5	3	16.4	14.2	12.9	11.1	14.9	21.2	12.1
mean barrier layer thickness (m)	27.5	29.9	14.1	11.3	9.0	12.2	28.7	29.3	39.7	47.6	33.7	45.3

N is the number of station, and B is the number of barrier layer occurrence (after Chu et al. 2001d, Journal of Physical Oceanography)

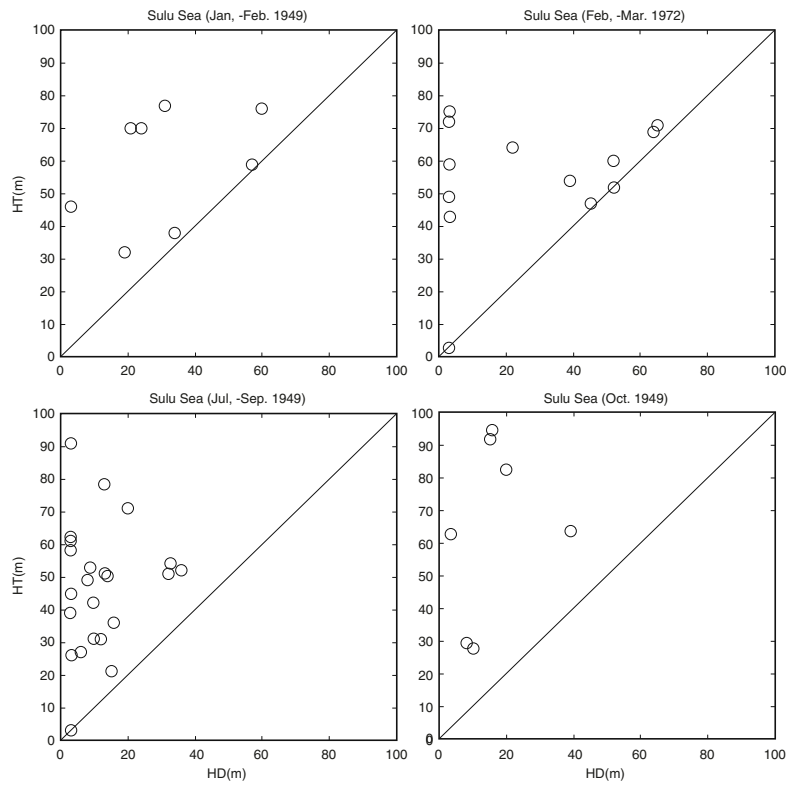


Fig. 2.23. Scatter diagrams (H_T versus H_D) of the Sulu Sea for the four selected periods: (a) January–February 1949, (b) February–March 1972, (c) July–September 1949, and (d) October–December 1973 (after Chu et al. 2001d, Journal of Physical Oceanography)

Scatter diagrams of H_T and H_D (Fig.2.23) show that the barrier layer occurs quite often in both summer and winter, with more evidence in the summer months. For example, H_D is lesser than H_T at almost all stations

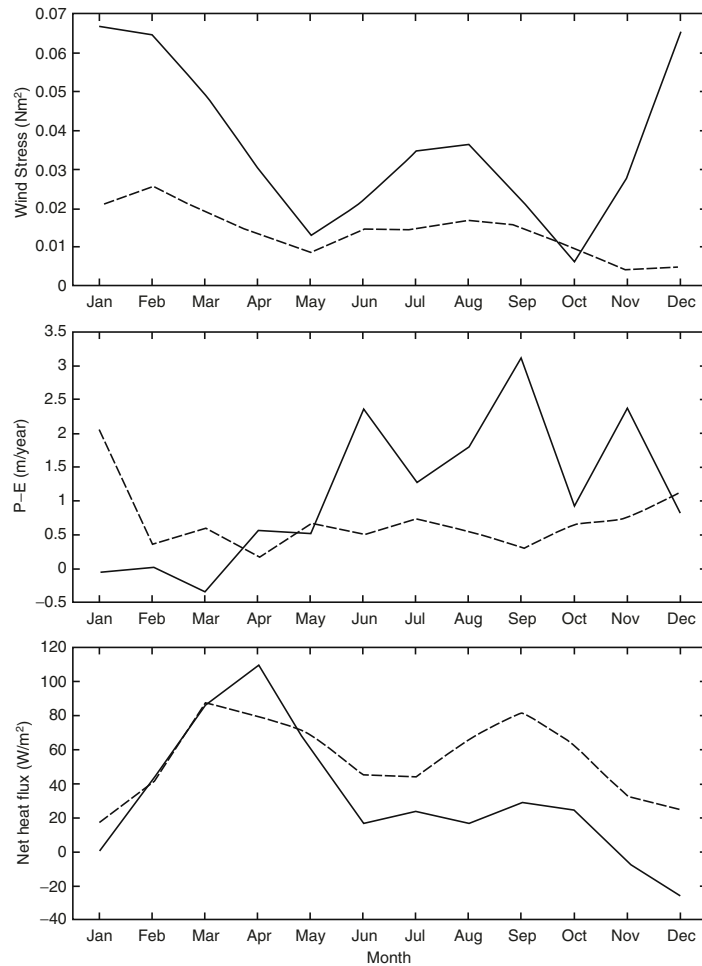


Fig. 2.24. Monthly mean COADS (a) surface wind stress (N m^{-2}), (b) $P-E$ (m yr^{-1}), and (c) net heat flux (W m^{-2}) averaged over the Sulu Sea (solid curve) and the Celebes Sea (dashed curve) (after Chu et al. 2001d, *Journal of Physical Oceanography*)

in October 1973. Comparing among the four periods, the barrier layer has relatively thin barrier layer in July–September 1949.

The Comprehensive Ocean-Atmosphere Data Set (COADS) provides monthly mean sea surface wind stress and net heat and freshwater fluxes (Fig. 2.24). The surface wind stress, net heat flux (F), and net freshwater flux ($P-E$) have seasonal variability in the Sulu Sea. The wind stress strengthens in December–February ($6.57\text{--}6.67 \times 10^{-2} \text{ N m}^{-2}$) and weakens in April–November ($0.63\text{--}3.66 \times 10^{-2} \text{ N m}^{-2}$). The net heat flux is negative in November–January (-25.4 to 0 W m^{-2} , surface cooling) and becomes largely

positive in March–May ($60\text{--}110.3\text{ W m}^{-2}$, strong surface warming). The surface fresh water flux ($P-E$) is weak in January–May ($<0.6\text{ m yr}^{-1}$) and strong in June–November ($>1\text{ m yr}^{-1}$).

In April and May the Sulu Sea is under the influence of weak winds ($1.3\text{--}3 \times 10^{-2}\text{ N m}^{-2}$), strong net heat flux ($60\text{--}110.3\text{ W m}^{-2}$), and weak surface fresh water flux ($0.52\text{--}0.56\text{ m yr}^{-1}$). The strong heat flux and weak winds cause shallow isothermal layer (small H_T). The weak fresh water flux cannot strengthen the salinity stratification. Thus, the frequency of the barrier layer is the least in April and May. In September and October the Sulu Sea is under the influence of weak winds ($0.63\text{--}2.19 \times 10^{-2}\text{ N m}^{-2}$), weak net heat flux ($24.6\text{--}29.2\text{ W m}^{-2}$), and strong surface fresh water flux (3.1 m yr^{-1} in September). These conditions lead to the detrainment regime for the upper ocean and favor the rain-formed mechanism (excessive precipitation over evaporation).

In December the Sulu Sea is under the influence of strong winds ($6.57 \times 10^{-2}\text{ N m}^{-2}$), surface cooling (-25.4 W m^{-2}), and relatively weak surface fresh water flux (0.8 m yr^{-1}). These conditions favor the entrainment regime in the upper ocean and the stratification-formed mechanism for the occurrence of barrier layer.

2.8.4 Barrier Layer in the Celebes Sea

The two depths (H_T and H_D) for the Celebes Sea are obtained from processing 179 CTD profiles. Monthly CTD stations (denoted by the symbol “o”) and the stations with the barrier layer occurrence ($H_D < H_T$, represented by the symbol “+”) in the Celebes Sea (Fig. 2.25) show a rather frequent occurrence of barrier layer in the Celebes Sea. For example, among 14 CTD stations in December, there are 13 stations where barrier layer occurs. The rate of occurrence reaches 93% (Table 2.2). The barrier layer thickness has a maximum value of 62.0 m in April and a minimum value of 9.6 m in June. The climatological features of barrier layer are outlined as follows: (a) barrier layer occurs most frequent in December with a frequency of 93% and least frequent in April with a frequency of 36%; (b) MLD has a minimum value of 7.3 m in March and a maximum value of 28.1 m in September; and (c) barrier layer thickness has a maximum value in March–April (49.7–62.0 m) and a minimum value of 9.6 m in June. These numbers might not have statistical significance due to the size of the sample being small.

Scatter diagrams of H_T and H_D (Fig. 2.26) show that the barrier layer occurs quite often in winter and fall and less often in spring. For example, H_D is lesser than H_T at almost all stations in January 1941. At Station 16, H_D and H_T are 25 and 100 m, respectively with a barrier layer thickness of about 75 m. Among the four periods, the barrier layer has relatively thin barrier layer in July 1941 and May–June 1972.

The surface wind stress, net heat flux (F), and net fresh water flux ($P-E$) have less seasonal variability in the Celebes Sea than in the Sulu Sea (Fig. 2.24). The wind stress varies between $0.45 \times 10^{-2}\text{ N m}^{-2}$ (November)

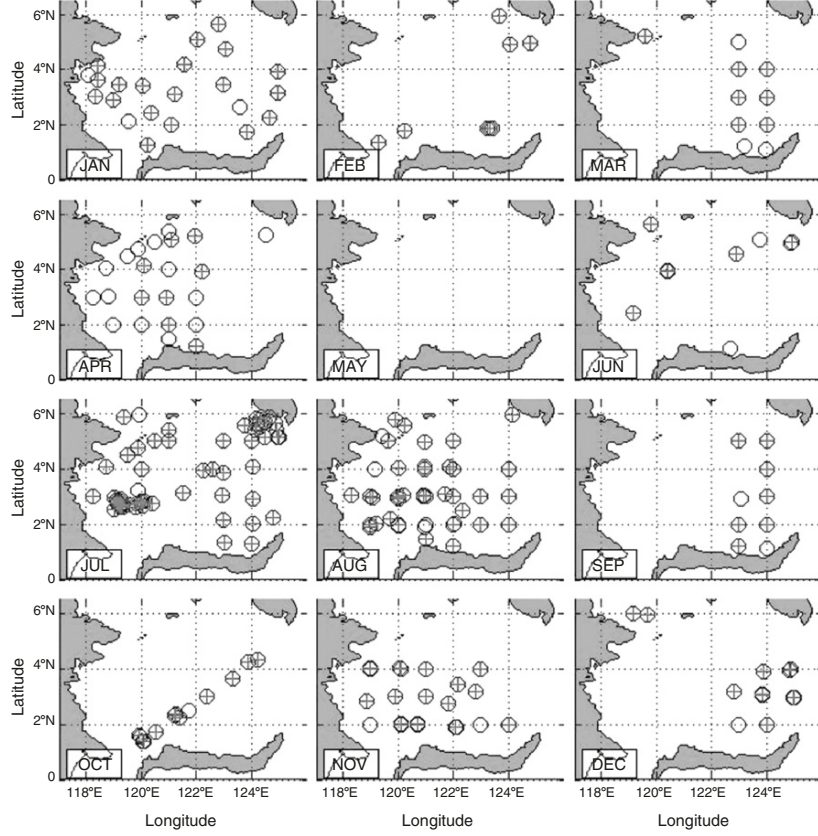


Fig. 2.25. Monthly CTD stations (denoted by the symbol “o”) and the stations with the barrier layer occurrence ($H_D < H_T$, represented by the symbol “r”) in the Celebes Sea (after Chu et al. 2001d, Journal of Physical Oceanography)

and $2.6 \times 10^{-2} \text{ Nm}^{-2}$ (February). The surface net heat and fresh water fluxes are positive all year round with F varying from 17.5 W m^{-2} (January) to 87.4 W m^{-2} (March) and $(P-E)$ varying from 0.17 m yr^{-1} (April) to 2.1 m yr^{-1} (January). Thus, the Celebes Sea is under the influence of weak winds, surface warming, and surface fresh water flux all year round. These conditions favor the rain-formed mechanism.

In December–January the Celebes Sea is experienced weak net heat flux ($17.5\text{--}24.5 \text{ W m}^{-2}$), and strong surface fresh water flux ($1.14\text{--}2.06 \text{ m yr}^{-1}$). These conditions may cause the detrainment regime for the upper ocean and favor the rain-formed mechanism (excessive precipitation over evaporation).

In April, the Celebes Sea experiences strong net heat flux (80.4 W m^{-2}), and weak surface fresh water flux (0.17 m yr^{-1}). The strong heat flux and weak winds cause shallow isothermal layer (small H_T). The weak fresh water flux

Table 2.2. Monthly occurrence frequency and climate features of the barrier layer in the Sulu Sea

	Jan	Feb	Mar	Apr	May	Jun	Jul	Aug	Sep	Oct	Nov	Dec
B	8	11	17	4	1	48	11	16	15	28	6	14
N	12	13	19	8	2	61	16	19	16	31	6	18
B/N (%)												
mean MLD (m)	67	85	89	50	50	79	69	84	94	90	100	78
mean barrier layer thick-ness (m)	29	30.5	19.5	16.5	3	16.4	14.2	12.9	11.1	14.9	21.2	12.1

N is the number of station, and *B* is the number of barrier layer occurrence (after Chu et al. 2001d, Journal of Physical Oceanography)

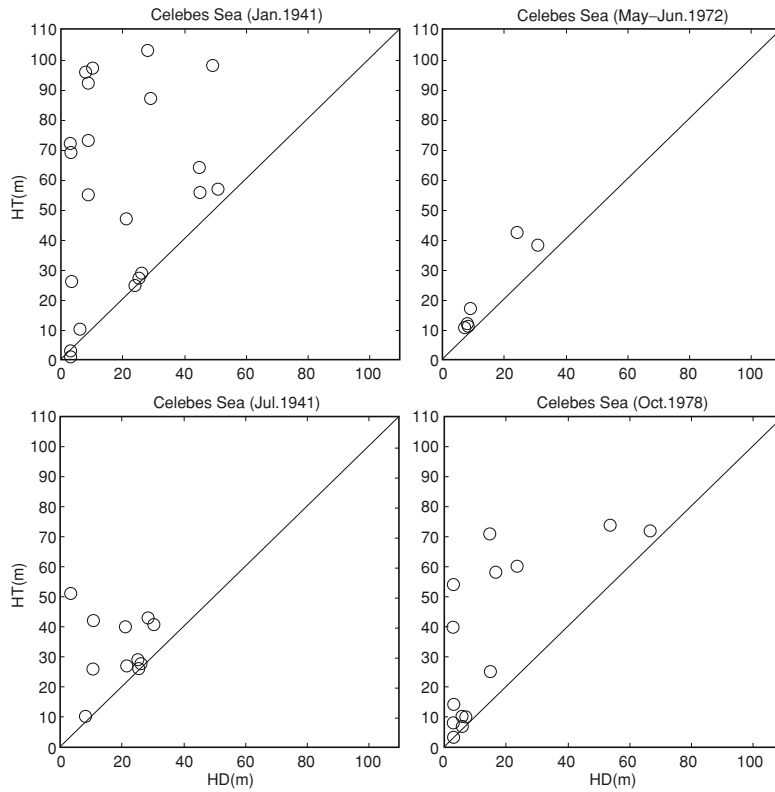


Fig. 2.26. Scatter diagrams (H_T versus H_D) of the Celebes Sea for the four selected periods: (a) January–February 1949, (b) February–March 1972, (c) July–September 1949, and (d) October–December 1973 (after Chu et al. 2001d, Journal of Physical Oceanography)

strengthens the salinity stratification slightly. Thus, the barrier layer occurs least frequently in April.

2.9 Determination of Vertical Temperature Structure from SST

The most difficult problem in physical oceanography is the lack of in situ observations. With the help of electromagnetic techniques, especially satellite remote-sensing, we may obtain global coverage of temporally varying surface data such as SST. Can we determine the vertical thermal structure from satellite SST observations? To answer this question we should first examine the linkage between SST and sub-surface thermal structure (Fig. 2.27). The key issue is how to compress a large profile data set into a small parameter (or coefficient) data set. Parametric models (see Sects. 2.4 and 2.5) uses the layered structure (mixed layer, entrainment zone, thermocline or halocline, and deep layer) to transform the profile data into a set of physical parameters such as SST, MLD_T , thermocline bottom depth, thermocline temperature gradient, and deep layer stratification (Chu et al. 2000a). Using parametric models depicted in Sects. 2.4 and 2.5, a vertical temperature profile can be transformed into several parameters: SST, MLD_T , thermocline bottom depth, thermocline temperature gradient, and deep layer stratification.

These parameters vary on different time scales: SST and MLD_T on scales of minutes to hours, the thermocline bottom depth and thermocline temperature gradient on months to seasons, and deep layer stratification on an even longer time-scale. If the long time-scale parameters such as the thermocline bottom

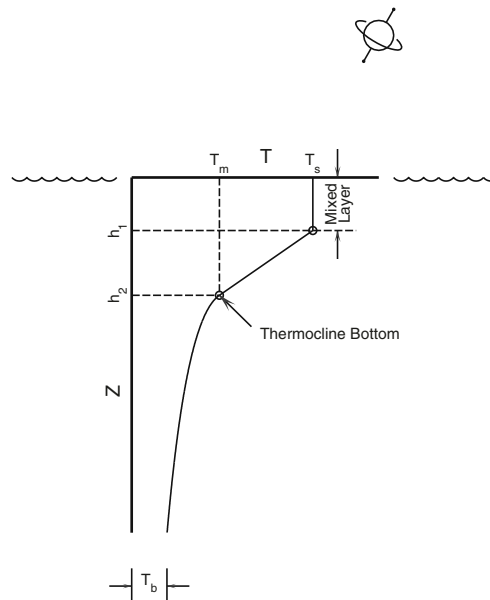


Fig. 2.27. SST and temperature profile (after Chu et al. 2000a, Journal of Atmospheric and Oceanic Technology)

depth, thermocline temperature gradient, and deep layer stratification are known (or given by climatological values), the degree of freedom of a vertical profile fitted by the model reduces to one: SST. When SST is observed, we may invert MLD_T , and, in turn, the vertical temperature profile with the known longtime-scale parameters. Using the parametric model, the inversion of the sub-surface thermal structure from satellite SST becomes a relationship between SST and sub-surface parameters.

2.9.1 Methodology

Keeping the minimal possible degrees of freedom, the thermal parametric model (2.2a)–(2.2f) can be simply depicted by (see Fig. 2.27),

$$T(z) = T_S, \quad (0 \geq z \geq h_1), \quad (2.34a)$$

$$T(z) = T_S + G_{th}(z + h_1), \quad (-h_1 \geq z \geq -h_2) \quad (2.34b)$$

$$T(z) = T_d + (T_{tb} - T_d) \exp \left[\frac{z_0^\alpha - (z_0 - z - h_2)^\alpha}{H^\alpha} \right], \quad (z \leq -h_2), \quad (2.34c)$$

where T_S , T_{tb} , and T_d are SST, temperature at the thermocline bottom depth, and a deep temperature; h_1 , h_2 , H are MLD_T , thermocline bottom depth, and a lower layer e-folding scale, respectively; and G_{th} is thermocline temperature gradient. The deep temperature, T_d , is the temperature at the deepest ocean depth such as 5,500 m in the climatological data (Levitus and Boyer 1994). For shallow water regions, T_d is, of course, not a real observed value but an extrapolated value to the deepest depth (e.g., 5,500 m). We use T_d to keep the data above the bathymetry, fitting the parametric model (2.34).

Here, the thermocline is featured by a linear profile (constant G_{th}), and the lower layer is characterized by a non-linear profile. To guarantee $T(z)$ and $dT(z)/dz$ continuous at $z = -h_2$,

$$T(h_2 + 0) = T(h_2 - 0), \quad \frac{dT(h_2 + 0)}{dz} = \frac{dT(h_2 - 0)}{dz} = G_{th} \quad (2.35)$$

determines the two additional parameters, z_0 and a . Differentiating (2.34) with respect to z and using (2.35) yield

$$z_0 = \left[\frac{HG_{th}}{a(T_{tb} - T_d)} \right]^{1/(a-1)}. \quad (2.36)$$

The parameter a cannot be zero nor be greater than or equal to one. Otherwise, z_0 becomes very large and distorts the e-folding decrease of temperature with depth. Chu et al. (2000a) use $a = 0.5$. Thus, from a vertical temperature profile we may extract three temperatures (T_S , T_{tb} , T_d), three depths

(h_1, h_2, H) , and one gradient G_{th} , seven parameters in total. We require continuity of temperature $z = -h_2$,

$$T_S - G_{\text{th}}(h_2 - h_1) = T_{\text{tb}}. \quad (2.37)$$

Therefore, any six of the seven parameters ($T_S, T_{\text{tb}}, T_d, h_1, h_2, H, G_{\text{th}}$) determine a vertical profile. Thus, the degrees of freedom of the thermal parametric model are six.

2.9.2 Example – South China Sea

The South China Sea has bottom topography (Fig. 2.28) that makes it a unique semi-enclosed ocean basin that is seasonally forced by a pronounced monsoon surface wind. Extended continental shelves (less than 100 m deep) exist along the north boundary and across the southwest portion of the basin, while steep slopes with almost no shelf are found along the eastern boundary. The deepest water is confined to an oblate bowl oriented SW–NE, centered at 13°N . The maximum depth is around 4,500 m. The MOODS temperature profiles of the South China Sea are used for the analysis. After quality control, a subset is used consisting of May (1932–1994) 10,153 profiles (Fig. 2.29).

In May, for the years 1986–1994, there are 40 daytime Multi-Channel SST (MCSST) and MOODS data points which are co-located in the same week,

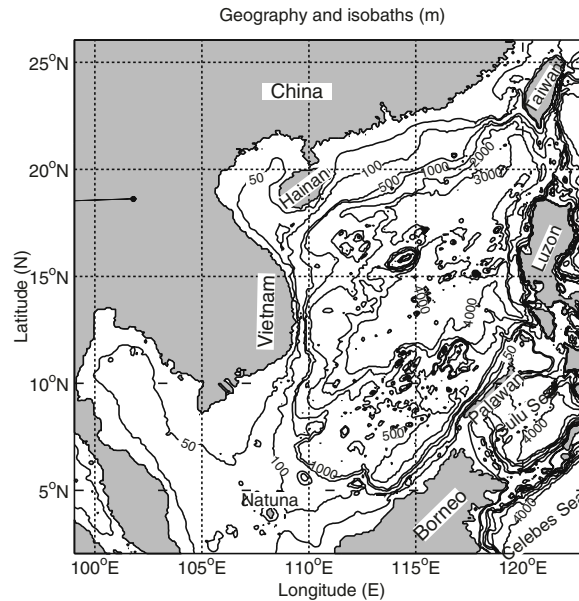


Fig. 2.28. Geography and isobaths showing the bottom topography of the South China Sea (from Chu et al. 2000a, *Journal of Atmospheric and Oceanic Technology*)

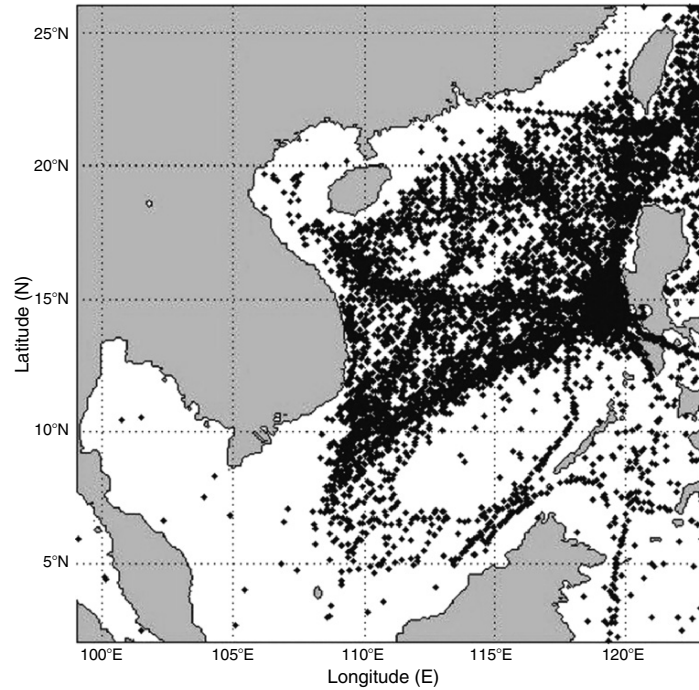


Fig. 2.29. Distribution of the MOODS profiles in May 1932–1994 (from Chu et al. 2000a, *Journal of Atmospheric and Oceanic Technology*)

marked by “*” in Fig. 2.30. Note that the number of “*” in Fig. 2.30 is much less than 40. This is due to several data points sharing the same spots. The 40 MOODS profiles were treated as a test data set. The MOODS data set excluding the test data is the training data set, consisting of 10,113 profiles.

The parametric model (2.34) and the iteration method illustrated in Sect. 2.4.3 are used to obtain a set of thermal parameters ($T_S, T_{tb}, h_1, h_2, H, G_{th}, T_d$) for each profile. The thermal parameters are averaged within $1^\circ \times 1^\circ$ grid. The averaged values are taken as the representative values for the grid cell. These values might not be representative in high gradient and coastal regions. Three types of cells were found in the South China Sea, representing co-located MCSST and MOODS data points (“*”), MOODS data points less than ten (“+”), and MOODS data points more than ten (“o”), as shown in Fig. 2.30.

Usually early May is the time of the summer monsoon onset in the South China Sea (Tao and Chen 1987). The thermal parameters obtained from processing the MOODS data set (May 1932–1994) may represent the thermal response of the South China Sea to the monsoon onset. Figure 2.31 shows the mean thermal parameter fields in May averaged over 1932–1994. Surface warm water (29.5°C) with a maximum temperature 30°C occupies most of

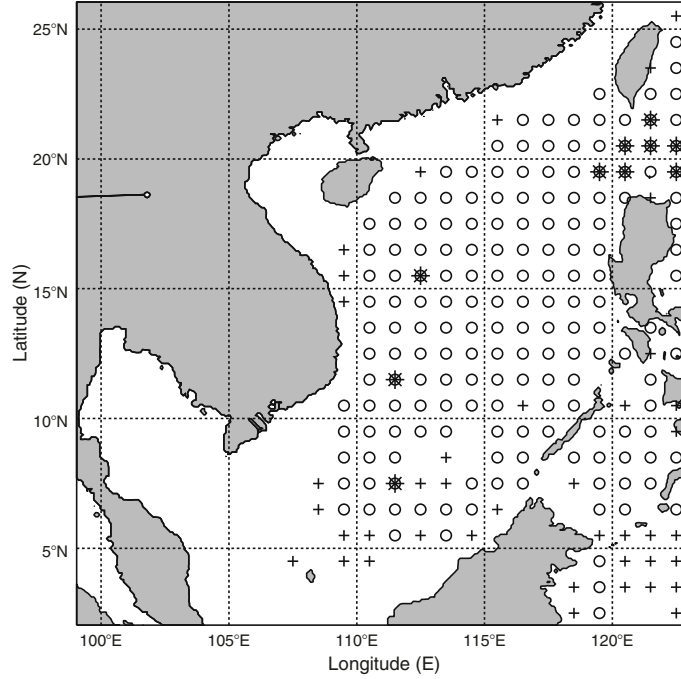


Fig. 2.30. Three types of $1^\circ \times 1^\circ$ cells represented by center grid points: co-locating and co-appearing of MCSST and MOODS data points (“*”), MOODS data points less than ten (“+”), and MOODS data points more than ten (“o”) (from Chu et al. 2000a, Journal of Atmospheric and Oceanic Technology)

the southern half of the South China Sea (Fig. 2.31a). The 29.5°C isotherm extended from the southeast corner of the Vietnam Coast (near $108^\circ\text{E}, 11^\circ\text{N}$) northeastward to the southwest coast of the Luzon Island (near $120^\circ\text{E}, 15^\circ\text{N}$). $\text{MLD}_T(h_1)$ varied from 10 to 40 m and had a latitudinal variation (Fig. 2.31b).

The southern South China Sea (south of 13°N) was characterized by a deep mixed layer ($h_1 \geq 20$ m) region with a maximum value of 40 m near Palawan Island. This suggests strong turbulent mixing in the southern part of the South China Sea immediately after the summer monsoon onset. The northern South China Sea (north of 13°N) has a shallow mixed layer ($h_1 \leq 20$ m) with a depth of 10 m. In the continental shelf regions, thermocline bottom depth (h_2) was quite shallow (≤ 100 m) and in the deep South China Sea basin, h_2 was deeper (> 100 m) with a maximum value of 400 m in Luzon Strait (Fig. 2.31c), where however, a weak thermocline (G_{th}) was found with a vertical temperature gradient around $0.04^\circ\text{C m}^{-1}$ (Fig. 2.31d). Temperature at $z = -h_2$ (T_{tb}) was coldest (12°C) in Luzon Strait and warmest (22°C) in the southern shelf region near Natuna Island (Fig. 2.31e). The lower layer e-folding thickness (H) represents the stratification in the layer below the thermocline. The smaller the value of H , the stratification of this layer is

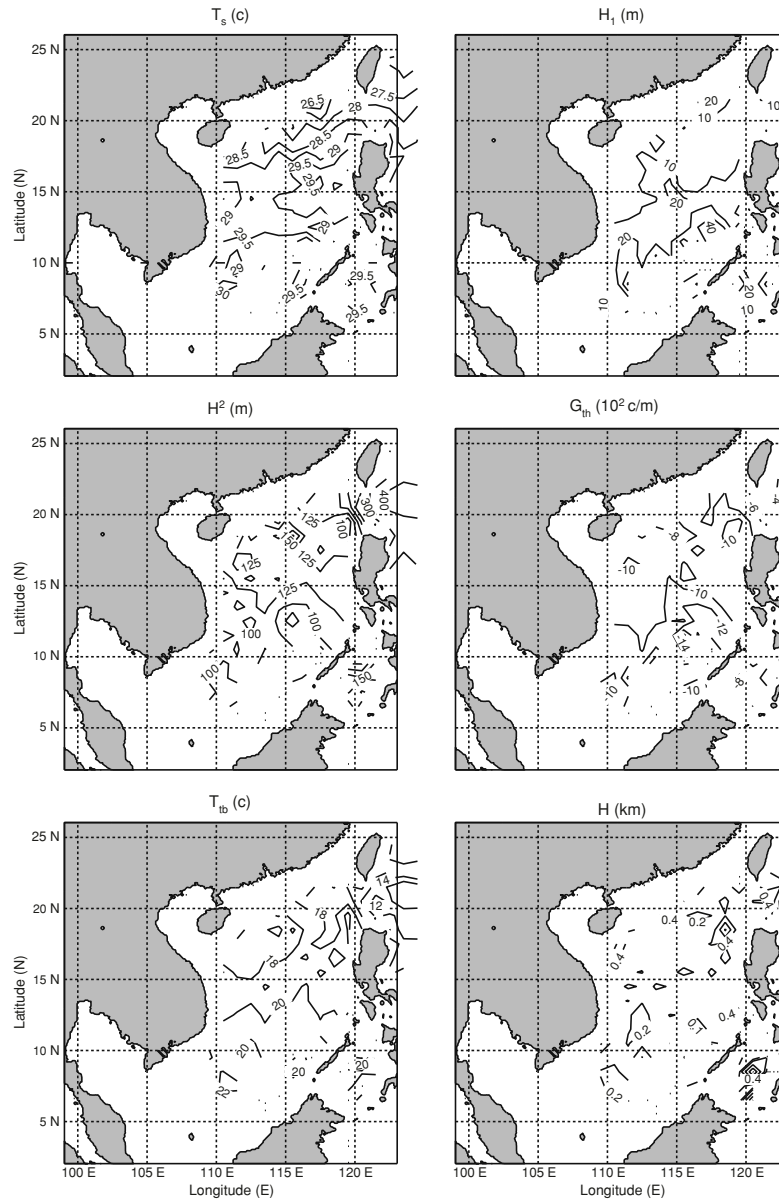


Fig. 2.31. Horizontal distributions of mean thermal parameters obtained from the training data set: (a) SST, (b) h_1 , (c) h_2 , (d) G_{th} , (e) T_{tb} , and (f) H (from Chu et al. 2000a, Journal of Atmospheric and Oceanic Technology)

stronger. In the deep basin, H is quite small (100–200 m), indicating weak stratification below the thermocline (Fig. 2.31f). Thus, the South China Sea

thermal response to the monsoon onset can be characterized by a northward advancement of warm surface water, strong turbulent mixing in the southern part with deeper mixed layers, and a relatively uniform deep layer below the thermocline in the deep basin.

2.9.3 Regression Method

For each $1^\circ \times 1^\circ$ grid cell, the mean values (for that cell) are subtracted from each of the thermal parameters ($T_S, T_{tb}, h_1, h_2, H, G_{th}$) to obtain the thermal parameter anomalies ($T'_S, T'_{tb}, h'_1, h'_2, H', G'_{th}$), to compute the correlation coefficients (Table 2.3), and to show the scatter diagrams (Fig. 2.32) between T'_S and the sub-surface parameter anomalies ($T'_{tb}, h'_1, h'_2, H', G'_{th}$). Both Table 2.3 and Fig. 2.32 indicate that among the sub-surface parameters, T'_S has the strongest linear association with h'_1 . The significance of the correlation can be evaluated by

$$t = \frac{r\sqrt{n-2}}{\sqrt{1-r^2}}, \quad (2.38)$$

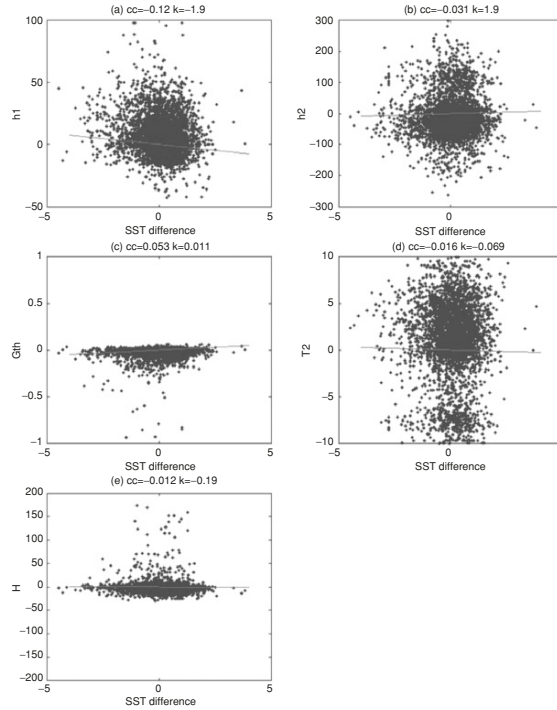


Fig. 2.32. Scatter diagrams of SST anomaly with various thermal parameter anomalies: (a) h'_1 , (b) h'_2 , (c) G'_{th} , (d) T'_{tb} , and (e) H' (from Chu et al. 2000a, Journal of Atmospheric and Oceanic Technology)

Table 2.3. Correlation coefficients with the SST anomaly

h'_1	h'_2	G'_{th}	T'_{th}	H'
-0.12	0.03	0.05	-0.01	-0.01

Table 2.4. The t -values of various correlation coefficients

h'_1	h'_2	G'_{th}	T'_{th}	H'
-15.77	3.98	6.64	-1.33	-1.33

which has a t -distribution with $(n - 2)$ degrees of freedom. Here, r is the correlation coefficient; n is the number of samples (10,153). We begin with the usual null hypothesis that there is no linear association between T'_S and the sub-surface parameter anomalies ($T'_{\text{tb}}, h'_1, h'_2, H', G'_{\text{th}}$). The critical t -value at significance level of 0.005 ($t_{0.005}$) is 2.576. Three absolute values of t computed by (2.38) are larger than the critical value (2.576): -15.77 between T'_S and h'_1 , 6.64 between T'_S and G'_{th} , and 3.98 between T'_S and h'_2 (Table 2.4).

Considering various correlation coefficients (Table 2.3) we may conclude that the correlation between the two short time-scale parameters T'_S and h'_1 is stronger than the correlation between T'_S and the long time-scale parameters ($T'_{\text{tb}}, h'_2, H', G'_{\text{th}}$). This in turn confirms the multi-time-scale hypothesis for the South China Sea thermal parameters.

A negative correlation between T'_S and h'_1 might not be true everywhere in the ocean. For example, Tully and Giovando (1963) found it difficult to establish such a relationship at least for a portion of the eastern sub-Arctic Pacific Ocean. However, Chu (1993) pointed out the possibility of such a negative correlation using an analytic ocean mixed layer model for the equatorial Pacific.

For each grid cell, the mean temperature profile, $\bar{T}(z)$, is computed. The temperature anomaly $T'(z)$ is obtained from subtracting the mean profile from each profile in the MOODS training data set. The simplest method of estimating sub-surface $T'(z)$ from SST' is to regress

$$T'(z) = b(z)\text{SST}', \quad (2.39)$$

where $b(z)$ is the regression coefficient obtained from the training data set.

2.9.4 Multi-Time-Scale Method

Having the current SST information in the inversion, we need to use the multi-decorrelation time-scale hypothesis. This hypothesis will reduce the degrees of freedom of the parameter space. The seven parameters vary on different time-scales: T_S and h_1 on a short decorrelation time-scale, $T_{\text{tb}}, T_d, h_2, H$, and G_{th} on a long decorrelation time-scale. The parameters on a long decorrelation time-scale are treated as a background data set which may be pre-determined by historical data. The parameters on the short time-scale are determined by

the inverse method. If the five parameters on the long time-scale are assumed to be pre-determined, the degree of freedom of this model reduces to one. Between the two short time-scale parameters T_S and h_1 , only one parameter is independent. Usually, we take T_S as the independent parameter. If T_S is given by satellite observation, (2.37) can be used to determine h_1 , and therefore the vertical profile. This is called the multi-time-scale method. The MOODS data for the South China Sea in May are used to verify this method.

If SST from the MOODS test data (40 data points) (Fig. 2.30) is taken as known values for the short time-scale parameter T'_S , we may use (a) the background long time-scale parameters: T_{tb}, h_2, H, G_{th} to determine h_1 (Figs. 2.31b,e); or (b) the temperature continuity condition at $z = -h_2$ (2.37) to determine h_1 ; in addition, the May climatological values for T_d (Levitus and Boyer 1994). With all the seven parameters given, vertical profiles $\hat{T}(z)$ can be easily constructed using (2.34). The 40 inverted profiles agree quite well with the observed profiles, however, the 40 regressed profiles have a larger mismatch with the observed profiles (Fig. 2.33).

2.9.5 Verification

Any model, including the regression and inverse models presented here, should be verified before claiming any practical usefulness. Usually, the model verification contains two parts: the rms error and the correlation coefficient between modeled and observed profiles.

The May climatological profiles at the MCSST points are used as the “least-effort” profiles. The standard deviation of the climatological profiles represents the first criterion for the model validity. If the model rms error is larger than the climatological standard deviation, the model does not have any practical usefulness. The model becomes valid only if its rms error is smaller than the climatological standard deviation.

Figure 2.34a shows the vertical distribution of the model rms and climatological standard over the whole test data area. The rms errors for both regression and inverse methods increase with depth from the surface to maximum values around 1.8°C near 100 m depth, and then reduce relatively with depth. At all depths except near 100 m depth, the rms errors for the inverse model are smaller than the rms errors for the regression model, which in turn are smaller than the climatological standard deviation. The depth of 100 m is approximately the mean thermocline bottom depth (Fig. 3.31). This implies some difficulty in inverting the temperature at the thermocline bottom depth. Overall, the vertically averaged inverse model rms error (around 0.72°C) is smaller than the regression model rms error (around 1.06°C), which in turn is smaller than the climatological standard deviation (1.51°C).

The correlation coefficients between modeled and observed profiles at all depths represent the second criterion for the model validity. The correlation coefficient for the inverse model varies with depth between 1 and 0.5 and has a vertical mean value of 0.79. Use of (6) leads to $t = 3.559$ for $n = 40$, and

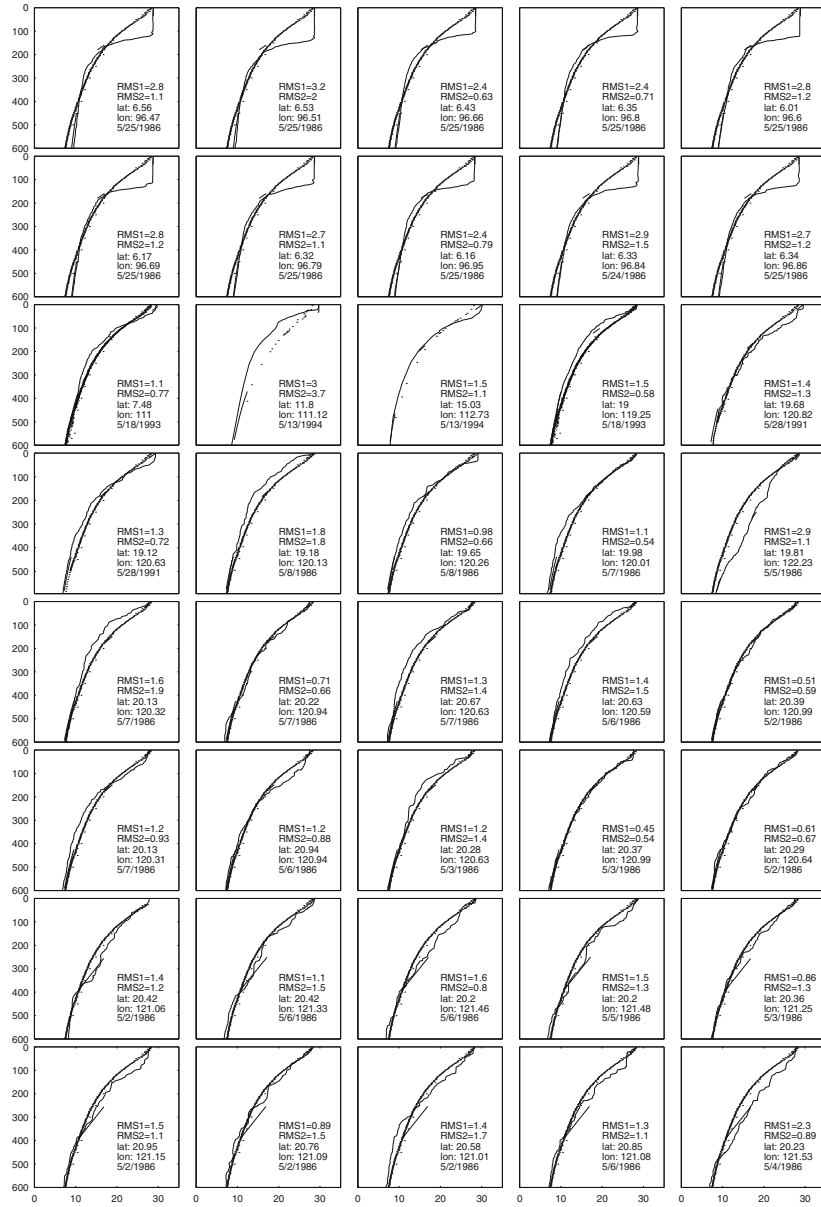


Fig. 2.33. Comparison between 40 regressed (*dotted*), inverted (*dash-dotted*), and observed (*solid*) profiles (from Chu et al. 2000a, Journal of Atmospheric and Oceanic Technology)

$r = 0.5$. This value is much larger than the critical t -value (2.576), which means significant correlations at confidence level of 0.005 between the in-

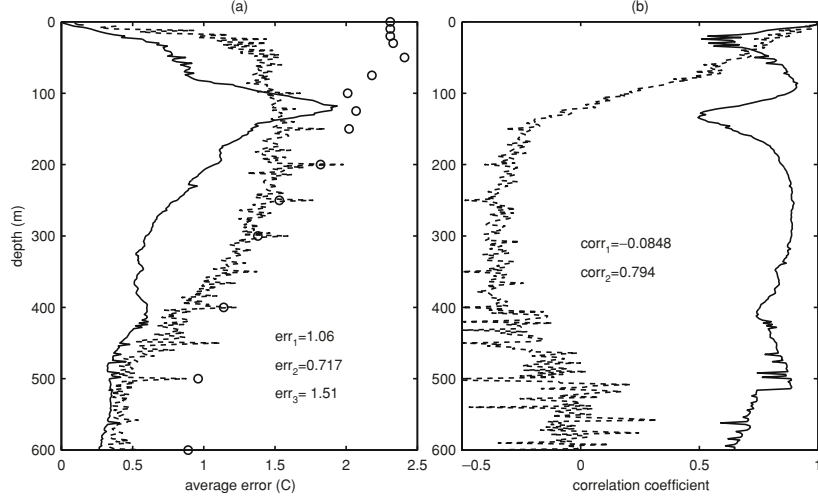


Fig. 2.34. Vertical distribution of (a) inverse model rms errors (*solid*), regression model rms errors (*dotted*) and climatological standard deviation (*circle*), and (b) correlation coefficients between observed and inverted (*solid*), observed and regressed (*dotted*) profiles (from Chu et al. 2000a, Journal of Atmospheric and Oceanic Technology)

verted and the observed profiles for all depths exist. However, the correlation coefficient for the regression model decreases rapidly from one at the surface to zero near 100 m depth, and then becomes negative below that depth (Fig. 2.34b), which indicates no significant positive correlations between the regressed and the observed profiles for the sub-layer depths. The small mean rms error (0.72°C) and high positive correlation coefficient (0.79) make this multi-time-scale inverse method valid for practical use.

2.9.6 Limitation of the Multi-Time Scale Hypothesis

The key issue of inverting sub-surface thermal structure from SST is to reduce the degree of freedom of the thermal parameter space by multi-time-scale hypothesis. To apply this method globally, we should first test the validity of this hypothesis. This can be done by the correlation analysis. If correlation between T'_S and h'_1 is stronger than the correlation between T'_S and the other parameters ($T'_{tb}, h'_1, h'_2, H', G'_{th}$), the multi-time-scale hypothesis is confirmed and the use of this inverse method is feasible. If correlation between T'_S and h'_1 is not significant, such as Tully and Giovando (1963) found in one region of the North Pacific, it is very hard to use this method for that region. Furthermore, the rms error and correlation tests should be conducted after the inversion to see the real usefulness.

2.10 Autocorrelation Functions

Various ocean systems such as fronts, eddies, and water masses have different temporal and spatial scales. These scales feature a system's life span and spatial extent both horizontally and vertically. For example, White et al. (1982) identified spatial correlation scales in the western Pacific of about 600 km in the tropics (south of 17.5°N) and 300 km in the sub-tropics (north of 17.5°N); Ozsoy et al. (1989) found the spatial scales to be 200–250 km in the Levantine Basin of the Mediterranean Sea; Chu et al. (1997a; 2002b) identified the seasonal variation of the temporal and spatial scales in the Yellow Sea and Sea of Japan (known as the East Sea in Korea) using the autocorrelation function: 90 km from 158 km in winter to 251 km in summer, and the seasonal variation of the surface temporal decorrelation scale is around 2.4 days from 14.7 days in winter to 12.3 days in summer.

The autocorrelation function of (T, S) fields,

$$\eta(l) = \frac{1}{s^2} \int_L \theta'(l_0)\theta'(l_0 + l)dl_0, \quad (2.40)$$

can be used to represent (temporally and spatially) thermohaline variability. Here, θ represents temperature or salinity and θ' is its anomaly; l_0 denotes the independent space/time vectors defining the location of points in a sampling space L ; l is the space/time lag; and s^2 is the variance of θ ; η is computed by paring the anomalies into bins depending upon their separation in space/time, l . The values η will be obtained from calculating the correlation coefficient for all the anomaly pairs in each bin, which will be constructed for the combination of different lags.

2.10.1 Bin Method

For quasi-isolated basin such as the Yellow Sea and the Japan Sea, it is reasonable to assume that the autocorrelation function depends only on the distance between two locations in order to reduce the number of bins. Without this assumption, the number of bins is very large, e.g., 27,000 if each of the temporal and spatial (x and y) lags has 30 bins.

Chu et al. (1997a; 2002b) proposed a simple bin method to calculate the autocorrelation function for the East Asian marginal seas such as the Yellow Sea and Sea of Japan. For each observation θ_{obs} at depth z (or some equivalent vertical coordinate), the closest grid point climatological value (such as GDEM described in Sect. 3.1.2) $\bar{\theta}_C$ is found and the anomaly,

$$\theta' = \theta_{\text{obs}} - \bar{\theta}_C,$$

is computed. Every individual anomaly, θ' , is paired with the other data points, $\hat{\theta}'$, within the temporal domain for analysis (such as same season). The temporal and spatial differences or lags are calculated between the two anomalies.

The anomaly pair $(\theta', \hat{\theta}')$ is then placed in the corresponding temporal lag bin with increment Δt (such as one day) and spatial lag bin with increment Δr (such as 10 km). If the spatial lag is within Δr_0 (5 km) and the temporal lag is within Δt_0 (0.5 day), the corresponding pair is placed into bin $(0, 0)$. If the horizontal lag is between $m \Delta r - \Delta r_0$ and $m \Delta r + \Delta r_0$, and the temporal lag is between $n \Delta t - \Delta t_0$ and $n \Delta t + \Delta t_0$, the pair is placed into the bin (m, n) with the pair number $P(m, n)$.

After the anomaly pairs have been spatially and temporally sorted, the autocorrelation function for each bin (m, n) is computed by

$$\eta(m, n) = \frac{\sum_{\text{bin}(m,n)} \theta' \hat{\theta}'}{\sum_{\text{bin}(m,n)} (\theta')^2}, \quad (2.41)$$

which varies with the spatial and temporal lags (m, n) . Equation (2.41) indicates that the computed η for the bin (m, n) is in fact the estimation of the autocorrelation coefficient of pairs in that bin. A t -value for verifying the significance of a sample correlation coefficient is given by (see a statistical text book

$$t = \frac{\eta \sqrt{P-2}}{\sqrt{1-\eta^2}}, \quad (2.42)$$

which is a value of the statistic T having a t -distribution with $(P-2)$ degree of freedom. Using α as the level of significance, a criterion η_α is obtained

$$\eta_\alpha = \frac{t_\alpha}{\sqrt{P-2+t_\alpha^2}}. \quad (2.43)$$

The estimated autocorrelation function is significant on the level of α if $\eta(m, n) > \eta_\alpha$.

The measured variance s^2 is divided into signal (s_s^2) and noise (s_n^2) whereby

$$s^2 = s_s^2 + s_n^2. \quad (2.44)$$

The noise variance is brought on from two sources, geophysical and instrumentation errors. Here, the geophysical error is unresolved thermal variability with scales smaller than the typical time and space scales between two temperature profiles. In this study the unresolved scales are 0.5 day and 5 km. The autocorrelation function at the first bin $(0, 0)$ does not represent the correlation between profiles paired by themselves, and therefore does not equal one. Following Sprintall and Meyers (1991), the signal-to-noise ratio (SNR) is computed by

$$\lambda = \frac{s_s}{s_n} = \sqrt{\frac{\eta(0,0)}{1-\eta(0,0)}}. \quad (2.45)$$

The larger the value of λ , the less geophysical error exists. If $\eta(0,0) = 1$, there is no noise, $\lambda = \infty$; and if $\eta(0,0) = 0$, there is no signal. If $\lambda > 2$, the ratio of the signal variance, s_s^2 , to the noise variance, s_n^2 , is greater than four, which is considered quite good conditions by White et al. (1982) and Sprintall and Meyers (1991).

2.10.2 Autocorrelation Function in Deep and Shallow Water

Difference is found in calculating the autocorrelation function between deep and shallow (such as continental shelf) water. The deep ocean temperature profiles tend to follow the pattern of mixed layer, a thermocline, and a deeper layer with a slow decrease in temperature with depth. Shallow water does not consistently mimic this pattern. It may range from the classical profile to completely isothermal. The coastal water is largely affected by bathymetry, river run-off, internal waves, and tides. Therefore, the temporal and horizontal scales are also under the strong influence of these forcing factors, and should have different vertical structure from the deep water. For deep waters, the vertical variation of the temporal and horizontal scales are usually obtained from the temperature fields at certain depths (e.g., 100, 200, and 300 m in White et al. 1982) or from SST and the depth of certain temperature (e.g., depth of 20°C in Sprintall and Meyers (1991)). For deep water, these depths are easily determined (Fig. 2.35a).

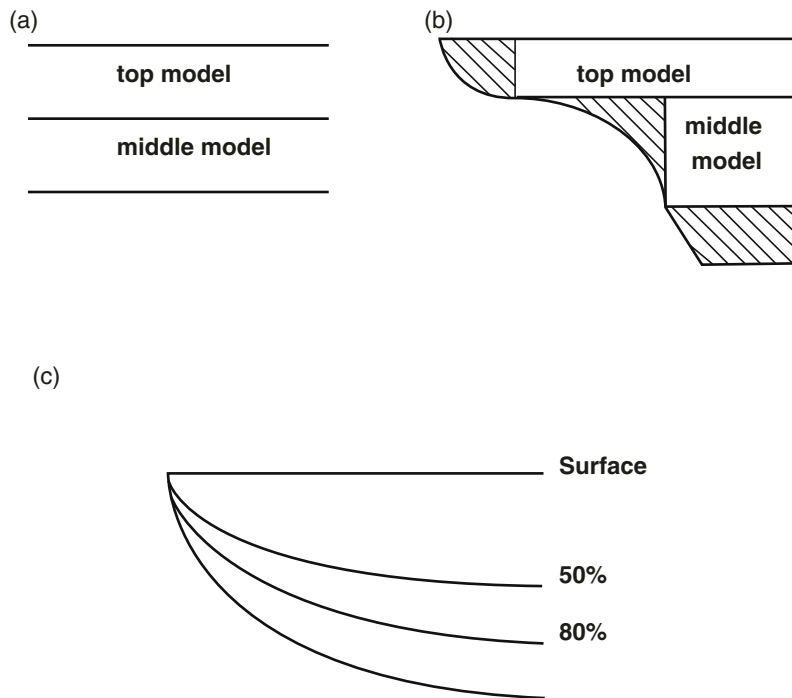


Fig. 2.35. Depths for computing autocorrelation function for the Yellow Sea: (a) horizontal levels for deep water, (b) horizontal levels for continental shelf, and (c) bottom following levels (from Chu et al. 1997a, *Journal of Geophysical Research*)

2.10.3 Shallow Water – Yellow Sea Temperature Field

(a) Topographic – following level. For shallow water (such as the Yellow Sea, see Fig. 2.6), horizontal and temporal scales should not be identified at given depths. This is because a single layer structure in the Yellow Sea appearing in winter, which makes the depth of certain isotherm non-representative for the sub-surface thermal fields; and because of a strong influence of horizontally varying bathymetry on the shallow water, which causes the temperature fields at different depths to be non-representative of sub-surface fields. A sloping bottom for shallow water, any chosen depths will lead to some areas (hashed area in Fig. 2.35b) not covered by any sub-models. Therefore, it is more reasonable to calculate the autocorrelation function at terrain-following coordinate,

$$\sigma_{\text{topo}} = -\frac{z}{H}. \quad (2.46)$$

Here H is the water depth, and z is the vertical coordinate. Mid-water properties are represented by $\sigma_{\text{topo}} = 5$, and the near-bottom water features are portrayed by $\sigma_{\text{topo}} = 8$ (Fig. 2.35c). The analysis on the σ_{topo} -coordinate system benefits initializing popular σ_{topo} -coordinate coastal models, such as the Princeton Ocean Model (Blumberg and Mellor 1987), but has disadvantage during weakly forced and stratified periods. The deeper σ_{topo} -levels will be within the mixed layer environment in shoal areas and below the mixed layer in the deeper portions of the basin.

(b) Pair-number. The MOODS data have approximately 35,658 profiles (during 1929–1991) for the Yellow Sea shelf. The pair-number distributions, $P(m, n)$, for the four seasons are depicted in Fig. 2.36. Uneven distribution is seen in the temporal and spatial bins. Almost everywhere $P(m, n)$ is equal or more than 500. The maximum $P(m, n)$ is located in bins with near 1–2 day temporal lags and 80–120 km spatial lags.

Since the pair-number for each bin, $P(m, n)$, is given, the criterion for the autocorrelation function (η_α) for a particular level of significance (α) can be calculated using (2.43). The criterion η_α has a strong seasonal variation (Fig. 2.37) due to the change of pair numbers $P(m, n)$. It is smaller for most bins in summer than in winter. Figure 2.38 shows the dependence of $\eta(m, n)$ on the temporal and spatial lags in winter and summer. The autocorrelation function decreases with temporal and spatial lags faster in winter than in summer.

When

$$\eta^{(\sigma)}(m, n) > \eta_\alpha, \quad (2.47)$$

the estimated autocorrelation function is significant on the level of α . Since both $\eta^{(\sigma)}(m, n)$ and η_α have seasonal variations, the significance level should also be changed with seasons. The significant surface autocorrelation function estimation ($\alpha = 0.10$) is limited to the left lower corner of the (τ, r) plane with $\tau < 15$ day and $r < 200$ km in winter (Fig. 2.37a) and occupies nearly the whole left part of the (τ, r) plane with $\tau < 20$ day in summer (Fig. 2.37b).

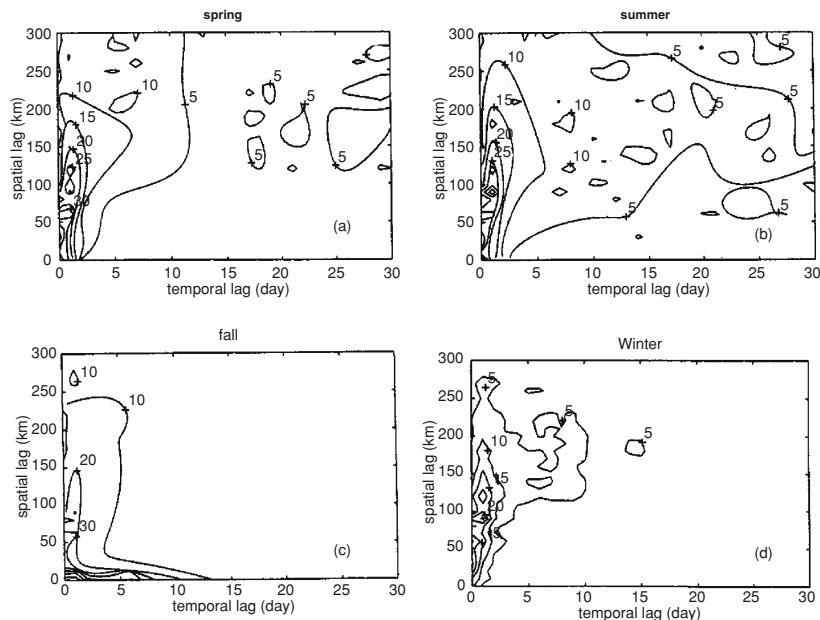


Fig. 2.36. The pair-number (in 100) distribution in the (m, n) space of the Yellow Sea for (a) spring, (b) summer, (c) fall, and (d) winter (from Chu et al. 1997a, *Journal of Geophysical Research*)

Such a seasonal variability in significant autocorrelation function estimations leads to a significant difference in statistical parameters such as decorrelation scales.

(c) Temporal lag. After the anomaly pairs have been spatially and temporally sorted, the autocorrelation function of temperature is computed using (2.41). Temporal dependence of the autocorrelation $\eta^{(\sigma)}(m, n)$ can be easily discussed by $\eta - n$ curves at several different spatial lags, e.g., $m = 0$ (“no lag”), $m = 1$ (10 km lag), and $m = 15$ (150 km lag). These curves are plotted for different seasons and three σ_{topo} levels (0, 0.5, and 0.8) in order to see the seasonal and vertical variations. The three winter curves, $\eta^{(\sigma)}(0, n)$, $\eta^{(\sigma)}(1, n)$, and $\eta^{(\sigma)}(15, n)$, are plotted for the surface, $\sigma_{\text{topo}} = 0$ (Fig. 2.39a), the mid-level, $\sigma_{\text{topo}} = 0.5$ (Fig. 2.39b), and the near-bottom, $\sigma_{\text{topo}} = 0.8$ (Fig. 2.39c).

The three summer curves, $\eta^{(\sigma)}(0, n)$, $\eta^{(\sigma)}(1, n)$, and $\eta^{(\sigma)}(15, n)$ are plotted for the surface, $\sigma_{\text{topo}} = 0$ (Fig. 2.40a), the mid-level, $\sigma_{\text{topo}} = 0.5$ (Fig. 2.40b), and the near-bottom, $\sigma_{\text{topo}} = 0.8$ (Fig. 2.40c). The autocorrelation function has the following features: (1) Its temporal variability weakens as the spatial lag increases, and becomes extremely small (near constantly low values) at the spatial lag $m = 15$ (150 km) except for the summer surface field (Fig. 2.40a), where it decreases quasi-linearly with the time lag (dotted curve line in Fig. 2.40a). (2) Its vertical variability is quite small during

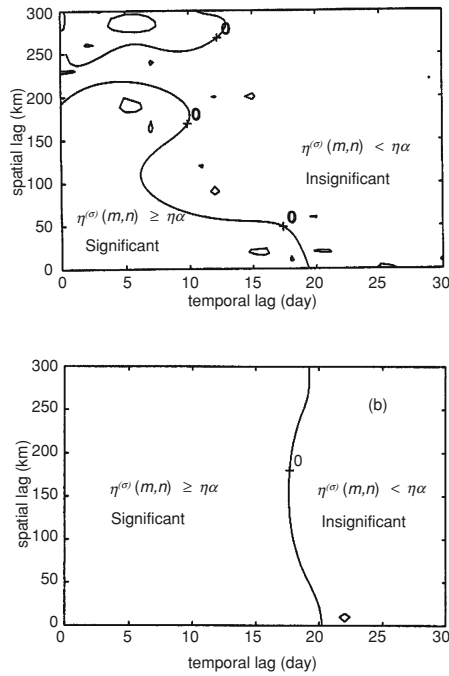


Fig. 2.37. Criterion ($\alpha = 0.10$) for the surface autocorrelation function estimation in the Yellow Sea: (a) winter, and (b) summer (from Chu et al. 1997a, Journal of Geophysical Research)

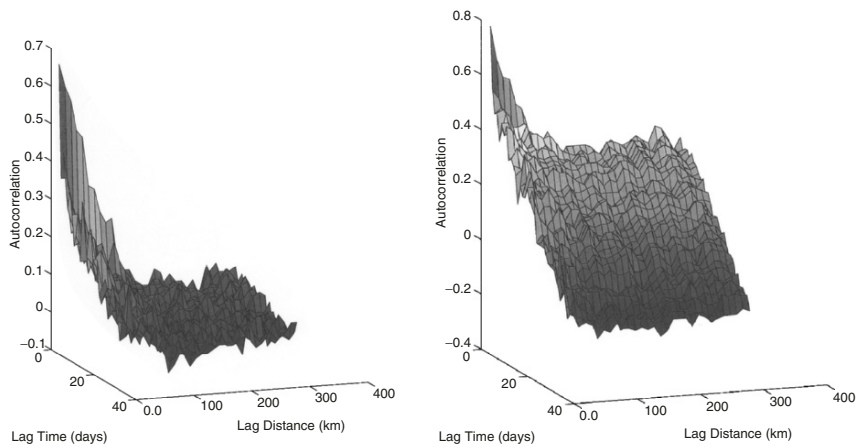


Fig. 2.38. Dependence of autocorrelation function η for the Yellow Sea temperature field on the temporal and spatial lags: (a) winter, and (b) summer. Note that the decrease of η with lag is faster in winter than in summer

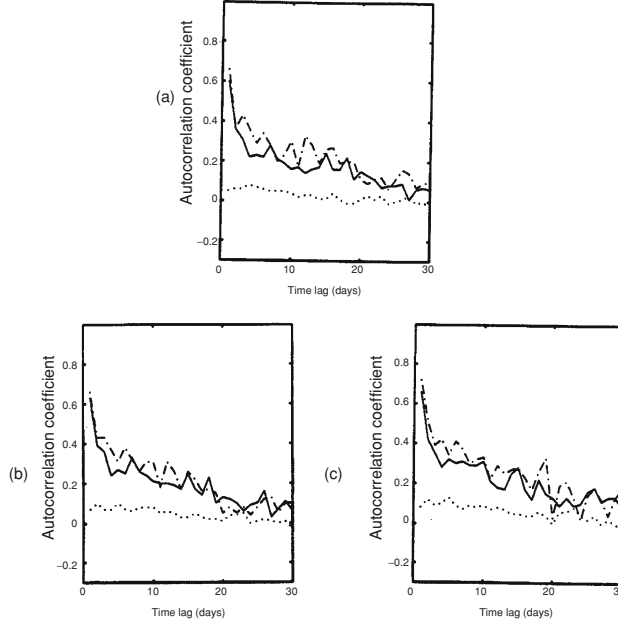


Fig. 2.39. Winter temporal variation of autocorrelation function at different spatial lags: $m = 0$ (no lag, *dash-dot curve*), $m = 1$ (10 km lag, *solid curve*), and $m = 15$ (150 km lag, *dotted curve*) for three levels: **(a)** surface ($\sigma_{\text{topo}} = 0$), **(b)** mid-level ($\sigma_{\text{topo}} = 0.5$), and **(c)** near bottom ($\sigma_{\text{topo}} = 0.8$) (from Chu et al. 1997a, Journal of Geophysical Research)

winter (Fig. 2.39) and not so small during summer (Fig. 2.40). This coincides with the single-layer structure in winter and the multi-layer structure in summer (see Sect. 2.4). (3) During summer its temporal variability weakens with depth. The surface autocorrelation function shows a fast reduction with time lag n (Fig. 2.40a). At mid-level ($\sigma_{\text{topo}} = 0.5$), it has slower reduction than the surface as n increases (Fig. 2.40b). At near-bottom ($\sigma_{\text{topo}} = 0.8$), it fluctuates around certain values (0.5 for no-spatial lag, 0.28 for 10 km lag, and almost 0 for 150 km) as n increases (Fig. 2.40c).

(d) Spatial lag. The spatial dependence of autocorrelation function, $\eta^{(\sigma)}(m, n)$, can be easily discussed by $\eta - m$ curves at several different temporal lags, e.g., $n = 0$ (no lag), $n = 1$ (one day lag), and $n = 15$ (15 day lag). These curves are plotted for different seasons and three σ_{topo} levels (0, 0.5, and 0.8) in order to see the seasonal and vertical variations. The three winter curves, $\eta^{(\sigma)}(m, 0)$, $\eta^{(\sigma)}(m, 1)$, and $\eta^{(\sigma)}(m, 15)$, are plotted for the surface, the surface, $\sigma_{\text{topo}} = 0$ (Fig. 2.41a), the mid-level, $\sigma_{\text{topo}} = 0.5$ (Fig. 2.41b), and the near-bottom, $\sigma_{\text{topo}} = 0.8$ (Fig. 2.41c).

The three summer curves, $\eta^{(\sigma)}(m, 0)$, $\eta^{(\sigma)}(m, 1)$, and $\eta^{(\sigma)}(m, 15)$, are plotted for the surface, $\sigma_{\text{topo}} = 0$ (Fig. 2.42a), the mid-level, $\sigma_{\text{topo}} = 0.5$

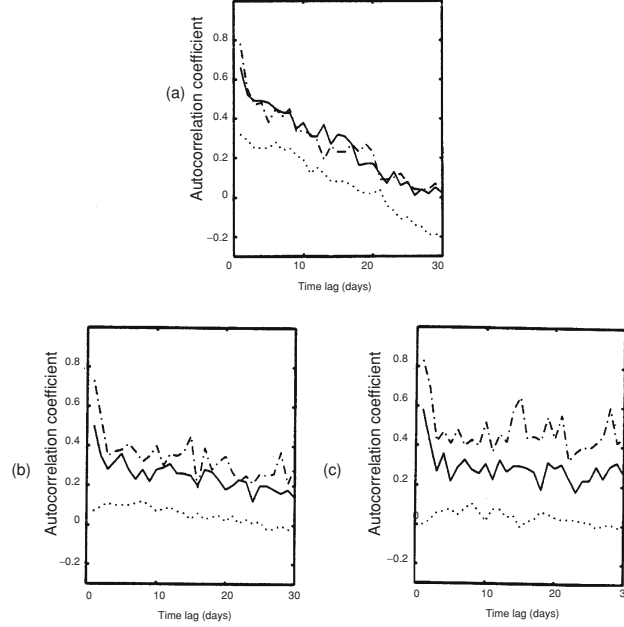


Fig. 2.40. Summer temporal variation of autocorrelation function at different spatial lags: $m = 0$ (no lag, *dash-dot curve*), $m = 1$ (10 km lag, *solid curve*), and $m = 15$ (150 km lag, *dotted curve*) for three levels: (a) surface ($\sigma_{\text{topo}} = 0$), (b) mid-level ($\sigma_{\text{topo}} = 0.5$), and (c) near bottom ($\sigma_{\text{topo}} = 0.8$) (from Chu et al. 1997a, Journal of Geophysical Research)

(Fig. 2.42b), and the near-bottom, $\sigma_{\text{topo}} = 0.8$ (Fig. 2.42c). The autocorrelation function has the following features: (1) Its spatial variability weakens as the temporal lag increases, and becomes very small (smaller than 0.2) at the time lag $n = 15$ day except for the summer near-bottom field (Fig. 2.42c), where the horizontal variability of the autocorrelation function at $n = 15$ day is quite close to that at $n = 0$ (no time lag) and $n = 1$ day lag, as shown in Fig. 2.42c. This indicates that during summer the tidal effect (on the time-scale is less or equal than one day) is important for the Yellow Sea bottom thermal field. (2) Its vertical variability is quite small during the winter (Fig. 2.41) and not so small during the summer (Fig. 2.42). This coincides with the single-layer structure in the winter and the multi-layer structure in the summer months (see Sect. 2.4.2). (3) During summer, the spatial variability of the autocorrelation function strengthens with depth. The surface autocorrelation function shows a relatively weak reduction versus spatial lag (Fig. 2.42a). The mid-level ($\sigma_{\text{topo}} = 0.5$) autocorrelation function has a stronger reduction than the surface as the spatial lag increases (Fig. 2.42b). The near-bottom ($\sigma_{\text{topo}} = 0.8$) autocorrelation function has the strongest reduction versus spatial lag (Fig. 2.42c).

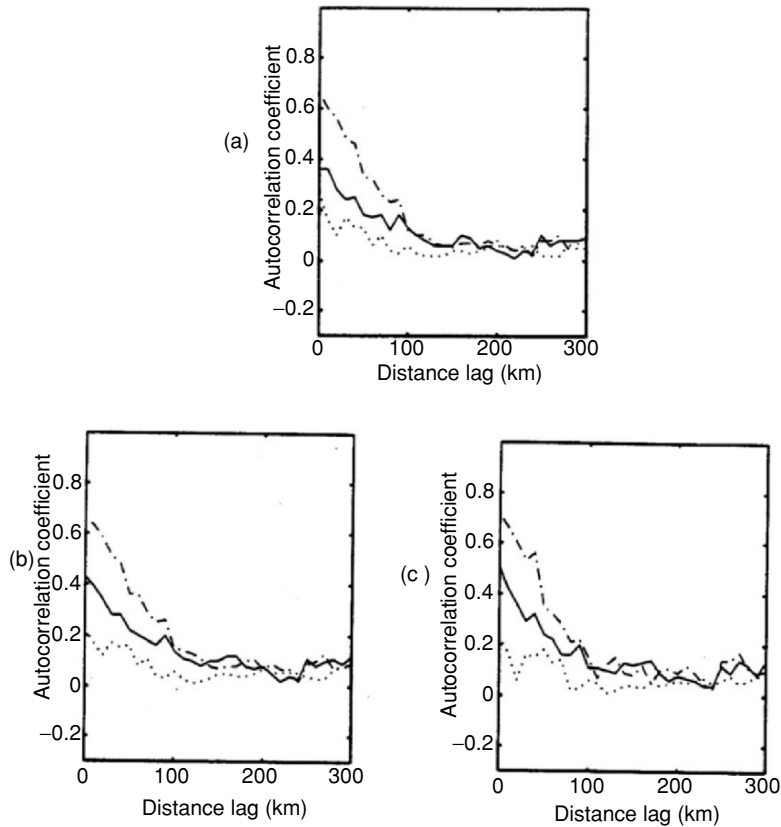


Fig. 2.41. Winter spatial variation of autocorrelation function at different temporal lags: $n = 0$ (no lag, *dash-dot curve*), $n = 1$ (one day lag, *solid curve*), and $n = 15$ (15 day lag, *dotted curve*) for three levels: (a) surface ($\sigma_{\text{topo}} = 0$), (b) mid-level ($\sigma_{\text{topo}} = 0.5$), and (c) near bottom ($\sigma_{\text{topo}} = 0.8$) (from Chu et al. 1997a, Journal of Geophysical Research)

2.11 Temporal and Spatial Decorrelation Scales

Various ocean systems such as fronts, eddies, and water masses have different temporal and spatial scales. These scales feature a system's life span and spatial extent both horizontally and vertically. For example, White et al. (1982) identified spatial decorrelation scales in the western Pacific of about 600 km in the tropics (south of 17.5°N) and 300 km in the sub-tropics (north of 17.5°N) while Ozsoy et al. (1989) found the spatial scales to be 200–250 km in the Levantine Basin of the Mediterranean Sea. Chu et al. (1997a; 2002b) use the Gaussian model to fit the autocorrelation function and then to identify the decorrelation scale as the scale for the spatial or temporal variability.

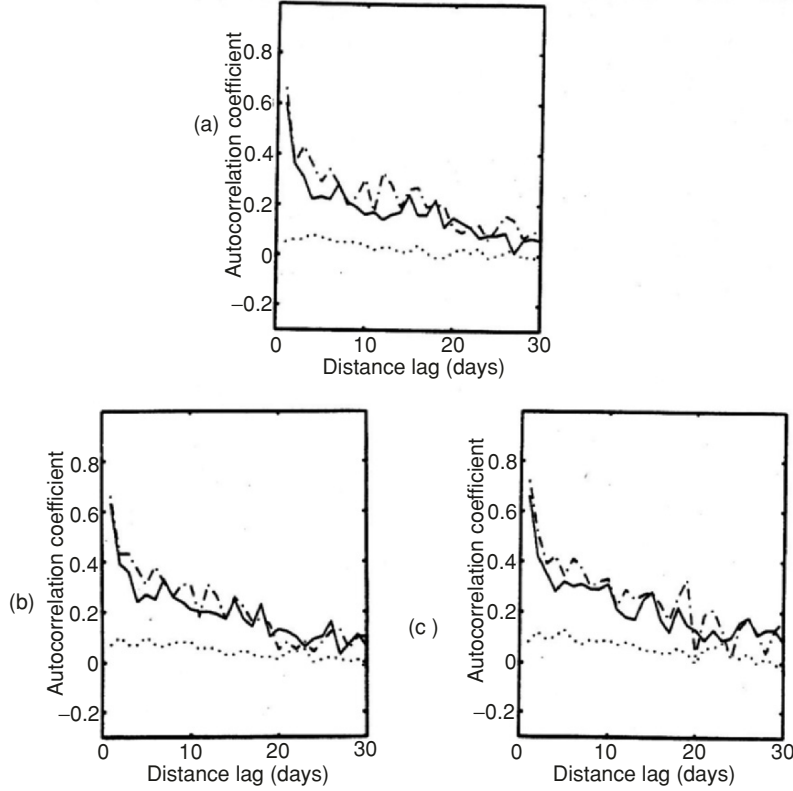


Fig. 2.42. Summer spatial variation of autocorrelation function at different temporal lags: $n = 0$ (no lag, *dash-dot curve*), $n = 1$ (one day lag, *solid curve*), and $n = 15$ (15 day lag, *dotted curve*) for three levels: **(a)** surface ($\sigma_{\text{topo}} = 0$), **(b)** mid-level ($\sigma_{\text{topo}} = 0.5$), and **(c)** near bottom ($\sigma_{\text{topo}} = 0.8$) (from Chu et al. 1997a, Journal of Geophysical Research)

2.11.1 Gaussian Model

The Gaussian model

$$\hat{\eta}^{(\sigma)}(m, n) = \hat{\eta}^{(\sigma)}(0, 0) \exp \left[-A_{\sigma}^2 (m \Delta r)^2 - C_{\sigma}^2 (n \Delta \tau)^2 \right], \quad (2.48)$$

is often used to fit the autocorrelation function (Clancy and Pollak 1983; Phoebus 1988; Chu et al. 1997a; 2002b). Here, $\hat{\eta}^{(\sigma)}(m, n)$ denotes the Gaussian fit of the autocorrelation function at the level σ_{topo} in the bin with the spatial separation $m \Delta r$, and the temporal separation $n \Delta \tau$ with $(\Delta r, \Delta \tau)$ the increments for the space/time separation. A_{σ}^{-1} and C_{σ}^{-1} are horizontal and temporal decorrelation scales at the level σ_{topo} . The dominant space/time scales obtained from the autocorrelation function are important not only in determining sampling density but also for the optimum interpolation of the

observed data. For example, the US Navy's Optimal Thermal Interpolation System runs everyday, combines real-time data, climatology, and predictions from ocean mixed layer models to represent an accurate picture of the ocean thermal structure on global and regional scales (Phoebus 1988; Clancy and Pollak 1983). Before running this system, the temporal and spatial scales, A_σ^{-1} and C_σ^{-1} , should specify.

2.11.2 *F*-Test for the Gaussian Model

One can test the null hypothesis H_0 to indicate that the Gaussian model (2.48) is not significant by merely forming the ratio (see any statistics book)

$$F = \frac{\text{SSR}/k}{\text{SSE}/(l - k - 1)}, \quad (2.49)$$

where $k = 2$, l is the total number of bins in either spatial or temporal lags, and

$$\text{SSR} = \sum_m \sum_n \left[\ln \hat{\eta}^{(\sigma)}(m, n) - \text{mean}(\ln \hat{\eta}^{(\sigma)}(m, n)) \right]^2, \quad (2.50)$$

$$\text{SSE} = \sum_m \sum_n \left[\ln \hat{\eta}^{(\sigma)}(m, n) - \ln \eta^{(\sigma)}(m, n) \right]^2, \quad (2.51)$$

denote a regression sum of squares and a residual mean square, respectively. When

$$F > F_\alpha(k, l - k - 1), \quad (2.52)$$

the null hypothesis H_0 is rejected. The Gaussian model is significant. Here $F_\alpha(k, l - k - 1)$ satisfies the F -distribution with $\nu_1 = k$, $\nu_2 = l - k - 1$, and a confidence level of α . The F -values for different levels and seasons are listed in Table 2.5. All the F -values exceed the critical value (5.45) of the F -distribution for 2 and 28 degrees of freedom at $\alpha = 0.01$. Therefore, the Gaussian model is reasonable for the Yellow Sea thermal autocorrelation function.

2.11.3 Seasonal Variability of the Decorrelation Scales

The computed autocorrelation function for different seasons and levels ($\sigma_{\text{topo}} = 0, 0.5, 0.8$) are then fitted to a Gaussian function of the form of (2.48) by the regression method, which lead to the spatial and temporal decorrelation scales,

Table 2.5. F -values for estimating the Yellow Sea autocorrelation function

σ_{topo} -level	winter	summer
surface	28.64	12.26
0.5	26.43	11.71
0.8	25.01	11.34

Table 2.6. Seasonal and vertical variations of decorrelation scales of the Yellow Sea

Season	Level	temporal scale (day)	spatial scale (km)	SNR (λ)
Winter	0	14.7	158	2.06
	0.5	14.7	167	1.88
	0.8	15.2	172	2.21
Summer	0	12.3	251	3.00
	0.5	15.8	169	2.21
	0.8	17.2	157	3.00

A_σ^{-1} and C_σ^{-1} , respectively. Table 2.6 presents these decorrelation scales and SNRs for winter and summer.

The SNR for both winter and summer are higher than that for the deep waters of the Eastern Equatorial Pacific, which is around 1.0 as reported by Sprintall and Meyers (1991). This infers that the temperature signal in the Yellow Sea shelf is stronger than in the open waters. In both winter and summer seasons, the largest noise occurs at the mid-level ($\sigma_{\text{topo}} = 0.5$). This is expected since this is the transition layer where both the meteorological and topographic effects occur. The SNR is greater in summer than in winter.

The vertical variation in temporal and spatial decorrelation scales is smaller in winter than in summer. In winter, the temporal scale varies only a half-a-day and the horizontal scale changes only 14 km among three different levels ($\sigma_{\text{topo}} = 0, 0.5, 0.8$). This vertically quasi-uniformity in decorrelation scales also represents the winter single-layer structure caused by the strong surface forcing. In the winter season, the Yellow Sea shelf has strong mixing due to both strong winds and the upward buoyancy flux. With a large part of the Yellow Sea having depths less than 50 m, vertical mixing reaches the bottom and creates isothermal profiles. Thus, decorrelation scales will be similar from the surface to the near-bottom ($\sigma_{\text{topo}} = 0.8$) water column. In summer, the temporal scale increases five days and the horizontal scale decreases 94 km from the surface ($\sigma_{\text{topo}} = 0$) to the near-bottom ($\sigma_{\text{topo}} = 0.8$) waters. This vertically varying decorrelation scales also implies the summer multi-layer structure.

Surface horizontal decorrelation scales are almost 100 km longer in summer than in winter. This is due to the strong solar heating in summer, causing a relatively uniform SST field. Surface temporal decorrelation scales are 2.4 days shorter in summer than in winter. This might be caused by the shallower surface mixed layer in summer (less thermal inertia). Only the upper layer water is affected in summer by the atmospheric forcing rather than the entire water column as in winter. The surface temporal decorrelation scale should be shorter in summer than in winter.

An interesting feature shown in Table 2.6 is the increase of temporal decorrelation scale with depth in both summer (evident) and winter (slight). The near-bottom water ($\sigma_{\text{topo}} = 0.8$) has the longest temporal scale in summer,

which could be directly related to the existence of the Yellow Sea Cold Water throughout the summer in the middle of the Yellow Sea.

2.11.4 Usefulness of the Decorrelation Scales

The decorrelation scales are widely used in the OI system to map irregular data into regular grid points and in the observational system design to determine the horizontal and temporal resolution of the observational network. Since interpolating irregular data into regular grid points will be discussed in the next chapter, we only discuss the application to the observational network design.

As mentioned in Sect. 2.10.1, the noise comes from instrumental and geophysical errors. Since the instrumental error in XBT measurements is usually about 0.1°C (Barnett and Bernstein 1980), and even smaller in CTD measurements, the instrumental error is generally neglected against the geophysical error. This implies that the curtailment of noise must be accomplished by the reduction of geophysical error. This is usually done by increasing the sample density. Having determined the statistical structure of thermal variability in the Yellow Sea shelf, the minimum sampling density required to detect thermal variability can now be arbitrated as two or three samples per decorrelation scale (Sprintall and Meyers 1991). This would mean that spatially, any temperature measurement in both summer and winter may be conducted at 50–80 km and 4–6 day intervals with the knowledge that the sub-surface features will also be adequately sampled.

Questions and Exercises

- (1) What are the major features of the ocean observational data such as CTD, XBT, or AXBT measurements?
- (2) What are the two kinds of representation of a temperature (or salinity) profile? What are the advantages and disadvantages of using each representation?
- (3) When are the major characteristics of the thermal parametric model for the non-polar regions depicted in Fig. 2.8? How many independent parameters are there in this thermal parametric model?
- (4) When are the major characteristics of the thermal and haline parametric models for the polar region depicted in Figs. 2.13 and 2.14? How many independent parameters are there in this thermal parametric model?
- (5) For the polar region, what are the major differences of the (T, S) profiles among the shallow-mixing, deep-mixing, and advection-types?
- (6) What are the major differences between parametric and curve-fitting models? Please discuss the advantages and disadvantages of each model.
- (7) What are the objective and subjective determination of ocean mixed layer depth? What is the major difficulty in objective determination of the mixed layer depth from the profile data?

- (8) There are two types of criteria (difference and gradient) in subjective determination of the mixed layer depth. Please discuss the difference between the two.
- (9) Work with your (T, S) profiles such as XBT measurements. Please (a) compute the second derivatives $\partial^2 F(z_j)/\partial z^2$ (F is T or S) using (2.6) and determine the mixed layer depth objectively; (b) determine the mixed layer depth subjectively using the difference criterion (2.26a) or (2.26b); (c) determine the mixed layer depth subjectively using the gradient criterion (2.26c). Compare the three sets of the mixed layer depth data and discuss the difference among them.
- (10) Under what conditions, the subjective (difference and gradient) and objective methods will cause large errors?
- (11) Two approaches exist to establish climatological mean mixed layer depth field: (a) determine the mean mixed layer depth from the climatological mean (T, S) profiles, (b) the synoptic mixed layer depth from observational (T, S) profiles and then average the synoptic mixed layer depth to get the climatological mean mixed layer depth (described in Sect. 2.7.2). Why is the mixed layer determined from the first approach always larger than that from the second approach? If you want to build up climatological mean mixed layer depth (or thermocline/halocline depth), which approach will you take? Why?
- (12) From the time-longitude plot of monthly mean mixed layer depth in the equatorial Pacific (Fig. 2.18), what kinds of wave motion can be identified?
- (13) What is the barrier layer? What are the major mechanisms causing the barrier layer? Why?
- (14) Can barrier layer occur in high latitude oceans? Why?
- (15) What are the major difficulties to determine temperature profile from SST? What is the advantage to use the multiple time-scale method?
- (16) What errors do you make when you use the bin method (2.41) to calculate the autocorrelation function η defined by (2.40)? Why?
- (17) What is the difference between deep and shallow water in computing the autocorrelation function from observational (T, S) profiles? Why?
- (18) What is the limitation of using the Gaussian model to fit the autocorrelation function computed from the observed (T, S) profiles?

$$\hat{\eta}^{(\sigma)}(m, n) = \hat{\eta}^{(\sigma)}(0, 0) \exp [-A_\sigma^2 (m \Delta r)^2 - C_\sigma^2 (n \Delta \tau)^2]$$

- (19) Discuss the usefulness and application of the autocorrelation function and associated decorrelation scales.

Establishment of Gridded (T, S) Fields

The P-vector inverse method is to determine absolute velocity using the gridded (T, S) data. Since the observational (T, S) data are usually sparse and irregularly distributed, the data analysis to establish gridded data should be conducted before using the P-vector method. Two methods, optimal interpolation (OI) and optimal spectral decomposition (OSD) are presented in this chapter.

3.1 Two Types of Climatological Data Sets

Two analyses are available to construct three-dimensional temperature and salinity climatology on regular grids from observed profiles (a) z -level analysis and (b) parameter analysis. The z -level analysis is to produce horizontally gridded mean temperature and salinity data for all standard depth levels. The parameter analysis is to produce gridded mean value of each thermohaline (or curve-fitting) parameter and then to compute mean temperature and salinity profiles at each horizontal grid from the mean parameters. This leads to the two major climatological datasets of three-dimensional T, S fields that are available for public use (a) the NOAA World Ocean Atlas (WOA) and the Joint US-Russian Environmental Working Group (EWG) Arctic Ocean Atlas with $1^\circ \times 1^\circ$ resolution, which was built using the z -level analysis (Levitus and Boyer 1994) and (b) the Navy's Generalized Digital Environmental Model (GDEM) with $0.5^\circ \times 0.5^\circ$ resolution (unclassified), which was produced using the parametric analysis (Teague et al. 1990).

3.1.1 z -Level Analysis

The z -level analysis is to interpolate the observed temperature and salinity data at standard depth levels. The NOAA WOA has 33 depth levels (Table 3.1). The static stability is usually checked for each observed profile before analysis. The horizontal interpolation of observed data onto

Table 3.1. The standard depth levels of the NOAA WOA data set

K	z -level (m)						
1	0	10	-200	19	-1,000	28	-3,000
2	-10	11	-250	20	-1,100	29	-3,500
3	-20	12	-300	21	-1,200	30	-4,000
4	-30	13	-400	22	-1,300	31	-4,500
5	-50	14	-500	23	-1,400	32	-5,000
6	-75	15	-600	24	-1,500	33	-5,500
7	-100	16	-700	25	-1,750		
8	-125	17	-800	26	-2,000		
9	-150	18	-900	27	-2,500		

grid points might cause (unphysical) static instability. The density is calculated from temperature and salinity at each grid point, and the density difference ($\Delta\rho = \rho_{\text{up}} - \rho_{\text{low}}$) is calculated for two consecutive depth levels within the same water column. For $\Delta\rho > 0$, the water is statically unstable.

The WOA data set has 1,124,708 undersea data points. Among them, $\Delta\rho > 0$ occurs at 5,693 points (0.51% of total data points), and $\Delta\rho > 0.05 \text{ kg m}^{-3}$ occurs at 2,510 points. Figure 3.1a shows the occurrence of the horizontal location of static instability ($\Delta\rho > 0.05 \text{ kg m}^{-3}$). Quite surprisingly, static instability points spread out in the world oceans especially in the Arctic Ocean and in the subtropical gyre of the North Pacific Ocean. The density difference $\Delta\rho$ is usually less than 0.1 kg m^{-3} , but it can be larger than 0.8 kg m^{-3} (Fig. 3.1b). The majority of the unstable points are located in the upper ocean within 30 m and near 300 m (Fig. 3.1c).

Since WOA has static instability occurring in a large area of the Arctic Ocean, it is not suitable for practical use. A gridded climatological (T, S) data set (annual mean, summer, and winter) was established at the same 33 z -levels (Table 3.1) on $1^\circ \times 1^\circ$ grid. This was the effort of the EWG established in June 1995 under the framework of the US-Russian Joint Commission on Economic and Technological Cooperation. In January 1996, the Arctic Climatology Subgroup took on the task of compiling digital data on arctic regions to expand scientific understanding of the Arctic. This work resulted in a set of three atlases on CD-ROM for arctic oceanography, sea ice, and meteorology.

The Atlas consists of separate CD-ROM volumes for winter and summer. More than 1.3 million individual temperature and salinity observations collected from Russian and western drifting stations, ice breakers, and airborne expeditions were used to develop the products contained in the winter atlas. The primary products on the atlas are gridded mean fields for decadal periods (1950s–1980s) of temperature, salinity, density and dynamic height, Atlantic water layer depth, temperature and salinity profiles, and transects. Note that the original individual observations are not provided on the CD-ROM. The

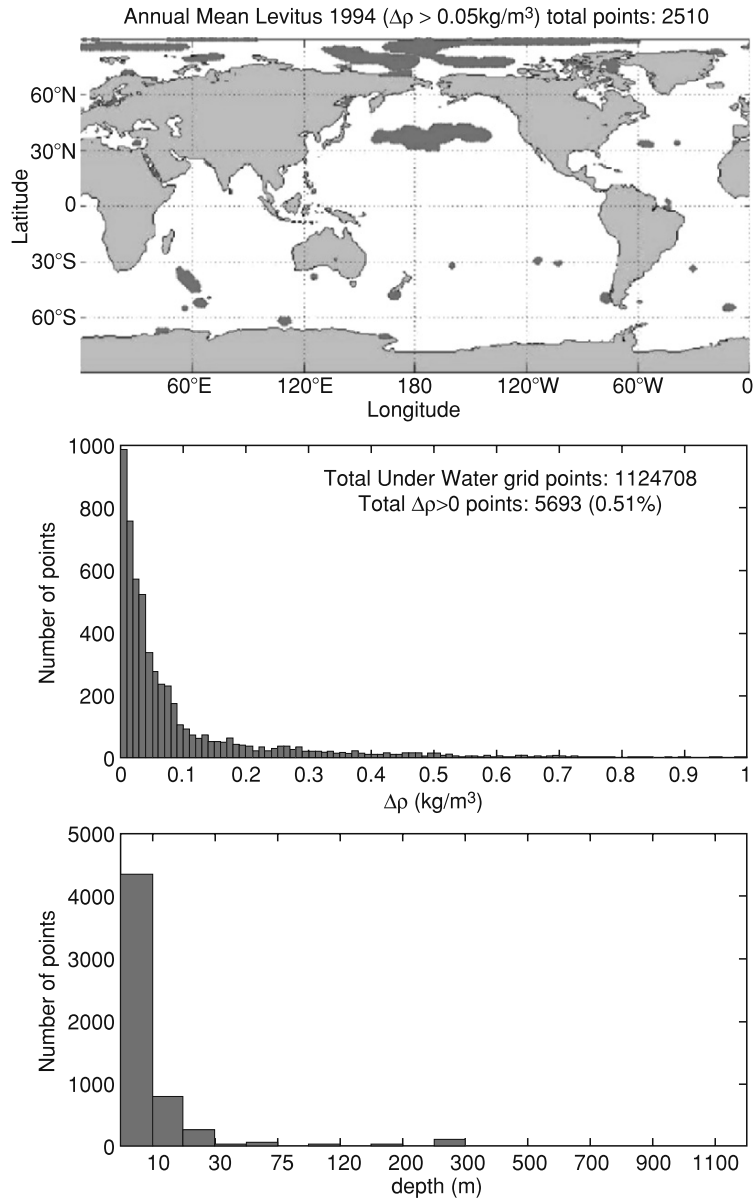


Fig. 3.1. Static instability in the WOA climatological annual mean temperature and salinity data: (a) horizontal location where $\Delta\rho > 0.05\text{ kg m}^{-3}$ occurs, (b) histogram of $\Delta\rho$, and (c) histogram of depth where $\Delta\rho > 0.05\text{ kg m}^{-3}$ occurs

CD-ROMs are in HTML format and are free of charge. For more detailed information, please look at the website: <http://nsidc.org/data/>.

3.1.2 Parametric Analysis

The parametric analysis is to interpolate the parameters of observed profiles onto the horizontal grids. Each observed profile is represented by same number of parameters. For example, the curve-fitting parametric model used to build GDEM has a total of 18 parameters with eight parameters in the shallow top submodel, seven parameters in the mid-depth submodel, and three parameters in the deep submodel (see Sects. 2.5 and 2.6). The observed profiles are transferred into 18 sets of two-dimensional data (horizontal). After 18 sets of the gridded two-dimensional parameters are calculated, the vertical profile at each grid point can be reconstructed using the parametric model. The parametric model is designed with stable stratification having different values of the parameters representing different strengths.

GDEM is gridded data in the form of a four-dimensional digital model (latitude, longitude, depth, and time). The gridded data are generated in three resolutions; 30', 20', and 10' latitude–longitude grids and 3, 6, and 12-month time intervals. The Global GDEM dataset, which covers much of the globe, is generated with a 30' resolution. Regions that are operationally important to the United States Navy are generated with higher horizontal resolutions of 20' and 10'. These regions predominantly consist of shallow water regions like the Mediterranean, the Yellow Sea, and the Persian Gulf (Fig. 3.2). The Naval Oceanographic Office has combined all these different types of resolution GDEM into a single database called GDEM Variable resolution (GDEM V) to allow for the highest resolution and most updated GDEM datasets to be available to the fleet.

As mentioned by Teague et al. (1990), large-scale oceanographic features are generally found to be similarly represented in both GDEM and the NOAA

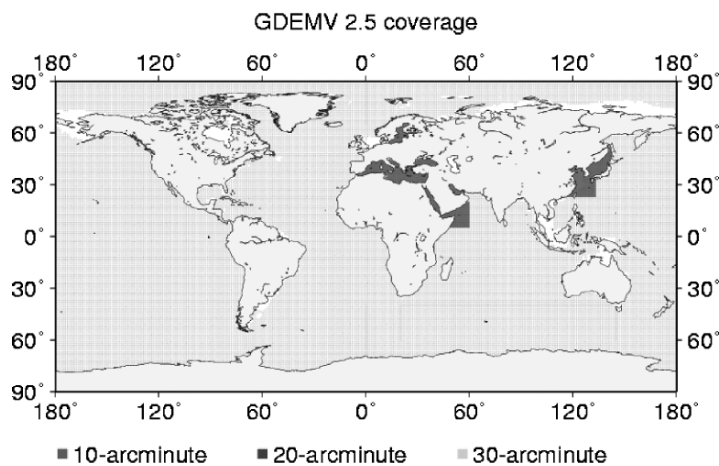


Fig. 3.2. GDEM coverage and horizontal resolutions from the Naval Oceanographic Office (2000)

WOA temperature and salinity. GDEM appears to render better representations of seasonal variability and regions of high current shear because of a different smoothing method and finer grid spacing. GDEM data contain the monthly mean temperature and salinity (T, S) and the annual mean temperature and salinity (\bar{T}, \bar{S}) fields.

3.2 Optimal Interpolation

3.2.1 Modular Ocean Data Assimilation System

Temperature and salinity are in ceaseless change on various time scales such as day (or 12 h), month, year, and longer. Three-dimensional gridded (T, S) fields with daily temporal resolution (or higher) are very useful to identify temporal and spatial variability of fronts and mesoscale eddies. Such fields are produced by the US Navy’s Modular Ocean Data Assimilation System (MODAS), by assimilating a wide range of ocean observations into a starting field. The MODAS products are used to generate the sound speed for ocean acoustic modeling applications (Fox et al. 2002).

MODAS, developed in the mid-1990s at the Naval Research Laboratory in Stennis Space Center, is a global ocean analysis tool presently running at various navy facilities. It produces three-dimensional grids of temperature and salinity with horizontal resolutions ranging from one-half to one-eighth of a degree and uses these fields to derive other oceanographic fields of interest, such as density, sound speed, mixed layer depth, and geostrophic velocity. Unlike traditional “static climatology,” such as WOA climatology and the GDEM that simply represent historical averages of ocean conditions, MODAS can assimilate real-time observations and produce an “adjusted” climatology that more closely represents the actual ocean conditions (Fox et al. 2002).

To produce its “dynamic climatology,” MODAS starts with a static, bi-monthly, gridded climatology of temperature and salinity that is derived from an archive of millions of profile measurements. The sea surface temperature (SST) and sea surface height (SSH) observations from satellites are used to generate two-dimensional, gridded fields of SST and SSH. This is accomplished by using optimum interpolation (OI) to calculate the SST and SSH values at the regularly spaced grid points within the fields. OI is the technique used for combining a background, or first guess, field and measured data by using a model to indicate how nearby data are correlated (Fox et al. 2002). In the case of SST for example, the interpolated temperature is calculated by adding an interpolated temperature anomaly to the first guess grid value, as shown in the following equation (Gandin 1965; Clancy and Pollak 1983)

$$T_k^a = T_k^f + \sum_{j=1}^N \alpha_{kj} (T_j^o - T_j^f), \quad (3.1)$$

where T_k^a is the analyzed SST at the k th grid point, T_k^f is the first guess temperature at the k th grid point valid at the analysis time, T_j^o is the observed SST at location j , T_j^f is the first guess temperature at location j valid at the observation time, α_{kj} is a weighting factor applied to the observation, and N is the number of observations assimilated at the k th grid point. The anomaly is, therefore, determined as the linear combination of observed anomalies after each one is weighted to account for spatial and temporal sampling.

The first guess fields used by MODAS for the OI calculations are the previous day's MODAS field for SST and a large-scale weighted average of 35 days of altimetry for SSH. For the first OI iteration, the static climatology is used for the SST first guess. Synthetic temperature profiles can then be created by projecting these fields downward in the water column to a depth of 1,500 m using relationships determined from a least-square regression analysis of historical temperature profiles that relate both SST and SSH to the subsurface temperature (Fox et al. 2002).

The weighting factors are estimated by minimizing the least-square difference between the interpolated and actual grid point values and solving the following set of equations for the space-time autocorrelation between location j and grid point k , η_{kj} (Clancy and Pollak 1983)

$$\sum_{j=1}^N (\eta_{ij} + \delta_{ij} \lambda_i^o) \alpha_{kj} = \eta_{kj}, \quad (3.2)$$

for $i = 1, 2, \dots, N$, where λ_i^o is the signal to noise ratio for the i th observation. To simplify this, the autocorrelation function for i th observation at location j , η_{ij} is given in the simple form of

$$\eta_{ij} = \exp(-A_k^2 \Delta x_{ij}^2 - B_k^2 \Delta y_{ij}^2 - C_k^2 \Delta t_{ij}^2), \quad (3.3)$$

where Δx_{ij} , Δy_{ij} and Δt_{ij} are the east–west, north–south, and time separation of location j from the grid point, respectively. The values of A_k^{-1} , B_k^{-1} , and C_k^{-1} are east–west, north–south, and temporal decorrelation scales, which are determined from the observational data using the autocorrelation function (see Sect. 2.11).

OI is also used to merge in situ temperature measurements into the dynamic climatology to produce a final temperature analysis. From this, a salinity analysis is produced using temperature–salinity regression relationships to estimate salinity at each depth. Similar to the temperature analysis, in situ salinity measurements can then be combined using OI to produce the final salinity analysis (Fox et al. 2002). An outline of the MODAS process is presented in Fig. 3.3. The final temperature and salinity analyses are what MODAS uses to produce the other derived fields, such as sound speed.

3.2.2 MODAS Evaluation

Chu et al. (2004a) used the South China Sea Monsoon Experiment (SCSMEX) T, S data to evaluate MODAS. SCSMEX is a large-scale experiment to study

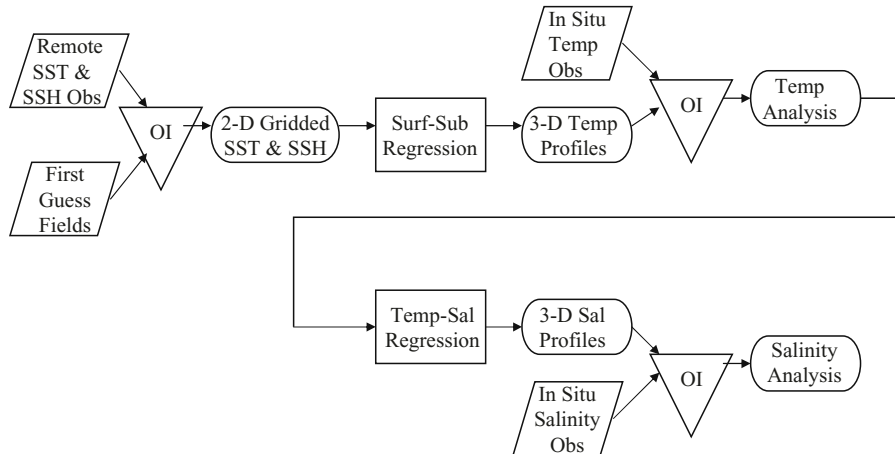


Fig. 3.3. Flow chart of MODAS operational procedure (Chu et al. 2004a, Journal of Oceanography)

the water and energy cycles of the Asian monsoon regions with the goal (SC-SMEX Science Working Group 1995) of providing a better understanding of the key physical processes responsible for the onset, maintenance, and variability of the monsoon over Southeast Asia and southern China, leading to improved predictions. The experiment involves the participation of all major countries and regions of East and Southeast Asia, as well as Australia and the United States.

SCSMEX had both atmospheric and oceanic components. The oceanic intensive observational period was from April through June 1998 with shipboard measurements, Autonomous Temperature Line Acquisition System (ATLAS) moored array, and drifters. The hydrographic data collected during the SCSMEX went through quality control procedures such as min-max check (e.g., disregarding any temperature data less than -2°C and greater than 40°C), error anomaly check (e.g., rejecting temperature data deviating more than 7°C from climatology), ship-tracking algorithm (screening out data with obvious ship position errors), max-number limit (limiting a maximum number of observations within a specified and rarely exceeded space-time window), and buddy check (rejecting contradicting data). After the quality control, the SCSMEX oceanographic dataset contains 1,742 CTD and mooring stations (Fig. 3.4). The majority of the CTDs were nominally capable of reaching a maximum depth of 2,000 m.

Figure 3.5 illustrates the T - S diagrams from SCSMEX (1,742 profiles), MODAS, and GDEM data. All three diagrams (opposite S-shape T - S curves) clearly show the existence of four water masses: the South China Sea Surface Water (warm and less fresh, 25.5 – 29.5°C , 32.75 – 33.5 ppt, depth <50 m), the South China Sea Subsurface Water (less warm and salty, 19.8 – 22.2°C ,

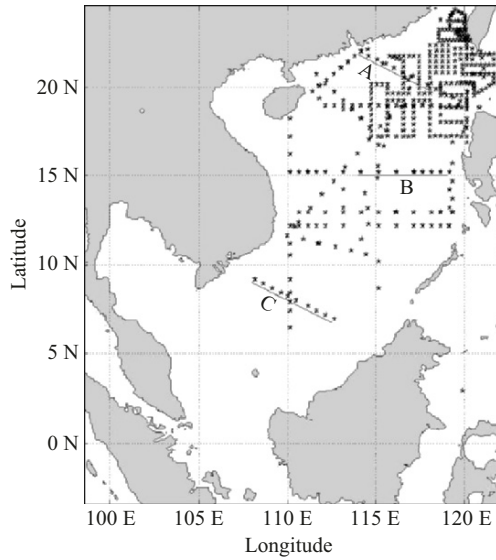


Fig. 3.4. The SCSMEX CTD stations (Chu et al. 2004a, Journal of Oceanography)

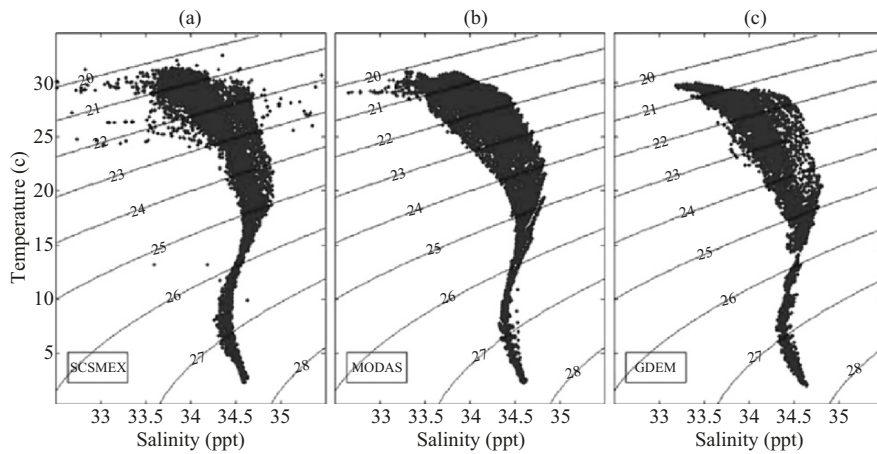


Fig. 3.5. T - S diagrams from (a) SCSMEX (1,742 profiles), (b) MODAS, and (c) GDEM data (Chu et al. 2004a, Journal of Oceanography)

33.85–34.72 ppt, depths 50–200 m), the South China Sea Intermediate Water (less cool and fresh, 5.3–10.0°C, 34.35–34.64 ppt, depths 200–600 m), and the South China Sea Deep Water (cool and fresher, 2.0–6.0°C, 34.4–34.64 ppt, depth >1,000 m).

The easiest way to verify MODAS performance is to plot the MODAS data against SCSMEX CTD data (Fig. 3.6). The scatter diagrams for temperature

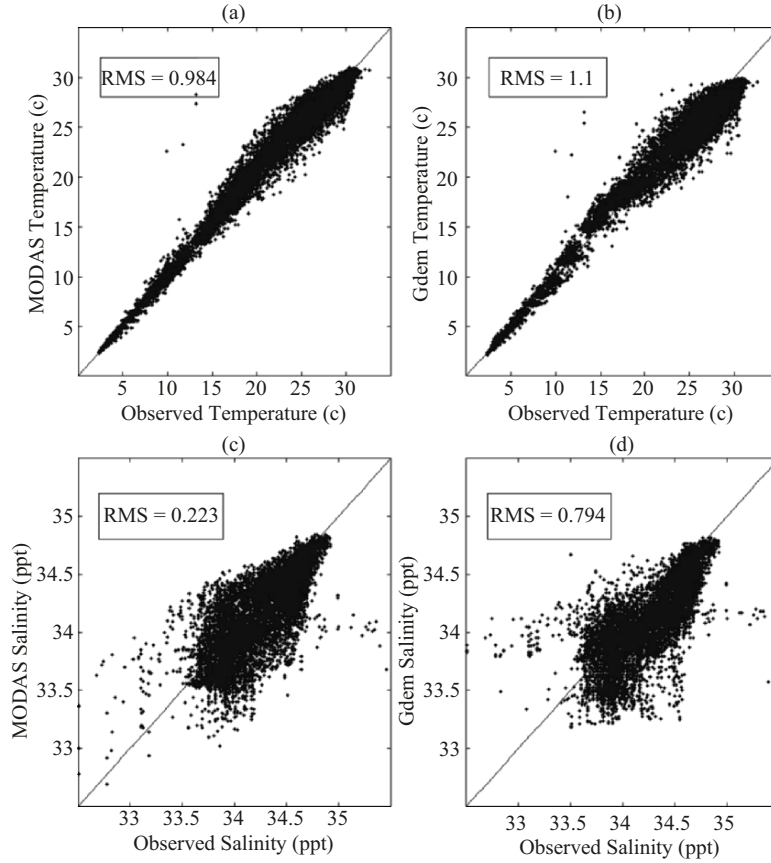


Fig. 3.6. Scatter diagrams of (a) MODAS versus SCSMEX temperature, (b) MODAS versus SCSMEX salinity, (c) GDEM versus SCSMEX temperature, and (d) GDEM versus SCSMEX salinity (Chu et al. 2004a, Journal of Oceanography)

show the points clustering around the line of $T_m = T_o$. The scatter diagrams for salinity show a greater spread of the points around the line of $S_m = S_o$.

This result indicates better performance in temperature nowcast than in salinity nowcast. The errors for temperature and salinity nowcasts have a Gaussian-type distribution with zero mean for temperature and -0.048 ppt for salinity with a standard deviation of 0.98°C for temperature and 0.22 ppt for salinity (Fig. 3.7). This result indicates that MODAS usually under-predicts the salinity.

3.2.3 Future MODAS Improvement

Two treatments distinguish MODAS from ordinary OI schemes (1) “synthetic” temperature profiles generated using surface height and temperature,

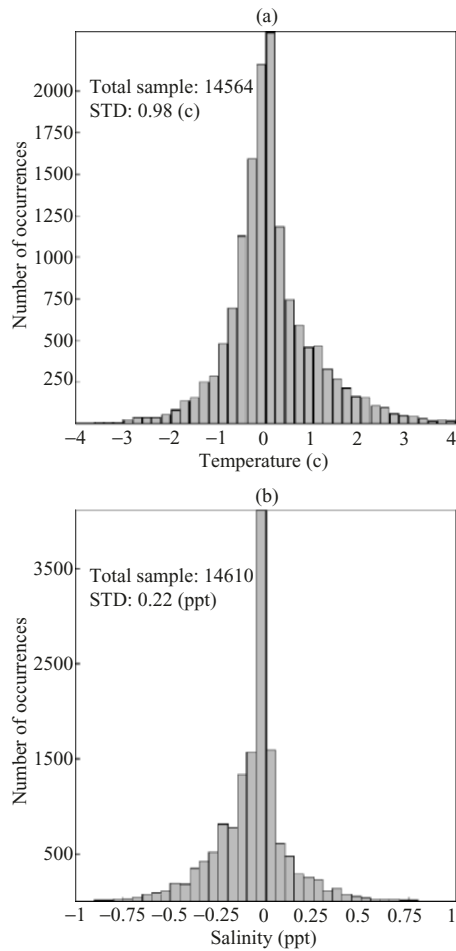


Fig. 3.7. Histogram of MODAS errors of (a) temperature ($^{\circ}\text{C}$) and (b) salinity (ppt) (Chu et al. 2004a, Journal of Oceanography)

and (2) salinity as a function of temperature. The first treatment of MODAS is to establish linear regression relationships between (SST, SSH) with temperature at a given depth. Synthetic temperature profiles extending to a maximum depth of 1,500m are computed from these regression relationships. It is difficult and unrealistic to achieve these characteristics from SST and SSH. Using parametric modeling concept, the synthetic temperature profiles will be obtained from the relationships between (SST, SSH) and $(d_1, d_2, d_3, d_4, d_5), [G^{(m)}, G^{(th)}, G^{(tr)}, G^{(d1)}, G^{(d2)}]$ in future MODAS, rather than from the relationships between (SST, SSH) and temperature at the given depth.

The second treatment of MODAS is to determine the relationship between salinity and temperature at each position, depth, and time of year, by locally weighted linear regression from the subset of observations having both temperature and salinity (Fox et al. 2002). This is on the basis of sole dependence of salinity on temperature. Chu and Garwood (1990, 1991) and Chu et al. (1990) found a two-phase thermodynamics of atmosphere and ocean, each medium having two independent variables: temperature and salinity for oceans, temperature and humidity (or cloud fraction) for the atmosphere. Both positive and negative feedback mechanisms are available between atmosphere and ocean. First, clouds reduce the incoming solar radiation at the ocean surface by scattering and absorption, which cools (relatively) the ocean mixed layer. The cooling of the ocean mixed layer lowers the evaporation rate, which will diminish the clouds. This is the negative feedback. Second, precipitation dilutes the surface salinity, stabilizing the upper ocean and reducing ocean mixed layer deepening. The MLD may be caused to shallow if the downward surface buoyancy flux is sufficiently enhanced by the precipitation. The reduction in MLD will increase SST by concentrating the net radiation and downward heat flux across the sea surface into thinner layer. The increase of SST augments the surface evaporation, which increases the surface salinity (for ocean) and produces more clouds (for atmosphere). This indicates that no unique T - S relationship exists, especially in the upper ocean.

A reasonable way to represent salinity profile is by depths and gradients: d_1 (MLD for salinity), d_2 (depth of the halocline top), d_3 (depth of the halocline bottom), d_4 (depth of the top of the first deep layer), and d_5 (bottom of the first deep layer), $G_S^{(m)}$ (~ 0 , mixed layer gradient), $G_S^{(ha)}$ (halocline gradient), $G_S^{(tr)}$ (mean entrainment zone gradient), $G_S^{(d1)}$ (mean gradient in the first deep layer), and $G_S^{(d2)}$ (mean gradient in the second deep layer). In a future MODAS, synthetic salinity profiles should be independent of the synthetic temperature profiles. They will be obtained from the relationships between surface data (SST, SSH, precipitation) and $(d_1, d_2, d_3, d_4, d_5)$, $[G_S^{(m)}, G_S^{(ha)}, G_S^{(tr)}, G_S^{(d1)}, G_S^{(d2)}]$.

3.3 Optimal Spectral Decomposition

3.3.1 Spectral Decomposition

The OSD method was described in detail for closed (Eremeev et al. 1994, 1995; Danilov et al. 1996; Ivanov et al. 2001) and semiclosed basins (Chu et al. 2003a, b; Ivanov et al. 2004). Any physical variable $c(\mathbf{x}, z, t)$ at depth z_k is decomposed using the generalized Fourier series (Chu 1999b; Ivanov et al. 2001; Chu et al. 2003a, b, 2005a, b)

$$c(\mathbf{x}, z_k, t) = A_0(z_k, t) + \sum_{m=1}^M A_m(z_k, t) \Psi_m(\mathbf{x}, z_k), \mathbf{x} \in R(z_k) \quad (3.4)$$

where M is the truncated mode number, $\Psi_m(\mathbf{x}, z_k)$ and $A_m(z_k, t)$ are the orthogonal basis functions (or called modes) and the spectral coefficients, respectively; $R(z_k)$ is the area bounded by the lateral boundary $\Gamma(z_k)$ at depth z_k .

The eigenfunctions $\{\Psi_m(\mathbf{x}, z_k)\}$ of the horizontal Laplace operator with the basin geometry and homogeneous Neumann boundary condition at $\Gamma(z)$ are taken as the basis functions

$$\nabla_h^2 \Psi_m = -\lambda_m \Psi_m, \quad \mathbf{n} \cdot \nabla_h \Psi_m|_{\Gamma} = 0, \quad m = 1, 2, \dots, M, \quad (3.5)$$

where $\nabla_h^2 \equiv \partial^2/\partial x^2 + \partial^2/\partial y^2$, and \mathbf{n} is the unit vector normal to $\Gamma(z)$. The basis functions $\{\Psi_m\}$ are independent of the data and therefore available prior to the data analysis.

The OSD method has two important procedures: optimal mode truncation and determination of spectral coefficients $\{A_m\}$. After the two procedures, the generalized Fourier spectrum (3) is used to provide data at regular grids in space and time.

3.3.2 Optimal Mode Truncation

The optimal mode truncation number (M_{opt}) is defined as the critical mode number with the set of spectral coefficients $\{A_m\}$ least sensitive to observational data sampling and noise. For sample size of P and mode truncation of M , the spectral coefficients $\{A_m\}$ are estimated by the least-square difference between observed and calculated values (Menke 1984)

$$J_{\text{emp}} = J(\tilde{A}_1, \dots, \tilde{A}_M, P, M) = \frac{1}{P} \sum_{j=1}^P \left(c^{(j)} - \sum_{m=1}^M \tilde{A}_m(z, t) \Psi_m^{(j)}(\mathbf{x}, z) \right)^2 \rightarrow \min, \quad (3.6)$$

where the symbol “ \sim ” represents the estimated value at (\mathbf{x}, t) . For homogeneously sampled data with low noise and without systematic error, the empirical cost function J_{emp} should tend to 0 monotonically as M increases to infinity. The set of the spectral coefficients $\{A_m\}$ depends on the mode truncation M . Optimal estimation of $\{A_m\}$ is equivalent to the determination of M_{opt} (Ivanov et al. 2001, 2004; Chu et al. 2003a, b).

A modified cost function (Vapnik and Chervonenkis 1974a, b),

$$J \leq \frac{J_{\text{emp}}}{1 - \sqrt{\frac{M(\ln \frac{P}{M} + 1) - \ln(1-\tau)}{P}}}, \quad (3.7)$$

is used to determine the optimal mode truncation M_{opt} . Here, τ is the probability of

$$|J - J_{\text{emp}}| \rightarrow 0 \text{ as } M \text{ increases.}$$

Usually, for a regional sea such as the Black Sea, M_{opt} is 30–50 for the basin-scale (~ 300 km) variability and 150 for the mesoscale (~ 20 km) variability

(Chu et al. 2005a). For sparse and noisy data, it is difficult to get reliable and stable estimates of all the necessary spectral coefficients, but the first few spectral coefficients $\tilde{A}_0(z_k, t), \tilde{A}_1(z_k, t), \dots, \tilde{A}_m(z_k, t)$ are reliable and stable.

3.3.3 Rotation Matrix Method for Regularization

Determination of the spectral coefficients is achieved by solving a set of linear algebraic equations of $\{\tilde{A}_m(z, t)\}$ that are obtained from the optimization procedure (3.4) and (3.7),

$$\mathbf{A}\hat{\mathbf{a}} = \mathbf{Q}\mathbf{Y}. \quad (3.8)$$

where $\hat{\mathbf{a}}$ is the estimated state vector (L -dimensional) for the exact state vector \mathbf{a} ; \mathbf{A} is a $P \times L$ coefficient matrix; \mathbf{Q} is a $P \times P$ square matrix ($P > L$); \mathbf{Y} is a P -dimensional observation vector, consisting of a signal $\bar{\mathbf{Y}}$ and a noise \mathbf{Y}' ,

$$\mathbf{Y} = \bar{\mathbf{Y}} + \mathbf{Y}'.$$

Due to the high level of noise contained in the observations, the set of algebraic equations is ill-posed and needs to be solved by a regularization method that requires (a) stability (robustness) even for data with high noise and (b) the ability to filter out errors with a priori unknown statistics.

The two known matrices \mathbf{A} and \mathbf{Q} are determined by the physical process or field. Let $\|\dots\|$ be the Euclidean norm and

$$\eta_1 = \frac{\|\mathbf{Q}\mathbf{Y}'\|}{\|\mathbf{Q}\bar{\mathbf{Y}}\|}, \quad \eta_2 = \frac{L}{P}, \quad \eta_3 = \frac{\max(\text{sigular values of } \mathbf{A})}{\min(\text{sigular values of } \mathbf{A})}, \quad (3.9a)$$

be the noise-to-signal ratio, dimension ratio, and condition number of the matrix \mathbf{A} . For a particular system, η_2 is given. Usually, η_1 and η_3 are large (called “imperfect”),

$$\eta_1 \geq 1, \quad \eta_3 \gg 1,$$

which makes (3.8) difficult to solve. Besides, the low-order noise statistics and the norm of the exact state vector ($\|\mathbf{a}\|$) are unknown. Reduction of η_1 and η_3 (i.e., reduction of imperfection) without a priori knowledge of noise statistics and $\|\mathbf{a}\|$ is an important step toward solving (3.8) accurately. If the matrix \mathbf{A} has no noise, the accuracy in determining $\hat{\mathbf{a}}$ is given by Tikhonov et al. (1990),

$$\|\chi\|^2 = \frac{\|\mathbf{a} - \hat{\mathbf{a}}\|^2}{\|\mathbf{a}\|^2} \leq \eta_1^2 \eta_3^2. \quad (3.9b)$$

Equation (3.8) can be transformed into a system with stable solution to small perturbations in \mathbf{Q} and \mathbf{Y} using traditional regularization methods (e.g., Tikhonov and Arsenin 1979; Bennett 1992). However, biased estimations $\hat{\mathbf{a}}$ is often obtained for \mathbf{a} and the following condition

$$\hat{\mathbf{a}} \rightarrow \mathbf{a} \text{ as } \eta_1 \rightarrow 0, \quad (3.9c)$$

is not guaranteed.

Furthermore, the traditional regularization methods require a priori knowledge of $\|\mathbf{a}\|$. To overcome these weaknesses, a new rotation method for $\eta_2 < 1$ is developed in this study to change (3.8) into a new system with possibly minimum coefficient matrix and noise-to-signal ratio without a priori knowledge of noise statistics.

Nonsingular orthogonal transformation is conducted through multiplication of (3.8) by a plane rotation matrix \mathbf{S} from the left,

$$\mathbf{S}\mathbf{A}\hat{\mathbf{a}} = \mathbf{S}\mathbf{Q}\mathbf{Y}, \quad (3.10)$$

which changes the coefficient matrix and the source term from $(\mathbf{A}, \mathbf{Q}\mathbf{Y})$ to $(\mathbf{S}\mathbf{A}, \mathbf{S}\mathbf{Q}\mathbf{Y})$ and provides the opportunity to minimize the imperfection of the new system (3.10),

$$\tilde{\eta}_3^2(1 + \tilde{\eta}_1^2) \rightarrow \min, \quad (3.11)$$

where

$$\tilde{\eta}_1 \equiv \frac{\|\mathbf{S}\mathbf{Q}\mathbf{Y}'\|}{\|\mathbf{S}\mathbf{Q}\bar{\mathbf{Y}}\|}, \quad \tilde{\eta}_3 \equiv \frac{\|\mathbf{S}\mathbf{Q}\bar{\mathbf{Y}}\|}{\|\mathbf{a}\|}. \quad (3.12)$$

Minimization (3.11) is obtained by the following maximization (Strakhov 1991; Ivanov et al. 2001)

$$J_1 = \|\mathbf{A}\|^2 - \frac{\|\mathbf{S}\mathbf{Q}\mathbf{Y}\|^2}{\|\mathbf{a}\|^2} \rightarrow \max, \quad (3.13)$$

where $\|\mathbf{A}\|$ is the spherical norm of the matrix \mathbf{A} . Substitution of (3.12) in (3.13) yields

$$J_1 = \|\mathbf{A}\|^2 - \tilde{\eta}_3^2 \left[1 + \frac{2(\mathbf{S}\mathbf{Q}\bar{\mathbf{Y}} * \mathbf{S}\mathbf{Q}\mathbf{Y}')}{\|\mathbf{S}\mathbf{Q}\bar{\mathbf{Y}}\|^2} + \tilde{\eta}_1^2 \right] \rightarrow \max, \quad (3.14)$$

which is the procedure to obtain minimum values of $\tilde{\eta}_1$ and $\tilde{\eta}_3$ without $\|\mathbf{a}\|^2$. Here, the symbol “*” indicates the scalar product in the Euclidean space. For a white noise \mathbf{Y}' , we have

$$(\mathbf{S}\mathbf{Q}\bar{\mathbf{Y}} * \mathbf{S}\mathbf{Q}\mathbf{Y}') \rightarrow 0 \text{ as } P \rightarrow \infty.$$

The maximization of J_1 using (3.14) is then equivalent to the minimization (3.11). Note that this minimization is not necessarily the same as

$$\tilde{\eta}_3^2 \rightarrow \min, \quad \tilde{\eta}_1^2 \rightarrow \min.$$

The new transformed system (3.10) can be solved by usual algebraic methods such as the Gauss method.

3.3.4 Accuracy of the Rotation Matrix Method

The accuracy of the reconstruction of (3.10) is estimated with the given norm of the exact state vector, $\|\mathbf{a}\|$. Since $\|\mathbf{a}\|$ is not a priori known, an effective norm $\|\mathbf{a}_{\text{eff}}\|$ is defined by

$$J_2 = \left| \frac{\|\hat{\mathbf{a}}\|^2}{\|\mathbf{a}_{\text{eff}}\|^2} - 1 \right| \rightarrow \min, \quad (3.15)$$

Simple analysis on (3.11)–(3.15) shows that two norms $\|\mathbf{a}_{\text{eff}}^*\|$ and $\|\mathbf{a}_{\text{eff}}^{**}\|$ (generally $\|\mathbf{a}_{\text{eff}}^*\| \neq \|\mathbf{a}_{\text{eff}}^{**}\|$) exist such that the functionals J_1 and J_2 reach their maximum values and

$$\|\mathbf{a}\| \leq \|\mathbf{a}_{\text{eff}}^*\|, \quad \|\mathbf{a}_{\text{eff}}^{**}\| \leq 2\|\mathbf{a}\|.$$

If $\|\mathbf{a}\| \rightarrow \|\mathbf{a}_{\text{eff}}^*\|$, then $\|\chi\|^2 \rightarrow 0$. When $\|\mathbf{a}\| \rightarrow \|\mathbf{a}_{\text{eff}}^{**}\|$ we have

$$\|\chi\|^2 \rightarrow \left[1 - \frac{\|\mathbf{a}_{\text{eff}}^{**}\|}{\|\mathbf{a}\|} \right]^2.$$

Therefore, replacement of $\|\mathbf{a}\|$ by $\|\mathbf{a}_{\text{eff}}^{**}\|$ will not deteriorate the accuracy of the solution of (3.8). A similar replacement of $\|\mathbf{a}\|$ is also suggested for color noises and deterministic perturbations. However, the reconstruction accuracy might deteriorate because the scalar product $(\mathbf{S}\mathbf{Q}\mathbf{Y}^*\mathbf{S}\mathbf{Q}\mathbf{Y}')$ does not tend to 0 for $P \rightarrow \infty$. For simplicity, we restrict the reconstruction to the data distorted by the white noise only.

3.3.5 Rotation Matrix Method for Linear Scalar Process

Consider a temporally varying linear scalar process,

$$\bar{Y}(t) = \alpha + \beta t, \quad t \in [0, T],$$

perturbed by a white noise $Y'(t)$. The noisy data are represented by

$$Y(t) = \bar{Y}(t) + Y'(t)$$

The Fourier series

$$X(t) = a_0 + \sum_{i=1}^{38} [a_i \sin(i\pi t/T) + a_{i+19} \cos(i\pi t/T)], \quad (3.16a)$$

is used to recover the signal, $\bar{Y}(t)$. The reconstruction is to determine the estimated state vector,

$$\hat{\mathbf{a}} = (a_1, a_2, \dots, a_L), \quad L = 38, \quad (3.16b)$$

such that the temporally integrated difference between $X(t)$ and $Y(t)$ reaches the minimum value,

$$J = \int_0^T [X(t) - Y(t)]^2 dt \rightarrow \min \quad (3.17)$$

Substitution of (3.16) in (3.17) yields (3.8) of $\hat{\mathbf{a}}$ with a very high condition number for the coefficient matrix.

The noisy data set $Y(t)$ is generated in such a way that the sensitivity of reconstruction quality to (η_1, η_2) can be investigated: 60–100 points (varying P and time step Δt) uniformly distributed into the interval $[0, T]$ are used to get $\bar{Y}(t)$, and white noises $Y'(t)$ with η_1 ranging from 0 to 3 are added to $\bar{Y}(t)$. Here,

$$T/60 \geq \Delta t \geq T/100.$$

The three-nondimensional parameters η_1, η_2 , and η_3 vary within the following ranges,

$$0 \leq \eta_1 \leq 3; \quad 0.4 \leq \eta_2 \leq 0.6; \quad \eta_3 \simeq 10^6. \quad (3.18)$$

For such a high condition number, (3.8) cannot be solved directly. The rotation matrix \mathbf{S} is calculated using the maximization procedure depicted in Sect. 3.3.3. The condition number of the coefficient matrix of the new system (3.10) reduces to

$$\tilde{\eta}_3 \simeq 1.5.$$

The reconstructed accuracy $\|\chi\|$ reduces with the decrease of η_1 (noise-to-signal ratio before the rotation) monotonically from 0.4 for $\eta_1 = 3.0$ to 0 for $\eta_1 = 0$ (Fig. 3.8a). The reconstructed process $\hat{X}(t)$ is closer to $\bar{Y}(t)$ as η_1 reduces (Fig. 3.8b).

3.3.6 Rotation Matrix Method for Two-Dimensional Field

Eremeev et al. (1992) reconstructed the Black Sea summer climatological surface temperature field (T_{clim}) using the traditional regularization method (Bennett 1992). The nondimensional parameters (η_1, η_2, η_3) vary within the following intervals,

$$0 \leq \eta_1 \leq 4, \quad 0.025 \leq \eta_2 \leq 0.67, \quad 3 \times 10^4 \leq \eta_3 \leq 3 \times 10^7 \quad (3.19)$$

For large values of (η_1, η_3) , the accuracy of the traditional regularization methods is not very good. The climatological surface temperature field, $T_{\text{clim}}(x, y)$, is perturbed by white noises $T'(x, y)$. The noisy data are represented by

$$T_{\text{data}}(x, y) = T_{\text{clim}}(x, y) + T'(x, y), \quad (x, y) \in \Omega, \quad (3.20)$$

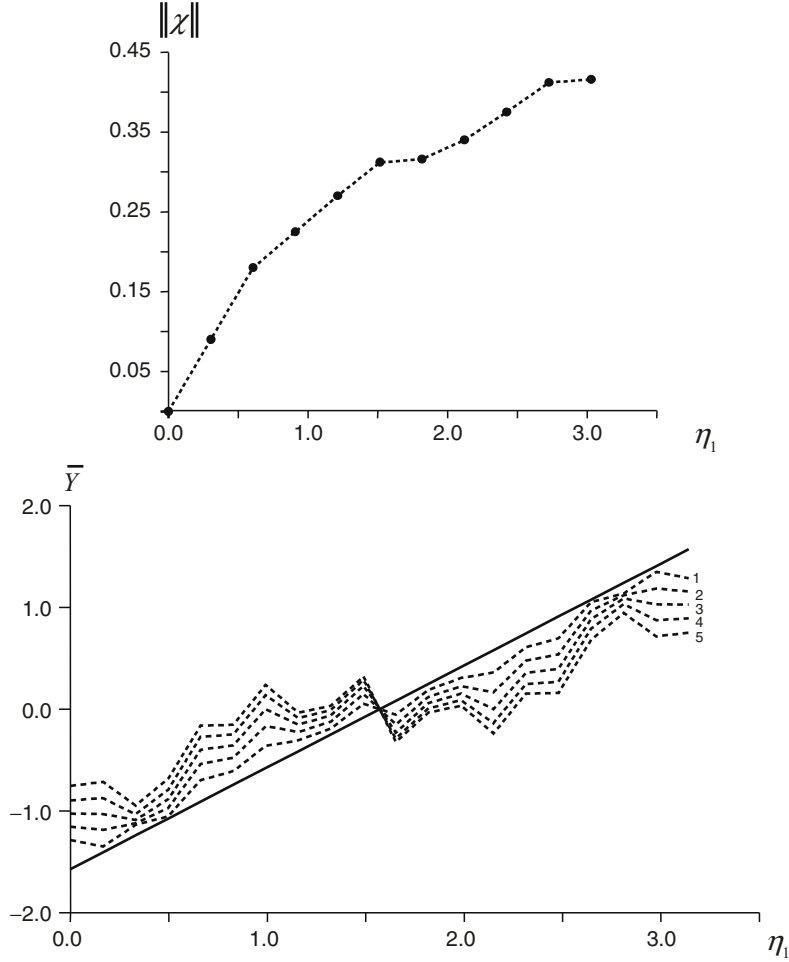


Fig. 3.8. Reconstruction of the one-dimensional linear process: **(a)** upper panel: reconstruction accuracy and **(b)** lower panel: comparison between $\bar{Y}(t)$ (solid line) and reconstructed processes $X(t)$ (dashed curves) with 1, 2, 3, 4, and 5 corresponding to $\eta_1 = 0.6, 1.2, 1.8, 2.4,$ and 3.0 (Chu et al. 2004b, International Journal of Bifurcation and Chaos)

where Ω is the Black Sea. The generalized Fourier series,

$$T(x, y) = T_0 + \sum_{i=1}^{30} a_i \Psi_i(x, y), \quad (3.21)$$

is used to recover the climatological signal, $T_{\text{clim}}(x, y)$. Here, T_0 is a constant (to be determined) and the basis functions $\{\Psi_i(x, y), i = 1, 2, \dots, 30\}$ are the eigenfunctions of the plane von Neumann operator with homogeneous

boundary conditions for the domain Ω (Eremeev et al. 1992). The reconstruction is to determine the estimated state vector,

$$\hat{\mathbf{a}} = (a_1, a_2, \dots, a_L), \quad L = 30, \quad (3.22)$$

such that the spatially integrated difference between $T_{\text{data}}(x, y)$ and $T(x, y)$ reaches the minimum value,

$$J = \int_{\Omega} \int_{\Omega} [T(x, y) - T_{\text{data}}(x, y)]^2 dx dy \rightarrow \min. \quad (3.23)$$

Substitution of (3.21) in (3.23) yields (3.8) of $\hat{\mathbf{a}}$ with a very high condition number for the coefficient matrix [see (3.19)].

After applying the rotation matrix \mathbf{S} with the maximization procedure [(3.14)], the condition number of the coefficient matrix of the new system (3.10) reduces to

$$\tilde{\eta}_3 \leq 5.0. \quad (3.24)$$

Reconstructed accuracy $\|\chi\|$ using the optimal spectral decomposition scheme is up bounded by η_1 (noise-to-signal ratio before the rotation)

$$\|\chi\| \leq \eta_1, \quad (3.25)$$

and usually decreases with decreasing η_1 and η_2 (Fig. 3.9). Note that the approach does not improve the reconstruction accuracy for $\eta_2 \leq 0.045$. For large noise-to-signal ratio, $\eta_1 > 3.0$, the reconstruction accuracy improves when the dimension ratio (η_2) increases from 0.3 to 0.67.

3.3.7 Rotation Matrix Method for Perturbed Lorenz Attractor

The Lorenz system, a truncated three-component atmospheric convection model, is represented by a three-dimensional vector

$$\mathbf{X} \equiv \begin{bmatrix} X_1 \\ X_2 \\ X_3 \end{bmatrix}, \quad (3.26)$$

which satisfies the following nonlinear ordinary differential equation with the initial condition,

$$\frac{d\mathbf{X}}{dt} = \mathbf{F}(\mathbf{X}, \mathbf{c}), \quad \mathbf{X}(t_0) = \mathbf{X}_0, \quad (3.27)$$

where the vector functional \mathbf{F} and state parameter vector are defined by Lorenz (1963)

$$\mathbf{F} = \begin{bmatrix} -b_1 X_1 + b_1 X_2 \\ -X_1 X_2 + b_2 X_1 - X_2 \\ X_1 X_2 - b_3 X_3 \end{bmatrix}, \quad \mathbf{b} \equiv \begin{bmatrix} b_1 \\ b_2 \\ b_3 \end{bmatrix}. \quad (3.28)$$

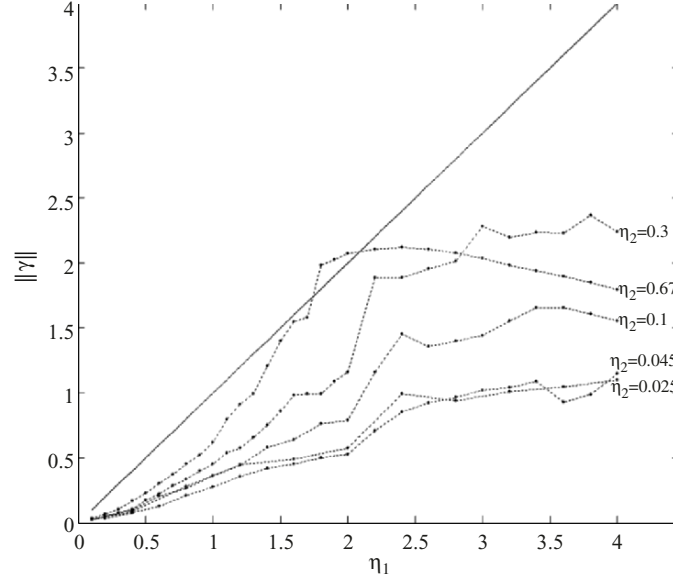


Fig. 3.9. Dependence of the accuracy $\|\chi\|$ on η_1 with different η_2 values for the two-dimensional temperature field in the Black Sea. Note that $\|\chi\|$ is usually smaller than η_1 (Chu et al. 2004b, International Journal of Bifurcation and Chaos)

The initial condition (\mathbf{X}_0) and the parameter vector (\mathbf{b}) affect the characteristics of the Lorenz system. Chu (1999a, b) shows the model parameter representing the boundary condition. We integrate (3.27) numerically with the time step as $\Delta t = 0.01$ and

$$\mathbf{X}_0 = \begin{bmatrix} 0.1 \\ 0.1 \\ 0.1 \end{bmatrix}, \quad \mathbf{b} \equiv \begin{bmatrix} 10 \\ 28 \\ 8/3 \end{bmatrix}, \quad (3.29)$$

to obtain the famous butterfly pattern for the track in the phase space (X_1, X_2) (Fig. 3.10) and unstable oscillation for temporal variation of X_3 (Fig. 3.11).

The signal $\bar{\mathbf{Y}}(t)$ is recovered from the noisy data $[Y_1(t), Y_2(t), Y_3(t)]$ (Figs. 3.12 and 3.13) through accurate estimation of the parameter vector $\hat{\mathbf{b}}$ and effective reduction of noises. Estimation of the state vector

$$\hat{\mathbf{b}} = (b_1, \dots, b_L), \quad L = 3, \quad (3.31)$$

is conducted using the minimization of the temporally integrated difference between $\mathbf{X}(t)$ and $\mathbf{Y}(t)$,

$$J = \int_{t_0}^T [\mathbf{X}(t) - \mathbf{Y}(t)] * [\mathbf{X}(t) - \mathbf{Y}(t)] dt \rightarrow \min. \quad (3.32)$$

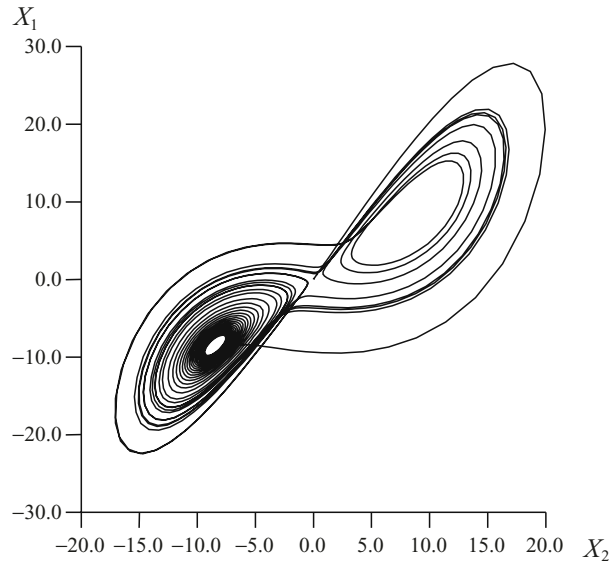


Fig. 3.10. Lorenz attractor without white noise: butterfly pattern of track in (X_1, X_2) phase space (Chu et al. 2004b, International Journal of Bifurcation and Chaos)

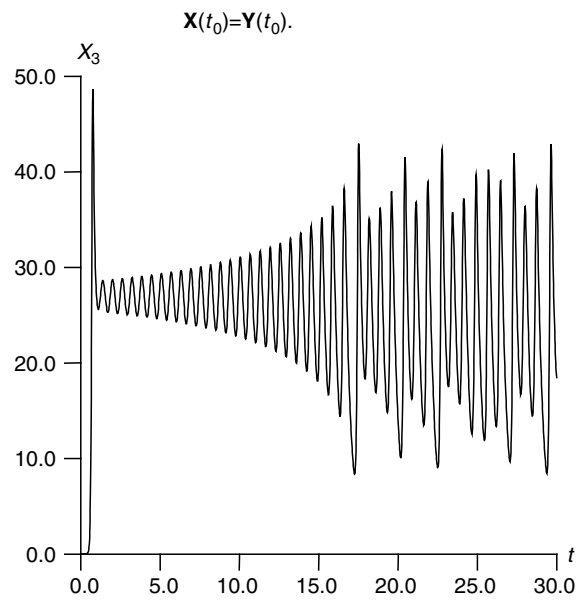


Fig. 3.11. Lorenz attractor without white noise: time series of X_3 (Chu et al. 2004b, International Journal of Bifurcation and Chaos)

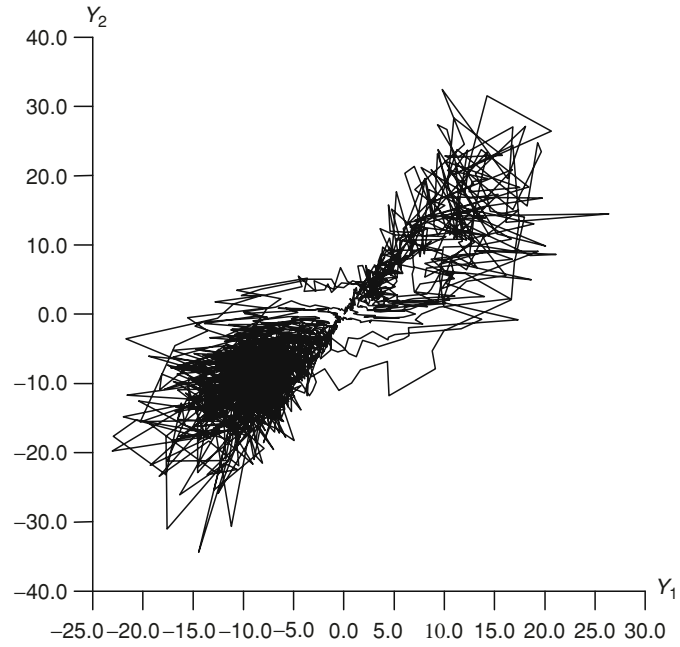


Fig. 3.12. Lorenz attractor distorted by white noise with $\eta_1 = 0.6$: noisy track in (Y_1, Y_2) phase space with no butterfly pattern (Chu et al. 2004b, International Journal of Bifurcation and Chaos)

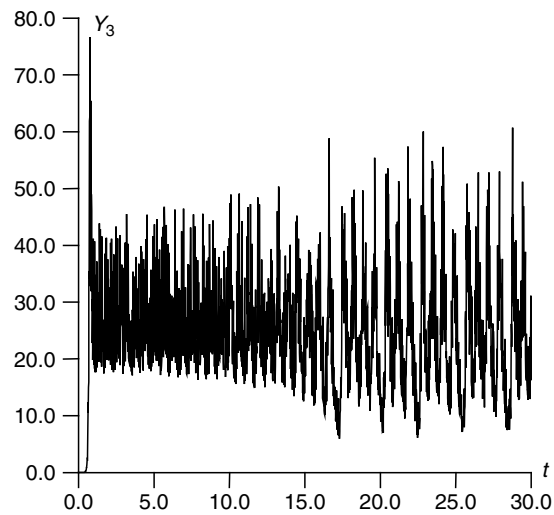


Fig. 3.13. Lorenz attractor distorted by white noise with $\eta_1 = 0.6$: time series of Y_3 (Chu et al. 2004b, International Journal of Bifurcation and Chaos)

Here, there is no explicit relationship between $\mathbf{X}(t)$ and \mathbf{b} . The minimization (3.32) becomes

$$\frac{\partial J}{\partial \hat{c}_j} = 0 \quad (3.33)$$

An iterative algorithm (Eykhoff 1973) is used with the initial conditions

$$\mathbf{X}(t_0) = Y(t_0). \quad (3.34)$$

Let the parameter vector be estimated by $\hat{\mathbf{b}}^{(n-1)}$ for the $(n-1)$ th iteration. Integration of the Lorenz system

$$\frac{d\mathbf{X}}{dt} = \mathbf{F}(\mathbf{X}, \hat{\mathbf{b}}) \quad (3.35)$$

gives the state vector $\mathbf{X}^{(n-1)}(t)$ for the $(n-1)$ th iteration. If the estimated parameter vector $\hat{\mathbf{b}}^{(n-1)}$ has an increment, $\Delta\mathbf{b}$, the state vector has a corresponding increment,

$$\Delta\mathbf{X}^{(n-1)}(t) = \mathbf{U}^{(n-1)}\Delta\mathbf{b}, \quad (3.36)$$

where \mathbf{U} is the sensibility matrix defined by

$$U_{ij} = \frac{\partial X_i}{\partial b_j}; \quad i, j = 1, 2, 3.$$

When the increment $\Delta\mathbf{b}$ is selected such that (3.33) is satisfied, and this leads to

$$\int_{t_0}^T (\mathbf{U}^t)^{(n-1)} \mathbf{U}^{(n-1)} \cdot \Delta\mathbf{b} dt = \int_{t_0}^T (\mathbf{U}^t)^{(n-1)} \cdot (\mathbf{Y} - \mathbf{X}^{(n-1)}) dt, \quad (3.37)$$

the temporally integrated difference between $\mathbf{Y}(t)$ and $\mathbf{X}^{(n-1)}(t) + \mathbf{U}^{(n-1)}\Delta\mathbf{b}$, reaches the minimum [see (3.32)]. Here, the matrix \mathbf{U}^t is the transpose of the matrix \mathbf{U} . The estimated parameter vector at the n th iteration is taken as

$$\hat{\mathbf{b}}^{(n)} = \hat{\mathbf{b}}^{(n-1)} + \Delta\mathbf{b}. \quad (3.38)$$

Equation (3.35) is solved with $\hat{\mathbf{b}}^{(n)}$ and the state vector at the n th iteration, $\mathbf{X}^{(n)}(t)$, is obtained.

At each iteration step, an ill-posed algebraic equation for $\Delta\mathbf{b}$ [(3.37)] should be solved. As per the two previous examples, the noise-to-signal ratio and the condition number are large,

$$\eta_1 \simeq 0.6, \quad \eta_3 \simeq 10^4. \quad (3.39)$$

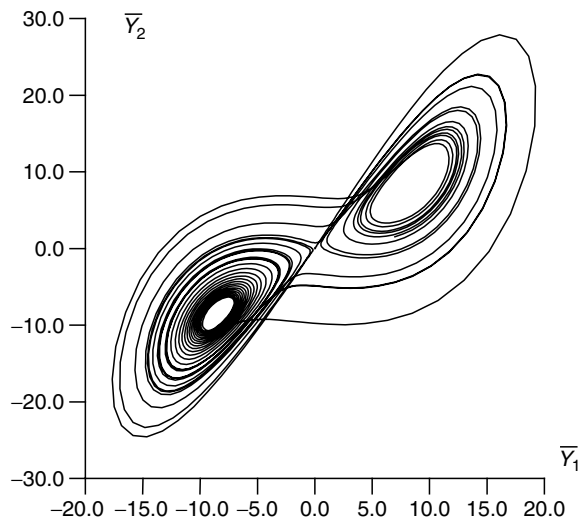


Fig. 3.14. Reconstructed Lorenz attractor from the “noisy data” with $\eta_1 = 0.6$ using the rotation method: butterfly pattern of track in (\bar{Y}_1, \bar{Y}_2) phase space (Chu et al. 2004b, International Journal of Bifurcation and Chaos)

The rotation method is used to get minimum $(\hat{\eta}_1, \hat{\eta}_3)$ at each iteration step. The ill-conditioning of (3.37) is greatly reduced because

$$\hat{\eta}_3 < 5 \quad (3.40)$$

at all the iteration steps. The iteration converges fast. The final estimated parameter vector is given by

$$\hat{\mathbf{b}} = \begin{pmatrix} 9.93 \\ 27.98 \\ 2.667 \end{pmatrix}.$$

After the reconstruction, we obtain the butterfly pattern of the track in the phase space (X_1, X_2) (Fig. 3.14) and the unstable oscillation for temporal variation of X_3 (Fig. 3.15). Comparison between Figs. 3.12 and 3.13, and Figs. 3.14 and 3.15 demonstrates the capability of the rotation method for reconstructing noisy data.

3.3.8 Bimodality of Temperature Field at Mid-Depth of North Atlantic

There are several attempts to construct the large-scale mid-depth circulation pattern for the whole North Atlantic using climate data (Schmitz and McCartney 1993; Reid 1994; Lozier et al. 1995) and for regional seas in the

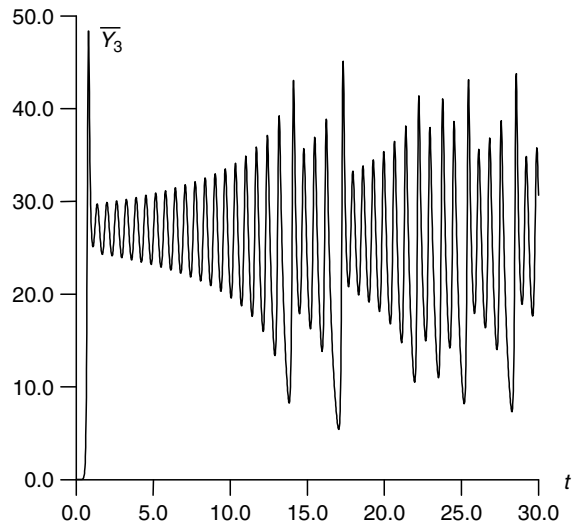


Fig. 3.15. Reconstructed Lorenz attractor from the “noisy data” with $\eta_1 = 0.6$ using the rotation method: time series of \bar{Y}_3 (Chu et al. 2004b, International Journal of Bifurcation and Chaos)

North Atlantic with higher resolution using subsurface float (SOFAR, RAFOS, ALACE, PALACE, SOLO) trajectories directly or combining with hydrological observations (Lavender et al. 2000, 2005; Bower et al. 2002). The basin scale and sub-basin scale mid-depth circulation and its variability can also be potentially extracted from the ARGO float data (ARGO science team 2001). However, analysis of ARGO data is not a trivial problem because the observation is sparse (up to 800 km spatial gap) and noisy.

Between November 2003 and January 2005, over 56,000 float days (cumulative) of data were collected in the North Atlantic ($10\text{--}60^\circ\text{N}$) in general at three parking depths: 1,000, 1,500, and 2,000 m. The floats parking at 2,000 m, depths shallower than 1,000 m, and unknown depths are excluded from the analysis. The temperature is represented by

$$T(x, y, t) = T_0 + \sum_{m=1}^M \sum_{n=1}^N a_{mn}(t) \Psi_{mn}(x, y), \quad (3.41)$$

where $\{\Psi_{mn}\}$ are the basis functions, $\{a_{mn}(t)\}$ are the spectral coefficients, and T_0 is the mean temperature. Using the OSD method, 14 monthly temperature fields at 950 m depth is reconstructed between December 2003 and January 2005 with

$$M_{\text{opt}} = N_{\text{opt}} = 38, \quad T_0 = 6.50^\circ\text{C}, \quad (3.42)$$

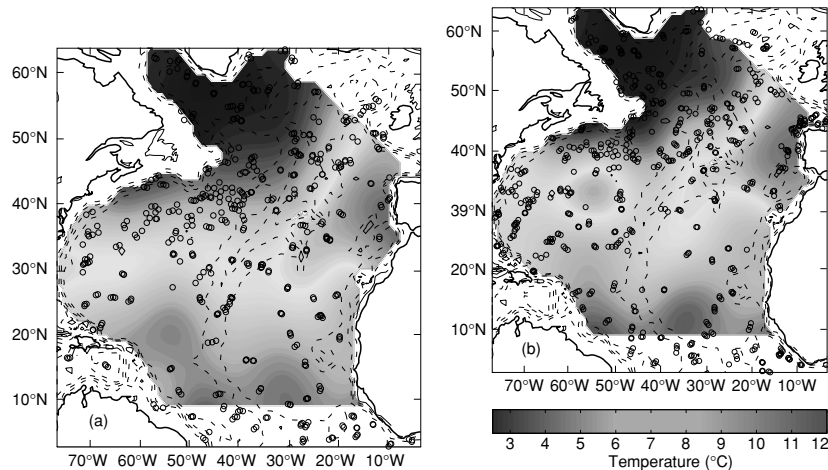


Fig. 3.16. North Atlantic temperature at 950 m depth in (a) February 2004 and (b) December 2004. Circles are points where temperature was measured (Chu et al. 2006, submitted to *Journal of Oceanography*)

and Ψ_{mn} on $1^\circ \times 1^\circ$ grid. These computations uniquely demonstrate the existence of two different temperature patterns for winter (2003 and 2004)—spring (2004) (Fig. 3.16a) and fall (2004)—winter (2004 and 2005) (Fig. 3.16b).

The principle distinction between the two patterns (Fig. 3.16a, b) appears at least in cross-Atlantic transport of heat and salt (not shown here) from the Mediterranean Sea. The first mode (Fig. 3.16a) implies the existence of advection pathways across the Mid-Atlantic Ridge, which may accelerate westward motion of the Mediterranean water in the North Atlantic. The second mode (Fig. 3.16b) slows down westward propagation of warm and salt water from this sea. Comparison of monthly temperature patterns consecutively from September to December 2004 (second mode period, not shown here) clearly demonstrates a largest portion of Mediterranean water slowly moving along the Mid-Atlantic ridge with speed of about $1\text{--}1.5\text{ cm s}^{-1}$. If the mid-depth temperature is taken as a tracer, the velocity can be roughly estimated from two consecutive temperature fields on the basis of displacements of 6, 7, 8, 9, and 10°C isotherms (Fig. 3.17) where the arrows show the mean direction of isotherm displacements during the three-month periods.

Reid (1994) identified the second mode as the steady state of the North Atlantic due to its high recurrence in data. Our computations indicate that this mode is one of the two possible North Atlantic modes. The two modes correspond to opposite mean values of the North Atlantic Oscillation (NAO) Index (www.cru.uea.ac.uk): negative value (-0.81) for the first mode (December 2003 to March 2004) and positive value (0.27) for the second (August–November 2004). The OSD reduces the noise-to-signal ratio for the ARGO

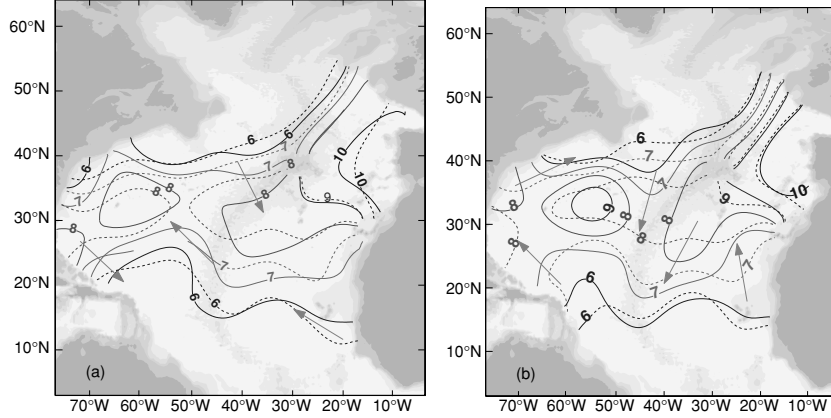


Fig. 3.17. Mid-depth circulation identified by isotherm displacement (a) from December 2003 (*dashed curves*) to March 2004 (*solid curves*) and (b) from September 2004 (*dashed curves*) to December 2004 (*solid curves*). The *gray arrows* show the water pathways (Chu et al. 2006, submitted to Journal of Oceanography)

data to 0.07–0.1 for temperature. With this noise level, the reconstructed temperature field is quite realistic (Chu et al. 2003a, b, 2004b).

3.4 Global Heat Storage

The climatological data (WOA and GDEM) show annual cycle of temperature and heat storage for the world oceans and individual ocean basins. The annual and monthly mean temperatures are represented by (\bar{T} and T_{mon}). Annual mean heat storage from the surface to depth z (negative value) at location (x, y) is defined by

$$\bar{H}_{\text{ST}}(x, y, z) = \int_z^0 \rho c_p \bar{T} dz'. \quad (3.43)$$

Monthly heat storage anomaly is defined by

$$\Delta H_{\text{ST}}(x, y, z) = \int_z^0 \rho c_p (T_{\text{mon}} - \bar{T}) dz'. \quad (3.44)$$

WOA contains the data from the surface to a maximum depth of 5,500 m. GDEM contains the data from the surface to bottom. The strength of the GDEM is the static stability for all the vertical profiles. Here, we present the results from GDEM data. The annual mean global heat storage per unit area from the surface to bottom (unit: 10^6 J m^{-2}) (Fig. 3.18) shows that a minimum contour of 10^8 J m^{-2} is located near Antarctic. Maximum contours of $4 \times 10^9 \text{ J m}^{-2}$ are found in the subtropical Atlantic and western Pacific. The contours nearly follow the bathymetry in the coastal regions.

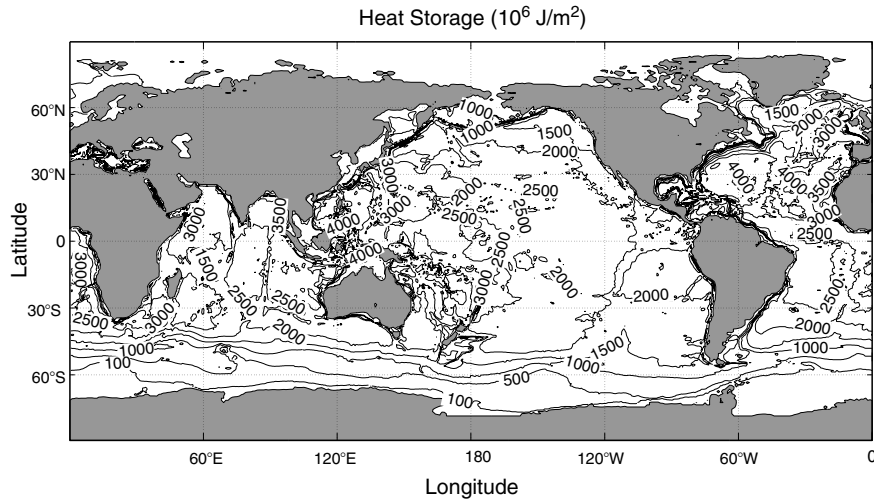


Fig. 3.18. Annual mean global heat storage per unit area from the surface to bottom (unit: 10^6 J m^{-2}). A minimum contour of 10^8 J m^{-2} is located near Antarctic. Maximum contours of $4 \times 10^9 \text{ J m}^{-2}$ are found in the subtropical Atlantic and western Pacific. The contours nearly follow the bathymetry in the coastal regions

The contours of the annual mean global heat storage per unit area from the surface to 550 m (Fig. 3.19a) and 275 m (Fig. 3.19b) depths are almost in zonal direction in high latitudes and align with the subtropical gyre in the low latitudes.

Figure 3.20 shows the horizontally integrated annual mean heat storage by 1° latitude belt from the surface to various depths. Almost no difference is found in the heat storage from the surface to these depths (including the ocean bottom) in the high latitudes (north of 60°N and south of 60°S). This indicates that for polar regions, the heat storage for the upper 275 m layer is quite representative for the whole water column. However, the heat storage has large difference in the subtropical regions (between 30°N and 30°S). For example, the heat storage from the surface to 275 m depth is nearly one-fourth of that for the whole water column. The heat storage from the surface to 3,000 m depth is nearly three-fourth of that for the whole water column.

Figure 3.21 shows similar features as from WOA (Levitus 1984) (1) heat storage has large annual cycle at midlatitudes of both hemispheres that lags the maximum of incoming solar radiation by about three months. (2) The heat storage of the Northern Hemisphere has a large annual cycle located at 12°N . The heat storage in this region is approximately three to four months out of phase with the annual cycle at midlatitudes of the Northern Hemisphere with the maximum at 12°N occurring around May. (3) The annual range of heat storage at 12°N is as large as the annual range at midlatitudes of the Northern Hemisphere. However, Fig. 3.21 also shows the large difference of the monthly

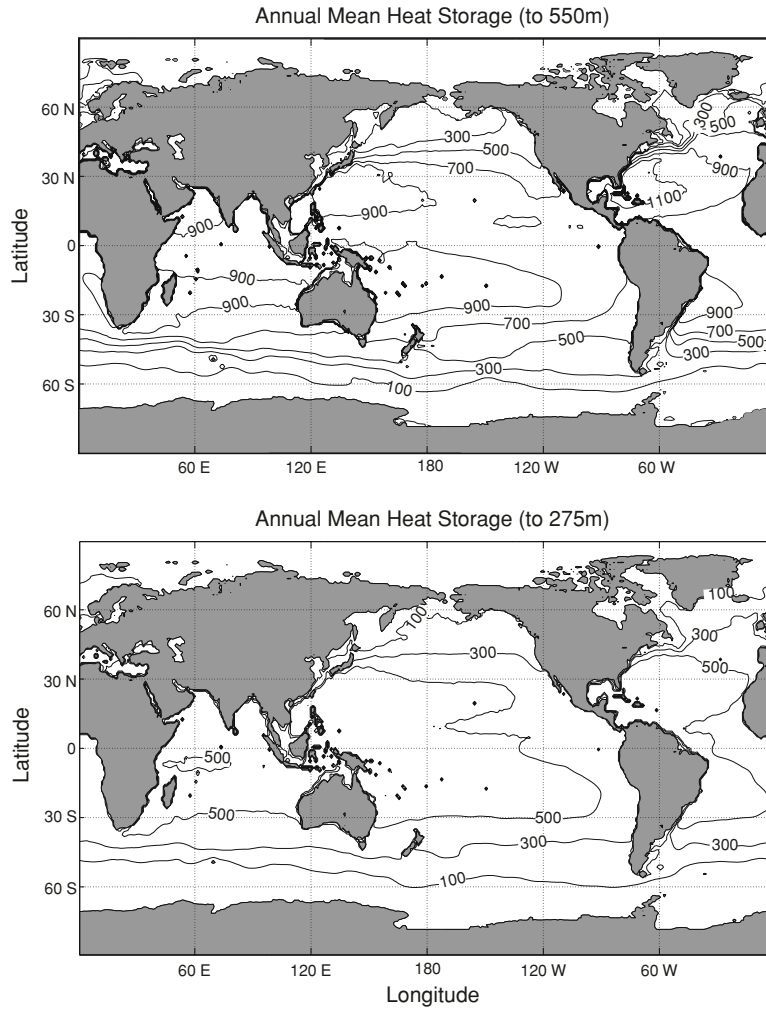


Fig. 3.19. Annual mean global heat storage per unit area from the surface to (a) 550 m and (b) 275 m depths (unit: 10^6 J m^{-2}). The contours of the heat storage almost align in zonal direction in high latitudes and with the subtropical gyre in the low latitudes

heat storage anomaly between the surface to 3,000 m depth and to the ocean bottom.

Questions and Exercises

- (1) What is the difference between the z -level and parameter analyses in building climatological data on the grid points? Why the z -level analysis

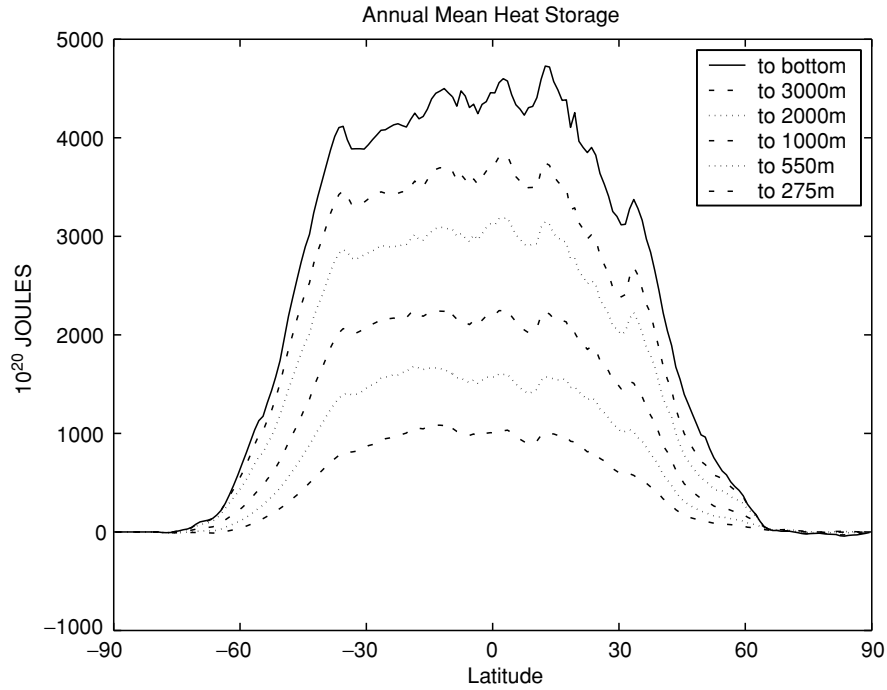


Fig. 3.20. Horizontally integrated annual mean heat storage by 1° latitude belt from the surface to various depths (275, 550, 1,000, 2,000, and 3,000 m, the ocean bottom). It shows almost no difference in the heat storage from the surface to these depths in the high latitudes (north of 60°N and south of 60°S), and a large difference in the subtropical regions (between 30°N and 30°S)

on the (T, S) profiles cannot guarantee the static stability? What does Fig. 3.1 tell us?

- (2) Discuss the advantages and disadvantages of z -level and parameter analyses in building climatological data on the grid points from observed profile data.
- (3) When the analyzed temperature (T_k^a) is computed at the grid point k from the first guess temperature (T_k^f) using the observational data (T_j^o)

$$T_k^a = T_k^f + \sum_{j=1}^N \alpha_{kj} (T_j^o - T_j^f), \quad (\text{E3.1})$$

use the least-square difference between the interpolated and actual grid point values to prove that the weighting factors (α_{kj}) satisfy the following equation

$$\sum_{j=1}^N (\eta_{ij} + \delta_{ij} \lambda_i^o) \alpha_{kj} = \eta_{kj}. \quad (\text{E3.2})$$

where η_{kj} is the autocorrelation between point k and point j .

Global Ocean Heat Storage by 1° Latitude Belts (solid line: 3000m, dashed line: bottom)

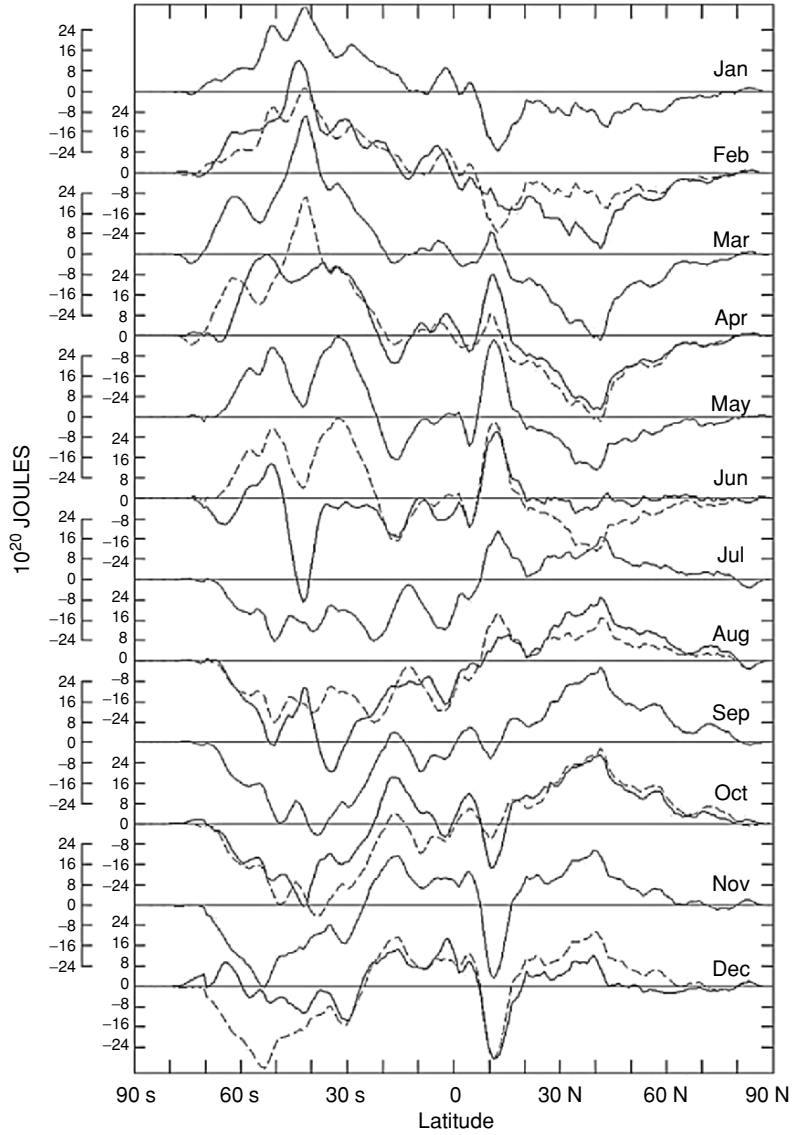


Fig. 3.21. Horizontally integrated monthly heat storage anomaly by 1° latitude belt from the surface to 3,000m depth (*solid curves*) and to the bottom (*dashed curves*)

- (4) Discuss the strength and weakness of MODAS. Suggest future improvement.
- (5) What is the interpretation of Gaussian-type MODAS errors shown in Fig. 3.7?

- (6) What is the major benefit of using the optimal spectral decomposition method (3.4)?

$$c(\mathbf{x}, z_k, t) = A_0(z_k, t) + \sum_{m=1}^M A_m(z_k, t) \Psi_m(\mathbf{x}, z_k), \quad \mathbf{x} \in R(z_k) \quad (\text{E3.3})$$

- (7) Do the eigenfunctions $\{\Psi_m(\mathbf{x}, z_k)\}$ in the optimal spectral decomposition depend on the observational data? Why?
- (8) What is the reason for the Vapnik–Chervonenkis cost function (3.7) to be used to determine the optimal mode truncation?
- (9) Why do we need to use the rotation matrix method to solve the algebraic equation (3.8)?
- (10) An ill-posed algebraic equation

$$\mathbf{A}\hat{\mathbf{a}} = \mathbf{Q}\mathbf{Y}, \quad (\text{E3.4})$$

is solved using the rotation matrix \mathbf{S} . Equation (d) is multiplied by \mathbf{S} from the left,

$$\mathbf{S}\mathbf{A}\hat{\mathbf{a}} = \mathbf{S}\mathbf{Q}\mathbf{Y}, \quad (\text{E3.5})$$

which changes the coefficient matrix and the source term from $(\mathbf{A}, \mathbf{Q}\mathbf{Y})$ to $(\mathbf{S}\mathbf{A}, \mathbf{S}\mathbf{Q}\mathbf{Y})$. Prove that the minimization process

$$\tilde{\eta}_3^2(1 + \tilde{\eta}_1^2) \rightarrow \min, \quad (\text{E3.6})$$

is equivalent to the maximization

$$J_1 = \|\mathbf{A}\|^2 - \frac{\|\mathbf{S}\mathbf{Q}\mathbf{Y}\|^2}{\|\mathbf{a}\|^2} \rightarrow \max, \quad (\text{E3.7})$$

where $\|\mathbf{A}\|$ is the spherical norm of the matrix \mathbf{A} and

$$\tilde{\eta}_1 \equiv \frac{\|\mathbf{S}\mathbf{Q}\mathbf{Y}'\|}{\|\mathbf{S}\mathbf{Q}\bar{\mathbf{Y}}\|}, \quad \tilde{\eta}_3 \equiv \frac{\|\mathbf{S}\mathbf{Q}\bar{\mathbf{Y}}\|}{\|\mathbf{a}\|}. \quad (\text{E3.8})$$

- (11) Prove (E3.7) to be the same as

$$J_1 = \|\mathbf{A}\|^2 - \tilde{\eta}_3^2 \left[1 + \frac{2(\mathbf{S}\mathbf{Q}\bar{\mathbf{Y}} * \mathbf{S}\mathbf{Q}\mathbf{Y}')}{\|\mathbf{S}\mathbf{Q}\bar{\mathbf{Y}}\|^2} + \tilde{\eta}_1^2 \right] \rightarrow \max. \quad (\text{E3.9})$$

- (12) Why is it that the reconstructed accuracy $\|\chi\|$ of the optimal decomposition scheme is up bounded by η_1 (noise-to-signal ratio before the rotation), $\|\chi\| \leq \eta_1$?
- (13) Please discuss the significance of the bimodality of the mid-depth North Atlantic circulation that is identified by using the ARGO data.

- (14) Select an area of your interest. Download the heat storage data provided in DVD-ROM in this book. Discuss the seasonal and depth variability of the heat storage.
- (15) The heat storage from the surface to 3,000 m depth is very different during the months April, June, August, and December from the surface to the bottom; and not so different in other months (see Fig. 3.21). Can you explain this phenomenon?
- (16) Download the heat storage data provided in DVD-ROM in this book. Compute the global heat storage below 5,500 m depth. Explain whether the heat storage below the depth of 5,500 m is negligible.

Coordinate Systems

The hydrographic data are usually represented in the z -coordinate (or using pressure to represent depth) system. However, many inverse methods use the isopycnal coordinate system such as the box model (Wunsch 1978), original β -spiral method (Stommel and Scott 1977), and the P-vector model (Chu and Li 2000). This chapter describes isopycnal coordinate system, semi-isopycnal coordinate system, and the transformation of hydrographic data from the z to isopycnal and semi-isopycnal coordinate systems.

4.1 Isopycnal Coordinate System

As pointed out by Wunsch and Grant (1982), in determining large-scale circulation from hydrographic data, we can be reasonably confident on the assumptions of geostrophic balance, mass conservation, and no major crossisopycnal mixing (except where water masses are in contact with the atmosphere). The potential density ρ of each fluid element would be conserved.

The isopycnal coordinate system is represented by (x, y, ρ) with x - and y -axes in the horizontal plane, ρ -axis in vertical with unit vectors $(\mathbf{i}, \mathbf{j}, \mathbf{k})$ in the three directions, repetitively. The benefit of using the isopycnal coordinate system is that the density ρ can be treated as constant in horizontal differentiation. The geostrophic balanced motion on an isopycnal surface (ρ) with a pressure p is given by Bleck and Smith (1990),

$$\mathbf{V} = \frac{1}{f} \mathbf{k} \times \nabla M, \quad (4.1)$$

where $\mathbf{V} = (u, v, 0)$, is the geostrophic velocity; $M = p/\rho + gz$, is the Montgomery potential. The hydrostatic balance is written by

$$\frac{p}{\rho^2} + \frac{\partial M}{\partial \rho} = 0. \quad (4.2)$$

The adiabatic density conservation and incompressible continuity equations are combined to give an equation for the thickness, $\partial p/\partial\rho$. The continuity equation is given by

$$\nabla \cdot \left(\frac{\partial p}{\partial \rho} \mathbf{V} \right) = 0. \quad (4.3)$$

Note that the differentiations with respect to x and y are on the isopycnal surface. Differentiation of (4.1) with respect to ρ and use of (4.2) lead to the thermal wind relation

$$\frac{\partial \mathbf{V}}{\partial \rho} = -\frac{1}{f\rho^2} \mathbf{k} \times \nabla p. \quad (4.4)$$

The continuity (4.3) can be rewritten by

$$\mathbf{V} \cdot \nabla \left(\frac{\partial p}{\partial \rho} \right) + \frac{\partial p}{\partial z} \nabla \cdot \mathbf{V} = 0, \quad (4.5)$$

Using (4.1) yields

$$\nabla \cdot \mathbf{V} = \nabla \left(\frac{1}{f} \right) \cdot (\mathbf{k} \times \nabla M) = -\frac{1}{f} \nabla f \cdot \mathbf{V}. \quad (4.6)$$

Substituting (4.6) in (4.5) yields the conservation of potential vorticity (q) on the isopycnal surface,

$$\mathbf{V} \cdot \nabla q = 0, \quad (4.7)$$

where

$$q = \frac{fg}{\partial p/\partial \rho}. \quad (4.8)$$

The derivative $\partial p/\partial\rho$ represents the thicknesses between two adjacent isopycnal levels. The (p, q) fields are computed on the isopycnal surface can be computed numerically after the hydrographic data are processed in the isopycnal surface. The climatological (p, q) fields on $\sigma^2 = 35.47(\text{kg m}^{-3})$ isopycnal surface are calculated using the NODC annual mean climatological T, S data (Fig. 4.1).

4.2 Semi-Isopycnal Coordinate System

Consider a series of potential density (σ_θ) surfaces, each marked by a constant value of σ with the depth,

$$z^{(\sigma)} = R(x, y, \sigma), \quad (4.9)$$

where R is the decreasing function with σ . The vertical distance between two closely spaced σ surfaces with increment of $\Delta\sigma$ is given by

$$h^{(\sigma)} = \frac{\partial z^{(\sigma)}}{\partial \sigma} \Delta\sigma. \quad (4.10)$$

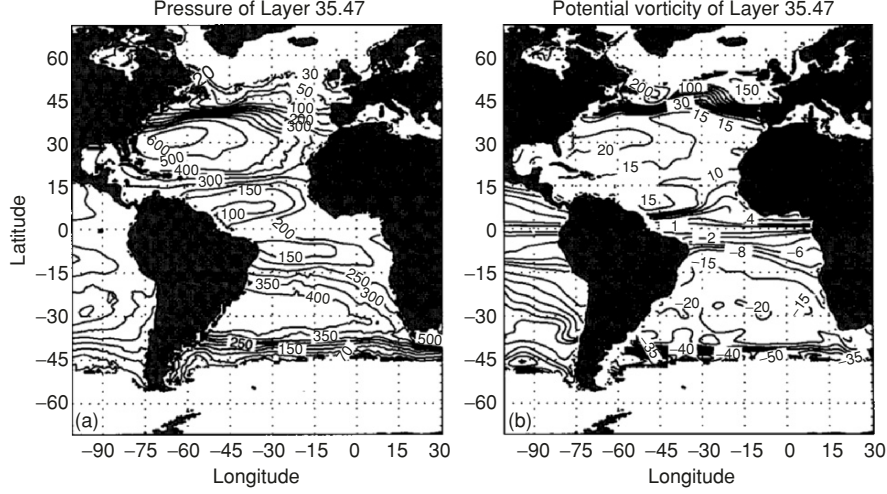


Fig. 4.1. Climatological (p, q) data on $\sigma_2 = 35.47(\text{kg m}^{-3})$ isopycnal surface: (a) pressure (unit: db) and (b) potential vorticity (unit: $10^{-11} \text{ m}^{-1} \text{ s}^{-1}$) (from Chu and Li 2000, Journal of Physical Oceanography)

The semi-isopycnal coordinate system is represented by $(x, y, z^{(\sigma)})$ with x - and y -axes in the horizontal plane, $z^{(\sigma)}$ -axis in vertical with unit vectors $(\mathbf{i}, \mathbf{j}, \mathbf{k})$ in the three directions, repetitively (McDougall 1988).

The geostrophic balanced motion in the $(x, y, z^{(\sigma)})$ is given by

$$\mathbf{V}^{(\sigma)} = \frac{1}{f\rho} \mathbf{k} \times \nabla_{\sigma} p, \quad (4.11)$$

which is similar to (1.1) for the z -coordinate system. Here, the gradient operator at the $z^{(\sigma)}$ -level is defined by

$$\nabla_{\sigma} \equiv \mathbf{i} \left. \frac{\partial}{\partial x} \right|_{\sigma} + \mathbf{j} \left. \frac{\partial}{\partial y} \right|_{\sigma}. \quad (4.12)$$

The continuity equation can be expressed by considering the flow between two isopycnal surfaces separated by an increment, $h^{(\sigma)}$, together with the diapycnal velocities $w_u^{(\sigma)}$ and $w_l^{(\sigma)}$ across the upper and lower isopycnal surfaces (Fig. 4.2). The continuity of an ocean is represented by

$$\frac{1}{h} \left. \frac{\partial(h^{(\sigma)}u)}{\partial x} \right|_{\sigma} + \left. \frac{\partial(h^{(\sigma)}v)}{\partial y} \right|_{\sigma} + \frac{w_u^{(\sigma)} - w_l^{(\sigma)}}{h} = 0. \quad (4.13)$$

For infinitesimally small h , (4.13) becomes

$$\mathbf{V}^{(\sigma)} \cdot \nabla_{\sigma} [\ln(h^{(\sigma)})] + \nabla_{\sigma} \cdot \mathbf{V}^{(\sigma)} + \frac{\partial w^{(\sigma)}}{\partial z} = 0. \quad (4.14)$$

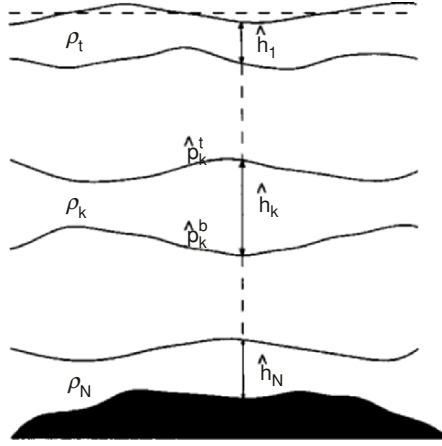


Fig. 4.2. Vertical discretization of the multilayer ocean with the k th layer having potential density ρ_k , layer thickness \hat{h}_k , top and bottom pressures (\hat{p}_k^t, \hat{p}_k^b), respectively (Chu and Li 2000, Journal of Physical Oceanography)

Horizontal divergence can be calculated from (4.11),

$$\nabla_\sigma \cdot \mathbf{V}^{(\sigma)} = -\frac{\nabla_\sigma f}{f^2 \rho} \cdot (\mathbf{k} \times \nabla_\sigma p) = -\frac{\nabla_\sigma f}{f} \cdot \mathbf{V}^{(\sigma)}. \quad (4.15)$$

Substituting (4.15) in (4.14) yields the conservation of potential vorticity,

$$\mathbf{V}^{(\sigma)} \cdot \nabla_\sigma [q^{(\sigma)}] = \frac{\partial w^{(\sigma)}}{\partial z}, \quad q^{(\sigma)} \equiv \ln[Q^{(\sigma)}], \quad Q^{(\sigma)} \equiv \frac{f}{h^{(\sigma)}}, \quad (4.16)$$

where $Q^{(\sigma)}$ is the potential vorticity; and $q^{(\sigma)}$ is a conservative quantity representing the potential vorticity (we may call it the pseudo potential vorticity). The diapycnal velocity $w^{(\sigma)}$ is not only from the vertical diffusivity, thermobaricity, and cabbeling, but also from lateral mixing along the neutral tangent plane (McDougall 1988).

4.3 Isopycnal Surfaces Determined from Data

Three reference levels: (surface, 2,000 decibar (db), 4,000 db) are used for potential density computation (Keffer 1985; Talley 1988): σ_0 (or sometime called σ_θ) using the surface, σ_2 using 2,000 db, and σ_4 using 4,000 db. The potential densities σ_2 and σ_4 provide better representations for levels near 2,000 and 4,000 db. Here,

$$\sigma_m = \rho_m - 1,000 \text{ kg m}^{-3}, \quad m = 0, 2, 4. \quad (4.17)$$

The following ranges for the σ_m -values are considered,

$$22.200 \leq \sigma_0 \leq 27.725, \quad 31.625 \leq \sigma_2 \leq 37.150, \quad 41.30 \leq \sigma_4 \leq 45.90. \quad (4.18)$$

Note that 27.725, 37.15, and 45.90 are maximum values for σ_0 , σ_2 , and σ_4 computed from the GDEM T , S data set. The potential densities (σ_0 , σ_2 , σ_4) are discretized with the increment,

$$\Delta\sigma = 0.025 \text{ kg m}^{-3}, \quad (4.19)$$

for σ_0 , σ_2 and

$$\Delta\sigma = 0.02 \text{ kg m}^{-3}, \quad (4.20)$$

for σ_4 . Thus, there are 222 σ_0 -layers, 222 σ_2 -layers, and 280 σ_4 -layers. Within each layer, the density is vertically uniform.

The cubic spline is used to interpolate T , S data into 246 z -levels with three different increments in order to well resolve isopycnal surfaces: 5 m from 0- to 100-m depth, 10 m from 100- to 1,000-m depth, 20 m from 1,000- to 2,500-m depth, and 50 m below 2,500-m depth. Thus, a high-resolution z -coordinate data set $[\hat{T}(z), \hat{S}(z), \hat{\sigma}_m(z)]$ has been built. The symbol ‘‘hat’’ indicates the data either directly from observations or computed from observational data. For simplicity and no loss of generality, we will use $\sigma_\theta(\sigma_0)$ for illustration.

4.4 Data Transformation

The transformation is fulfilled by comparing the z -coordinate potential density data $\hat{\sigma}_\theta(z_j)$ with the discrete σ_θ -values at the bottom of the k th isopycnal layer, $\sigma_\theta^b(k)$,

$$\sigma_\theta^b(k) = 22.1875 + (k - 1)\Delta\sigma_\theta, \quad \sigma_\theta(k) = \frac{1}{2}[\sigma_\theta^b(k) + \sigma_\theta^b(k + 1)], \quad (4.21)$$

where the superscript b indicates the bottom of the k th isopycnal layer. The geometric depth for the bottom of the $\sigma_\theta(k)$ -layer is obtained by

$$\hat{D}_k^b = -z_j, \quad \text{if } \hat{\sigma}_\theta(z_j) = \sigma_\theta^b(k), \quad (4.22)$$

and

$$\hat{D}_k^b = -z_j - \frac{\sigma_\theta(k) - \hat{\sigma}_\theta(z_j)}{\hat{\sigma}_\theta(z_{j+1}) - \hat{\sigma}_\theta(z_j)}, \quad \text{if } \hat{\sigma}_\theta(z_j) < \sigma_\theta^b(k) < \hat{\sigma}_\theta(z_{j+1}). \quad (4.23)$$

The thickness of the k th isopycnal layer is calculated by

$$\hat{h}_k = \hat{D}_k^b - \hat{D}_{k-1}^b. \quad (4.24)$$

After \hat{h}_k is obtained, we may compute the hydrostatic pressure field. Starting from the surface ($k = 1$), the k th layer has density ρ_k and thickness \hat{h}_k , as shown in Fig. 4.2. Pressure is not uniform within the layer with

$$\hat{p}_k^t = g \sum_{i=1}^{k-1} \rho_i \hat{h}_i, \quad (4.25)$$

at the top of the k th layer, and

$$\hat{p}_k^b = g \sum_{i=1}^k \rho_i \hat{h}_i, \quad (4.26)$$

at the bottom of the k th layer. The mean value

$$\hat{p}_k \equiv \frac{\hat{p}_k^t + \hat{p}_k^b}{2} = g \left(\sum_{i=1}^{k-1} \rho_i \hat{h}_i + \frac{1}{2} \rho_k \hat{h}_k \right), \quad (4.27)$$

can be used to represent the pressure at the middle of the k th layer (Fig. 4.2). The potential vorticity (4.18) is discretized by

$$\hat{q}_k = \frac{fg\delta\sigma_\theta}{\hat{p}_k^b - \hat{p}_k^t}. \quad (4.28)$$

Earlier work of McCartney (1982), Keffer (1985), and Talley (1988) also shows the benefit of using potential vorticity in ocean circulation studies.

Questions and Exercises

- (1) Derive the conservation of the potential vorticity equation for the isopycnal coordinate system from the geostrophic balance,

$$\mathbf{V} = \frac{1}{f} \mathbf{k} \times \nabla M, \quad (E4.1)$$

the hydrostatic balance,

$$\frac{p}{\rho^2} + \frac{\partial M}{\partial \rho} = 0, \quad (E4.2)$$

and the continuity equation,

$$\nabla \cdot \left(\frac{\partial p}{\partial \rho} \mathbf{V} \right) = 0. \quad (E4.3)$$

- (2) The potential vorticity is defined by

$$q = \frac{fg}{\partial p / \partial \rho}, \quad (E4.4)$$

in the isopycnal surface coordinate and by

$$q^{(\sigma)} \equiv \ln \left[\frac{f}{h^{(\sigma)}} \right], \quad (E4.5)$$

in the semi-isopycnal surface coordinate, discuss the difference between the two.

- (3) What is the similarity and difference between the isopycnal and semi-isopycnal coordinate systems? When you analyze the (T, S) profile data, what coordinate system will you choose among z -coordinate, isopycnal-coordinate, and semi-isopycnal coordinate? Why?

P-Vector

A perfect unit vector (i.e., P-vector) can be defined by the density only. This vector represents the orientation of the absolute velocity. Existence of the P-vector and its vertical turning guarantees the validity of the velocity inversion.

5.1 z -Coordinate System

5.1.1 Definition

When the constant ρ and q surfaces intersect (Fig. 5.1), it is true that

$$\nabla\rho \times \nabla q \neq 0. \quad (5.1)$$

A unit vector, called the perfect vector (or P-vector) by (Chu 1995a,b), can be defined by

$$\mathbf{P} = \frac{\nabla\rho \times \nabla q}{|\nabla\rho \times \nabla q|}. \quad (5.2)$$

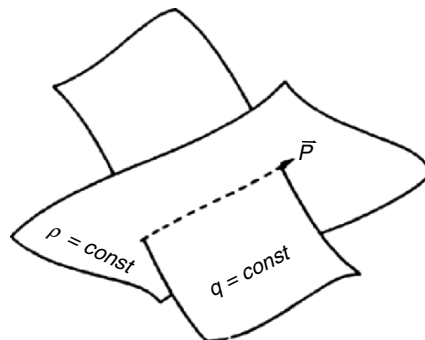


Fig. 5.1. Intersection of surfaces of ρ and q (from Chu 1995a, Marine Technology Society Journal)

The Needler's formula (1.19) becomes

$$\mathbf{V} = \gamma \mathbf{P}, \quad (5.3)$$

where γ is a scalar and its absolute value $|\gamma|$ is the speed. Thus, γ is called the speed parameter. The benefits of using the vector \mathbf{P} are in two-folds: two-step determination of \mathbf{V} and easy inclusion of three necessary conditions. A two-step method was proposed by Chu (1995a) (i.e., the P-vector inverse method): (a) determination of the unit vector \mathbf{P} , and (b) determination of the scalar γ from the thermal wind relation.

5.1.2 Horizontal P-Vector Field

Climatological \mathbf{P} field in the North Atlantic Ocean was constructed from the climatological mean potential density field (ρ) which was computed from NOAA WOA annual mean temperature and salinity fields (Fig. 5.2). The data has 33 vertical levels (Table 3.1) with $1^\circ \times 1^\circ$ horizontal resolution,

$$\Delta x = \frac{2\pi R}{360} \cos \phi, \quad \Delta y = \frac{2\pi R}{360}, \quad (5.4)$$

where ϕ is the latitude, R the earth radius.

The vertical grid is the difference between the two vertical levels as illustrated in Table 3.1,

$$\Delta z_k = z_k - z_{k+1}. \quad (5.5)$$

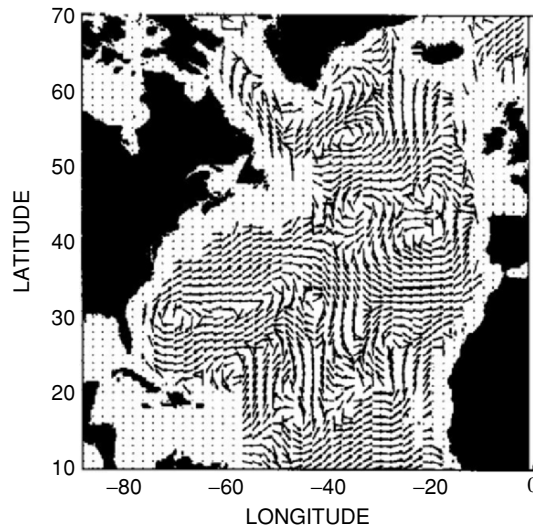


Fig. 5.2. North Atlantic Ocean \mathbf{P}_h field at 150m depth computed from WOA climatological annual mean T, S data (from Chu 1995a, Marine Technology Society Journal)

The potential vorticity q is calculated from ρ using (1.9), and the vector \mathbf{P} is computed from (ρ, q) using (5.2). Although the unit vector, \mathbf{P} , only carries partial information about the velocity field [see (5.3)], it is rather surprising that its horizontal components, $\mathbf{P}_h = (P_x, P_y)$, catches the most important features of the North Atlantic general circulation. For example, at 150 m depth \mathbf{P}_h resembles the classical views (Schmitz and McCartney 1993) quite well. The important features are: (1) anticyclonic subtropical gyre in the western part of the ocean between 20°N and 45°N , (2) recirculation cell on the western side (west of 40°W) of the subtropical gyre, (3) cyclonic–anticyclonic dipole in the areas ($30^\circ\text{W} - 10^\circ\text{W}$, about 30°N), and (4) high latitude cyclonic gyre ($50^\circ\text{N} - 60^\circ\text{N}$, $20^\circ\text{W} - 50^\circ\text{W}$).

5.1.3 P-Spiral

The three components of the vector \mathbf{P} can be written by [see (5.2)],

$$P_x = \frac{J^{(x)}(\rho, q)}{J_2(\rho, q)}, \quad P_y = \frac{J^{(y)}(\rho, q)}{J_2(\rho, q)}, \quad P_z = \frac{J^{(z)}(\rho, q)}{J_2(\rho, q)}, \quad (5.6)$$

where $J^{(x)}(A, B)$, $J^{(y)}(A, B)$, and $J^{(z)}(A, B)$ are two-dimensional Jacobians,

$$J^{(x)}(A, B) \equiv \begin{vmatrix} \partial A/\partial y & \partial A/\partial z \\ \partial B/\partial y & \partial B/\partial z \end{vmatrix}, \quad J^{(y)}(A, B) \equiv \begin{vmatrix} \partial A/\partial z & \partial A/\partial x \\ \partial B/\partial z & \partial B/\partial x \end{vmatrix}, \\ J^{(z)}(A, B) \equiv \begin{vmatrix} \partial A/\partial x & \partial A/\partial y \\ \partial B/\partial x & \partial B/\partial y \end{vmatrix}, \quad J_2 = \sqrt{[J^{(x)}]^2 + [J^{(y)}]^2 + [J^{(z)}]^2}.$$

Let α be the angle between \mathbf{P}_h and the x -axis,

$$P_x = \sin \alpha, \quad P_y = \cos \alpha. \quad (5.7)$$

Change of α with depth from z_m to z_k ,

$$\Delta \alpha_{km} = \alpha_k - \alpha_m, \quad (5.8a)$$

is called the **P**-spiral and

$$\sin(\Delta \alpha_{km}) = \left| \begin{vmatrix} P_x^{(k)} & P_x^{(m)} \\ P_y^{(k)} & P_y^{(m)} \end{vmatrix} \right| \quad (5.8b)$$

can be used to identify the **P**-spiral between two levels. If $\sin(\Delta \alpha_{km}) \neq 0$, the **P**-spiral exists; otherwise the **P**-spiral does not exist (Fig. 5.3).

The **P**-vector expression (5.6) is used to explore the existence of the **P**-spiral. Substituting (5.6) into (5.7) yields,

$$\sin \alpha = \frac{J^{(y)}(\rho, q)}{\sqrt{[J^{(x)}(\rho, q)]^2 + [J^{(y)}(\rho, q)]^2}}, \quad (5.9) \\ \cos \alpha = \frac{J^{(x)}(\rho, q)}{\sqrt{[J^{(x)}(\rho, q)]^2 + [J^{(y)}(\rho, q)]^2}}.$$

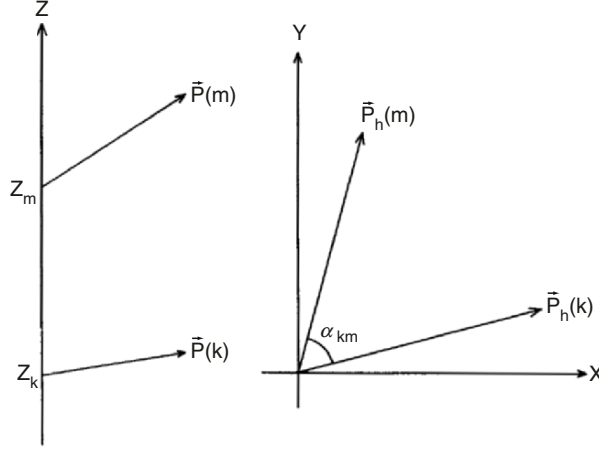


Fig. 5.3. (a) **P**-spiral and (b) turning angle α_{km} between two levels (from Chu 1995a, Marine Technology Society Journal)

Differentiation of $\sin \alpha$ with respect to z gives

$$\frac{\partial(\sin \alpha)}{\partial z} = \cos \alpha \frac{\partial \alpha}{\partial z}, \quad (5.10)$$

Substituting (5.9) into (5.10) yields

$$\Lambda \equiv \frac{\partial \alpha}{\partial z} = \frac{1}{[J^{(x)}]^2 + [J^{(y)}]^2} \left[J^{(x)} \frac{\partial J^{(y)}}{\partial z} - J^{(y)} \frac{\partial J^{(x)}}{\partial z} \right], \quad (5.11)$$

which represents the vertical turning of \mathbf{P}_h when $\partial \alpha / \partial z \neq 0$, the **P**-spiral exists. The parameter Λ is called the **P**-vector turning parameter.

Since the potential vorticity q is calculated from ρ with $q = f \partial \rho / \partial z$, substitution of this relationship into (5.6) yields

$$J^{(x)}(\rho, q) = f J^{(x)}(\rho, \rho_z) - \beta \rho_z^2, \quad J^{(y)}(\rho, q) = f J^{(y)}(\rho, \rho_z), \quad (5.12)$$

$$\frac{\partial}{\partial z} J^{(x)}(\rho, q) = f J^{(x)}(\rho, \rho_{zz}) - 2\beta \rho_x \rho_{zz}, \quad (5.13a)$$

$$\frac{\partial}{\partial z} J^{(y)}(\rho, q) = f J^{(y)}(\rho, \rho_{zz}), \quad (5.13b)$$

where the subscript “ z ” denotes the vertical derivative. Substituting (5.12) and (5.13) into (5.11) yields

$$\Lambda = \frac{\rho_z J_3(\rho, \rho_z, \rho_{zz}) + \beta [2\rho_x \rho_{zz} J^{(y)}(\rho, \rho_z) - \rho_z^2 J^{(y)}(\rho, \rho_{zz})] / f}{[J^{(x)}(\rho, \rho_z) - \beta \rho_z^2 / f]^2 + [J^{(y)}(\rho, \rho_z)]^2}, \quad (5.14)$$

where

$$J_3(A, B, C) \equiv \begin{vmatrix} \partial A/\partial x & \partial A/\partial y & \partial A/\partial z \\ \partial B/\partial x & \partial B/\partial y & \partial B/\partial z \\ \partial C/\partial x & \partial C/\partial y & \partial C/\partial z \end{vmatrix}, \quad (5.15)$$

is the three-dimensional Jacobian for (A, B, C) .

What are the necessary conditions for the existence of the **P**-spiral? Equation (5.14) shows that

$$\Lambda = 0, \quad \text{for } \rho_z = 0, \quad (5.16)$$

which is the first necessary condition – the **P**-spiral exists when the density is stratified (i.e., $\rho_z \neq 0$). For the f -plane approximation ($\beta = 0$), (5.14) becomes

$$\Lambda = \frac{\rho_z J_3(\rho, \rho_z, \rho_{zz})}{[J^{(x)}(\rho, \rho_z)]^2 + [J^{(y)}(\rho, \rho_z)]^2}, \quad (5.17)$$

which leads to the second necessary condition, the **P**-spiral exists, when ρ, ρ_z , and ρ_{zz} are functionally independent, i.e.,

$$J_3(\rho, \rho_z, \rho_{zz}) \neq 0. \quad (5.18)$$

This also indicates that the β -effect does not play any roles in the existence of **P**-spiral.

5.2 Isopycnal Coordinate System

5.2.1 **P**-vector

The potential vorticity conservation requires that any water particle should move along q -isoline on the isopycnal surface, i.e., any q -isoline is a trajectory of water particles (Fig. 5.4). For each trajectory, the **P**-vector is defined as the unit tangential vector,

$$\mathbf{P} = \frac{1}{|\nabla q|} (\mathbf{k} \times \nabla q) = \frac{1}{|\nabla q|} \left(-\frac{\partial q}{\partial y} \mathbf{i} + \frac{\partial q}{\partial x} \mathbf{j} \right). \quad (5.19)$$

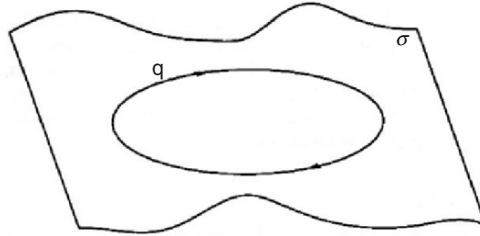


Fig. 5.4. Isolines of potential vorticity (q) are trajectories on the isopycnal surface (from Chu and Li 2000, *Journal of Physical Oceanography*)

Equation (5.19) shows that the existence of \mathbf{P} requires

$$\nabla q \neq 0, \quad (5.20)$$

showing the heterogeneity of potential vorticity on the isopycnal surface. At any point on the isopycnal surface, the vector \mathbf{P} indicates the tangential direction of the trajectory and therefore, is parallel to the absolute velocity vector,

$$\mathbf{V} = \gamma(x, y, \rho)\mathbf{P}, \quad (5.21)$$

where the absolute value of γ is the speed of the currents,

$$|\gamma| = |\mathbf{V}|. \quad (5.22)$$

Now, the determination of the velocity on the isopycnal surface is also divided into two steps: (a) determination of the unit vector \mathbf{P} , and (b) determination of γ . The positive (negative) values of γ indicate the same (opposite) direction of \mathbf{V} with \mathbf{P} .

5.2.2 Absolute Velocity Formula

Substituting (5.21) into the thermal wind relation (4.4) leads to

$$\frac{\partial \gamma}{\partial \rho} \mathbf{P} + \gamma \frac{\partial \mathbf{P}}{\partial \rho} = -\frac{1}{f\rho^2} \mathbf{k} \times \nabla p. \quad (5.23)$$

Vector-product of both sides of (5.23) by the vector \mathbf{P} gives

$$\gamma(\mathbf{P} \times \frac{\partial \mathbf{P}}{\partial \rho}) = -\frac{1}{f\rho^2} \mathbf{P} \times (\mathbf{k} \times \nabla p). \quad (5.24)$$

Scalar-product of both sides of (5.24) by the vector \mathbf{P} yields

$$\gamma = \frac{\mathbf{P} \cdot \nabla p}{f\rho^2 \mathbf{P} \cdot (\mathbf{k} \times \partial \mathbf{P} / \partial \rho)}. \quad (5.25)$$

Substituting (5.25) into (5.21) yields the absolute velocity,

$$\mathbf{V} = \frac{\mathbf{P} \cdot \nabla p}{f\rho^2 \mathbf{P} \cdot (\mathbf{k} \times \partial \mathbf{P} / \partial \rho)} \mathbf{P}, \quad (5.26)$$

which is similar to Needler's formula (1.19).

5.2.3 P-Vector Spiral

The angle between \mathbf{P} and the x -axis on the isopycnal surface that changes with the isopycnal level is called the \mathbf{P} -spiral. Figure 5.5 shows the turning between the two levels k and m with the turning angle (Chu 2000),

$$\Delta \alpha_{km} = \alpha_k - \alpha_m.$$

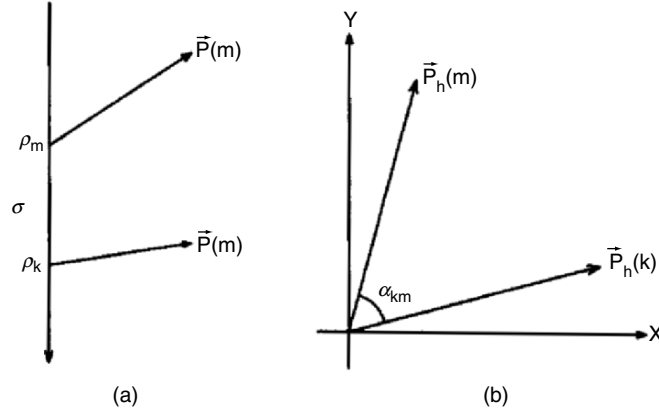


Fig. 5.5. Vertical turning of the P-vector: (a) P-vector at two isopycnal levels, and (b) turning angle between two isopycnal levels (from Chu 2000, Journal of Oceanography)

From the P-vector definition (5.19), we have

$$\sin \alpha = P_x = -\frac{1}{|\nabla q|} \frac{\partial q}{\partial y}, \quad \cos \alpha = P_y = \frac{1}{|\nabla q|} \frac{\partial q}{\partial x}. \quad (5.27)$$

Differentiating $\sin \alpha$ with respect to ρ and using (5.27) yield the \mathbf{P} turning parameter

$$\Lambda \equiv \frac{\partial \alpha}{\partial \rho} = -\mathbf{P} \cdot \left(\mathbf{k} \times \frac{\partial \mathbf{P}}{\partial \rho} \right). \quad (5.28)$$

Substituting (5.19) into (5.28) yields

$$\Lambda = \frac{J(q, q_\rho)}{|\nabla q|^2}, \quad (5.29)$$

where

$$J(A, B) \equiv \frac{\partial A}{\partial x} \frac{\partial B}{\partial y} - \frac{\partial B}{\partial x} \frac{\partial A}{\partial y}.$$

Two necessary conditions should be satisfied such that the \mathbf{P} -spiral exists (i.e., $\partial \alpha / \partial \rho \neq 0$): (a) heterogeneity of potential vorticity on the isopycnal surface (i.e., $\nabla q \neq 0$), and (b) no functional dependence between q and q_ρ .

5.3 Semi-Isopycnal Coordinate

5.3.1 P-Vector

The conservation of potential vorticity is given by [see (4.16)]

$$\mathbf{V}^{(\sigma)} \cdot \nabla_\sigma \left[q^{(\sigma)} \right] = \frac{\partial w^{(\sigma)}}{\partial z}, \quad q^{(\sigma)} \equiv \ln \left[Q^{(\sigma)} \right], \quad Q^{(\sigma)} \equiv \frac{f}{h^{(\sigma)}}.$$

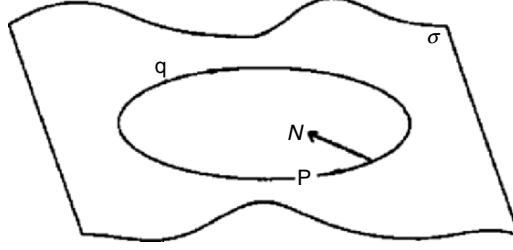


Fig. 5.6. Isoline of potential vorticity (q) is the trajectory of the water particle on the isopycnal surface. Here, (P, N) are the tangential and normal unit vectors of the trajectory (from Chu 2000, Journal of Oceanography)

The two vectors $\mathbf{V}^{(\sigma)}$ and $\nabla_{\sigma}[q^{(\sigma)}]$ are usually not perpendicular if the vertical convergence of the diapycnal velocity exists ($\partial w^{(\sigma)}/\partial z \neq 0$). The velocity does not parallel the tangential direction of the $q^{(\sigma)}$ -isoline. However, the tangential and normal unit vectors of the $q^{(\sigma)}$ -isoline (Fig. 5.6) on the potential density surface can be defined by (Fig. 5.6),

$$\mathbf{P} = \frac{1}{|\nabla_{\sigma}q^{(\sigma)}|} \left[\frac{\partial q^{(\sigma)}}{\partial y} \mathbf{i} - \frac{\partial q^{(\sigma)}}{\partial x} \mathbf{j} \right], \quad \mathbf{N} = \frac{\nabla_{\sigma}q^{(\sigma)}}{|\nabla_{\sigma}q^{(\sigma)}|}. \quad (5.30)$$

The horizontal velocity at the isopycnal surface can be represented by (Chu 2000)

$$\mathbf{V}^{(\sigma)} = \gamma \mathbf{P} + \frac{\partial w^{(\sigma)}/\partial z}{|\nabla_{\sigma}q^{(\sigma)}|} \mathbf{N}. \quad (5.31)$$

Here, γ is the parameter to be determined by the thermal wind relation. Nonzero vertical convergence of diapycnal velocity ($\partial w^{(\sigma)}/\partial z \neq 0$) causes the crossing $q^{(\sigma)}$ -isoline motion.

Substitution of $q^{(\sigma)} \equiv \ln [f/h^{(\sigma)}]$ into (5.30) yields

$$P_x = \left[\frac{\beta}{f} - \frac{\partial \ln(h^{(\sigma)})}{\partial y} \right] / \left[\left(\frac{\beta}{f} - \frac{\partial \ln(h^{(\sigma)})}{\partial y} \right)^2 + \left(\frac{\partial \ln(h^{(\sigma)})}{\partial x} \right)^2 \right]^{1/2}, \quad (5.32)$$

$$P_y = \frac{\partial \ln(h^{(\sigma)})}{\partial x} / \left[\left(\frac{\beta}{f} - \frac{\partial \ln(h^{(\sigma)})}{\partial y} \right)^2 + \left(\frac{\partial \ln(h^{(\sigma)})}{\partial x} \right)^2 \right]^{1/2}, \quad (5.33)$$

where P_x and P_y are the two components of the unit vector \mathbf{P} . Without vertical change of the diapycnal velocity equation, (5.31) becomes,

$$\mathbf{V}^{(\sigma)} = \gamma \mathbf{P}, \quad (5.34)$$

and any water particle that moves along $q^{(\sigma)}$ -isoline on the potential density, i.e., any $q^{(\sigma)}$ -isoline, is a trajectory of water particles (Fig. 5.6). We call this case ($\partial w^{(\sigma)}/\partial z = 0$) as the no diapycnal exchange case.

5.3.2 P-Spiral

From the P-vector definition (5.30), the angle (α) from the x -axis to the vector \mathbf{P} counterclockwise is given by

$$P_x = \sin \alpha, \quad P_y = \cos \alpha. \quad (5.35)$$

Existence of the \mathbf{P} -spiral between potential-density levels becomes the nonzero ($\partial\alpha/\partial z \neq 0$). A nondimensional \mathbf{P} -spiral parameter defined by

$$\Lambda = h^{(\sigma)} \frac{\partial\alpha}{\partial z^{(\sigma)}} \quad (5.36)$$

is used to represent the \mathbf{P} -spiral. Substituting (5.35) into (5.36) yields

$$\Lambda = -h^{(\sigma)} \frac{\partial P_x / \partial z^{(\sigma)}}{P_y} = h^{(\sigma)} \frac{\partial P_y / \partial z^{(\sigma)}}{P_x}, \quad (5.37)$$

and substituting (5.32) and (5.33) into (5.37) yields

$$\Lambda = h^{(\sigma)} \frac{J(q^{(\sigma)}, \partial q^{(\sigma)} / \partial z^{(\sigma)})}{|\nabla_{\sigma} q^{(\sigma)}|^2}. \quad (5.38)$$

Thus, the necessary condition for the existence of the \mathbf{P} -spiral is the nonzero Jacobian of $q^{(\sigma)}$ and $\partial q^{(\sigma)} / \partial z^{(\sigma)}$, that is, the nonzero $q^{(\sigma)}$ and $\partial q^{(\sigma)} / \partial z^{(\sigma)}$, and the independence between $q^{(\sigma)}$ and $\partial q^{(\sigma)} / \partial z^{(\sigma)}$.

Substituting (4.16) into (5.38) yields

$$\Lambda = h^{(\sigma)} \frac{-\frac{\beta}{f} \frac{\partial^2 [\ln h^{(\sigma)}]}{\partial x \partial z^{(\sigma)}} + J \left[\ln h^{(\sigma)}, \frac{\partial (\ln h^{(\sigma)})}{\partial z^{(\sigma)}} \right]}{\left[\frac{\partial (\ln h^{(\sigma)})}{\partial x} \right]^2 + \left[\frac{\beta}{f} - \frac{\partial (\ln h^{(\sigma)})}{\partial y} \right]^2}, \quad (5.39)$$

which indicates that the \mathbf{P} -spiral can be generated by laterally and vertically inhomogeneous thickness between two closely-spaced potential-density surfaces (Chu 2000). The spatial variability of the parameter Λ represents the spatial variability of the \mathbf{P} -spirals. For illustration, we chose six locations (Fig. 5.7), A (54°W, 20°N), B (36°W, 28°N), C (20°W, 55°N), D (57°W, 40°N), E (18°W, 6°S), and F (30°W, 45°N), where the first three locations were studied extensively in the past (e.g., Stommel and Schott 1997; Schott and Stommel 1978). These six points represent the Antilles Current, North Atlantic Gyre, Norwegian Current, Gulf Stream, South Equatorial Current, Antarctic Circumpolar Current, respectively. The P-vector turning angles between the two consecutive isopycnal layers ($\Delta \alpha_{km}$) are computed for the six locations (Fig. 5.8). For $\Delta \alpha_{km} = 0.2$, the vertical turning angle is around 11°. For $\beta = 0$, (5.39) becomes

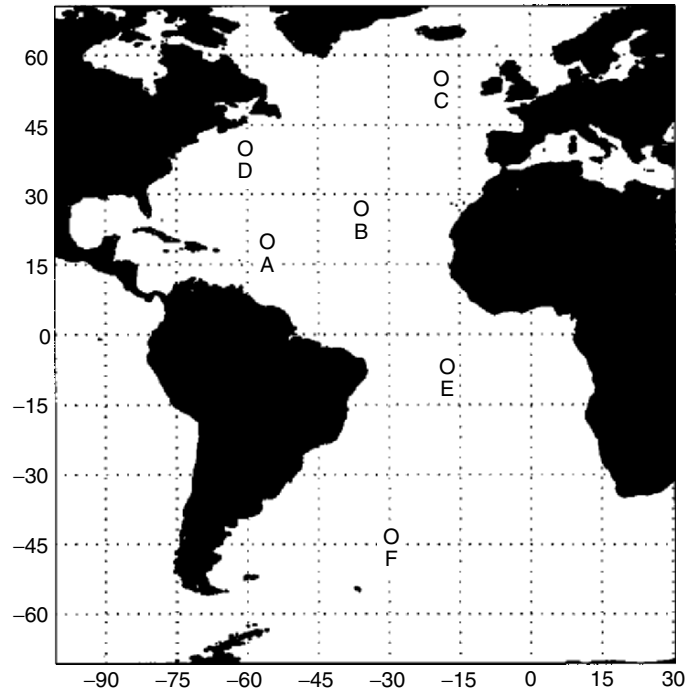


Fig. 5.7. Six locations: Antilles Current (A), North Atlantic Gyre (B), Norwegian Current (C), Gulf Stream (D), South Equatorial Current (E), Antarctic Circumpolar Current (F) (from Chu 2000, *Journal of Oceanography*)

$$\Lambda = h(\sigma) \frac{J \left[\ln h(\sigma), \frac{\partial(\ln h(\sigma))}{\partial z(\sigma)} \right]}{\left[\frac{\partial(\ln h(\sigma))}{\partial x} \right]^2 + \left[\frac{\partial(\ln h(\sigma))}{\partial y} \right]^2}, \quad (5.40)$$

showing the existence of the **P**-spiral without the β -effect.

Questions and Exercises

- (1) What are the most important features of the **P**-vector defined by (5.3) for the z -coordinate system?
- (2) Why the **P**-vector lie on the interface of isopycnal surface and iso-potential vorticity surface?
- (3) What is the **P**-spiral? Why is the **P**-spiral so important in determining absolute velocity from hydrographic data?
- (4) Is the β -effect important in determining absolute velocity from hydrographic data? If the answer is no, please explain why.
- (5) What are the three necessary conditions for the determination of absolute velocity from hydrographic data using the **P**-vector?

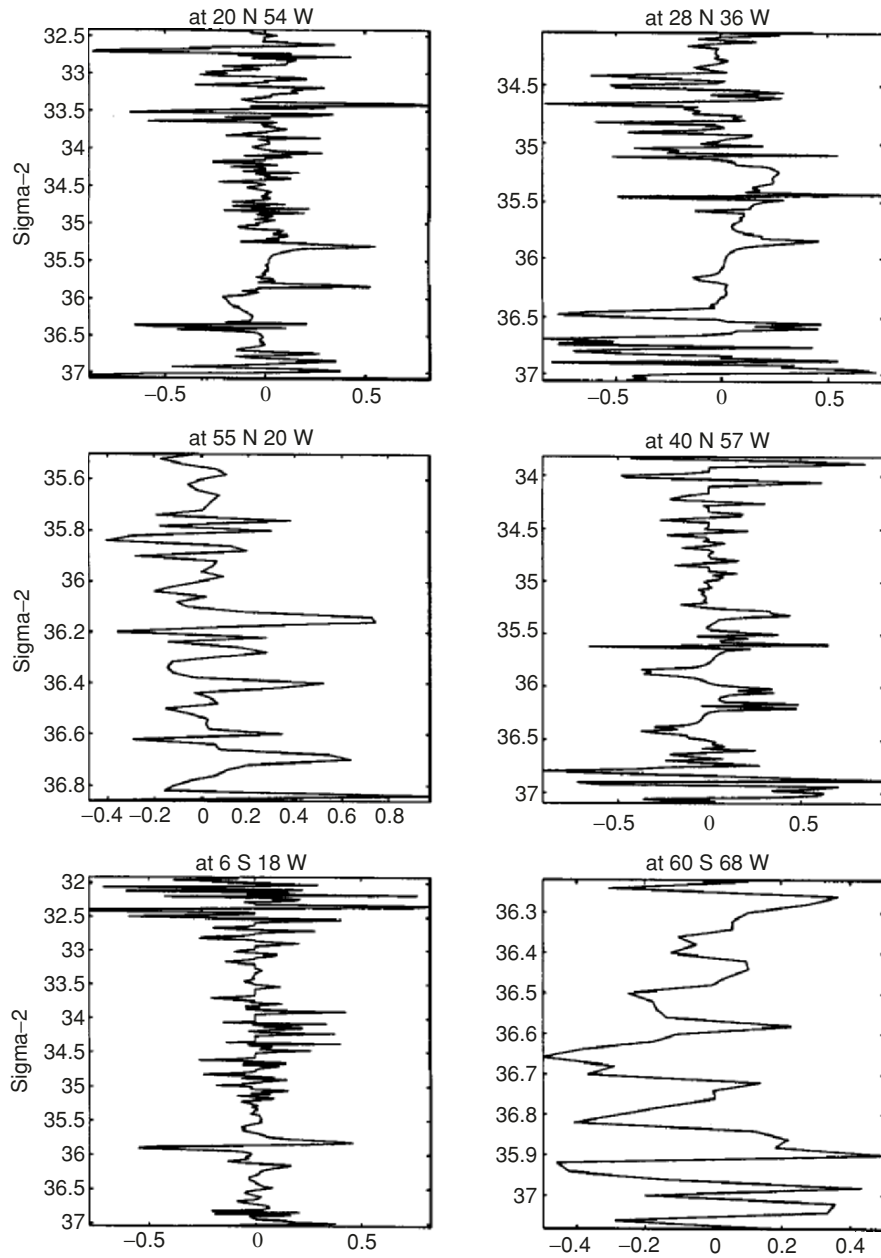


Fig. 5.8. The values of $\Delta\alpha$ for two consecutive isopycnal levels are usually small in the upper isopycnal layers, and become large in deeper isopycnal layers (from Chu 2000, *Journal of Oceanography*)

(6) Form the geostrophic balance

$$\mathbf{V} = \frac{1}{f} \mathbf{k} \times \nabla M, \quad (\text{E5.1})$$

and the hydrostatic balance,

$$\frac{p}{\rho^2} + \frac{\partial M}{\partial \rho} = 0, \quad (\text{E5.2})$$

for the isopycnal coordinate system. Derive the absolute velocity equation,

$$\mathbf{V} = \frac{\mathbf{P} \cdot \nabla p}{f \rho^2 \mathbf{P} \cdot (\mathbf{k} \times \partial \mathbf{P} / \partial \rho)} \mathbf{P}. \quad (\text{E5.3})$$

Discuss the physical significance of (E5.3).

- (7) Compare the P-vector turning parameters in z -coordinate, isopycnal-coordinate, and semi-isopycnal coordinate. Find in which coordinate system the P-vector turning parameter provides more concise information.
- (8) What is the physical interpretation of Fig. 5.8? Does it imply that the isopycnal- or semi-isopycnal coordinate is a good choice in determining absolute velocity from hydrographic data? Why?

Determination of Speed Parameter

The P-vector inverse method has two steps (a) determination of \mathbf{P} and (b) determination of the parameter γ (or called the speed parameter). When \mathbf{P} exists and vertical convergence of diapycnal velocity does not exist, the absolute velocity \mathbf{V} parallels \mathbf{P} . Determination of \mathbf{V} is reduced to the determination of the scalar γ .

6.1 Algebraic Equations

Applying the thermal wind relations (1.4) and (1.5) [or (4.4)] for the z -coordinate (or the isopycnal coordinate) at two different levels z_k and z_m (or ρ_k and ρ_m), a set of algebraic equations for determining the parameter γ are obtained (Chu 1995a)

$$\gamma^{(k)} P_x^{(k)} - \gamma^{(m)} P_x^{(m)} = \Delta u_{km}, \quad (6.1)$$

$$\gamma^{(k)} P_y^{(k)} - \gamma^{(m)} P_y^{(m)} = \Delta v_{km}. \quad (6.2)$$

In the z -coordinate system,

$$\Delta u_{km} \equiv \frac{g}{f\rho_0} \int_{z_m}^{z_k} \frac{\partial \rho}{\partial y} dz', \quad \Delta v_{km} \equiv -\frac{g}{f\rho_0} \int_{z_m}^{z_k} \frac{\partial \rho}{\partial x} dz' \quad (6.3)$$

are geostrophic shear at depth z_k relative to z_m . For the isopycnal coordinate system,

$$\Delta u_{km} \equiv \frac{1}{f} \int_{\rho_m}^{\rho_k} \frac{1}{\rho^2} \frac{\partial p}{\partial y} d\rho, \quad \Delta v_{km} \equiv -\frac{1}{f} \int_{\rho_m}^{\rho_k} \frac{1}{\rho^2} \frac{\partial p}{\partial x} d\rho \quad (6.4)$$

are geostrophic shear at level ρ_k relative to ρ_m . If the determinant

$$\begin{vmatrix} P_x^{(k)} & P_x^{(m)} \\ P_y^{(k)} & P_y^{(m)} \end{vmatrix} \neq 0, \quad (6.5)$$

the algebraic equations (6.1) and (6.2) have unique solution for $\gamma^{(k)} (m \neq k)$,

$$\gamma^{(k)} = \frac{\begin{vmatrix} \Delta u_{km} & P_x^{(m)} \\ \Delta v_{km} & P_y^{(m)} \end{vmatrix}}{\begin{vmatrix} P_x^{(k)} & P_x^{(m)} \\ P_y^{(k)} & P_y^{(m)} \end{vmatrix}}. \quad (6.6)$$

As soon as $\gamma^{(k)}$ is obtained, the absolute velocity \mathbf{V} is easily computed using (5.3), (5.21), or (5.34). Equation (5.8b) shows that the condition (6.5) is the existence of \mathbf{P} -spiral. This is to indicate that, for water columns satisfying the two necessary conditions (\mathbf{P} and \mathbf{P} -spiral exist) the absolute velocity can be computed.

6.2 Necessary Conditions

Necessary conditions for determination of \mathbf{V} solely from ρ become conditions regarding the vector \mathbf{P} . The ρ surface does not parallel the q surface, which requires

$$\nabla \rho \times \nabla q \neq 0, \quad (6.7)$$

which leads to the first necessary condition.

Necessary Condition 1: The vector \mathbf{P} exists.

Stommel and Scott (1977) pointed out that because the horizontal component of velocity rotates with depth in the open ocean (earlier called the β -spiral), absolute velocities can be obtained from observations of the density field alone. For the set of algebraic equations (6.1) and (6.2) having unique solutions (i.e., the \mathbf{P} -vector method works), it requires

$$\sin(\Delta \alpha_{km}) = \begin{vmatrix} P_x^{(k)} & P_x^{(m)} \\ P_y^{(k)} & P_y^{(m)} \end{vmatrix} \neq 0, \quad (6.8)$$

which leads to the second necessary condition.

Necessary Condition 2: The horizontal component of \mathbf{P} has vertical turning [see (6.8)], or the existence of \mathbf{P} -spiral (Chu 2000).

Before using any inverse method, these two necessary conditions should be checked. If one of them is not satisfied, no inverse method can be used to obtain the velocity field from the T , S fields for that water column.

6.3 Optimization Scheme

For a given level, $z = z_k$, there are $(N-1)$ sets ($m = 1, 2, k-1, k+1, \dots, N$) of equations (6.1) and (6.2) for calculating $\gamma^{(k)}$. Here N is the total number of vertical levels of the water column. All the $N-1$ sets of equations are compatible under the thermal wind constraint and have to provide the same solution. However, because of errors in measurements (instrumentation errors) and computations (truncation errors), the parameter $\gamma^{(k)}$ may vary with m . A least square error algorithm should be used to minimize the error. If the absolute velocity at depth z_m ($u^{(m)}, v^{(m)}$) is known, we may use the thermal wind relation (1.4) and (1.5) to calculate the absolute velocity at any level z_k ,

$$\begin{aligned} u^{(k)} &= u^{(m)} + \Delta u_{km}, & v^{(k)} &= v^{(m)} + \Delta v_{km}, \\ w^{(k)} &= -\frac{u^{(k)} \partial \rho^{(k)} / \partial x + v^{(k)} \partial \rho^{(k)} / \partial y}{\partial \rho^{(k)} / \partial z}. \end{aligned} \quad (6.9)$$

The computed $[u^{(k)}, v^{(k)}, w^{(k)}]$ may not be in the same direction as the vector \mathbf{P} $[P_x^{(k)}, P_y^{(k)}, P_z^{(k)}]$ at the depth z_k . If we assume that the vector \mathbf{P} exists at the depth z_k and that the velocity vector parallels the vector $\mathbf{P}^{(k)}$, an error can be easily defined by (Fig. 6.1)

$$E^{(k)} = \left| \gamma^{(k)} \mathbf{P}^{(k)} - \mathbf{V}^{(k)} \right| = 2\gamma^{(k)} \sin \left[\frac{1}{2}(\theta^{(k)}) \right] \cong \gamma^{(k)} \sin \theta^{(k)}, \quad (6.10)$$

where $\theta^{(k)}$ is the angle between $\mathbf{P}^{(k)}$ and $\mathbf{V}^{(k)}$.

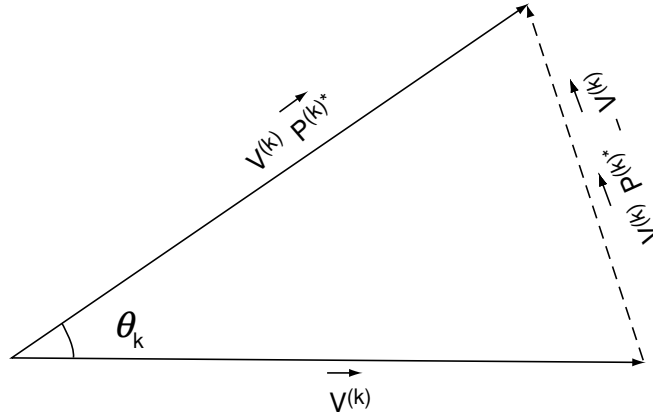


Fig. 6.1. Error at the level k (from Chu et al. 1998d, Journal of Geophysical Research-Oceans)

The total error of the water column velocity caused by the uncertainty of $[u^{(m)}, v^{(m)}]$ is

$$E = \sqrt{\sum_k (h_k E_k)^2}, \quad (6.11)$$

where $h_k = 0.5(z_{k-1} - z_{k+1})$, is the thickness of the layer centered at the k th level. The velocity $[u^{(m)}, v^{(m)}]$ is determined such that the total error E reaches the minimum,

$$\frac{\partial E}{\partial u^{(m)}} = 0, \quad \frac{\partial E}{\partial v^{(m)}} = 0, \quad (6.12)$$

which leads to a 2×2 algebraic equations for determining $[u^{(m)}, v^{(m)}]$,

$$A_{11}u^{(m)} + A_{12}v^{(m)} = F_1, \quad (6.13a)$$

$$A_{21}u^{(m)} + A_{22}v^{(m)} = F_2, \quad (6.13b)$$

where

$$A_{11} = \sum_k a_{11}^{(k)}, \quad A_{12} = \sum_k a_{12}^{(k)}, \quad A_{21} = A_{12}, \quad A_{22} = \sum_k a_{22}^{(k)}, \quad (6.14a)$$

$$F_1 = - \sum_k [a_{11}^{(k)} \Delta u_{km} + a_{12}^{(k)} \Delta v_{km}], \quad F_2 = - \sum_k [a_{21}^{(k)} \Delta u_{km} + a_{22}^{(k)} \Delta v_{km}], \quad (6.14b)$$

and

$$a_{11}^{(k)} \equiv [P_y^{(k)}]^2 \chi^{(k)}, \quad a_{12}^{(k)} = a_{21}^{(k)} \equiv -P_x^{(k)} P_y^{(k)} \chi^{(k)}, \quad a_{22}^{(k)} \equiv [P_x^{(k)}]^2 \chi^{(k)},$$

$$\chi^{(k)} \equiv \left[1 + \left(\frac{\partial \rho^{(k)} / \partial x}{\partial \rho^{(k)} / \partial z} \right)^2 + \left(\frac{\partial \rho^{(k)} / \partial y}{\partial \rho^{(k)} / \partial z} \right)^2 \right] h_k^2. \quad (6.15)$$

If the determinant of (6.13a, b) is nonzero,

$$\begin{vmatrix} A_{11} & A_{12} \\ A_{21} & A_{22} \end{vmatrix} \neq 0, \quad (6.16)$$

the absolute velocity at the level $z = z_m$ can be determined by

$$u^{(m)} = \frac{\begin{vmatrix} F_1 & A_{12} \\ F_2 & A_{22} \end{vmatrix}}{\begin{vmatrix} A_{11} & A_{12} \\ A_{21} & A_{22} \end{vmatrix}}, \quad v^{(m)} = \frac{\begin{vmatrix} A_{11} & F_1 \\ A_{21} & F_2 \end{vmatrix}}{\begin{vmatrix} A_{11} & A_{12} \\ A_{21} & A_{22} \end{vmatrix}}. \quad (6.17)$$

6.4 Evaluation Using the Modular Ocean Model (MOM)

Any inverse method involves two different kinds of errors: observational and modeling errors. The best way to verify the model is to use a no-error data set. Since there is no such data set, we may use a set of steady state solutions from a numerical model as a no-error data set. Chu et al. (1998a) use the steady-state solutions of temperature and salinity from Pacanowski et al. (1991) version of the Modular Ocean Model (MOM), which is based on the work of Bryan (1987).

6.4.1 MOM Implementation

The model domain consists of a $60 \times 65^\circ$ box in latitude-longitude space from 10°N to 70°N and 10°W to 75°W . An idealized shelf with a structure similar to that in Holland (1973) is included along the western boundary. The horizontal grid spacing is 2° latitude by 2° longitude. The model has 12 levels in the vertical, and the depth distribution is listed in Table 6.1.

Values assigned to the various model parameters are listed in Table 6.2. No-slip and insulating boundary conditions are applied at the lateral boundaries. The model uses the Cox (1987) parameterization to compute vertical diffusion and convection implicitly. The enhanced vertical diffusivity in regions of static instability is set at $10 \text{ m}^2 \text{ s}^{-1}$. The convective adjustment is used in the model.

The temperature and salinity of upper-most level are eased under a Haney (1971) restoration to a zonally uniform temperature [unit: $^\circ\text{C}$] field,

$$T_a(\varphi) = 30.0 - \frac{33.0}{80.0}\varphi + 40.0 \sin \left[\frac{2\pi}{75.0}(\varphi - 5.0) \right], \quad (6.18)$$

Table 6.1. Vertical levels for MOM modeling

k	z -level (m)	k	z -level (m)
1	-12.5	7	-635.0
2	-37.5	8	-1,025.0
3	-70.0	9	-1,575.0
4	-125.0	10	-2,350.0
5	-215.0	11	-3,250.0
6	-370.0	12	-4,150.0

Table 6.2. MOM parameters

parameter	symbol	value
horizontal diffusivity	A_{TH}	$1 \times 10^3 \text{ m}^2 \text{ s}^{-1}$
horizontal viscosity	A_{MH}	$2 \times 10^5 \text{ m}^2 \text{ s}^{-1}$
vertical diffusivity	A_{TV}	$1 \times 10^{-4} \text{ m}^2 \text{ s}^{-1}$
vertical viscosity	A_{MV}	$1 \times 10^{-4} \text{ m}^2 \text{ s}^{-1}$
characteristic density	P_0	$1,025 \text{ kg m}^{-3}$
heat capacity	C_w	$4 \times 10^3 \text{ J kg}^{-1} \text{ K}^{-1}$

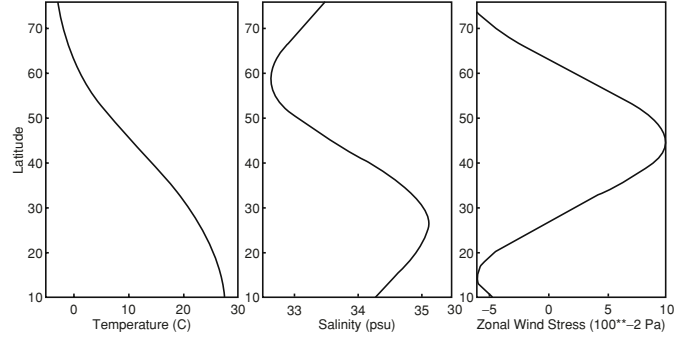


Fig. 6.2. Surface boundary conditions. Temperature and salinity fields used in the Haney-type restoring forcing condition and the surface wind stress (from Chu et al. 1998a, *Journal of Oceanography*)

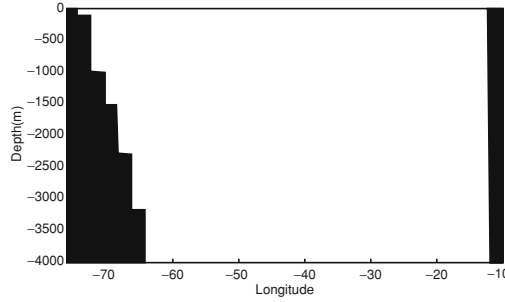


Fig. 6.3. The x -dependent bottom topography used in the MOM model (from Chu et al. 1998a, *Journal of Oceanography*)

and a salinity [unit: ppt] field

$$S(\varphi) = 35.0 - \frac{1.32}{50.0}\varphi + 0.84 \sin \left[\frac{2\pi}{55.0}(\varphi - 15.0) \right], \quad (6.19)$$

with relaxation time-scale of 25 days (over a modeled top mixed 25 m). Figure 6.2 shows the surface boundary conditions and the zonal wind stress. The bottom topography is assumed to be only dependent on x , and has a staircase-type change west of 64°W and no change east of 64°W (Fig. 6.3).

The techniques of Bryan (1987) for acceleration equilibration of the model solution are used. This includes using a longer time-step at any depth. The acceleration factor increases from one at the surface level to eight at the bottom level. After 750 surface years (6,000 years at the bottom) the model reaches a statistically steady state (total kinetic energy reaches equilibrium).

6.4.2 MOM Generated Steady-State (ρ, q) Data

The MOM model output includes potential temperature, salinity, and velocity (u, v, w). The statistically steady potential density field (ρ) is computed from the temperature and salinity fields. Figure 6.4 shows the σ_θ ($\equiv \rho - 1,000$) field at different depths. The most evident features are listed as follows. The maximum values ($29.2\text{--}29.3 \text{ kg m}^{-3}$) appear at the high latitudes (near 70°N) at all depths. The horizontal σ_θ gradient reduces as the depths increases. The low σ_θ water appears at the equatorial region near surface and stretches northward as the depth increases. Near the surface (Fig. 6.4a) the σ_θ contours are almost zonal except at the western boundary, where the σ_θ contours bend towards the north, indicating the northward movement of low σ_θ equatorial water. At the depths of 37.5 m (Fig. 6.4b) and 70 m (Fig. 6.4c), the northward movement of the equatorial low σ_θ water becomes more evident. At the depth of 215 m (Fig. 6.4d), the low σ_θ zone shifts northward. Two centers of low σ_θ (27.4 kg m^{-3}) are found at the southwest corner ($25^\circ\text{N}, 74^\circ\text{W}$) and at the middle of the eastern boundary. At the deep levels (Figs. 6.4e and 6.4f), σ_θ is very uniform. The minimum zone of σ_θ is located at around 60°N .

The statistically steady potential vorticity field (q) is computed from σ_θ . Figure 6.5 shows the $q(=f\partial\rho/\partial z)$ field at different depths. The most evident features are listed as follows. The values of q are either negative or zero. There is an anticyclonic gyre occupying the majority of the domain. In upper levels (12.5 m, 37.5 m, and 70 m), the strongest negative q center (with a value around $-1.4 \times 10^{-6} \text{ kg m}^{-4} \text{ s}^{-1}$) is located near the southwest corner ($60^\circ\text{--}70^\circ\text{W}, 20^\circ\text{--}35^\circ\text{N}$). As depth increases, the magnitude of q -values reduces. The strongest negative q center, with values around $-2.5 \times 10^{-8} \text{ kg m}^{-4} \text{ s}^{-1}$ at 1,575 m depth and $-2.2 \times 10^{-9} \text{ kg m}^{-4} \text{ s}^{-1}$ at 3,250 m depth (2–3 orders of magnitude smaller than the upper levels), is located near the northeast corner ($20^\circ\text{--}10^\circ\text{W}, 55^\circ\text{--}65^\circ\text{N}$).

6.4.3 MOM Generated Statistically Steady-State Velocity Field

Figure 6.6 shows the MOM generated statistically steady horizontal velocities at several depths (a) 12.5 m, (b) 37.5 m, (c) 70 m, (d) 215 m, (e) 1,575 m, and (f) 3,250 m. The circulation patterns can be outlined as follows. Westward-moving equatorial currents are evident in upper levels ($z \geq -215 \text{ m}$) and disappear in the deeper layer ($z < -215 \text{ m}$). The width of the upper layer equatorial current is around 6° in latitude.

When the upper layer equatorial current approaches the western boundary, it turns direction and becomes the western boundary current. The maximum velocity of the western boundary current reaches 13 cm s^{-1} . The intermediate level (1,575 m) and deep level (3,250 m) feature a westward current originating at the northeast corner. This current turns southwestward at around 50°W and branches into two western boundary currents (northward and southward)

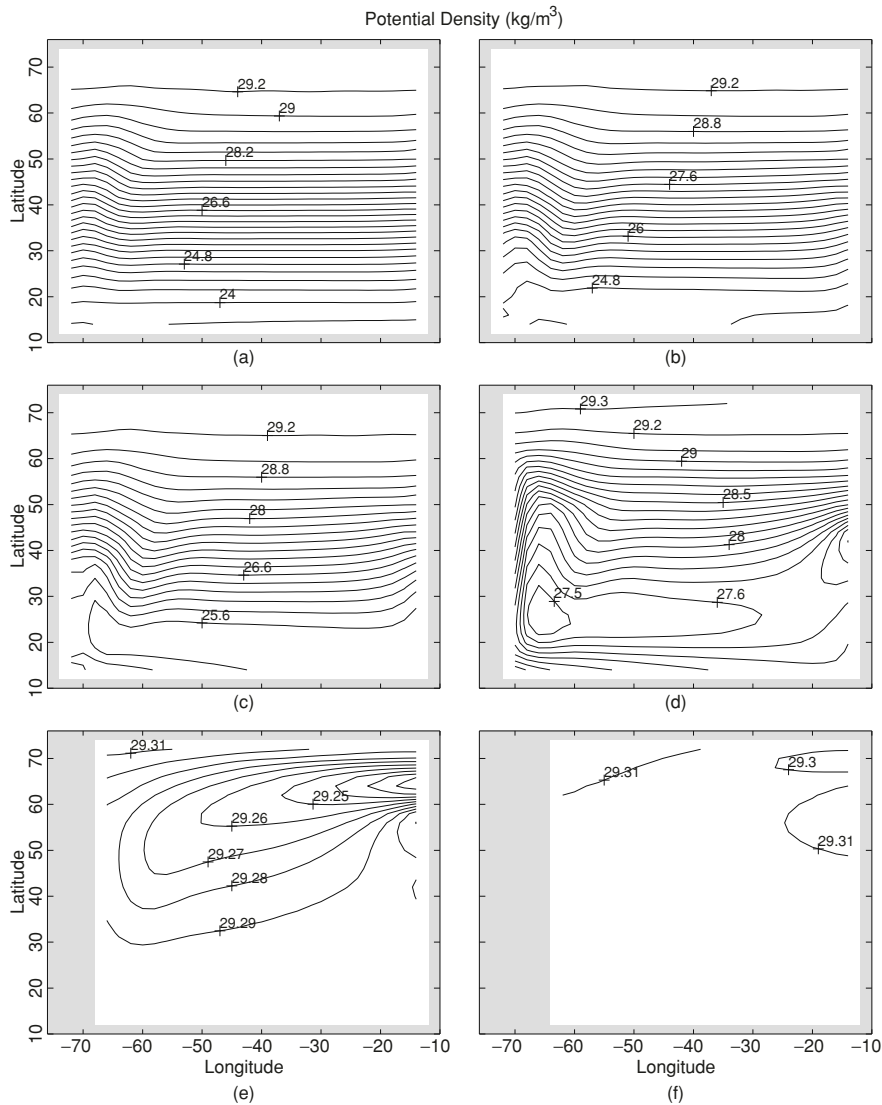


Fig. 6.4. Statistically steady potential density (kg m^{-3}) from the MOM simulation at different depths (a) 12.5 m, (b) 37.5 m, (c) 70 m, (d) 215 m, (e) 1,575 m, and (f) 3,250 m (from Chu et al. 1998a, *Journal of Oceanography*)

while approaching the western boundary. The bifurcation is found at 40°N for the depth of 1,575 m, and at 60°N for the depth of 3,250 m. The deep currents are weak ($\leq 2 \text{ cm s}^{-1}$).

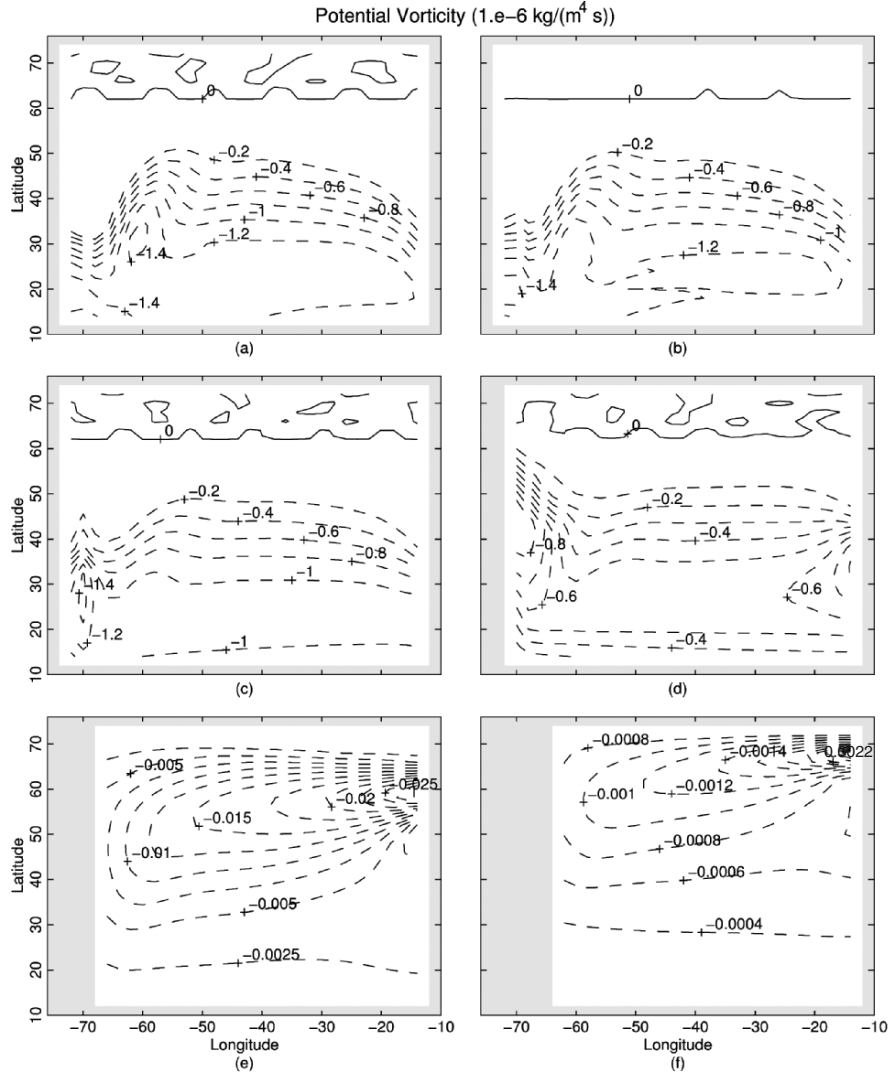


Fig. 6.5. Statistically steady potential vorticity (in $10^{-6} \text{ kg m}^{-4} \text{ s}^{-1}$) from the MOM simulation at different depths (a) 12.5 m, (b) 37.5 m, (c) 70 m, (d) 215 m, (e) 1,575 m, and (f) 3,250 m (from Chu et al. 1998a, *Journal of Oceanography*)

6.4.4 Necessary Condition Check-up

Before testing the P-vector method, the MOM (ρ, q) data are checked if the two necessary conditions are satisfied. The vector product of $\nabla\rho$ and ∇q is given by

$$\nabla\rho \times \nabla q = \mathbf{P} |\nabla\rho| |\nabla q| \sin \delta, \quad (6.20)$$

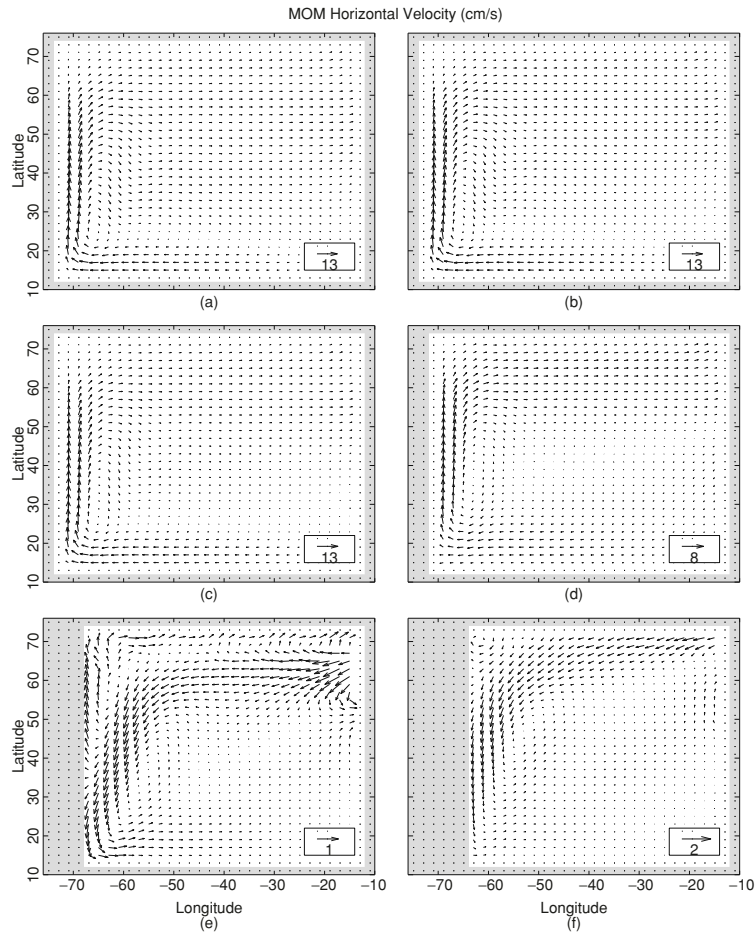


Fig. 6.6. Statistically steady horizontal velocity vector (in cm s^{-1}) from the MOM simulation at different depths (a) 12.5 m, (b) 37.5 m, (c) 70 m, (d) 215 m, (e) 1,575 m, and (f) 3,250 m (from Chu et al. 1998a, *Journal of Oceanography*)

where δ is the intersection angle between $\nabla\rho$ and ∇q . Since δ cannot be exactly zero when computed from data. A small value (10^{-5}) is taken as the criterion, if $|\sin\delta| \leq 10^{-5}$, the ρ surface is thought to be parallel to the q surface. Figure 6.7 shows the regions at six different depths where the first necessary condition fails.

The velocity spiral from the MOM simulation can be identified for each grid point by the plot of the horizontal velocity of all depths (Fig. 6.8). There are 12 vectors at each grid. Coincidence of the vectors indicates that there is no vertical turning. Two numbers given at each grid indicate the maximum turning between two consecutive levels such as from 370-m (level 6) to 635-m (level 7) in the subtropical regions (10° – 30° N) and from 1,025-m (level 8)

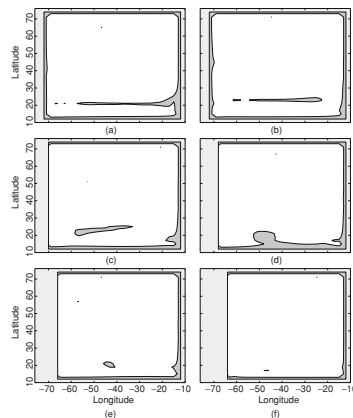


Fig. 6.7. Regions with $|\sin \delta| \leq 10^{-5}$ at different depths (a) 12.5 m, (b) 37.5 m, (c) 70 m, (d) 215 m, (e) 1,575 m, and (f) 3,250 m (from Chu et al. 1998a, *Journal of Oceanography*).

to 1,575-m (level 9) in the mid- and high- latitudes (north of 40°N) regions. At some locations, the maximum turning occurs at deeper levels. Usually, strong vertical turning of the horizontal velocity indicates a strong baroclinicity. This also implies that the second necessary condition (existence of spiral) is satisfied.

6.4.5 Absolute Velocities Obtained from the P-Vector Inverse Method Using MOM T, S Output

Taking the statistically steady potential temperature and salinity fields as no-error data sets, we employed the P-vector inverse method to obtain the 3-D absolute velocity (u, v) . Figure 6.9 shows the vector plots of the horizontal velocities at several different depths (a) 12.5 m, (b) 37.5 m, (c) 70 m, (d) 215 m, (e) 1,575 m, and (f) 3,250 m. The circulation patterns are very similar to the MOM statistically steady-state velocity fields in the upper four levels (12.5 m, 37.5 m, 70 m, and 215 m). The circulation patterns can be outlined as follows. Westward-moving equatorial currents are evident with a width of 6° in latitude. When the equatorial current approaches the western boundary, it turns direction and become the western boundary current. The current velocities are similar at the three levels: 12.5 m, 37.5 m, and 70 m, but weaker in the P-vector inverse method. The lower level (1,575 and 3,250 m) velocity fields are very weak. The major difference between the MOM and the inverse solutions is the western boundary flow bifurcation. The MOM model shows the high latitude westward flow bifurcated at 40°N for the depth of 1,575 m, and at 60°N for the depth of 3,250 m into two western boundary currents (northward and southward). However, the P-vector inverse model does not show this bifurcation.

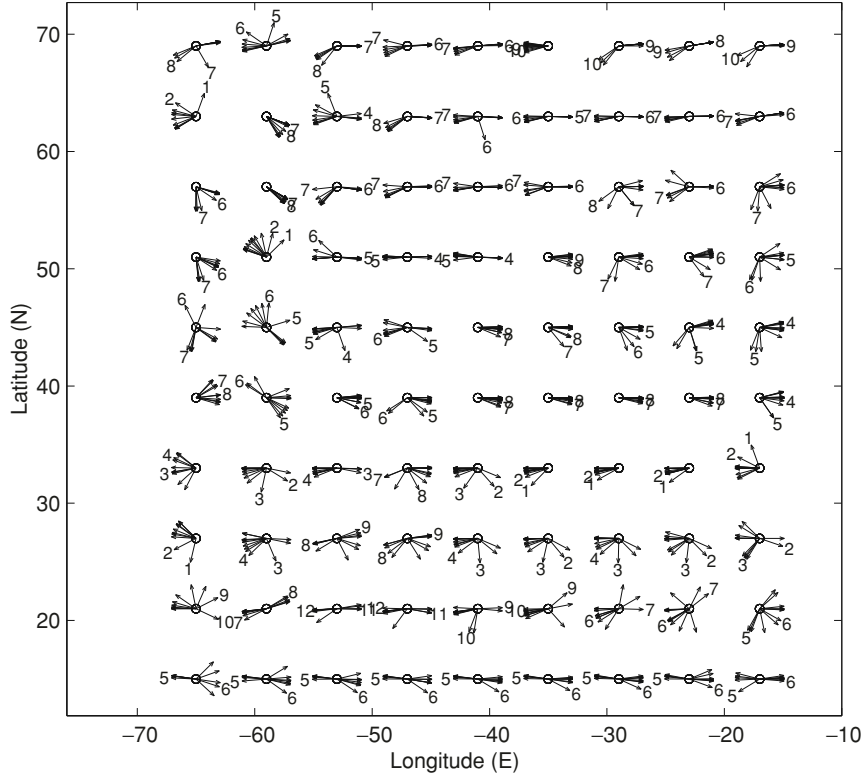


Fig. 6.8. P-Spirals of the horizontal velocity (12 vectors at each grid). Two numbers given at each grid indicate the maximum turning between two consecutive levels (from Chu et al. 1998a, *Journal of Oceanography*)

6.4.6 Comparison between Nondivergent Portions of Two Flow Fields

Given that the MOM model flow field derives from primitive equation dynamics, we do not expect that the velocity fields from the P-vector method (assuming geostrophic dynamics) match the MOM model velocity fields. The only valid comparison should be with the nondivergent portion of the flow field,

$$\nabla^2 \Psi_{\text{MOM}} = \frac{\partial(fv_{\text{MOM}})}{\partial x} - \frac{\partial(fu_{\text{MOM}})}{\partial y}, \quad (6.21)$$

$$\nabla^2 \Psi = \frac{\partial(fv)}{\partial x} - \frac{\partial(fu)}{\partial y}, \quad (6.22)$$

which are solved by taking $(u_{\text{MOM}}, v_{\text{MOM}})$, (u, v) as forcing functions under the boundary conditions

$$\Psi_{\text{MOM}}|_{\Gamma} = 0, \quad \Psi|_{\Gamma} = 0, \quad (6.23)$$

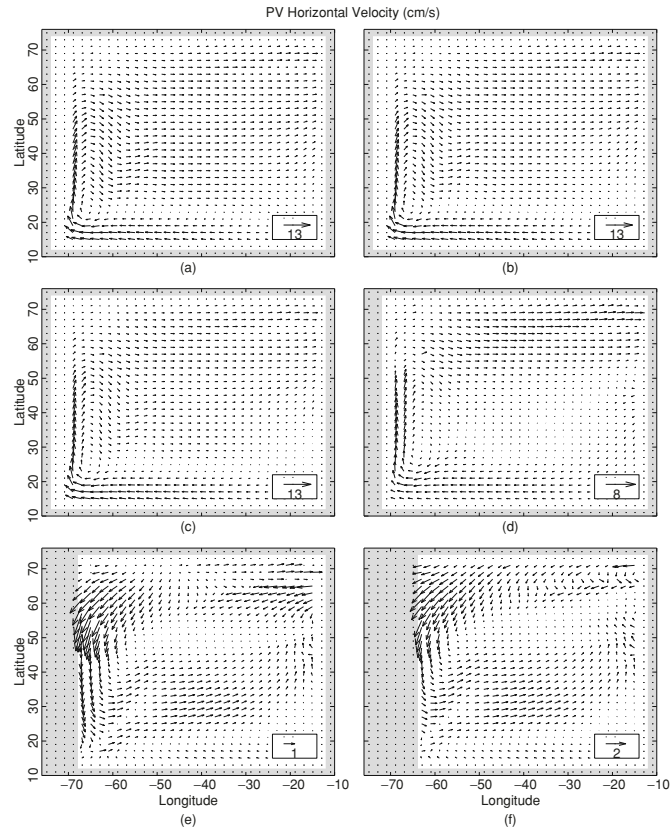


Fig. 6.9. Absolute velocity fields computed using the P-vector method at different depths (a) 12.5 m, (b) 37.5 m, (c) 70 m, (d) 215 m, (e) 1,575 m, and (f) 3,250 m (from Chu et al. 1998a, *Journal of Oceanography*)

where Γ represents the lateral boundaries. The Ψ_{MOM} field has the following features (Fig. 6.9): a nearly basin-wide anticyclonic gyre in the upper levels (12.5 m, 37.5 m, 70 m, and 215 m) and a nearly basin-wide cyclonic gyre in the lower levels (1,575 m, 3,250 m).

These gyres are evident by closed Ψ_{MOM} contours with a maximum value for the anticyclonic gyre and with a minimum value for the cyclonic gyre. Both basin-wide gyres are asymmetric. The center of the gyres (both upper and lower levels) is towards the west, with a strong western boundary current. In the upper levels, a weak and narrow cyclonic gyre appears in the high latitudes (north of 60°N east of 55°W (south of Greenland and Iceland.) This weak high latitude cyclonic gyre reduces its size with depth and becomes an anticyclonic gyre which stretches westward to the western boundary in the intermediate level (1,575 m). In the deep level (3,250 m), the cyclonic gyre fills the whole basin.

The streamfunction Ψ (Fig. 6.9) at the six different depths shows that the pattern of the two fields are quite similar: a nearly basin-wide anticyclonic gyre in the upper levels (12.5 m, 37.5 m, 70 m, and 215 m) and a nearly basin-wide cyclonic gyre in the lower levels (1,575 m, 3,250 m). These gyres are featured by closed Ψ contours with a maximum value for the anticyclonic gyre and a minimum value for the cyclonic gyre. The center of the basin-wide gyres (both upper and lower levels) is towards the west, and has a strong western boundary current. The patterns are very similar between Ψ_{MOM} and Ψ at all depths.

The differences between Ψ_{MOM} and Ψ are (a) the nearly basin-wide gyre is stronger in the MOM model than in this P-vector model except for the intermediate level (1,575 m), where the cyclonic gyre obtained by the P-vector method is stronger; (b) in the upper levels (12.5 m, 37.5 m, 70 m, and 215 m) the high latitude (north of 60°N) cyclonic gyre obtained by the P-vector model stretches from the eastern boundary to the western boundary; and (c) in the intermediate level (1,575 m), the high latitude anticyclonic gyre by the P-vector model is located in the eastern part (east of 40°W) rather than stretching to the western boundary in the MOM model.

Relative difference (I_{Ψ}) between Ψ_{MOM} and Ψ for each level can be depicted by a ratio between root-mean-square difference and standard deviation of MOM results ($\text{dev}_{\Psi_{\text{MOM}}}$),

$$I_{\Psi} = \frac{\sqrt{\frac{1}{M-1} \sum (\Psi_{\text{MOM}} - \Psi)^2}}{\sigma_{\Psi_{\text{MOM}}}}, \quad (6.24)$$

$$\text{dev}_{\Psi_{\text{MOM}}} = \sqrt{\frac{1}{M-1} \sum (\Psi_{\text{MOM}} - \bar{\Psi}_{\text{MOM}})^2}, \quad (6.25)$$

where M is the total number of the horizontal grid points, and $\bar{\Psi}_{\text{MOM}}$ is the horizontal mean. The numerator and denominator of (6.24) show the mean difference between two streamfunctions and the variability of Ψ_{MOM} . The smaller the I_{Ψ} , the smaller is the difference between the inverse and MOM solutions. Near the surface, I_{Ψ} is small (~ 0.15), increases with depth until 1,000 m (level eight) with the maximum value of 0.8, and then decreases with depth (Fig. 6.10). In deep levels ($z \leq -2,500$ m), I_{Ψ} reduces with depth from 0.3 to 0.2. Near the bottom, I_{Ψ} is around 0.2. The maximum value of I_{Ψ} may be caused by strong baroclinicity near that level (Fig. 6.10).

6.5 z -Coordinate System

In this section, the Japan/East Sea is used as an example to illustrate the ordinary P-vector inverse method in the z -coordinate system (Chu 1995a; Chu et al. 2001a).

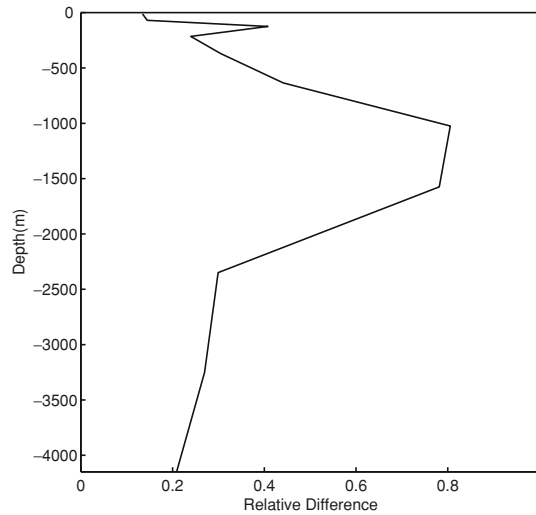


Fig. 6.10. Vertical variation of the relative difference I_{Ψ} (from Chu et al. 1998a, Journal of Oceanography)

6.5.1 Japan/East Sea

The Japan Sea, known as the East Sea in Korea, has steep bottom topography (Fig. 6.11) that makes it a unique semienclosed ocean basin overlaid by a pronounced monsoon surface wind. The Japan Sea covers an area of 10^6 km^2 , has a maximum depth in excess of 3,700 m, and is isolated from open oceans except for small (narrow and shallow) straits which connect the Japan Sea to the Pacific Ocean.

The Japan/East Sea contains three major basins called the Japan Basin, Ulleng/Tsushima Basin, and Yamato Basin, and a high central seamount called the Yamato Rise. The Japan Sea is of a great scientific interest as it is taken as a miniature prototype of the ocean. Its basin-wide circulation pattern, boundary currents, Subpolar Front, mesoscale eddy activities, and deep water formation are similar to those in a large ocean. It experiences two monsoons, winter and summer, every year. During the winter monsoon season, a cold northwest wind blows over the Japan Sea as a result of the Siberian High Pressure System located over the East Asian continent. Radiative cooling and persistent cold air advection maintain cold air over the Japan/East Sea. The northwest-southeast oriented Jet Stream is positioned above it. Such a typical winter monsoon pattern lasts nearly six months (November–April). During the summer monsoon, a warm and weaker southeast wind blows over

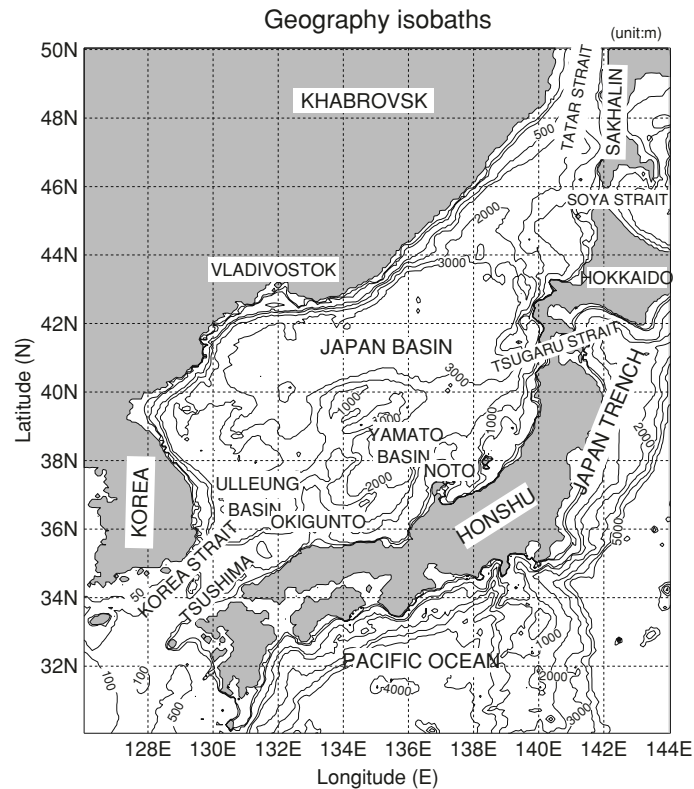


Fig. 6.11. Geography and isobaths showing the bottom topography (in meters) of the Japan/East Sea (from Chu et al. 2001a, *Journal of Physical Oceanography*)

the Japan/East Sea. Such a typical summer monsoon pattern lasts nearly four months (mid-May to mid-September).

The Japan/East Sea thermohaline structure and general circulation have been investigated for several decades. The Tsushima Warm Current (Mitta and Ogawa 1984), dominating the surface layer, flows in from the Tsushima Strait, and carries warm water from the south up to 40°N where a polar front forms (Seung and Yoon 1995). Most of the nearly homogeneous water in the deep part of the basin is called the Japan Sea Proper Water (Moriyasu 1972) and is of low temperature and low salinity. Above the Proper Water, warm and saline water flows in through the Tsushima Strait, transports northeastward, and flows out through the Tsugaru and Soya Strait.

The Tsushima Warm Current separates north of 35°N into western and eastern channels (Uda 1934; Kawabe 1982a,b; Hase et al. 1999; Senjyu 1999). The flow through the western channel closely follows the Korean coast (called the East Korean Warm Current) until it bifurcates into two branches near 37°N . The eastern branch follows the Subpolar Front to the western coast

of Hokkaido Island, and the western branch moves northward and forms a cyclonic eddy at the Eastern Korean Bay. The flow through the eastern channel follows the Japanese coast, called the Near-shore Branch by Yoon (1982). More accurately, we may call it the Japan Near-shore Branch, which is usually weaker than the East Korean Warm Current. The Tsushima Warm Current at both channels reduces with depth. The East Korean Warm Current meets the southward coastal current, the North Korean Cold Current, at about 38°N with some seasonal meridional migration. After separation from the coast, the East Korean Warm Current and the North Korean Cold Current converge and form a strong front (i.e., the Subpolar Front) that stretches in a west-east direction across the basin. The North Korean Cold Current makes a cyclonic recirculation gyre in the north but most of the East Korean Warm Current flows out through the outlets (Uda 1934). The formation of the North Korean Cold Current and the separation of the East Korean Warm Current are due to a local forcing by wind and buoyancy flux (Seung 1992). Large meanders develop along the front and are associated with warm and cold eddies.

Between the Tsushima Warm Current water and the Japan Sea Proper Water, a vertical salinity minimum south of the Subpolar Front, usually accompanied by the dissolved oxygen maximum, was first found and named the Japan Sea Intermediate Water by Miyazaki (1952, 1953), and further depicted by Kajiura et al. (1958) and Moriyasu (1972). The collocation of the salinity minimum and the dissolved oxygen maximum implies that the Intermediate Water originates from the descending surface water around the Subpolar Front (Miyasaki 1952, 1953; Miyasaki and Abe 1960). Later, Kim and Chung (1984) found very similar property in the Ulleung/Tsushima Basin and proposed the East Sea Intermediate Water (i.e., Japan Sea Intermediate Water used by the Japanese oceanographers); and Kim and Kim (1999) found the high salinity water with high oxygen in the eastern Japan Basin (i.e., north of Subpolar Front) and named the water the High Salinity Intermediate Water ($S > 34.07$ ppt).

The seasonal variability of both the Japan Sea circulation and thermohaline structure has been studied based on limited datasets such as the seasonal SST variability (Isoda and Saitoh 1988, 1993; Kano 1980; Maizuru Marine Observatory 1997). Based on the satellite infrared images in the western part of the Japan Sea and the routine hydrographic survey by the Korea Fisheries Research and Development Agency in 1987, Isoda and Saitoh (1993) found SST patterns in winter and spring which are characterized as follows: A small meander of a thermal front was first originated from the Tsushima Strait near the Korean coast and gradually grew into an isolated warm eddy with a horizontal scale of 100 km. The warm eddy intruded slowly northward from spring to summer. Chu et al. (1998a) reported the seasonal occurrence of Japan Sea eddies from the composite analysis on the U.S. National Centers for Environmental Prediction (NCEP) monthly SST fields (1981–1994). For example, they identified a warm center appearing in later spring in the East Korean Bay. Recently, Park and Chu (2006a) investigate the interannual SST

variability from the reconstructed NOAA/AVHRR Oceans Pathfinder best SST data (1985~2002) using the complex empirical function (CEOF) analysis. The first CEOF mode represents a standing oscillation and a maximum belt in the central Japan/East Sea. There are two near 7-year events and one 2–3-year event during the period of 1985–2002. The first mode oscillates by adjacent atmospheric systems such as the Aleutian Low, the North Pacific High, the Siberian High, and the East Asian jet stream. Positive correlation in a zonal belt between the first mode SST anomaly and the background surface air temperature/SST anomaly shows the intensive ocean–atmosphere interaction near the Polar Front in the North Pacific.

6.5.2 GDEM for the Japan/East Sea

Data for building the current version of GDEM climatology for the Japan Sea were obtained from the MOODS, which has 136,509 temperature and 52,572 salinity profiles during 1930–1997. The main limitation of the MOODS data is its irregular distribution in time and space. Certain periods and areas are over sampled while others lack enough observations to gain any meaningful insights. Vertical resolution and data quality are also highly variable depending much on instrument type and sampling expertise (Chu et al. 1997a–d). The monthly distributions of the Japan Sea temperature (Fig. 6.12a) and salinity (Fig. 6.12b) stations show that the number of temperature stations is 2–3 times more than the number of salinity stations. January has the least profiles while August has the most.

The seasonal T , S variation reduces as the depth increases. At 300-m depth there is almost no seasonal variability. Thus, we only present the horizontal fields at the surface and the intermediate level (150-m) for illustration. In order to see the seasonal variation of the vertical thermohaline structure, we present the latitudinal and zonal cross-sections of the monthly mean fields. To identify the variability in both monthly-mean and monthly-mean anomaly fields, we use a cold (warm) center to represent temperature minimum (maximum), and a fresh (salty) center to represent salinity minimum (maximum).

6.5.3 Temperature

(a) *Sea surface.* Although monthly SST field (Fig. 6.14) shows an evident seasonal variation, the Subpolar Front exists continuously through the year. Its position is quite stationary, but its intensity strengthens in the winter (especially the east part) and weakens in the summer. Such a pattern is similar to earlier description (Maizuru Marine Observatory 1997). The location of the Subpolar Front in spring is quite consistent with Isoda and Saitoh's (1988) estimations using ten NOAA-8 Advanced Very High Resolution Radiometer (AVHRR) images in spring 1984.

The SST is always found higher than 5°C year-round in the Ulleung/Tsushima Basin and the Yamato Basin, which is consistent with Kim and

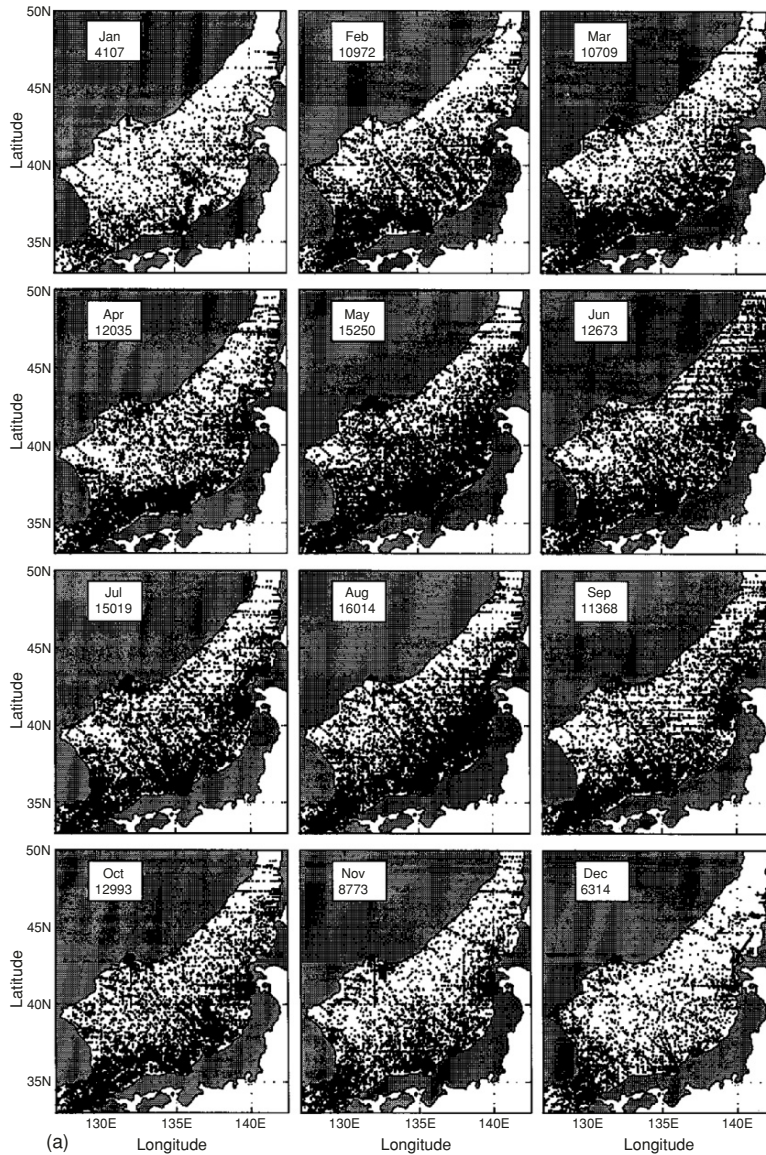


Fig. 6.12. Spatial distribution of the MOODS stations during 1930–1997 (a) temperature, and (b) salinity (from Chu et al. 2001a, *Journal of Physical Oceanography*) Yearly temperature (Fig. 6.13a) and salinity (Fig. 6.13b) profile numbers show temporally uneven distribution with almost no observations in the entire Japan Sea in certain years (e.g., 1944, 1989 for temperature, and 1944, 1987–1993 for salinity) and many observations in other years (e.g., nearly 6,500 temperature profiles in 1969, and 3,700 salinity profiles in 1967). Spatial and temporal irregularities along with the lack of data in certain regions must be carefully weighted in order to avoid statistically induced variability.

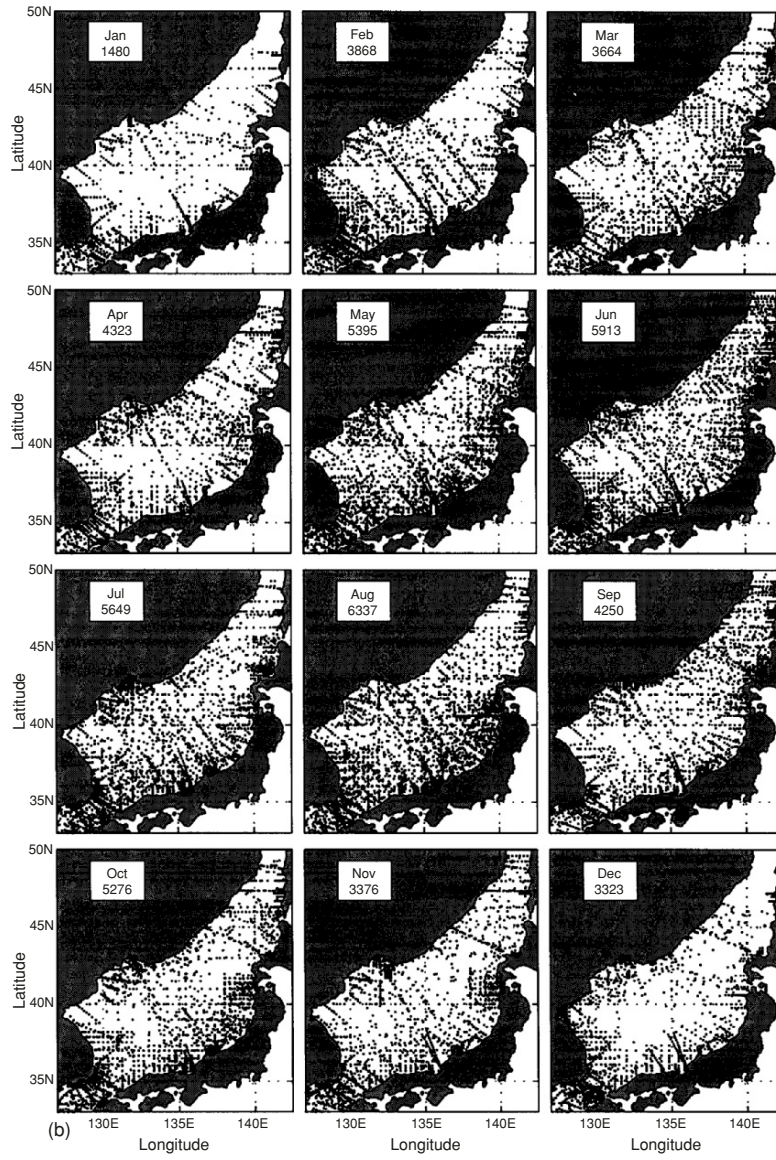


Fig. 6.12. Continued.

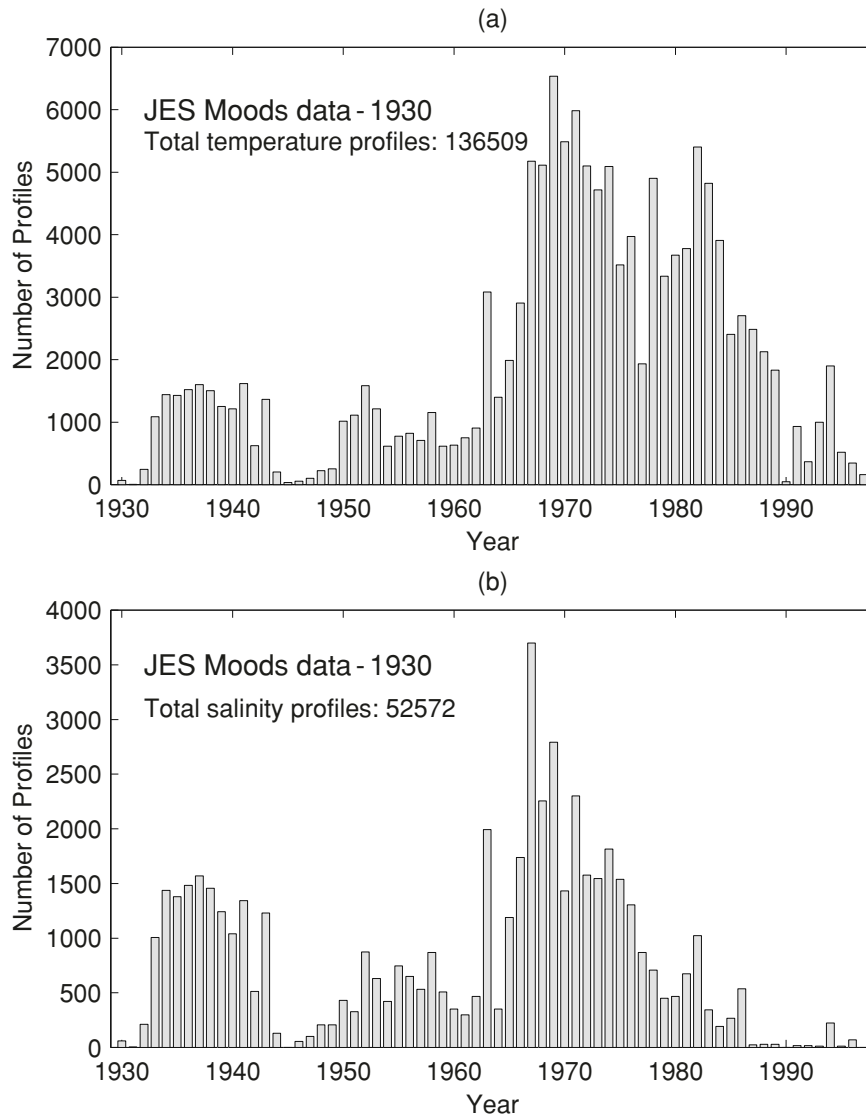


Fig. 6.13. Temporal distribution of the MOODS stations during 1930–1997 (a) temperature, and (b) salinity (from Chu et al. 2001a, *Journal of Physical Oceanography*)

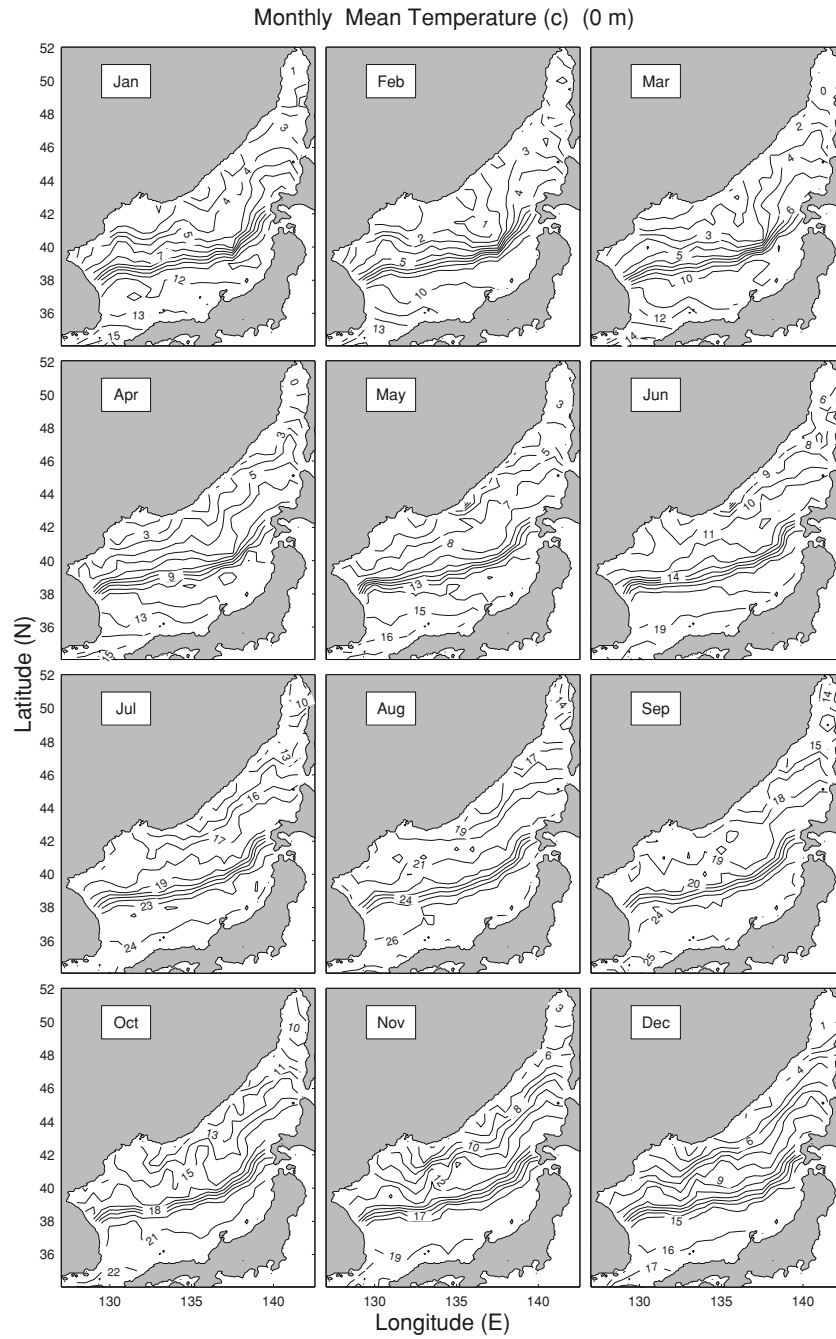


Fig. 6.14. Monthly mean temperature ($^{\circ}\text{C}$) field at the ocean surface (from Chu et al. 2001a, *Journal of Physical Oceanography*)

Kim (1999) observational studies. The maximum SST gradient is found as $16^{\circ}\text{C}/100\text{ km}$ near 137°E , 40°N in February and March, and the minimum SST gradient is found as $8^{\circ}\text{C}/100\text{ km}$ from July to September. The SST gradient across the Subpolar Front is two times as strong in the winter as in the summer. The weakening of the Subpolar Front in the summer is caused by the faster warming of the water mass north of this Front than south of the Front in spring. A second front occurs north of the Subpolar Front (bifrontal structure) during the fall-to-winter transition season, especially in November and December. This front parallels the Russian coast with the maximum SST gradient around $4^{\circ}\text{C}/100\text{ km}$ in November.

(b) *Temperature at intermediate level (150-m)*. The seasonal thermal variability at the 150 m depth is much weaker than at the surface (Fig. 6.15). The Subpolar Front still occurs throughout the year and is located at almost the same location as at the surface. At the north of the Subpolar Front, temperature is uniformly cold (1° – 3°C) throughout the year; south of the Subpolar Front, temperature changes from 5° to 9°C . The Subpolar Front meandering at 131°E , 134°E , and 138°E forms several mesoscale eddies. The meandering near Okin Gunto (134°E) in spring was previously reported by Isoda and Saitoh (1988; 1993). Besides, a second front occurs (bifrontal structure) south of the Subpolar Front along the west coast of Japan during the winter and spring seasons.

(c) *Zonal cross-sections (37°N and 43°N)*. The zonal cross-sections (37°N and 43°N) of the monthly mean temperature show a strong seasonal/permanent thermocline structure south of the Subpolar Front (Fig. 6.16a) and a strong seasonal/weak permanent thermocline structure north of the Front (Fig. 6.16b).

South of the Front at 37°N (Fig. 6.16), the permanent thermocline is located at 80–125 m and appears all year round with the maximum strength ($0.12^{\circ}\text{C m}^{-1}$) in August. Above it, the seasonal thermocline occurs from the surface to 50 m depth in June ($0.15^{\circ}\text{C m}^{-1}$), which intensifies during the summer monsoon season to a maximum value of around $0.36^{\circ}\text{C m}^{-1}$ in August, and weakens in September. In October, the seasonal thermocline erodes and the ocean mixed layer starts to occur. In November, the mixed layer is well established with the temperature near 18°C and the depth around 75 m.

During the prevailing winter monsoon season (December–March), the mixed layer deepens to 80–130 m with a westward uplift of the mixed layer depth: 80 m near the Korean coast and 130 m near the Japanese coast. The mixed layer temperature is around 10°C , starts to warm at a rate of $2^{\circ}\text{C}/\text{month}$ from March to May, and its depth shoals. For example, the mixed layer temperature increases from 12°C in April to 14°C in May, and the mixed layer depth decreases from 50 to 70 m in April to less than 50 m in May. This process (warming and shoaling) continues during the summer monsoon season (June–August).

North of the Subpolar Front at 43°N (Fig. 6.17), the permanent thermocline is quite weak and located near the surface to 300 m depth with an evident westward uplift from the Japanese coast (thickness around 300 m) to

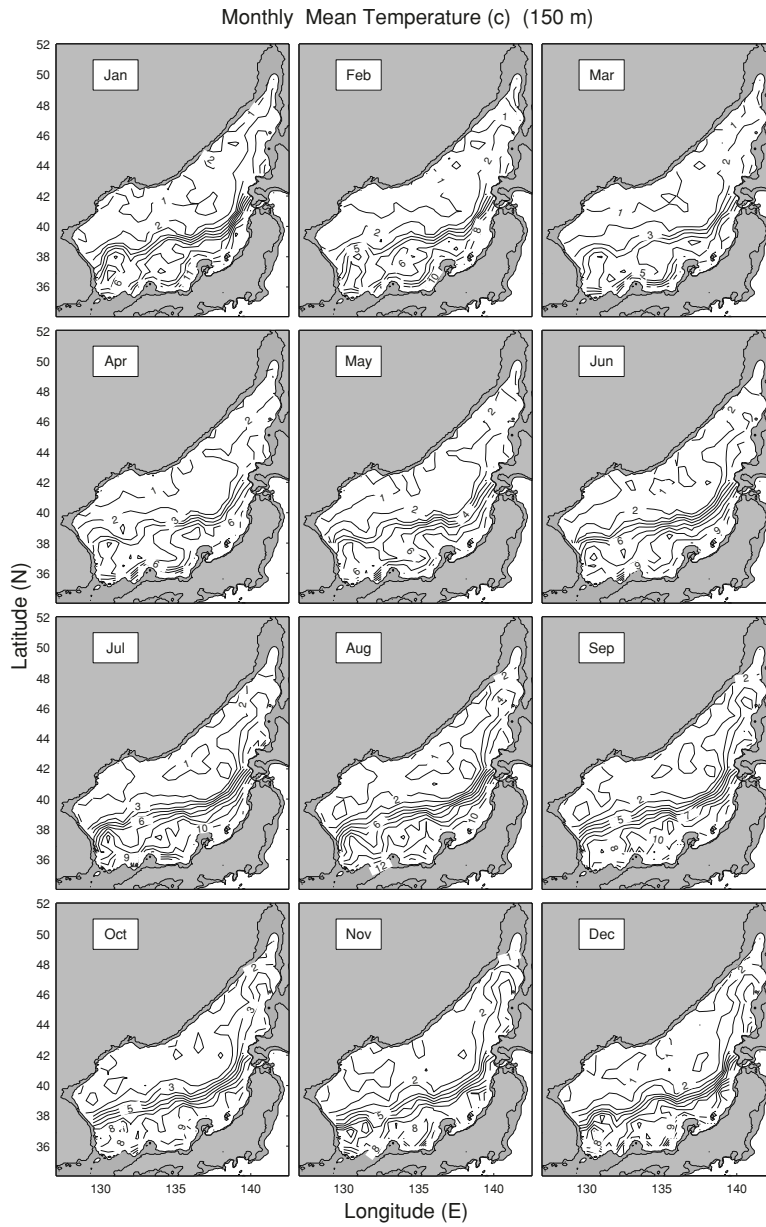


Fig. 6.15. Monthly mean temperature ($^{\circ}\text{C}$) field at 150 m depth (from Chu et al. 2001a, Journal of Physical Oceanography)

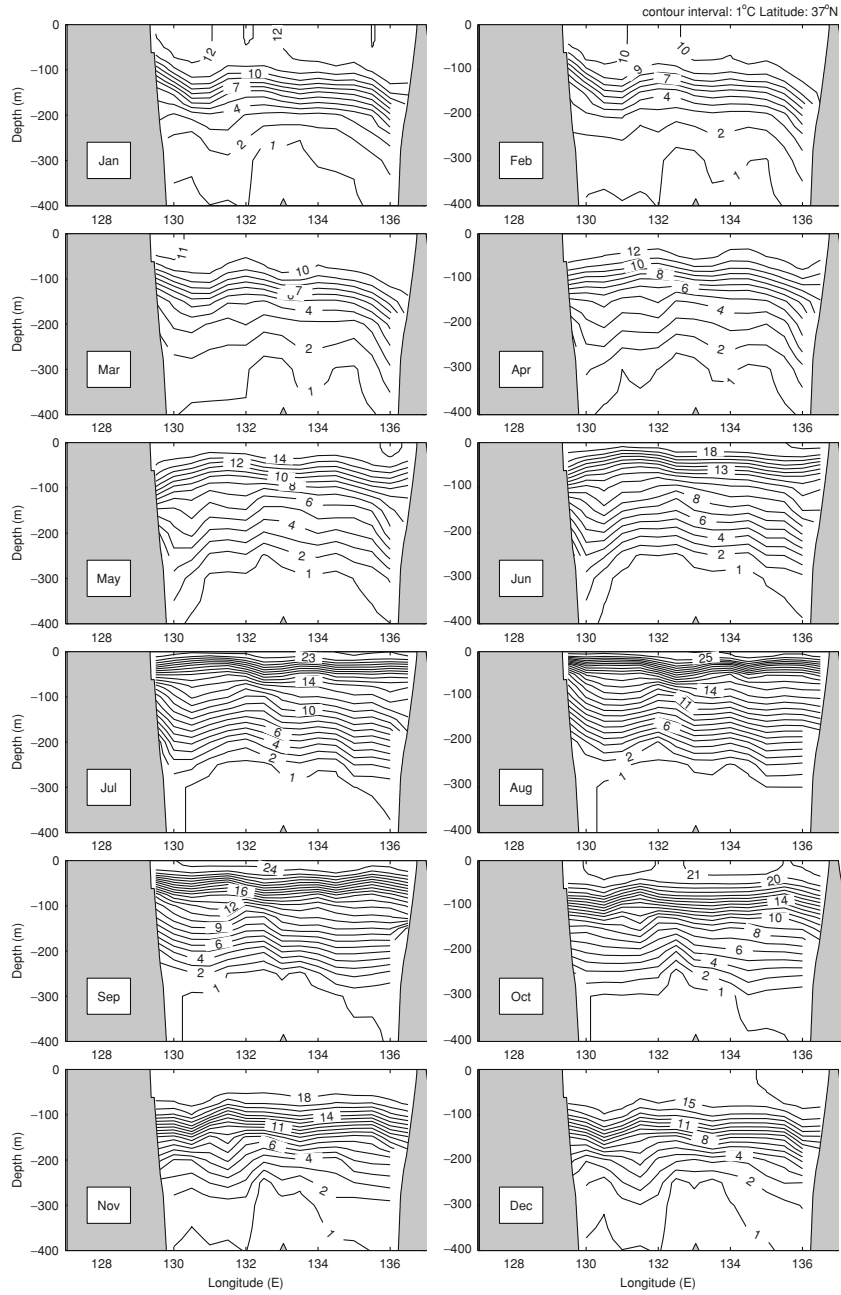


Fig. 6.16. Zonal cross-section of monthly mean temperature ($^{\circ}\text{C}$) at 37°N . Contour interval: 1°C (from Chu et al. 2001a, Journal of Physical Oceanography)

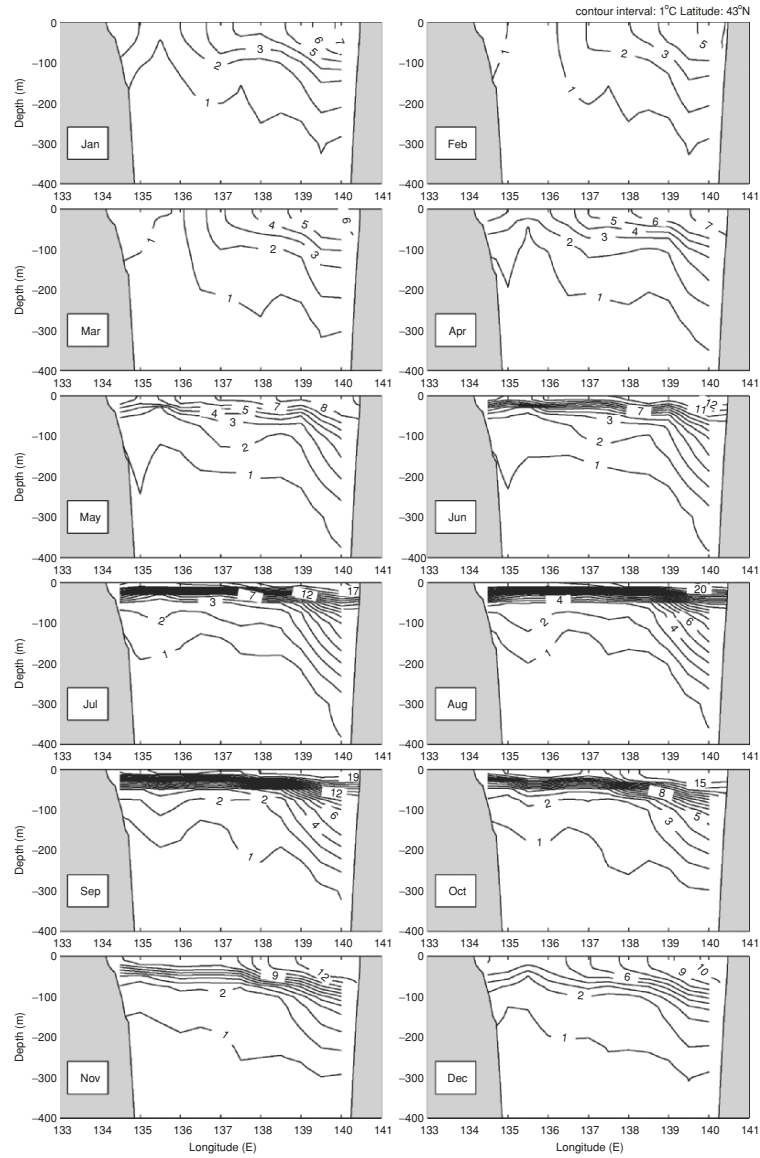


Fig. 6.17. Zonal cross-section of monthly mean temperature ($^{\circ}\text{C}$) at 43°N . Contour interval: 1°C (from Chu et al. 2001a, *Journal of Physical Oceanography*)

the Russian coast (thickness around 100 m). The seasonal thermocline occurs from the surface to 50 m depth in May ($0.08^{\circ}\text{C m}^{-1}$), which intensifies during the summer monsoon season to a maximum value of around $0.5^{\circ}\text{C m}^{-1}$ in August and September, and weakens in October. In November, the seasonal

thermocline erodes and becomes the part of the permanent thermocline, which weakens during the prevailing winter monsoon season. In February, the permanent thermocline is so weak that the water column is almost uniformly cold (1°C) west of 136°E and weakly stratified ($\leq 0.01^{\circ}\text{C m}^{-1}$) east of 136°E .

(d) *Latitudinal cross-section* (135°E). The strong north–south thermal asymmetry across the Subpolar Front is also identified from the latitudinal cross-section (135°E) of the monthly mean temperature (Fig. 6.18). During the prevailing winter monsoon season (December–March), the permanent thermocline is identified at 100–250 m depths south of the Subpolar Front with a vertical temperature gradient weakening from December (near $0.1^{\circ}\text{C m}^{-1}$) to March (near $0.05^{\circ}\text{C m}^{-1}$). The permanent thermocline is identified at 25–100 m depths north of the Subpolar Front in December with a vertical gradient near $0.06^{\circ}\text{C m}^{-1}$, which is much weaker than that south of the Front. From January to March, there is almost no evident thermocline north of the Front.

During the prevailing summer monsoon season (June–August), a shallow seasonal thermocline occurs in the whole Japan Sea basin with a stronger strength north of than south of the Subpolar Front; and overlays relatively uniform water north of the Front and stratified water (the permanent thermocline) south of the Front. A seasonal thermocline appears near the surface at the North of the Front (above 50 m depth) with a vertical gradient enhancing from $0.25^{\circ}\text{C m}^{-1}$ in June to $0.36^{\circ}\text{C m}^{-1}$ in August.

This strong and shallow thermocline isolates the exchange of the seawater below the thermocline from the atmospheric forcing and makes this water (north of the Subpolar Front under the thermocline) quite uniform. South of the Subpolar Front, a seasonal thermocline is wider (25–100 m depths) and weaker with a vertical gradient around $0.13^{\circ}\text{C m}^{-1}$. Such a north–south asymmetric pattern in July was previously presented by Kim and Kim (1999) using the Circulation Research of the East Asian Marginal Seas data taken mainly in the summer of 1995. However, the seasonal thermocline north of the Subpolar Front is stronger from the GDEM data than from the Circulation Research of the East Asian Marginal Seas data.

The seasonal thermocline has a strong asymmetry across the Subpolar Front. North of the Subpolar Front, the seasonal thermocline occurs near the surface in April and May, enhances drastically during the summer monsoon season, survives in Fall, and is still quite strong with a vertical gradient of $0.12^{\circ}\text{C m}^{-1}$ in November. It weakens drastically in December. South of the Subpolar Front, the seasonal thermocline occurs in the summer monsoon season, survives in the early fall, and disappears in November.

6.5.4 Salinity

(a) *Sea surface*. The monthly sea surface salinity field (Fig. 6.19) shows a strong seasonal variation with less (more) horizontal variability in the winter (summer). The saline Kuroshio water (>34.2 ppt) enters the Japan Sea

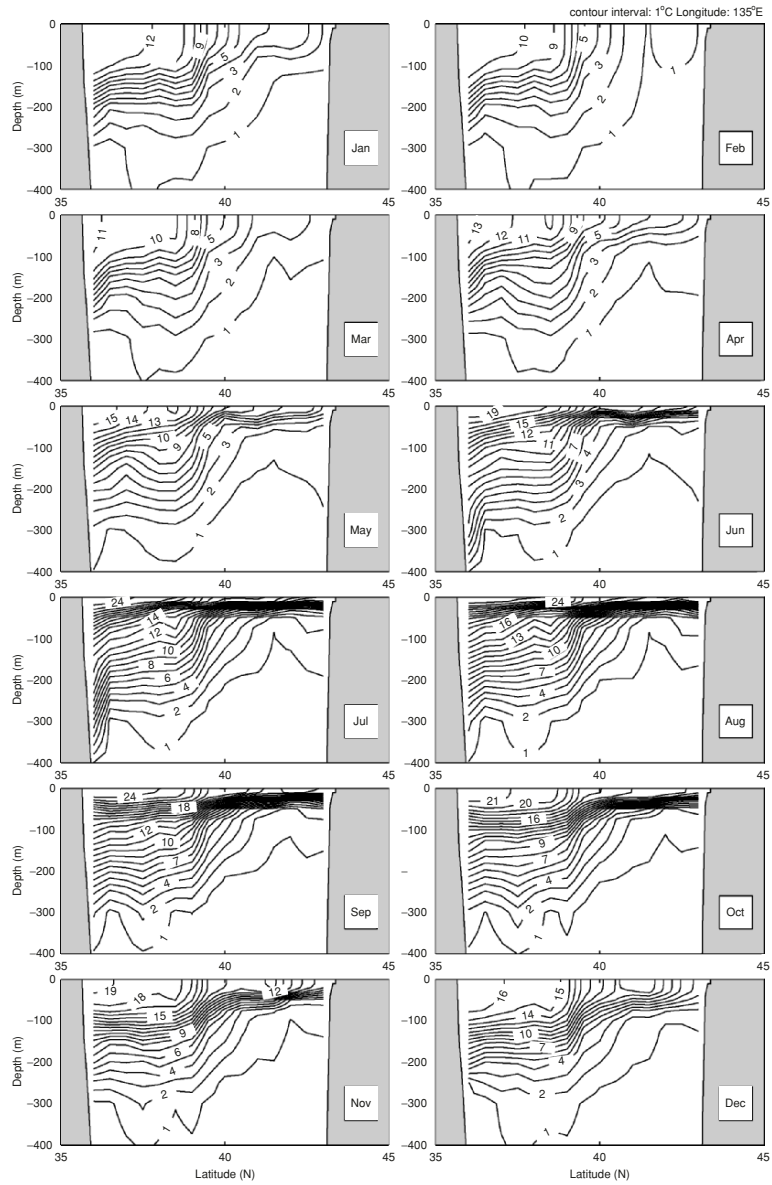


Fig. 6.18. Latitudinal cross-section of monthly mean temperature ($^{\circ}\text{C}$) at 135°E . Contour interval: 1°C (from Chu et al. 2001a, *Journal of Physical Oceanography*)

from the Tsushima/Korean Strait into the Japan Sea and forms two permanent salty centers located in the northern Japan Basin (west of the Hokkaido Island) with the salinity higher than 34.0 ppt, and the area between the Ullung/Tsushima and Yamato Basins with the maximum salinity of 34.3 ppt in

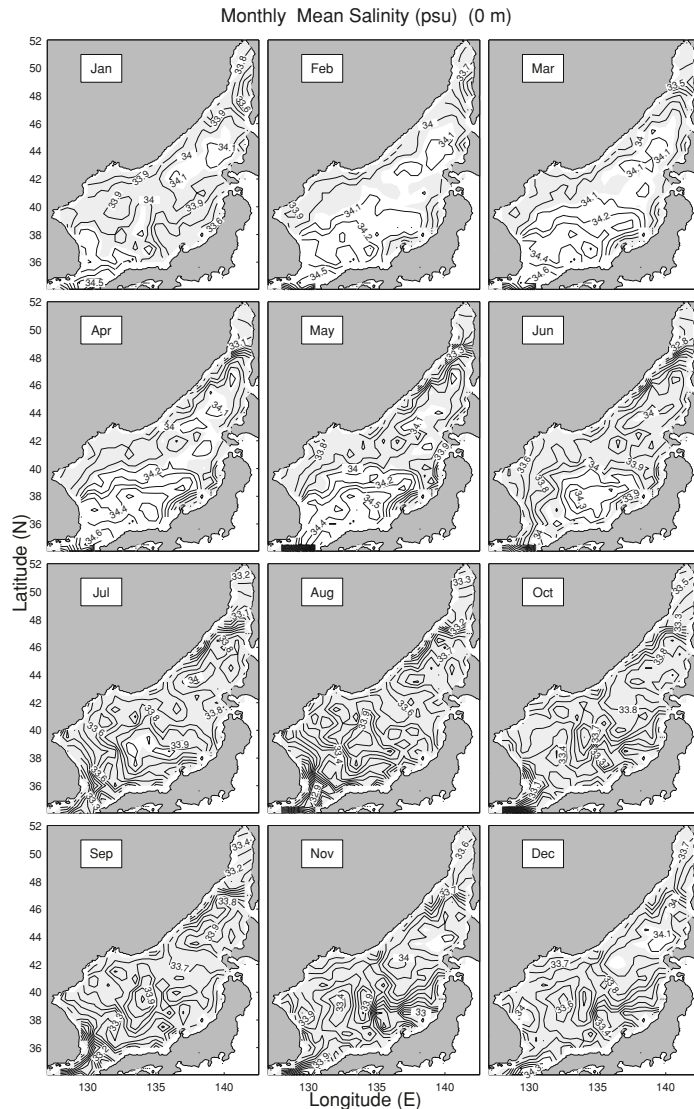


Fig. 6.19. Monthly mean salinity (ppt) field at the ocean surface (from Chu et al. 2001a, *Journal of Physical Oceanography*)

June, respectively. The salty center has less seasonal variation in the northern Japan Basin than the Ulleung/Tsushima and Yamato Basins. The winter (February) field is consistent with that reported by Kim and Kim (1999) using the data set of the Japan Oceanographic Data Center during 1930 to 1990.

(b) *Intermediate level (150 m)*. Figure 6.20 shows horizontal depictions of the monthly mean salinity at 150 m depth with a contour interval of 0.1 ppt.

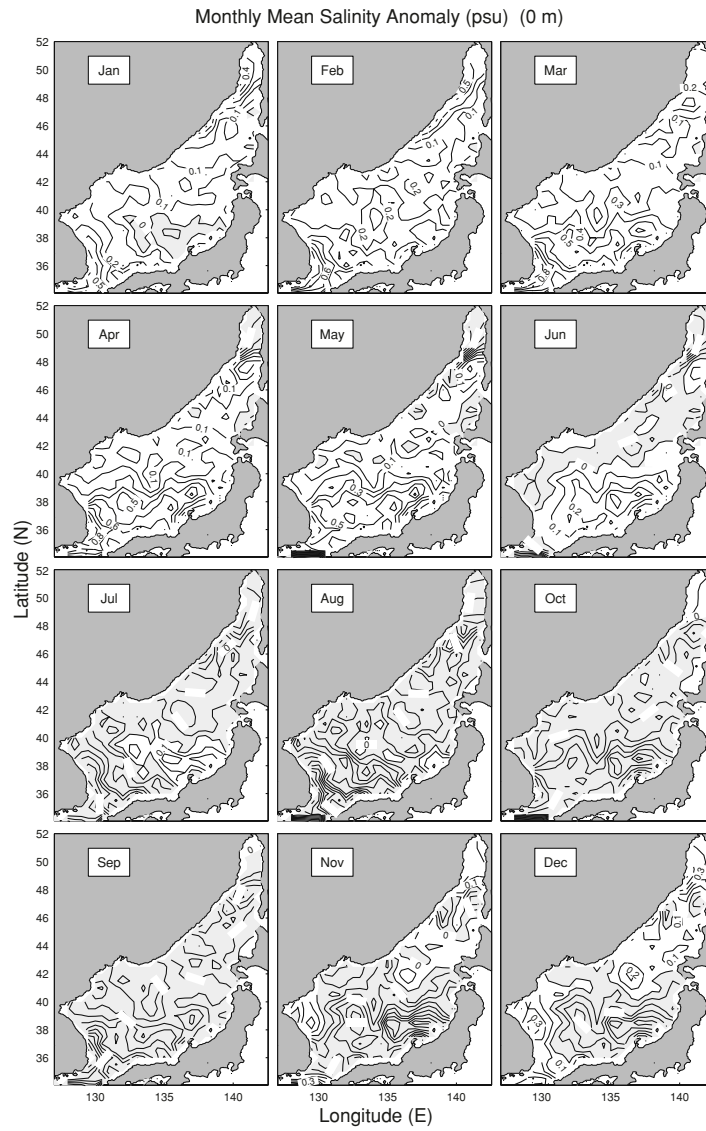


Fig. 6.20. Monthly mean salinity (ppt) field at 150 m depth (from Chu et al. 2001a, Journal of Physical Oceanography)

The depth of 150 m corresponds to the middle level of the Japan Sea Intermediate Water (low salinity) as well as the High Salinity Intermediate Water (high salinity).

Low salinity in the Japan Sea Intermediate Water (less than 34.06 ppt, shaded areas in Fig. 6.20) dominates the western Japan Basin and the Ulle-

ung/Tsushima Basin. It expands eastward during the summer monsoon season (June–September) and retreats westward during the winter monsoon season (December–March).

High salinity of the High Salinity Intermediate Water occupies the eastern Japan Basin. This is consistent with earlier work by Kim and Kim (1999). The saline water occupies the east and south and less of it appears in the north and west, especially in the northwestern boundary. The isohaline of 34.1 is collocated with the Subpolar Front (Fig. 6.15) with the salinity above (below) 34.1 in the south (north) of the Front. Salinity is relatively uniform (34.0–34.1 ppt) throughout the year, north of the Subpolar Front. South of the Subpolar Front the salinity changes from 34.1 to 34.5 ppt.

(c) *Zonal cross-sections* (37°N and 43°N). The zonal cross-sections (37°N and 43°N) of the monthly mean salinity show an evident salinity minimum south of the Subpolar Front (Fig. 6.21) and absence of a salinity minimum north of the Front (Fig. 6.22). This consistency exists with many earlier studies such as Miyazaki (1952,1953), Miyasaki and Abe (1960), Kim and Chung (1984), Senjyu (1999), and Kim and Kim (1999).

South of the Subpolar Front at 37°N (Fig. 6.21), a strong (seasonal) halocline occurs from the surface to 30 m depth in June (0.01 ppt m^{-1}), which intensifies during the summer monsoon season to a maximum value of around 0.03 ppt m^{-1} in August, and weakens from September to December.

In January, the halocline erodes and disappears. During the summer monsoon season (June–September), the salinity minimum shifts eastward from the Ulleung/Tsushima Basin (131° – 133°E) in June to the southern Yamato Basin (132° – 135°E) in July–September. A horizontally oriented SMAX ($S > 34.2 \text{ ppt}$) appears above the salinity minimum with the interface at 200–300 m depths.

In October, this horizontally oriented salinity maximum is broken into two parts with each part enclosed by the 34.2 ppt isoline. A narrow relatively low salinity area, sandwiched by the two SMAX centers, occurs in the central Ulleung/Tsushima Basin (near 132°E) beneath 100 m depth and strengthens from November to January accompanying the erosion of the surface halocline.

In January, the near surface halocline disappears, the salinity minimum (enclosed by 34.1 ppt isoline) appears in the Ulleung/Tsushima Basin (131° – 133°E) and reaches the surface, eventually the two salinity maximum centers weaken (especially the west one). The salinity minimum expands horizontally, descending vertically, and becomes very evident in February. From February to June, the salinity minimum continues to descend. The top of the salinity minimum occurs at 150–200 m depths in February and at 200–300 m in April–June.

North of the Subpolar Front at 43°N (Fig. 6.22), the salinity minimum shows up in the upper layer (above 100 m) of the western Japan Basin (west of 136°E) all the year round. This is consistent with Kim and Kim's (1999) identification that the Japan Sea Immediate Water in the western Japan Basin is characterized by a low salinity ($S < 34.06$). The high salinity water ($S >$

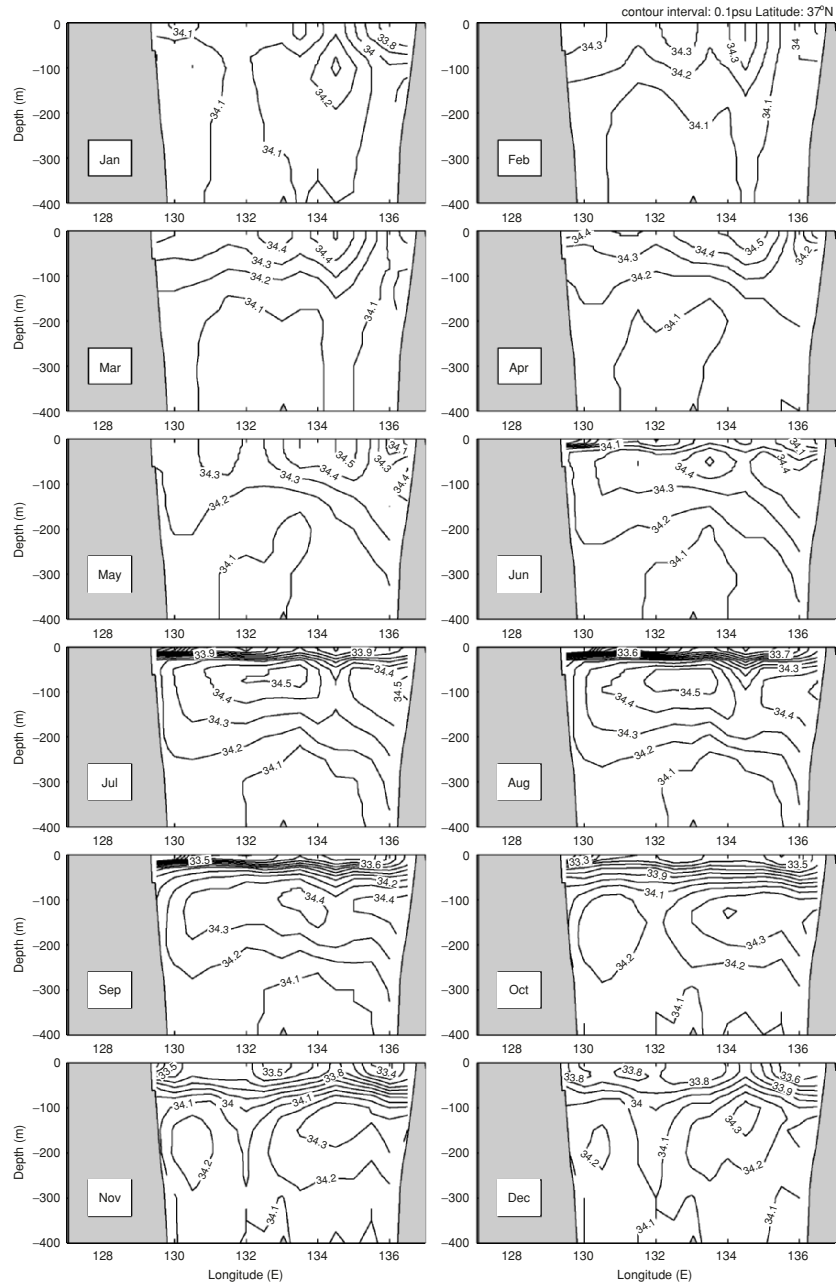


Fig. 6.21. Zonal cross-section of monthly mean salinity (ppt) at 37°N. Contour interval: 0.1 ppt (from Chu et al. 2001a, Journal of Physical Oceanography)

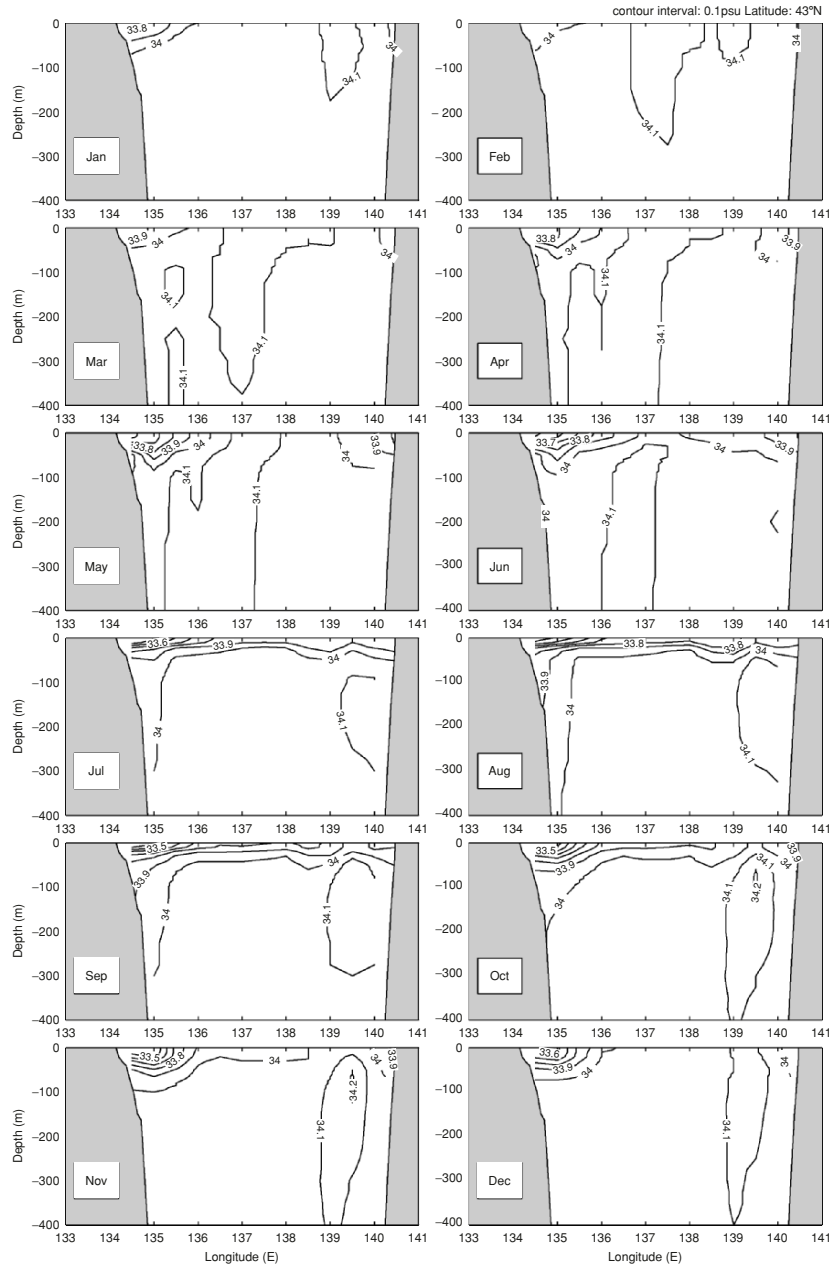


Fig. 6.22. Zonal cross-section of monthly mean salinity (ppt) at 43°N. Contour interval: 0.1 ppt (from Chu et al. 2001a, *Journal of Physical Oceanography*)

34.1 ppt) of the High Salinity Immediate Water appears in the central (136°–138°E) and the eastern (138.5°–140°E) Japan Basin. The eastern Japan Basin salinity maximum appears almost all the year round except the spring season (March–May). The central Japan Basin salinity maximum is not as evident as the eastern one except in February and March.

(d) *Latitudinal cross-section* (135°E). The strong north–south haline asymmetry across the Subpolar Front is also identified from the latitudinal cross-section (135°E) of the monthly mean salinity: the appearance (disappearance) of the salinity minimum south (north) of the Subpolar Front (Fig. 6.23). South of the Subpolar Front, the salinity minimum ($S < 34.06$ ppt) occurs during the summer monsoon season (July–October) underneath a horizontally oriented salinity maximum with a salty core ($S > 34.5$ ppt) at 100 m depth. The salinity maximum with a salty core ($S = 34.3$ ppt) was observed in October 1969 when a hydrographic survey for the whole Japan Sea basin was carried out by the Japan Meteorological Agency (Kim and Kim 1999). The interface between the salinity minimum and maximum is located at 200–300 m depth. During the winter monsoon season, the salinity minimum is not evident. North of the Subpolar Front, high salinity water ($S > 34.1$ ppt) of the High Salinity Intermediate Water appears in the central Japan Basin (40°–43°N) with strengthening in the winter and weakening in the summer.

6.5.5 Absolute Velocity

The inverted absolute velocity field (Fig. 6.24) coincides with earlier descriptions of the Japan Sea circulation (e.g., Uda 1934; Suda and Hidaka 1932; Suda et al. 1932). However, the currents at the four major straits are not well inverted. For example, the velocity at the Tsushima/Korea Strait is too small, and there is no velocity inverted at the other straits such as the Tartar Strait. This may be caused by the narrowness and shallowness of the straits.

The inverted absolute velocity field shows an evident branching of the Tsushima Warm Current. North of 35°N, the Tsushima Warm Current bifurcates into an eastern channel (first branch) and a western channel. The strength of the Tsushima Warm Current at both channels reduces with depth. The flow through the western channel (i.e., the East Korean Warm Current) closely follows the Korean Coast until it separates near 37°–38°N into two branches: the off-shore branch (or the second branch) follows the Polar Front to the western coast of Hokkaido Island, and the long-shore branch (or the third branch), moves northward (i.e., the East Korean Warm Current). Such a three-branch pattern was first identified by Suda and Hidaka (1932) and Suda et al. (1932) using hydrographic and current meter data observed from the month of June to September in 1929 and in 1930, respectively. Since then, the existence of three branches has been believed to be the typical Tsushima Warm Current flow pattern. Using temperature and salinity data mainly obtained in 1973, Kawabe (1982a) investigated the seasonal variation of the Tsushima Warm Current branching and found that the first branch exists in

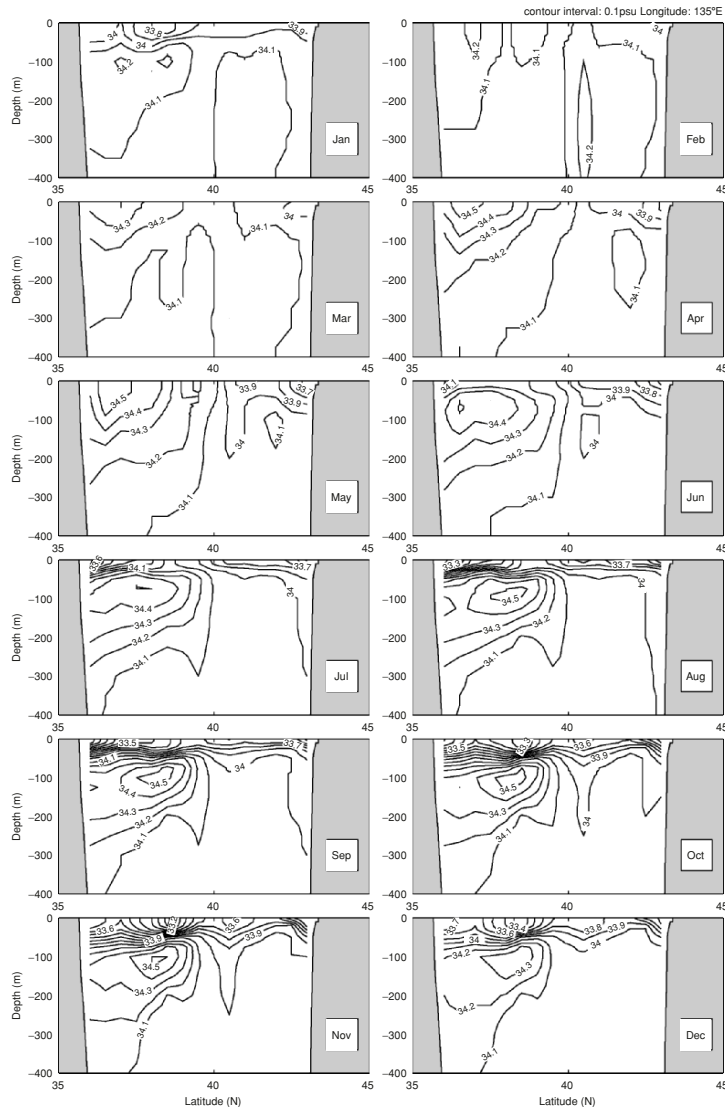


Fig. 6.23. Latitudinal cross-section of monthly mean salinity (ppt) at 135°E. Contour interval: 0.1 ppt (from Chu et al. 2001a, *Journal of Physical Oceanography*)

spring and summer, the second branch only in summer from the month of June to August, and the third branch in all seasons. His observational results were simulated using a two-layer numerical model (Kawabe 1982b; Sekine 1986).

The inverted flow through the eastern channel (first branch) closely follows the Japanese coast (i.e., Japan Near-Shore Branch) and is weaker than the flow through the western channel (Fig. 6.24). The maximum speed of the first

branch is found to be around 0.1 m s^{-1} , occurring near the Japanese coast (135°E , 35.5°N) at the surface. The Japan Near-Shore Branch is too weak to be identified in winter (December–February). In March, the Japan Near-Shore Branch starts to occur along the Japanese coast, and strengthens in spring and reaches the maximum velocity in July. This coincides with Kawabe’s (1982a) observational results.

The inverted flow along the Subpolar Front (second branch) may be called as the Polar Front Current. The maximum speed of the Polar Front Current is found at the surface around 0.2 m s^{-1} (Fig. 6.24). An asymmetric cyclonic gyre is found in the MidJapan Sea ($135^\circ\text{--}140^\circ\text{E}$, $38^\circ\text{--}44^\circ\text{N}$) in the winter monsoon season (December–March) with the flow associated with the Polar Front Current as the southern and eastern flanks and the flow from the north (MidJapan Sea cold current) as the northern and western flanks. The Polar Front Current has a weak seasonal variation in flow pattern and a strong seasonal variation in current speed. The seasonal variability of this gyre is largely determined by the seasonal variability of the Polar Front Current.

An interesting feature is the out-of-phase variation between the Polar Front Current and the Japan Near-Shore Branch (along the west coast of Japan). For example, the Polar Front Current (Japan Near-Shore Branch) strengthens (weakens) from July to September, and weakens (strengthens) in spring from March to April.

The seasonal variation of the Japan Sea major currents is also shown in the latitudinal cross-section of the monthly mean u -component (Fig. 6.25). Two eastward flowing currents, the Japan Near-Shore Branch (near 36°N) and the Polar Front Current ($38^\circ\text{--}40^\circ\text{N}$), are well represented. The Polar Front Current has the maximum speed of 0.22 m s^{-1} (minimum speed of 0.12 m s^{-1}) occurring in September (February–April) at the surface. During the summer monsoon season (July–September), the Polar Front Current strengthens (maximum speed increases from 0.18 m s^{-1} to 0.22 m s^{-1}) and the Japan Near-Shore Branch weakens (maximum speed decreases from 0.12 m s^{-1} to 0.04 m s^{-1}). During winter monsoon season (December–April), the Polar Front Current weakens (maximum speed decreases from 0.18 to 0.12 m s^{-1}) and the Tsushima Warm Current strengthens (maximum speed increases from 0.02 m s^{-1} in January to 0.1 m s^{-1} in April). The volume transport of the Polar Front Current shows an evident seasonal variation with the maximum value of 1.32 Sv ($1 \text{ Sv} = 10^6 \text{ m}^3 \text{ s}^{-1}$) in November–December and the minimum value of 0.88 Sv in April (Fig. 6.26).

This example shows the usefulness of the P-vector method. The inverted absolute geostrophic velocities represent the Japan Sea circulation reasonably well, especially the Tsushima Current and its bifurcation. The Polar Front Current has a weak seasonal variation in flow pattern, a strong seasonal variation in current speed, and out-of-phase variability with the Tsushima Warm Current. When the Polar Front Current strengthens from July (0.18 m s^{-1}) to September (0.22 m s^{-1}), the Tsushima Warm Current weakens from 0.12 to 0.04 m s^{-1} . When the Polar Front Current weakens from

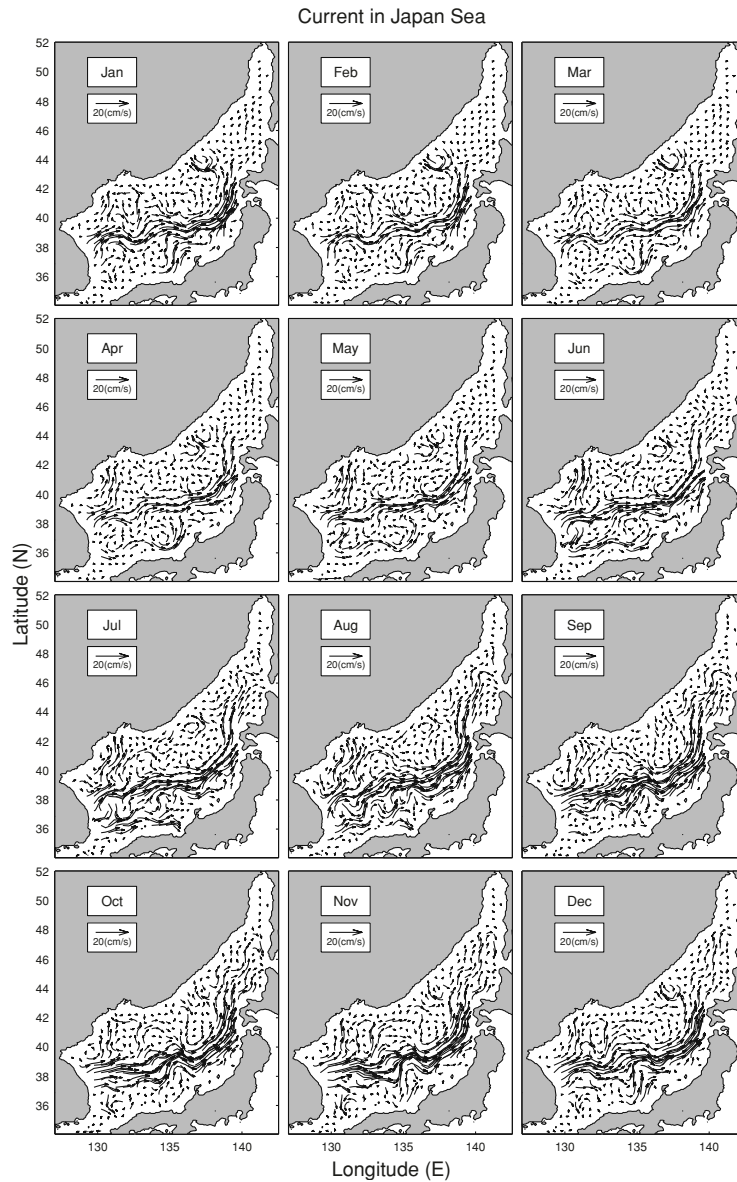


Fig. 6.24. Inverted monthly mean surface circulation (from Chu et al. 2001a, Journal of Physical Oceanography)

January (0.18 m s^{-1}) to April (0.12 m s^{-1}), the Tsushima Current strengthens from 0.02 to 0.1 m s^{-1} . The seasonal variability of the Mid-Japan Sea cyclonic gyre is largely determined by the seasonal variability of the Polar Front Current. The volume transport of the Polar Front Current has the maximum

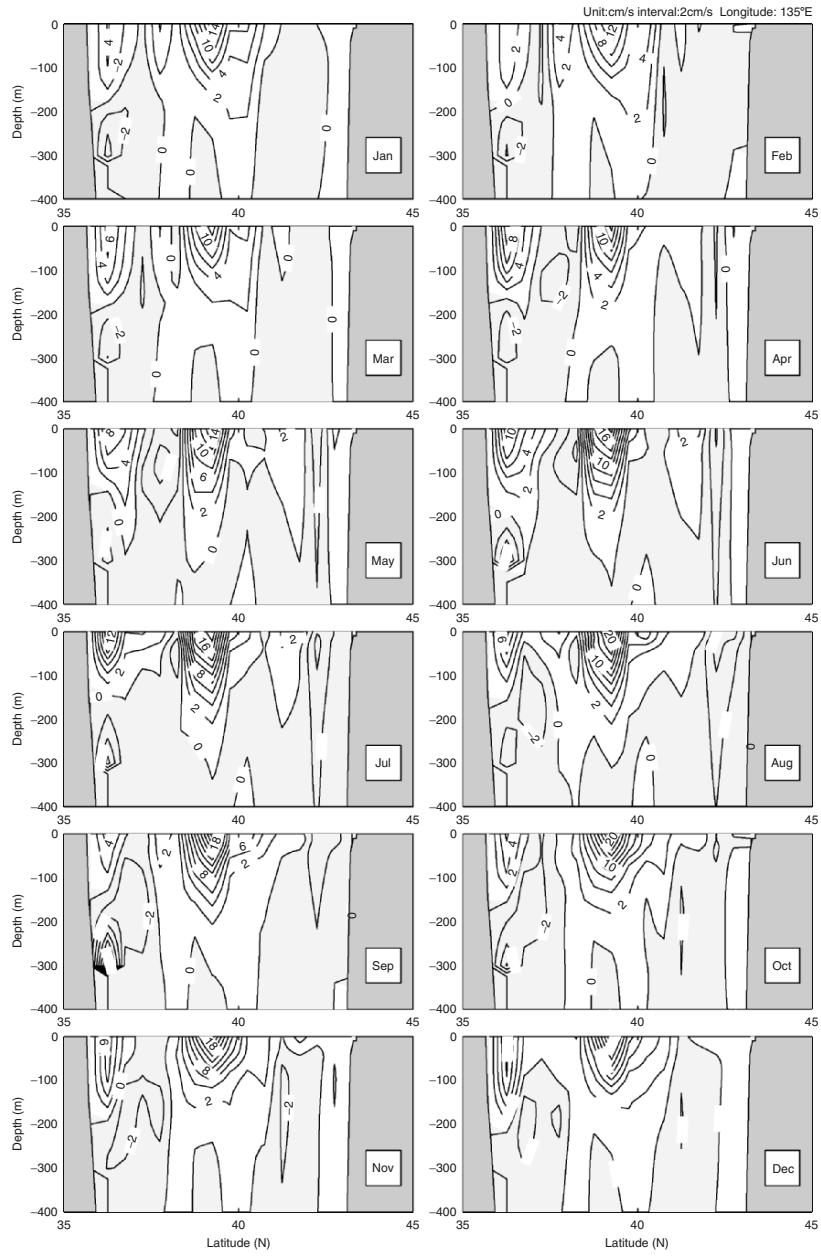


Fig. 6.25. Latitudinal cross-section of monthly mean u velocity (10^{-2} m s^{-1}) at 135°E . Contour interval: 10^{-2} m s^{-1} (from Chu et al. 2001a, Journal of Physical Oceanography)

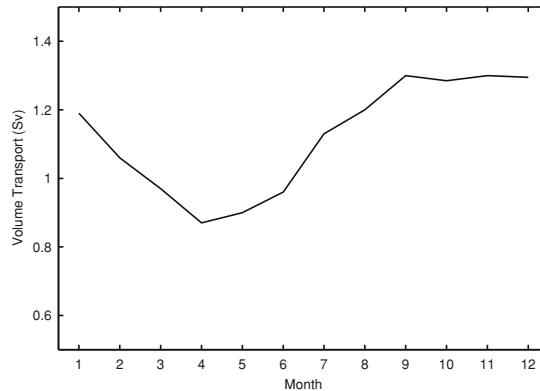


Fig. 6.26. Monthly variation of the volume transport (Sv) of the Polar Front Current at 135°E cross-section (from Chu et al. 2001a, *Journal of Physical Oceanography*)

value of 1.32 Sv in November–December and the minimum value of 0.88 Sv in April.

6.6 Isopycnal Coordinate System

In this section, the South China Sea is used as an example to illustrate the P-vector inverse method in the isopycnal-coordinate system (Chu and Li 2000; Chu et al. 2002a).

6.6.1 South China Sea

South China Sea, the largest marginal sea in the West Pacific Ocean, is separated from adjacent oceans by a chain of islands. It contains a broad shallow shelf on the south, extending along the Vietnamese-Chinese coast to the Taiwan Strait on the north, a deep sea basin in the center, and a dangerous ground near Nansha with numerous reef islands over the southeast (Fig. 6.27). It has a bottom topography that makes it a unique semienclosed ocean basin overlaid by a pronounced monsoon surface wind. Extensive continental shelves (less than 100 m deep) are found on the western and southern parts, while steep slopes with almost no shelves are found in the eastern part of South China Sea. The deepest water is confined to a bowl-type trench and the maximum depth is approximately 4,700 m. The South China Sea joins the Pacific Ocean through the Luzon Strait between Taiwan and Philippine. The combination of geometry, connectivity with the Pacific Ocean, and strongly variable atmospheric forcing contributes to the complex dynamics of the flow in that region (Metzger 1996).

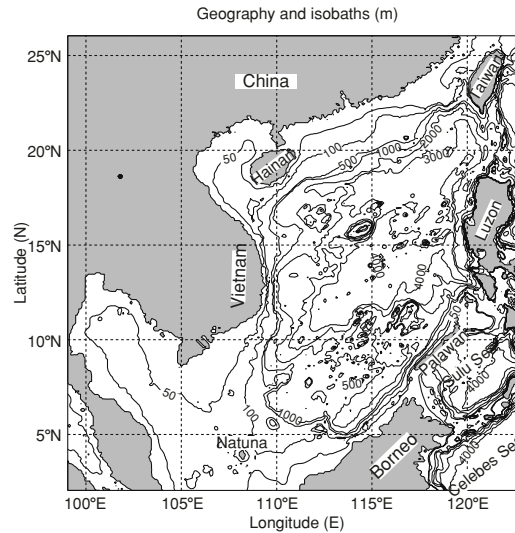


Fig. 6.27. Geography and isobaths showing the bottom topography of the South China Sea (from Chu and Li 2000, *Journal of Physical Oceanography*)

6.6.2 Oceanic Conditions

The Kuroshio, originating from the North Equatorial Current, flows northward as a western boundary current east of Luzon and Taiwan (Nitani 1970). The Luzon Strait is the principal passage through which the Pacific water enters the South China Sea; therefore the mass transport through the Luzon Strait is critical in determining the characteristics of the South China Sea waters (Shaw 1989, 1991). For example, Hu et al. (1992) believed this flow to contribute to currents in Taiwan Strait. However, Li et al. (1992) showed, by using a numerical model, that this flow did not contribute to currents in the Taiwan Strait. The volume transport through the Luzon Strait is uncertain. Different authors reported values ranging from 8 to 10 Sv by Huang et al. (1994) to 3 Sv outflow in summer and 3 Sv inflow in winter by Wyrтки, (1961a, b). Metzger (1996) estimated that the mean Kuroshio intrusion through the Luzon Strait is around 2.4–4.4 Sv (higher resolution with lower transport values) using the Navy’s Layered Ocean Model forced by wind stress climatology having various resolutions.

The seasonally reversing monsoon winds also play an important role in determining the upper ocean circulation (Shaw and Chao 1994). From April to August, the weaker southwesterly summer monsoon winds result in a wind stress of over 0.1 N m^{-2} and drive a northward coastal jet off Vietnam coast and an anticyclonic basin-scale circulation. From November to March, the stronger northeasterly winter monsoon winds correspond to a maximum wind stress of nearly 0.3 N m^{-2} and cause a southward coastal jet and cyclonic basin-scale circulation. Such a seasonal variability of the surface circulation

was simulated by several numerical models (e.g., Chu et al. 1998c, 1999b–d, 2000b; Chao et al. 1996). However, Metzger (1996) pointed out that the surface currents observed by Wyrтки, (1961a, b) are subjected to Ekman drift in this highly variable wind regime.

Seasonal occurrence of the South China Sea eddies have been reported by several authors. Dale (1956) and Uda and Nakao (1972) reported a cold eddy off the central Vietnam coast in summer. Nitani (1970) found a cold eddy located northwest of Luzon in summer. Reports from the South China Sea Institute of Oceanology (1985) indicate that a warm-core eddy appears in summer and winter in the central South China Sea, but in summer, it is closer to Vietnam at the surface. Recently, a cold-core eddy was detected in the central South China Sea during December 29, 1993, to January 5, 1994, from the analysis of TOPEX/Poseidon data (Soong et al. 1995). Chu et al. (1997d) and Chu and Chang (1997) identified the existence of a central South China Sea surface warm-core eddy in midMay from a historical data set: the MOODS data. From the composite analysis on the US NCEP monthly SST fields (1982–1994), Chu et al. (1997d) found that during the spring-to-summer monsoon transition (March–May) a warm anomaly (greater than 1.8°C) is formed in the central South China Sea at 112° – $119^{\circ}30'\text{E}$, 15° – $19^{\circ}30'\text{N}$. Emery and Csanady (1973) reported that many large stratified lakes and semiencloded marginal seas and estuaries exhibit a persistent cyclonic circulation. Integrating the Navy’s Layered Ocean Model to the statistically equilibrium state, Metzger (1996) simulated a persistent cyclonic circulation in the upper layer of the South China Sea with an approximate thickness of 250 m.

Questions arise: is the viewpoint of Emery and Csanady’s (1973) or Metzger and Hurlburt’s (1996) cyclonic circulation pattern representative for the South China Sea circulations below the mixed layer? What is the seasonal variability of the Kuroshio intrusion through the Luzon Strait? The P-vector method is used to invert the absolute geostrophic circulations (both barotropic and baroclinic parts) on the isopycnal surfaces from the Navy’s public domain GDEM climatological monthly mean temperature and salinity data set with 0.5° resolution (Teague et al. 1990).

6.6.3 Monthly Mean Temperature Field

The monthly mean 3-D temperature field obtained from the GDEM dataset is similar to the climatological monthly mean fields directly computed from the MOODS as depicted in Chu et al. (2002c). The SST variation obtained from the GDEM data is quite consistent with earlier investigations based on the NCEP data (Chu et al. 1997d) and based on the MOODS data (Chu et al. 1997c, 2002c).

Figure 6.28 is the horizontal depiction of monthly mean temperature at 150 m depth. The contour interval is 0.5°C . In them, we see that the basin is dominated by a cool pool with several cold centers located northwest of

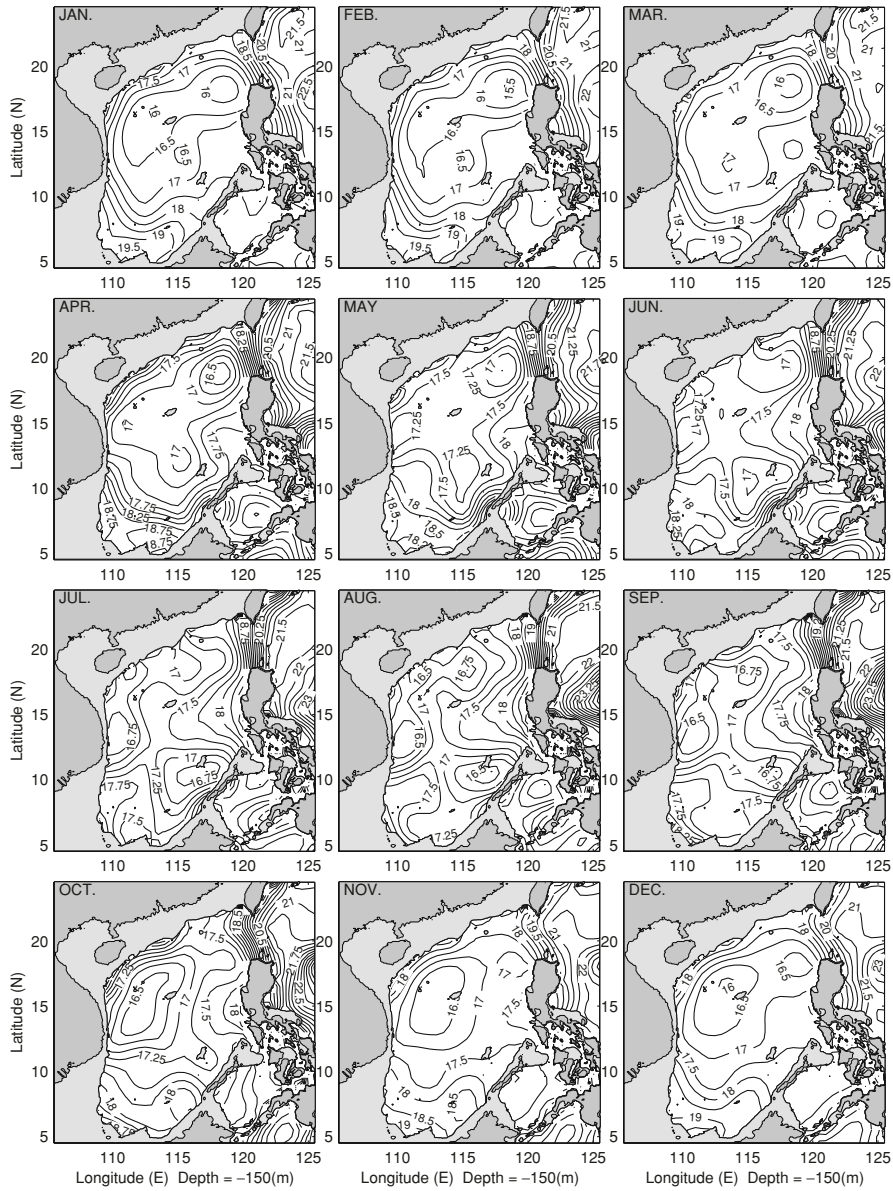


Fig. 6.28. Monthly mean temperature ($^{\circ}\text{C}$) fields at 150-m depth obtained from GDEM (from Chu and Li 2000, *Journal of Physical Oceanography*)

Luzon and south of Dongsha, near Vietnamese Bight, Xisha, and Liyue Bank. Dale (1956) and Uda and Nakao (1972) reported a cold eddy off the central Vietnam Bight in summer. Nitani (1970) found a cold eddy located northwest

of Luzon in summer. These two cold centers occurring in summer were also simulated by Chao et al. (1996) with the help of a primitive equation model. The warm water appears in the vicinity of the cool water. A transient central warm pool was identified in spring (Chu et al. 1997c,d, 2002c). A warm water mass is situated in the Philippine Sea all the year round, east of the Luzon Strait, where a strong front appears between the warm Kuroshio water and cool South China Sea water. Other two warm centers appear southwest of Luzon, and northwest of Borneo.

The South China Sea seasonal thermal variability can be characterized by strengthening/weakening of the major cool pool. The basin-wide cool pool expands during winter and shrinks during summer. In December, this cool pool occupies the vast area of the South China Sea from 9°N to 20°N with two evident cold centers: the Northwest Luzon cold center (located at 116° – 120°E , 16° – 19°N) strengthens during the winter monsoon season and however, the Xisha cold center weakens and disappears in February and March. On the other hand, the cold center near the Vietnamese Bight (located at 109° – 112°E , 12° – 16°N) appears in May and strengthens during the summer monsoon season and, however, at the same time the Northwest Luzon cold center weakens and disappears.

The warm tongue penetrates northwestward right after passing through the Luzon Strait from Kuroshio and then stretches southwestward along the western boundary of the South China Sea with a very narrow width (100–200 km). This is consistent with other research on climatological data (Shaw 1989; 1991) and historical observational data (Li et al. 1998; Qu et al. 2000; Liu et al. 2001).

The Southwest Luzon warm center (located at 116° – 120°E , 12° – 14°N) occurs in March. The warm tongue associated with this warm center expands westward during the spring-to-summer transition, and occupies the east part of central South China Sea basin in the summer monsoon season (June–September). During the autumn-to-winter transition (October–November) the Xisha cold center occurs and strengthens in December.

6.6.4 Monthly Mean Salinity Field

Figure 6.29 is the horizontal depiction of monthly mean salinity at 150 m depth. The contour interval is 0.05 ppt. The most evident feature is the advance/retreat of the salty tongue represented by 34.60 ppt isoline from the Philippine Sea through Luzon Strait. This salty tongue penetrates northwestward right after passing through the Luzon Strait and then stretches southwestward along the western boundary of the South China Sea. The salty tongue has the minimum penetration into the South China Sea in October. As the salt tongue advances into the northwestern South China Sea along the Chinese–Vietnamese coast, a salty center occurs near Dongsha (115° – 117°E , 19° – 21°N) in December. As the salty tongue further advances for the next six months (January–June), the Dongsha salty center weakens

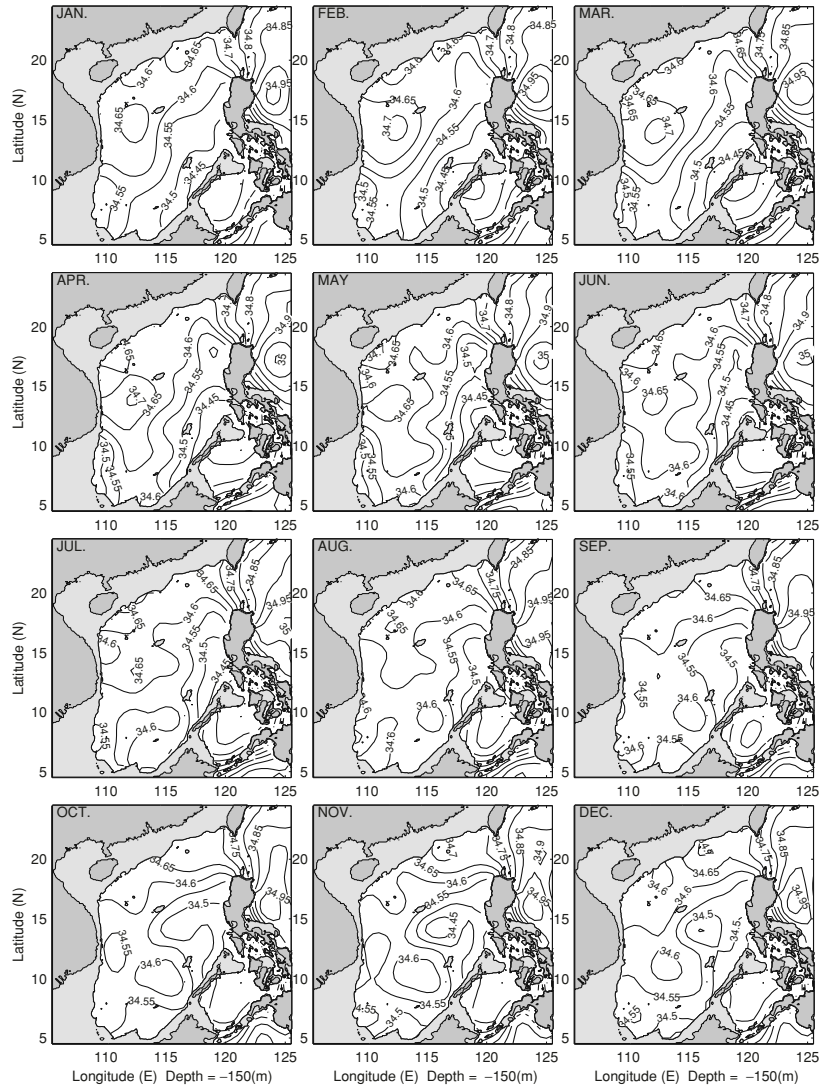


Fig. 6.29. Monthly mean salinity (ppt) fields at 150-m depth obtained from GDEM (from Chu and Li 2000, *Journal of Physical Oceanography*)

and disappears in March, and an evident salty center shows up near the Vietnamese Bight (110° – 113° E, 14° – 16° N) for six months (January–June) with salinity greater than 34.7ppt in February, March, April, and greater than 34.65ppt in other months. June is characterized as the maximum penetration of the salty tongue into the South China Sea. The salty tongue starts to retreat in July and the salty center near Vietnamese Bight weakens. A salty center appears in southeastern South China Sea west of Palawan-Borneo

(114° – 116° E, 8° – 11° N) enclosed by 34.6 ppt. This salty center expands toward the west until December.

Such a feature is to some extent inconsistent with the earlier studies (e.g., Shaw 1991). This is due to the sparse salinity observations in the South China Sea. The MOODS dataset for building the GDEM climatology has lesser salinity than temperature stations. The seasonal variability depicted here is not reliable for certain regions such as the region between Liyue Bank and Nansha, where there is no observational data.

6.6.5 Monthly Mean Pressure Field

We use the formulae described in Sect. 4.3 to transform (T, S) data from z - to isopycnal- coordinate system and (4.25) and (4.26) to calculate the monthly mean pressure field at the isopycnal surfaces. Let the isopycnal surfaces $\sigma_{\theta} = 23.0$, and 26.2 (kg m^{-3}) represent subsurface, and intermediate-level, respectively. Inhomogeneous pressure distribution on the isopycnal surface indicates upwelling (low pressure) and downwelling (high pressure) of that surface.

(a) *Subsurface* ($\sigma_{\theta} = 23.0 \text{ kg m}^{-3}$). The typical pattern (Fig. 6.30) is the pressure increase from the northwest boundary (Chinese–Vietnamese coast) to the southeast boundary (Luzon–Palawan–Borneo). The isoline of $p = 70$ decibar (db) separates the South China Sea into two parts: northwest low pressure and southeast high pressure regions. The southeast South China Sea (high pressure region) has less seasonal variation than the northwest South China Sea (low pressure region). The southeast high pressure near Luzon–Palawan–Borneo expands northwestward in summer and retreats in winter. The Luzon–Palawan–Borneo high pressure is broken into two centers in June: One is enclosed by 80 db isoline and located at the southwest South China Sea (110° – 112° E, 8° – 10° N), and the other is near Luzon–Palawan. The southwest South China Sea high pressure center expands northeastward in July and August, and joins the Luzon–Palawan–Borneo high pressure in October.

The seasonal variation of the northwest South China Sea low pressure region is depicted as follows. A small low pressure center with a closed isoline of 50 db occurs near the Vietnamese Bight in September. This low pressure center expands northeastward from October to December, and occupies the northern South China Sea (north of 15° N) until February. From April to August the low pressure ($p \leq 50$ db) retreats toward the Chinese–Vietnamese coast accompanying with the northwestward expansion of the Luzon–Palawan–Borneo high pressure. In September, the low pressure region shrinks to a small center near the South Vietnam Bight.

(b) *Intermediate level* ($\sigma_{\theta} = 26.2 \text{ kg m}^{-3}$) Seasonal variation of the intermediate level is weaker than the subsurface level. The typical pattern is the existence of a permanent South China Sea basin-scale low pressure with one permanent and two seasonal low pressure centers (Fig. 6.31).



Fig. 6.30. Monthly mean subsurface ($\sigma_\theta = 23.0 \text{ kg m}^{-3}$) pressure field (unit: db) (from Chu and Li 2000, *Journal of Physical Oceanography*)

The isoline of $p = 310 \text{ db}$ may be used to separate low and high pressure regions. The permanent low pressure center is located near Dongsha (called the Dongsha Low). Two seasonal low pressure centers are found near Vietnamese Bight from May to September and near Luzon–Palawan in July and August. Note that there exists a strong pressure gradient across the Luzon Strait from higher pressure ($p > 420 \text{ db}$) in the Philippine Sea to lower pressure in the South China Sea ($p < 340 \text{ db}$). If Kuroshio intrusion occurs at this level ($\sigma_\theta = 26.2 \text{ kg m}^{-3}$) then the intruded Kuroshio water moves upward through Luzon Strait.

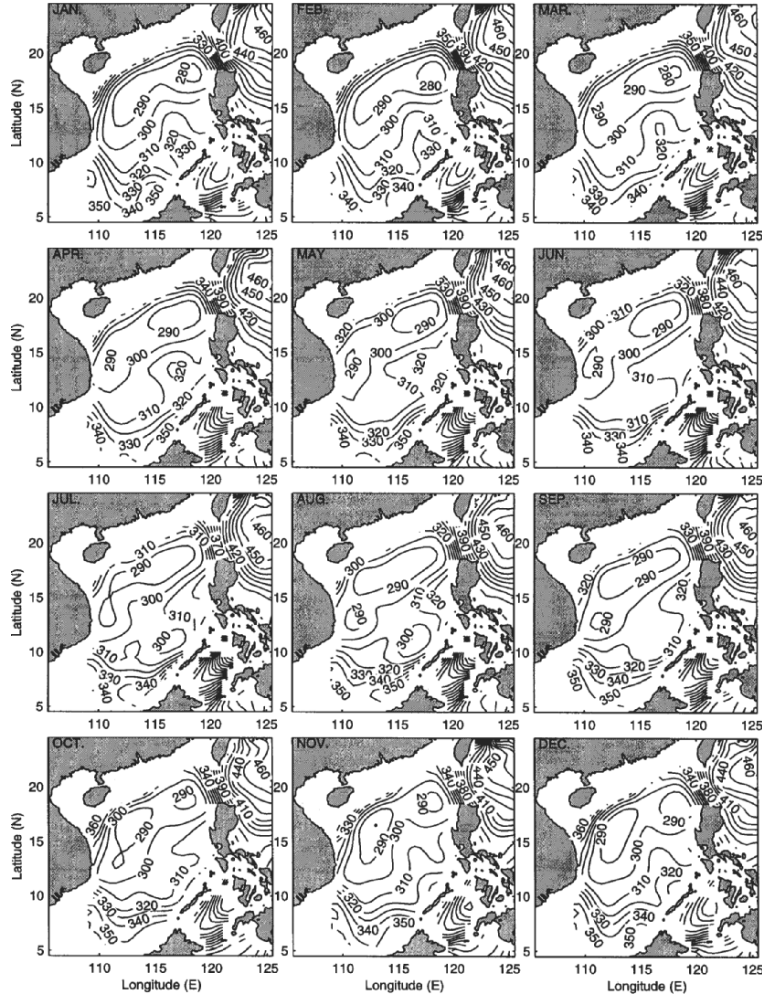


Fig. 6.31. Monthly mean intermediate level ($\sigma_\theta = 26.2 \text{ kg m}^{-3}$) pressure field (unit: db) (from Chu and Li 2000, *Journal of Physical Oceanography*)

6.6.6 Monthly Mean Potential Vorticity Field

Equation (4.28) is used to calculate the potential vorticity at isopycnal surfaces. Inhomogeneous potential vorticity distribution on the isopycnal surface indicates that the P-vector can be determined as the tangential unit vector of the q -isolines.

(a) *Subsurface* ($\sigma_\theta = 23.0 \text{ kg m}^{-3}$). Seasonal variation of the potential vorticity is characterized by the domination of a closed high over the South China Sea with the maximum value greater than $1.8 \times 10^{-9} \text{ m}^{-1} \text{ s}^{-1}$ in winter, and the northwestward monotonically increasing of the potential vorticity over the

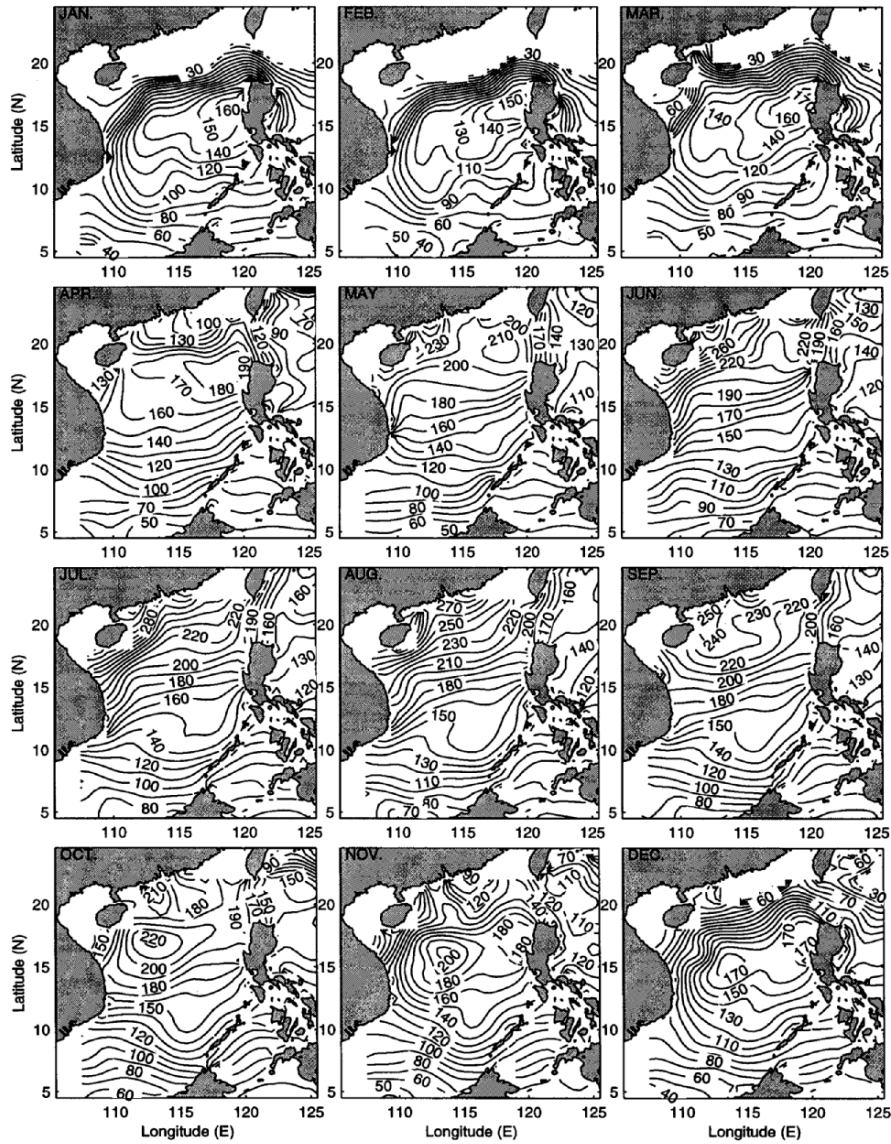


Fig. 6.32. Monthly mean subsurface ($\sigma_\theta = 23.0 \text{ kg m}^{-3}$) potential vorticity (unit: $10^{-11} \text{ m}^{-1} \text{ s}^{-1}$) (from Chu and Li 2000, *Journal of Physical Oceanography*)

South China Sea basin from the southern boundary in summer. The q -isolines intersect with the Luzon Strait in winter and run parallel to the Luzon Strait in summer (Fig 6.32). Since the geostrophic velocity is along the q -isolines, there is crossing Luzon Strait flow during winter and paralleling Luzon Strait flow during summer. Several authors (Shaw 1989; Chu and Li 2000) discussed

the Kuroshio intrusion into the South China Sea during winter. We may call the winter (summer) q -pattern as the intrusion (nonintrusion) pattern. The evident seasonal variation (intrusion and nonintrusion) on the subsurface may be caused by its shallow depths (Fig. 6.32). As depth increases, the seasonal reversal of the transport across the Luzon Strait weakens. At 150 m depth, the salinity field (Fig. 6.29) does not imply such a seasonal reversal.

The winter intrusion pattern begins in November with a basin-scale high potential vorticity over the South China Sea. This high potential vorticity expands and occupies the whole basin from December to March. Since the Kuroshio water enters the South China Sea through Luzon Strait in winter, it is reasonable to expect a basin-scale cyclonic gyre. In April, the potential vorticity high shrinks and retreats northward. The q -isolines become paralleling to the Luzon Strait. This tendency continues in May and eventually becomes the summer (June–September) nonintrusion q pattern with the disappearance of the basin-scale potential vorticity high. It reoccurs in the northern South China Sea in October with a maximum value greater than $2.2 \times 10^{-9} \text{ m}^{-1} \text{ s}^{-1}$ near Xisha, and expands southward in November. The winter intrusion q -pattern begins.

(b) *Intermediate level* ($\sigma_\theta = 26.2 \text{ kg m}^{-3}$). Seasonal variation of potential vorticity at the intermediate level is weaker than at the subsurface level. The seasonal variation (Fig. 6.33) is characterized by strengthening (weakening) of a potential vorticity high over the basin in summer (winter). The basin-scale northeast-to-southwest oriented potential vorticity high is weak in December and January. A small closed high occurs near ($114^\circ\text{E}, 18^\circ\text{N}$) with the maximum value greater than $2.5 \times 10^{-10} \text{ m}^{-1} \text{ s}^{-1}$ in February, and strengthens slowly in spring and the closed potential vorticity high ($2.5 \times 10^{-10} \text{ m}^{-1} \text{ s}^{-1}$) shifts toward west near Dongsha in May. This Dongsha potential vorticity high center becomes stationary throughout the whole of summer monsoon season (June–September) and the transition season (October–November).

6.6.7 Monthly Mean Circulations

Most important features from the P-vector method are the Kuroshio intrusion, basin gyre, flow separation, and mesoscale eddies. The inverted monthly circulation agrees quite well with earlier observational study (Wyrтки, 1961a, b) at the surface and with modeling results (Chu et al., 1999cd, 2001c) at the deeper levels.

(a) *Subsurface* ($\sigma_\theta = 23.0 \text{ kg m}^{-3}$). The subsurface shows a strong seasonal variation (Fig. 6.34). Due to the shallowness of the level, $\sigma_\theta = 23.0$, the Kuroshio east of the Luzon Strait is not well inverted. Warm and salty Kuroshio water enters the South China Sea through Luzon Strait evidently in October–March, the transition and during the winter monsoon season. The winter circulation pattern is the basin-wide cyclonic gyre. A cyclonic mesoscale eddy splits from the gyre near Dongsha in February, strengthens afterwards, and becomes evident through the whole of summer monsoon season. The

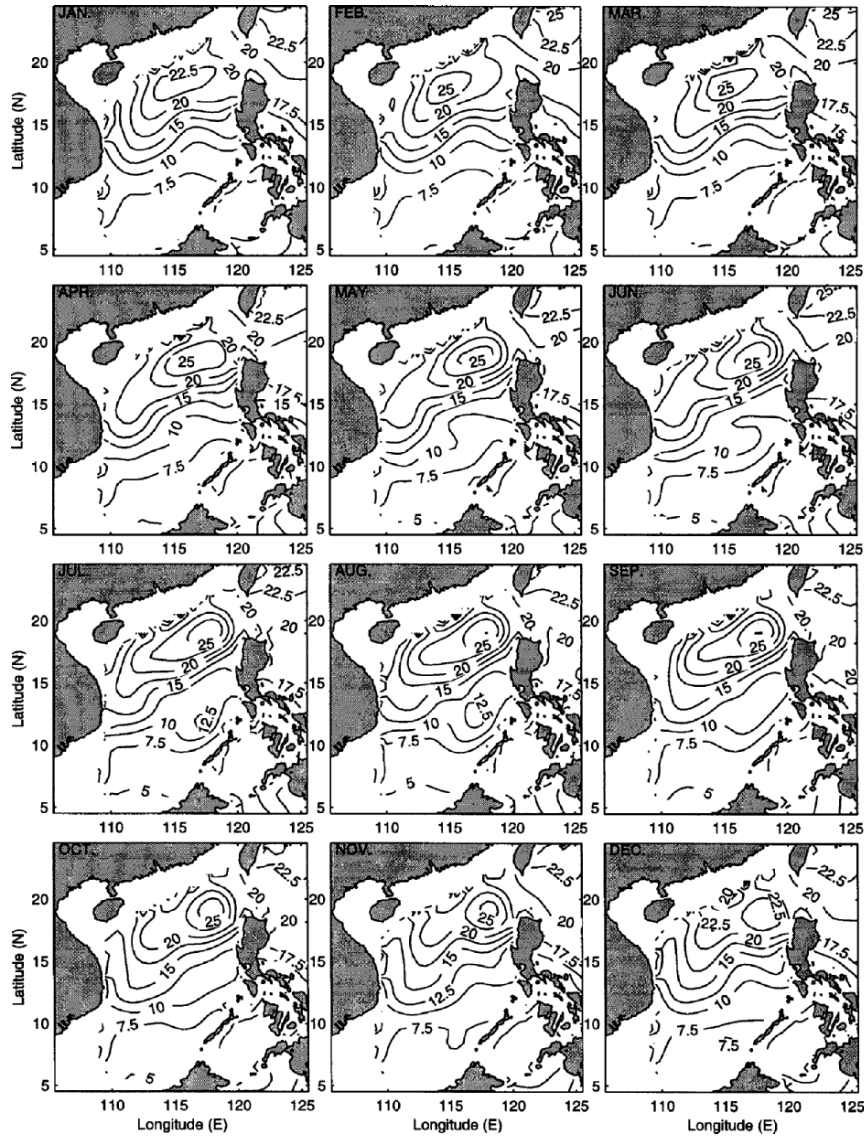


Fig. 6.33. Monthly mean intermediate level ($\sigma_\theta = 26.2 \text{ kg m}^{-3}$) potential vorticity (unit: $10^{-11} \text{ m}^{-1} \text{ s}^{-1}$) (from Chu and Li 2000, *Journal of Physical Oceanography*)

Kuroshio intruded flow is expected to be confined near the continental slope south of China. The Dongsha cyclonic eddy is undetectable from November to January. On the other hand, the basin-wide cyclonic gyre weakens in April with the disappearance of the southward western boundary currents near the Vietnamese coast.

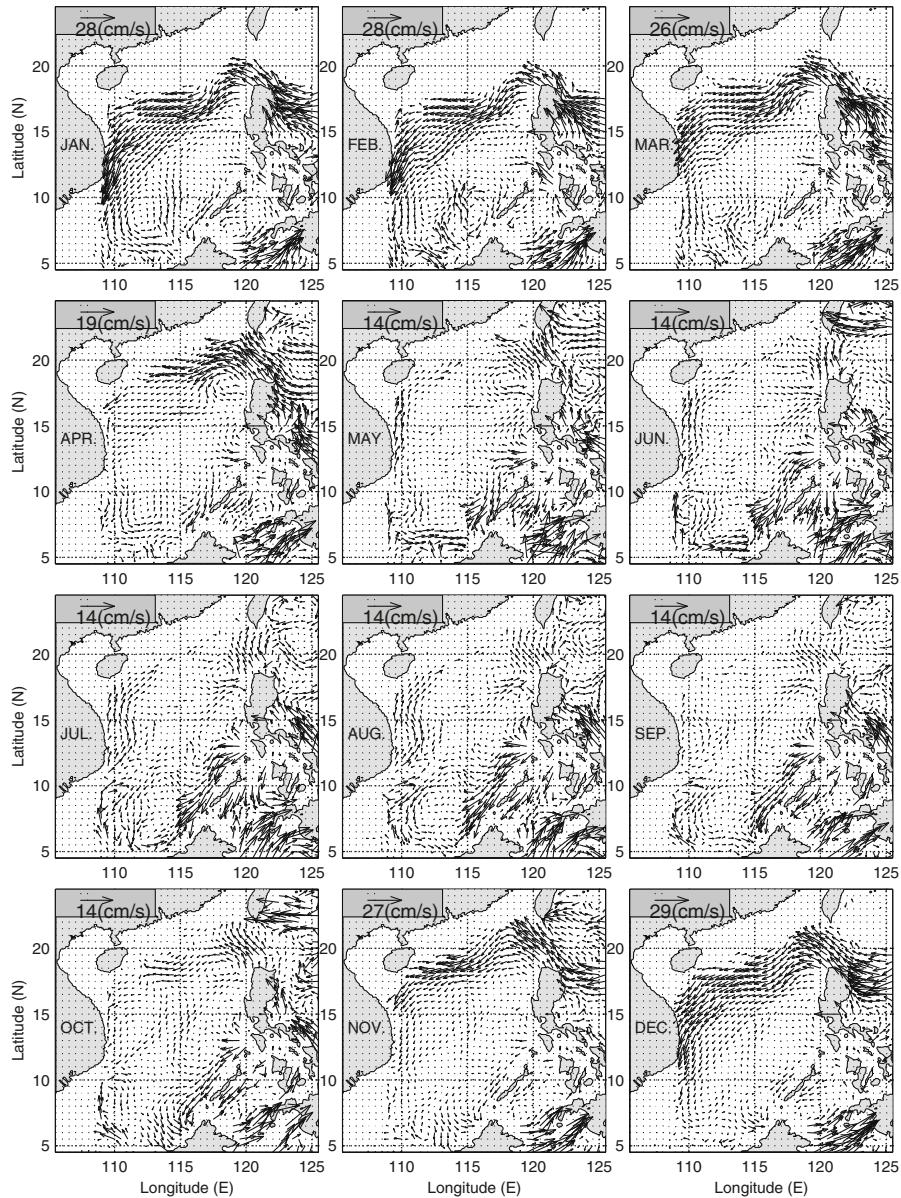


Fig. 6.34. Monthly mean subsurface ($\sigma_\theta = 23.0 \text{ kg m}^{-3}$) velocity vector field (from Chu and Li 2000, *Journal of Physical Oceanography*)

The summer (June–August) pattern is generally a weak anticyclonic gyre. A northward western boundary current occurs from the south to the Vietnamese coast with a weaker speed (less than 0.1 m s^{-1}) than its counterpart

(southward western boundary current) in winter. The western boundary current splits into two currents at 10°N : the coastal current and the off-shore current. The off-shore current recirculates and forms a mesoscale anti-cyclonic eddy near Natuna Island. The Natuna eddy was simulated using a numerical model (Chu et al. 1999d). The coastal branch continues north and then east at Hainan Island.

(b) *Intermediate level* ($\sigma_{\theta} = 26.2 \text{ kg m}^{-3}$). As the water depth increases, the seasonal variation of the inverted velocity reduces with depth. The intermediate level ($\sigma_{\theta} = 26.2$), changing from 280 to 460 db, has a persistent basin-scale cyclonic gyre as the major feature of the circulation. There is no seasonal reversal of the western boundary current. The seasonal circulation variability is featured by strengthening, weakening, and splitting of a basin-wide cyclonic gyre (Fig. 6.35). This gyre is evident and strong in winter and weakens in summer. As spring approaches (April–May), the western boundary currents (southward) near the South Vietnam Bight weaken. This “broken” gyre feature continues in the whole of summer (June–August). The western boundary currents (southward) intensify in the Fall. The cyclonic basin-scale gyre all the year round at the intermediate level consists of the numerical models (Metzger and Hurlburt 1996; Chu et al. 1999c, d).

6.6.8 Kuroshio Intrusion Through Luzon Strait

The seasonal variation of the intrusion of the Kuroshio Water into the South China Sea through the Luzon Strait has been investigated in earlier studies (Shaw 1989; 1991). As pointed out by Shaw (1991), the intrusion process is important not only to the transport of water masses into the South China Sea, but also to the shelf circulation off the southeast coast of China. Shaw (1989) used the discriminant-analysis method to classify the water mass T, S characteristics at 150, 200, and 250 m, and found that water characteristics of the Philippine Sea (Kuroshio) were identifiable along the continental margin south of China from October to January. The presence of this water indicated an intrusion current from the Philippine Sea into the South China Sea.

The inverted east–west velocities on the isopycnal surfaces along $120^{\circ}45'\text{E}$ longitude with the minimum distance between Taiwan and Luzon are used to represent the flow across the Luzon Strait (Fig. 6.36). Positive values show the outflow from the South China Sea to the Philippine Sea, and negative values represent the inflow from the Philippine Sea to the South China Sea (Kuroshio intrusion).

The estimate of the transport through the Luzon Strait is sensitive to the cross-section selection due to larger gradient of the property (temperature, salinity, and Montgomery potential, etc.) in the zonal direction than in the latitudinal direction. The signal of the zonal flow might be contaminated by the fluctuation of the Kuroshio.

The flow through the Luzon Strait has a strong seasonal variation in the upper and intermediate layers. Evident Kuroshio intrusion occurs from

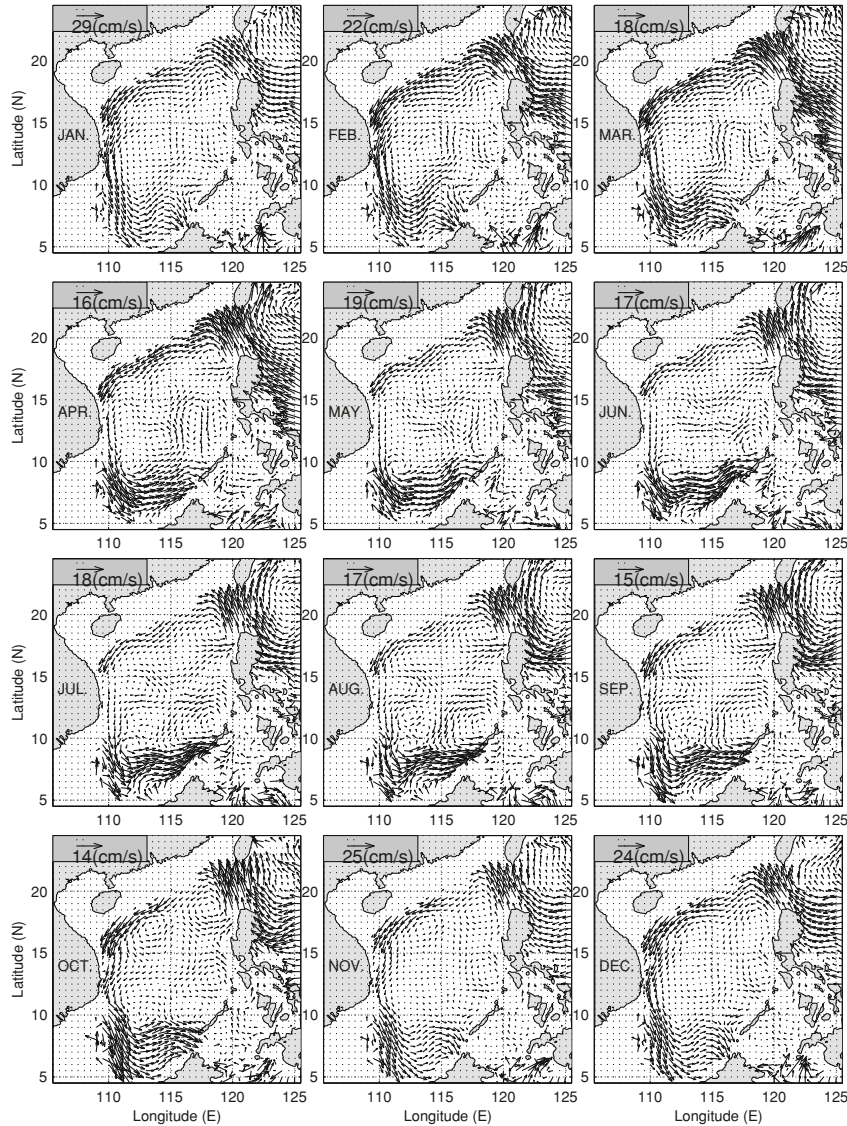


Fig. 6.35. Monthly mean intermediate level ($\sigma_\theta = 26.2 \text{ kg m}^{-3}$) velocity vector field (from Chu and Li 2000, *Journal of Physical Oceanography*)

November to April from the surface to $\sigma_\theta = 27.0$ with the maximum speed of 0.18 m s^{-1} in the middle of the Strait at $\sigma_\theta = 23.75$ in December. From January to March the core of this jet splits into two jet-cores. The upper jet-core ($\sigma_\theta = 24.0$) shifts toward the south (Luzon Island) with the maximum speed reducing from 0.17 m s^{-1} (January) to 0.14 m s^{-1} (March). The lower jet-core

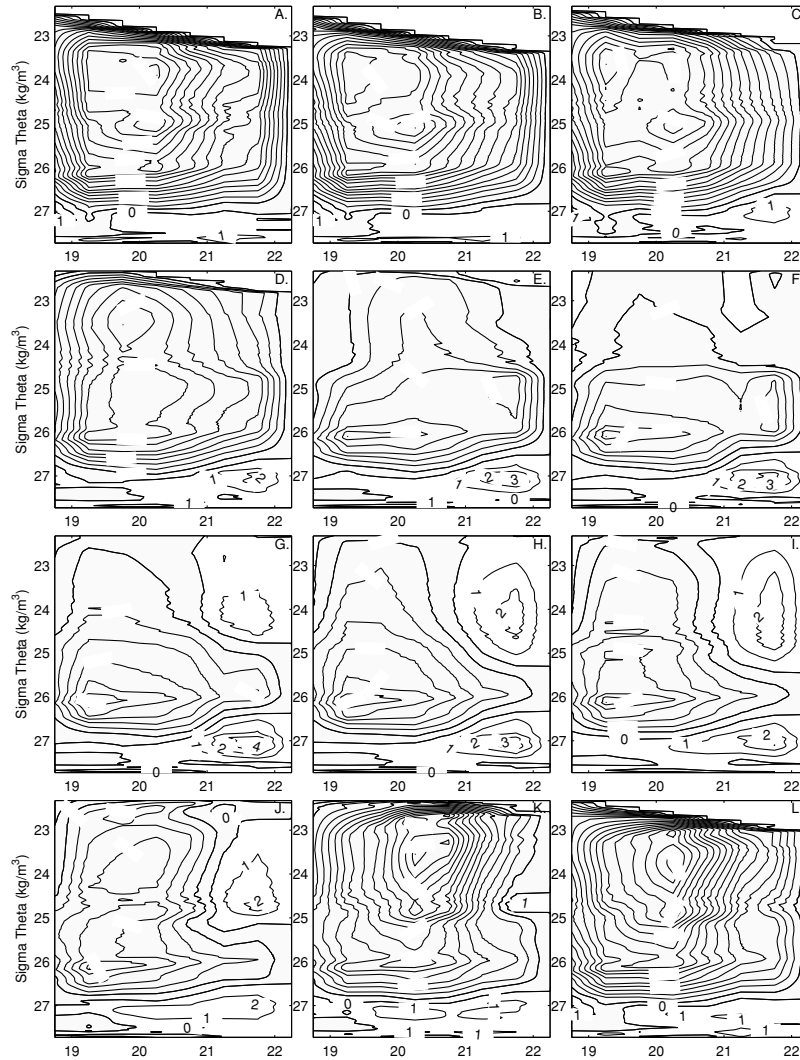


Fig. 6.36. Monthly mean east–west velocities (eastward positive) on the isopycnal surfaces along $120^{\circ}45'E$ longitude representing the flow across Luzon Strait (unit: 10^{-2} m s^{-1}) (from Chu and Li 2000, *Journal of Physical Oceanography*)

($\sigma_{\theta} = 25.0$) keeps the same location in the middle of the Strait ($20^{\circ} - 20^{\circ}30' \text{ N}$). In spring and summer, the Kuroshio intrusion weakens drastically. The maximum speed becomes 0.06 m s^{-1} at the intermediate level ($\sigma_{\theta} = 26.0$) in the southern part of the Luzon Strait (near 19.5° N) from May to October. Weak outflow (0.02 m s^{-1}) to the Philippine Sea occurs in the northern part of the Luzon Strait (north of $20^{\circ}45' \text{ N}$) from the surface to $\sigma_{\theta} = 25.5$ during the summer monsoon season.

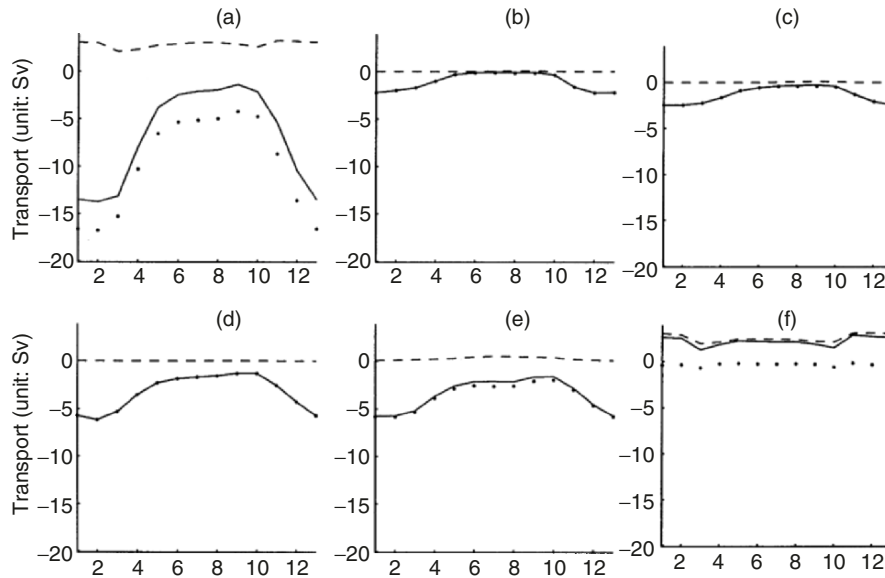


Fig. 6.37. Monthly mean east–west velocity (eastward positive) on the isopycnal surfaces along $120^{\circ}45'$ E longitude representing the flow across the Luzon Strait (unit: 10^{-2} m s^{-1}) (from Chu and Li, 2000, *Journal of Physical Oceanography*)

Figure 6.37 and Tables 6.3–6.8 show the monthly total and layered (between two σ_{θ} levels) volume transports through Luzon Strait. The dashed, dotted, and solid curves indicate outflow (eastward), inflow (westward), and net transports. The outflow is much weaker than the inflow for the total transport and the most layered transports except the deep layer ($\sigma_{\theta} \geq 27.025$), where the outflow is dominant. The total transport is negative (inflow) all year round with a minimum value of -13.7 Sv in February and a maximum value of -1.4 Sv in September with the annual transport of -6.5 Sv , which is between Metzger and Hurlburt's (1996) estimation ($2.4 - 4.4 \text{ Sv}$) and Huang et al.'s (1994) estimation ($8 - 10 \text{ Sv}$). The total and layered volume transports at the Luzon Strait might be useful for South China Sea numerical modeling.

There is a time-lag in seasonal variations between the Kuroshio intrusion and the salty tongue penetration (Fig. 6.29) at 150-m depth (near $\sigma_{\theta} = 25.0$): the Kuroshio intrusion (Fig. 6.33) is the strongest in January, and the salty tongue has the maximum penetration in June. Such a lag (4–5 months) is approximately the travel time for the Kuroshio water penetrating from Luzon Strait into the southern South China Sea. For a rough estimation, water particles in winter (December–February) enter the Luzon Strait with a speed around of 0.10 m s^{-1} at 150 m depth and travel 8.64 km each day. The distance between the Luzon Strait and the southern South China Sea is nearly 1,200–1,400 km. It will take approximately 5 months for the water particles traveling from Luzon Strait to the southern South China Seas.

Table 6.3. Monthly variation of the total inflow (westward) and outflow (eastward) volume transport (Sv) at the Luzon Strait (from Chu and Li 2000, Journal of Physical Oceanography)

	Ann	Jan	Feb	Mar	Apr	May	Jun	Jul	Aug	Sep	Oct	Nov	Dec
in	9.35	16.59	16.75	15.25	10.30	6.56	5.36	5.14	4.98	4.23	4.75	8.70	13.61
out	2.85	3.09	3.01	2.10	2.33	2.77	2.90	3.05	3.04	2.86	2.60	3.27	3.20
net (in)	6.50	13.50	13.74	13.15	7.97	3.79	2.46	2.09	1.94	1.37	2.15	5.43	6.50

Table 6.4. Monthly variation of the total inflow (westward) and outflow (eastward) volume transport (Sv) between $\sigma_\theta = 22.20$ and $\sigma_\theta = 24.00$ at the Luzon Strait (from Chu and Li 2000, Journal of Physical Oceanography)

	Ann	Jan	Feb	Mar	Apr	May	Jun	Jul	Aug	Sep	Oct	Nov	Dec
In	0.99	2.20	1.98	1.69	0.97	0.30	0.11	0.10	0.13	0.15	0.35	1.63	2.23
Out	0.02	0.00	0.00	0.00	0.00	0.01	0.02	0.05	0.06	0.08	0.03	0.00	0.00
net (in)	0.97	2.20	1.98	1.69	0.97	0.29	0.09	0.05	0.07	0.07	0.32	1.63	2.23

Table 6.5. Monthly variation of the total inflow (westward) and outflow (eastward) volume transport (Sv) between $\sigma_\theta = 24.00$ and $\sigma_\theta = 25.00$ at the Luzon Strait (from Chu and Li, 2000, Journal of Physical Oceanography)

	Ann	Jan	Feb	mar	Apr	May	Jun	Jul	Aug	Sep	Oct	Nov	Dec
In	1.27	2.46	2.44	2.22	1.62	0.88	0.55	0.41	0.40	0.37	0.47	1.31	2.08
Out	0.03	0.00	0.00	0.00	0.00	0.00	0.01	0.04	0.10	0.13	0.08	0.01	0.00
net (in)	1.24	2.46	2.44	2.22	1.62	0.88	0.54	0.37	0.30	0.24	0.39	1.30	2.08

Table 6.6. Monthly variation of the total inflow (westward) and outflow (eastward) volume transport (Sv) between $\sigma_\theta = 25.00$ and $\sigma_\theta = 26.00$ at the Luzon Strait (from Chu and Li 2000, Journal of Physical Oceanography)

	Ann	Jan	Feb	Mar	Apr	May	Jun	Jul	Aug	Sep	Oct	Nov	Dec
In	3.13	5.71	6.14	5.30	3.53	2.30	1.87	1.69	1.57	1.31	1.31	2.55	4.27
Out	0.00	0.00	0.00	0.00	0.00	0.00	0.00	0.00	0.01	0.03	0.01	0.00	0.00
net (in)	3.13	5.71	6.14	5.30	3.53	2.30	1.87	1.69	1.56	1.28	1.30	2.55	4.27

Table 6.7. Monthly variation of the total inflow (westward) and outflow (eastward) volume transport (Sv) between $\sigma_\theta = 26.00$ and $\sigma_\theta = 27.00$ at the Luzon Strait (from Chu and Li 2000, Journal of Physical Oceanography)

	Ann	Jan	Feb	Mar	Apr	May	Jun	Jul	Aug	Sep	Oct	Nov	Dec
In	3.61	5.80	5.83	5.34	3.91	2.88	2.56	2.63	2.62	2.09	1.98	3.01	4.66
Out	0.27	0.05	0.09	0.14	0.21	0.29	0.42	0.52	0.47	0.43	0.36	0.18	0.09
net (in)	3.34	5.75	5.74	5.20	3.70	2.59	2.14	2.11	2.15	1.66	1.62	2.83	4.57

Table 6.8. Monthly variation of the total inflow (westward) and outflow (eastward) volume transport (Sv) between $\sigma_\theta = 27.00$ and $\sigma_\theta = 27.725$ at the Luzon Strait (from Chu and Li 2000, Journal of Physical Oceanography)

	Ann	Jan	Feb	Mar	Apr	May	Jun	Jul	Aug	Sep	Oct	Nov	Dec
In	0.36	0.41	0.36	0.69	0.26	0.21	0.28	0.31	0.26	0.31	0.63	0.20	0.37
Out	2.53	3.04	2.92	1.95	2.11	2.47	2.46	2.44	2.40	2.20	2.12	3.08	3.10
net (out)	2.17	2.63	2.56	1.26	1.85	2.26	2.18	2.13	2.14	1.89	1.49	2.88	2.73

Questions and Exercises

- (1) In determining the parameter γ from two different levels z_k and z_m (or ρ_k and ρ_m), a set of algebraic equations

$$\gamma^{(k)} P_x^{(k)} - \gamma^{(m)} P_x^{(m)} = \Delta u_{km}, \quad (\text{E6.1})$$

$$\gamma^{(k)} P_y^{(k)} - \gamma^{(m)} P_y^{(m)} = \Delta v_{km}. \quad (\text{E6.2})$$

is used. For determining the parameter at k -level, $\gamma^{(k)}$, you may use $(N - 1)$ levels ($m = 1, 2, \dots, k - 1, k + 1, \dots, N$), where N is total number of levels. Prove that the parameter $\gamma^{(k)}$ is the same whichever m -level is used if there is no observational error in the hydrographic data.

- (2) If there is observational error in the hydrographic data, do you still get the same value of $\gamma^{(k)}$ using different m -levels? Why?
- (3) In the optimization scheme to determine the parameter $\gamma^{(k)}$, a necessary condition (6.16)

$$\begin{vmatrix} A_{11} & A_{12} \\ A_{21} & A_{22} \end{vmatrix} \neq 0,$$

is obtained. Discuss the physical significance of this condition.

- (4) In evaluating the P-vector method using MOM, the streamfunction is applied [see (6.24) and (6.25)]. What conditions are assumed? Are they realistic?
- (5) What are the major thermal features for the Japan/East Sea from Figs. 6.14 and 6.15?
- (6) Discuss the mesoscale thermal characteristics for the Japan/East Sea from Figs. 6.16 to 6.18.
- (7) What are the major haline features from Figs. 6.19 and 6.20? Does the salinity show evident features of the Polar Front in the Japan/East Sea?
- (8) What are the halocline characteristics in the Japan/East Sea from Figs. 6.21 to 6.23? Discuss these features associated with the Polar Front.
- (9) What are the major features of the inverted Japan/East Sea surface current velocities that can be observed from Fig. 6.24? Discuss the current features associated with the thermohaline structure.

- (10) Discuss mesoscale eddy features in central Japan/East Sea from Fig. 6.25.
- (11) Search the literature to see if the monthly mean volume transport of the Polar Front Current at 135°E shown in Fig. 6.26 is consistent with the earlier results.
- (12) Do large stratified lakes and semienclosed marginal seas and estuaries exhibit a persistent cyclonic circulation?
- (13) What are the major thermal features for the South China Sea from Fig. 6.28?
- (14) What are the major haline features for the South China Sea from Fig. 6.29?
- (15) What features can you identify from the isopycnal surface pressure shown in Fig. 6.30 (subsurface) and Fig. 6.31 (intermediate level)? What does strong pressure gradient imply?
- (16) What features can you identify from the isopycnal surface potential vorticity shown in Fig. 6.32 (subsurface) and Fig. 6.33 (intermediate level)? Does the water parcel move along the isoline of the potential vorticity? Why?
- (17) What are the major features for the South China Sea circulations obtained from Fig. 6.32 (subsurface) and Fig. 6.33 (intermediate level)? What are the major differences of the circulations at the two different levels?
- (18) Does Fig. 6.36 show evidence of Kuroshio intrusion? In conjunction with Figs. 6.34 and 6.35, discuss the path of the Kuroshio Water in the South China Sea.
- (19) Search the literature to find agreement and disagreement of the Kuroshio intrusion into the South China Sea obtained from Fig. 6.36 with the estimation from other authors.

Variational P-Vector Method

The P-vector inverse method described in chaps. 5 and 6 is to determine the absolute velocity for each water column independently (local determination). This method is simple and straight forward. However, local determination of the absolute velocity field might not guarantee global mass conservation. The variational P-vector method is developed for solving this problem.

7.1 Weakness of the P-Vector Method

Let $(u^{(P)}, v^{(P)})$ be the absolute velocity determined by the P-vector method, and $(U^{(P)}, V^{(P)})$ be their vertical integrations (i.e., volume transport),

$$(U^{(P)}, V^{(P)}) = \int_{-H}^0 (u^{(P)}, v^{(P)}) dz. \quad (7.1)$$

Due to the local determination of the absolute velocity, the current P-vector method does not always guarantee the mass conservation over a domain Ω , i.e.,

$$\iint_{\Omega} \left[\frac{\partial U^P}{\partial x} + \frac{\partial V^P}{\partial y} \right] dx dy \neq 0 \quad (7.2)$$

may happen. Such a deficiency largely affects the quality of the inversion. For example, the Tsushima Warm Current in the shallow Tsushima/Korea Strait was not well-inverted (see Fig. 6.24). Thus, a variational algorithm is used to make the left-hand side of (7.2) close to zero as possible.

7.2 Variational Algorithm

Let (U, V) be the vertically integrated velocity optically determined by minimizing the following functional (called the cost function),

$$J(U, V) = \frac{1}{2} \iint_{\Omega} \left[(U - U^{(P)})^2 + (V - V^{(P)})^2 \right] dx dy, \quad (7.3)$$

with the constraint (mass conservation)

$$\frac{\partial U}{\partial x} + \frac{\partial V}{\partial y} = 0$$

This problem becomes an unconstrained optimization using

$$L(U, V, \lambda) = J(U, V) + \iint_{\Omega} \lambda \left[\frac{\partial U}{\partial x} + \frac{\partial V}{\partial y} \right] dx dy, \quad (7.4)$$

where λ is the Lagrangian parameter.

Let the dependent variable be defined on the interval, $0 \leq x \leq L_x, 0 \leq y \leq L_y$. Use a uniform grid,

$$0 = x_1 < x_2 < \dots < x_{N_x} = L_x, 0 = y_1 < y_2 < \dots < y_{N_y} = L_y \quad (7.5a)$$

with grid spacing of $(\Delta x, \Delta y)$, as shown in Fig. 7.1a. Here, N_x and N_y are numbers of grid points in x and y directions, and

$$\Delta x = x_{i+1} - x_i = L_x/N_x, \quad \Delta y = y_{j+1} - y_j = L_y/N_y. \quad (7.5b)$$

Let ρ, λ be evaluated at the grid point (i, j) , and the integrated velocity components $U, V, U^{(P)}, V^{(P)}$ be evaluated at the staggered points, respectively (Fig. 7.1b). The functional (8.4) is discretized by

$$\begin{aligned} \hat{L} &= \frac{1}{2} \sum_{i=1}^{N_x-1} \sum_{j=1}^{N_y-1} \left[(U_{ij} - U_{ij}^{(P)})^2 + (V_{ij} - V_{ij}^{(P)})^2 \right] \Delta x \Delta y \\ &+ \frac{1}{2} \sum_{i=1}^{N_x-1} \sum_{j=1}^{N_y-1} \lambda_{ij} (U_{ij} + U_{i,j-1} - U_{i-1,j} - U_{i-1,j-1}) \Delta y \\ &+ \frac{1}{2} \sum_{i=1}^{N_x-1} \sum_{j=1}^{N_y-1} \lambda_{ij} (V_{ij} + V_{i,j-1} - V_{i-1,j} - V_{i-1,j-1}) \Delta x. \end{aligned} \quad (7.6)$$

7.3 Combined Local-Global Determination

Minimization of \hat{L} is a combination of local determination at the staggered grid (i, j) for velocity

$$U_{ij} \rightarrow U_{ij}^{(P)}, \quad V_{ij} \rightarrow V_{ij}^{(P)}, \quad (7.7)$$

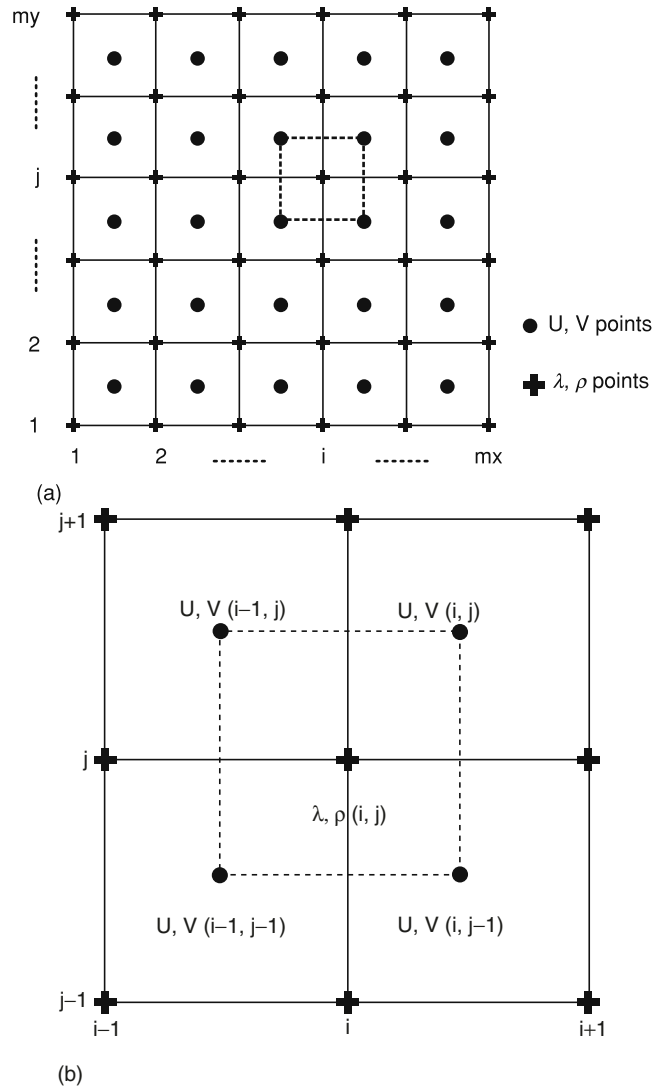


Fig. 7.1. Staggered grid used for the computation: (a) grid distribution and (b) staggered grids for (u, v) and standard grids for (ρ, λ) (from Chu et al. 2001b, Journal of Physical Oceanography)

and global determination (box model)

$$\frac{1}{\Delta x} (U_{ij} + U_{i,j-1} - U_{i-1,j} - U_{i-1,j-1}) + \frac{1}{\Delta y} (V_{ij} + V_{i,j-1} - V_{i-1,j} - V_{i-1,j-1}) \rightarrow 0, \quad (7.8)$$

leads to the mass conservation at any box centered at the nonstaggered grid for ρ and λ (Fig. 7.1b). Thus, this variational P-vector method can be treated as a P-vector box model. The variational problem is the determination of $(U_{ij}, V_{ij}, \lambda_{ij})$ through minimizing the cost function

$$\frac{\partial \hat{L}}{\partial U_{ij}} = 0, \quad \frac{\partial \hat{L}}{\partial V_{ij}} = 0, \quad \frac{\partial \hat{L}}{\partial \lambda_{ij}} = 0. \quad (7.9)$$

Substituting (7.6) into (7.9) yields

$$U_{ij} = U_{ij}^P - \frac{1}{2\Delta x} (\lambda_{ij} + \lambda_{i,j+1} - \lambda_{i+1,j} - \lambda_{i+1,j+1}), \quad (7.10)$$

$$V_{ij} = V_{ij}^P - \frac{1}{2\Delta y} (\lambda_{ij} + \lambda_{i,j+1} - \lambda_{i+1,j} - \lambda_{i+1,j+1}), \quad (7.11)$$

$$\begin{aligned} & \frac{1}{\Delta x} (U_{ij} + U_{i,j-1} - U_{i-1,j} - U_{i-1,j-1}) \\ & + \frac{1}{\Delta y} (V_{ij} + V_{i,j-1} - V_{i-1,j} - V_{i-1,j-1}) = 0. \end{aligned} \quad (7.12)$$

Substituting (7.10) and (7.11) into (7.12) yields a linear algebraic equation for the Lagrange parameter,

$$\begin{aligned} & a_{11}\lambda_{i-1,j-1} + a_{21}\lambda_{i,j-1} + a_{31}\lambda_{i+1,j-1} + a_{12}\lambda_{i-1,j} + a_{22}\lambda_{i,j} + a_{32}\lambda_{i+1,j} \\ & + a_{13}\lambda_{i-1,j+1} + a_{23}\lambda_{i,j+1} + a_{33}\lambda_{i+1,j+1} = S_{ij}, \end{aligned} \quad (7.13)$$

where $i = 2, 3, \dots, N_x - 1, j = 2, 3, \dots, N_y - 1$, and

$$\begin{aligned} a_{11} = a_{12} = a_{31} = a_{33} &= -\frac{1}{4} \left(\frac{1}{\Delta x^2} + \frac{1}{\Delta y^2} \right), \quad a_{22} = \frac{1}{2} \left(\frac{1}{\Delta x^2} + \frac{1}{\Delta y^2} \right), \\ a_{21} = a_{23} &= -a_{12} = -a_{32} = \frac{1}{2} \left(\frac{1}{\Delta x^2} - \frac{1}{\Delta y^2} \right), \end{aligned} \quad (7.14)$$

and

$$\begin{aligned} S_{ij} &= \frac{1}{2\Delta x} \left(U_{ij}^{(P)} + U_{i,j+1}^{(P)} - U_{i-1,j}^{(P)} - U_{i+1,j+1}^{(P)} \right) \\ &+ \frac{1}{2\Delta y} \left(V_{ij}^{(P)} + V_{i,j+1}^{(P)} - V_{i-1,j}^{(P)} - V_{i+1,j+1}^{(P)} \right). \end{aligned} \quad (7.15)$$

The alternative-direction implicit (ADI) method (Press et al. 1986) is used to obtain the value of the Lagrange parameter at the grid point, λ_{ij} solving

(7.13). Substituting the given value of λ_{ij} into (7.10) and (7.11) yield the optimal estimation of U_{ij} and V_{ij} .

After the vertically integrated velocity (U, V) is calculated, the bottom velocity can be determined. Let $h = h(x, y)$ be the bottom topography and (u_{-h}, v_{-h}) be the bottom velocity. Applying the thermal wind relations (1.4) and (1.5) to the two levels z and $-h$, we have

$$(u, v)_z - (u, v)_{-h} = \frac{g}{f\rho_0} \int_{-h}^z \left(\frac{\partial \rho}{\partial y}, -\frac{\partial \rho}{\partial x} \right) dz'. \quad (7.16)$$

Vertical integration of (7.16) from the bottom ($z = -h$) to the surface ($z = 0$) yields

$$(u, v)_{-h} = \frac{1}{h}(U, V) - \frac{g}{fh\rho_0} \int_{-h}^0 dz \int_{-h}^z \left(\frac{\partial \rho}{\partial y}, -\frac{\partial \rho}{\partial x} \right) dz'. \quad (7.17)$$

With the computed bottom velocity $(u, v)_{-h}$, we use the thermal wind relations (1.4) and (1.5) to obtain the absolute velocity from the density field.

7.4 Annual Mean Velocity

Figure 7.2 shows the inverted horizontal velocity vectors at 0-, 50-, 100-, 150-, 200-, and 300-m deep, respectively. The variational P-vector method inverts the velocity well at the three major straits: Tsushima/Korea, Tsugaru, and Soya Straits. However, the flow in Tatar Strait is not well resolved due to the poor data quality.

We take the velocity field at 0-, 50-, and 100-m (150-, 200-, and 300-m) deep to represent the upper (intermediate) layer circulation features. The inverted velocity field agrees well with early results using the ordinary P-vector method (see Sect. 6.5.5) except for flow in the straits which is more improved.

7.4.1 Upper Layer

The most striking feature of the upper layer circulation is its three-branch structure. North of 35°N , the Tsushima Warm Current bifurcates into an eastern portion (the first branch, or the Japan Near-Shore Branch) and a western portion. The strength of the Tsushima Warm Current at both portions reduces with depth. Flow through the western portion (i.e., East Korean Warm Current) closely follows the Korean Coast until it separates near $37^\circ - 38^\circ\text{N}$ into two branches: the off-shore branch (the second branch, i.e., the Polar Front Current) follows the Polar Front to the western coast of Hokkaido Island, and the along-shore branch (or the third branch) moves northward (i.e.,

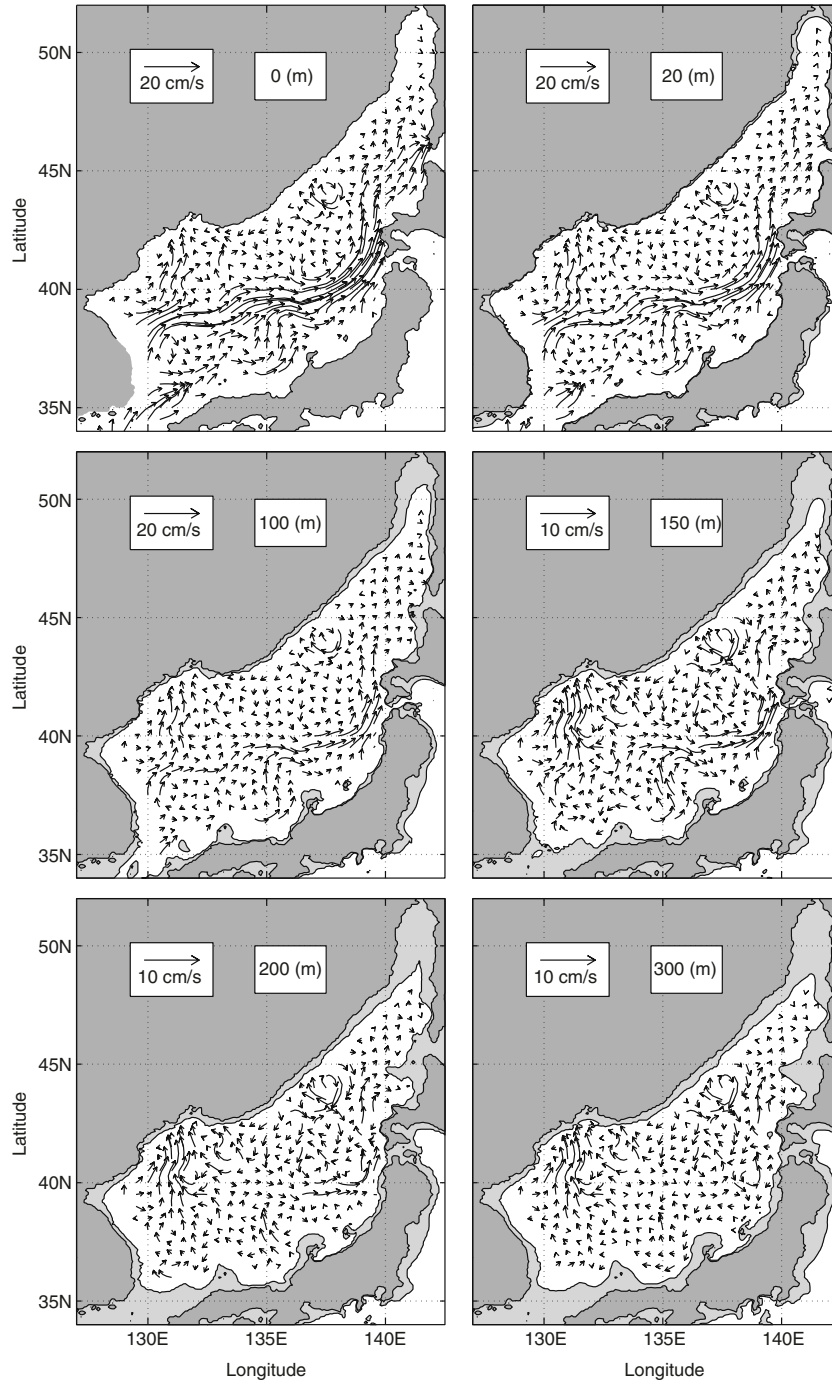


Fig. 7.2. Inverted annual mean horizontal velocity vectors at different depths: (a) 0 m, (b) 50 m, (c) 100 m, (d) 150 m, (e) 200 m, and (f) 300 m (from Chu et al. 2001b, *Journal of Physical Oceanography*)

the East Korean Warm Current). Such a three-branch pattern was first identified by Suda and Hidaka (1932) and Suda et al. (1932) using hydrographic and current meter data from June to September in 1929 and in 1930, respectively. Since then, the existence of three branches has been believed to be the typical Tsushima Warm Current flow pattern. The second branch (i.e., the Polar Front Current) is stronger than the first branch (i.e., the Japan Near-Shore Branch).

The maximum speed of the Polar Front Current is found around 0.2 m s^{-1} at the surface. The maximum speed of the Japan Near-Shore Branch is found to be around 0.1 m s^{-1} , occurring near the Japanese coast (135°E – 35.5°N) at the surface. The second feature of the upper layer circulation is its multieddy structure. An evident cyclonic gyre is identified in the Japan Basin (135° – 140°E , 38° – 44°N) with the flow associating with the Polar Front Current as its southern and eastern flanks and the flow from the north as its western flank. A mesoscale anticyclonic eddy is identified in the Ulleng/Tsushima Basin (130° – 132°E , 36° – 38°N) with the Polar Front Current as its northern and western flanks. The velocity field weakens with depth.

7.4.2 Intermediate Layer

The most striking feature of the intermediate layer circulation is its multieddy structure. The Polar Front Current weakens at 150 m deep and disappears at 200 and 300 m depth. The cyclonic gyre in the Japan Basin (135° – 140°E , 38° – 44°N) is evident with a maximum speed to be around 0.1 m s^{-1} . The Ulleng/Tsushima Basin anticyclonic eddy is evident at 150 and 200 m depth and weakens drastically at 300 m depth.

7.5 Seasonal Variability

The seasonal variability of the inverted absolute velocity (not in the straits) is quite similar to an early study using the ordinary P-vector method (see Sect. 6.5.5).

7.5.1 Surface Circulation

The velocity variability reduces with depth since the seasonal density variability weakens with depth. The Polar Front Current has a weak seasonal variation in flow pattern and a strong seasonal variation in current speed. The Japan Near-Shore Branch is too weak to be identified in winter (December–February). In March, it starts to occur along the Japan coast, and strengthens in spring and reaches the maximum velocity in July.

An interesting feature in the surface currents (Fig. 7.3) is the out-of-phase variation between Polar Front Current (along the Polar Front) and Japan Near-Shore Branch (along the west coast of Japan). For example, the Polar

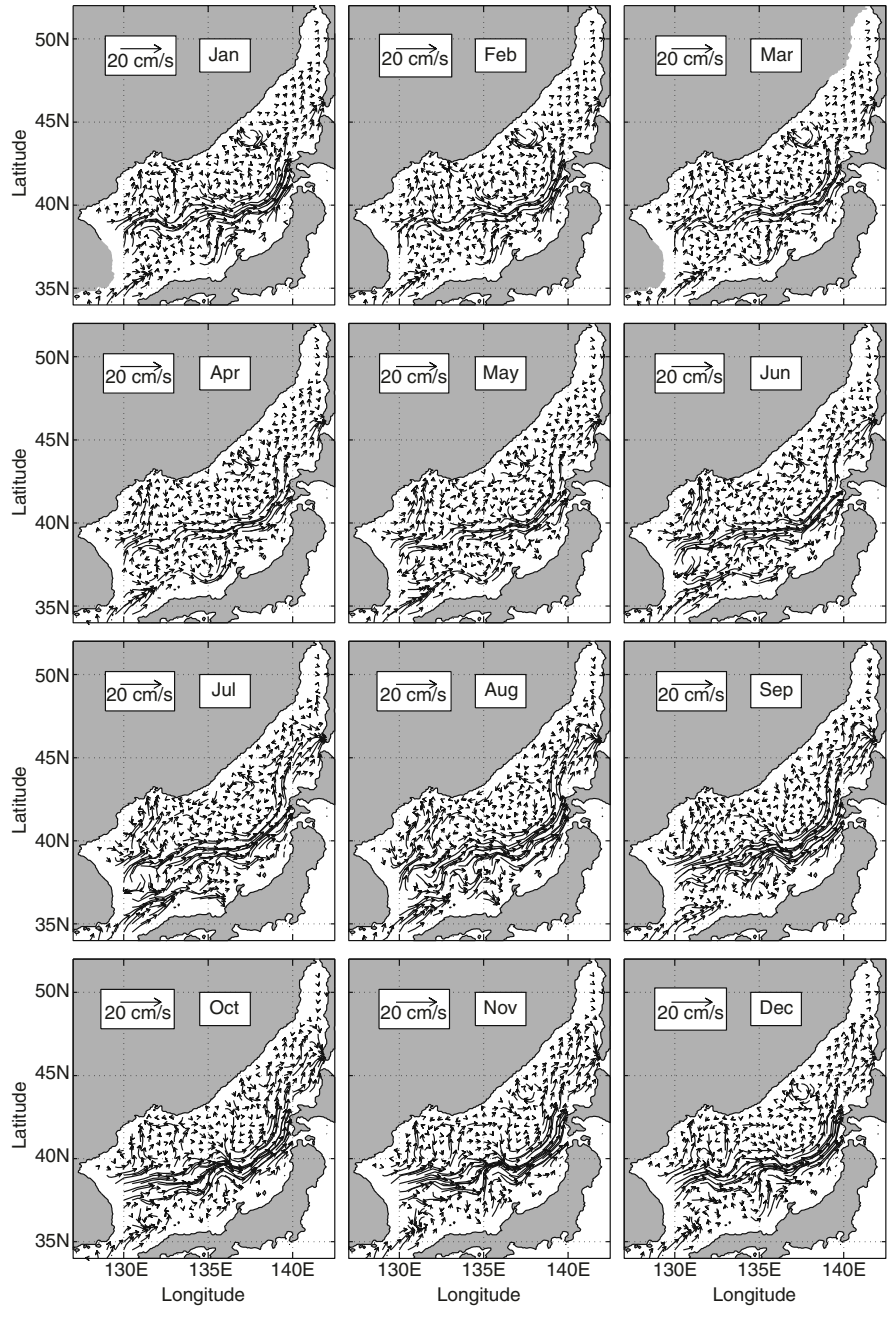


Fig. 7.3. Inverted monthly mean surface horizontal velocity vectors (from Chu et al. 2001b, *Journal of Physical Oceanography*)

Front Current (Japan Near-Shore Branch) strengthens (weakens) from July to September, and weakens (strengthens) from January to April.

The Japan Basin cyclonic gyre occurs all the year round with the flow associated with the Polar Front Current as the southern and eastern flanks and the flow from the north as the western flank. The seasonal variability of this gyre is largely determined by the seasonal variability of the Polar Front Current.

7.5.2 Out-of-Phase Variation

The seasonal variation of the Japan/East Sea major currents is also shown in the meridional cross-section (135°E) of the monthly mean u -component (7.4). Two eastward flowing currents, the Polar Front Current (38° – 40°N) and Japan Near-Shore Branch (36° – 37°N), are well represented. The Polar Front Current is strong from September to December with the maximum speed of 0.2 m s^{-1} and weak from February to June with a minimum speed of 0.1 m s^{-1} . During the summer monsoon season (June–October), the Polar Front Current strengthens (maximum speed increases from 0.12 to 0.18 m s^{-1}), and the Japan Near-Shore Branch weakens (maximum speed decreases from 0.12 to 0.04 m s^{-1}). During the winter monsoon season (December–April), the Polar Front Current weakens (maximum speed decreases from 0.18 to 0.12 m s^{-1}), and the Japan Near-Shore Branch strengthens (maximum speed increases from 0.04 to 0.12 m s^{-1}).

7.5.3 Ulleung/Tsushima Basin Anticyclonic Eddy

The seasonal variation of the Ulleng/Tsushima Basin anticyclonic eddy is shown in the zonal cross-section (37°N) of monthly mean v -component (Fig. 7.5) between 130°E and 132°E : the northward flow in the west and the southward flow in the east. The inverted Ulleng/Tsushima Basin eddy has a core from the surface to 100 m deep with a maximum swirl velocity of 0.06 m s^{-1} . It is quite evident during the whole winter season (December–February) and weakens in March. It cannot be identified at the 37°E cross-section from spring to early summer (April–June) and becomes evident again in late summer (August).

7.5.4 Flow through Tsushima/Korea Strait

The monthly mean surface velocity vector field in Tsushima/Korea Strait (Fig. 7.6) shows the capability of the variational P-vector method to invert the currents in shallow straits. The inverted general circulation pattern agrees with the observational circulation pattern using Acoustic Doppler Current Profiler (ADCP) reported by Egawa et al. (1993): The main axis of the Tsushima Warm Current exists in the western channel at 34°N for all months, and the current in the eastern channel is relatively weak. The seasonal variation of the current magnitude is quite small. Northeastward steady flow always exists in the middle of the strait with a maximum current speed of 0.1 m s^{-1} .

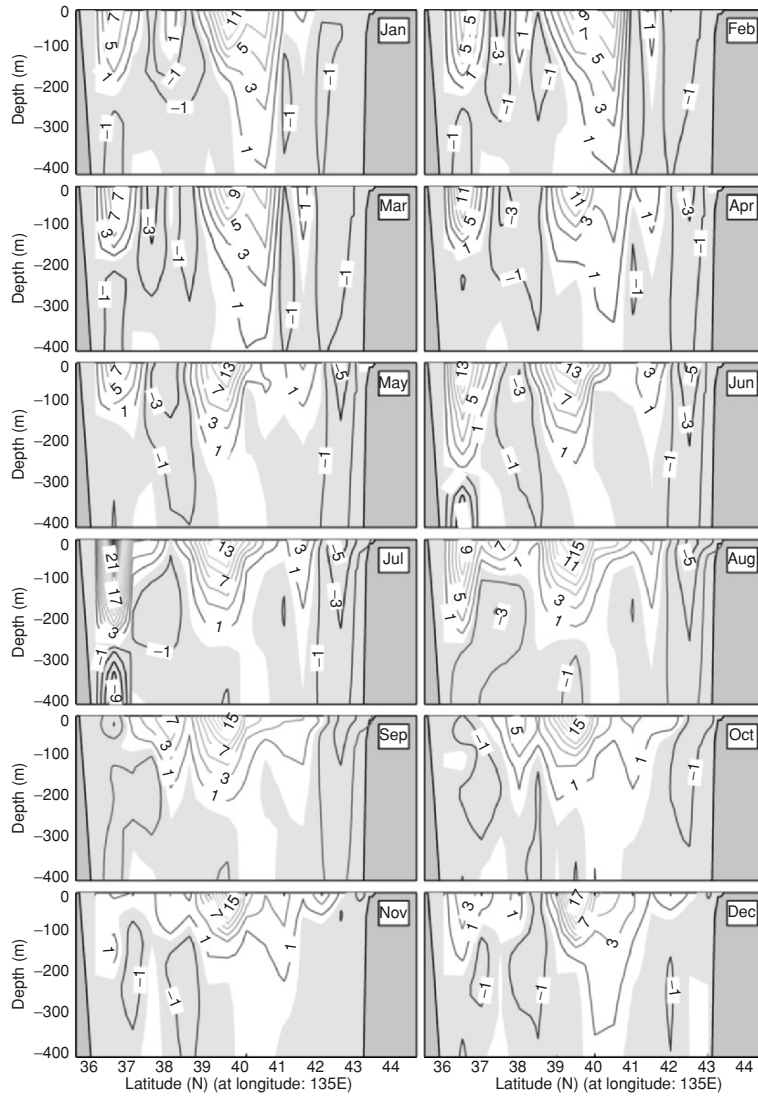


Fig. 7.4. Meridional cross-sections of the inverted monthly mean u velocity (unit: 10^{-2} m s^{-1}) along 135°E (from Chu et al. 2001b, Journal of Physical Oceanography)

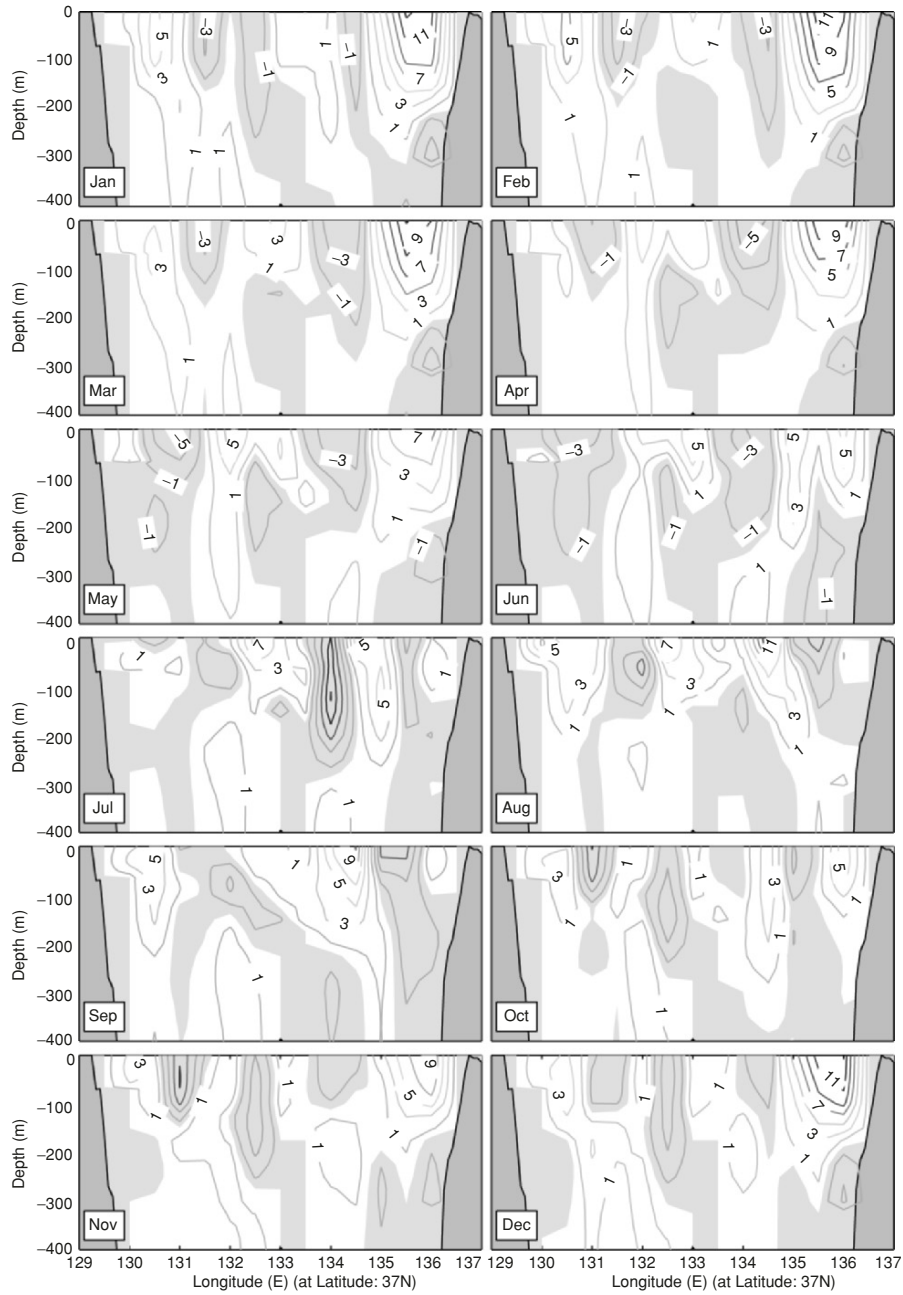


Fig. 7.5. Zonal cross-sections of inverted monthly mean v velocity (unit: 10^{-2} m s^{-2}) along 37°N (from Chu et al. 2001b, *Journal of Physical Oceanography*)

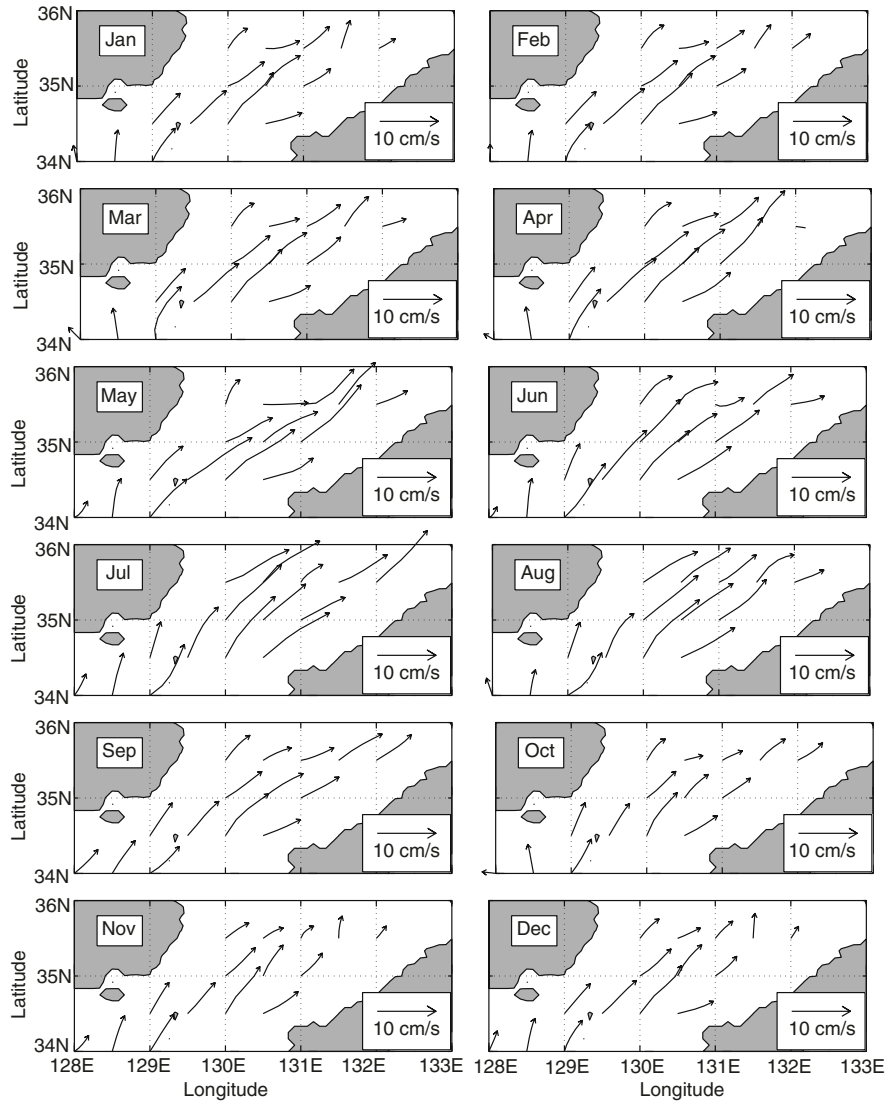


Fig. 7.6. Inverted monthly mean surface horizontal velocity vectors in the Tsushima/Korean Strait (from Chu et al. 2001b, Journal of Physical Oceanography)

7.6 Volume Transport Through Tsushima/Korea, Tsugaru, and Soya Straits

Warm water enters the Japan Sea through the Tsushima/Korea Strait with the Tsushima Warm Current from the East China Sea and exits the Japan Sea through the Tsugaru and Soya straits. An evident volume transport through Tatar Strait is not found (Martin and Kawase 1998). Using the inverted absolute velocity field, we calculate the monthly mean volume transport through the four straits. The transport through Tatar Strait is zero. The transports through Tsushima/Korea, Tsugaru, and Soya Straits are shown in Fig. 7.7. An evident seasonal variation is found in Tsushima/Korea Strait with a minimum value of 1.9 Sv in November and a maximum value of 2.9 Sv in July (Table 7.1). The annual mean volume transport is 2.3 Sv, and the range (maximum minus minimum) of the seasonal variation is 1.0 Sv. This range (1.0 Sv) is larger than Isobe's (1994) estimation (0.7 Sv) using the sea level difference across the strait, smaller than Inoue et al.'s (1985) estimation (1.61 Sv) with 3.43 Sv in summer and 1.82 Sv in winter, and Yi's (1966) estimation (1.9 Sv) with a maximum of 2.2 Sv in October and a minimum of 0.3 Sv in February.

The volume transport in Soya Strait (outflow) has a similar seasonal variation to that in Tsushima/Korea Strait. The maximum (minimum) outflow from Soya Strait is 1.4 Sv (0.5 Sv) in July (December). The annual range is 0.9 Sv. The volume transport in Tsugaru Strait (outflow) has a rather weak seasonal variability. The maximum (minimum) outflow from Tsugaru Strait is 1.6 Sv (1.2 Sv) in December (September). The annual range is 0.4 Sv. The ratio of the outflow through Tsugaru vs. Soya Strait varies from a maximum value of 3.2 in December to a minimum value of 1.1 in July. The inverted circulation pattern agrees well with the numerical modeling results (Chu et al. 2000c, 2003c).

The inverted inflow transport through Tsushima/Korea Strait equals the total outflow transport through Tsugaru and Soya Straits (a mass-conservation pattern, see Table 7.1). Such a feature indicates the improvement of the variational P-vector method over the original P-vector method, and might be practically useful in determining open boundary conditions for regional numerical models. For example, some Japan Sea circulation models use constant outflow partitioning: Chu et al. (2001b) (or Bang et al. 1996) assumed that 75% (80%) of the total inflow transport flows out of the Japan Sea through Tsugaru Strait, and 25% (20%) through Soya Strait. Such an uncertainty in the open boundary conditions can be eliminated when the variational P-vector method is used.

The variational P-vector method is a combined box/P-vector model. It has the capability to invert the Japan Sea circulation reasonably well and in particular at the three major straits: Tsushima/Korea, Tsugaru, and Soya Straits. The inverted absolute velocity field coincides with earlier observational depiction of the Japan/East Sea circulation.

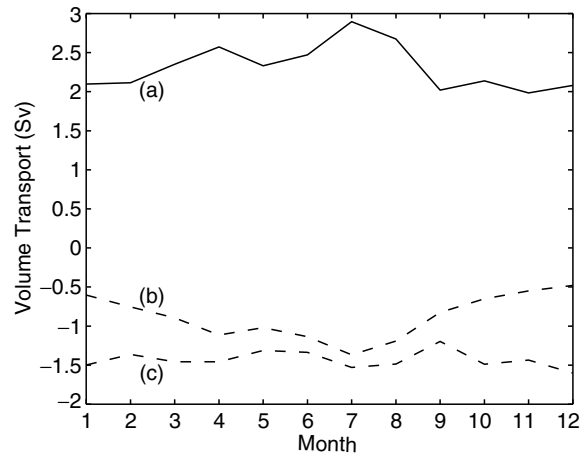


Fig. 7.7. Inverted monthly mean surface horizontal velocity vectors in the Tsushima/Korean Strait (from Chu et al. 2001b, Journal of Physical Oceanography)

Table 7.1. Inverted monthly variation of volume transport (Sv) at the three major straits. The positive/negative values mean inflow/outflow (from Chu et al. 2001b, Journal of Physical Oceanography)

	Jan	Feb	Mar	Apr	May	Jun	Jul	Aug	Sep	Oct	Nov	Dec
soya	0.6	0.7	0.9	1.1	-1.0	-1.1	-1.4	-1.2	-0.8	-0.7	0.5	-0.5
tsugaru	1.5	1.4	1.5	1.5	-1.3	-1.3	-1.5	-1.5	-1.2	-1.5	-1.4	-1.6
tsushima	2.1	2.1	2.4	2.6	2.3	2.4	2.9	2.7	2.0	2.2	1.9	2.1

Questions and Exercises

- (1) What is the major weakness of the P-vector inverse method? Why?
- (2) The variational P-vector method is to minimize

$$L(U, V, \lambda) = J(U, V) + \iint_{\Omega} \lambda \left[\frac{\partial U}{\partial x} + \frac{\partial V}{\partial y} \right] dx dy, \tag{E7.1}$$

where λ is the Lagrangian parameter. What conditions do you get from $\partial L / \partial U = 0$, $\partial L / \partial V = 0$, or $\partial L / \partial \lambda = 0$?

- (3) What improvement can you identify from the comparison between Fig. 7.3 and Fig. 6.24 when the variational scheme is used for the P-vector method?
- (4) What are the major features of the Japan/East Sea multieddy structure?

- (5) Discuss the current features and transports at the Tsushima/Korean Strait from Figs. 7.6 and 7.7
- (6) The volume transports at the three major straits of the Japan/East Sea (Soya, Tsugura, and Tsushima/Korean) are calculated using the variational P-vector method as shown in Table 7.1. Search the literature to find agreement and disagreement with other authors.

Determination of Volume Transport Stream Function

The P-vector inverse method has been successfully used to invert the absolute velocity from hydrographic data for the extra-equatorial hemispheres, but not for the equatorial region since it is based on the geostrophic balance. A smooth interpolation scheme across the equator is described in this chapter to bring together the two already known solutions (P-vectors) for the extra-equatorial hemispheres, using the volume transport stream function Ψ .

8.1 Vertically Integrated Velocity

Starting from the basic (1.1a)–(1.1d), compute the depth-integrated (total) horizontal velocity

$$(\hat{U}, \hat{V}) = \int_{-H}^0 (\hat{u}, \hat{v}) dz, \quad (8.1)$$

and geostrophic velocity,

$$(U, V) = \int_{-H}^0 (u, v) dz \quad (8.2)$$

where $z = -H(x, y)$ represents the ocean bottom, and $z = 0$ refers to the ocean surface. Depth-integration of (1.1a) and (1.1b) from the ocean bottom to the ocean surface leads to

$$\begin{aligned} -f(\hat{V} - V) &= A_z \left. \frac{\partial \hat{u}}{\partial z} \right|_{z=\eta} - A_z \left. \frac{\partial \hat{u}}{\partial z} \right|_{z=-H} \\ &+ A_h \nabla_2^2 \hat{U} - 2A_h \nabla_2 u_{-H} \cdot \nabla_2 H - A_h u_{-H} \nabla_2^2 H, \end{aligned} \quad (8.3)$$

$$f(\hat{U} - U) = A_z \left. \frac{\partial \hat{v}}{\partial z} \right|_{z=\eta} - A_z \left. \frac{\partial \hat{v}}{\partial z} \right|_{z=-H} + A_h \nabla_2^2 \hat{V} - 2A_h \nabla_2 v_{-H} \cdot \nabla_2 H - A_h v_{-H} \nabla_2^2 H, \quad (8.4)$$

where (u_{-H}, v_{-H}) are velocity components at the ocean bottom. The turbulent momentum flux at the ocean surface is calculated by

$$A_z \left(\frac{\partial \hat{u}}{\partial z}, \frac{\partial \hat{v}}{\partial z} \right) \Big|_{z=\eta} = \frac{(\tau_x, \tau_y)}{\rho_0}, \quad (8.5)$$

where (τ_x, τ_y) are the surface wind stress components. The turbulent momentum flux at the ocean bottom is parameterized by

$$A_z \left(\frac{\partial \hat{u}}{\partial z}, \frac{\partial \hat{v}}{\partial z} \right) \Big|_{z=-H} = C_D \sqrt{u_{-H}^2 + v_{-H}^2} (u_{-H}, v_{-H}), \quad (8.6)$$

where $C_D = 0.0025$ (Blumberg and Mellor 1987) is the drag coefficient. Substituting the thermal wind relations (1.4) and (1.5) into (8.2) yields

$$(U, V) = (U_{\text{den}} + H u_{-H}, V_{\text{den}} + H v_{-H}), \quad (8.7)$$

where

$$(U_{\text{den}}, V_{\text{den}}) = \frac{g}{f \rho_0} \left(\int_{-H}^0 \int_{-H}^z \frac{\partial \rho}{\partial y} dz' dz, - \int_{-H}^0 \int_{-H}^z \frac{\partial \rho}{\partial x} dz' dz \right) \quad (8.8)$$

is the density driven transport. Rearrange (8.3) and (8.4) into

$$A_h \nabla^2 \hat{U} + f \hat{V} = f V_{\text{den}} + f V_b - \frac{\tau_x}{\rho_0} + A_h Q_1, \quad (8.9)$$

$$-A_h \nabla^2 \hat{V} + f \hat{U} = f U_{\text{den}} + f U_b + \frac{\tau_y}{\rho_0} - A_h Q_2, \quad (8.10)$$

where

$$Q_1 \equiv (2 \nabla u_{-H} \cdot \nabla H + u_{-H} \nabla^2 H), \quad Q_2 \equiv (2 \nabla v_{-H} \cdot \nabla H + v_{-H} \nabla^2 H),$$

and

$$U_b = \left(H - \frac{C_D}{f} \sqrt{u_{-H}^2 + v_{-H}^2} \right) u_{-H}, \quad V_b = \left(H + \frac{C_D}{f} \sqrt{u_{-H}^2 + v_{-H}^2} \right) v_{-H}, \quad (8.11)$$

are the transport due to the bottom currents, or in simple terms, it is called the bottom transport. With the known bottom velocity vector (u_{-H}, v_{-H}) , the depth-integrated velocity (U, V) can be determined from the wind, density, and topographic data.

For the extra-equatorial regions, the horizontal diffusion can be neglected (see Sect. 1.1.2). Equations (8.10) and (8.9) become

$$U^* = U_{\text{den}} + U_{\text{b}} + \frac{\tau_y}{f\rho_0}, \quad (8.12)$$

$$V^* = V_{\text{den}} + V_{\text{b}} - \frac{\tau_x}{f\rho_0}. \quad (8.13)$$

With the known (u_{-H}, v_{-H}) , the depth-integrated flow (U^*, V^*) may be directly calculated using (8.12) and (8.13). However, the computed (U^*, V^*) field using (8.12) and (8.13) is quite noisy and cannot be the final product. Thus, the superscript “*” is used to represent the interim depth-integrated velocity calculated using (8.12) and (8.13).

8.2 Volume Transport Stream Function

Integration of the continuity (1.1d) with respect to z from the bottom to the surface yields,

$$\frac{\partial \hat{U}}{\partial x} + u_{-H} \frac{\partial H}{\partial x} + \frac{\partial \hat{V}}{\partial y} + v_{-H} \frac{\partial H}{\partial y} - w_{-H} = 0. \quad (8.14)$$

The water follows the bottom topography,

$$w_{-H} = u_{-H} \frac{\partial H}{\partial x} + v_{-H} \frac{\partial H}{\partial y}. \quad (8.15)$$

Equation (8.14) becomes

$$\frac{\partial \hat{U}}{\partial x} + \frac{\partial \hat{V}}{\partial y} = 0, \quad (8.16)$$

which leads to the definition of the volume transport stream function (Ψ),

$$\hat{U} = -\frac{\partial \Psi}{\partial y}, \quad \hat{V} = \frac{\partial \Psi}{\partial x}. \quad (8.17)$$

Subtracting differentiation of (8.10) with respect to y from the differentiation of (8.9) with respect to x yields

$$\nabla^2 \Psi = \Pi, \quad (8.18)$$

where

$$\begin{aligned} \Pi \equiv & \frac{1}{f} \left[\frac{\partial(fV_{\text{den}})}{\partial x} - \frac{\partial(fU_{\text{den}})}{\partial y} \right] + \frac{1}{f} \left[\frac{\partial(fV_{\text{b}})}{\partial x} - \frac{\partial(fU_{\text{b}})}{\partial y} \right] \\ & - \frac{1}{f} \left[\frac{\partial}{\partial x} \left(\frac{\tau_x}{\rho_0} \right) + \frac{\partial}{\partial x} \left(\frac{\tau_y}{\rho_0} \right) \right] + \frac{A_h}{f} \left(\frac{\partial Q_1}{\partial x} + \frac{\partial Q_2}{\partial y} \right), \end{aligned} \quad (8.19)$$

is the volume transport vorticity. Equation (8.18) is called the Poisson Ψ -equation.

8.3 Volume Transport Vorticity

8.3.1 Extra-Equatorial Region

For extra-equatorial region, the horizontal diffusion can be neglected, (8.19) becomes

$$\begin{aligned} \Pi \equiv & \frac{1}{f} \left[\frac{\partial(fV_{\text{den}})}{\partial x} - \frac{\partial(fU_{\text{den}})}{\partial y} \right] + \frac{1}{f} \left[\frac{\partial(fV_{\text{b}})}{\partial x} - \frac{\partial(fU_{\text{b}})}{\partial y} \right] \\ & - \frac{1}{f} \left[\frac{\partial}{\partial x} \left(\frac{\tau_x}{\rho_0} \right) + \frac{\partial}{\partial x} \left(\frac{\tau_y}{\rho_0} \right) \right]. \end{aligned} \quad (8.20)$$

The volume transport vorticity Π for the extra-equatorial regions can be computed from observational data using (8.21). This is because $(U_{\text{den}}, V_{\text{den}})$ depend on ρ only; (τ_x, τ_y) are wind stress components; and $(U_{\text{b}}, V_{\text{b}})$ are determined by the bottom current velocity (u_{-H}, v_{-H}) . The P-vector inverse method described in Chaps. 5 and 6 is used to determine (u_{-H}, v_{-H}) from hydrographic data.

The calculated volume transport vorticity Π is quite noisy even from climatological data (Fig. 8.1). In this case, the climatological hydrographic data (e.g., GDEM or WOA) are used to compute $(U_{\text{den}}, V_{\text{den}})$ [see (8.8)]. The climatological surface wind stress (τ_x, τ_y) data are obtained from climatological wind data such as the Comprehensive Ocean-Atmosphere Data Set (da Silva et al. 1994). The bottom topography is obtained from the Navy's Digital Bathymetry Data Base 5-minute (DBDB5).

8.3.2 Equatorial Region (between 8°S and 8°N)

In the equatorial region, the Coriolis parameter f is small. The horizontal gradient of the Reynolds stress cannot be neglected and (8.21) cannot be used to determine the function Π . Summation of the differentiation of (8.9) with respect to y and the differentiation of (8.10) with respect to x and the use of (8.18) yield the volume transport vorticity equation,

$$\nabla^2 \Pi = \frac{\beta}{A_h} (\hat{V} - V_{\text{den}} - V_{\text{b}}) - \frac{1}{A_h \rho_0} \left(\frac{\partial \tau_y}{\partial x} - \frac{\partial \tau_x}{\partial y} \right) + \left(\frac{\partial Q_2}{\partial x} - \frac{\partial Q_1}{\partial y} \right). \quad (8.21)$$

For the extra-equatorial regions, $A_h \cong 0$, (8.21) becomes the Sverdrup (1947) relation

$$\beta(\hat{V} - V_{\text{den}} - V_{\text{b}}) = \frac{1}{\rho_0} \left(\frac{\partial \tau_y}{\partial x} - \frac{\partial \tau_x}{\partial y} \right). \quad (8.22)$$

The northern and southern boundary values of Π are computed using (8.20). The volume transport vorticity (8.21) is solved with the boundary values of Π (Fig. 8.2) and the cyclic eastern and western boundary conditions, and the Π -values in the equatorial region between 8°N and 8°S are obtained. Figure 8.3 shows annual, January, and July mean distributions of Π -values for the equatorial region (8°S–8°N). The computed Π -field is quite smooth.

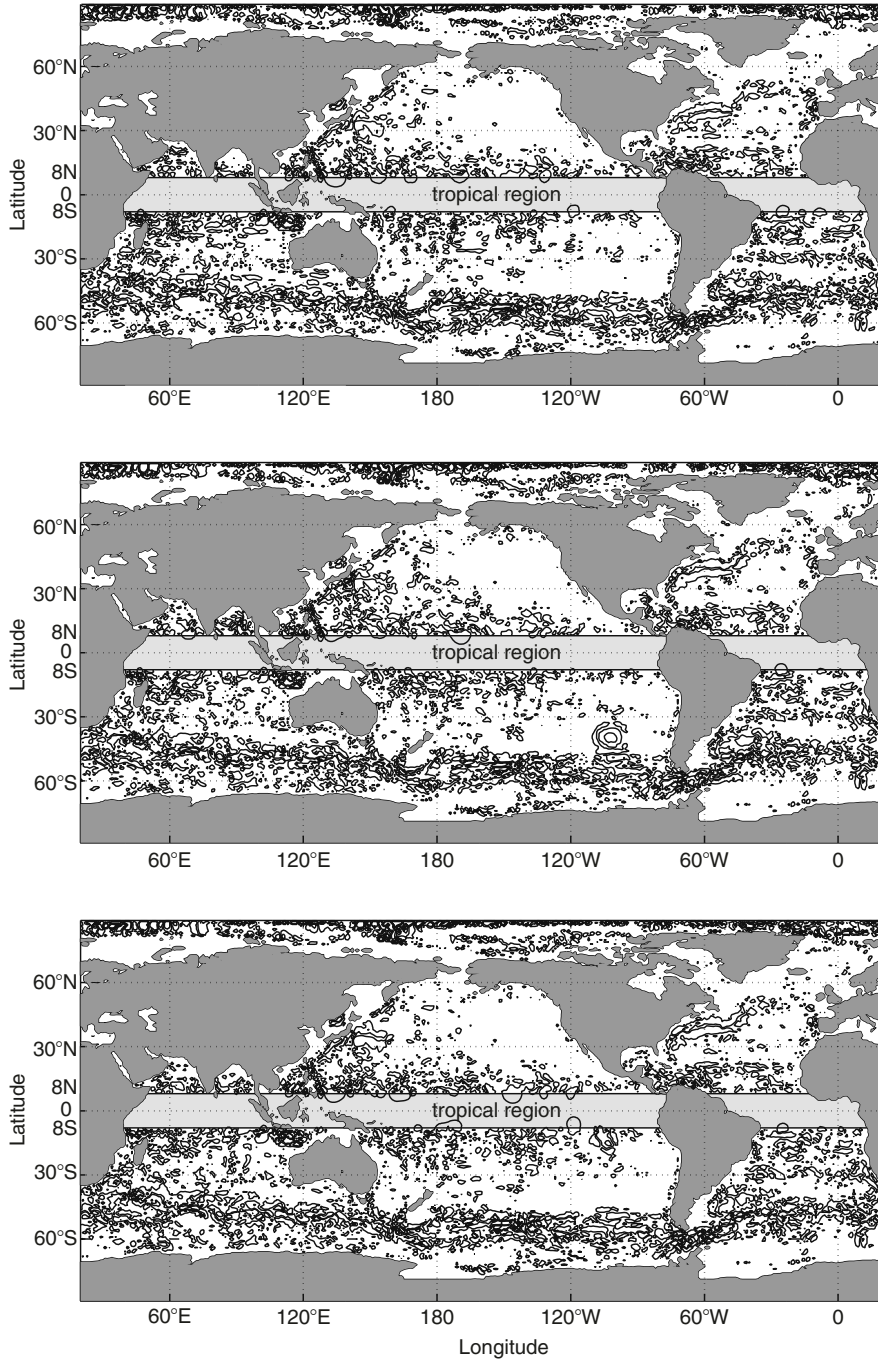


Fig. 8.1. Distributions of Π for the extra-equatorial regions (a) annual mean, (b) January, and (c) July (from Chu and Fan 2006, *Journal of Marine Systems*)

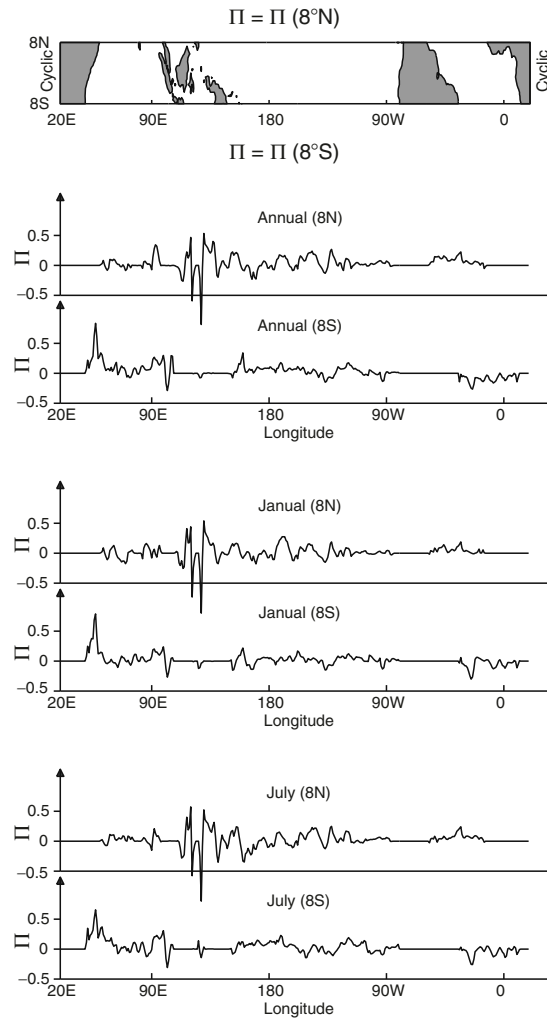


Fig. 8.2. Northern (8°N) and southern (8°S) boundary conditions of Π for the tropical regions (from Chu and Fan 2006, *Journal of Marine Systems*)

8.4 Boundary Conditions for Poisson Ψ -Equation

The computation described in Sect. 8.3 yields the global volume transport vorticity (Π), which is the forcing term of the Poisson Ψ -equation (8.18). In order to solve (8.18), we need boundary conditions. The flow across the Antarctic Continent does not lead to the southern boundary condition

$$\Psi = C_1, \quad \text{at the southern boundary } y = y_s \quad (8.23)$$

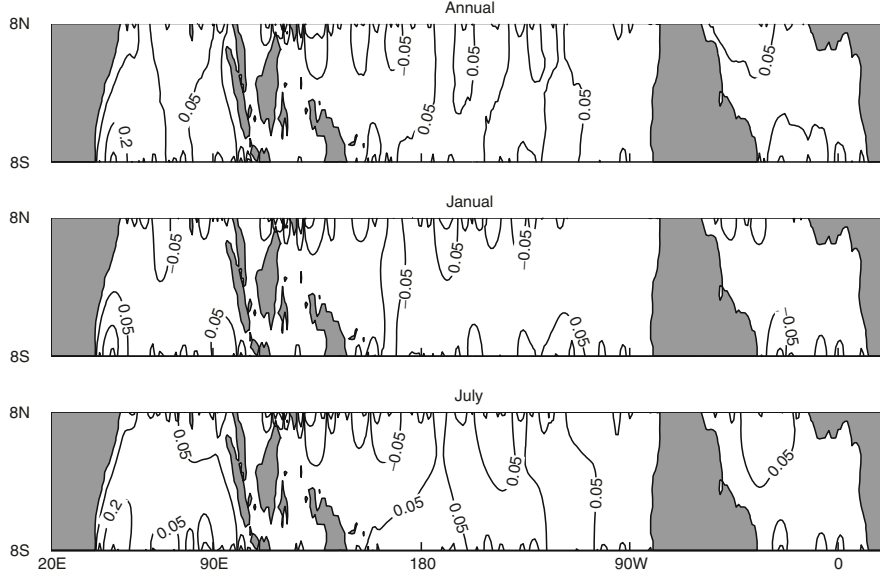


Fig. 8.3. Solutions of the volume transport vorticity (8.21) representing the distributions of Π for the equatorial regions (a) annual mean, (b) January, and (c) July (from Chu and Fan 2006, *Journal of Marine Systems*)

The horizontal convergence of the 2D flow (\hat{U}, \hat{V}) at the North Pole does not lead to the northern boundary condition

$$\Psi = C_2, \quad \text{at the northern boundary } y = y_n, \quad (8.24)$$

where C_1 and C_2 are constants (to be determined). The cyclic boundary condition is applied to the western and the eastern boundaries (Fig. 8.4).

We integrate $\partial\Psi/\partial y = -U^*$ with respect to y along the western (or eastern) boundary from the southern boundary ($\Psi = 0$) to the northern boundary to obtain

$$\Psi|_{\text{west}}(y) = - \int_{y_s}^y U^*(x_{\text{west}}, y') dy'. \quad (8.25)$$

The cyclic boundary condition gives

$$\Psi|_{\text{east}}(y) = \Psi|_{\text{west}}(y) \quad (8.26)$$

8.5 Determination of Ψ -Values at Islands

Before solving the Poisson Ψ -equation (8.18) with the boundary conditions (8.23)–(8.26), the Ψ -values at all islands should be given. These values

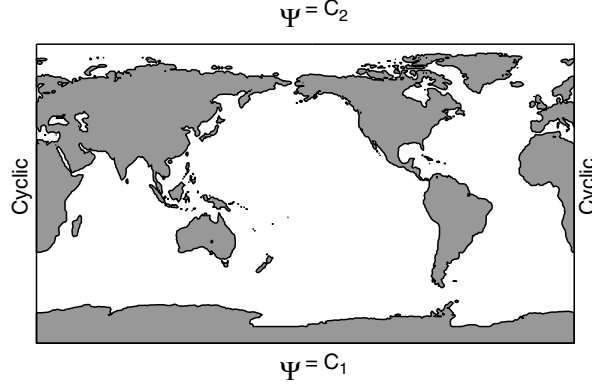


Fig. 8.4. Boundary conditions of Ψ for the global ocean (from Chu and Fan 2006, *Journal of Marine Systems*)

were subjectively set up in earlier studies. For example, in calculating the geostrophic transport in the Pacific Ocean, Reid (1997) set up Ψ -value to be 0 for Antarctic, 135 Sv for Australia, and 130 Sv for America. In calculating the geostrophic transport in the South Atlantic Ocean, Reid (1989) set up Ψ -value to be 0 for Antarctic, 132 Sv for Africa, and 130 Sv for America. Such a treatment subjectively prescribes 130 Sv through the Drake Passage and 132 Sv through the area between Africa and Antarctica. Godfrey (1989) used the Sverdrup model to compute Ψ -values at islands. In this section, a more general method on the basis of the Stokes circulation theorem is presented for determining Ψ -value at islands.

8.5.1 Stokes Theorem

Let the ocean basin be defined as a domain Ω and islands as $\Omega_j (j = 1, \dots, N)$ in (x, y) space with uniform grids $(\Delta x, \Delta y)$ and assume the multiple connection with horizontal boundaries of closed solid-wall segments (i.e., islands) of $\delta\Omega_j, j = 1, \dots, N$. The domain Ω may have open boundaries. Figure 8.5 shows a schematic illustration of such a domain with open boundary segments and islands.

In order to determine the boundary conditions for islands, McWilliams 1977 defined a simply connected fluid region between an island ($\delta\Omega_j$) and a clockwise circuit in the fluid interior ($\delta\omega_j$). Let C_j denote the closed area bounded by $\delta\Omega_j$ and $\delta\omega_j$, and (\mathbf{n}, \mathbf{s}) be the normal (positive outward) and tangential unit vectors along the boundaries of C_j .

The circulation around the boundary of C_j is calculated using the Stokes Theorem,

$$-\oint_{\delta\Omega_j} \hat{\mathbf{V}} \cdot \mathbf{s} dl + \oint_{\delta\omega_j} \hat{\mathbf{V}} \cdot \mathbf{s} dl = \iint_{C_j} \mathbf{k} \cdot (\nabla \times \hat{\mathbf{V}}) dx dy \quad (8.27)$$

where l is the path along the boundary of C_j . The direction of closed integration \oint is defined as anticlockwise. Substituting the volume transport stream function (8.17) into the first term in the left-hand side of (8.27) yields

$$\oint_{\delta\Omega_j} \nabla\Psi \cdot \mathbf{n} \, dl = \oint_{\delta\omega_j} \hat{\mathbf{V}} \cdot \mathbf{s} \, dl - \iint_{C_j} \mathbf{k} \cdot (\nabla \times \hat{\mathbf{V}}) \, dx \, dy, \quad (8.28)$$

and determines the Ψ -value at Island- Ω_j .

The smaller the area of C_j , the smaller the value of the second term in the right-hand side of (8.28), i.e.,

$$\oint_{\delta\Omega_j} \nabla\Psi \cdot \mathbf{n} \, dl \rightarrow \Gamma_j \quad \text{as } C_j \rightarrow 0, \quad (8.29)$$

where

$$\Gamma_j = \oint_{\delta\omega_j} \mathbf{V} \cdot \mathbf{s} \, dl$$

Thus, selection of $\delta\omega_j$ with a minimum C_j becomes a key issue in determining the stream function, $\Psi|_{\Omega_j}$. Such a circuit ($\delta\omega_j^*$) is called the minimum circuit along the island Ω_j (Fig. 8.5). Let (I_l, J_l) ($l = 1, \dots, N + 1$) be the anticlockwise rotating grid points along $\delta\omega_j^*$ with $(I_{N+1}, J_{N+1}) = (I_1, J_1)$, and let the circulation along $\delta\omega_j^*$ be denoted by $\hat{\Gamma}_j$ and computed by

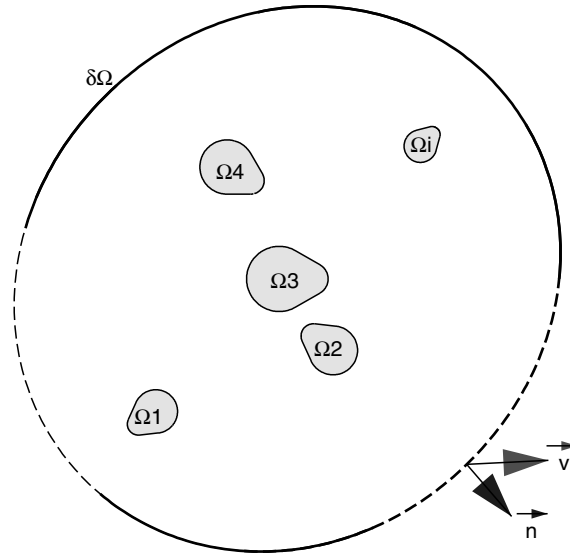


Fig. 8.5. Multiple connected domain. The *arrows* indicate the directions of integration along the line as the integral paths defined in the text (from Chu and Fan 2006, Journal of Marine Systems)

$$\hat{\Gamma}_j = \frac{1}{2} \sum_{l=1}^N [\hat{\mathbf{V}}(I_l, J_l) + \hat{\mathbf{V}}(I_{l+1}, J_{l+1})] \cdot [\mathbf{i}(I_{l+1} - I_l)\Delta x + \mathbf{j}(J_{l+1} - J_l)\Delta y], \quad (8.30)$$

which depends solely on the island geometry and the velocity field ($\hat{\mathbf{V}}$).

8.5.2 Algebraic Equation for Ψ -Value at Island- Ω_j

The left-hand side of (8.29) is discretized by

$$\begin{aligned} \oint_{\delta\Omega_j} \nabla\Psi \cdot \mathbf{n} \, dl &\doteq \sum_{l=1}^N \frac{(I_{l+1} - I_l)\Delta x}{\Delta y} [\Psi(I_l, J_l - 1) + \Psi(I_{l+1}, J_{l+1} - 1) \\ &\quad - \Psi(I_l, J_l + 1) - \Psi(I_{l+1}, J_{l+1} + 1)] + \sum_{l=1}^N \frac{(J_{l+1} - J_l)\Delta y}{\Delta x} \\ &\quad \times [\Psi(I_l + 1, J_l) + \Psi(I_{l+1} + 1, J_{l+1}) \\ &\quad - \Psi(I_l - 1, J_l) - \Psi(I_{l+1} - 1, J_{l+1})]. \end{aligned} \quad (8.31)$$

Since the grid points on the island Ω_j are always on the left side of the anticlockwise circulation $\hat{\Gamma}_j$ (Fig. 8.6), half grid points of (8.31) are in the island and half in the water. Thus, (8.31) can be rewritten by

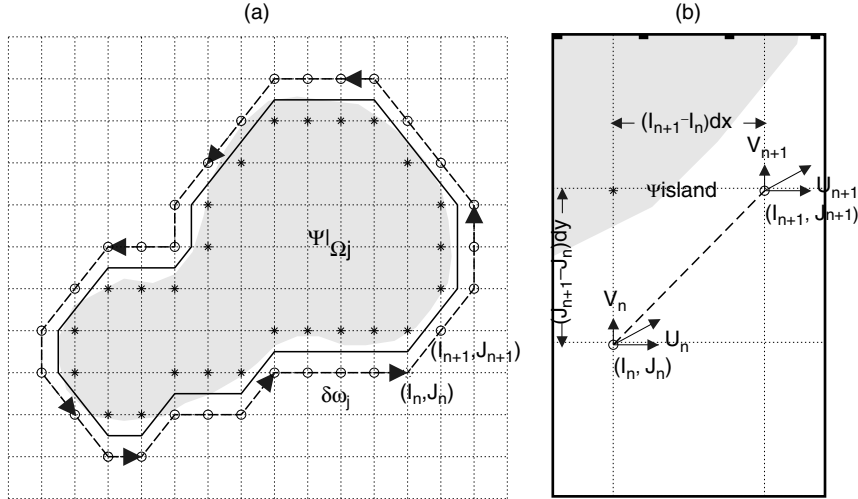


Fig. 8.6. Grid points around the island, Ω_j (from Chu and Fan 2006, Journal of Marine Systems)

$$\hat{\Gamma}_j = A\Psi|_{\Omega_j} + \Gamma_j^{(w)}, \quad (8.32)$$

where $\Gamma_j^{(w)}$ is the circulation in the water and

$$A = -\sum_{l=1}^N \left(\frac{|J_{l+1} - J_l|\Delta y}{2\Delta x} + \frac{|I_{l+1} - I_l|\Delta x}{2\Delta y} \right). \quad (8.33)$$

The volume transport stream function at Island- Ω_j is computed by

$$\Psi|_{\Omega_j} = \frac{\hat{\Gamma}_j - \Gamma_j^{(w)}}{A}. \quad (8.34)$$

8.5.3 Iteration Process

Equation (8.34) cannot be directly used to compute $\Psi|_{\Omega_j}$ even if the vertically integrated velocity (\hat{U}, \hat{V}) is given. This is because that the Ψ -values at surrounding water is still undetermined. Thus, we use an iterative process to determine $\Psi|_{\Omega_j}$ from a first guess value. Suppose all the islands Ω_j ($j = 2, \dots, N$) in Fig. 8.5 has to be removed, with the given boundary conditions at $\delta\Omega_1$, we solve the Poisson Ψ -equation (8.18) and obtain the solution $\Psi^*(x, y)$. The average of Ψ^* over Ω_j leads to the first guess Ψ -values at islands Ω_j ($j = 2, \dots, N$),

$$\Psi|_{\Omega_j}(0) = \iint_{\Omega_j} \Psi^*(x, y) dx dy. \quad (8.35)$$

Let Ψ -values and the circulation $\hat{\Gamma}_j$ be given at the m th iteration such that

$$\Psi|_{\Omega_j}(m) = \frac{\Gamma_j^*(m) - \sum_k B_k \Psi_k(m)}{A}, \quad (8.36)$$

where the minimum circuit circulation at the m th iteration, $\Gamma_j^*(m)$, might not be the same as $\hat{\Gamma}_j$. We update $\Psi|_{\Omega_j}$ using

$$\Psi|_{\Omega_j}(m) = \frac{\Gamma_j^*(m) - \sum_k B_k \Psi_k(m)}{A}. \quad (8.37)$$

Subtracting (7.40) from (7.41) yields

$$\Psi|_{\Omega_j}(m+1) = \Psi|_{\Omega_j}(m) + \frac{\hat{\Gamma}_j - \Gamma_j^*(m)}{A}, \quad (8.38)$$

which indicates the iteration process (a) solving the Poisson Ψ -equation (8.18) with $\Psi|_{\Omega_j}(m)$ to obtain solutions and in turn to get $\Gamma_j^*(m)$, (b) replacing the Ψ -values at islands using (8.38). The iteration process (Fig. 8.7) repeats until it reaches a certain criterion

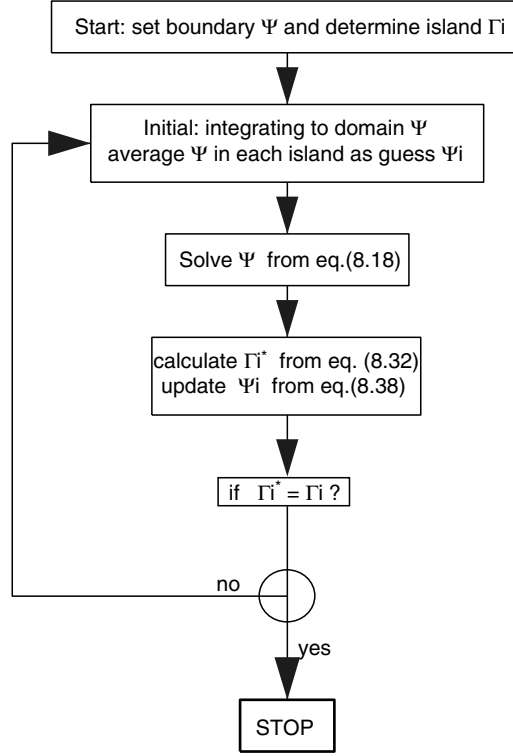


Fig. 8.7. Flow chart, showing the iteration method for determining $\Psi|_{\Omega_j}$

$$\frac{|\delta\mathbf{\Gamma}^*|}{|\hat{\mathbf{\Gamma}}|} \leq \varepsilon, \quad (8.39)$$

where

$$|\hat{\mathbf{\Gamma}}| \equiv \sqrt{\frac{1}{N} \sum_{j=1}^N [\hat{\Gamma}_j]^2}, \quad |\delta\mathbf{\Gamma}^*| \equiv \sqrt{\frac{1}{N} [\Gamma_j^*(m+1) - \Gamma_j^*(m)]^2}, \quad (8.40)$$

and ε is a small positive number (user input), which is set to be 10^{-6} in this study. As soon as the inequality (8.39) is satisfied, the iteration stops and the final set of $\{\Psi|_{\Omega_j}, j = 1, 2, \dots, N\}$ become the optimal Ψ -values for islands.

8.6 Verification of Island Algorithm

8.6.1 A Channel with Two Islands

Consider a channel (length: L , width: W) with a uniform depth and two irregular shaped islands (Fig. 8.8), where a larger one (Island-1) is located in

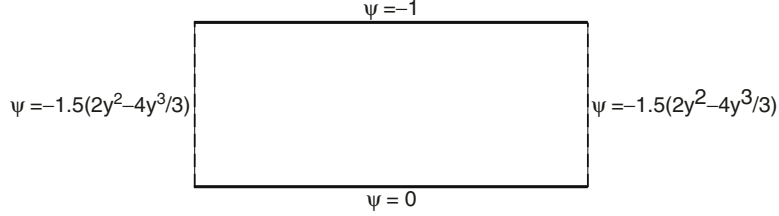


Fig. 8.8. Boundary conditions of the channel flow. Note that y is nondimensional

the middle of the channel, and a smaller one (Island-2) is located southwest of Island-1.

Let x - and y -axes be along the southern and western boundaries with the origin at the southwest corner and be nondimensionalized by W . The northern and southern boundaries of the channel are rigid, and the western and eastern boundaries are cyclic. A nondimensional mathematical model for the test consists of the Poisson equation [see (8.18)]

$$\nabla^2 \Psi = \Pi,$$

with the boundary conditions (Fig. 8.8)

$$\Psi|_{y=0} = 0, \quad \Psi|_{y=1} = -1, \quad \Psi|_{x=0} = \Psi|_{x=L/W} = -1.5 \left(2y^2 - \frac{4}{3}y^3 \right), \quad (8.41)$$

where the mean inflow (outflow) velocity is taken as a unit velocity. We will test if the method has the capability to determine Ψ -values at the islands for a given forcing

$$\Pi = \frac{d^2 \Psi(0)}{dy^2} = -6(1 - 2y). \quad (8.42)$$

8.6.2 Twin Experiments

Twin experiments are designed to test the validity of the method and to get the “exact” Ψ data for the verification. In the first experiment (control run), we integrate the Poisson Ψ -equation (8.18) with (8.41) and with the given Ψ -values at the two islands ($\Psi_1^{(I)}, \Psi_2^{(I)}$), we obtain the solution $\Psi^{(\text{ex})}(x, y)$ as the “exact” data for the evaluation. Here,

$$\Psi_1^{(I)} = (-1, -7/8, -3/4, -1/2, -3/8, -1/4, -1/8, 0) \Psi_2^{(I)} = -0.1. \quad (8.43)$$

The varying $\Psi_1^{(I)}$ changes the flow pattern. As $\Psi_1^{(I)} = -0.5$, the flow is almost symmetric north and south of Island-1. As $\Psi_1^{(I)} = 0$, the flow almost totally passes through between the north boundary and Island-1. As $\Psi_1^{(I)} = -1$, the flow almost totally passes through between the south boundary and Island-1 (Fig. 8.9). Also, the velocity field computed by

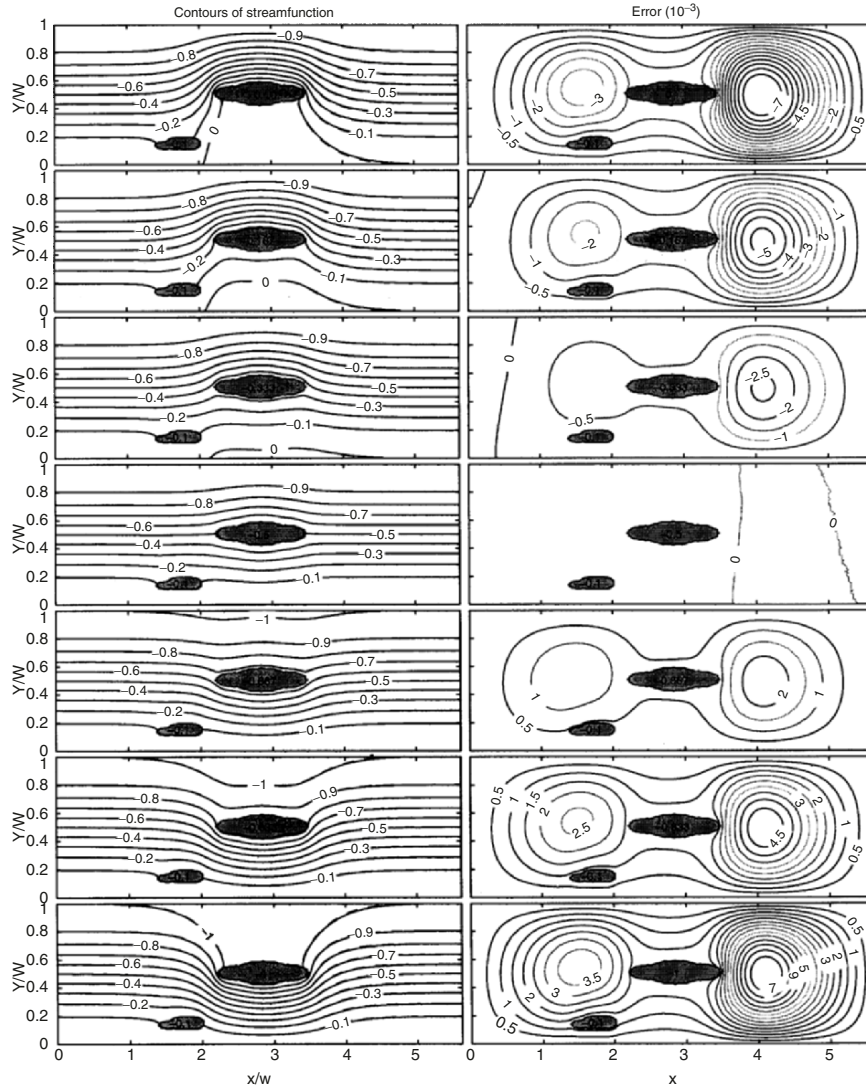


Fig. 8.9. *Left panels:* comparison between $\Psi^{(\text{ex})}(x, y)$ (solid contours) and $\Psi(x, y)$ (dashed contours) for $\Psi_1^{(I)}$ varying from -1 to 0 (keeping Island-1 at the same location) in the control run of the twin experiments. *Right panels:* The corresponding difference, $\Psi^{(\text{ex})}(x, y) - \Psi(x, y)$, for each case

$$\hat{U}^{(\text{ex})} = -\frac{\partial \Psi^{(\text{ex})}}{\partial y}, \quad \hat{V}^{(\text{ex})} = \frac{\partial \Psi^{(\text{ex})}}{\partial x}, \quad (8.44)$$

is used to compute the circulation $\hat{\Gamma}_1$ and $\hat{\Gamma}_2$ around the two islands for the second experiment (sensitivity run).

In the second experiment (sensitivity run), the Ψ -values at the two islands are unknown. We use (8.30) and (8.38) to compute the Ψ -values at the two islands and then to solve the Poisson Ψ -equation (8.18). The evaluation is achieved through the comparison of the two solutions. To test the capability of the scheme, we perform several sensitivity studies by varying the location and $\Psi_1^{(I)}$ -value for Island-1 and keeping them the same for Island-2, i.e., $\Psi_2^{(I)} = -0.1$.

8.6.3 Sensitivity to $\Psi_1^{(I)}$ -Value

Island-1 is kept as the same location and the $\Psi_1^{(I)}$ -value is varied [see (8.43)]. The “exact” solutions $\Psi^{(\text{ex})}(x, y)$ for seven different $\Psi_1^{(I)}$ -values are the solid contours in the left panels of Fig. 8.9. The corresponding solution, $\Psi(x, y)$, for the second experiment is represented by the dashed contours (Fig. 8.9). The difference between the two experiments (control minus sensitivity run), as illustrated in the right panels of Fig. 8.9, reveals a dual cyclonic-eddy (anticyclonic-eddy) structure in the leeward side and upwind side, respectively, when the $\Psi_1^{(I)}$ -value is larger (smaller) than -0.5 . The leeward eddy (i.e., the error) is twice as strong as the upwind eddy. Its absolute values reach a maximum around 0.007 (leeward) as $\Psi_1^{(I)} = 0, -1$. The errors decrease (increase) with $\Psi_1^{(I)}$ -value from 0 to -0.5 (from -0.5 to -1). When $\Psi_1^{(I)} = -0.5$, we have a minimum difference between the two experiments.

In the sensitivity run, using the method, the computed stream function at the two islands (Ψ_1, Ψ_2) might not be the same as $(\Psi_1^{(I)}, \Psi_2^{(I)})$, and the solution of (8.18), $\Psi(x, y)$, might not be the same as $\Psi^{(\text{ex})}(x, y)$. We calculate the relative root mean square error (rrmse) between $\Psi(x, y)$ and $\Psi^{(\text{ex})}(x, y)$

$$\text{rrmse} = \frac{\sqrt{\sum_i \sum_j [\Psi^{(\text{ex})}(x_i, y_j) - \Psi(x_i, y_j)]^2}}{\sum_i \sum_j [\Psi^{(\text{ex})}(x_i, y_j)]^2}, \quad (8.45)$$

for the whole channel and the relative errors

$$E_1 = \frac{|\Psi_1^{(I)} - \Psi_1|}{|\Psi_1^{(I)}|}, \quad E_2 = \frac{|\Psi_2^{(I)} - \Psi_2|}{|\Psi_2^{(I)}|}, \quad (8.46)$$

for the two islands.

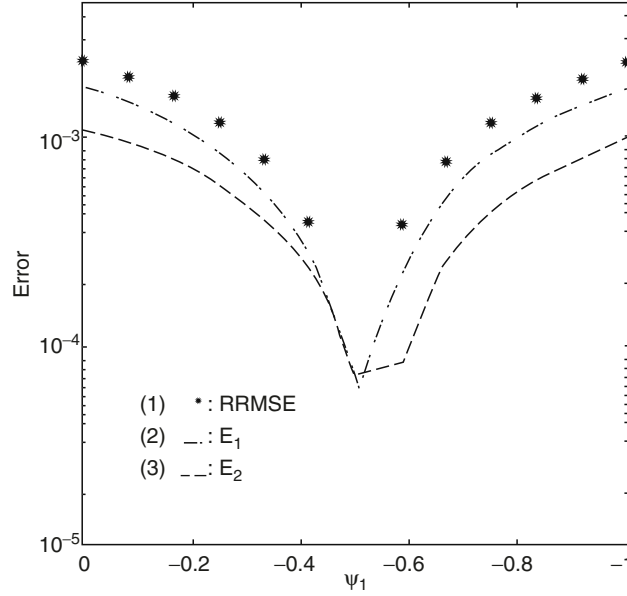


Fig. 8.10. Dependence of rrmse between $\Psi(x, y)$ and $\Psi^{(\text{ex})}(x, y)$ over the whole channel (denoted by *asterisk*), and the relative errors E_1 (*dash-dotted*) and E_2 (*dashed*) on varying $\Psi_1^{(1)}$ -values

Figure 8.10 shows the dependence of rrmse , E_1 , and E_2 on $\Psi_1^{(1)}$. The three relative errors have the following features (a) they are lesser than 1% with the maximum relative errors,

$$\max(\text{rrmse}, E_1, E_2) = (5.7, 2.0, 1.2) \times 10^{-3}; \quad (8.47)$$

(b) Minimum relative errors occur when the volume transport is relatively symmetric to Island-1 $\Psi_1^{(1)} = -0.5$,

$$\min(\text{rrmse}, E_1, E_2) = (0.92, 0.61, 0.72) \times 10^{-4}; \quad (8.48)$$

(c) The three relative errors have a similar dependence on $\Psi_1^{(1)}$. They all decrease with $\Psi_1^{(1)}$ monotonically from the maximum errors $[(5.7, 2.0, 1.2) \times 10^{-3}]$ at $\Psi_1^{(1)} = -1$ (flow mostly south of Island-1) to the minimum errors $[(0.92, 0.61, 0.72) \times 10^{-4}]$ at $\Psi_1^{(1)} = -0.5$ (flow relatively symmetric north and south of Island-1); and then increase with $\Psi_1^{(1)}$ monotonically to the maximum errors at $\Psi_1^{(1)} = 0$ (flow mostly north of Island-1).

8.6.4 Sensitivity to Location of Island-1

The $\Psi_1^{(1)}$ -value (-0.5) is kept unchanged and its location (in the y -direction) is varied. The solutions $\Psi^{(\text{ex})}(x, y)$ for seven different locations are shown as the

solid contours in the left panels of Fig. 8.11. The corresponding results for the second experiment are shown as the dashed contours. The difference between the two experiments (first minus second experiment), as illustrated in the right panels of Fig. 8.11, reveals an elliptic anticyclonic-eddy structure with the maximum value of 0.01 (maximum error). As Island-1 “moves” northward, the “anticyclone” weakens and splits into two smaller “anticyclones” with the leeward one being stronger than the other. When Island-1 “moves” to the center of the channel, the errors become very small. As Island-1 continues to “move” northward, a cyclonic-eddy first occurs at the leeward side of Island-1, expands toward the west, and reveals an elliptic cyclonic-eddy structure with the maximum error of 0.011.

In the second experiment, the computed stream function at the two islands (Ψ_1, Ψ_2) using this method is usually not be exactly the same as $(\Psi_1^{(I)}, \Psi_2^{(I)})$, and the solution $\Psi(x, y)$ might not be exactly the same as $\Psi^{(\text{ex})}(x, y)$. Figure 8.12 shows the dependence of rmse , E_1 , and E_2 on the location of Island-1. The three relative errors have the following features (a) they are lesser than 1% with the maximum relative errors

$$\max(\text{rmse}, E_1, E_2) = (3.7, 3.2, 1.9) \times 10^{-3}; \quad (8.49)$$

and (b) the three relative errors have a similar dependence on the location of Island-1. They all decrease with northward “displacing” Island-1 monotonically from the maximum errors [(3.7, 3.2, 1.9)] when Island-1 is located near the southern boundary (first on the left panels) to the minimum errors [(0.92, 0.61, 0.72) $\times 10^{-4}$] when Island-1 is located near the middle of the channel; and then increase with northward “displacing” Island-1 monotonically to the maximum errors [(6.7, 3.2, 2.0) $\times 10^{-3}$] when Island-1 is located near the northern boundary.

8.6.5 Sensitivity to Noise

In reality, the velocity data contain errors. In order to test if the noisy data destroy the solution, or in other words, to test the model capability in handling the noisy data, we use a random number generator to produce a white noise ($U_{\text{noise}}, V_{\text{noise}}$) with different noise levels (0.00417–0.05) for each grid pointing independently and adding it to the “exact” velocity,

$$\tilde{U} = \hat{U}^{(\text{ex})} + U_{\text{noise}}, \quad \tilde{V} = \hat{V}^{(\text{ex})} + V_{\text{noise}}, \quad (8.50)$$

which is used to calculate $(\hat{\Gamma}_1, \hat{\Gamma}_2)$ around the two islands for the second experiment.

The “exact” solution $\Psi^{(\text{ex})}(x, y)$ is obtained for

$$\Psi_1^{(I)} = -0.5, \quad \Psi_2^{(I)} = -0.1, \quad (8.51)$$

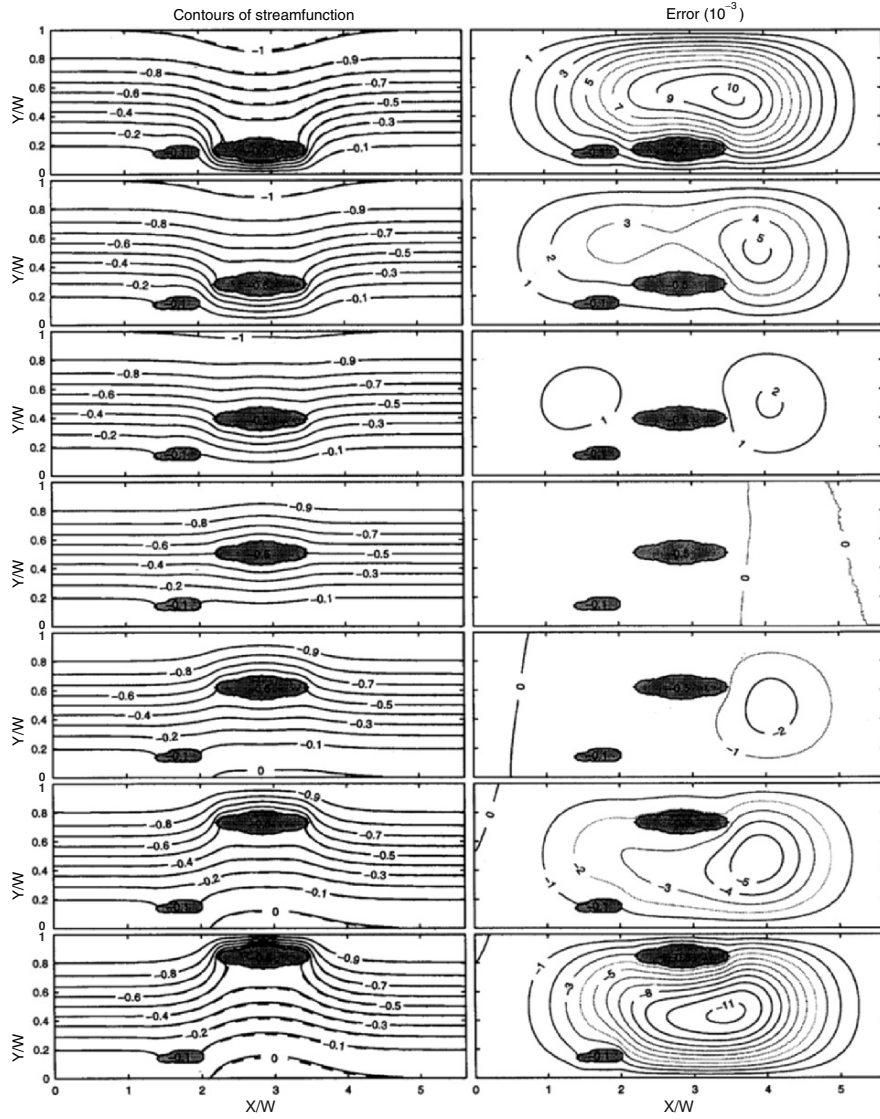


Fig. 8.11. Left panels: Comparison between $\Psi^{(ex)}(x,y)$ (solid contours) and $\Psi(x,y)$ (dashed contours) for varying location of Island-1 (keeping $\Psi_1^{(1)} = -0.5$) in the control run of the twin experiments. Right panels: The corresponding difference, $\Psi^{(ex)}(x,y) - \Psi(x,y)$, for each case

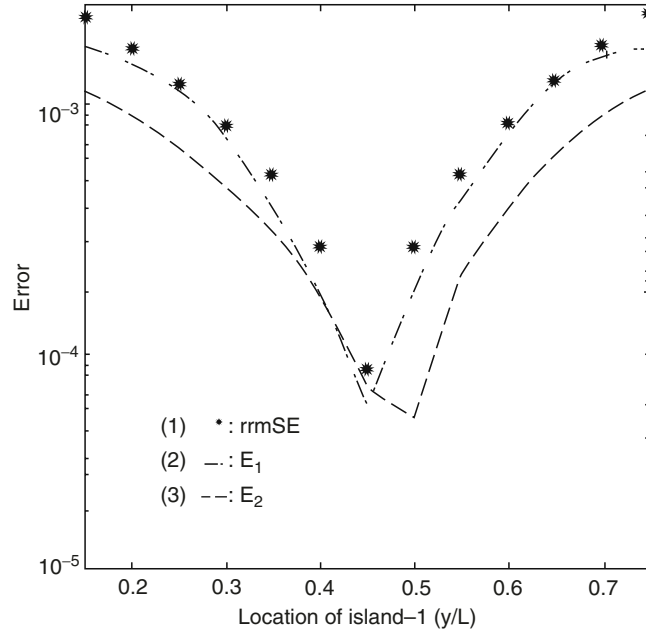


Fig. 8.12. Dependence of rrmse between $\Psi(x, y)$ and $\Psi^{(\text{ex})}(x, y)$ over the whole channel (denoted by *asterisk*), and the relative errors E_1 (*dash-dotted*) and E_2 (*dashed*) on varying location of Island-1

and Island-1 located at the middle of the channel for the first experiment (shown in middle panels of Fig. 8.11). This “exact” solution has the minimum root mean square error in the twin experiments.

The solution $\Psi^{(\text{ex})}(x, y)$ is also shown as the solid contours in Fig. 8.13. The corresponding results for the second experiment are shown as the dashed contours. As the noise level increases, the solution from the second experiment becomes noisy, but the flow pattern is quite stable. Figure 8.14 shows the rrmse between $\Psi(x, y)$ and $\Psi^{(\text{ex})}(x, y)$ for the whole channel and the errors E_1 and E_2 for different noise levels. Generally, the rrmse increases with the noise level from 1.6×10^{-3} (at the noise level of 0.0125) to 0.01 (at the noise level of 0.05). For the noise level of 0.05, the errors E_1 and E_2 are 0.053 and 0.02, respectively. This indicates that the use of this method to estimate the Ψ -values for islands will bring the error similar to (0.05 for Island-1’s stream function) and less than (0.02 for Island-2’s stream function) the noise level.

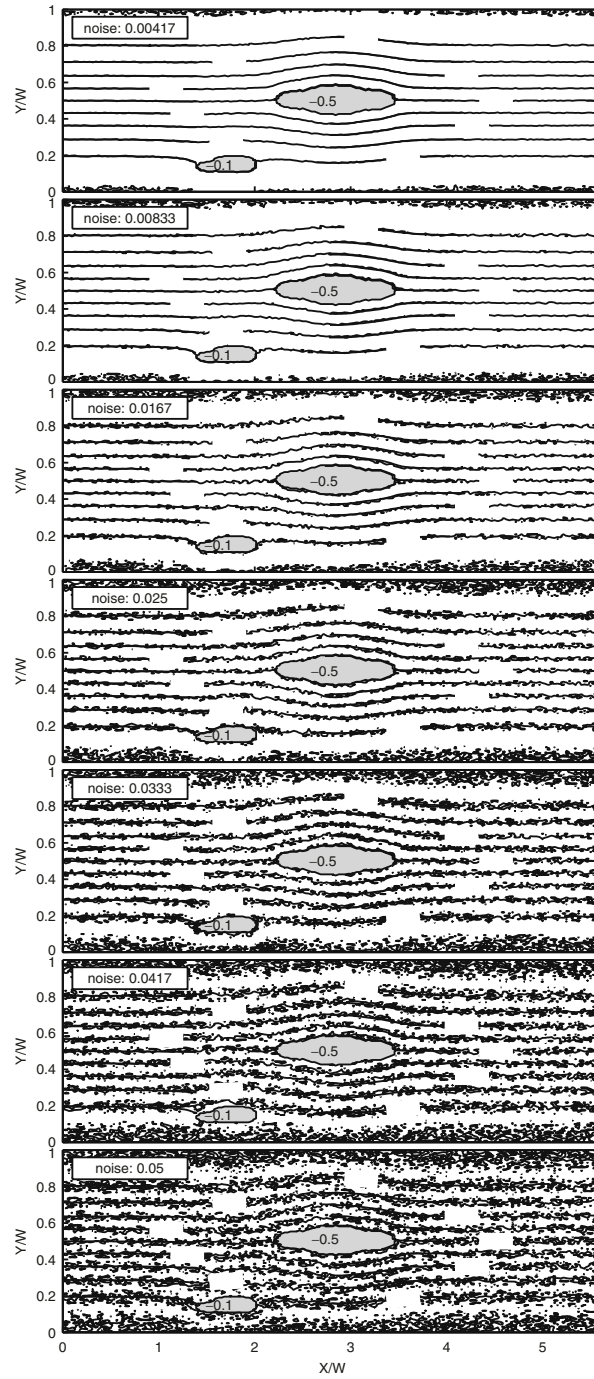


Fig. 8.13. Comparison between $\Psi^{(ex)}(x, y)$ (solid contours) and $\Psi(x, y)$ (dashed contours) for various noise levels from 0.00417 to 0.05

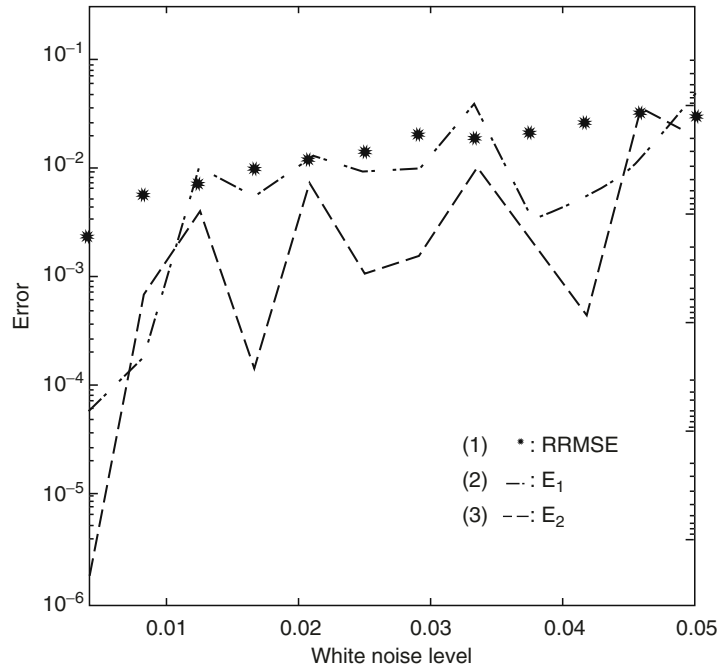


Fig. 8.14. Dependence of rrmse between $\Psi(x, y)$ and $\Psi^{(\text{ex})}(x, y)$ over the whole channel (denoted by *asterisk*), and the relative errors E_1 (*dash-dotted*) and E_2 (*dashed*) on varying noise levels

8.7 Global Volume Transport Stream Function

8.7.1 Ψ -Values for Global Islands

The iteration method developed in Sect. 8.5 is used to determine Ψ -values at islands. Figure 8.15 shows the distribution of Ψ -values for each continent/island computed from the annual, January, and July mean hydrographic and wind data. Taking the annual mean as an example, we have: 0 Sv for the American Continent, 157.30 Sv for Antarctica, -21.74 Sv for Australia, -27.17 Sv for Madagascar, and -21.74 Sv for New Guinea.

8.7.2 Ψ -Values for Global Oceans

With the given values at the boundaries and islands, the Poisson Ψ -equation (8.18) is solved with the climatological annual and monthly Π -fields and obtain annual and monthly global Ψ -fields. After that, we use (8.17) to recompute the depth-integrated velocity (\hat{U}, \hat{V}) . Since the NOAA WOA $1^\circ \times 1^\circ$ hydrographic (Levitus and Boyer 1994; Levitus et al. 1994) and wind data (da Silva et al. 1994) are used to compute Ψ -fields, small-scale topographic features

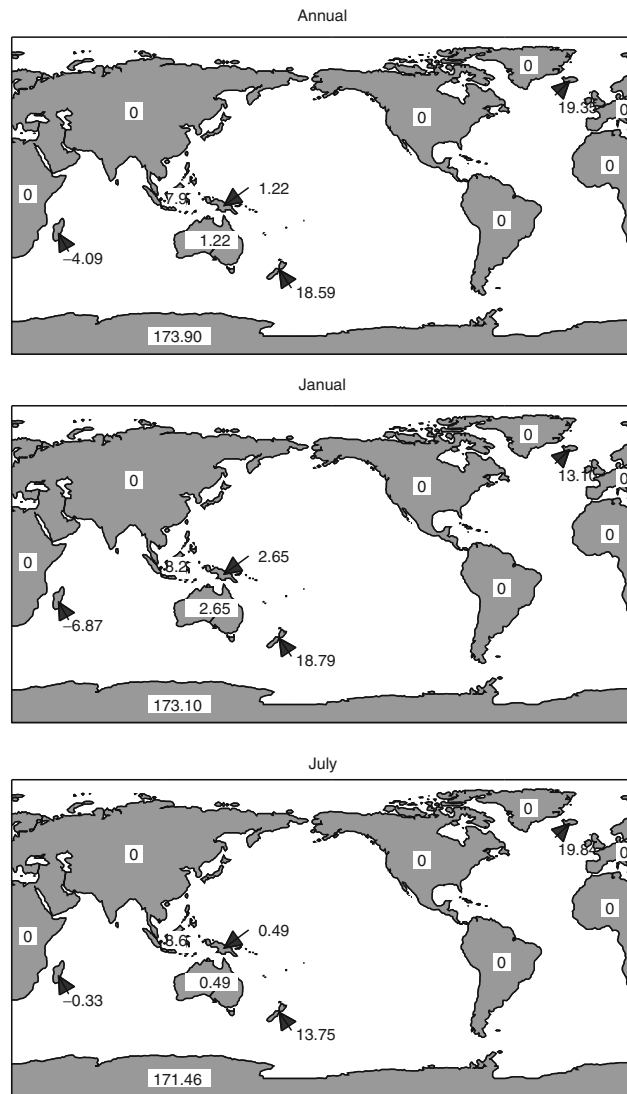


Fig. 8.15. Computed Ψ -values for each continent/island (a) annual mean, (b) January, and (c) July (from Chu and Fan 2006, *Journal of Marine Systems*)

such as English Channel, Taiwan Strait, Gibraltar Strait, and Bering Strait cannot be resolved. The global Ψ -field (Fig. 8.16) and depth-integrated velocity vector (\hat{U}, \hat{V}) field (Fig. 8.17) agree reasonably well with earlier studies (e.g., Reid 1989, 1994, 1997; Semtner and Chervin 1992) and show the capability of the P-vector method for determining main characteristics of global

circulation, such as the strong Antarctic Circumpolar Current, the well-defined subtropical and subpolar gyres, and the equatorial current system.

8.8 Sensitivity to Observational Errors

Usually, errors occur in hydrographic and wind data (observational errors) and in model discretization (i.e., computational errors). Sensitivity study is conducted on the solutions to the observational data errors before discussing the calculated circulation characteristics. Suppose the observational data errors have to be represented by a Gaussian-type random variable with a zero mean and a standard deviation of σ , then a random number generator (FORTRAN function, Ranf) is used to produce two sets of random noises for each grid point independently, with mean value of zero and standard deviation of σ (1) three-dimensional temperature error field with standard deviation of 0.2°C and (2) two-dimensional surface wind stress error field with standard deviation of 0.05 N m^{-2} .

Stability of the inverse model is confirmed through the comparison between the annual mean Ψ -field with random errors in temperature data and surface wind stress data (Fig. 8.18b) and with the Ψ -field having no error added (Fig. 8.16). The inverse model has the capability to filter out noise in the forcing terms because of the major mathematical procedures of the model containing two integrations of the Poisson equation.

Questions and Exercises

- (1) Derive the equations for the depth-integrated horizontal velocity

$$-f(\hat{V} - V) = A_z \left. \frac{\partial \hat{u}}{\partial z} \right|_{z=\eta} - A_z \left. \frac{\partial \hat{u}}{\partial z} \right|_{z=-H} + A_h \nabla_2^2 \hat{U} - 2A_h \nabla_2 u_{-H} \cdot \nabla_2 H - A_h u_{-H} \nabla_2^2 H, \quad (\text{E8.1})$$

$$f(\hat{U} - U) = A_z \left. \frac{\partial \hat{v}}{\partial z} \right|_{z=\eta} - A_z \left. \frac{\partial \hat{v}}{\partial z} \right|_{z=-H} + A_h \nabla_2^2 \hat{V} - 2A_h \nabla_2 v_{-H} \cdot \nabla_2 H - A_h v_{-H} \nabla_2^2 H, \quad (\text{E8.2})$$

from the basic (1.1a)–(1.1d).

- (2) Discuss the physical significance of each term of the interim depth-integrated flow (U^* , V^*),

$$U^* = U_{\text{den}} + U_{\text{b}} + \frac{\tau_y}{f\rho_0}, \quad (\text{E8.3})$$

$$V^* = V_{\text{den}} + V_{\text{b}} - \frac{\tau_x}{f\rho_0}. \quad (\text{E8.4})$$

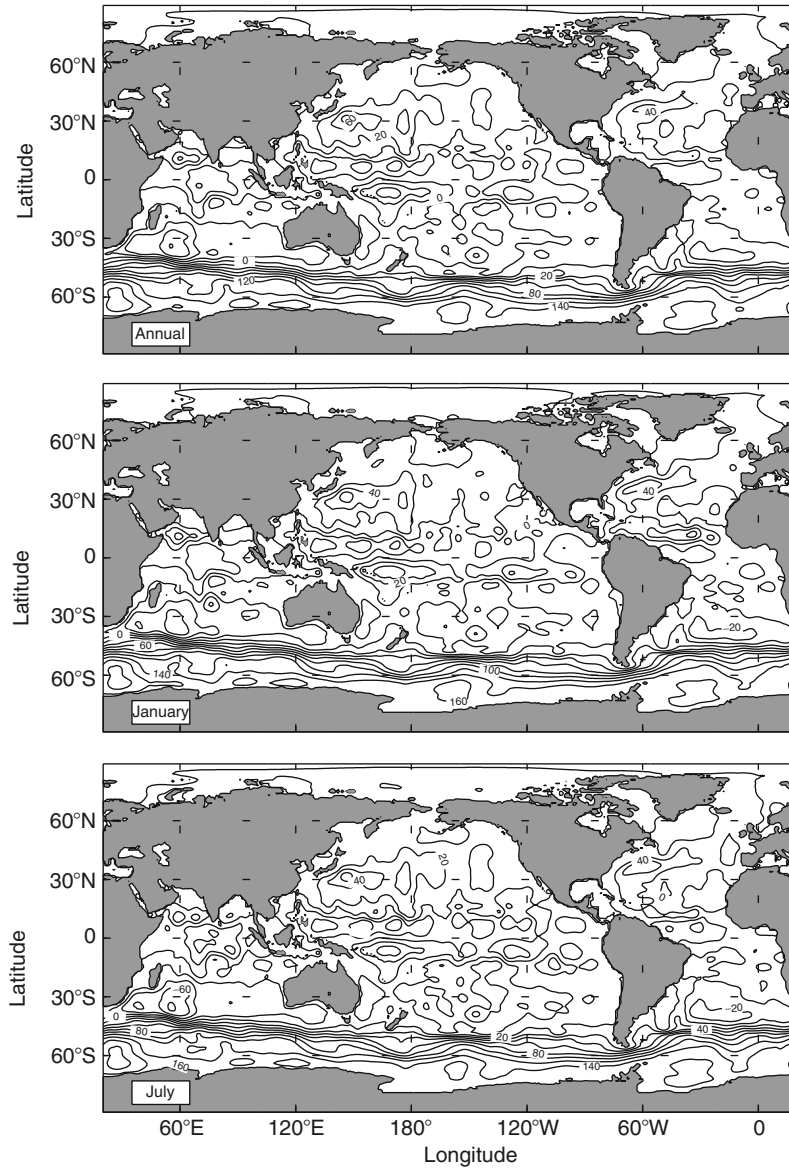


Fig. 8.16. Computed global volume transport stream function (Ψ) (a) annual mean, (b) January, and (c) July (from Chu and Fan 2006, *Journal of Marine Systems*)

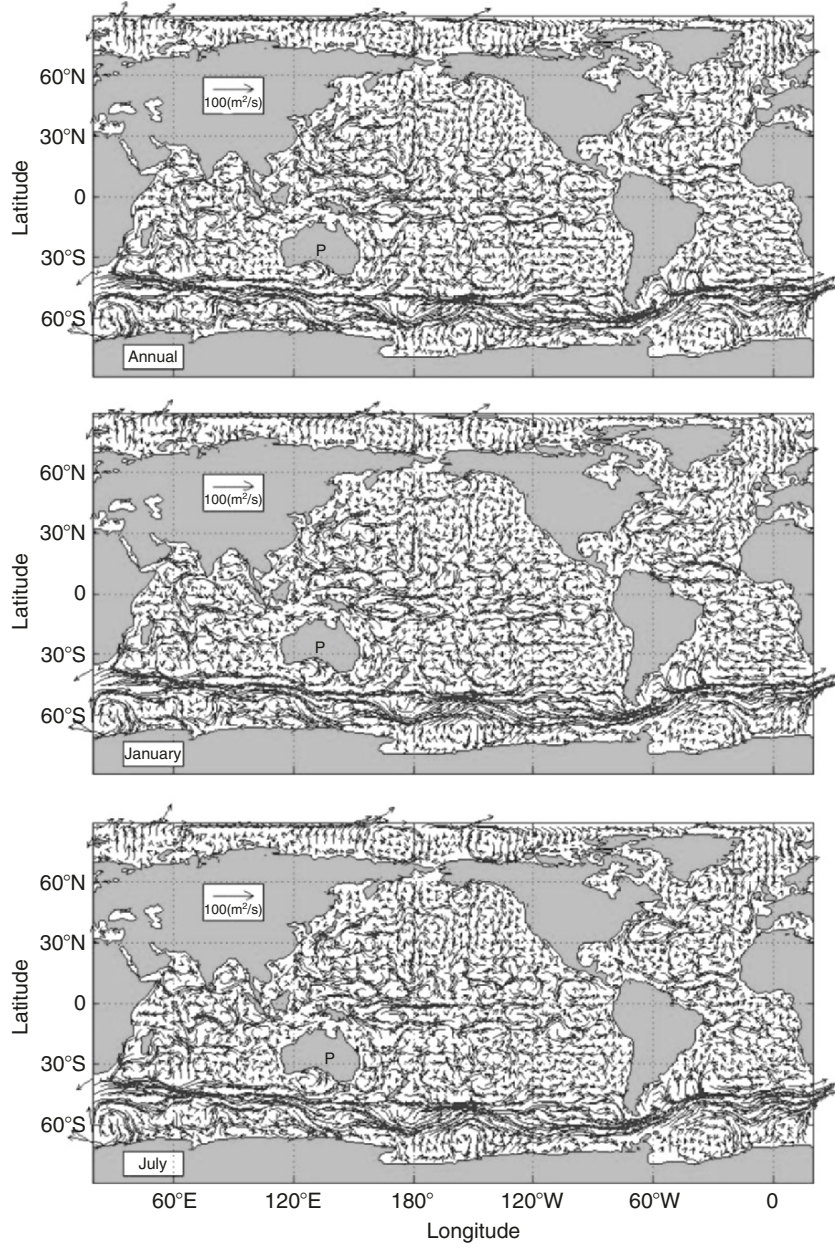


Fig. 8.17. Computed global depth-integrated velocity (U, V) vectors (a) annual mean, (b) January, and (c) July (from Chu and Fan 2006, *Journal of Marine Systems*)

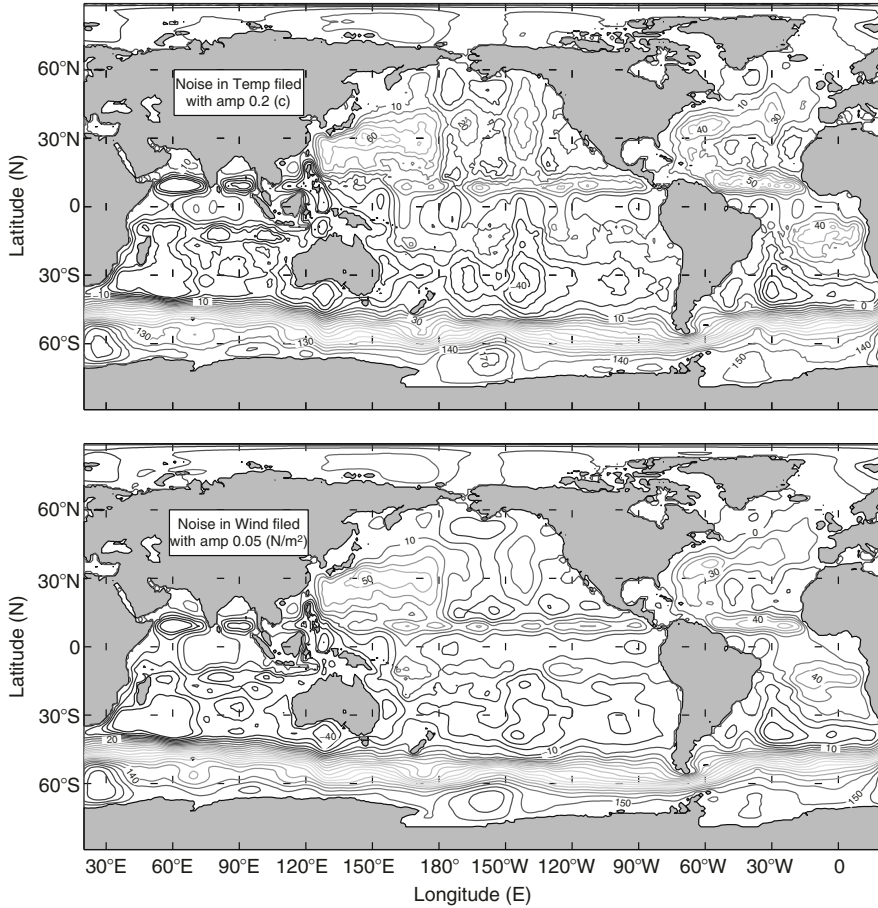


Fig. 8.18. Annual mean global volume transport stream function (Ψ) computed using the P-vector method with (a) three-dimensional Gaussian-type temperature errors (0-mean, 0.2°C -standard deviation) and (b) two-dimensional Gaussian-type surface wind stress errors (0-mean, 0.02 N m^{-2} -standard deviation). The stochastic errors are introduced into all the grid points by random number generator

(3) Discuss the similarity and dissimilarity of the following equation

$$\nabla^2\Pi = \frac{\beta}{A_h}(\hat{V} - V_{\text{den}} - V_b) - \frac{1}{A_h\rho_0} \left(\frac{\partial\tau_y}{\partial x} - \frac{\partial\tau_x}{\partial y} \right) + \left(\frac{\partial Q_2}{\partial x} - \frac{\partial Q_1}{\partial y} \right), \tag{E8.5}$$

and the Munk equation.

(4) For a domain Ω with islands as $\Omega_j (j = 1, \dots, N)$ shown in Fig. 8.5, prove that the volume transport stream function at Island- Ω_j can be computed approximately by

$$\Psi|_{\Omega_j} = \frac{\hat{\Gamma}_j - \Gamma_j^{(w)}}{A}, \quad (\text{E8.6})$$

where $\Gamma_j^{(w)}$ is the circulation in the water and

$$A = - \sum_{l=1}^N \left(\frac{|J_{l+1} - J_l| \Delta y}{2\Delta x} + \frac{|I_{l+1} - I_l| \Delta x}{2\Delta y} \right),$$

$$\hat{\Gamma}_{j_j} = \frac{1}{2} \sum_{l=1}^N [\hat{\mathbf{V}}(I_l, J_l) + \hat{\mathbf{V}}(I_{l+1}, J_{l+1})]$$

$$\cdot [\mathbf{i}(I_{l+1} - I_l)\Delta x + \mathbf{j}(J_{l+1} - J_l)\Delta y].$$

- (5) Search the literature and compare the Ψ -values of global islands identified using the Stokes Theorem and other methods.
- (6) What are the major characteristics of the global circulation identified from the global volume transport stream function (Fig. 8.16) and depth-integrated horizontal velocity (Fig. 8.17)?
- (7) Are the effects of noises in the temperature and wind observations large on the calculated annual mean global volume transport stream function form in comparison between Fig. 8.18 and Fig. 8.16a? Justify your answer.

C-Vector for Identifying Oceanic Secondary Circulations

Secondary circulation, referring to the motion, relative to a basic flow (geostrophic and hydrostatic balanced), occurs often in the ocean such as deep convection and circulations driven by fronts and eddies. It affects the general circulation and the mass, heat, salt, and energy balance. The oceanic secondary circulation is difficult to measure directly, but is easy to be identified by pseudovorticity using the C-vector method from routine temperature and salinity observations.

9.1 C-Vector

The thermal wind relation (1.3) can be rewritten by

$$f \frac{\partial u}{\partial z} = -\frac{\partial b}{\partial y}, \quad f \frac{\partial v}{\partial z} = \frac{\partial b}{\partial x}, \quad b = -g \frac{(\rho - \rho_0)}{\rho_0}, \quad (9.1)$$

where the variable b is usually called the buoyancy. The total flow, $\hat{\mathbf{V}} = (u, v, w)$, is decomposed into geostrophic (\mathbf{V}) and ageostrophic (\mathbf{V}_{ag}) velocities,

$$\hat{\mathbf{V}} = \mathbf{V} + \mathbf{V}_{\text{ag}}.$$

If the advection of momentum and buoyancy is dominated by the geostrophic advection (i.e., quasigeostrophic system),

$$\hat{\mathbf{V}} \cdot \nabla \hat{\mathbf{V}} \approx \mathbf{V} \cdot \nabla \mathbf{V}, \quad \hat{\mathbf{V}} \cdot \nabla b = \mathbf{V} \cdot \nabla b, \quad (9.2)$$

then the ageostrophic velocity is determined by Bannon and Chu (1988)

$$-fv_{\text{ag}} = \frac{1}{\rho_0} \frac{\partial X}{\partial z} - \left(\frac{\partial}{\partial t} + \mathbf{V} \cdot \nabla \right) u, \quad (9.3)$$

$$fu_{\text{ag}} = \frac{1}{\rho_0} \frac{\partial Y}{\partial z} - \left(\frac{\partial}{\partial t} + \mathbf{V} \cdot \nabla \right) v, \quad (9.4)$$

$$N^2 w_{\text{ag}} = \frac{\partial B}{\partial z} - \left(\frac{\partial}{\partial t} + \mathbf{V} \cdot \nabla \right) b, \quad (9.5)$$

where (X, Y) and B are the vertical turbulent momentum and buoyancy fluxes (downward positive), and N is the Brunt–Vaisala frequency.

Cross derivatives among (9.3)–(9.5) lead to the definition of pseudovorticity (Xu 1992; Chu 2002),

$$\frac{\partial}{\partial y}(N^2 w_{\text{ag}}) - \frac{\partial}{\partial z}(f^2 v_{\text{ag}}) = 2f^3 C_x, \quad (9.6a)$$

$$\frac{\partial}{\partial z}(f^2 u_{\text{ag}}) - \frac{\partial}{\partial x}(N^2 w_{\text{ag}}) = 2f^3 C_y, \quad (9.6b)$$

$$\frac{\partial}{\partial x}(f^2 v_{\text{ag}}) - \frac{\partial}{\partial y}(f^2 u_{\text{ag}}) = 2f^3 C_z, \quad (9.6c)$$

where

$$C_x = -\frac{1}{f^2} \frac{\partial(u, v)}{\partial(y, z)} + \frac{1}{2f^3} \frac{\partial}{\partial z} \left(f \frac{\partial X}{\partial z} + \frac{\partial B}{\partial y} \right), \quad (9.7a)$$

$$C_y = -\frac{1}{f^2} \frac{\partial(u, v)}{\partial(z, x)} + \frac{1}{2f^3} \frac{\partial}{\partial z} \left(f \frac{\partial Y}{\partial z} - \frac{\partial B}{\partial x} \right), \quad (9.7b)$$

$$C_z = -\frac{1}{f^2} \frac{\partial(u, v)}{\partial(x, y)} - \frac{1}{2f^2} \frac{\partial}{\partial z} \left(\frac{\partial X}{\partial x} + \frac{\partial Y}{\partial y} \right) - \frac{\beta}{2f^3} \frac{\partial Y}{\partial z}, \quad (9.7c)$$

are (nondimensional) components of vector \mathbf{c} . Thus, the pseudovorticity of the secondary circulation is determined by three forcing factors (a) geostrophic forcing (i.e., distinct water masses across the front), $-f\partial(u, v)/\partial(y, z)$, $-f\partial(u, v)/\partial(z, x)$, and $-f\partial(u, v)/\partial(x, y)$, (b) turbulent momentum flux (X, Y) , and (c) buoyancy flux (B) . In the upper ocean, the last two factors are mainly caused by the surface wind stress and buoyancy flux. As pointed by Xu (1992), the C-vector is the ageostrophic vortex line (Fig. 9.1) whose horizontal components (C_x, C_y) represent the secondary circulation in vertical cross section.

Observations generally show a well-mixed upper ocean by turbulent motion. The transition between the turbulent mixed layer and the stratified water below is a thin entrainment zone with large gradients of density and

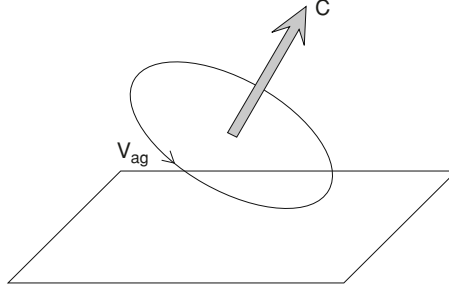


Fig. 9.1. C-vector and the secondary circulation (from Chu 2002, Geophysical Research Letters)

velocity. All turbulent fluxes are usually assumed to vanish below the ocean mixed layer. The mixed layer depth h_1 is defined as the depth above which temperature, salinity, or velocity (geostrophic plus ageostrophic) is vertically uniform to certain critical value. The vertical uniformity leads to the bulk model parameterization (e.g., Price et al. 1986; Chu et al. 1990; Chu and Garwood 1990, 1991) of turbulent fluxes (X, Y, B) ,

$$(X, Y) = (\tau_x, \tau_y) + \left[(\tau_x, \tau_y) - (X, Y)_{-h} \frac{z}{h_1} \right],$$

$$B = B_0 + (B_0 - B_{-h}) \frac{z}{h_1}, \quad \text{for } z > -h_1, \quad (9.8a)$$

$$(X, Y, B) \simeq 0, \quad \text{for } z < -h_1 \quad (9.8b)$$

where (τ_x, τ_y) is the surface wind stress and B_0 is the surface buoyancy flux. $(X, Y)_{-h}$ and B_{-h} are turbulent fluxes at the base of the mixed layer, which are computed from the surface fluxes.

From (9.8a) and (9.8b) we obtain

$$\frac{\partial^2 X}{\partial z^2} = 0, \quad \frac{\partial^2 Y}{\partial z^2} = 0, \quad (9.9)$$

for the whole water column. On computing the horizontal components of the C-vector (C_x, C_y) , the turbulent momentum flux can be neglected for the whole water column, and the turbulent buoyancy flux can be neglected for the water column below the surface mixed layer. Note that the nonuniform currents may exist in the upper ocean such as the Ekman layer, where (9.9) does not hold good. However, (9.9) may be used below the Ekman layer.

Since B is a linear function of z in the surface mixed layer [see (9.8a)], the contribution of B to (C_x, C_y) in the surface mixed layer is depth-independent [see (9.8a)]. Since B_{-h} is computed from the surface turbulent fluxes (τ_x, τ_y) and B_0 (bulk models), the atmosphere may control the scale of the horizontal variability of B_{-h} and B_0 .

9.2 Secondary Circulations Across Arctic Fronts in the Fram Strait

Fram Strait (Fig. 9.2) is the only deep connection between the Arctic Ocean and the rest of the world ocean through the Greenland Sea, Iceland Sea, and Norwegian Sea (GIN Sea). Water masses in the Fram Strait are imported from the neighboring Atlantic and polar oceans, and are encountered in various stages of modification. The North Atlantic Water is relatively warmer and saline ($T > 2^{\circ}\text{C}$, $S > 34.9$ ppt). The Polar Water is cooler and fresher ($T < 0^{\circ}\text{C}$, $S < 34.7$ ppt) (van Aken et al. 1991). Analyzing the 1984 marginal ice zone experiment observations in the Fram Strait, Gascard et al. (1988) found that the West Spitzbergen Current and the East Greenland Current are two main generators for eddies in the Fram Strait.

In the transition, different water masses interface and form frontal zones that not only separate water bodies with different hydrographic characteristics but also the regional biological systems. The different water masses encountered in the GIN Sea and the Fram Strait often form fronts. The Arctic front or frontal zone is oriented more or less meridionally. It separates the warm and salty North Atlantic Water in the Norwegian and West Spitzbergen currents from the cool and fresh Arctic Water (Dietrich 1969). After analyzing hydrographic data along $74^{\circ}45'\text{N}$ in February 1989 during cruise VA78 of R/V Valdivia, van Aken et al. (1991) identified four Arctic fronts south of the Fram Strait.

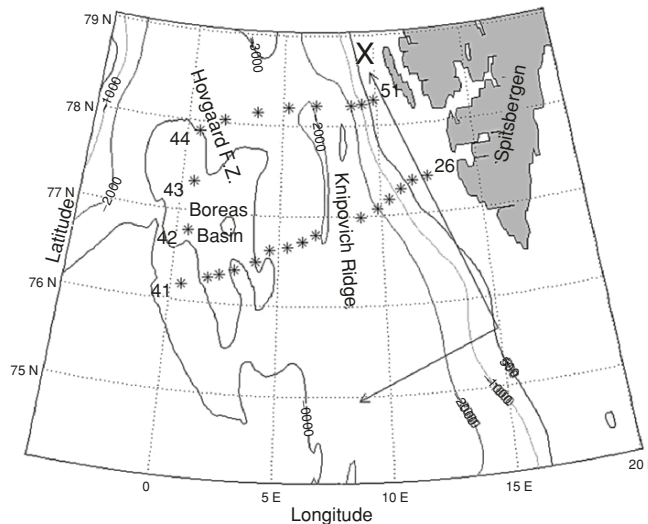


Fig. 9.2. Geography of the East Fram Strait, coordinate system, and CTD stations of R/V Valdivia cruise 54 in the Fram Strait from 16 March to 5 April 1987 (from Chu 2002, Geophysical Research Letters)

The physical–biological effect arises from the significant vertical component of the three-dimensional ageostrophic flow (called the secondary circulation) associated with the fronts, where vertical upward motion may act as a fertilizer of the upper water column. A better knowledge of the secondary circulation is therefore crucial. However, direct measurement of the secondary circulation in the ocean is difficult. The C-vector can be used to diagnose three-dimensional oceanic secondary circulations from observational data.

The atmosphere has most of its energy in scales of several hundreds of kilometers and more, it is reasonable to assume that

$$\frac{\partial}{\partial z} \left(\frac{\partial B}{\partial y} \right) = 0, \quad \frac{\partial}{\partial z} \left(\frac{\partial B}{\partial x} \right) = 0, \quad (9.10)$$

across the Arctic front, and therefore the horizontal C-vector components are computed from the geostrophic forcing only. The geostrophic forcing has been recognized as the major factor to cause the atmospheric frontal secondary circulation (Hoskins et al. 1978; Xu 1992). It may also be important for oceanic frontal secondary circulation.

9.3 Hydrographic Data Collection

CTD data, collected during a large-scale hydrographic survey on RV/VALDIVIA cruise-54 of the eastern Greenland Sea and the Fram Strait from 16 March to 5 April 1987 (Quadfasel and Ungewiß 1988), are used to illustrate the advantage of using the C-vector method in analyzing oceanic secondary circulation. The major task of this cruise was to map the vertical distribution of temperature, salinity, and dissolved oxygen in the Greenland Sea as a measure of the large-scale circulation and transport. A secondary objective was to search active convection events. Along seven sections a total of 73 CTD profiles were taken (Fig. 9.2). Four of these sections crossed the Arctic Front that separates the Greenland Sea gyres from the warm and saline northward flowing Norwegian Atlantic Current and the West Spitzbergen Current. The sections were designed to form three closed boxes to allow calculation of transport budgets. An usual station spacing was 56 km except along the Fram Strait section at 78°25'N and across the Hovgaard Fracture Zone, where the spacing was decreased to less than 28 km. All CTD profiles were run to the depth of within 5 m of the bottom.

9.4 Potential Density

The potential density excess referred to 500 db computed from the CTD data shows the existence of multifrontal zones in the Fram Strait. For example, three Arctic fronts are identified from the north cross section (Stations 44–51) (Fig. 9.3) (a) eastern front occurring near the west coast of Spitzbergen

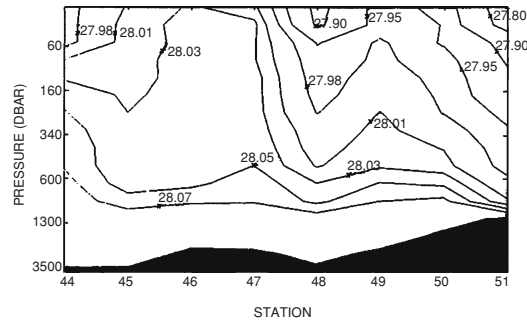


Fig. 9.3. Potential density excess referred to 500 db along the north cross section in the Fram Strait (from Stations 44–51) (from Chu 2002, Geophysical Research Letters)

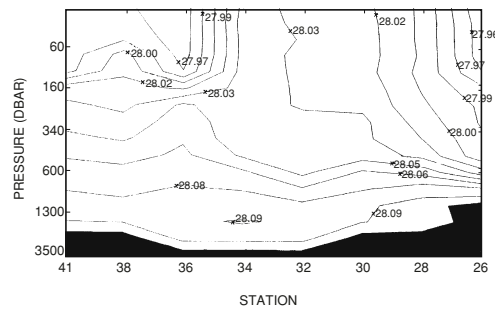


Fig. 9.4. Potential density excess referred to 500 db along the south cross section in the Fram Strait (from Stations 26–41) (from Chu 2002, Geophysical Research Letters)

(Stations 49–51), (b) shallow western front (above 160 m depth) occurring near 0° longitude (Stations 44–46) in the Hovgaard Fracture Zone, and (c) a deep midfront (Stations 47–48) in the north Knipovich Ridge. Within the south cross section in the Fram Strait (Stations 26–41, Fig. 9.4), only two fronts can be identified with a strong and shallow front in the Boreas Basin (Stations 34.36) and a weak deep front near the west coast of Spitzbergen (Stations 26–30).

Usually, upward (downward) bending of isopycnal is used to identify upward (downward) motion. For example, in Fig. 9.3 the isopycnal bend upward near Stations 46–47, 49, and downward near Stations 45 (to 250 m depth), 48 (surface to 1,000 m depth), and 51. Since such identification is very qualitative, it is hard to sketch the secondary circulation pattern and strength. Is it possible to get quantitative information using the same density data? The answer is “yes” because the secondary circulation can be represented by the horizontal component of the C-vector (i.e., horizontal pseudovorticity).

9.5 Horizontal Pseudovorticity

The geostrophic current (u, v) is computed from density, and then the horizontal components of the C-vector are computed from (u, v) . Figure 9.5 shows the x -component of the nondimensional pseudovorticity (C_x/f^2) along the north cross section (Stations 44–51). Looking toward north the positive (negative) values of C_x/f^2 imply a clockwise (anticlockwise) circulation. Two clockwise and two anticlockwise secondary circulations are identified. Among them, the clockwise secondary circulations are deeper than the anticlockwise secondary circulations (depth less than 60 m). Note that in this study, the geostrophic current is computed as 2,500 db which is to be assumed as the level of no motion. This may affect the C-vector computation, especially in large horizontally sheared barotropic current such as in the Fram Strait (Fahrbach et al. 2001). However, Fig. 9.5 keeps almost the same geostrophic current as 2,000 db which is chosen as the reference level.

The most striking feature is the existence of a shallow (surface to 60 m), strong anticlockwise secondary circulation with a minimum value of C_x/f^2 around -9.01 , located near the Knipovich Ridge (Stations 46–48). We may call it the Knipovich cell. The upward and downward branches of this cell are connected to two clockwise secondary cells from the east (upward branch) and west (downward branch). Below the Knipovich cell, between 340 and 1,000 m depth, there is a very weak clockwise vorticity (a maximum value of C_x/f^2 around 0.01).

East of the Knipovich cell, a deep (surface to 1,000 m), clockwise secondary circulation with a maximum pseudovorticity of 1.95 is identified near the West

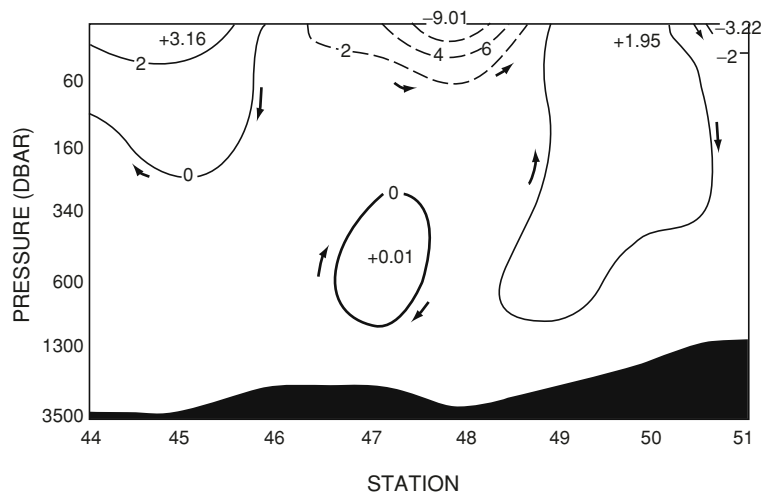


Fig. 9.5. Nondimensional horizontal pseudovorticity, C_x , along the north cross section in the Fram Strait (from Chu 2002, *Geophysical Research Letters*)

Spitzbergen slope (Stations 48–50). We may call it the West Spitzbergen cell. Its downward branch follows the slope. Its upward branch connects to the Knipovich cell. West of the Knipovich cell, a relatively shallow (to 250 m depth) clockwise secondary circulation with a maximum pseudovorticity of 3.16 is identified in the Hovgaard Fracture Zone (Stations 44–46). The downward branch connects to the Knipovich cell (Stations 46–48). The upward branch is located at Stations 44–45. We may call it the Hovgaard cell. The horizontal pseudovorticity (C_x/f^2) represents the secondary circulation around the x -axis. The larger the C_x/f^2 , the secondary circulation is stronger. Strong upwelling is identified between the Knipovich Ridge and the West Spitzbergen slope.

9.6 Two Scalar Functions

For large-scale motion, the horizontal variability of B_h and B_0 cannot be assumed as zero, and (9.10) is not valid. However, (9.9) can be considered as valid because it does not depend on the horizontal scale. The C-vector for the large-scale motion can be written by

$$C_x = -\frac{1}{f^2} \frac{\partial(u, v)}{\partial(y, z)} + \frac{1}{2f^3} \frac{\partial}{\partial z} \left(\frac{\partial B}{\partial y} \right), \quad (9.11a)$$

$$C_y = -\frac{1}{f^2} \frac{\partial(u, v)}{\partial(z, x)} - \frac{1}{2f^3} \frac{\partial}{\partial z} \left(\frac{\partial B}{\partial x} \right), \quad (9.11b)$$

$$C_z = -\frac{1}{f^2} \frac{\partial(u, v)}{\partial(x, y)} - \frac{1}{2f^2} \frac{\partial}{\partial z} \left(\frac{\partial X}{\partial x} + \frac{\partial Y}{\partial y} \right) - \frac{\beta}{2f^3} \frac{\partial Y}{\partial z} \quad (9.11c)$$

where the thermohaline circulation can be represented by the horizontal components (C_x, C_y) and the wind-driven circulation can be represented by the vertical component C_z .

Defining the two scalar functions used by Chu et al. (2003a, b),

$$u_{\text{ag}} = -\frac{\partial\psi}{\partial y} + \frac{\partial^2\phi}{\partial z\partial x}, \quad v_{\text{ag}} = \frac{\partial\psi}{\partial x} + \frac{\partial^2\phi}{\partial z\partial y}, \quad w_{\text{ag}} = -\nabla_2^2\phi, \quad (9.12)$$

the three-dimensional scalar functions (ψ, ϕ) may be called generalized stream function and velocity potential. Substituting (9.12) into (9.6) yields

$$\frac{1}{f^2} \frac{\partial}{\partial y} \left(N^2 \nabla_2^2 \phi + f^2 \frac{\partial^2 \phi}{\partial z^2} \right) - \frac{\partial^2 \psi}{\partial x \partial z} = -2fC_x, \quad (9.13a)$$

$$\frac{1}{f^2} \frac{\partial}{\partial x} \left(N^2 \nabla_2^2 \phi + f^2 \frac{\partial^2 \phi}{\partial z^2} \right) + \frac{\partial^2 \psi}{\partial y \partial z} = 2fC_y, \quad (9.13b)$$

$$\nabla_2^2 \psi + \frac{2\beta}{f} \frac{\partial\psi}{\partial y} - \frac{2\beta}{f} \frac{\partial^2\phi}{\partial x\partial z} = 2fC_z. \quad (9.14)$$

Cross differentiation of (9.13a) and (9.13b) yields

$$\begin{aligned} & \frac{\partial}{\partial x} \left[\frac{1}{f^2} \frac{\partial}{\partial x} \left(N^2 \nabla_2^2 \phi + f^2 \frac{\partial^2 \phi}{\partial z^2} \right) \right] + \frac{\partial}{\partial y} \left[\frac{1}{f^2} \frac{\partial}{\partial y} \left(N^2 \nabla_2^2 \phi + f^2 \frac{\partial^2 \phi}{\partial z^2} \right) \right] \\ &= 2 \left[\frac{\partial}{\partial x} (f C_y) - \frac{\partial}{\partial y} (f C_x) \right]. \end{aligned} \quad (9.15)$$

Here, (9.14) and (9.15) are the two diagnostic equations for determining (ψ, ϕ) from hydrographic data. Equation (9.15) shows that the generalized velocity potential (ϕ) is solely forced by the horizontal components of the C-vector (C_x, C_y) . However, (9.14) shows that the generalized stream function (ψ) is affected by ϕ , only if the β -effect is considered.

9.7 Three Types of Forcing Terms for Ageostrophic Circulation

Substituting (9.11) into (9.14) and (9.15) yield

$$\nabla_2^2 \psi + \frac{2\beta}{f} \frac{\partial \psi}{\partial y} - \frac{2\beta}{f} \frac{\partial^2 \phi}{\partial x \partial z} = S_{\text{geo}}^{(\psi)} + S_w, \quad (9.16)$$

$$\begin{aligned} & \frac{\partial}{\partial x} \left[\frac{1}{f^2} \frac{\partial}{\partial x} \left(N^2 \nabla_2^2 \phi + f^2 \frac{\partial^2 \phi}{\partial z^2} \right) \right] + \frac{\partial}{\partial y} \left[\frac{1}{f^2} \frac{\partial}{\partial y} \left(N^2 \nabla_2^2 \phi + f^2 \frac{\partial^2 \phi}{\partial z^2} \right) \right] \\ &= S_{\text{geo}}^{(\phi)} + S_B, \end{aligned} \quad (9.17)$$

where

$$S_{\text{geo}}^{(\psi)} \equiv -\frac{2}{f} \frac{\partial(u, v)}{\partial(x, y)}, \quad S_{\text{geo}}^{(\phi)} \equiv -2 \left\{ \frac{\partial}{\partial x} \left[\frac{1}{f} \frac{\partial(u, v)}{\partial(z, x)} \right] - \frac{\partial}{\partial y} \left[\frac{1}{f} \frac{\partial(u, v)}{\partial(y, z)} \right] \right\}, \quad (9.18)$$

are the geostrophic forcing terms;

$$S_w \equiv -\frac{1}{f} \frac{\partial}{\partial z} \left(\frac{\partial X}{\partial x} + \frac{\partial Y}{\partial y} \right) - \frac{\beta}{f^2} \frac{\partial Y}{\partial z}, \quad (9.19)$$

is the wind forcing term; and

$$S_B \equiv - \left[\frac{\partial}{\partial x} \left(\frac{1}{f^2} \frac{\partial^2 B}{\partial z \partial x} \right) - \frac{\partial}{\partial y} \left(\frac{1}{f^2} \frac{\partial^2 B}{\partial z \partial y} \right) \right], \quad (9.20)$$

is the buoyancy forcing term. Without the β -effect ($\beta = 0$), the two functions (ψ, ϕ) can be independently solved from

$$\nabla_2^2 \psi = S_{\text{geo}}^{(\psi)} + \bar{S}_w, \quad (9.21)$$

$$\nabla_2^2 \left(N^2 \nabla_2^2 \phi + f^2 \frac{\partial^2 \phi}{\partial z^2} \right) = \bar{S}_{\text{geo}}^{(\phi)} + \bar{S}_{\text{B}}, \quad (9.22)$$

where

$$\bar{S}_{\text{geo}}^{(\phi)} \equiv 2f \left[\frac{\partial}{\partial y} \frac{\partial(u, v)}{\partial(y, z)} - \frac{\partial}{\partial x} \frac{\partial(u, v)}{\partial(z, x)} \right], \quad \bar{S}_{\text{B}} \equiv -\nabla_2^2 \left[\frac{(B_0 - B_{-h})}{h_1} \right],$$

$$\bar{S}_{\text{w}} \equiv -\frac{1}{f} \frac{\partial}{\partial z} \left(\frac{\partial X}{\partial x} + \frac{\partial Y}{\partial y} \right). \quad (9.23)$$

Thus the two scalar functions (ψ, ϕ) can be obtained independently.

Questions and Exercises

- (1) What features can you get between $\nabla \times \mathbf{C}$ and the ageostrophic velocity \mathbf{V}_{ag} ? Here, $\mathbf{V}_{\text{ag}} = (u_{\text{ag}}, v_{\text{ag}}, w_{\text{ag}})$, $\mathbf{C} = (C_x, C_y, C_z)$,

$$\frac{\partial}{\partial y} (N^2 w_{\text{ag}}) - \frac{\partial}{\partial z} (f^2 v_{\text{ag}}) = 2f^3 C_x, \quad (E9.1)$$

$$\frac{\partial}{\partial z} (f^2 u_{\text{ag}}) - \frac{\partial}{\partial x} (N^2 w_{\text{ag}}) = 2f^3 C_y, \quad (E9.2)$$

$$\frac{\partial}{\partial x} (f^2 v_{\text{ag}}) - \frac{\partial}{\partial y} (f^2 u_{\text{ag}}) = 2f^3 C_z, \quad (E9.3)$$

- (2) What is the divergence of \mathbf{C} ?
 (3) Discuss the feasibility of using the linear representation of the turbulent momentum and buoyancy fluxes in the mixed layer

$$(X, Y) = (\tau_x, \tau_y) + \left[(\tau_x, \tau_y) - (X, Y)_{-h} \frac{z}{h_1} \right], \quad (E9.4)$$

$$B = B_0 + (B_0 - B_{-h}) \frac{z}{h_1}, \quad \text{for } z > -h_1, \quad (E9.5)$$

$$(X, Y) \simeq 0, \quad \text{for } z < -h_1, \quad (E9.6)$$

where h_1 is the mixed layer depth, (τ_x, τ_y) is the surface wind stress, and B_0 is the surface buoyancy flux. $(X, Y)_{-h}$ and B_{-h} are turbulent fluxes at the base of mixed layer, which are computed from the surface fluxes.

- (4) Discuss the difference of the turbulent momentum flux represented by (E9.4) and the Ekman flow model.
 (5) Why the conditions

$$\frac{\partial}{\partial z} \left(\frac{\partial B}{\partial y} \right) = 0, \quad \frac{\partial}{\partial z} \left(\frac{\partial B}{\partial x} \right) = 0, \quad (E9.7)$$

are realistic across the Arctic Front?

- (6) Discuss the characteristics for the potential density field shown in Figs. 9.3 and 9.4? Can you identify Polar Front on these figures?
- (7) What are the major characteristics of the secondary circulation across the Fram Strait as shown in Fig. 9.5?
- (8) Discuss the physical significance of (ψ, ϕ) equations for the ageostrophic flow,

$$\nabla_2^2 \psi + \frac{2\beta}{f} \frac{\partial \psi}{\partial y} - \frac{2\beta}{f} \frac{\partial^2 \phi}{\partial x \partial z} = S_{\text{geo}}^{(\psi)} + S_w, \quad (\text{E9.8})$$

$$\begin{aligned} & \frac{\partial}{\partial x} \left[\frac{1}{f^2} \frac{\partial}{\partial x} \left(N^2 \nabla_2^2 \phi + f^2 \frac{\partial^2 \phi}{\partial z^2} \right) \right] + \frac{\partial}{\partial y} \left[\frac{1}{f^2} \frac{\partial}{\partial y} \left(N^2 \nabla_2^2 \phi + f^2 \frac{\partial^2 \phi}{\partial z^2} \right) \right] \\ & = S_{\text{geo}}^{(\phi)} + S_B. \end{aligned} \quad (\text{E9.9})$$

- (9) Discuss dynamically the difference between the two scalar functions (ψ, ϕ) . Why does the β -effect connect the ϕ -function to the ψ -function?
- (10) Since the scalar ϕ is determined by buoyancy and geostrophic forcing, can you use ϕ to represent the thermohaline circulation? Why?
- (11) The ψ -function is basically forced by the winds and geostrophic flow. Why equation (E9.8) is so different from the stream function in the wind-driven-circulation models such as the Stommel model?

Datasets

This book includes several datasets (in DVD-ROM) that are calculated from (T, S) data and written in the Network Common Data Form (netCDF) format. They are climatological annual and monthly mean global absolute velocity in z -coordinate, absolute velocity in isopycnal coordinate, (T, S) in isopycnal coordinate, volume transport stream function (Ψ), volume transport vorticity (Π), and heat storage from the ocean surface to a given depth.

10.1 General Description

Hydrographic and inverted velocity data described in this book are all in the netCDF, which is an interface for array-oriented data access, a library for implementation of interface, and a machine-independent format for representing data. The netCDF software was developed at the Unidata (<http://www.unidata.ucar.edu>) Program Center in Boulder, Colorado, which is a National Science Foundation-sponsored program empowering US universities, through innovative applications of computers and networks, to make the best use of atmospheric, oceanic, and related data for enhancing education and research.

The netCDF software functions as an I/O library, callable from C, FORTRAN, C++, Perl, or other language for which a netCDF library is available. The library stores and retrieves data in self-describing, machine-independent datasets. Each netCDF dataset can contain multidimensional, named variables (of differing types that include integers, real numbers, characters, bytes, etc.). Each variable may be accompanied by ancillary data, such as units of measure or descriptive text. The interface includes a method for appending data to existing netCDF datasets in prescribed ways and functionality that is more or less like a (fixed length) record structure. However, the netCDF library also allows direct-access storage and retrieval of data by variable name and index and therefore is useful only for disk-resident (or memory-resident) datasets (Unidata 2004).

10.2 NetCDF Data Model

10.2.1 General Structure

A netCDF dataset contains dimensions, variables, and attributes, which all have both a name and an ID number by which they are identified. These components can be used together to capture the meaning of data and relations among data fields in an array-oriented dataset. The netCDF library allows simultaneous access to multiple netCDF datasets which are identified by dataset ID numbers, in addition to ordinary file names.

In the enclosed data DVD-ROM, the inverted three-dimensional velocity (u, v, w) data are in netCDF format. Using Matlab, the velocity dataset contains a symbol table for variables having their name, data type, rank (number of dimensions), dimensions, and initial disk address (Fig. 10.1) in the table. Each element is stored at a disk address which is a linear function of the array indices (subscripts) by which it is identified. Hence, these indices need not be stored separately (as in a relational database). This provides a fast and compact storage method.

Figure 10.1 is used to illustrate the concepts of the netCDF data model, which includes dimensions, variables, and attributes. For the variable u , the dimension names are declared in the left box: lat, lon, lev, and month. The dimension lengths are shown in the narrow box: [50 80 33 12].

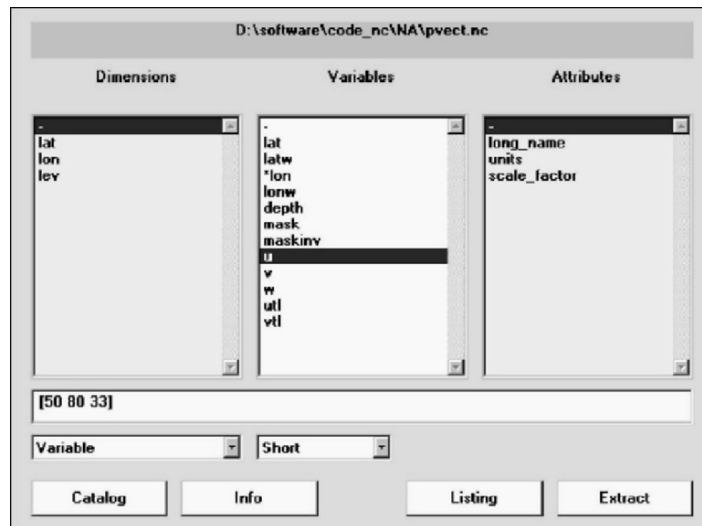


Fig. 10.1. Dimensions, variables, and attributes of netCDF data model. Note that this window is generated using MATLAB

10.2.2 Dimension

A dimension may be used to represent a real physical dimension, for example, time, latitude, longitude, and level (or depth). A dimension might also be used to give an index with other quantities, for example station or model-run-number. A netCDF dimension has both a name and a length. A dimension length is an arbitrary positive integer, except that one dimension in a netCDF dataset can have the length unlimited. Such a dimension is called the unlimited dimension or the record dimension. A variable with an unlimited dimension can grow to any length along that dimension. The unlimited dimension index is like a record number in conventional record-oriented files. A netCDF dataset can have at the most one unlimited dimension, but need not have any. If a variable has an unlimited dimension, that dimension must be the most significant (slowest changing) one.

10.2.3 Variable

Data Variables

The basic unit of named data in a netCDF dataset is a variable. When a variable is defined, its shape is specified as a list of dimensions. Variables are used to store the bulk of the data in a netCDF dataset. A variable represents an array of values of the same type. A scalar value is treated as a zero-dimensional array (or rank 0). A variable has a name, a data type, and a shape described by its list of dimensions specified when the variable is created. In the enclosed DVD-ROM, the variables are three-dimensional (u , v , w), two-dimensional vertically integrated velocity (U , V), and two-dimensional volume transport stream function (Ψ). An external data type variable is one of a small set of netCDF types that have the following names nc-byte, nc-char, nc-short, nc-int, nc-float, and nc-double in the C interface. The name nc-long is a deprecated synonym for nc-int in the C interface. A variable may also have associated attributes, which may be added, deleted, or changed after the variable is created.

Coordinate Variables

A variable with the same name as a dimension is called a coordinate variable. It typically defines a physical coordinate corresponding to that dimension. The coordinate variables shown in Fig. 10.1 are latitude, longitude, level, and time. These define the latitudes, longitudes, depth level, and times corresponding to positions along these dimensions. Note that each coordinate variable is a vector and has a shape consisting of the dimension with the same name. A position along a dimension can be specified using an index. This is an integer with a minimum value of 0 for C programs.

If a dimension has a corresponding coordinate variable, then this provides an alternative, and often a more convenient means of specifying position along it. Current application packages that make use of coordinate variables commonly assume that they are numeric vectors and strictly monotonic (all values are different and either increasing or decreasing).

10.2.4 Attributes

NetCDF attributes are used to store data that refers to the existing data (ancillary data or metadata), similar in many ways to the information stored in data dictionaries and schema in conventional database systems. Most attributes provide information about a specific variable. These are identified by the name (or ID) of that variable, together with the name of the attribute. An attribute has an associated variable, a name, a data type, a length, and a value. The netCDF treats all attributes as vectors; scalar values are treated as single-element vectors. Conventional attribute names should be used wherever applicable. New names should be as meaningful as possible. The attributes shown in Fig. 8.1 are long-name, units, and scale-factor.

The external type of an attribute is specified when it is created. The types permitted for attributes are the same as the netCDF external data types for variables. Attributes with the same name for different variables should sometimes be of different types. For example, the attribute valid-max specifying the maximum valid data value for a variable of type int should be of type int, whereas the attribute valid-max for a variable of type double should instead be of type double. Attributes are more dynamic than variables or dimensions; they can be deleted and have their type, length, and values changed after they are created, whereas the netCDF interface provides no way of deleting a variable or changing its type or shape.

Some attributes provide information about the dataset as a whole and are called global attributes. These are identified by the attribute name together with a blank variable name or a special null “global variable” ID (in C or Fortran). One global attribute (data source) is defined for the example netCDF dataset. This is a character array intended for documenting the data. Actual netCDF datasets might have more global attributes to document the origin, history, conventions, and other characteristics of the dataset as a whole.

In contrast to variables, which are intended for bulk data, attributes are intended for ancillary data, or information about the data. The total amount of ancillary data associated with a netCDF object, and stored in its attributes, is typically small enough to be memory-resident. However, variables are often too large to fit entirely in the memory and have to be split into sections for processing.

Another difference between attributes and variables is that variables may be multidimensional. Attributes are all either scalars (single-valued) or vectors (a single, fixed dimension). Variables are created with a name, type, and shape before they are assigned data values. So a variable may exist with no values.

The value of an attribute must be specified when it is created, so no attribute ever exists without a value.

A variable may have attributes, but an attribute cannot have attributes. Attributes assigned to variables may have the same units as the variable (for example, valid range) or have no units (for example, scale factor). If you want to store data that requires units different from those of the associated variable, it is better to use a variable than an attribute. More generally, if data require ancillary data to describe them are multidimensional, require any of the defined netCDF dimensions to index their values, or require a significant amount of storage, then that data should be represented using variables rather than attributes.

10.3 Data Extraction

Any data listed in the variable box (Fig. 10.1) can be extracted. On highlight the specific data variable you want to extract (e.g., *u* in the variable box). Click the extraction button in the lower right corner. This enables the data extraction window to pop out (Fig. 10.2). The default name for the extracted data is *ncx*. On clicking the okay button after checking the dimension of the data variable, the data can be extracted. The external types supported by the netCDF interface are listed in Table 10.1.

These types are chosen to provide a reasonably wide range of trade-offs between data precision and number of bits required for each value. These external data types are independent from whatever internal data types are supported by a particular machine and language combination. These types of extracted data are called “external”, because they correspond to the portable external representation for netCDF data. When a program reads external netCDF data into an internal variable, the data is converted, if necessary, into the specified internal type. Similarly, if you write internal data into a netCDF variable, this may cause it to be converted to a different external

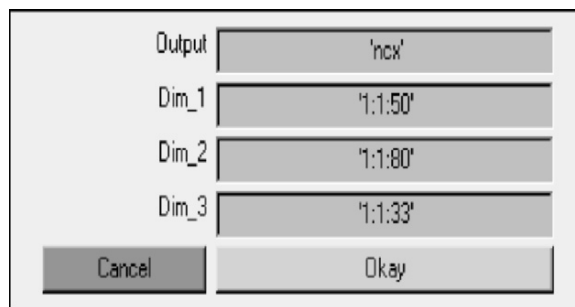


Fig. 10.2. Data extraction window

Table 10.1. Extracted data type and characteristics

data type	Characteristics
char	8-bit characters intended for representing text
byte	8-bit signed or unsigned integers
short	16-bit signed integers
int	32-bit signed integers
float or real	32-bit IEEE floating-point
double	64-bit IEEE floating-point

type, provided the external type for the netCDF variable differs from the internal type.

The separation of external and internal types and automatic type conversion has several advantages. You need not be aware of the external type of numeric variables, since automatic conversion to or from any desired numeric type is available. You can use this feature to simplify code, by making it independent of external types, using a sufficiently wide internal type, e.g., double precision, for numeric netCDF data of several different external types. Programs need not be changed to accommodate a change to the external type of a variable.

10.4 Datasets

Along with this book, several datasets are released in CD-ROM regarding the global circulation and basin-scale circulations. They include heat storage, depth and potential vorticity at isopycnal surfaces, volume transport stream function, vertically integrated horizontal velocity (U , V), and three-dimensional velocity fields in z -coordinate and isopycnal coordinate. The isopycnal surface (T , S) fields are also included.

10.4.1 Heat Storage

The global heat storage dataset includes annual mean $[\bar{H}_{ST}(x, y, z)]$ and monthly anomaly $[\Delta H_{ST}(x, y, z)]$, totaling to 13 subsets. They are calculated from GDEM. This dataset has 13 subsets with one annual mean and 12 monthly anomalies. Each subdataset is three-dimensional in which the vertical coordinate z indicates the depth of the lower boundary of the water column that the heat storage is calculated.

10.4.2 Depth of Isopycnal Surface

Depth of isopycnal surface is computed from WOA and GDEM annual and monthly mean (T , S) data. For either WOA or GDEM data, there are 13 fields (annual and monthly mean) for each of $(\sigma_0, \sigma_2, \sigma_4)$. The depth of k th

isopycnal surface is given by \hat{D}_k^b [see (4.22)]. The thickness between the two isopycnal levels [k th and $(k - 1)$ th] is calculated by $\hat{h}_k = \hat{D}_k^b - \hat{D}_{k-1}^b$ [see (4.24)]. The depth data \hat{D}_k^b can also be used for the ocean modeling, using the isopycnal coordinate system.

10.4.3 Potential Vorticity at Isopycnal Surface

Global potential vorticity at isopycnal surface is computed from WOA and GDEM annual and monthly mean (T, S) data. For either WOA or GDEM data, there are 13 fields (annual and monthly mean) for each of $(\sigma_0, \sigma_2, \sigma_4)$. The potential vorticity of k th isopycnal surface is given by \hat{q}_k [see (4.27), (4.28)].

10.4.4 Absolute Velocity in z -Coordinate

Global three-dimensional absolute velocity field in the z -coordinate [$u(x_i, y_j, z_k), (x_i, y_j, z_k)$] is computed from the WOA (T, S) data. This dataset has 13 subsets including the annual and monthly mean values. The horizontal and vertical resolutions are the same as the corresponding WOA and GDEM data.

10.4.5 Absolute Velocity in Isopycnal Coordinate

Global three-dimensional absolute velocity field in the isopycnal coordinate [$u(x_i, y_j, \sigma), (x_i, y_j, \sigma)$] is computed from the GDEM (T, S) data using σ_0 . This dataset has 13 subsets including the annual and monthly mean values. The horizontal resolution is the same as the corresponding GDEM data. The vertical resolution is higher than the z -coordinate. For example, there are 222 isopycnal levels in the South China Sea.

10.4.6 Volume Transport Stream Function and Vertically Integrated Velocity

Global volume transport stream function $\Psi(x, y)$ and vertically integrated velocity [$U(x, y), V(x, y)$] are calculated using the NOAA WOA $1^\circ \times 1^\circ$ hydrographic (Levitus and Boyer 1994; Levitus et al. 1994) and wind data (da Silva et al. 1994). Each of the [$\Psi(x, y), U(x, y), V(x, y)$] contains 13 subsets including the annual and monthly mean values. The horizontal resolution is $1^\circ \times 1^\circ$.

Inverted Circulations in the Pacific Basin

Detailed description of the world oceans can be obtained from the datasets presented in Chap. 10. In this chapter, characteristics of the inverted circulations in the Pacific Ocean are presented.

11.1 General Features

Figure 11.1 shows the inverted annual mean volume transport stream function (Ψ) and vertically integrated velocity (U, V) for the Pacific Basin that is calculated by using the method depicted in Chap. 8. The annual mean northward transport across the equator in the west is 21.7 Sv, between the -21.7 Sv isoline at the western boundary (northeast coast of New Guinea) to the 0 Sv isoline near 170°W (Fig. 11.1a). This current meanders and generates several eddies such as the Mindanao Eddy (cyclonic), near the southern Philippines (Masumoto and Yamagata 1991) and the Halmahera eddy (anticyclonic) near Indonesia. The northward current joins the North Equatorial Current with 30 Sv transport (from 0 to 30 Sv isolines) east of the Philippines (10 – 15°N). Of these 51.7 Sv of water, 21.7 Sv are lost to the Indonesian Seas directly, or through the South China Sea indirectly. The remaining 30 Sv of water continues northward to Japan and then eastward with the anticyclonic gyre. This subtropical gyre recirculates 20 Sv between 25 and 35°N (from 30 to 50 Sv isolines) and makes 50 Sv of the Kuroshio Current, east of Japan. The seasonal variability is small in the inverted volume transport stream function and vertically integrated velocity (Fig. 11.2).

There are several low-latitude cyclonic gyres, with axes along 8°N and 8°S (Chu and Fan 2006). Among them, an evident cyclonic gyre occurs in the north equatorial region between 180 and 120°E , and three smaller cyclonic eddies (also called broken gyres) appear in the south equatorial region, east of 170°E . The north equatorial gyre appeared clearly on the study by Munk (1950) of the wind-driven circulation of the North Pacific, and was identified by Reid (1997) using hydrographic data. The south equatorial gyre identified using the

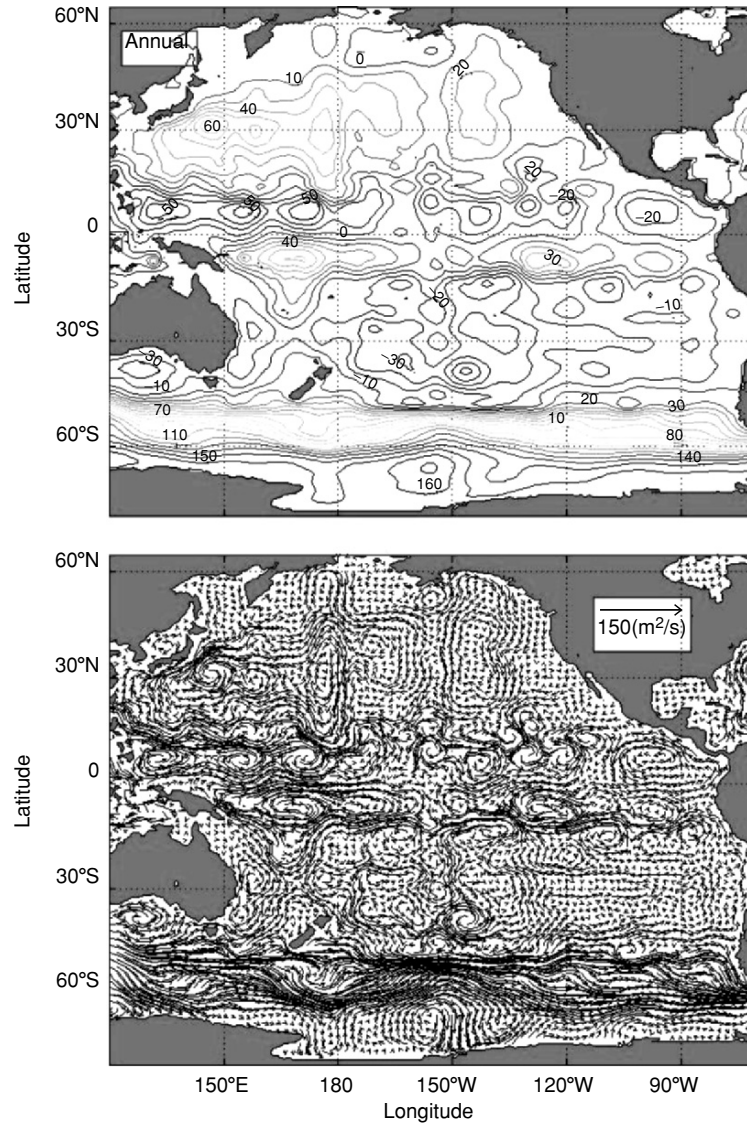


Fig. 11.1. Annual mean (a) volume transport stream function (Ψ) and (b) vertically integrated velocity (U, V) for the Pacific basin (from Chu and Fan 2006, *Journal of Marine Systems*)

P-vector method (broken gyre) is different from Reid's (1989) description of a complete gyre structure. The south subtropical anticyclonic gyre occurs east of 180°E between 12°S and 45°S and recirculates 30 Sv of water.

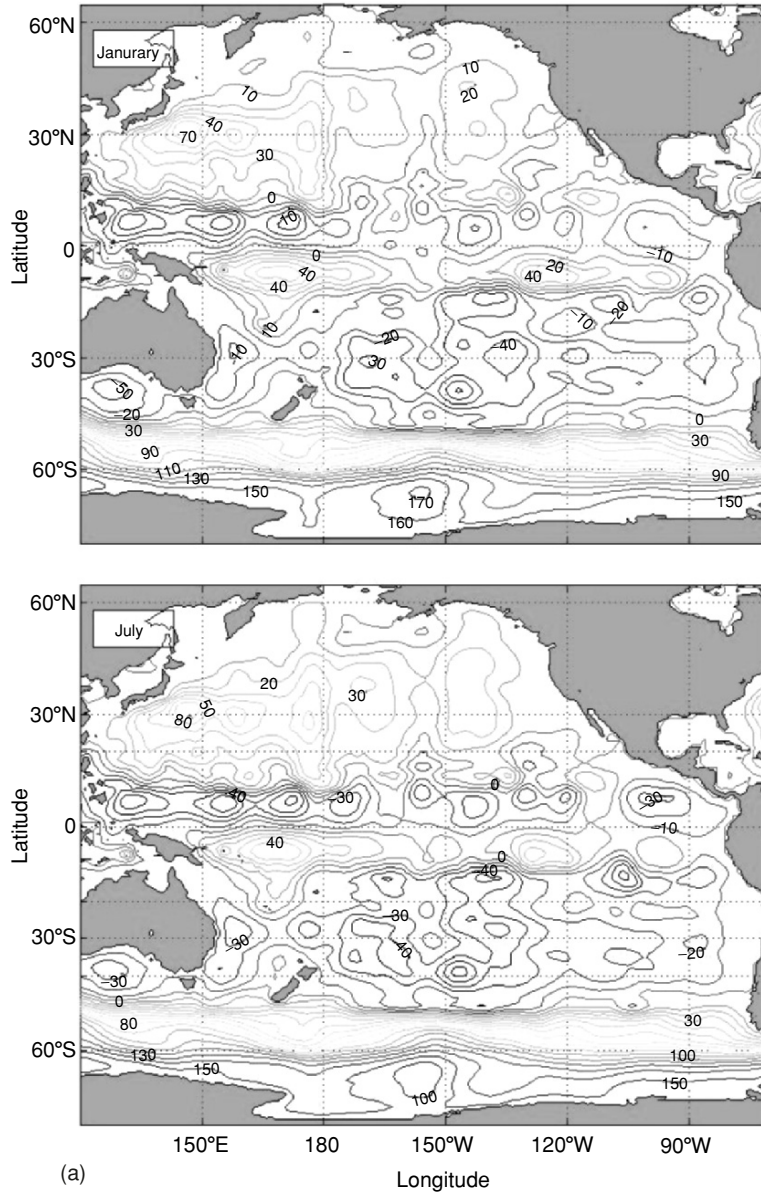


Fig. 11.2. (a) Seasonal variation of volume transport stream function (Ψ) for the Pacific Ocean (from Chu and Fan 2006, *Journal of Marine Systems*).

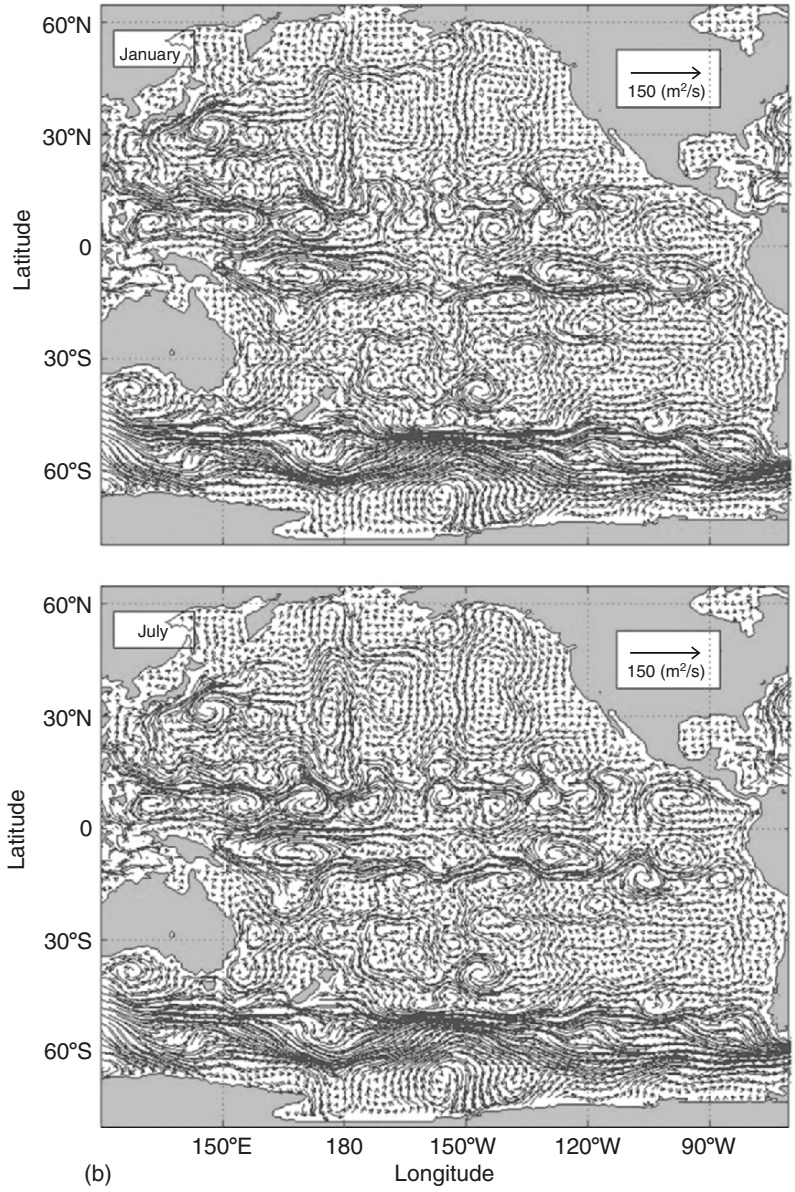


Fig. 11.2. (b) Seasonal variation of vertically integrated velocity (U, V) for the Pacific basin (from Chu and Fan 2006, *Journal of Marine Systems*)

11.2 Water Mass Crossroads

The western equatorial Pacific, particularly the southernmost Philippine Sea, is called “water mass crossroads” by Fine et al. (1994) due to the confluence of several water masses from higher latitudes of both hemispheres (Wyrki, 1961a, b; Fine et al. 1994). The volume transport stream function and vertically integrated velocity are calculated using the method described in Chap. 7, as shown in Fig. 11.3.

11.2.1 General Description

The annual mean northward transport across the equator in the west is around 20 Sv, between the -20 Sv isoline at the western boundary (northeast coast of New Guinea) to the 0 Sv isoline near 170°W (Fig. 11.3a). This current meanders and generates several eddies such as the Mindanao Eddy (cyclonic) near southern Philippines and the Halmahera Eddy (anticyclonic) near Indonesia. The northward current joins the North Equatorial Current with 30 Sv transport (from 0 to 30 Sv isolines) east of the Philippines (10 – 15°N). Of these 50 Sv of water, 20 Sv are lost to the Indonesian Seas directly, or via the South China Sea indirectly. The remaining 30 Sv of water continues northward to Japan and then eastward with the anticyclonic gyre. This subtropical gyre recirculates 20 Sv between 25 and 35°N (from 30 to 50 Sv isoline) and makes 50 Sv of the Kuroshio Current east of Japan.

There are several low-latitude cyclonic gyres, with axes along 8°N and 8°S . Among them, an evident cyclonic gyre occurs in the north equatorial region between 180° and 120°E , and three smaller cyclonic eddies (also called broken gyres) appear in the south equatorial region, east of 170°E . The north equatorial gyre appeared clearly on the study by Munk (1950) of the wind-driven circulation of the North Pacific, and was identified by Reid (1997) using hydrographic data. The south equatorial gyre identified using the P-vector method (broken gyre) is different from Reid’s (1989) description of a complete gyre structure. The south subtropical anticyclonic gyre occurs east of 180°E between 12°S and 45°S and recirculates 30 Sv of water.

After encountering the western boundary along the Philippine coast, the North Equatorial Current bifurcates into the northward flowing Kuroshio and the southward flowing Mindanao Current (Masuzawa 1969; Nitani 1970; Wijffels et al. 1995). The Mindanao Current and the New Guinea Coastal Undercurrent flow equatorward, feeding both the North Equatorial Counter Current, the New Guinea Coastal Current, and the flow from the Pacific to the Indian Ocean, that is, the Indonesian Throughflow.

The Mindanao Current is unique because it is the only northern hemisphere low-latitude western boundary current that has a mean flow toward the equator (Lukas et al. 1996), and is important because it feeds the Indonesian Throughflow (Field and Gordon 1992), and, in turn, sends impacts on the stratification of the Indian Ocean (Lukas et al. 1996; Godfrey 1996).

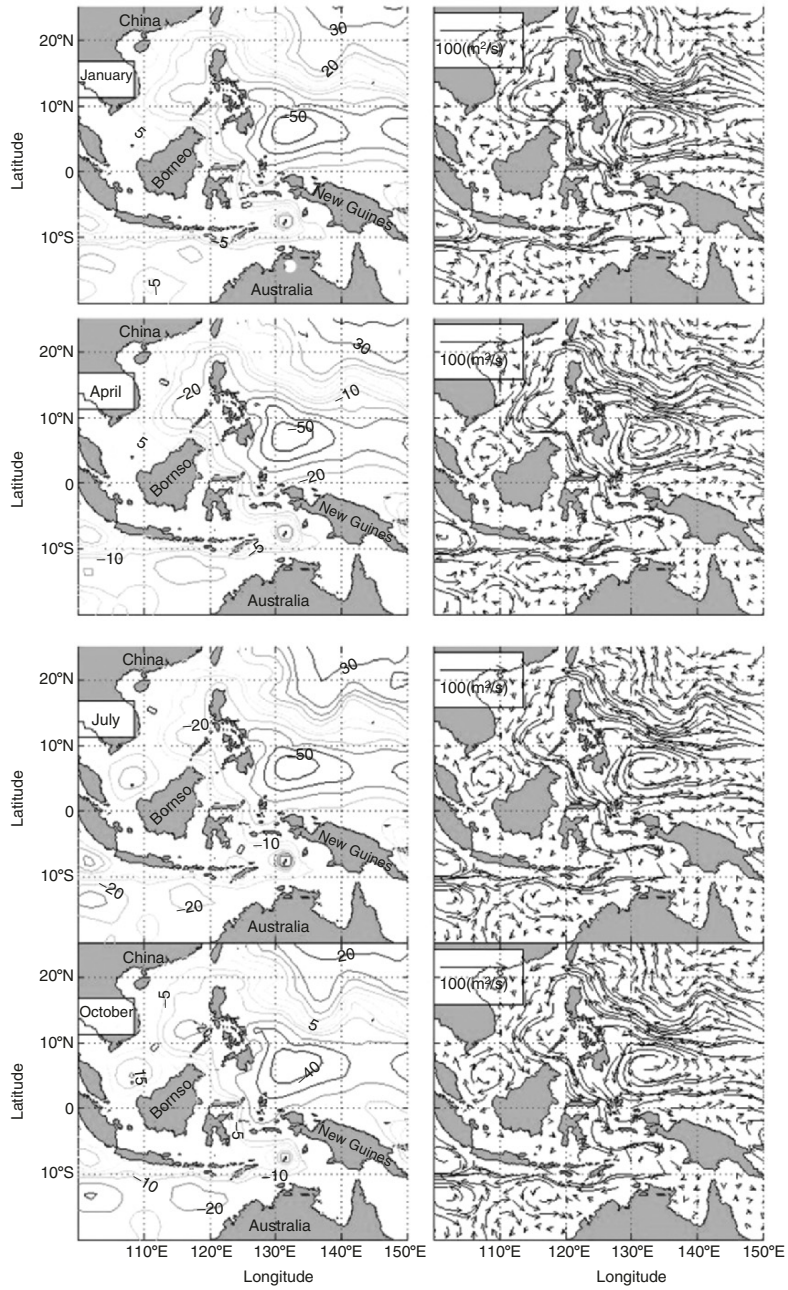


Fig. 11.3. The inverted monthly mean Ψ and (U, V) vector fields in the vicinity of water mass crossroads: (a) January, (b) April, (c) July, and (d) October

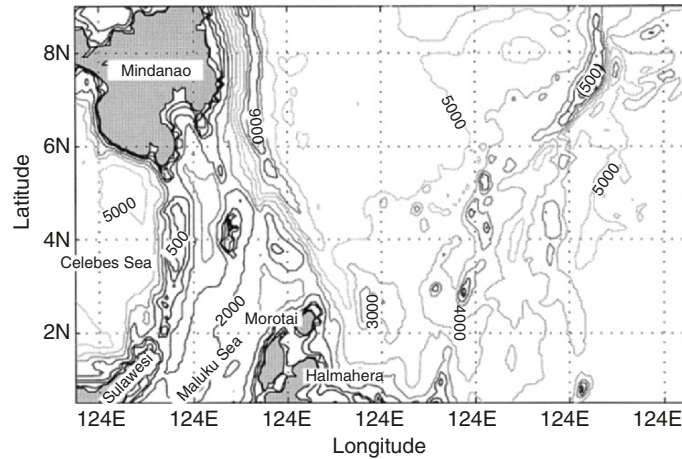


Fig. 11.4. Geography and isobaths showing the bottom topography of the southwestern Pacific near Midanao Island (from Chu et al. 2003d, Chinese Journal of Oceanology and Limnology)

The North Equatorial Counter Current bifurcates into three branches near 130°E . The central branch continues to flow eastward as the North Equatorial Counter Current. The northern branch moves northwestward and forms a cyclonic eddy near Mindanao Island, which is called the Mindanao Eddy. The southern branch moves southwestward, joins the northwest moving currents from the New Guinea Coastal Current and the New Guinea Coastal Undercurrent, which are parts of the South Equatorial Current, and forms an anticyclonic eddy near the Halmahera Sea, which is called the Halmahera Eddy.

Metzger and Hurlburt (1996) adopted a high horizontal resolution six-layer model driven by monthly climatological winds to analyze the coupled dynamics among the Sulu Sea, the South China Sea, and the Pacific Ocean. Their model simulates the existence of the dual eddy structure. The Mindanao Eddy and the Halmahera Eddy are in the middle of the water mass crossroads, surrounded by complicated topography (Fig. 11.4), and connected to major equatorial currents. Seasonal variability (thermohaline structure and circulation) of the two eddies represents the seasonal variability in low latitude dynamics and interbasin water mass exchange.

Water mass characteristics have been used to infer the flow along the isopycnal surfaces. For example, between 300 and 1,000 m the North Pacific Intermediate Water (around $\sigma_{\theta} = 26.8 \text{ kg m}^{-3}$) and Antarctic Intermediate Water (around $\sigma_{\theta} = 27.2 \text{ kg m}^{-3}$) reach this area (Reid 1997; Tschlya 1991; Talley 1993; Bingham and Lukas 1994, 1995; Fine et al. 1994). Kashino et al. (1996) confirm the existence of the North Pacific Intermediate Water and Antarctic Intermediate Water in the far western equatorial Pacific near the entrances

to the Celebes and Halmahera Seas. They also provide further evidence for the flow of waters from the southern hemisphere across the equator, turning eastward into the North Equatorial Counter Current.

In order to obtain current signal quantitatively from hydrographic data in this area is not easy. Godfrey (1996) pointed out that there are a number of special difficulties such as active internal tides and the geostrophy that can only be used with caution to estimate the current distribution in the area. To overcome these difficulties, the P-vector method on the isopycnal surfaces can be used to invert the absolute velocity from GDEM (Chu et al. 2003d).

11.2.1 (T, S) Fields

In the pycnocline layer (100–300 m) there are salinity maximum layers from the North and South Pacific. These water masses are called North Pacific Tropical Water and South Pacific Tropical Water by Kashino et al. (1996). It is not the intention to present a detailed climatological thermohaline structure, but only as representative features on $\sigma_\theta = 25.0 \text{ kg m}^{-3}$ (in pycnocline) as illustration. This level is generally considered to be the level where the salinity maximum occurs (Kashino et al. 1996).

Temperature

Bimonthly mean temperature on $\sigma_\theta = 25.0 \text{ kg m}^{-3}$ (Fig. 11.5 shows a cool (northern) – warm (southern) eddy-like structure with a strong seasonal variability. The cool (warm) eddy is enclosed by 18.25°C (20°C) isoline. The cool eddy shows up almost all year round and is located at $128\text{--}133^\circ\text{E}$ and $6\text{--}9^\circ\text{N}$, and the warm eddy is evident only in winter (February) and spring (April). A weak thermal front exists between the cool and warm eddies with horizontal temperature gradient less than $1^\circ\text{C}/100 \text{ km}$. This front strengthens from December to April, and weakens from April to December.

Salinity

Salinity is generally used for identifying the water masses in the area. For example, Kashino et al. (1996) used 35.0 ppt contour as the boundary of high salinity South Pacific Tropical Water in analyzing R/V Kaiyo World Ocean Circulation Experiment (WOCE) expedition I in October 1992 and II in February 1994. Both expeditions covered the same area as ours (Fig. 11.6).

Horizontal salinity distribution on $\sigma_\theta = 25.0 \text{ kg m}^{-3}$ observed during Kaiyo WOCE I and II, shows the high-salinity South Pacific Tropical Water in the southern area. In October 1992, this water reached 2°N near Morotai Island and 3°N along 134°E . In February 1994, the South Pacific Tropical Water reached farther north than in October 1992, i.e., north of Morotai Island and 5°N along 130°E (Kashino et al. 1996).

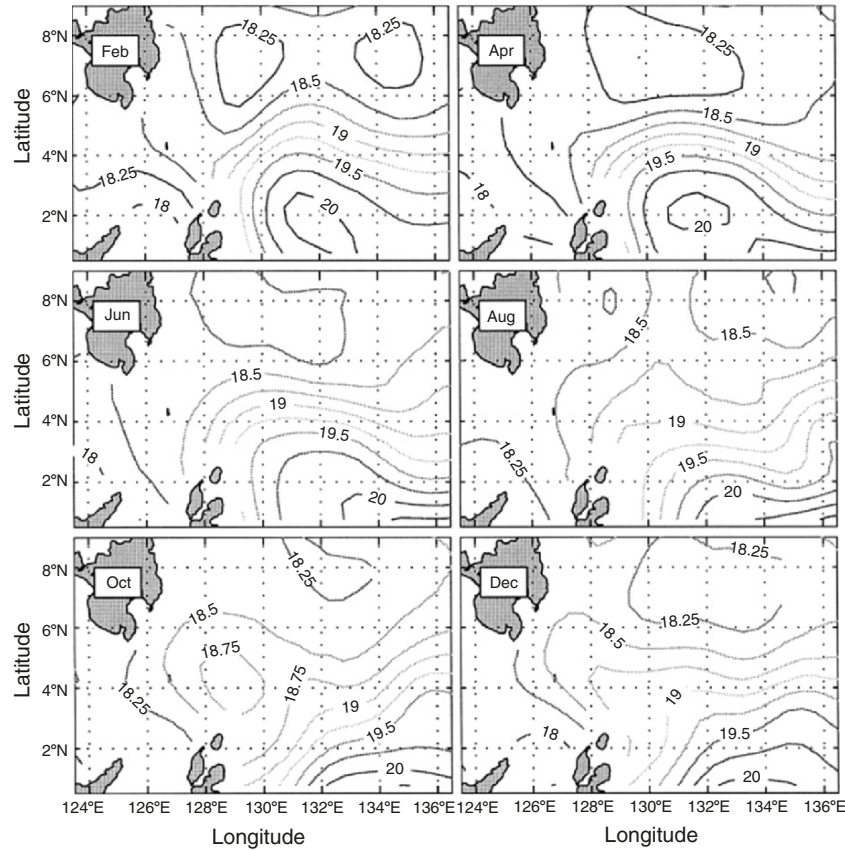


Fig. 11.5. Bimonthly mean temperature ($^{\circ}\text{C}$) fields on $\sigma_{\theta} = 25.0 \text{ kg m}^{-3}$ from GDEM (from Chu et al. 2003d, Chinese Journal of Oceanology and Limnology)

The monthly mean salinity on $\sigma_{\theta} = 25.0 \text{ kg m}^{-3}$ (Fig. 11.6) shows the similar feature depicted by Kashino et al. (1996). The high-salinity South Pacific Tropical Water (≥ 35.0 ppt) is located in the southern part of the area, and expands toward the northwest in February–June, and retreats toward the southeast in August–December. In February and April, a high salinity center enclosed by 35.3 ppt occurs at $131\text{--}133^{\circ}\text{E}$, $1\text{--}3^{\circ}\text{N}$, which coincides with the warm center (Fig. 11.5).

11.2.2 Velocity Field

Most important current system is featured as the southward flowing Mindanao Current, the eastward flowing North Equatorial Counter Current, the north-westward flowing New Guinea Coastal Current, and the New Guinea Coastal Undercurrent and associated mesoscale eddies such as the cyclonic Mindanao

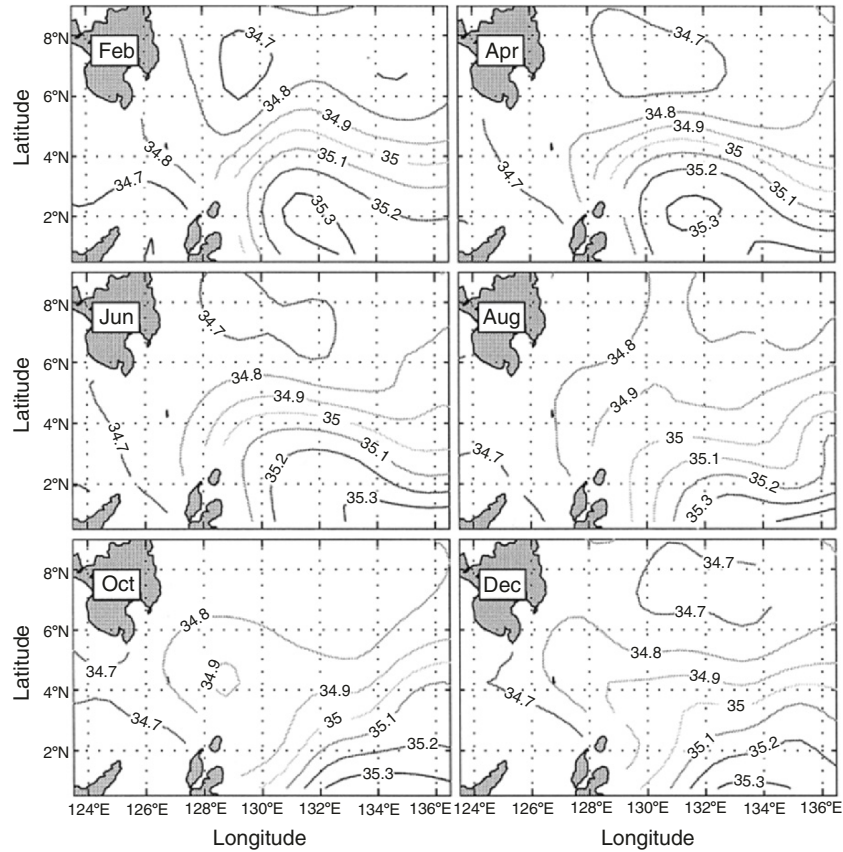


Fig. 11.6. Bimonthly mean salinity (ppt) fields on $\sigma_\theta = 25.0 \text{ kg m}^{-3}$ from GDEM (from Chu et al. 2003d, Chinese Journal of Oceanology and Limnology)

Eddy and the anticyclonic Halmahera Eddy. Figure 11.7 shows the horizontal velocity vectors on three different σ_θ levels: pycnocline ($\sigma_\theta = 25.0 \text{ kg m}^{-3}$), intermediate ($\sigma_\theta = 26.5 \text{ kg m}^{-3}$), and deep ($\sigma_\theta = 27.2 \text{ kg m}^{-3}$) levels. The last two levels may represent North Pacific Intermediate Water and Antarctic Intermediate Water in this area.

Pycnocline Level ($\sigma_\theta = 25.0 \text{ kg m}^{-3}$)

Three major currents (Mindanao Current, New Guinea Coastal Undercurrent, and North Equatorial Counter Current) and dual eddies (Mindanao Eddy and Halmahera Eddy) are easily identified. They have strong seasonal variability. The Mindanao Current strengthens from October to February and weakens from April to August. After leaving the south tip of Mindanao Island, it flows southeastward following the continental slope (see Figs. 10.7 and 10.4) and

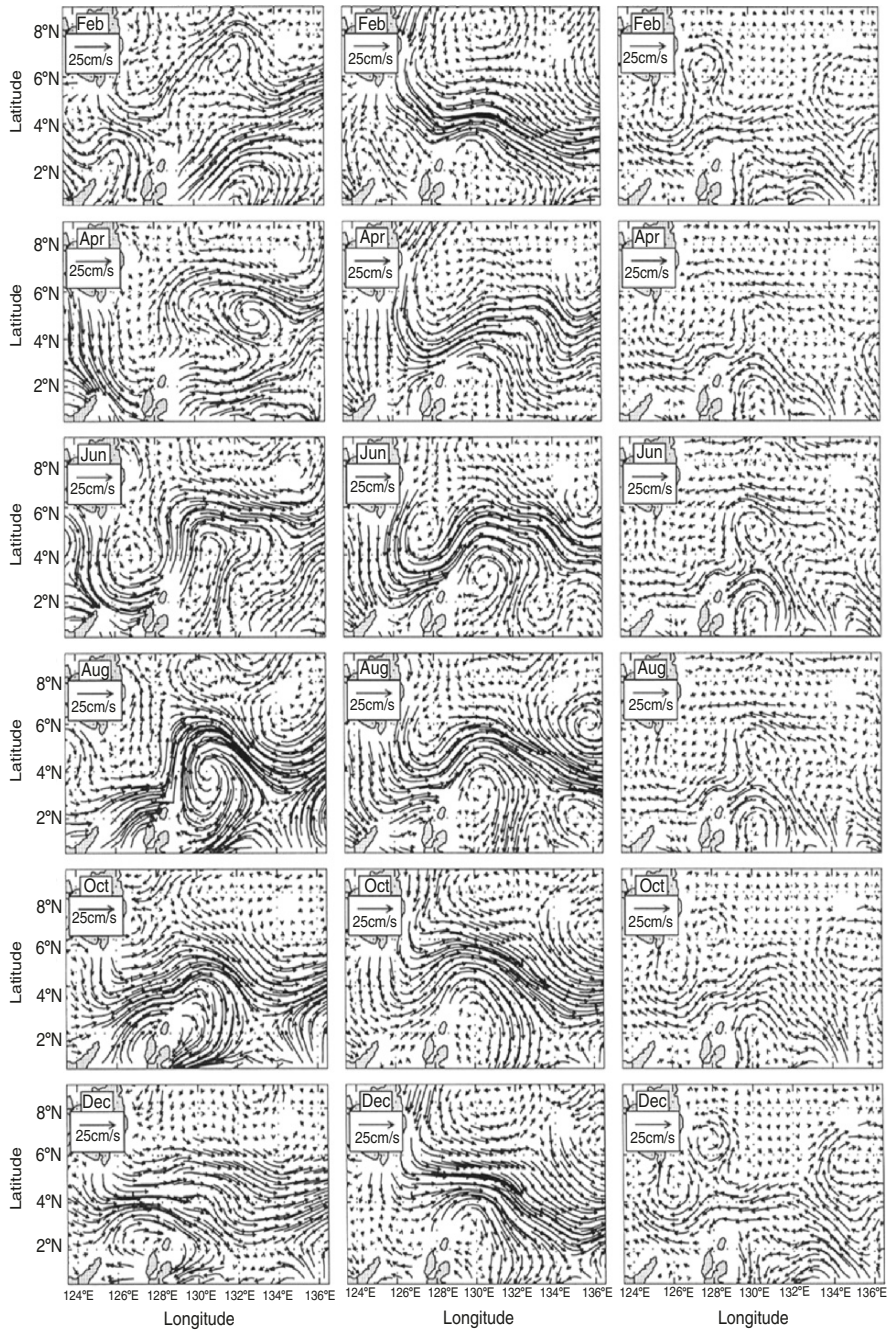


Fig. 11.7. Bimonthly mean velocity vector field east of Midanao Island on the surface of (a) $\sigma_\theta = 25.0 \text{ kg m}^{-3}$, (b) $\sigma_\theta = 26.5 \text{ kg m}^{-3}$, and (c) $\sigma_\theta = 27.2 \text{ kg m}^{-3}$ (from Chu et al. 2003d, Chinese Journal of Oceanology and Limnology)

recirculates northeastward near Morotai Island. Such a recirculation leads to the formation of the cyclonic eddy (Mindanao Eddy). The Mindanao Current is very weak from April to August, strengthens in October, and becomes strong in the winter with the maximum speed around 0.25 m s^{-1} in February. New Guinea Coastal Undercurrent flows northwestward along the northern New Guinea Island (Fig. 10.3). After leaving the north tip of New Guinea Island, it continues to move northward and feeds into an anticyclonic eddy, the Halmahera Eddy. This eddy strengthens in summer (June–August) and weakens in winter (December). In August, the Halmahera Eddy is located at $128\text{--}133^\circ\text{E}$, $2\text{--}6^\circ\text{N}$ with a maximum tangential velocity around 0.3 m s^{-1} .

Intermediate Level ($\sigma_\theta = 26.5 \text{ kg m}^{-3}$)

As the water depth increases, the seasonal variation of the velocity reduces. The intermediate level ($\sigma_\theta = 26.5 \text{ kg m}^{-3}$) is close to the level ($\sigma_\theta = 26.8 \text{ kg m}^{-3}$), where North Pacific Intermediate Water is located. The Mindanao Current is energetic; nearly 150 km wide, a southward and coastal trapped jet. It turns east after leaving Mindanao Island and feeds into the North Equatorial Counter Current, which separates into three branches near 130°E . The north and south branches feed into the Mindanao eddy (cyclonic) and the Halmahera eddy (anticyclonic). The central branch continues as the North Equatorial Counter Current. In winter (December–February), the dual eddies are north–south oriented with the Mindanao Eddy (maximum tangential velocity around 15 cm s^{-1}) located at $128\text{--}133^\circ\text{E}$, $6\text{--}9^\circ\text{N}$, and the Halmahera Eddy (maximum tangential velocity around 0.25 m s^{-1}) located at $128\text{--}133^\circ\text{E}$, $0.5\text{--}4^\circ\text{N}$. In April, Mindanao eddy (Halmahera eddy) expands toward the southwest (northeast). In June, the dual eddies are east–west oriented with the Mindanao eddy in the west and the Halmahera eddy in the east. The size of both eddies is smaller in the summer than in the winter.

Deep Level ($\sigma_\theta = 27.2 \text{ kg m}^{-3}$)

At the deep level, where the Antarctic Intermediate Water is located, the flow pattern is quite different from the pycnocline and intermediate levels. An evident westward flowing current is identified between 2 and 6°N which is in the opposite direction of North Equatorial Counter Current on the pycnocline and intermediate level. The flow pattern clearly shows New Guinea Coastal Undercurrent entering the eastern part of southern boundary ($134\text{--}136^\circ\text{E}$) and flowing northwestward with a maximum velocity larger than 20 cm s^{-1} in winter (December–February).

In winter (December–February), the New Guinea Coastal Undercurrent bifurcates at 133°E , 4°N into two branches (northward and westward). The northward branch recirculates at 6°N and forms an anticyclonic mesoscale eddy (around 200 km in diameter). The westward branch flows zonally (under North Equatorial Counter Current) to a longitude near 129°E and splits into

three branches moving southward, westward, and northward. The westward branch transports Antarctic Intermediate Water into the Celebes Sea. The northward branch turns to west at 8°N , recirculates along the west coast of Mindanao Island, and forms a cyclonic eddy (i.e., the Mindanao Eddy). In summer (June–August), the cyclonic Mindanao Eddy is identified southeast of the southern tip of Mindanao Island with 200 km in diameter and a maximum swirl velocity of 0.15 m s^{-1} .

11.2.3 Seasonal Variability of Major Currents

Mindanao Current Along $7^{\circ}15'\text{N}$

As mentioned earlier, the Mindanao Current is a major current in the water mass crossroads and feeds into the North Equatorial Counter Current and the Indonesia Throughflow. The seasonal variability of the Mindanao Current affects the seasonal variability of the two current systems, and, in turn, sends impacts on the seasonal variability of the Mindanao eddy (due to the variability of the North Equatorial Counter Current) and the Indian Ocean stratification (due to the variability of the Indonesia Throughflow). Kashino et al. (1999) investigated the current variability at the Pacific entrance of the Indonesia Throughflow. Shriver and Hurlburt (1997) identified the Throughflow from the global thermohaline circulation.

The north–south geostrophic velocities on isopycnal surfaces along $7^{\circ}15'\text{N}$ are used to represent the seasonal variability of the Mindanao Current (Fig. 11.8a). Positive (negative) values show the poleward (equatorward) flow. The negative values (equatorward flow) are shaded in gray. The top-to-bottom black vertical bars represent the islands. The small black bars occurring at the top or the bottom represent those σ_{θ} that do not reach these values. The equatorward flowing Mindanao Current has two jet-cores, located in the upper layer above the pycnocline (from the surface to $\sigma_{\theta} = 25.0\text{ kg m}^{-3}$) and deep layer ($\sigma_{\theta} > 26.5\text{ kg m}^{-3}$), respectively. The upper layer jet-core has a strong seasonal variability. Evident equatorward Mindanao Current occurs from December to March with a maximum speed of 0.1 m s^{-1} in January and February and 0.05 m s^{-1} in March, near the east coast of Mindanao Island at $\sigma_{\theta} = 23.25\text{ kg m}^{-3}$. The Mindanao Current disappears from April to November. The deep layer jet-core exists all year round with a weak seasonal variability. Its strength reaches the maximum (0.25 m s^{-1}) in winter and the minimum (0.1 m s^{-1}) in summer.

The v -component is converted from σ_{θ} to z levels (Fig. 11.8b), and shows the existence of upper layer (around 50 m) jet-core and the deep layer jet-core (300–600 m), respectively. A maximum speed of 100 cm s^{-1} in the Mindanao Current was measured along 7°N (Lukas et al. 1991) using the ADCP. The absolute velocities calculated from GDEM underestimate the actual velocities.

Figure 11.8b also shows the existence of three northward velocity cores. Among them, two cores are close to the coast (west of 130°E) and one core

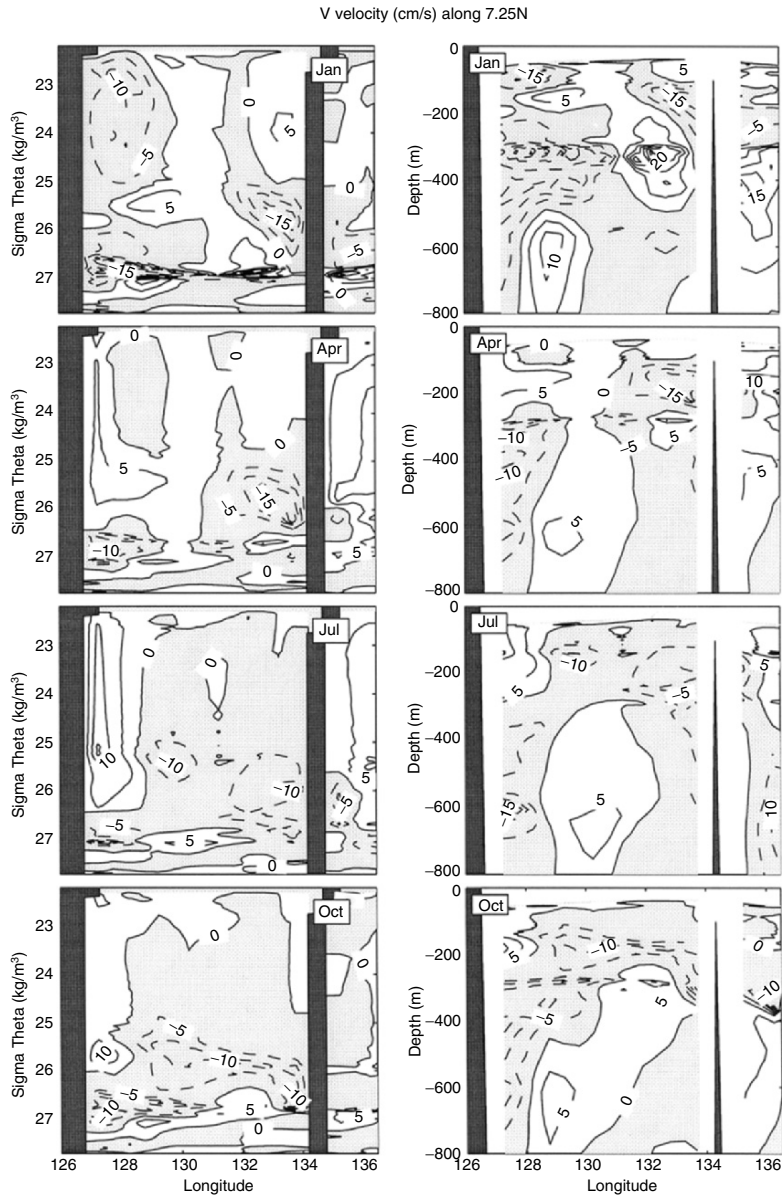


Fig. 11.8. Seasonal variation of north-south velocities (unit: cm s^{-1} ; northward positive) along $7^{\circ}15'N$ latitude representing the flow east of Mindanao Island: (a) on σ_{θ} levels, and (b) on z levels (from Chu et al. 2003d, Chinese Journal of Oceanology and Limnology)

(centered at 300 m deep) is away from the coast (130–134°E). The two coastal cores represent the Mindanao Undercurrent described by Hu and Cui (1989), and the third core represents the eastern part of the Mindanao Eddy. The Mindanao Undercurrent has an evident seasonal variation. From April to September, the upper layer of this current, occurring from 50 to 300 m (centered at 200 m), is close to the coast with a width around 200 km and a maximum velocity of 0.1 m s^{-1} . It retreats toward the coast from October to December with a width less than 100 km, and expands toward the east to a longitude near 132°E from January to March having a maximum velocity of 0.1 m s^{-1} at around 150 m deep. The lower layer of the Mindanao Undercurrent, occurring below 400 m, is around 100 km away from the coast and has a weak seasonal variability in its location and a strong seasonal variability in its strength. It reaches a maximum strength (0.2 m s^{-1}) in February and a minimum strength (0.05 m s^{-1}) from March to October.

Mindanao Eddy along 7°15'N

The Mindanao Eddy is a subsurface system, represented by the alternate southward flow west of and northward flow east of 130°E (Fig. 11.8b). In November, the Mindanao Eddy extends from 200 to 500 m with a jet core at 300 m deep. From November to March, its position keeps quite steady, but its strength varies drastically. The Mindanao eddy enhances through February and weakens in March. The northward branch increases to 0.2 m s^{-1} in December and January and the southward branch enhances to 0.25 m s^{-1} in February. From April to October, the Mindanao Eddy shifts southwestward to 128–133°E and south of 6°N (Fig. 11.7).

New Guinea Coastal Undercurrent along 1°15'N

Similar to the Mindanao Current, the New Guinea Coastal Undercurrent is a major current from the Southern Hemisphere to the water mass crossroads and feeds into the North Equatorial Counter Current and Indonesia Throughflow. The seasonal variability of New Guinea Coastal Undercurrent affects the seasonal variability of the North Equatorial Counter Current and Indonesia Throughflow, and, in turn, sends impacts on the seasonal variability of Mindanao eddy (due to variability of the North Equatorial Counter Current) and the Indian Ocean stratification (due to variability of the Indonesia Throughflow).

Since the geostrophic balance is not generally good, we use the computed v velocities on isopycnal surfaces along 1°15'N to imply the seasonal variability of the New Guinea Coastal Undercurrent approximately (Fig. 11.9a). Positive (negative) values show the poleward (equatorward) flow. The negative values (equatorward flow) are shaded in gray. Similar to Fig. 11.8a, the top-to-bottom black vertical bars represent the islands. The vertical bars between 127°15' and 128°45'E represent Halmahera Island (Fig. 11.4). The small black bars

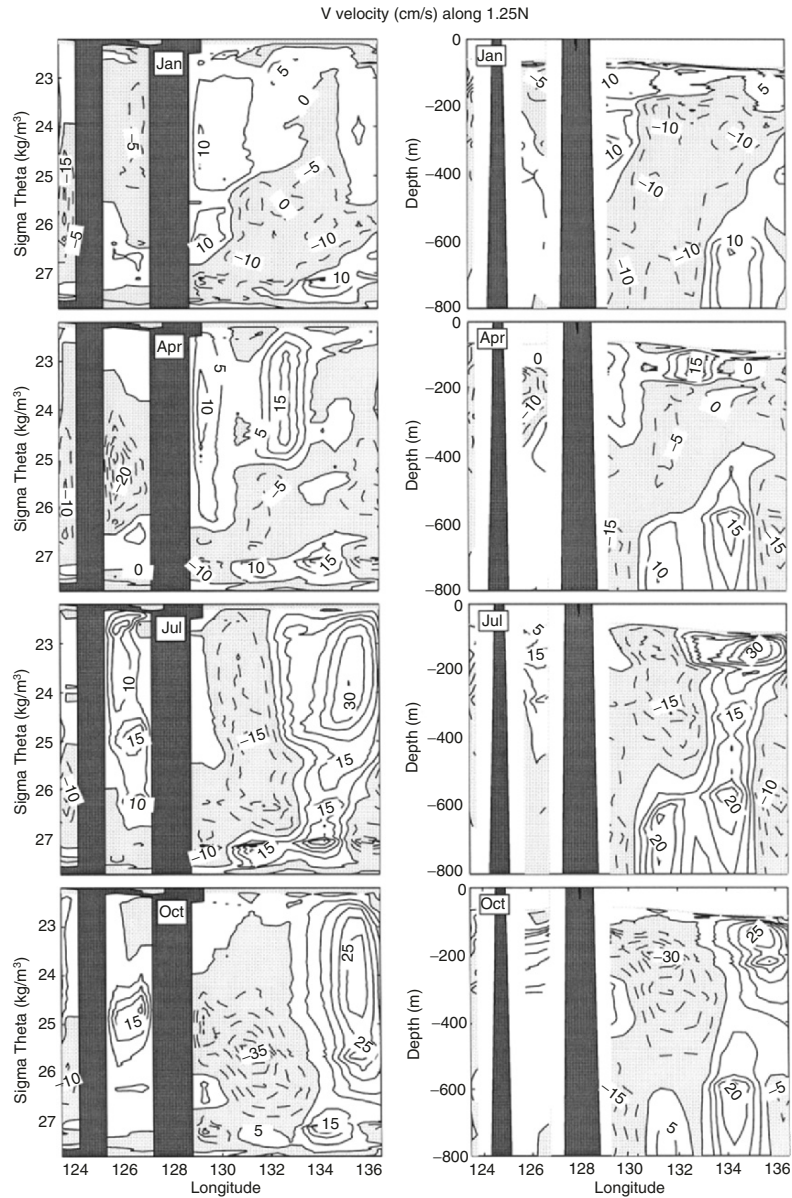


Fig. 11.9. Seasonal variation of north–south velocities (unit: cm s^{-1} ; northward positive) along $1^\circ 15' \text{N}$ latitude representing the flow east of Halmahera Island: (a) on σ_θ levels, and (b) on z levels (from Chu et al. 2003d, Chinese Journal of Oceanology and Limnology)

occurring at the top or the bottom represent those σ_θ that do not reach the value at that position. The New Guinea Coastal Undercurrent has two branches with the first one along the east coast of Halmahera Island with a width of around 400 km (coastal branch) and the second one located east of 133°E with a width around 300 km (open water branch).

An interesting feature is the out-of-phase variation between the coastal and open water branches. For example, the coastal (open water) branch strengthens (weakens) from September to March and weakens (strengthens) in spring (from March to September). From January to April, the coastal branch is strong with two cores, one in the upper layer (above the pycnocline, i.e., $\sigma_\theta < 25.0 \text{ kg m}^{-3}$) and the other in the intermediate layer ($25.0 \text{ kg m}^{-3} < \sigma_\theta < 26.5 \text{ kg m}^{-3}$). The maximum northward velocity is around 0.15 m s^{-1} . The open water branch is located in the deep layer ($\sigma_\theta > 26.5 \text{ kg m}^{-3}$) with a maximum northward velocity of 0.15 m s^{-1} . From April to October, the coastal (open water) branch weakens (strengthens) with a maximum northward velocity around 0.05 m s^{-1} (0.4 m s^{-1} in August). Besides, the open water branch extends from near surface to deep layer. Such an out-of-phase variation is also easily seen in the cross section of v -component on z level (Fig. 11.9b).

North Equatorial Counter Current (Along 130°E)

The North Equatorial Counter Current, originated from the confluence of southward flowing Mindanao Current and northward flowing New Guinea Coastal Undercurrent, is an eastward equatorial flow that is centered at around 5°N (e.g., Lukas et al. 1991). We use the east–west geostrophic velocities on isopycnal surfaces along 130°E longitude to represent the seasonal variability of the North Equatorial Counter Current (Fig. 11.10a). Positive (negative) values show the eastward (westward) flow. The negative values (westward flow) are shaded in gray.

The North Equatorial Counter Current extends from the surface to the level of $\sigma_\theta = 27.0 \text{ kg m}^{-3}$ all the year round. It occurs between 3° and 8°N from June to December and south of 8°N with two branches separated by an upper layer westward current from January to May, with two jet-cores, located in the pycnocline layer (centered around $\sigma_\theta = 25.0 \text{ kg m}^{-3}$) and in the intermediate layer ($27.0 \text{ kg m}^{-3} > \sigma_\theta > 26.0 \text{ kg m}^{-3}$), respectively. The pycnocline layer jet-core has a strong seasonal variability with a maximum speed of 0.4 m s^{-1} (0.1 m s^{-1}) in August (February). The intermediate layer jet-core is usually stronger than the pycnocline layer core with less seasonal variability. The maximum speed in the intermediate layer jet-core is found to be 0.45 m s^{-1} in February and 0.2 m s^{-1} in May.

Halmahera Eddy (Along 130°E)

The v -component on σ_θ is converted to that on z levels (Fig. 11.10b). The North Equatorial Counter Current separates near 130°E into three branches,

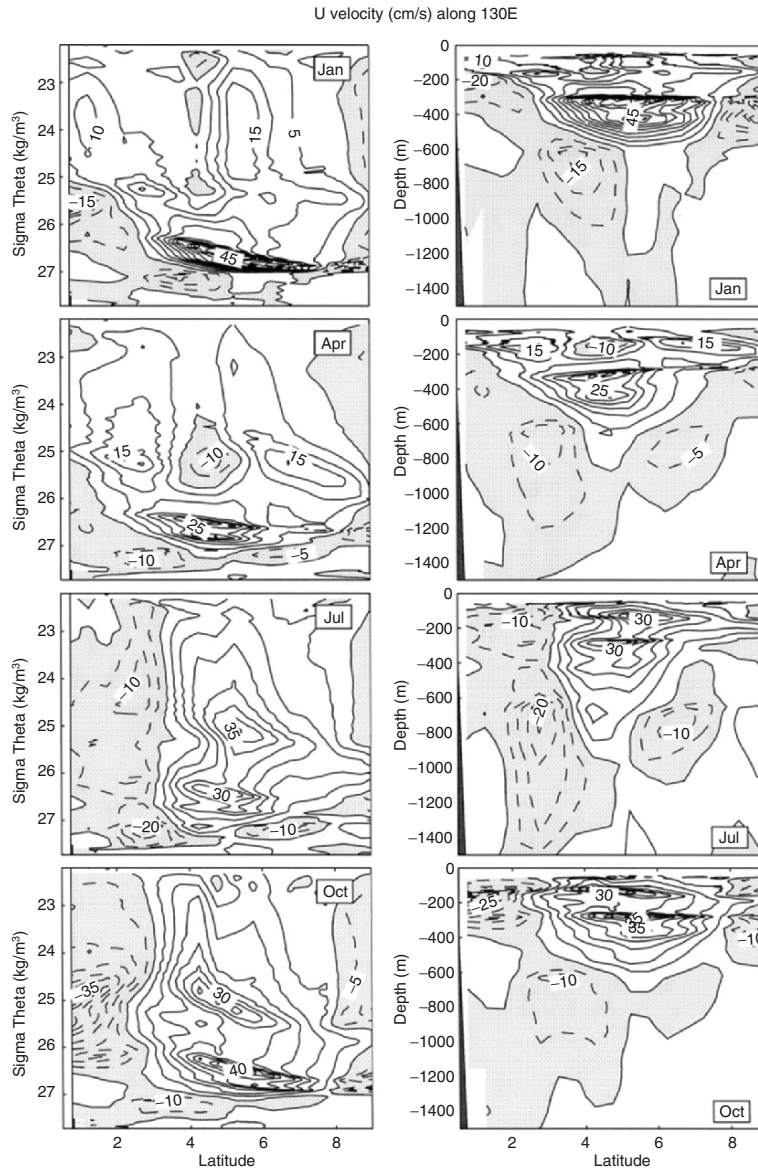


Fig. 11.10. Seasonal variation of east-west velocities (unit: cm s^{-1} ; eastward positive) along 130°E longitude representing the North Equatorial Counter Current: (a) on σ_θ levels, and (b) on z levels (from Chu et al. 2003d, Chinese Journal of Oceanology and Limnology)

the central branch (continuation of the North Equatorial Counter Current), the north branch feeding into the Mindanao Eddy, and south branch feeding into the Halmahera Eddy. The strength of the Halmahera Eddy is represented by the velocity of the westward flow. It strengthens in summer (June–August) and weakens in winter (December). The maximum westward speed in the southern flank reaches 0.2 m s^{-1} in summer and 0.10 m s^{-1} in winter.

11.2.5 Vertically Integrated Velocity

Monthly mean vertically integrated (for the whole water column) velocity is computed to represent the volume transport (Fig. 11.11). Three major currents (Mindanao Current, New Guinea Coast Undercurrent, and North Equatorial Counter Current) and dual eddies (Mindanao eddy and Halmahera eddy) are also identified in the integrated flow field whose seasonal variation is evident. The integrated Mindanao Current strengthens from October to February and weakens from April to August. After leaving the south tip of Mindanao Island, it flows southeastward following the continental slope and recirculates northeastward near Morotai Island and then turns towards the east. The recirculation leads to the formation of the Mindanao eddy (cyclonic eddy), and the eastward flow feeds into the North Equatorial Counter Current. The New Guinea Coastal Undercurrent flows northwestward into the area between 134° and 136°E at 0.5°N latitude and then joins the North Equatorial Counter Current at 133°E , 3°N . The dual eddy pattern is evident from June to August.

11.2.6 Volume Transport

Mindanao Current

The computed monthly total and layered (between two σ_θ levels) volume transports across $7^\circ 15'\text{N}$ (northward positive) between $126^\circ 45'$ (Mindanao coast) and $130^\circ 45'\text{E}$ longitudes (Fig. 11.12) are used to represent the seasonal variability of Mindanao Current volume transport. The dashed, dotted, and solid curves indicate northward, southward, and net transports, respectively. The northward flow is weaker than the southward flow for the total transport and the most layered transports except the deep layer ($\sigma_\theta \geq 27.025 \text{ kg m}^{-3}$), where the northward flow is dominant. The total transport is negative (southward) all the year round with a minimum value of -40.2 Sv in January and a maximum value of -5.3 Sv in June and July having the annual mean transport of -23.4 Sv , which agrees with many existing estimations such as -26 , -20 Sv by Lukas et al. (1991).

North Equatorial Counter Current

Monthly total and layered (between two σ_θ levels) volume transports are computed across 130°E (eastward positive) between $0^\circ 45'\text{N}$ and $8^\circ 15'\text{N}$

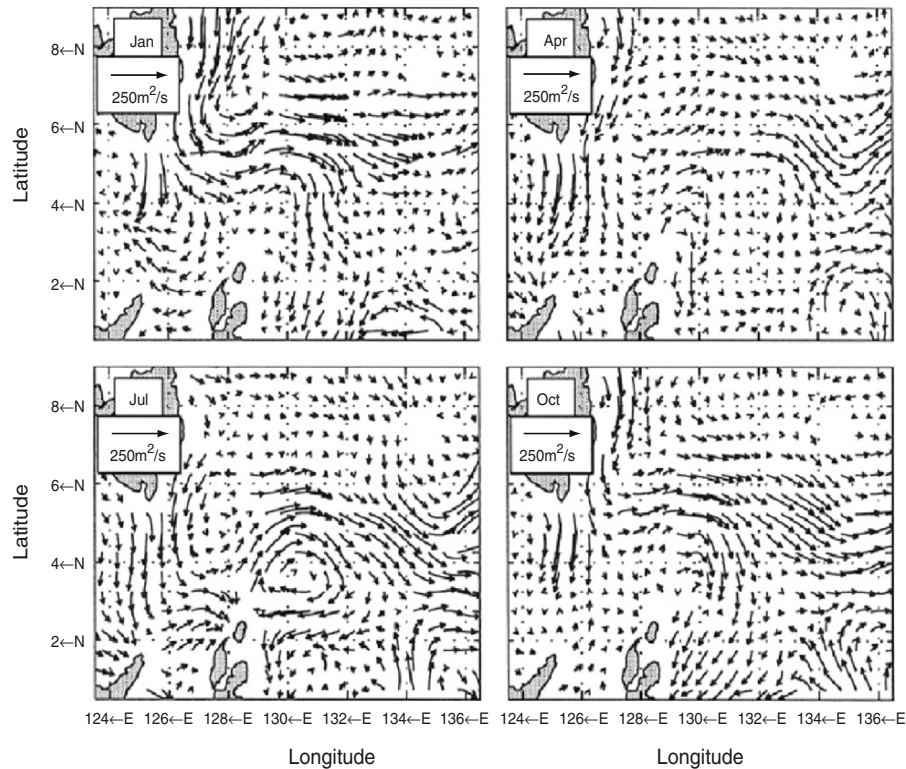


Fig. 11.11. Seasonal variability of vertically integrated velocity vectors (from Chu and Fan 2006, *Journal of Marine Systems*)

(Fig. 11.13) to represent the seasonal variability of North Equatorial Counter Current volume transport. The dashed, dotted, and solid curves indicate eastward, westward, and net eastward transports, respectively. The westward flow is weaker than the eastward flow for the total transport and the layered transports.

The total transport is positive (eastward) all the year round with a maximum value of 45.7 Sv in January and a minimum value of 20.0 Sv in April with the annual mean transport of 34.4 Sv, which is consistent with the estimation (35 Sv) of Johnson and McPhaden (1999) using the geostrophic calculations relative to a reference surface of 900 dbar.

Transport to the Celebes Sea

Monthly total and layered (between two σ_θ levels) volume transports are computed across $125^\circ 15' E$ (eastward positive) between $2^\circ 15' N$ and $5^\circ 45' N$ (Fig. 11.14) to represent the seasonal variability of volume transport to the

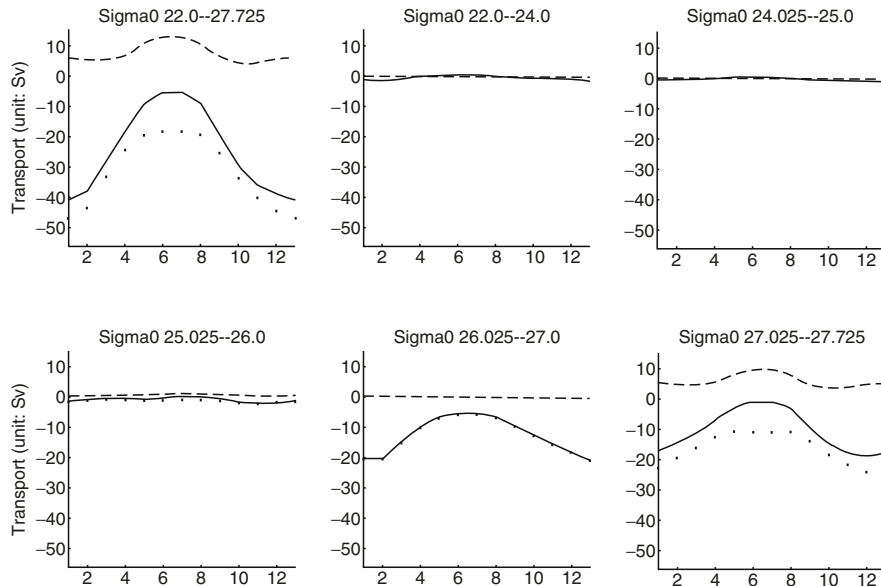


Fig. 11.12. Monthly variation of total and layered (between two σ_θ levels) latitudinal volume transports (northward positive) across $7^\circ 15' 6''$ N latitude between $126^\circ 45'$ and $130^\circ 45'$ E, representing the Mindanao Current transport (Sv): (a) total, (b) $\sigma_\theta < 24.0$, (c) σ_θ from 24.0 to 25.0, (d) σ_θ from 25.0 to 26.0, (e) σ_θ from 26.0 to 27.0, and (f) $\sigma_\theta > 27.0$. The *dashed*, *dotted*, and *solid* curves indicate the northward, the southward, and the net transports, respectively (from Chu et al. 2003d, Chinese Journal of Oceanology and Limnology)

Celebes Sea. The dashed, dotted, and solid curves indicate eastward, westward, and net transports, respectively. The eastward flow is weaker than the westward flow for the total transport (denoting water entering the Celebes Sea) in January (-16.7 Sv). The strength of the volume transport of the Mindanao Current into the Celebes Sea weakens from winter to spring, and in summer (August), the net transport (4.6 Sv) is eastward that indicates outflow from the Celebes Sea to the Pacific Ocean. The most layered transports are negative (westward) all the year round except the midlayer ($26.0 \text{ kg m}^{-3} \geq \sigma_\theta \geq 25.025 \text{ kg m}^{-3}$), where the eastward flow is dominant.

Transport to the Molucca Sea

Monthly total and layered (between two σ_θ levels) volume transports across $1^\circ 45'$ N (northward positive) between $125^\circ 45'$ E and $127^\circ 25'$ E (Fig. 11.15) to represent the seasonal variability of volume transport to the Malacca Sea. The dashed, dotted, and solid curves indicate northward, southward, and net transports, respectively. The southward flow (into the Malacca Sea) is

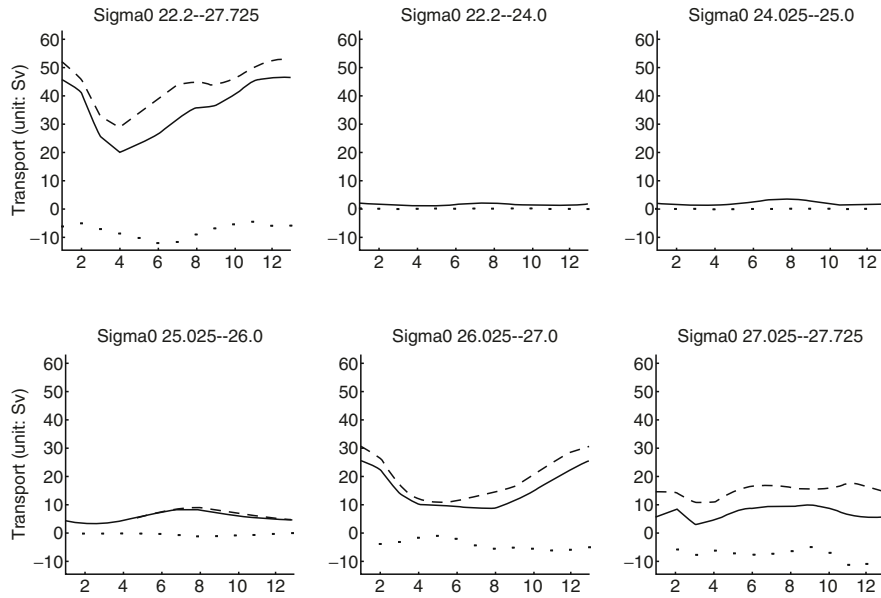


Fig. 11.13. Monthly variation of total and layered (between two σ_θ levels) zonal volume transports across 130°E longitude between $0^\circ45'$ and $6^\circ15'\text{E}$, representing the North Equatorial Counter Current transport (Sv): (a) total, (b) $\sigma_\theta < 24.0$, (c) σ_θ from 24.0 to 25.0, (d) σ_θ from 25.0 to 26.0, (e) σ_θ from 26.0 to 27.0, and (f) $\sigma_\theta > 27.0$. The *dashed*, *dotted*, and *solid* curves indicate the northward, the southward, and the net transports, respectively (from Chu et al. 2003d, Chinese Journal of Oceanology and Limnology)

little weaker than the northward flow (out of the Malacca Sea) for the total transport in January (1.5 Sv).

The net northward volume transport decreases with time. From February to May, the net volume transport is southward with the minimum value of -1.8 Sv in May. After May, the net volume transport becomes northward and enhances from 2.8 Sv in June to 7.9 Sv (maximum value) in August. The southward volume transport (into the Malacca Sea) is evident from January to June in the midlayer ($26.0\text{ kg m}^{-3} \geq \sigma_\theta \geq 25.025\text{ kg m}^{-3}$).

Transport to the Halmahera Sea

Monthly total and layered (between two σ_θ levels) volume transports across $1^\circ45'\text{N}$ (northward positive) between $129^\circ30'\text{E}$ and $136^\circ30'\text{E}$ (Fig. 11.16) to represent the seasonal variability of volume transport to the Halmahera Sea. The dashed, dotted, and solid curves indicate northward, southward, and net transports, respectively. The southward flow (into the Halmahera Sea) is stronger than the northward flow (out of the Halmahera Sea) for the total transport in most of the year except in June and July. The net

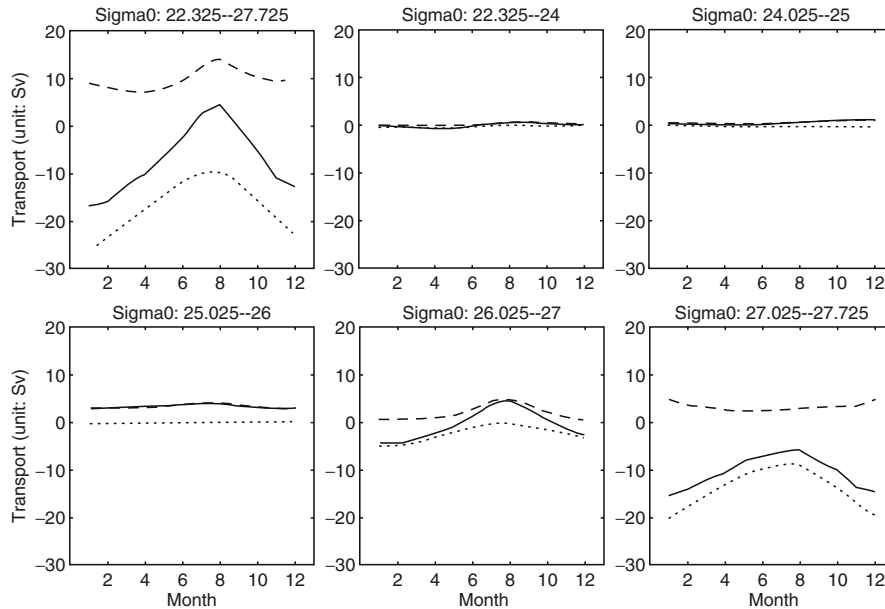


Fig. 11.14. Monthly variation of total and layered (between two σ_θ levels) zonal volume transports across $125^\circ 15'E$ (eastward positive) longitude between $2^\circ 15'N$ and $5^\circ 45'N$, representing the volume transport (Sv) between the Celebes Sea and Pacific Ocean: (a) total, (b) $\sigma_\theta < 24.0$, (c) σ_θ from 24.0 to 25.0, (d) σ_θ from 25.0 to 26.0, (e) σ_θ from 26.0 to 27.0, and (f) $\sigma_\theta > 27.0$. The *dashed*, *dotted*, and *solid* curves indicate the northward, the southward, and the net transports, respectively (from Chu et al. 2003d, Chinese Journal of Oceanology and Limnology)

southward volume transport (into the Halmahera Sea) reaches the maximum strength (-19.6 Sv) in January. The net southward volume transport weakens from January to March (-4.5 Sv) and then strengthens from March to May (-16.4 Sv) with time. The net volume transport is positive (out of the Halmahera Sea) in June (5.6 Sv) and July (11.9 Sv). The net volume transport is southward from August (-3.5 Sv) to December (-18.2 Sv). The southward volume transport (into the Halmahera Sea) is dominant in the two deep layers ($27.0\text{ kg m}^{-3} \geq \sigma_\theta \geq 26.025\text{ kg m}^{-3}$) and ($27.725\text{ kg m}^{-3} \geq \sigma_\theta \geq 27.025\text{ kg m}^{-3}$).

11.3 Indonesia Throughflow

The Indonesian Throughflow is the only interbasin exchange of water at low latitudes from the Pacific to the Indian Ocean. The calculated monthly mean Ψ and (U, V) fields in the vicinity of Indonesia (Fig. 11.17) shows the volume transport and the depth-integrated circulation pattern have weak

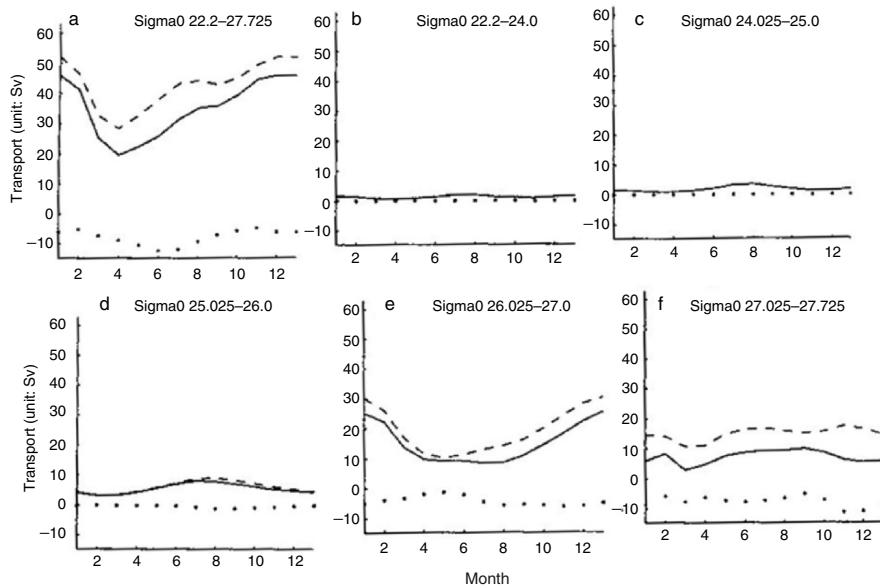


Fig. 11.15. Monthly variation of total and layered (between two σ_θ levels) latitudinal volume transports (northward positive) across $1^\circ 45' N$ latitude between $125^\circ 45' E$ and $127^\circ 25' E$, representing the seasonal variability of volume transport to the Malacca Sea: (a) total, (b) $\sigma_\theta < 24.0$, (c) σ_θ from 24.0 to 25.0, (d) σ_θ from 25.0 to 26.0, (e) σ_θ from 26.0 to 27.0, and (f) $\sigma_\theta > 27.0$. The *dashed*, *dotted*, and *solid* curves indicate the northward, the southward, and the net transports, respectively (from Chu et al. 2003d, Chinese Journal of Oceanology and Limnology)

seasonal variations and are quite similar from the surface to intermediate depth currents shown in the earlier description (e.g., Fine et al. 1994; Lukas et al. 1996; Godfrey 1996): Water from the Pacific Ocean enters the Indonesian seas near the region where the New Guinea Coast Current (10 Sv) meets the Mindanao Current (10–20 Sv), as well through the South Sulu Sea from the South China Sea (Fig. 11.3). The New Guinea Coastal Current transports 10 Sv of water around the Halmahera Eddy and joins the southeastward flowing North Equatorial Counter Current. The North Equatorial Current bifurcates east of the Philippines, with the southern branch becoming the Mindanao Current and the northern branch becoming the Kuroshio. Part of the water flowing southward in the Mindanao Current recirculates 10–20 Sv around the Mindanao Eddy to join the North Equatorial Counter Current while the remainder enters the Celebes Sea, where some South Pacific water passes into the Indonesian seas near Halmahera. The majority of the Indonesian Throughflow water exits to the Indian Ocean through the Timor Strait, with smaller transport through the Savu Sea and Lomok Strait. The

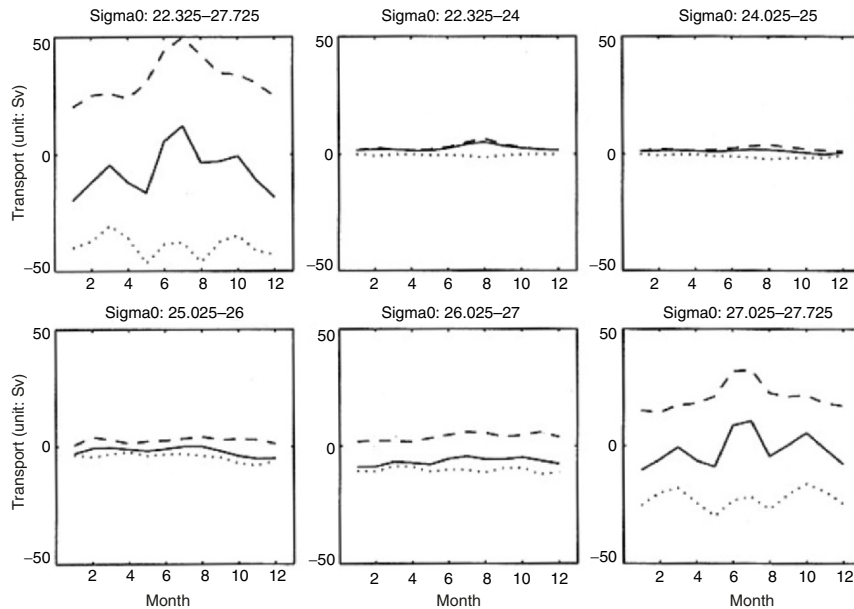


Fig. 11.16. Monthly variation of total and layered (between two σ_θ levels) latitudinal volume transports (northward positive) across $1^\circ 45'N$ latitude between $129^\circ 30' E$ and $136^\circ 30' E$, representing the seasonal variability of volume transport to the Halmahera Sea: (a) total, (b) $\sigma_\theta < 24.0$, (c) σ_θ from 24.0 to 25.0, (d) σ_θ from 25.0 to 26.0, (e) σ_θ from 26.0 to 27.0, and (f) $\sigma_\theta > 27.0$. The *dashed*, *dotted*, and *solid* curves indicate the northward, the southward, and the net transports, respectively (from Chu et al. 2003d, Chinese Journal of Oceanology and Limnology)

Mindanao Eddy (cyclonic) near the southern Philippines and the Halmahera Eddy (anticyclonic) near Indonesia are well represented in the inverted Ψ and (U, V) fields (Fig. 11.3). No strong flow is obtained through the Makassar Strait in the present computation, which is the discrepancy with earlier studies.

The monthly volume transport between Bali ($8^\circ S, 113.5^\circ E$) and northwest coast of Australia ($20^\circ S, 120^\circ E$) represents most of the Indonesian Throughflow (Fig. 11.17) and shows a weak seasonal variability with a maximum value of 22.9 Sv in December and a minimum value of 20.3 Sv in August. This agrees qualitatively well with the observational data (16.2 Sv) collected along the same section (Bali to Australia) in August 1989 by Fieux et al. (1994) and with the numerical simulated data (25.7 Sv using the 1.5 reduced gravity model, 15.8 Sv using the nonlinear six-layer model) reported by Morey et al. (1999).

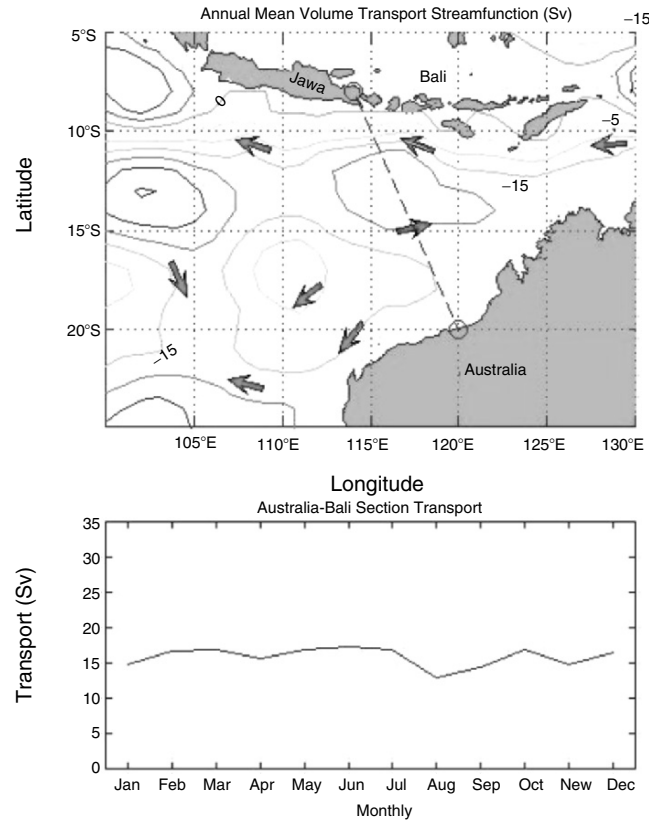


Fig. 11.17. Inverted volume transport between Bali (8°S , 113.5°E) and northwest coast of Australia (20°S , 120°E): (a) annual mean Ψ -field, and (b) monthly variability (from Chu and Fan 2006, *Journal of Marine Systems*)

11.4 Kuroshio Transport and its Intrusion into the South China Sea

Difference of the Ψ -values is used between Japan and the center of the subtropical gyre as the Kuroshio volume transport (Fig. 11.18). The monthly Kuroshio volume transport is very steady (very weak seasonal variation) with the transport from 57.7 to 62.4 Sv (Fig. 11.18). Our calculation of the Kuroshio volume transport agrees with Schmitz's (1996b) estimation (52.4 Sv), and larger than Bingham and Talley (1991) estimation (26.3 Sv), using an inverse method and Chen et al.'s (1992) estimation (30.3 Sv), using the geostrophic calculation (referenced to ADCP).

The seasonal variation of the intrusion of the Kuroshio Water into the South China Sea through the Luzon Strait has been investigated by many authors (e.g., Shaw 1989; Chu and Li 2000). Shaw (1989) used the discriminant

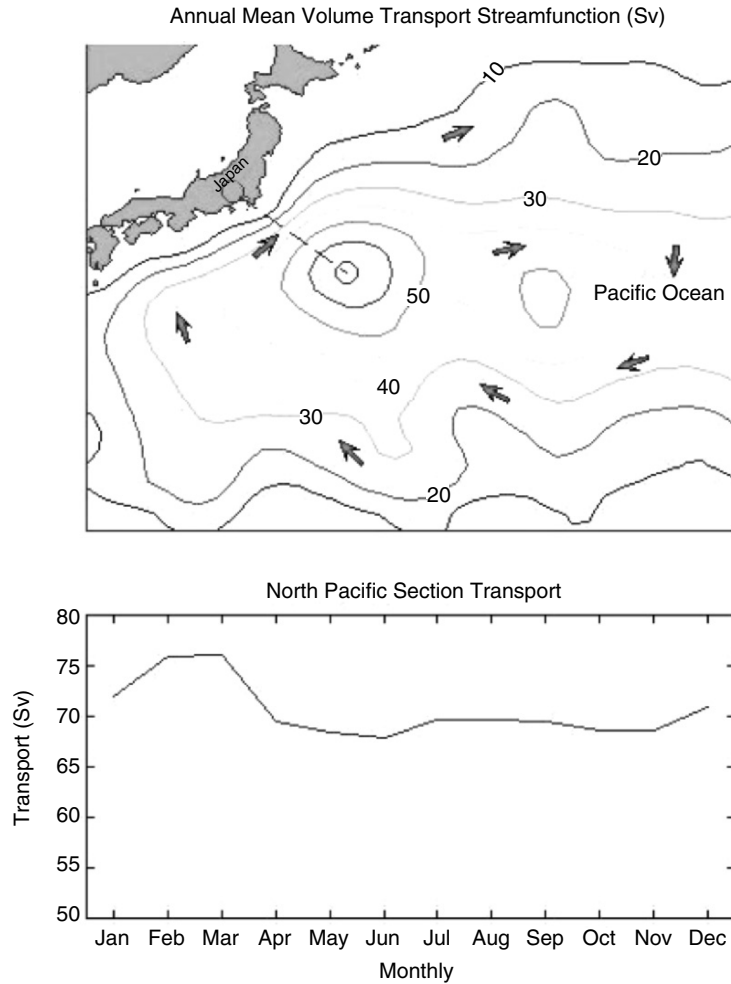


Fig. 11.18. (a) Annual mean Ψ field and (b) Monthly variation of the Kuroshio transport (from Chu and Fan 2006, *Journal of Marine Systems*)

analysis method to classify the water mass T, S characteristics at 150, 200, and 250 m, and found that water characteristics of the Philippine Sea (Kuroshio) were identifiable along the continental margin south of China from October to January. The presence of this water indicated an intrusion current from the Philippine Sea into the South China Sea. Chu and Li (2000) used the P-vector inverse method (Chu 1995a, b, 2000) to determine the isopycnal surface geostrophic velocities in the South China Sea. The annual and monthly mean volume transports through the Luzon Strait (Fig. 11.19) show Kuroshio intrusion all the year round with a seasonal variation (8–15 Sv). This estimation is larger than the existing estimations such as 2–3 Sv (Wyrтки 1961a, b), 8–10 Sv

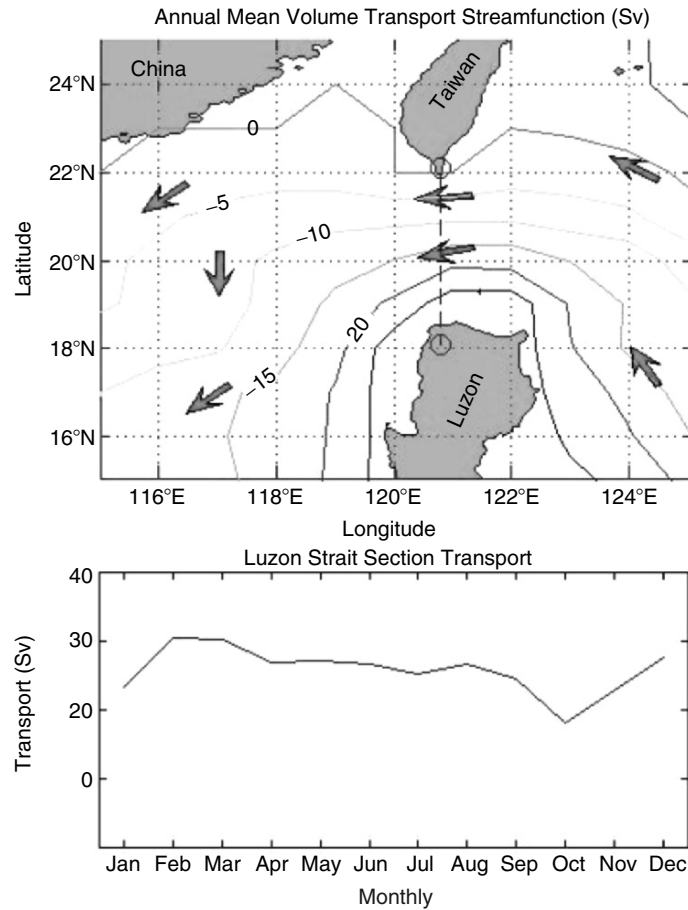


Fig. 11.19. (a) Annual mean Ψ field and (b) monthly variation of volume transport through the Luzon Strait into the South China Sea (from Chu and Fan 2006, *Journal of Marine Systems*)

(Huang et al. 1994), 2.4–4.4 Sv (Metzger and Hurlburt 1996), and 1.4–13.7 Sv (Chu and Li 2000) (see Table 6.3).

11.5 Northwest Pacific Subtropical Counter Current on Isopycnal Surface

11.5.1 General Features

One expects a westward flow in the subtropical northwest Pacific (Fig. 11.20), feeding the western boundary current based on the classical wind-driven theory. However, early observations (e.g., Uda 1955) show the occurrence of

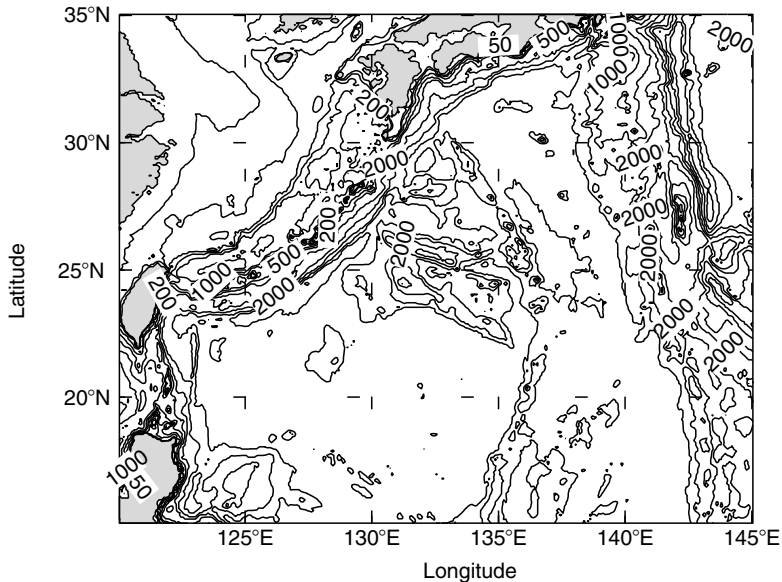


Fig. 11.20. Geography and bottom topography of the Northwest Pacific (from Chu et al. 2002a, *Geophysical Research Letters*)

eastward flow segment north of 15°N . Yoshida and Kidokoro (1967a, b) predicted the existence of an eastward current in the subtropical region especially $20\text{--}25^{\circ}\text{N}$ after computing the Sverdrup transport currents from the surface wind stress, and named it as the Subtropical Counter Current. This current was subsequently confirmed by Uda and Hasunuma (1969) from direct current meter observations and geostrophic calculations, and by White et al. (1978), using historical XBT data. Qiu (1999) inferred temporal and spatial variability of Subtropical Counter Current using the altimeter data from the first $5\frac{1}{4}$ -year TOPEX/Poseidon mission, and found that the eddy kinetic energy of Subtropical Counter Current is maximum in April/May and minimum in December/January. Regardless of the advancement of the knowledge on Subtropical Counter Current, there is still lack of quantitative description of this current such as its origin and spatial variability especially on the isopycnal surface.

11.5.2 Circulations

The P-vector method on the isopycnal surfaces (see Chap. 6) is used to compute the absolute velocity in the northwest Pacific [$15\text{--}35^{\circ}\text{N}$, $120\text{--}145^{\circ}\text{E}$] from the Navy's GDEM climatological June temperature and salinity data set with $0.5^{\circ} \times 0.5^{\circ}$ resolution (Teague et al. 1990). It is noted that only the geostrophic velocity is obtained using the P-vector method. Near the surface

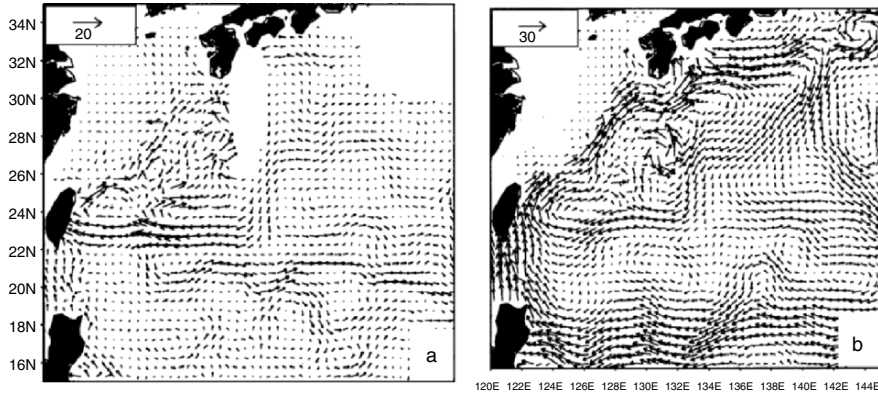


Fig. 11.21. Absolute velocity vectors (unit: cm s^{-1}) in June on isopycnal surface (a) $\sigma_\theta = 23.5$, and (b) $\sigma_\theta = 25.0$ (from Chu et al. 2002a, Geophysical Research Letters)

the geostrophic current is strong, at least in the Kuroshio. Since the isopycnal $\sigma_\theta = 23.5 \text{ kg m}^{-3}$ outcrops at $26\text{--}30^\circ\text{N}$ (Fig. 11.21a), the isopycnal surface circulations near $\sigma_\theta = 23.5 \text{ kg m}^{-3}$ might not be consistent when the direct measurements are taken, with current meters south of Honsu. Thus, the velocity at $\sigma_\theta = 25.0 \text{ kg m}^{-3}$ is chosen to represent the Kuroshio Current and its extension near Honsu (Chu et al. 2002a).

Most important features from the computation are the westward flowing North Equatorial Current, the northeast flowing Kuroshio Current and the associated eddies and recirculation current from Kuroshio, and the eastward flowing Subtropical Counter Current. At $\sigma_\theta = 23.5$, the North Equatorial Current is very weak. The eastward flowing Subtropical Counter Current originates mainly from the southward turning of Recirculation Current from Kuroshio (westward flowing) at ($127\text{--}128^\circ\text{E}$, 23°N).

At $\sigma_\theta = 25.0$ (Fig. 11.21b), the North Equatorial Current is quite strong. Between 128 and 134°E a weak current flowing eastward along 21°N is the north flank of an anticyclonic eddy located at $18\text{--}21^\circ\text{N}$, $128\text{--}134^\circ\text{E}$ (Fig. 10.21b). Evident eastward flow (i.e., Subtropical Counter Current) occurs east of 135°E , which is different from the Subtropical Counter Current at $\sigma_\theta = 23.5$. At deeper level ($\sigma_\theta = 25.8$), there is no eastward current in the subtropics.

Two theories are available to explain the formation of the Subtropical Counter Current: (a) the Ekman convergence (e.g., Roden 1980) induced by westerlies to the north and trade winds to the south, and (b) the geostrophic convergence, which causes the midgyre front and its associated zonal current (Cushman-Roisin 1984; Kubokawa 1997). Since the velocity is wholly determined by the density structure, the identification of the Subtropical Counter Current at this point tends to confirm the validity of the geostrophic convergence theory. Comparison between Fig. 11.21a, and b shows a strong vertical

shear in the Subtropical Counter Current. The baroclinic instability associated with the vertical shear causes Subtropical Counter Current to meander between 19 and 25°N with the main axis at around 21.5°N, and makes the eddy generation along it. As the Subtropical Counter Current flows eastward entraining water from eddies, it becomes wider with a maximum width of 6° of latitude (18–24°N) at 136–140°E.

11.5.3 Spatial Variability of the Subtropical Counter Current

The spatial variability of the Subtropical Counter Current is represented by four meridional cross sections (127.5°E, 129.5°E, 133.5°E, 138.5°E) of the east–west absolute velocities on isopycnal surfaces (Fig. 11.22).

The Subtropical Counter Current is the eastward flow near the Tropic of Cancer (23.5°N), and occurs in the upper layer above $\sigma_\theta = 25.8$. The core of Subtropical Counter Current is not located at the surface. The axis of this

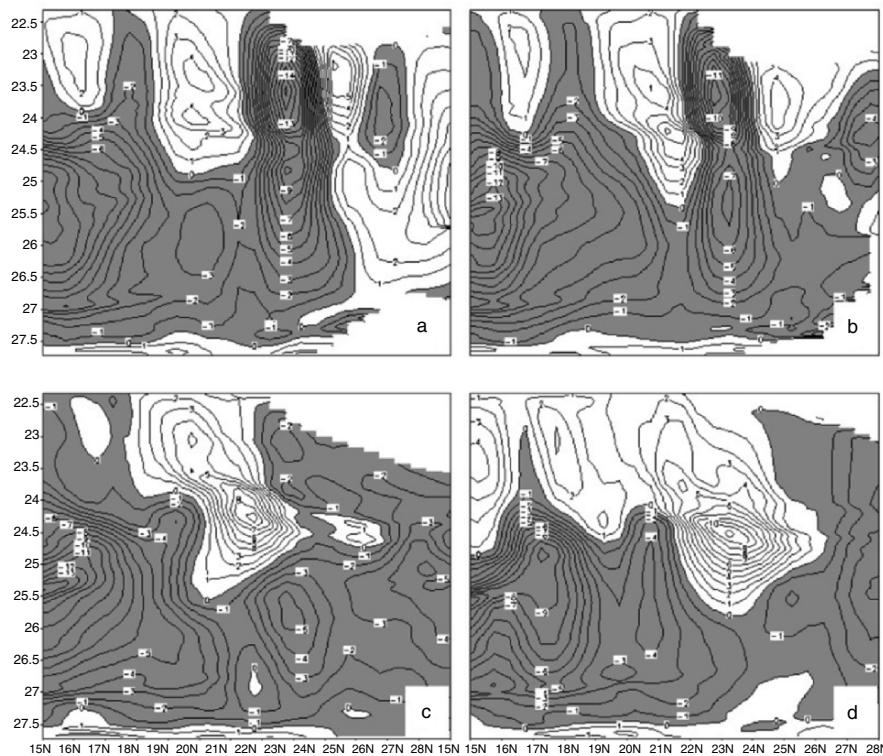


Fig. 11.22. East–west absolute velocity (unit: cm s^{-1}) in June at meridional cross sections: (a) 127.5°E, (b) 129.5°E, (c) 133.5°E, and (d) 138.5°E. Here, the shaded part (negative values) refers to the westward velocity (from Chu et al. 2002a, *Geophysical Research Letters*)

Current shifts northward as σ_θ increases and the speed increases eastward. For example, the maximum velocity of Subtropical Counter Current is around 0.04 m s^{-1} near 20°N between $\sigma_\theta = 23.0$ and $\sigma_\theta = 24.0$ at 127.5°E cross section (Fig. 11.22a), greater than 0.06 m s^{-1} near 21°N and $\sigma_\theta = 24.2$ at 129.5°E cross section (Fig. 11.22b), greater than 0.09 m s^{-1} near 21.5°N and $\sigma_\theta = 24.3$ at 133.5°E cross section (Fig. 11.22c), and greater than 0.12 m s^{-1} near 23°N and $\sigma_\theta = 24.5$ at 138.5°E cross section (Fig. 11.22d). At the σ_θ level, where the core of the Subtropical Counter Current is located, the speed of this Current is usually higher than the speed of the North Equatorial Current. This is because the core of the North Equatorial Current is located at deeper layers. The volume transport of the Subtropical Counter Current at 138.5°E is estimated as 8 Sv.

11.5.4 Potential Vorticity

The Subtropical Counter Current mainly comes from southward turning of the recirculation current from Kuroshio, which originates at the southern latitudes ($\sim 15^\circ\text{N}$) where the potential vorticity is relatively low. Scale analysis shows that the dissipative force alone is not sufficient to remove the low potential vorticity anomalies (Pedlosky 1987) for a narrow boundary current such as the Kuroshio and the recirculation from the Kuroshio. Talley (1988) pointed out the existence of a minimum potential vorticity area corresponding to the subtropical mode water located at $\sigma_\theta = 25.4$ level in the western Pacific. The minimum potential vorticity enclosed by $2.5 \times 10^{-7} \text{ m}^{-1} \text{ s}^{-1}$ at the cross section of 138.5°E (Fig. 11.23) indicates the location of the subtropical mode water. The core of the Subtropical Counter Current is located above the southern boundary of the subtropical mode water (i.e., minimum potential vorticity) from the comparison between Figs. 11.22d and 11.23. This result consists of the recent modeling studies (e.g., Kubokawa 1997).

11.5.5 Major Features

The eastward currents at upper levels (above $\sigma_\theta = 24.5$) reveal multicore structure. The Subtropical Counter Current is located at $19\text{--}23^\circ\text{N}$. Eastward flow segments occurring south of 17°N are usually the southern flanks of local cyclonic eddies rather than a part of a continuous current. Below the level of $\sigma_\theta = 24.5$, the Subtropical Counter Current has a single core located $19\text{--}23^\circ\text{N}$ west of 134°E and $22\text{--}26^\circ\text{N}$ east of 134°E .

The Subtropical Counter Current originates at 122.5°E at $\sigma_\theta = 23.5$. As σ_θ increases, the origin of the Subtropical Counter Current shifts eastward. The major source of the Current is the southeastward turning of the recirculation current from Kuroshio. This Current strengthens and broadens as it flows eastward. The volume transport of the Subtropical Counter Current at 138.5°E is estimated as 8 Sv.

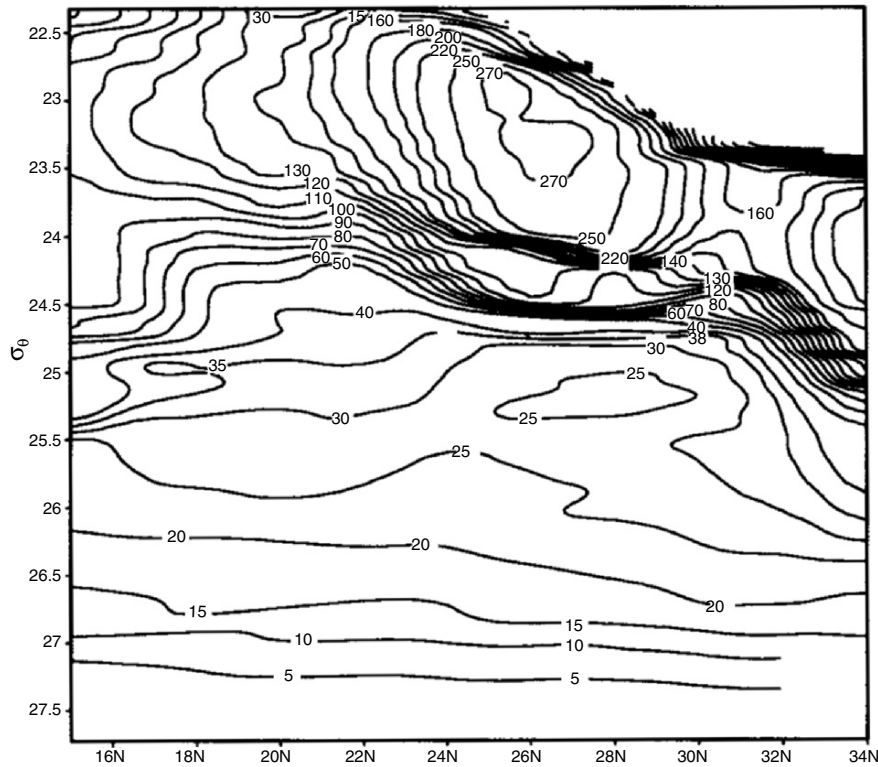


Fig. 11.23. Meridional cross section (138.5°E) of June potential vorticity (in $10^{-10} \text{ cm}^{-1}\text{s}^{-1}$) (from Chu et al. 2002a, *Geophysical Research Letters*)

The core of the Subtropical Counter Current is not located at the surface, but in the layer between $\sigma_{\theta} = 23.0$ and $\sigma_{\theta} = 24.7$, where this Current is stronger than North Equatorial Current. Moreover, the Subtropical Counter Current core is above the southern boundary of the subtropical mode water. The Subtropical Counter Current disappears below the level of $\sigma_{\theta} = 25.8$, that is to say, this Current is an upper ocean current. Its maximum depth is around 300 m.

11.6 Seasonal Variability of the South China Sea Thermohaline Structure

11.6.1 General Thermal Characteristics

The South China Sea is the largest marginal sea in the West Pacific Ocean. It has a bottom topography that makes it a unique semienclosed ocean basin overlaid by a pronounced monsoon surface wind. Based on limited data sets,

studies show that surface eddies in the South China Sea are predominantly cyclonic in winter and spring and anticyclonic in summer, with sizes ranging from small to mesoscale (Wyrski 1961a, b; Huang et al. 1994). Both cold and warm eddies exist in the South China Sea. Dale (1956) and Uda and Nakao (1972) reported a cold eddy off the central Vietnamese Coast in summer, and Nitani (1970) found a cold eddy located to the northwest of Luzon. Reports from the South China Sea Institute of Oceanology (1985) indicate that in the central South China Sea a warm-core eddy appears in summer and winter, which is closer to Vietnam in summer at the surface. In addition, a cold-core eddy was detected in the central South China Sea from the 29th December 1993 to 5th January 1994 according to analysis of the TOPEX/Poseidon data (Soong et al. (1995)).

Chu et al. (1997c) and Chu and Chang (1997) identified a central South China Sea surface warm-core eddy in mid-May from a more complete historical data set – the MOODS. From the composite analysis of the US National Centers for Environmental Prediction (NCEP) monthly SST fields (1982–1994), Chu et al. (1997d) found that during the spring-to-summer monsoon transition (March to May) a warm anomaly (greater than 1.8°C) is formed in the central South China Sea at 112°E – $119^{\circ}30'\text{E}$, 15°N – $19^{\circ}30'\text{N}$. This warm eddy appears in the central South China Sea (west of Luzon Island) during the late spring season and strengthens until the onset of the summer monsoon (mid-May) and then weakens and disappears at the end of May. Although its size and intensity varies, the warm eddy releases large moisture and heat fluxes into the atmosphere and in turn affects the monsoon circulation. Most of the existing studies on the seasonal eddy variability were based on the surface data. Recently, the seasonal and interannual variability of temperature field was identified by Wang et al. (1999) using the XBT data; and the seasonal and interannual variability of (T, S) fields was identified by Chu et al. (2002c) using the MOODS data. In this section, we present the thermohaline variability using the MOODS data.

11.6.2 Establishment of Monthly Gridded Data from the MOODS

The MOODS for the South China Sea contains 116,019 temperature and 9,617 salinity profiles (Fig. 11.24) from 1964 to 1984. The primary editing procedures included removal of profiles with obviously erroneous location, profiles with large spikes, and profiles displaying features that do not match the characteristics of surrounding profiles. In the shallow water, this procedure can be partially automated, but it also involves subjective interpretation because of the under sampling of MOODS, compared to the spatial and temporal variability of the ocean. Furthermore, vertical resolution and data quality are also highly variable depending much on instrument type and sampling expertise. Temporal and spatial irregularities along with the data resolution and quality problems must be carefully weighed in order to avoid mathematically induced variability.

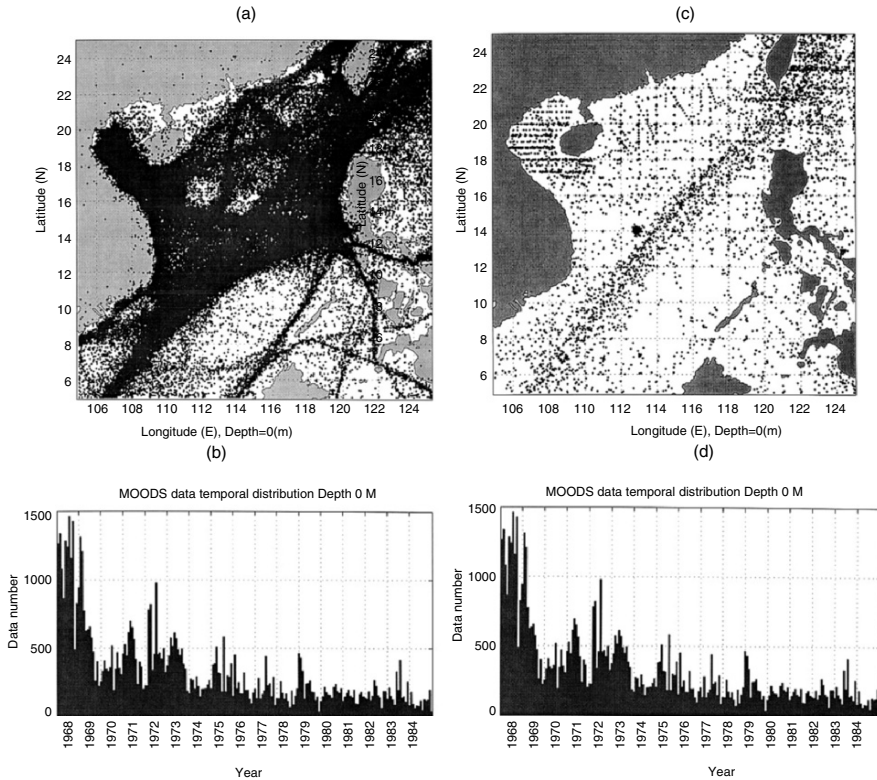


Fig. 11.24. (a) Spatial and (b) temporal distributions of the MOODS temperature stations, (c) spatial and (d) temporal distributions of the MOODS salinity stations, during 1964–1984 (from Chu et al. 2002c, *Acta Oceanologia Sinica*)

The temperature profiles are binned from 1968 to 1984 into monthly data for an individual year which produced 204 temperature data sets. The salinity profiles are binned into monthly climatology data which have 12 mean monthly salinity data sets.

The climatological T, S data are computed from the MOODS data using the z -level analysis. A two-scale optimal interpolation (OI) scheme (Gandin 1965; Lozano et al. 1996) is used to map the MOODS observations to a $0.5^\circ \times 1^\circ$ grid (finer resolution in the zonal direction) at 13 levels (Table 11.1) and to establish monthly climatology of temperature and salinity data set (total 12 fields). The large-scale OI was used to estimate the background mean with a decorrelation scale of 450 km. The mesoscale OI was used to map the observational anomaly from the background mean field into a regular grid with a spatial decorrelation scale of 75 km and a temporal decorrelation scale of 10 days. The spatial and temporal decorrelation scales associated to the mean field were estimated from the covariance matrix obtained from the MOODS

Table 11.1. Standard vertical levels

level	depth (m)	level	depth (m)	level	depth (m)	level	depth (m)
1	0	5	50	9	150	13	400
2	10	6	75	10	200		
3	20	7	100	11	250		
4	30	8	125	12	300		

for the South China Sea (Chu et al. 1997c). The large-scale mean was computed using the temperature and salinity profiles. The decorrelation length scale for the fluctuations from the mean was estimated from the MOODS data. The results shown below are relatively insensitive to the length scale in the range of 60–90 km. The decorrelation timescale was selected to ensure synopticity. Our interpolated fields are quite similar to the fields depicted by Chu et al. (2002c), using the cubic spline method.

11.6.3 Composite Analysis

Let $\psi(x_i, y_j, z_k, \tau_l, t_m)$ represent temperature and salinity (without τ_l) gridded data, where (x_i, y_j) are the horizontal grids; $z_k = 1, 2, \dots, 13$, represents vertical levels; $\tau_l = 1968, 1969, \dots, 1984$, is the time sequence in years; and $t_m = 1, 2, \dots, 12$, is the time sequence in months. Two temporal averages are defined before investigating the seasonal variation,

$$\bar{\psi}(x_i, y_j, z_k, t_m) = \frac{1}{\Delta\tau} \sum_l \psi(x_i, y_j, z_k, \tau_l, t_m),$$

$$\Delta\tau \equiv 17 \text{ yr (1968 – 1984)}, \quad (11.1)$$

which is the long-term monthly (t_m) mean value and

$$\bar{\bar{\psi}}(x_i, y_j, z_k) = \frac{1}{12} \sum_{m=1}^{12} \bar{\psi}(x_i, y_j, z_k, t_m), \quad (11.2)$$

which is the annual mean.

Annual Mean Temperature Field

The annual mean (1968–1984) temperature $\bar{\bar{T}}(x_i, y_j, z_k)$ over the South China Sea shows the pattern of northeast–southwest oriented isotherms at the upper layer from the surface to 75 m depth (Fig. 11.25). The annual surface mean temperature has a rather weak horizontal temperature gradient, decreasing from 28.5°C near the Borneo coast to 25°C near the southeast China coast. A strong temperature front is found near the Luzon Strait in the subsurface layer from 100 to 400 m. In that layer, the water temperature is quite uniform (e.g.,

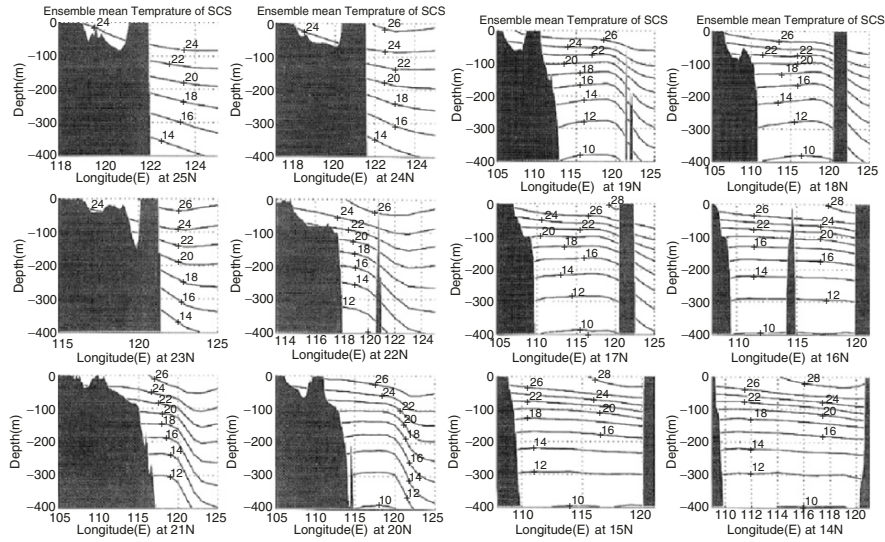


Fig. 11.26. Zonal cross sections of annual mean temperature ($^{\circ}\text{C}$) field from 25°N to 14°N with 1° increment (from Chu et al. 2002c, *Acta Oceanologica Sinica*)

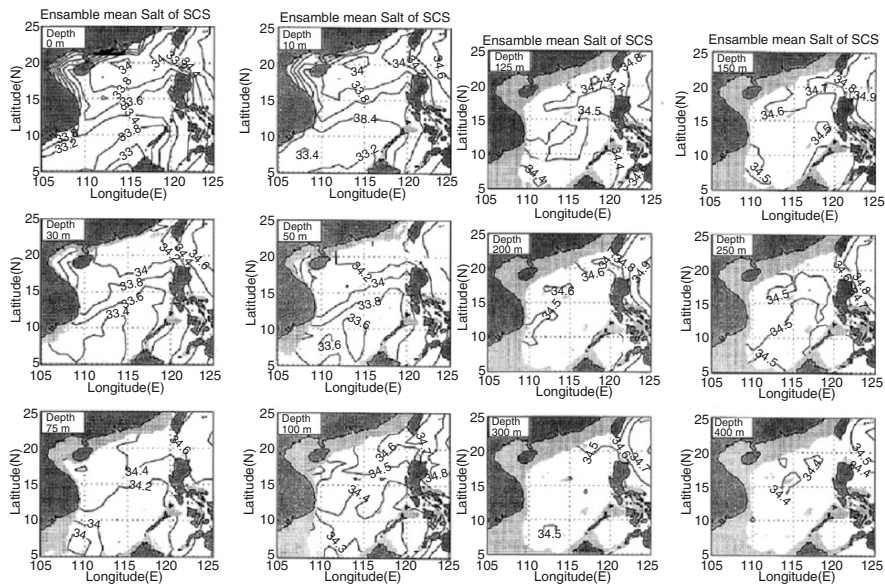


Fig. 11.27. Annual mean salinity (ppt) field at various depths from the surface to 400m depth (from Chu et al. 2002c, *Acta Oceanologica Sinica*)

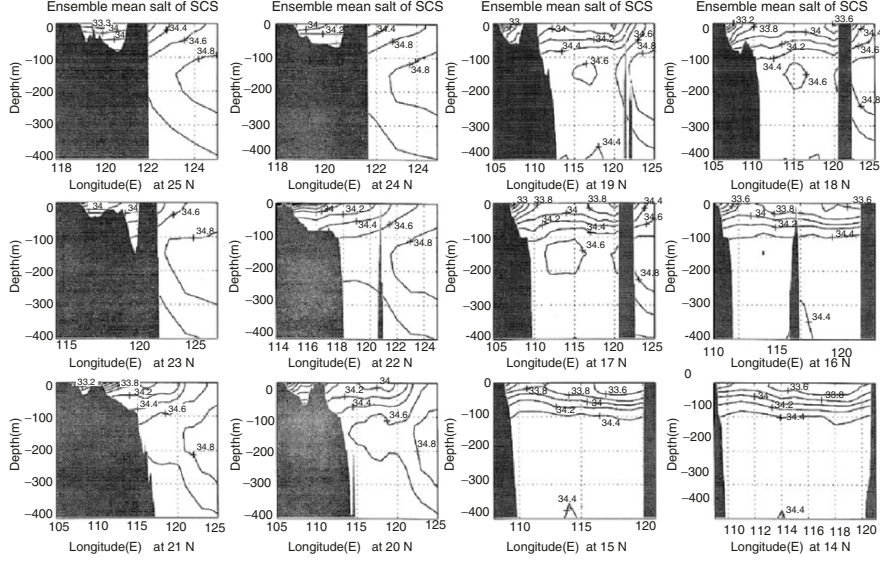


Fig. 11.28. Zonal cross sections of annual mean salinity (ppt) field from 25 to 14°N with 1° increment (from Chu et al. 2002c, *Acta Oceanologia Sinica*)

In the central region near 15°N zonal cross section (Fig. 11.28), the isohalines of \bar{S} are almost parallel to the isobaths in the upper 100 m. Below 100 m depth, the salinity is very uniform (34.4 ppt). However, in the northern region near 20°N zonal cross section (Fig. 11.28), the 34.6 ppt isohaline clearly shows the Kuroshio intrusion from the Luzon Strait into the northern South China Sea in the layer between 100 and 220 m reaching 115°E.

Monthly Mean Temperature Anomalies

The long-term monthly mean values relative to the ensemble mean, $\hat{T}(x_i, y_j, z_k)$,

$$\hat{T}(x_i, y_j, z_k, t_m) = \bar{T}(x_i, y_j, z_k, t_m) - \bar{\bar{T}}(x_i, y_j, z_k), \quad (11.3)$$

is defined as the monthly mean anomalies, which represent the composite features of the monthly mean thermal variability. The seasonal SST variation obtained from the MOODS consists of the earlier investigations based on the NCEP data (Chu et al. 1997d). During winter (January), \hat{T} is negative almost everywhere throughout the whole South China Sea (Fig. 11.29).

The typical winter (January) pattern contains northeast-to-southwest oriented isotherms in the northern South China Sea (north of 12°N), a warm anomaly ($\hat{T} > -1.2^\circ\text{C}$) west of Borneo–Palawan islands, and a cool anomaly ($\hat{T} < -2.4^\circ\text{C}$) near the South Vietnam coast (south of 12°N). The spring-to-summer transition (March to May) pattern shows the northward expansion of the warm anomaly west of Borneo–Palawan islands and the formation

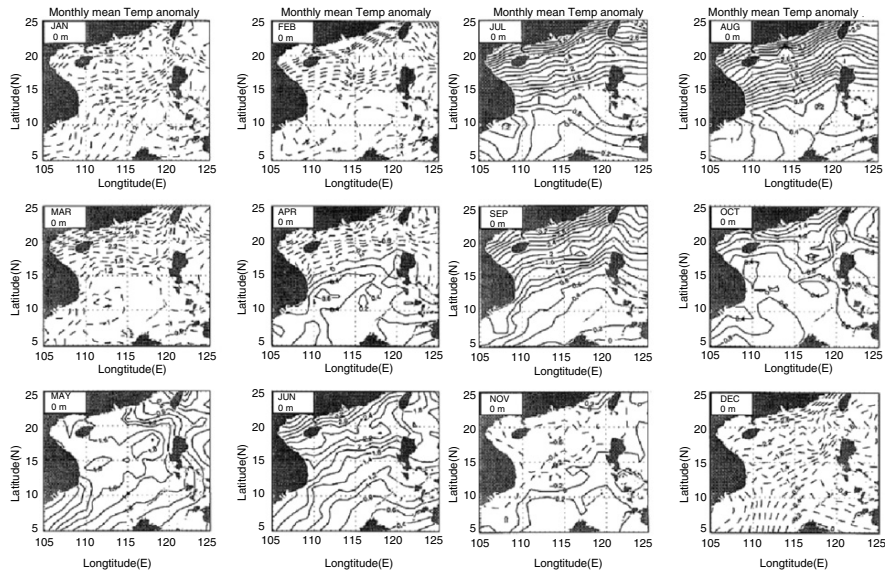


Fig. 11.29. Monthly mean surface temperature anomalies ($^{\circ}\text{C}$) (from Chu et al. 2002c, *Acta Oceanologica Sinica*)

of a central South China Sea ($10\text{--}15^{\circ}\text{N}$) warm anomaly with $\hat{T} > 0.6^{\circ}\text{C}$. The isotherm line of 1°C encloses almost all the South China Sea in May.

The summer (July) pattern is characterized by northeast-to-southwest oriented isotherms in the northern South China Sea (north of 15°N) (Fig. 11.29), a cool anomaly ($\hat{T} < 0.4^{\circ}\text{C}$) occurs west of Borneo–Palawan islands, and a warm anomaly ($\hat{T} > 1.2^{\circ}\text{C}$) near the South Vietnamese coast (south of 12°N). The summer pattern is opposite to the winter pattern. The fall-to-winter transition (September to November) pattern shows the northward expansion of the cool anomaly west of Borneo–Palawan islands and the formation of the central South China Sea ($10\text{--}15^{\circ}\text{N}$) cool anomaly.

At 200 m depth (intermediate level), the seasonal variation of temperature is featured by a basin-wide cool eddy ($\hat{T} < -0.8^{\circ}\text{C}$), a strong warm eddy ($\hat{T} > 0.8^{\circ}\text{C}$) near the South Chinese coast, and a weak warm eddy ($\hat{T} > 0.2^{\circ}\text{C}$) west of Borneo–Palawan islands during winter (Fig. 11.28) and a basin-wide warm eddy ($\hat{T} > 0.4^{\circ}\text{C}$), and a weak cool eddy ($\hat{T} < 0^{\circ}\text{C}$) near the South Vietnamese coast (south of 12°N) during summer (Fig. 11.30).

Near the western Luzon coast, a cool eddy ($\hat{T} < -1.0^{\circ}\text{C}$) occurs in winter and a warm eddy ($\hat{T} > -0.8^{\circ}\text{C}$) appears in summer. The weak WBP warm eddy strengthens, expands toward the northeast in spring (Fig. 11.30), gradually occupies the whole South China Sea, and turns to the summer pattern in July (Fig. 11.30). In autumn, the weak cool eddy near the South Vietnamese coast strengthens and expands toward northeast, and gradually occupies the

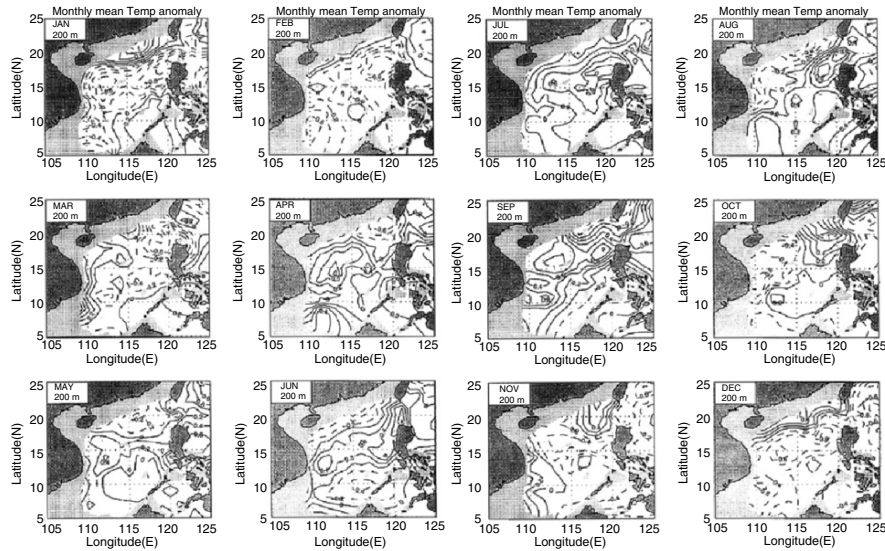


Fig. 11.30. Monthly mean temperature anomalies ($^{\circ}\text{C}$) at 200 m depth (from Chu et al. 2002c, *Acta Oceanologia Sinica*)

whole South China Sea, and turns to the winter pattern in January. Below 300 m depth, there is no significant seasonal variability.

The zonal cross section of \hat{T} along 19°N , shows the vertical structure of the winter cool eddy and the summer warm eddy near the western Luzon coast (Fig. 11.31). Both winter cool-core and summer warm-core eddies reach 250 m depth. The winter cool-core ($\hat{T} < -3^{\circ}\text{C}$) and the summer warm-core ($\hat{T} > 2.5^{\circ}\text{C}$) are located between 50 and 100 m depth.

Monthly Mean Salinity Anomalies

The monthly mean salinity anomaly \hat{S} is evident only in the layer above 200 m depth, and very weak below 200 m depth. Surface salinity has a strong seasonal variability. During winter (January), \hat{S} is positive almost everywhere throughout the whole South China Sea except near the South Vietnamese coast and the Gulf of Tonkin (Fig. 11.32).

A salty tongue with $\hat{S} > 0.4$ ppt stretches from the Luzon Strait to the continental shelf along the southeast China coast, representing a strong Kuroshio intrusion. Another weak fresh eddy with $\hat{S} < -0.2$ ppt is found west of Luzon Island. During summer (July), a salty tongue with \hat{S} around 0.4 ppt stretches from the Vietnamese coast to 118°E between 10 and 17°N , occupying the central South China Sea (Fig. 11.32). The rest of the area is occupied by negative \hat{S} . A strong fresh tongue occupies the continental shelf along the southeast China coast and the Gulf of Tonkin.

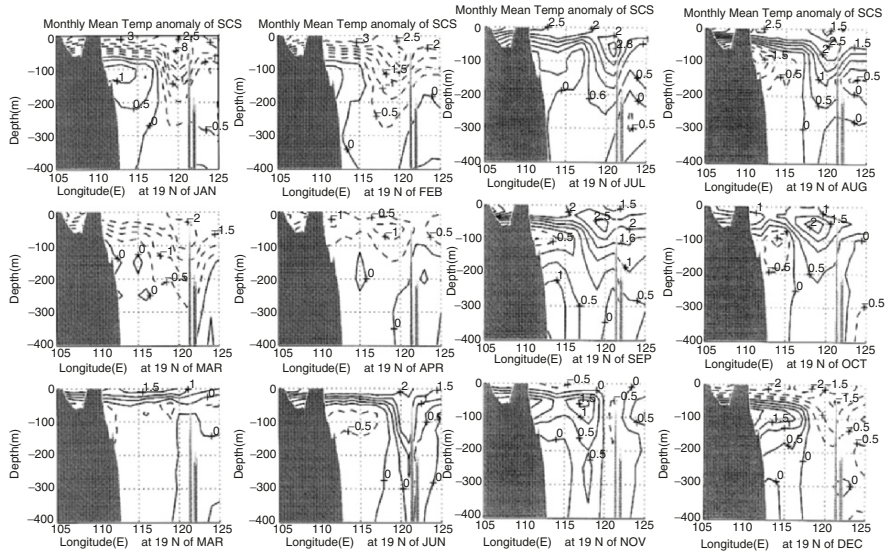


Fig. 11.31. Zonal cross sections of monthly mean temperature anomalies ($^{\circ}\text{C}$) at 19°N (from Chu et al. 2002c, *Acta Oceanologia Sinica*)

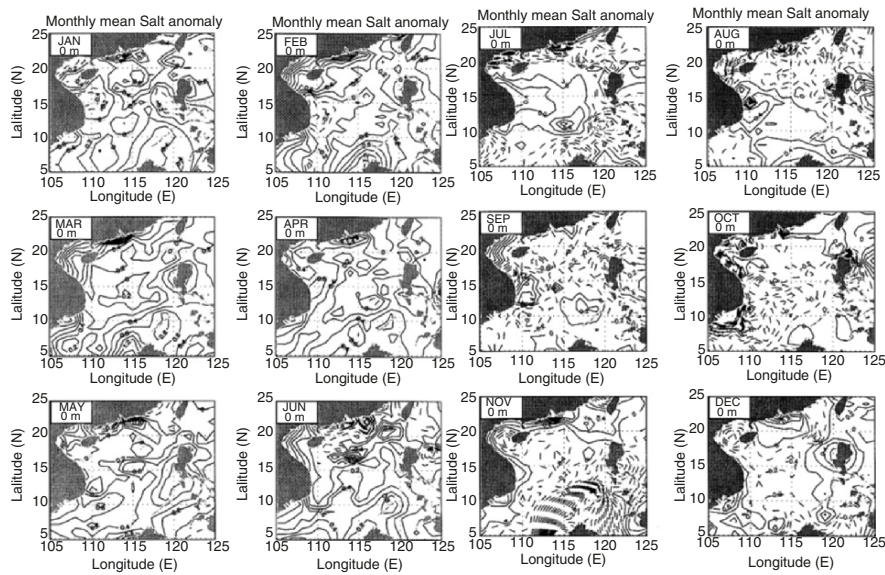


Fig. 11.32. Monthly mean surface salinity anomalies (ppt) (from Chu et al. 2002c, *Acta Oceanologia Sinica*)

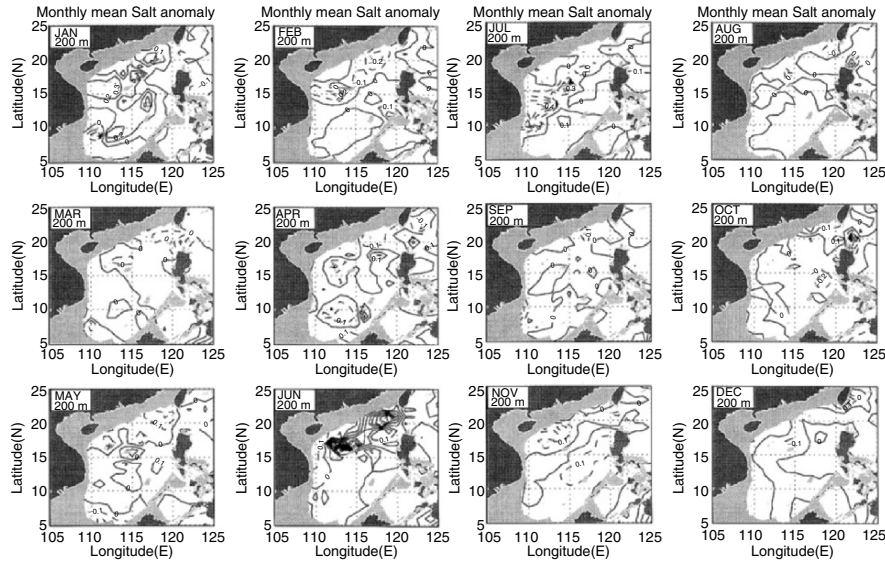


Fig. 11.33. Monthly mean salinity anomalies (ppt) at 200 m depth (from Chu et al. 2002c, *Acta Oceanologica Sinica*)

At 200 m depth, the seasonal variation of \hat{S} is also evident. In winter (Fig. 11.33), positive \hat{S} with a maximum value of 0.3 ppt occupies most of the area of the South China Sea, except the southwest corner near the Mekong River, where \hat{S} is negative (-0.4 ppt). In summer (Fig. 11.33), a narrow fresh tongue with a minimum value of -0.4 ppt stretches northeastward from the southwest corner near the Mekong River to 20°N (Fig. 11.33).

11.7 Seasonal Variability of the South China Sea Circulation

The P-vector inverse method in z -coordinate (see Chap. 6) is used to compute the absolute velocity from monthly mean T, S fields described in the previous section.

11.7.1 General Description

The most obvious features of the inverted summer and winter South China Sea circulation are flow separation, basin gyres, and mesoscale eddies. Hinted in Wyrski's (1961a, b) depiction but more explicit in our computation, are the upper level (10 m depth) west-to-east cross-basin currents, which are almost parallel to 16°N latitude from February to July. The inverted monthly South China Sea circulation agrees quite well with earlier observational

study (Wyrтки 1961a, b). As the commonly used inverse methods, the P-vector inverted western boundary currents are rather small. This could be caused by the neglect of relative vorticity in the potential vorticity calculation (Chu 1995a).

11.7.2 Surface Circulation

During the winter monsoon period (November to March), the winter Asian high pressure system brings strong winds from the northeast and the South China Sea surface circulation pattern is cyclonic (Wyrтки 1961a, b). At the surface inflow from the Luzon Strait (the Kuroshio intrusion) turns southwest along the Asian continental shelf, then turns south along the coast of Vietnam (Fig. 11.34). In November, this current splits into two currents at 12°N : a southward along-shore current and an eastward off-shore current. The southward branch turns east at 6°N , then turns northeast and joins the eastern branch at 115°E . An evident multieddy structure is obtained with two cyclonic eddies in the northern South China Sea (north of 12°N) and cyclonic and anticyclonic eddies in the southern South China Sea (south of 12°N). The eddy near Luzon was first identified by Nitani (1970) from the surface data. It is called the Luzon cyclonic eddy. The flow pattern does not change very much from November to December, except the cyclonic eddy near the Luzon Strait strengthens. In January, the west cyclonic eddy in the northern South China Sea expands toward the south. In March, the west cyclonic eddy in the northern South China Sea disappears and instead a cross-basin flow appears along 16°N latitude and joins the cyclonic eddy near the Luzon Strait. The southern South China Sea is occupied by an anticyclonic eddy. This anticyclonic eddy expands to the north and forms the only evident eddy in the central South China Sea in March (Fig. 11.34). This eddy is associated with the central South China Sea warm eddy in spring (Fig. 11.34) and expands toward the south in April. May is the month of the summer monsoon transition. The anticyclonic eddy reduces its strength and becomes unidentifiable.

During the summer monsoon period (mid-May to August), winds blow from the southwest and the surface circulation generally follows suit with anticyclonicity in the southern basin (Wyrтки 1961a). Inflow is through the southern boundary and outflow is through the northern Taiwan Strait and eastern Luzon Strait. The position of the inverted July indicates that the general circulation pattern has the following features. Velocities reach 0.2 m s^{-1} near the Vietnam Coast and split into two currents at 12°N : the coastal current and off-shore current. The off-shore current further bifurcates and partially leaves the coast; the bifurcation point is at 110°E . The northern branch moves northeast to 113°E and then turns zonally between 15 and 18°N . The southern branch moves zonally until on reaching Palawan Island, then turns north and joins with the north branch at 16°N . A cyclonic eddy appears in July near the South Vietnam coast and strengthens in August. This eddy was reported by Dale (1956) and Uda and Nakao (1974).

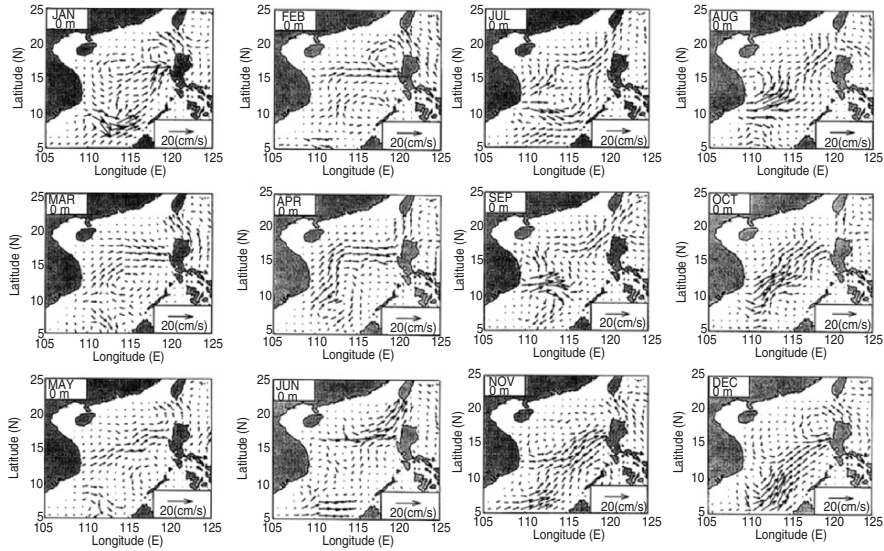


Fig. 11.34. Inverted monthly mean surface circulation (from Chu et al. 2002c, *Acta Oceanologia Sinica*)

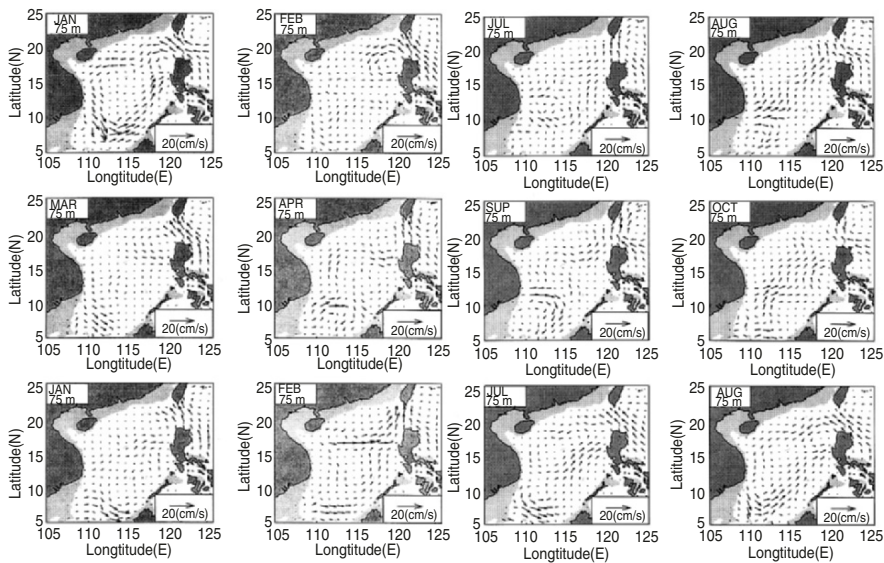


Fig. 11.35. Inverted monthly mean subsurface (75 m) circulation (from Chu et al. 2002c, *Acta Oceanologia Sinica*)

11.7.3 Subsurface (75 m)

The subsurface (75 m) shows a strong seasonal variation (Fig. 11.35). Warm and salty Kuroshio water enters the South China Sea through the Luzon Strait

in October–March, the transition to and during the winter monsoon season. The winter circulation pattern is the basin-wide cyclonic gyre. A cyclonic mesoscale eddy splits from the gyre near the Luzon Strait in January and keeps its strength in February. On the other hand, the basin-wide cyclonic gyre weakens and shrinks toward the southwest in February and disappears in March.

During the summer monsoon period (June–September), the Kuroshio intrusion through the Luzon Strait ceases. A weak anticyclonic eddy occurs in June near the South Vietnam coast and strengthens in July. A cross-basin current establishes in August from the north branch of that eddy to the Luzon Strait and forms a weak cyclonic gyre in the northwest and an anticyclonic gyre in the southeast. During the winter monsoon transition period, the southeast anticyclonic gyre weakens and the northeast cyclonic gyre gains strength and eventually it occupies the whole South China Sea, indicating the beginning of the winter circulation pattern.

11.7.4 Intermediate Level (150 m)

As the water depth increases, the inverted velocity generally reduces with depth. We choose 150 m depth as a representative of the intermediate level (Fig. 11.36). The seasonal circulation variability is featured by strengthening, weakening, and splitting of a basin-wide cyclonic gyre. This gyre is evident to strengthen in winter and weakens in summer. As spring approaches (March),

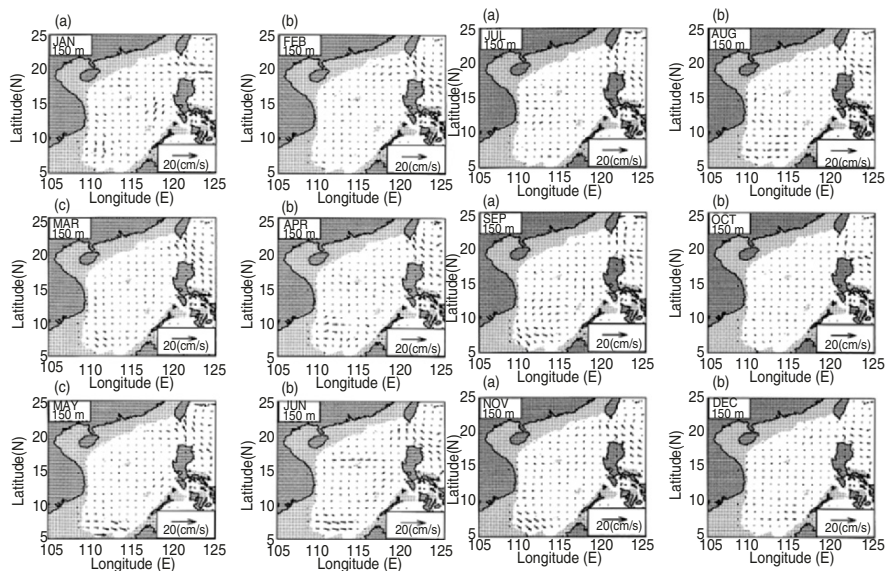


Fig. 11.36. Inverted monthly mean intermediate level (150 m) circulation (from Chu et al. 2002c, *Acta Oceanologia Sinica*)

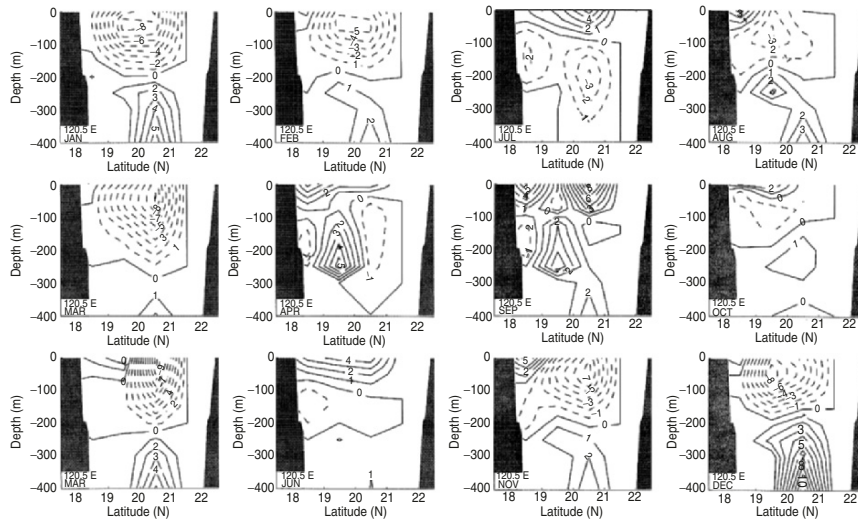


Fig. 11.37. Inverted monthly upper layer (0–400 m) mean zonal velocity across the Luzon Strait (120°E) (from Chu et al. 2002c, Chinese Journal of Oceanology)

a cyclonic eddy in the area northwest of Luzon occurs and the cyclonic gyre is located south of 16°N. In summer (July), the cyclonic gyre is pushed further south and a cyclonic eddy appears off the central Vietnam coast (14–18°N).

The South China Sea joins the Pacific Ocean through the Luzon Strait. The seasonal variations of the intrusion of the Kuroshio Water into the South China Sea through the Luzon Strait have been investigated in earlier studies (Fan and Yu 1981; Shaw 1989, 1991). As pointed out by Shaw (1991), the intrusion process is important not only to the transport of water masses into the South China Sea, but also to the shelf circulation off the southeast coast of China. Shaw (1989, 1991) used the discriminant analysis method to classify the water mass T, S characteristics at 150, 200, and 250 meters, and found that water characteristics of the Philippine Sea (Kuroshio) were identifiable along the continental margin south of China from October to January. The presence of this water indicated an intrusion current from the Philippine Sea into the South China Sea. The monthly zonal velocity in 120.5°E cross section is given in Fig. 11.37. The negative values indicate westward flow through the Luzon Strait (Kuroshio intrusion). The positive values show the outflow from the South China Sea to the Philippine Sea. Flow through the Luzon Strait has a strong seasonal variation, as well as a vertical shear. Evident Kuroshio intrusion (negative values) occurs during the winter monsoon season (November–March) in the upper 200 m. Below 200 m, the velocity is quite small, and most values are positive.

11.8 South China Sea Thermohaline Front

NASA's MCSST data clearly show the appearance of a cross basin, thermal front in winter (Fig. 11.38a) and disappearance of such a front in summer (Fig. 11.38b). In Sect. 10.6, the monthly mean upper layer (0–400 m) T, S data are computed at 13 depths (z -level analysis) using the OI method. An upper layer thermohaline front across the South China Sea basin can also be identified from Figs. 11.25 and 11.27 from the South Vietnamese coast (around 15°N) to Luzon Island (around 19°N). Is this thermohaline front realistic or unrealistic (computationally generated)? To answer this question, the climatological T, S dataset calculated using the curve-fitting model (i.e., GDEM) is used to identify the existence of this front (Chu and Wang 2003).

11.8.1 Thermohaline Front Identified Using GDEM

The SST variation obtained from the GDEM data is quite consistent with the monthly mean data obtained using the z -level analysis (Fig. 11.25). An important feature, yet to be explored, is the thermohaline front across the South China Sea basin from Vietnam Bight (109°E, 10°N) to the northwestern tip of Luzon (120°E, 19°N). Figure 11.39 shows the monthly mean sea surface temperature with contour interval of 0.5°C.

The horizontal gradient across the thermohaline front strengthens in the winter monsoon season (November to April) with a maximum value of 1.4°C/100 km and weakens drastically in the summer monsoon seasons (June to September). Figure 11.40 shows the monthly mean temperature at 50 m depth. Different from the surface, the temperature gradient is evident all the year round.

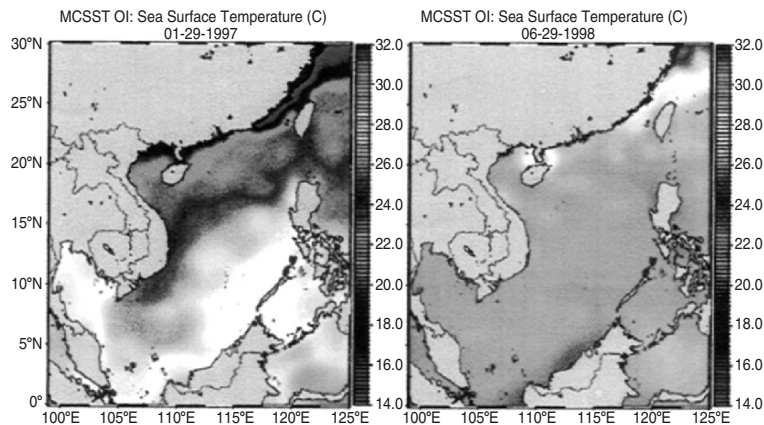


Fig. 11.38. NASA's MCSST data for (a) January 29, 1997, and (b) June 29, 1998. The data were interpolated by the Naval Research Laboratory (from Chu and Wang 2003, *Journal of Oceanography*)

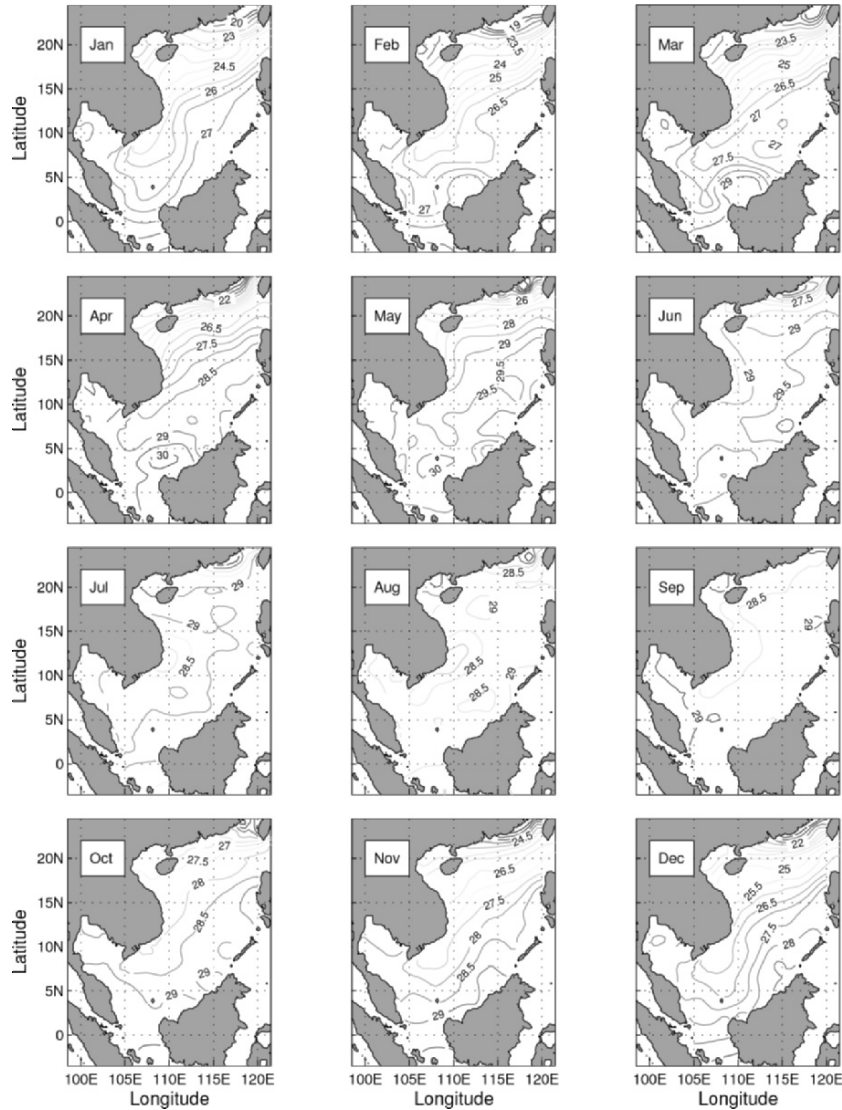


Fig. 11.39. Monthly mean sea surface temperature ($^{\circ}\text{C}$) field with 0.5°C contour interval (from Chu and Wang 2003, *Journal of Oceanography*)

Figure 11.41 shows the monthly mean surface salinity with contour interval of 0.25 ppt. The isoline of 33.75 ppt (or 33.5 ppt) in February to April (or May to January) divides the South China Sea into saltier northwestern Sea and fresher southeastern Sea. The horizontal salinity gradient across thermohaline front in winter is comparable to that in summer (nearly $0.25 \text{ ppt}/100 \text{ km}$).

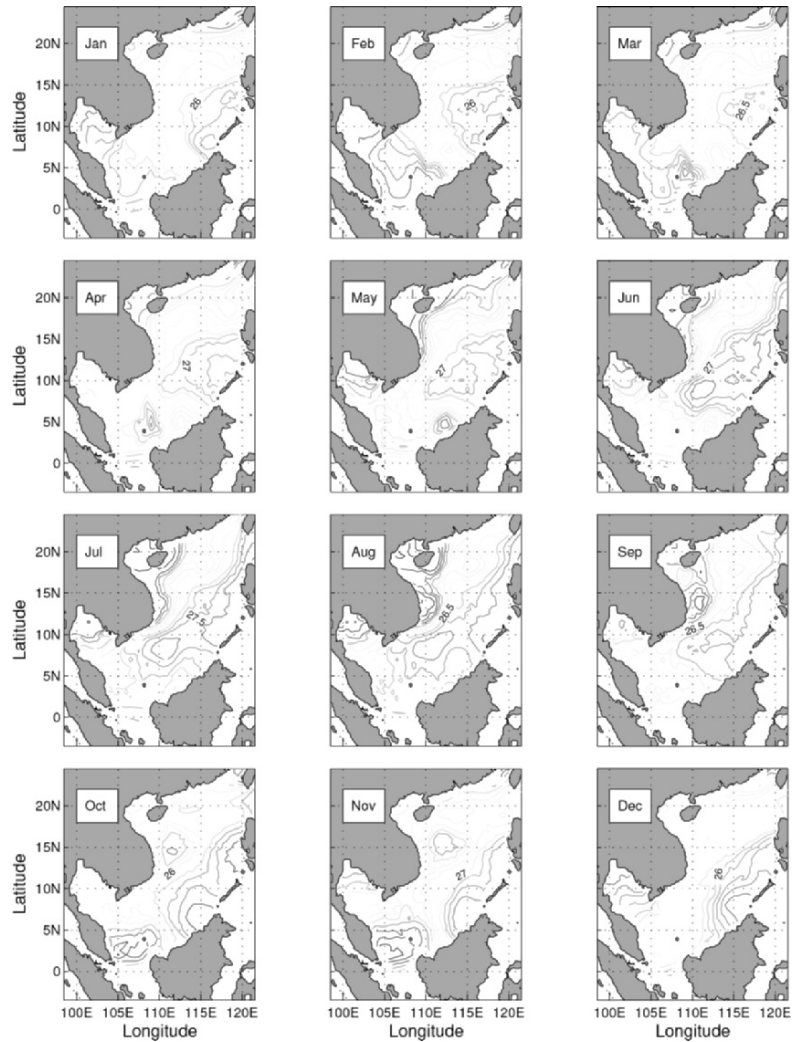


Fig. 11.40. Monthly mean temperature ($^{\circ}\text{C}$) field at 50 m depth with 0.5°C contour interval (from Chu and Wang 2003, *Journal of Oceanography*)

Figure 11.42 shows the monthly mean salinity at 50 m depth. The 34.0 ppt isoline separates the saltier, northwestern South China Sea from the fresher, southeastern Sea. A strong horizontal salinity gradient ($0.1 \text{ ppt}/100 \text{ km}$) is found near the Vietnam Bight in the summer monsoon season (July to October). The thermohaline front appears strong all the year round at the surface and subsurface (50 m).

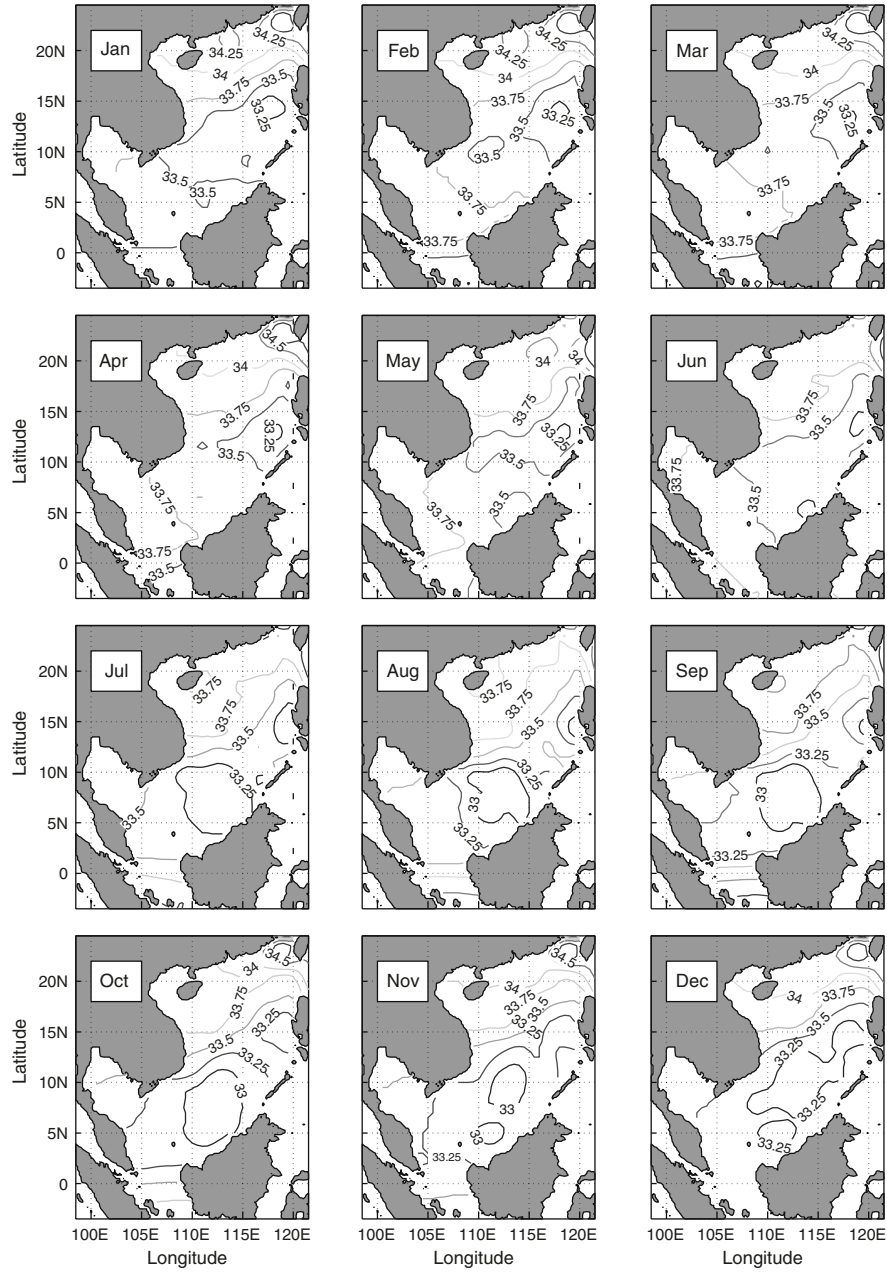


Fig. 11.41. Monthly mean sea surface salinity (ppt) field with 0.025 ppt contour interval (from Chu and Wang 2003, *Journal of Oceanography*)

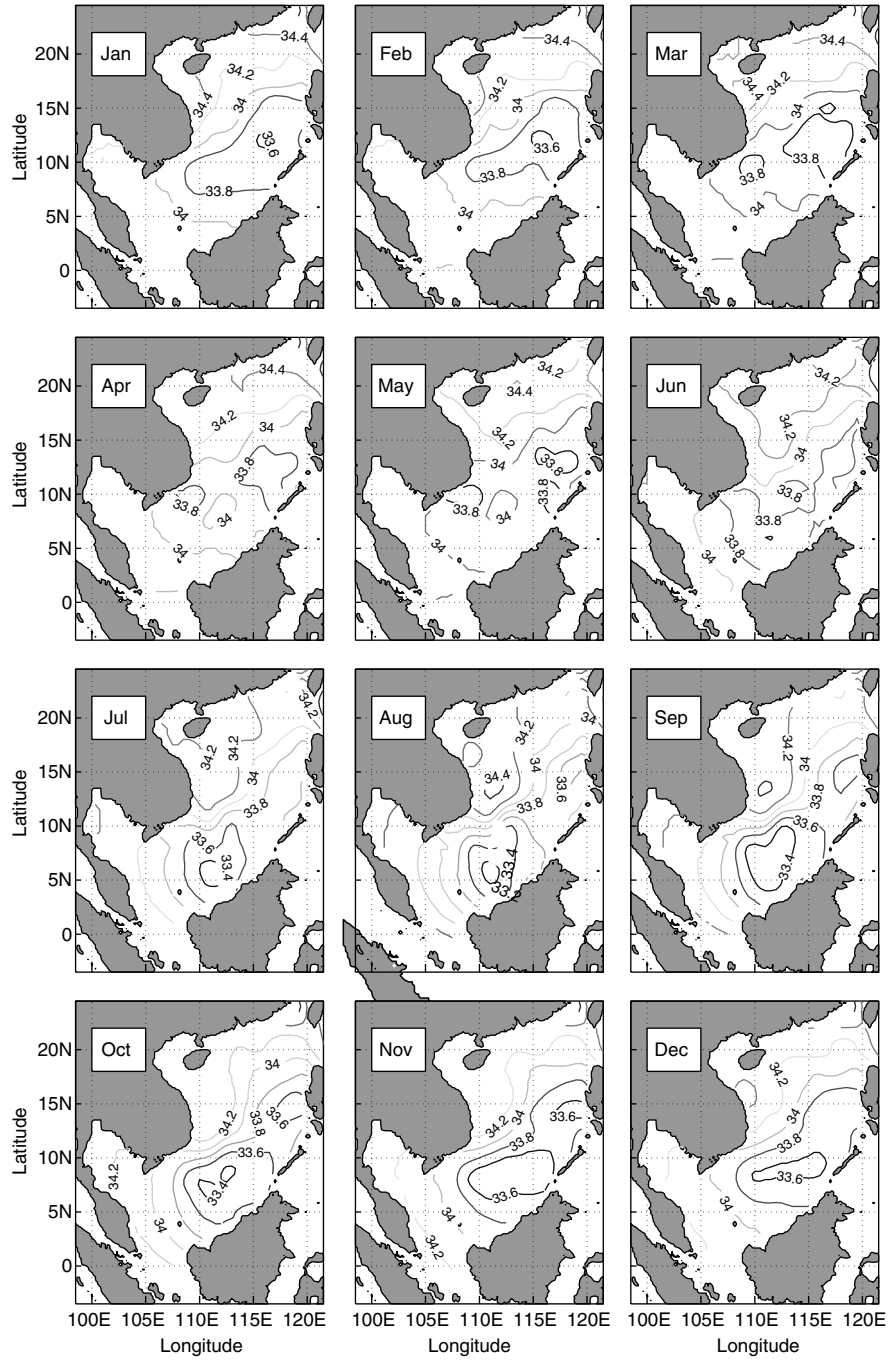


Fig. 11.42. Monthly mean salinity (ppt) field at 50 m depth with 0.02 ppt contour interval (from Chu 2003, *Journal of Oceanography*)

11.8.2 Forcing Mechanism

Preconditioning

The South China Sea is occupied by two separate water masses. In the north, the waters are cold and saline. The annual variability of salinity is small, due to the inflow and diffusion of high salinity water from the Pacific Ocean through the Luzon Strait. However, in the south the tropical conditions cause the waters to be warmer and fresher (Wyrтки 1961a). High temperature and low salinity water in the south, and low temperature and high salinity water in the north is the precondition for the thermohaline front formation in the central South China Sea.

Sverdrup Transport

For the ensemble mean (Fig. 11.43a) and winter (Fig. 11.43b) wind stress curl (ζ) fields, the northeast-to-southwest oriented zero-curl line separates the South China Sea into anticyclonic curls (causing southward Sverdrup transport) northwest of it and cyclonic curls (causing northward Sverdrup transport) southeast of it.

This process forces the two water masses to converge at the zero-curl line, causing the formation and/or strengthening of the thermohaline front. For the summer (Fig. 11.43b) ζ field, the zero-curl line separates the South China Sea into cyclonic curls (causing northward Sverdrup transport) northwest of it and anticyclonic curls (causing southward Sverdrup transport) southeast of it. This process forces the two water masses to divergence at the zero-curl line, weakening the thermohaline front. Use of the Sverdrup theory also predicts the existence of a jet-like flow associated with the zero-curl line.

11.8.3 Cross-Basin Current

Flow Pattern

Wyrтки (1961a) published an overview of South China Sea seasonal surface circulations and postulated a cross-basin current flowing northeastward all the year round. A wind-driven circulation is formed with the beginning of the southwest monsoon in May and June. Off the coast of Vietnam a northward flowing western boundary current is clearly visible. The wide, uniform drift in the northern South China Sea shows a deflection of the current to the right of the wind and forms the cross-basin current from the Vietnam bight to Luzon island. In September the strength of the currents decreases and in October the northeast monsoon starts blowing with considerable strength. Under the influence of the winds, water masses of the North Equatorial Current are intruded through Luzon Strait into South China Sea. This water flows along the coast of China to the southwest with a remarkable westward intensification

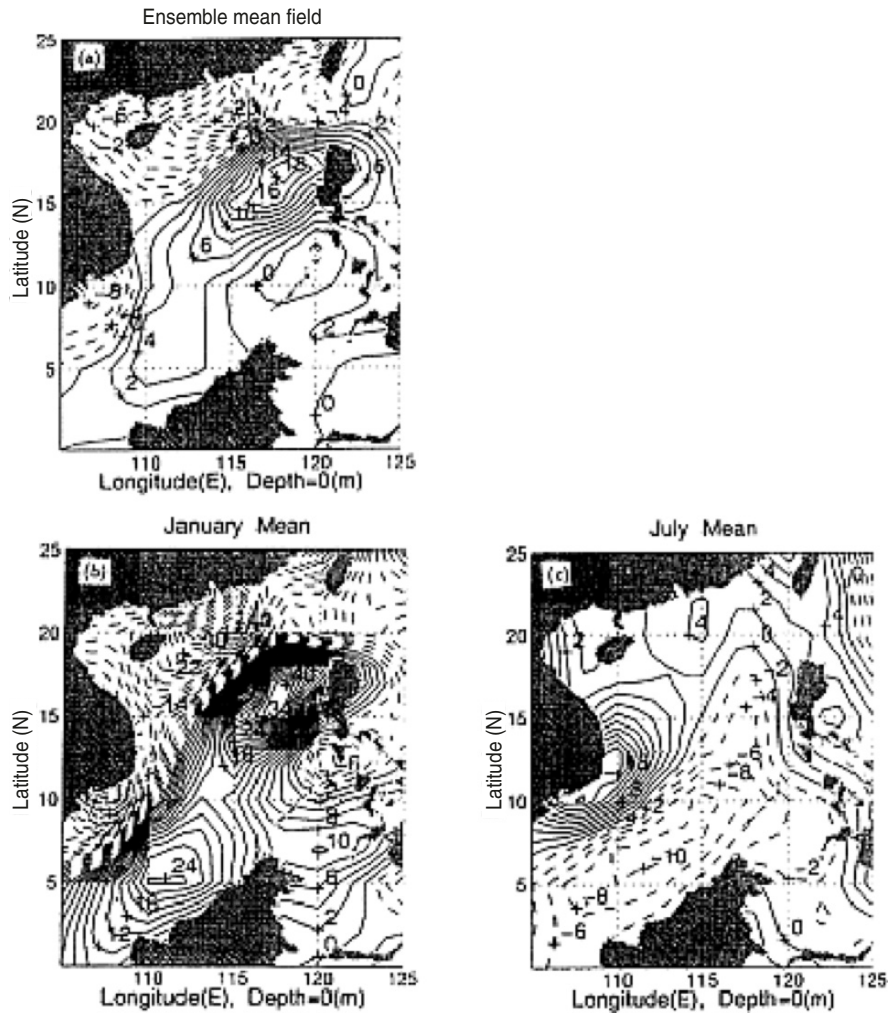


Fig. 11.43. Surface wind stress curl: (a) ensemble mean, (b) January, and (c) July. The unit is 10^{-8} N m^{-3} (from Chu et al. 1997d, *Journal of Geophysical Research*)

of the current. In the central South China Sea a counter current (i.e., cross-basin current) is developed north of 10°N .

The calculated absolute velocity field (Figs. 11.44 and 11.45) using the z -level P-vector method clearly shows the existence of the cross-basin current flowing northeastward from the Vietnam bight to Luzon island. Different from Wyrтки's cartoons, the coastal currents are not well obtained using the P-vector method. A comparison of Figs. 11.44, 11.45 with Figs. 11.39–11.42 shows the colocation of the crosscoastal current and the thermohaline front.

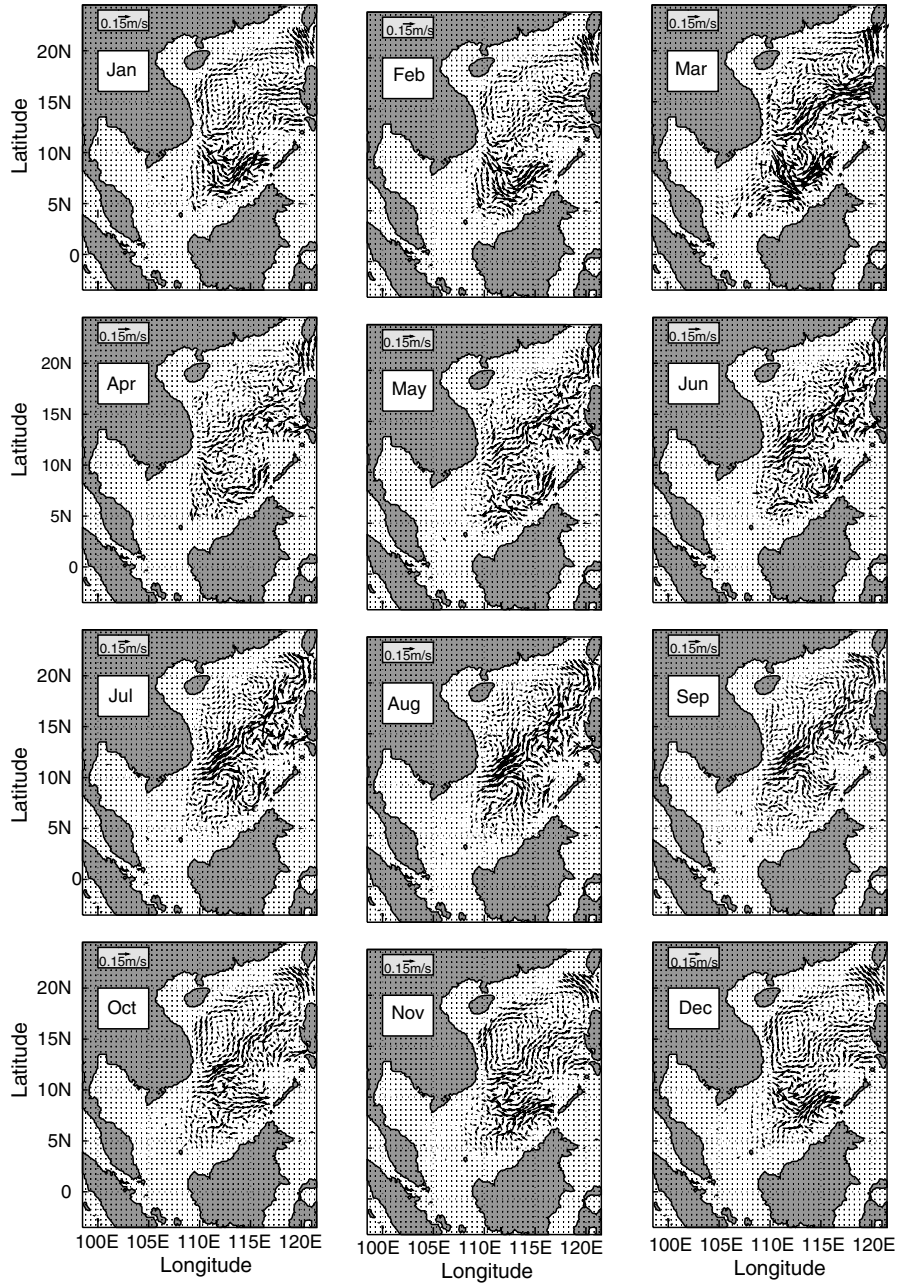


Fig. 11.44. Inverted monthly mean velocity field at the surface using the P-vector method (from Chu and Wang 2003, *Journal of Oceanography*)

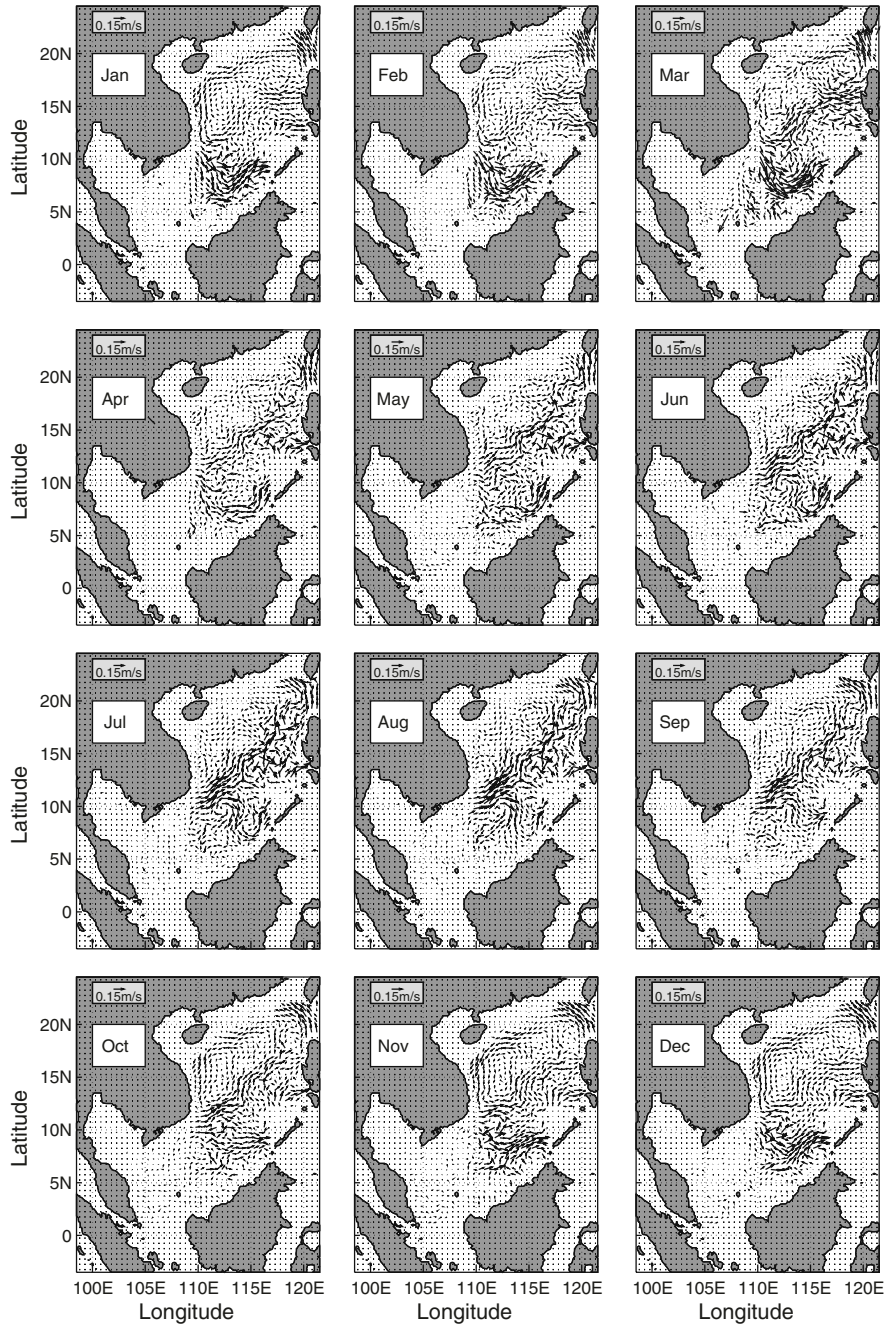


Fig. 11.45. Inverted monthly mean velocity field at 50 m depth using the P-vector method (from Chu and Wang 2003, *Journal of Oceanography*)

The cross-basin current has a weak seasonal variation in flow direction and a strong seasonal variation in current speed. It strengthens in summer and weakens in winter. In July and August, the maximum speed of the cross-basin current reaches 0.25 m s^{-1} (0.2 m s^{-1}) in the southern part near the Vietnam bight at the surface (50 m depth). In January and February the cross-basin current is very weak, around 0.05 m s^{-1} at the surface and 50 m deep. The seasonal variation of the cross-basin current is well reproduced by numerical modeling (e.g., Shaw and Chao 1994).

The cross-basin current meanders and generates cyclonic (anticyclonic) eddies to the northwest (southeast). For example, it meanders at ($110^\circ\text{E}, 10^\circ\text{N}$) from June to August. An anticyclonic eddy has been identified with its center at ($112^\circ\text{E}, 9^\circ\text{N}$) and a size of around 300 km. The tangential velocity of this eddy is nearly 0.2 m s^{-1} . This multieddy structure will be discussed in the next section.

Axis of the Cross-Basin Current

The orientation of the maximum velocity along the cross-basin current is defined as the axis that extends from ($110^\circ\text{E}, 10^\circ\text{N}$) to ($120^\circ\text{E}, 18^\circ\text{N}$) in a straight line at 50 m depth (as an example) from April to September (Fig. 11.46).

In October, the axis maintains as a straight-line course and shifts southward with a larger displacement in the northern part (250 km in the north tip) than in the southern part (100 km in the south tip). From November to March, the axis of the cross-basin current is no longer a straight line. The western part of the axis (west of 115°E) jumps around 200 km northward compared to October. The eastern part (east of 115°E) of the axis becomes zonal along 15°N latitude.

11.8.4 Water Mass Characteristics across the Front

Subareas

As described in Sect. 11.8.3, the water masses have different characteristics north and south of the thermohaline front, with high temperature low salinity water in the south, and low temperature high salinity water in the north. Analysis of T , S data in the latitudinal strip (112.5 – 115°E) is necessary to quantify the thermohaline variability across the thermohaline front and for a further understanding of the driving and variation mechanism of the thermohaline front.

This strip is divided from 6 to 22°N into eight rectangles with 2.5° in the zonal direction and 2° in the latitudinal direction (Fig. 11.47). These boxes can be grouped into three subareas: the thermohaline front (4 and 5), south of the thermohaline front (1–3), and north of the thermohaline front (6–8). The change of T – S features among these boxes leads to an understanding of the structure and the forcing mechanism of the thermohaline front.

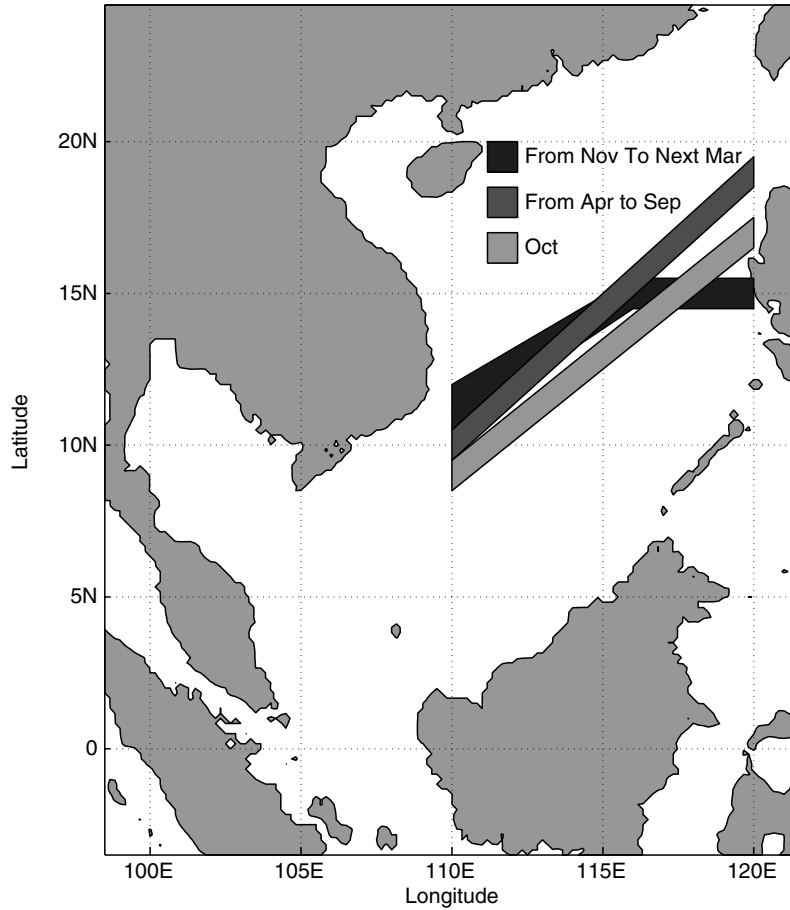


Fig. 11.46. Seasonal variation of the axis of the cross-basin current at 50 m depth (from Chu and Wang 2003, *Journal of Oceanography*)

***T-S* Diagrams**

The upper layer (0–300 m deep) *T-S* diagrams are plotted for each box in January (Fig. 11.48) and July (Fig. 11.49), respectively. The *T-S* curves in all boxes are of the same type (reverse-C shape) with a salinity maximum (nearly 34.65 ppt north of the thermohaline front and around 34.52 ppt south of the thermohaline front) layer. The maximum salinity has been previously discussed by Qu (2000) using *T, S* profiles from NODC. The location and the strength of the maximum salinity are comparable whether they are studied using the GDEM (Chu and Wang 2003) or NODC data (Qu 2000).

The *T-S* curves, however, have a larger range in both *T* and *S* south of the thermohaline front (Boxes 1–3) than to the north (Boxes 6–8), and the salinity maximum occurs at a shallower depth, north of the thermohaline front

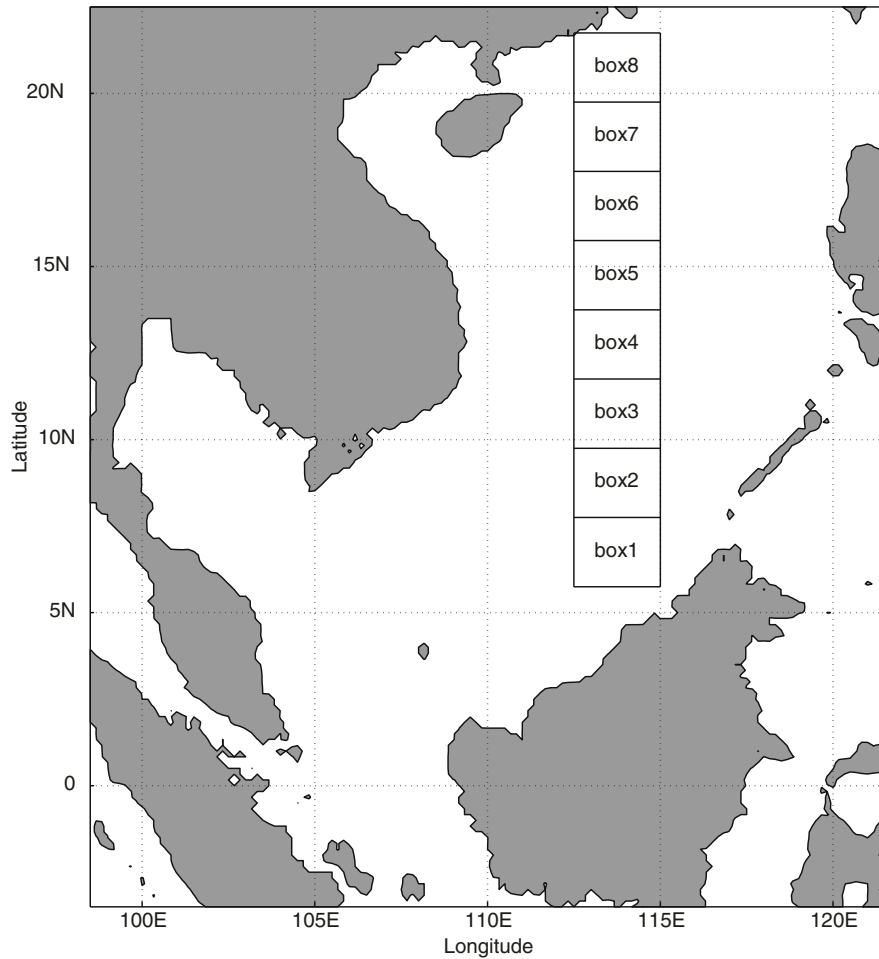


Fig. 11.47. Division of subareas across the thermohaline front (from Chu and Wang 2003, *Journal of Oceanography*)

($\sigma_t \simeq 25 \text{ kg m}^{-3}$ in Boxes 6–7) than to the south ($\sigma_t \simeq 25.6\text{--}25.8 \text{ kg m}^{-3}$ in Boxes 1–3). Thus, the thermohaline variability is larger at the south than at the north of the thermohaline front.

***T–S* Profiles**

The mean vertical T and S profiles are plotted for each box in January (Fig. 11.50) and July (Fig. 11.51), respectively. The thermohaline structure below 150 m is quite uniform horizontally and has weak seasonal variability between January and July, which indicates that the thermohaline front is an upper layer phenomenon. The halocline is stronger at the south than at the

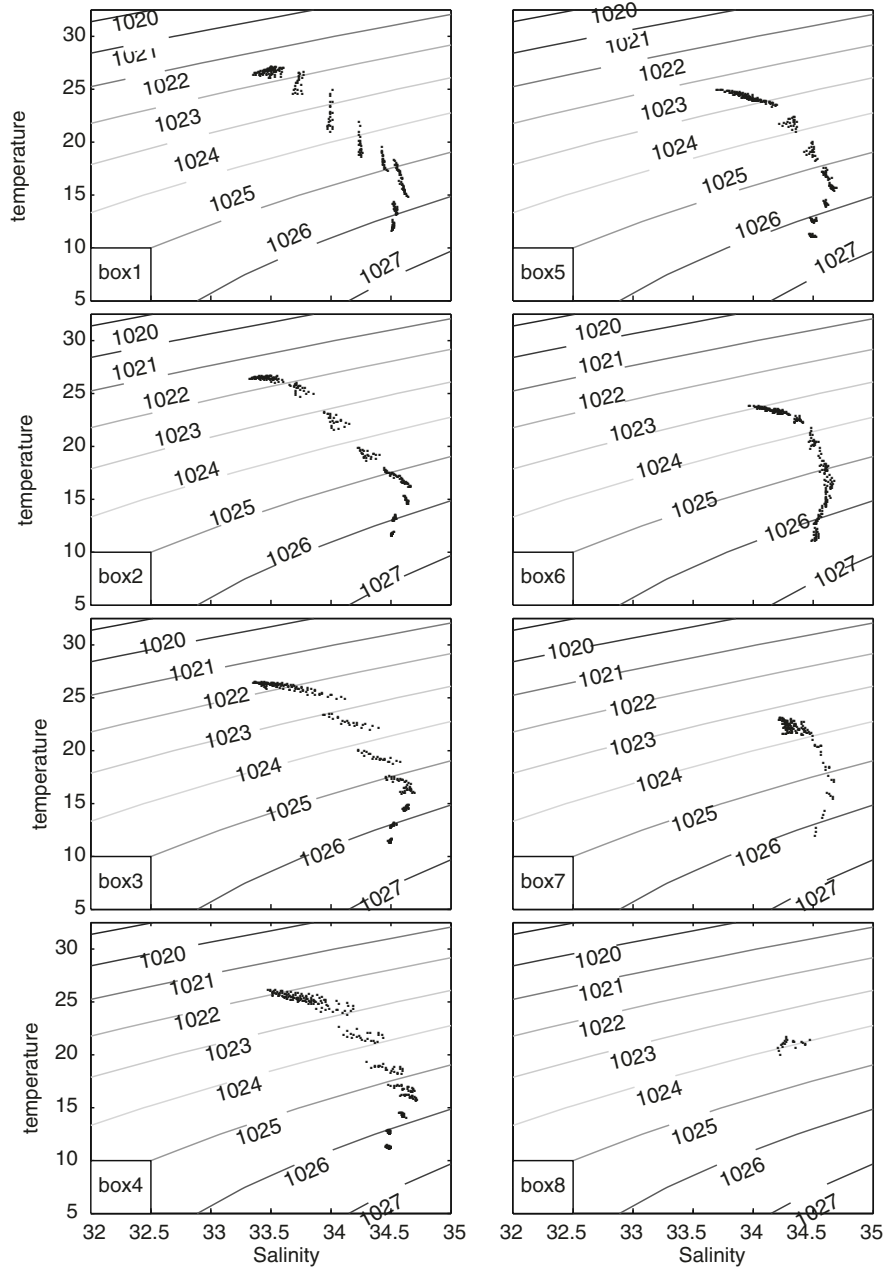


Fig. 11.48. Change of T - S diagrams across the thermohaline front in January (from Chu and Wang 2003, *Journal of Oceanography*)

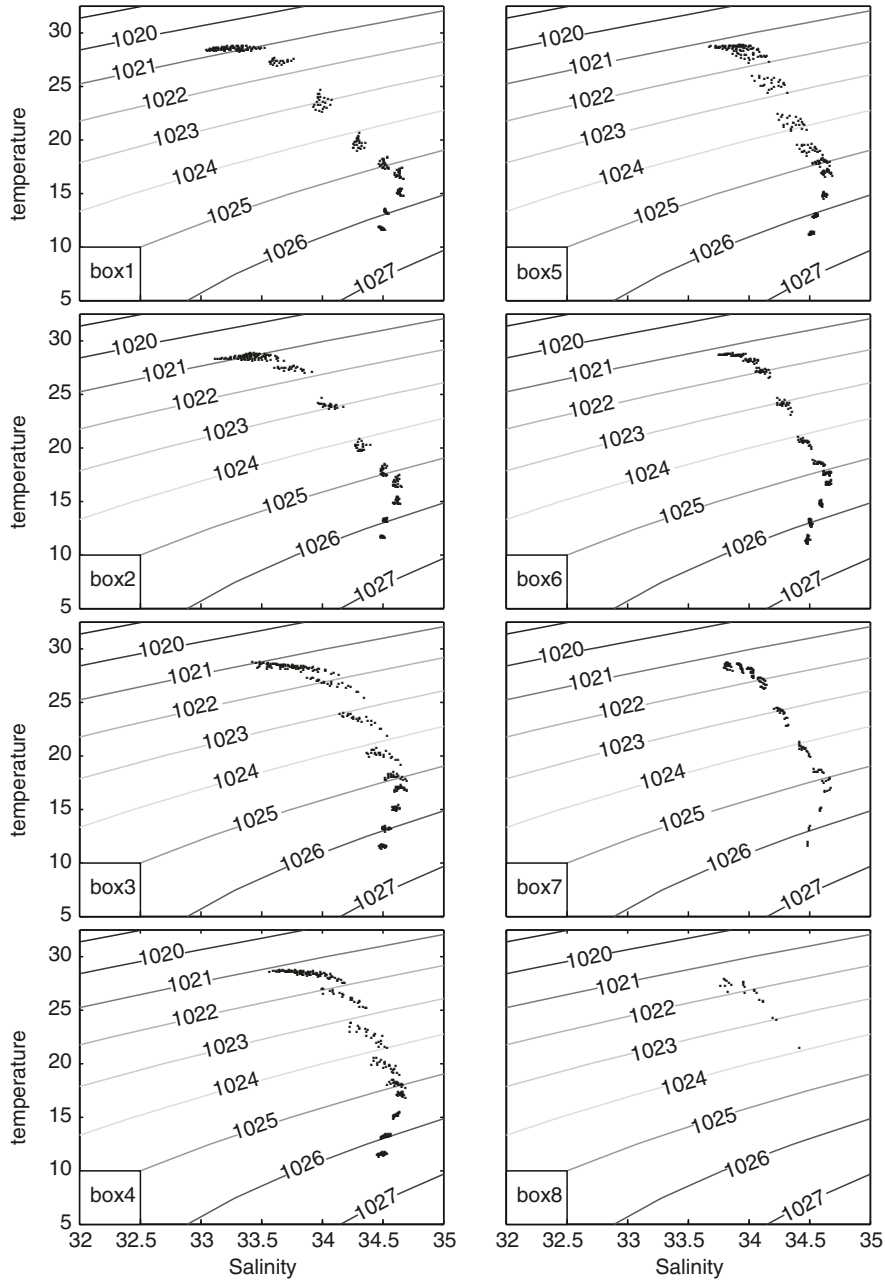


Fig. 11.49. Change of T - S diagrams across the thermohaline front in July (from Chu and Wang 2003, *Journal of Oceanography*)

north of the thermohaline front in both seasons (January and July). For example, the vertical salinity gradient in January is around 0.83 ppt/100 m in Box 2 (south of the thermohaline front) and nearly 0.38 ppt/100 m in Box 6 (north of the thermohaline front), and the vertical salinity gradient in July is around 0.92 ppt/100 m in Box 2 (south of the thermohaline front) and nearly 0.56 ppt/100 m in Box 6 (north of the thermohaline front). The salinity maximum (~ 34.65 ppt) occurs at shallower depth north of the thermohaline front (around 150 m deep in Boxes 6–7) than south of the thermohaline front (around 200 m deep in Boxes 1–3). There is no noticeable seasonal variability.

Seasonal thermohaline variability is evident above 150 m depth, and is stronger north than south of the thermohaline front. For example, January temperature profiles (Fig. 11.50) show deeper mixed layers north of the thermohaline front (e.g., around 60 m in Box 6) than south of the thermohaline front (e.g., 35 m in Box 2). This is caused by the dipole of the surface wind stress curl with anticyclonic (cyclonic) curl north (south) of the thermohaline front. July temperature profiles (Fig. 11.51) show shallower mixed layers north of the thermohaline front (e.g., around 10 m in Box 6) than south of the thermohaline front (e.g., 30 m in Box 2) with the same mechanism as January.

Surface Temperature

Monthly mean SST data show a larger seasonal variability north (Box-6) than south (Box-2) of the thermohaline front (Fig. 10.52a, b). The coldest SST occurs in February in both boxes: 23.5°C in Box-6 (north of the thermohaline front), and 26.6°C in Box-2 (south of the thermohaline front). The warmest SST north (south) of the thermohaline front is 29.1°C(29.6°C) appearing in July (May). The seasonal variability (warmest minus coldest temperature) is around 5.6°C in Box-6 and 3°C in Box-2.

The SST difference $\Delta\text{SST} = \text{SST}_{\text{Box-2}} - \text{SST}_{\text{Box-6}}$ is used to represent the strength of the surface thermohaline front in temperature (Fig. 11.52c). The difference (ΔSST) reaches a maximum value (3.1°C, strongest surface thermohaline front) in January, and a minimum value of 0.2°C in July and August (no surface thermohaline front).

Subsurface Temperature (50 m)

Monthly mean temperature at 50 m depth shows a larger seasonal variability at the north (Box-6) than at the south (Box-2) of the thermohaline front (Fig. 11.53a, b). The coldest temperature occurs in February in both boxes: 23.3°C in Box-6 (north of the thermohaline front), and 25.5°C in Box-2 (south of thermohaline front). The warmest temperature north (south) of the thermohaline front is 26.8°C(27.8°C) appearing in October (June). The seasonal variability is around 3.5°C in Box-6 and 2.3°C in Box-2.

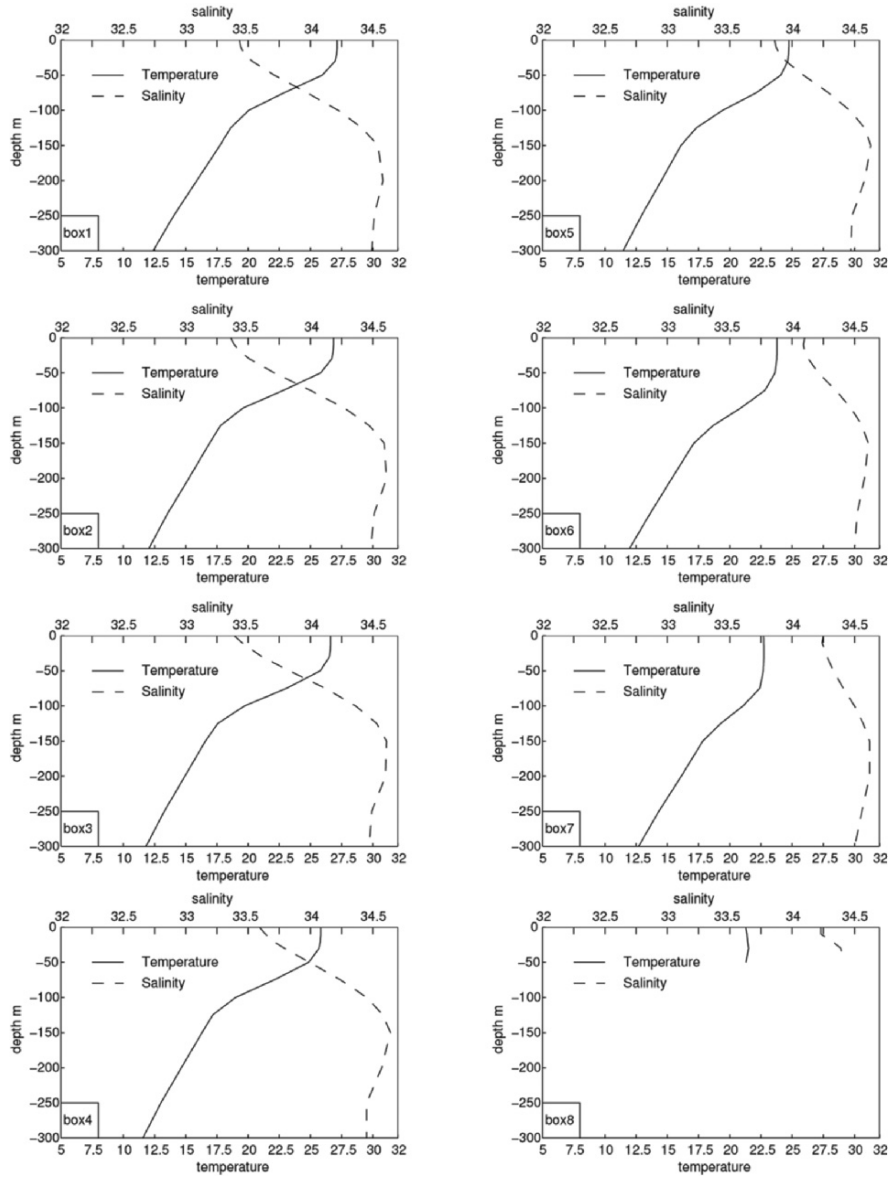


Fig. 11.50. Change of T and S profiles across the thermohaline front in January (from Chu and Wang 2003, Journal of Oceanography)

The temperature difference,

$$\Delta T = T_{\text{Box-2}} - T_{\text{Box-6}}$$

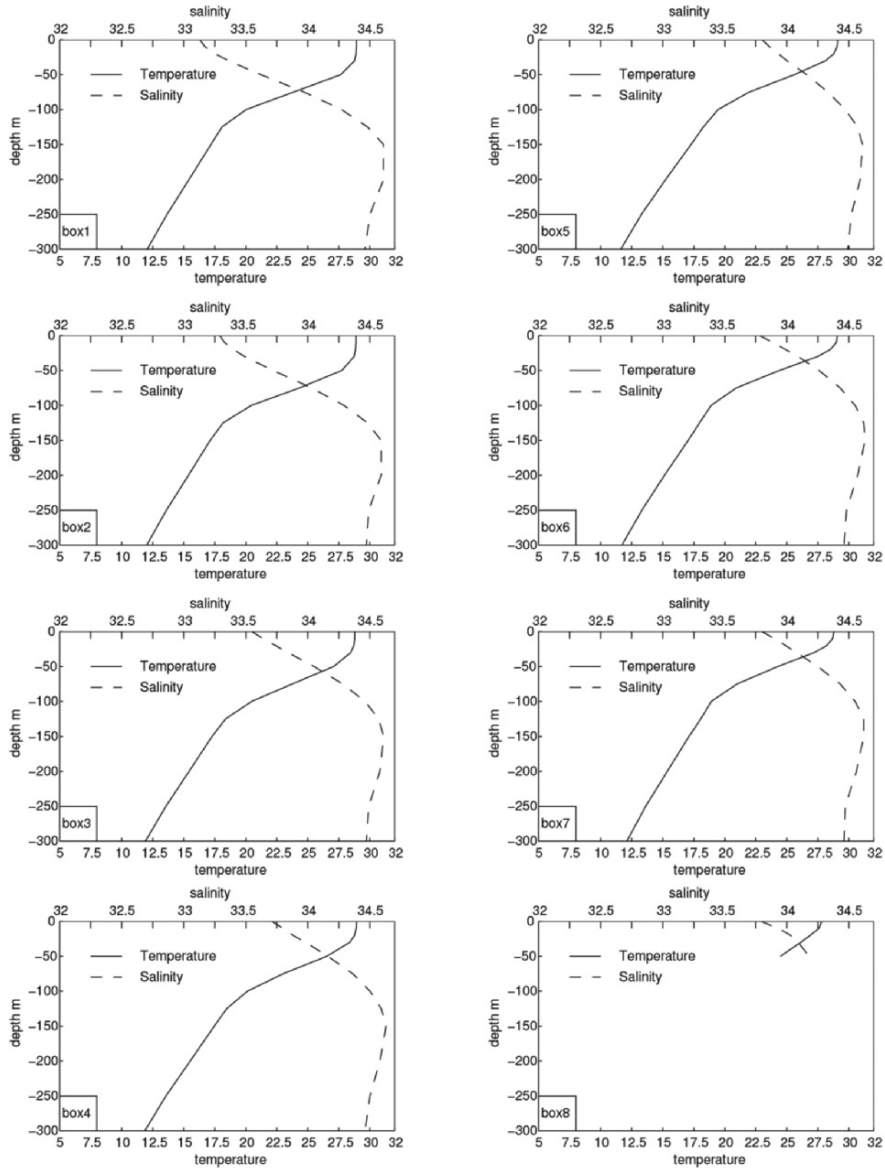


Fig. 11.51. Change of T and S profiles across the thermohaline front in July (from Chu and Wang 2003, *Journal of Oceanography*)

is used to represent the strength of the thermohaline front (Fig. 11.53c) at 50 m depth. The difference (ΔT) is larger in summer than in winter, and reaches 3.6°C (strongest subsurface thermohaline front) in June, and 0.9°C in October (weak subsurface thermohaline front).

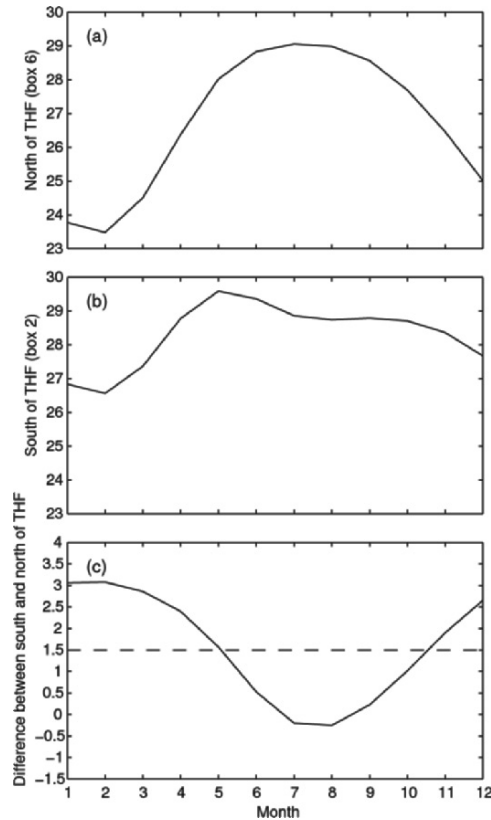


Fig. 11.52. Monthly evolutions of (a) SST ($^{\circ}\text{C}$) north of the thermohaline front (Box-6), (b) SST ($^{\circ}\text{C}$) south of the thermohaline front (Box-2), and (c) the difference between the two (ΔS_{ST}). A criterion of $\Delta S_{ST} = 1.5^{\circ}\text{C}$ (denoted by the *dashed line*) is used to represent the occurrence of the thermohaline front. Below the *dashed line*, $\Delta S_{ST} \leq 1.5^{\circ}\text{C}$, the temperature difference is not evident across the thermohaline front (from Chu and Wang 2003, *Journal of Oceanography*)

Surface Salinity

Monthly mean surface salinity shows different seasonal variability north (Box-6) and south (Box-2) of the thermohaline front (Fig. 11.54a, b). Low salinity is 33.78 ppt (32.96 ppt) north (south) of thermohaline front appearing in July and August (October and November). High salinity is 34.14 ppt (33.57 ppt) north (south) of the thermohaline front appearing in February (March). The seasonal variability is around 0.61 ppt (0.36 ppt) north (south) of the thermohaline front.

The difference,

$$\Delta S = S_{\text{Box-2}} - S_{\text{Box-6}},$$

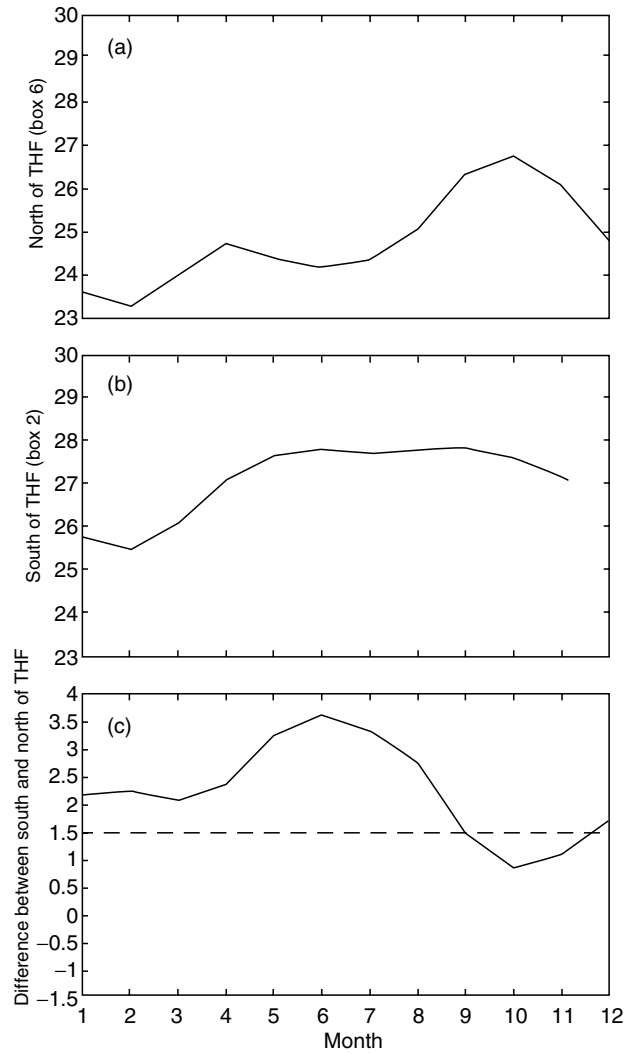


Fig. 11.53. Monthly evolutions at 50 m depth of (a) temperature ($^{\circ}\text{C}$) north of the thermohaline front (Box-6), (b) temperature ($^{\circ}\text{C}$) south of the thermohaline front (Box-2), and (c) the difference between the two (ΔT). A criterion of $\Delta T = 1.5^{\circ}\text{C}$ (denoted by the *dashed* line) is used to represent the occurrence of the thermohaline front. Below the dashed line ($\Delta T < 1.5^{\circ}\text{C}$), the temperature difference evident across the thermohaline front (from Chu and Wang 2003, *Journal of Oceanography*)

is used to represent the strength of the surface thermohaline front in salinity (Fig. 11.54c). The values of ΔS are all negative, indicating that the surface water is more saline to the north than south of the thermohaline front. The difference (ΔS) reaches a maximum value (0.96 ppt, strongest surface

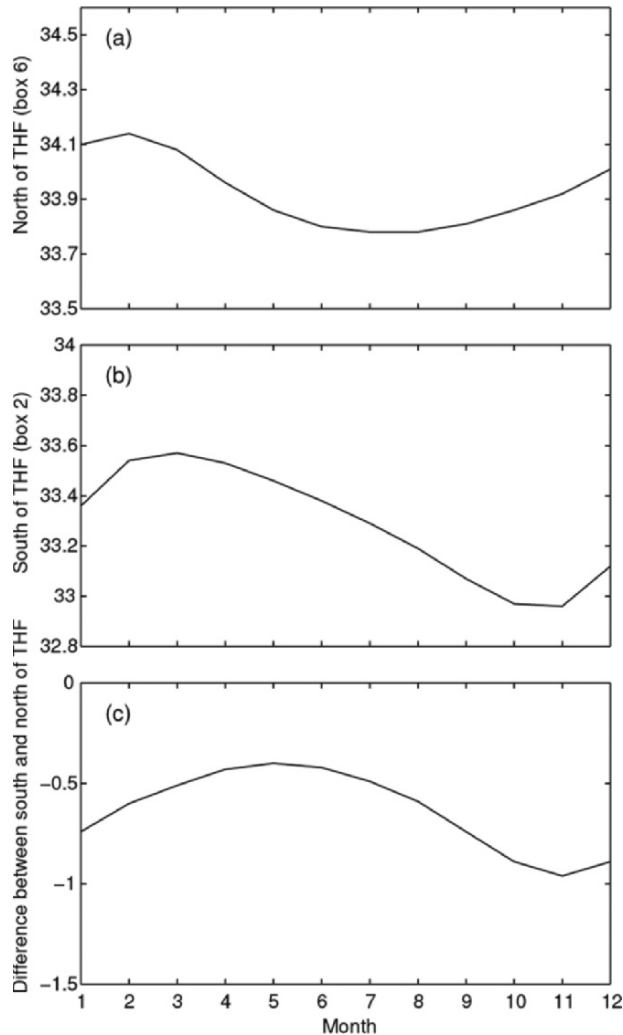


Fig. 11.54. Monthly evolutions at the surface of (a) salinity (ppt) north of the thermohaline front (Box-6), (b) salinity (ppt) south of the thermohaline front (Box-2), and (c) the difference between the two (ΔS) (from Chu and Wang 2003, Journal of Oceanography)

thermohaline front in salinity) in November, and a minimum value of 0.4 ppt in May (weak surface thermohaline front in salinity). The seasonal variation of ΔS is mainly caused by the salinity decrease in the southern South China Sea (Fig. 11.54b). This confirms that the major mechanism for the formation of the thermohaline front is the local expansion-blocking mechanism described in Sect. 11.8.3.

Subsurface (50 m) Salinity

Monthly mean salinity values at 50 m depth show a nearly in-phase seasonal variability north (Box-6) and south (Box-2) of thermohaline front (Fig. 11.55a, b). The minimum salinity north (south) of thermohaline front is 34.14 ppt (33.64 ppt) appearing in November (August and September). The maximum salinity occurs in May: 34.36 ppt north of thermohaline front, and 33.87 ppt south of thermohaline front. The seasonal variability is around 0.22 ppt in Box-6 and 0.23 ppt in Box-2, representing comparable seasonal variability north and south of the thermohaline front.

The salinity difference between Box-2 and Box-6 (Fig. 11.55c) represents the strength of the subsurface thermohaline front in salinity. The values of ΔS are all negative, indicating that the subsurface water is more saline at the north than at the south of the thermohaline front. The difference ΔS is nearly 0.5 ppt all the year round.

11.9 MultiEddy Structure Detected from AXBT Data

Climatological data (i.e., GDEM) show the existence and seasonal variability of the thermohaline front and associated cross-basin current in the central South China Sea. Lateral temperature and salinity gradients across the front may cause baroclinic instability which makes the cross-basin current to meander. Mesoscale eddies may be generated by the baroclinic instability. Wang et al. (2003) identified the multi-eddy structure using the satellite altimetry data. This section will discuss the multi-eddy structure in the South China Sea.

11.9.1 General Description

Seasonal occurrence of the South China Sea eddies have been reported by several authors. Dale (1956) and Uda and Nakao (1972) reported a cold eddy off the central Vietnam coast in summer. Nitani (1970) found a cold eddy located northwest of Luzon in summer. Reports from the South China Sea Institute of Oceanology (1985) indicate that a warm-core eddy appears in summer and winter in the central South China Sea, but in summer, it is closer to Vietnam at the surface. Recently, a cold-core eddy was detected in the central South China Sea during December 29, 1993, to January 5, 1994, from the analysis of TOPEX/Poseidon data (Soong et al. 1995). Chu et al. (1997c) and Chu and Chang (1997) identified a central surface warm-core eddy in mid-May from a historical data set: the MOODS. From the composite analysis on the NCEP monthly SST fields (1982–1994), Chu et al. (1997d) found that during the spring-to-summer monsoon transition (March–May) a warm anomaly (greater than 1.8°C) is formed in the central South China Sea at 112°–119°30'E, 15°–19°30'N.

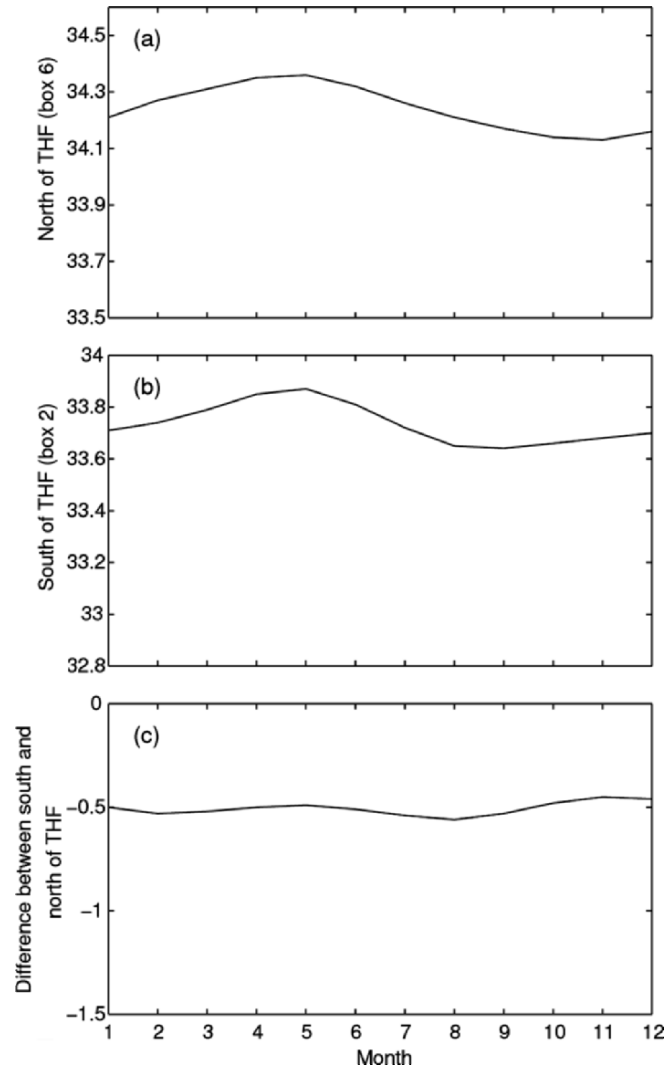


Fig. 11.55. Monthly evolutions at 50 m depth of (a) salinity (ppt) north of the thermohaline front (Box-6), (b) salinity (ppt) south of the thermohaline front (Box-2), and (c) the difference between the two (ΔS) (from Chu and Wang 2003, Journal of Oceanography)

The Naval Oceanographic Office conducted an intensive AXBT survey during May 14–25, 1995, over the majority of the South China Sea down to about 300 m depth. Figure 11.56 shows the daily AXBT deployment. This data set provides something close to a “snapshot” of the temperature in the upper ocean in the South China Sea during the transition time before the onset of the monsoon. Since only temperature-measuring AXBTs were used,

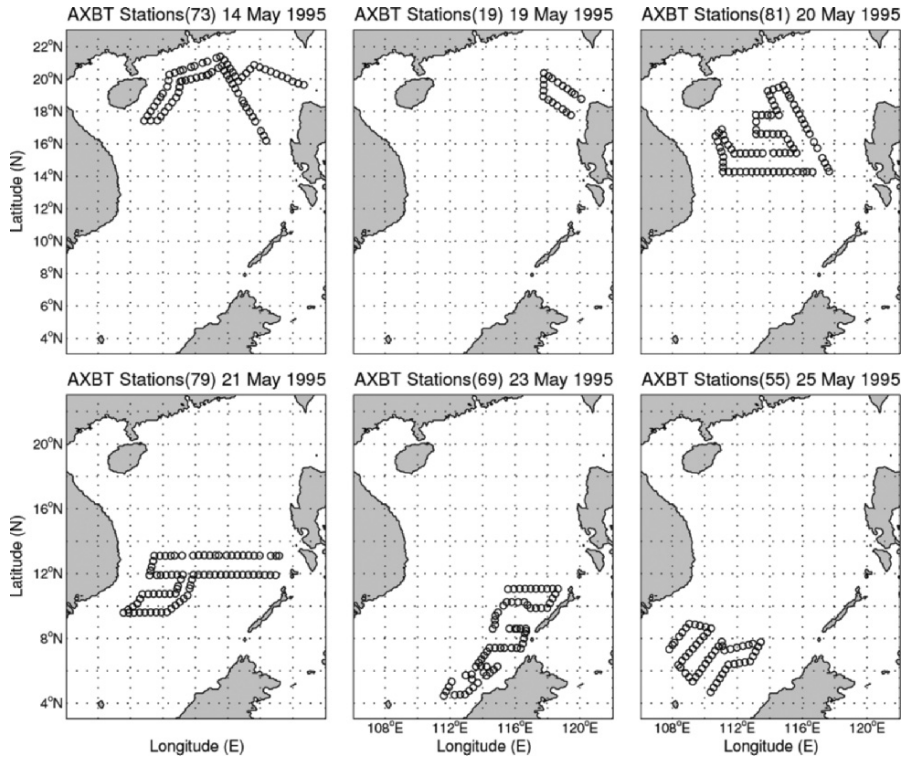


Fig. 11.56. Deployment pattern of AXBT survey during May 14–25, 1995 (from Chu et al. 1998d, *Journal of Geophysical Research*)

no salinity measurements were made at the same time. The three-dimensional velocity field is inverted from analysis of this temperature data set using climatological salinity data (Levitus et al. 1994) in lieu of in situ salinity data. Chu et al. (1998d) identified three dimensional multieddy structures from the AXBT data using the P-vector method.

11.9.2 AXBT Measurements

Most of the 376 AXBTs were deployed at six intervals over a 12 day period from May 14–25, 1995 (Chu et al. 1998d; Fig. 11.56). The majority of the AXBTs were nominally capable of reaching a depth of 360–400 m. The ensemble of temperature profiles (Fig. 11.57a) and the mean profile with an envelope of a standard deviation (Fig. 11.57b) show the existence of a mixed layer with depths ranging from 20 to 60 m and a thermocline with a vertical temperature gradient of 6–7°C per 100 m below the mixed layer.

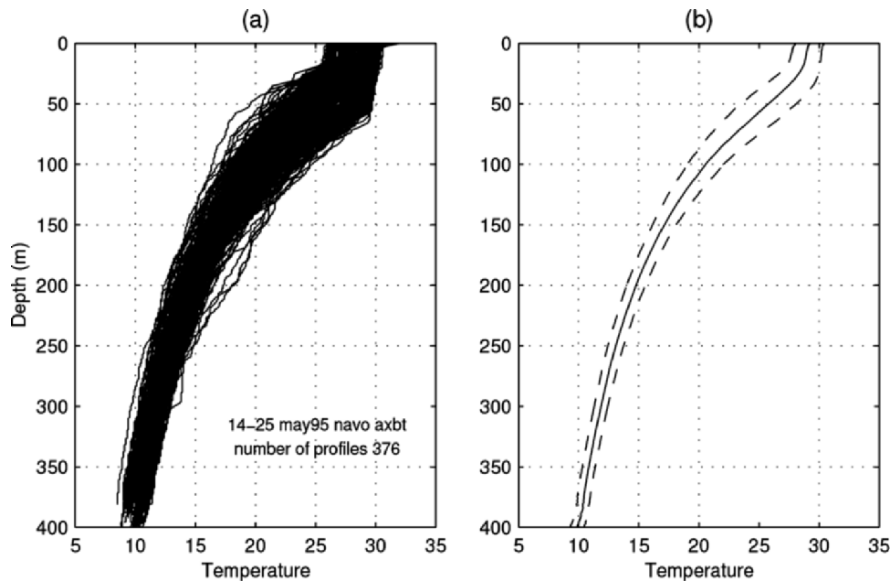


Fig. 11.57. Temperature profiles of AXBT survey during May 14–25, 1995. (a) Ensemble of profiles and (b) the mean profile with an envelope of a standard deviation. Both show the existence of a mixed layer with depths ranging from 20 to 60 m and a thermocline with a vertical temperature gradient of $6\text{--}7^\circ\text{C}/100\text{ m}$ below the mixed layer (from Chu et al. 1998d, *Journal of Geophysical Research*)

The AXBT observations were mapped to a regular grid at 12 levels (Table 11.1) using a two-scale OI scheme (Gandin 1965; Lozano et al. 1996). The large-scale OI was used to estimate the background mean with a decorrelation scale of 450 km. The mesoscale OI was used to map the observational anomaly from the background mean field into a regular grid with a spatial decorrelation scale of 75 km and a temporal decorrelation scale of 10 days. The spatial and temporal decorrelation scales associated to the mean field was estimated from the covariance matrix obtained from the MOODS for the South China Sea (Chu et al. 1997c). The large-scale mean was computed using the temperature and salinity profiles. The large-scale pattern for the surface (not shown) resembles the pattern previously estimated by Chu et al. (1997c). The decorrelation length scale for the fluctuations from the mean was estimated from the AXBT data. The results shown below are relatively insensitive to the length scale in the range of 60–90 km. The decorrelation timescale was selected to ensure synopticity. The SST horizontal scales seem rather larger than temperatures in the seasonal thermocline. Here, we choose horizontal scales to be uniform in the vertical for convenience and for lack of sufficient data to discriminate these differences properly.

11.9.3 Temperature

Horizontal Structures

Figure 11.58a–e shows horizontal depictions of temperature at 0, 50, 100, 200, and 300 m depths, respectively. The contour interval is 0.5°C . In them, we see that warmer water is situated at the central South China Sea with surrounding cooler water.

At 50 m depth, 28°C isotherm separates the warm central South China Sea water from the surrounding cooler water. The maximum temperature reaches 29°C . This central South China Sea warm pool extended to the 300 m depth and was surrounded by Dongsha, Hainan, South-Vietnamese Bight, and Liyue cool pools and also Xisha warm pool. The location and thermal features of these warm and cool pools are listed in Table 11.2.

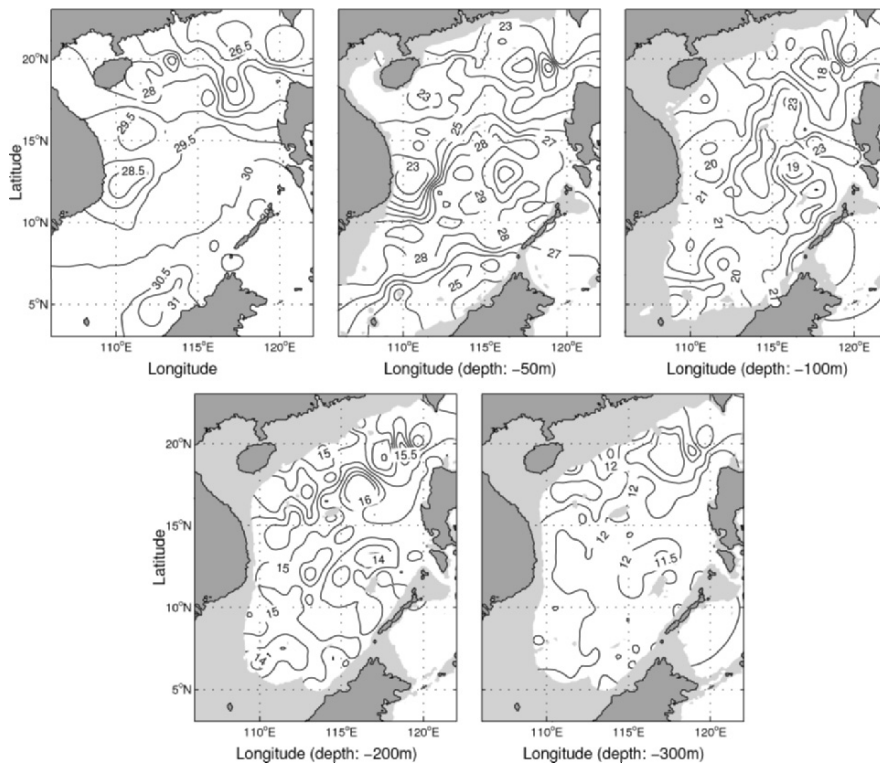


Fig. 11.58. Horizontal temperature fields at different depths: (a) 0 m, (b) 50 m, (c) 100 m, (d) 200 m, and (e) 300 m. The central South China Sea warm pool was surrounded by Dongsha, Hainan, South-Vietnamese Bight, and Liyue cool pools and Xisha warm pool (from Chu et al. 1998d, *Journal of Geophysical Research*)

Table 11.2. Locations, typical temperatures, and tangential velocities of the South China Sea warm-core and cool-core eddies detected during May 14–25, 1995 (from Chu et al. 1998d, Journal of Geophysical Research)

depth (m)	central (W)	Xisha (W)	Dongsha (C)	Hainan (C)	South Viet- namese Bight (C)	Liyue (C)
0	112–117°E 12–18°N 29.5–30°C 0.4 ms ⁻¹	110–112°E 14–16°N 29.5°C 0.2 ms ⁻¹	116–118°20'E 18–20°20'N 27°C 0.4 ms ⁻¹	110–112°E 18–20°N 28°C 0.1 ms ⁻¹	108–112°E 10–14°N 28.5°C 0.2 ms ⁻¹	115–118°E 12–14°N 29.5–30°C 0.3 ms ⁻¹
30	112–117°E 12–18°N 29°C 0.3 ms ⁻¹	110–112°E 14–16°N 24°C 0.1 ms ⁻¹	116–118°20'E 8–20°20'N 22°C 0.25 ms ⁻¹	110–112°E 16–18°N 23°C 0.08 ms ⁻¹	108–112°E 10–14°N 23°C 0.1 ms ⁻¹	115–118°E 12–14°N 26°C 0.3 ms ⁻¹
100	112–117°E 12–18°N 23°C 0.25 ms ⁻¹	110–112°E 14–15°N 21°C 0.08 ms ⁻¹	116–118°20'E 18–20°20'N 18°C 0.2 ms ⁻¹	109–111°30'E 16°40'–20°N 18°C 0.05 ms ⁻¹	110–112°E 12–14°N 20°C 0.1 ms ⁻¹	115–118°E 12–14°N 19°C 0.2 ms ⁻¹
200	112–117°E 12–18°N 16°C 0.1 ms ⁻¹	110–112°E 14–15°N 15°C 0.04 ms ⁻¹	116–118°20'E 18–20°20'N 13°C 0.1 ms ⁻¹	109–113°E 16–18°N 13.5°C 0.04 ms ⁻¹		114–117°E 11–14°N 14°C 0.09 ms ⁻¹
300	115–117°E 12–18°N 12°C 0.02 ms ⁻¹		110–113°E 18–20°20'N 11°C 0.03 ms ⁻¹	116–118°20'E 16–18°N 11°C 0.01 ms ⁻¹		114–116°E 10–14°N 11.5°C 0.03 ms ⁻¹

Vertical Structures

Four zonal cross sections (19°N, 17°N, 13°N, and 7°N) of temperature show the vertical structure of the mixed layer and the thermocline as well as the warm and cool pools (Fig. 11.59). The mixed layer was not evident at 19°N cross section but develops as latitude decreases. For 17°N and 7°N cross sections, the mixed layer shallows toward the east. At 13°N cross section, the mixed layer deepens at 114°E. The trough and ridge of the isotherms may be considered as centers of warm and cool pools.

At 19°N cross section, it shows the existence of Dongsha cool pool near 117°E from the uplifting (ridge) of isotherms. The ridge is located at 117°E at the surface, eastward shifted with depth, and kept at 117°E below the 100 m depth. The longitudinal span of Dongsha cool pool is around 2°.

The two cross sections at 17°N and 13°N show the occurrence of a central South China Sea warm pool from the downward bending (trough) of isotherms: 116°E at 17°N and 114°E at 13°N. The longitudinal span of central South China Sea warm pool is around 4° for both latitudes. The warm water is nearly isolated from the surrounding cooler water. This may suggest

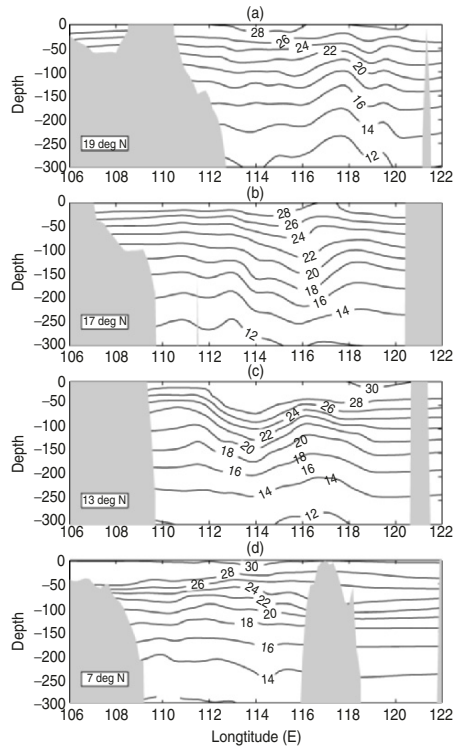


Fig. 11.59. Temperature distribution at several zonal cross sections: (a) 19°N, (b) 17°N, (c) 13°N, and (d) 7°N (from Chu et al. 1998d, *Journal of Geophysical Research*)

that local forcing might be important for the central South China Sea warm pool formation.

At 7°N cross section, it shows the eastward uplift of the thermocline depth from 50 m at 110°E to 25 m at 115°E. A surface warm pool with SST higher than 30°C is found between 112 and 115°E, and a midlevel (100 m) cool pool is detected between 110 and 112°E. In the eastern part (113–115°E), an isolated warm pool appeared below the 175 m depth.

Three latitudinal cross sections (111°E, 114°E, and 117°E) of temperature also show the vertical structure of the mixed layer and the thermocline as well as the warm and cool pools (Fig. 11.60). The mixed layer had a shallow-deep-shallow pattern in the latitudinal direction. Taking 114°E cross section as an example, the mixed layer had a shallow depth (about 10 m) near 5°N. Its depth increased with latitude to about 60 m at 13°30'N and decreased with latitude to almost zero (no mixed layer) near 20°N.

The trough and ridge of the isotherms may be considered as centers of warm and cool pools. The three cross sections indicated the occurrence of

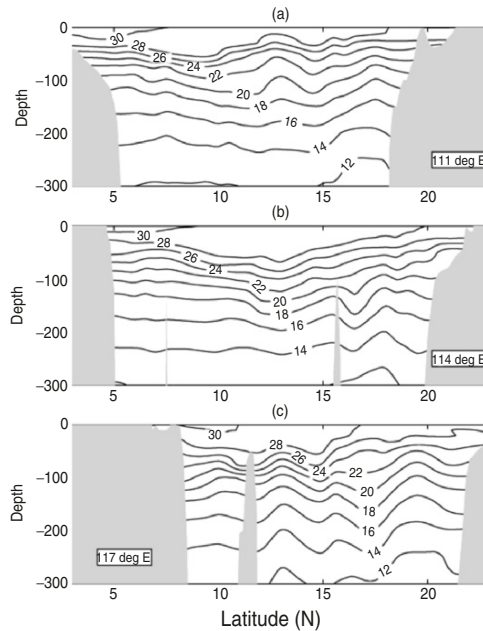


Fig. 11.60. Temperature distribution at several latitudinal cross sections: (a) 111°E, (b) 114°E, and (c) 117°E (from Chu et al. 1998d, *Journal of Geophysical Research*)

central South China Sea warm eddy evident from the downward bending (trough) of isotherms: 9°N at 111°E, 13°N at 114°E, and 15°N and 17°N at 117°E.

11.9.4 Circulations

T - S and $T - \bar{S}$ relations

The P-vector method for z -level is used to determine the velocity field from hydrographic data. Since there were no salinity (S) observations in the South China Sea during May 14–25, 1995, May WOA climatological salinity is interpolated to the AXBT stations and those salinity values (\bar{S}) were used for the P-vector computation. To validate this technique, we plotted two T - S diagrams: one diagram (Fig. 11.61a) is the plot of 3,478 (T , S) profiles from the MOODS in May 1933–1986 and the other diagram (Fig. 11.61b) is the plot of 376 T (AXBT) and \bar{S} profiles. The spatial and temporal distributions of the MOODS data are illustrated in Fig. 11.62a, b. A comparison between the two diagrams shows that the T - S characteristics remain stable. However, we should be aware of the shortcomings in using the climatological salinity values (\bar{S}). If the temperature field is relatively homogeneous in space, the density

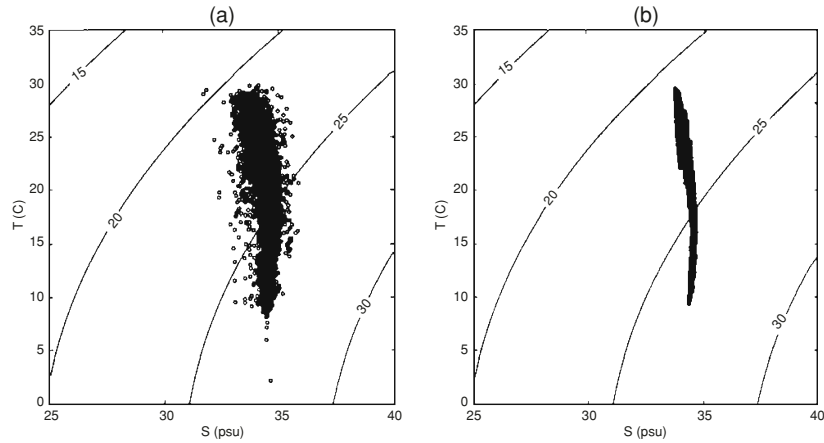


Fig. 11.61. T - S diagrams for (a) the MOODS data set in May 1933–1986 and (b) the AXBT temperature and May climatological salinity (from Chu et al. 1998d, *Journal of Geophysical Research*)

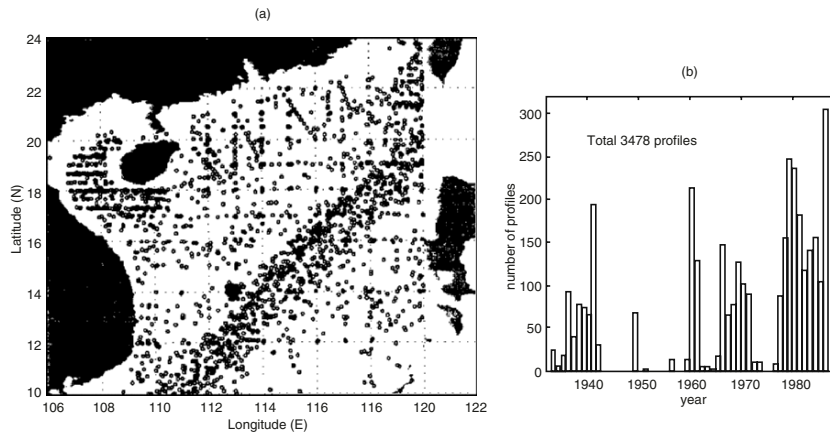


Fig. 11.62. The MOODS data distribution: (a) spatial and (b) temporal (from Chu et al. 1998d, *Journal of Geophysical Research*)

gradient depends mostly on the salinity gradient. Under that circumstance, the use of the climatological salinity values may bring large errors in inverting the velocity field.

Horizontal Velocity Fields

The available historical data (Wyrtki 1961a) show two totally different circulation patterns for the months preceding and following the AXBT survey in the central South China Sea: a cyclonic gyre in April (Fig. 11.63a) and an

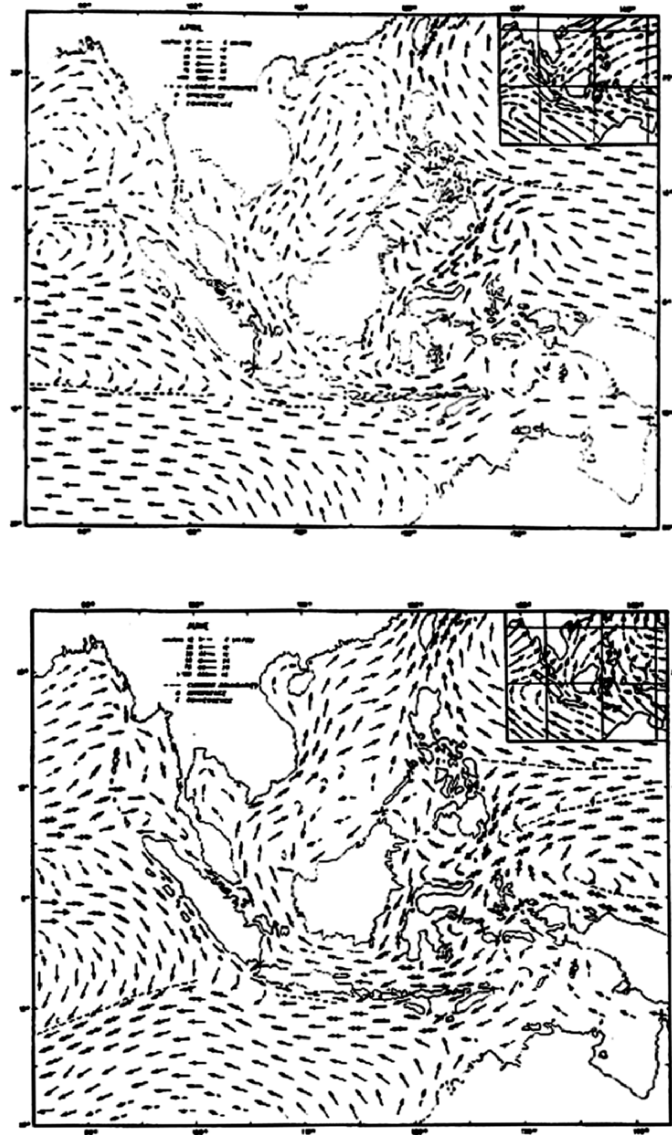


Fig. 11.63. A drastic change of the surface circulation from (a) April to (b) June (from Wyrтки 1961a)

anticyclonic gyre in June (Fig. 11.63b). We may treat the May circulation as the transition between the two patterns.

The inverted velocity data set (Fig. 11.64) indicates the existence of a central South China Sea anticyclonic gyre surrounded by several cyclonic and anticyclonic eddies. Generally, the anticyclonic (cyclonic) eddies are associated

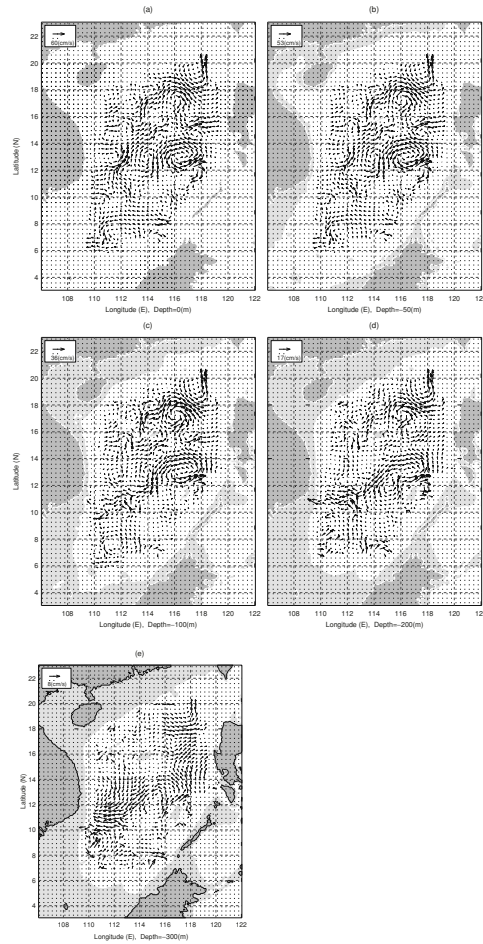


Fig. 11.64. Absolute velocity at different depths: (a) 0 m, (b) 50 m, (c) 100 m, (d) 200 m, and (e) 300 m. The central South China Sea anticyclonic eddy was surrounded by Dongsha, Hannan, South Vietnamese Bight, and Liyue cyclonic eddies and Xisha anticyclonic eddy (from Chu et al. 1998d, *Journal of Geophysical Research*)

with the warm (cool) pools. The kinetic features of these eddies are listed in Table 11.2. Furthermore, the magnitude of inverted velocities decreases with depth and is quite small at 300 m. This implies that the geostrophic calculation with the level-of-no-motion at or below about a 300 m depth could have been used to give results close to the P-vector method.

The observed three-dimensional temperature and inverted velocity fields indicate the existence of a central South China Sea warm-core anticyclonic eddy with surrounding Dongsha, Hannan, South Vietnamese Bight, and Liyue cool-core cyclonic eddies and Xisha warm-core anticyclonic eddy (Fig. 11.65).

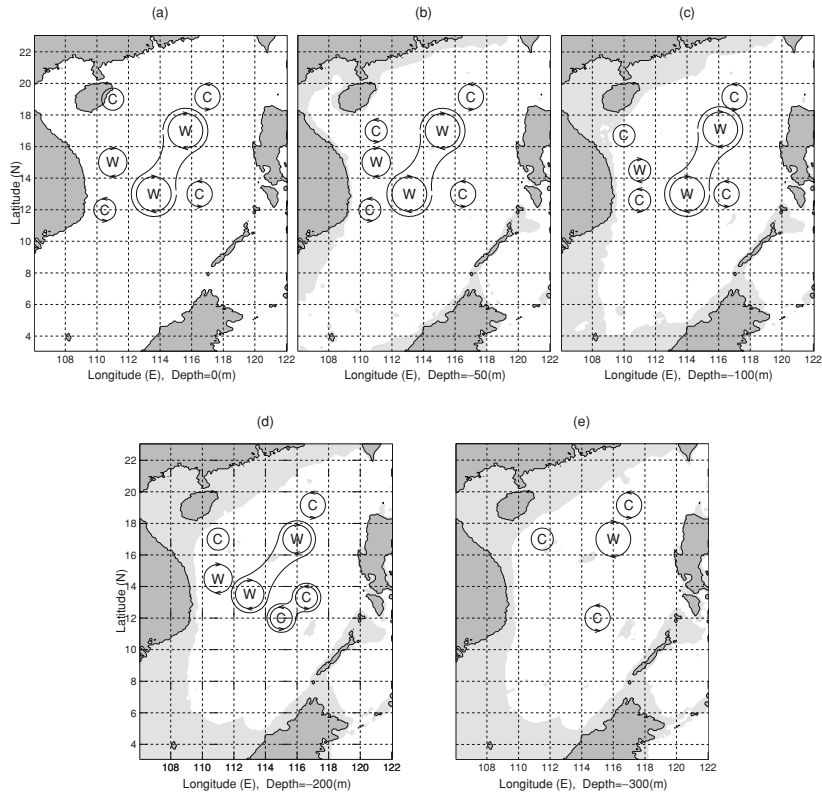


Fig. 11.65. Illustration of South China Sea warm-core and cool-core eddies in May 1995 (from Chu et al. 1998d, Journal of Geophysical Research)

Zonal Cross Sections of *v*-Component

Four zonal cross sections (19°N, 17°N, 13°N, and 7°N) of *v* velocity show the vertical eddy structure (Fig. 11.66). The positive values indicate northward velocity, and the negative values refer to the southward velocity. Alternate positive and negative areas indicate the occurrence of cyclonic and anticyclonic eddies. At each zonal cross section, a neighboring eastern negative/western positive pattern refers to an anticyclonic eddy, and, a neighboring western negative/eastern positive pattern refers to a cyclonic eddy.

At 19°N cross section, it shows the existence of the Dongsha cyclonic eddy near 117°E. The diameter of the Dongsha eddy is around 300 km. The depth of the eddy is around 200 m. This eddy reveals an asymmetric feature. The northward velocity with a maximum speed of 0.4 ms⁻¹ in the eastern part is stronger than the southward velocity with a maximum speed of 0.1 ms⁻¹ in the western part.

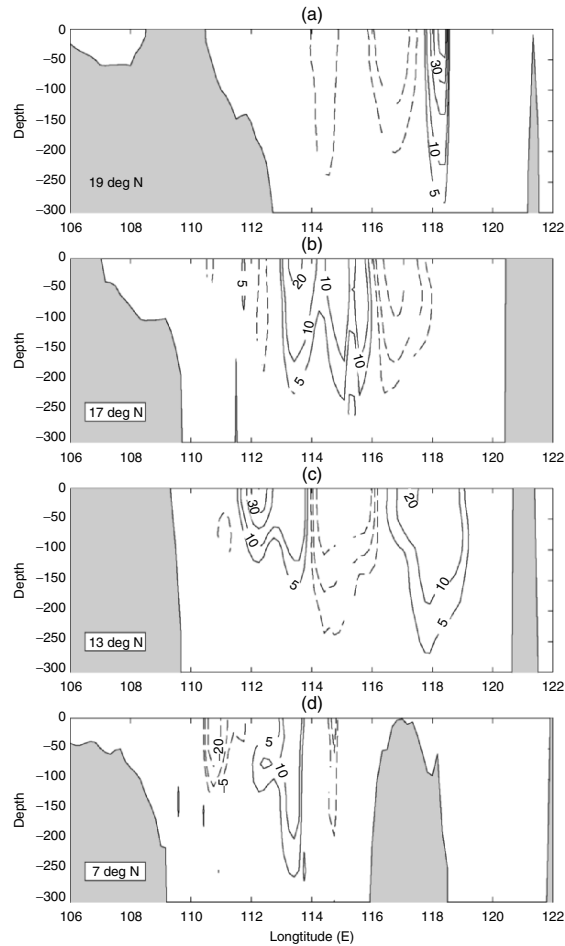


Fig. 11.66. Distribution of velocity v component at several zonal cross sections: (a) 19°N , (b) 17°N , (c) 13°N , and (d) 7°N (from Chu et al. 1998d, *Journal of Geophysical Research*)

At 17°N cross section, it shows the existence of the central South China Sea anticyclonic eddy that is centered at 116°E . The zonal span of the central South China Sea eddy is around 500 km. The depth of the eddy is around 300 m. The maximum tangential velocity is around 0.2 m s^{-1} . This eddy is quite symmetric with a maximum southward velocity in the eastern part similar to the northward velocity in the western part.

At 13°N cross section, it shows the existence of a double-eddy structure. Between 112 and 116°E there was a strong anticyclonic eddy (the central South China Sea eddy) with a maximum tangential speed of 0.3 m s^{-1} (appearing in the upper 50 m) and that is centered at 114°E . The zonal span of

this eddy is around 500 km. This anticyclonic eddy is associated with the central South China Sea warm pool. The depth of the eddy is around 250 m. To the east of the anticyclonic eddy, a cyclonic eddy appeared between 114 and 119°E that is centered at 116°20'E. This cyclonic eddy is associated with the Liyue cool pool, and therefore called the Liyue cool-core (cyclonic) eddy. The central South China Sea warm-core eddy and Liyue cool-core eddy shared the same southward branch. Furthermore, the northward flow at the eastern part of the Liyue cool-core eddy (maximum tangential speed around 0.1 m s^{-1}) is weaker than the southward flow in the western part.

At 7°N cross section, it shows the occurrence of a cyclonic eddy (110–114°E). This cyclonic eddy is quite asymmetric. The southward flow (maximum tangential speed around 0.2 m s^{-1}) in the western part is stronger than the northward flow (maximum tangential speed around 0.1 m s^{-1}) in the eastern part. The depth of the eddy is around 150 m. To the east of the anticyclonic eddy, a cyclonic eddy appeared between 114 and 119°E that is centered at 116°20'E.

Latitudinal Cross Sections of u -Component

Three latitudinal cross sections (111°E, 114°E, and 117°E) of u velocity also show the vertical eddy structure (Fig. 11.67). The positive values indicate eastward velocity, and the negative values refer to westward velocity. Alternate positive and negative areas indicate the occurrence of cyclonic and anticyclonic eddies. At each latitudinal cross section, a neighboring southern negative/northern positive pattern refers to an anticyclonic eddy. However, a neighboring northern negative/southern positive pattern refers to a cyclonic eddy.

The area with a southern negative/northern positive u pattern (anticyclonic eddy) coincides with the area of the downward bending isotherms (warm pool). At 111°E cross section, the central South China Sea warm-core eddy is identified by an isotherm trough located at 9°N (Fig. 11.65), and an anticyclonic eddy is identified by the southern negative/northern positive u pattern that is centered at 9°N (Fig. 11.67). At the 114°E cross section, the central South China Sea warm-core eddy is identified by an isotherm trough located at 13°N (Fig. 11.65), and an anticyclonic eddy is identified by the southern negative/northern positive u pattern that is centered at 13°N (Fig. 11.67).

11.9.5 Mechanisms

In searching mechanisms for the formation of this recurring seasonal signal, a central South China Sea warm anomaly, Chu et al. (1997d) found a high correlation between surface wind stress curl and SST anomaly from correlation analysis of the European Center for Medium-range Weather Forecast (ECMWF) analyzed wind stress data and the NCEP SST data. The high correlation leads to a hypothesis for the wind-driven central South China Sea warm pool during the spring-to-summer monsoon transition. The bowl-type

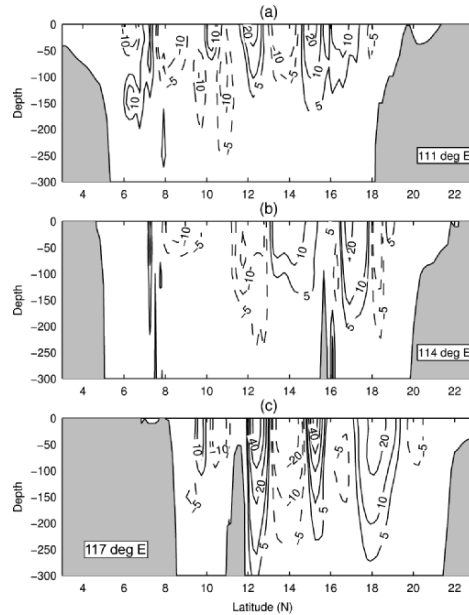


Fig. 11.67. Distribution of velocity u component at several latitudinal cross sections: (a) 111°E , (b) 114°E , and (c) 117°E (from Chu et al. 1998d, *Journal of Geophysical Research*)

bottom topography (Fig. 11.68) provides a favorable condition for the central South China Sea warm pool formation in the spring-to-summer monsoon transition. In spring, a surface anticyclone usually appears over the central South China Seas (Cheang 1980). Ekman downwelling will occur in the central part of the “bowl,” and mass balance will cause upwelling near the boundary of the bowl. The downwelling prevents the deep cold water from upward advection, while the upwelling along the boundary helps the upward advection of deep cold water. This makes the central part of the bowl warm and the side part of the bowl cool and leads to the generation of the central South China Sea warm pool surrounded by several cool pools. Furthermore, other mechanisms such as remote forcing and topographic influence could be significant. This wind-driven mechanism for the formation of a central South China Sea warm-core eddy with surrounding cool-core eddies during the spring-to-summer transition was confirmed by a numerical study (Chu et al. 1998c).

11.10 Low Salinity Cold-Core Cyclonic Eddy Northwest of Luzon

Last section shows the existence of six eddies in the South China Sea from an AXBT survey conducted in May 1995 and historical salinity data using the

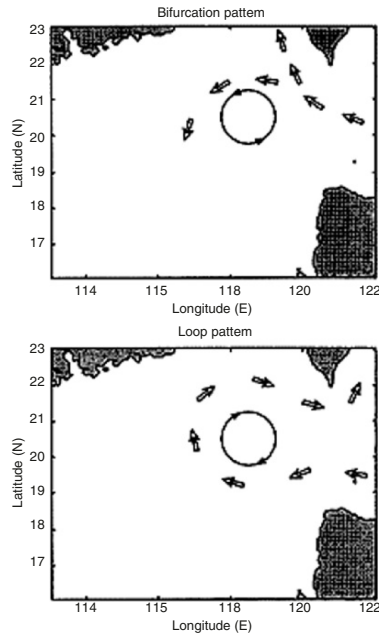


Fig. 11.69. Two regimes of the northeast South China Sea circulation: (a) bifurcation pattern, and (b) loop pattern (from Chu and Fan 2001, *Journal of Oceanography*)

istics of the major eddy (i.e., the northwestern Luzon eddy) in the area. If this eddy is cyclonic (Qiu et al. 1985; Chu and Fan 2001), the northeast South China Sea circulation takes the bifurcation pattern: The Kuroshio water is intruded into the South China Sea through the whole Luzon Strait and bifurcated into northward and northwestward branches before impinging the eddy. The northwestward branch was circulating around the cyclonic eddy (Fig. 11.69a). If this eddy is anticyclonic (Li et al. 1998), the northeast South China Sea circulation takes the loop pattern (Metzger and Hurlburt 1996). The Kuroshio water is intruded into the South China Sea through the southern Luzon Strait. It loops around the anticyclone, exits the South China Sea through the northern Luzon Strait, and rejoins the Kuroshio currents (Fig. 11.69b).

The northwestern Luzon eddy was claimed to be either cold-core cyclonic or warm-core anticyclonic from geostrophic shear calculated from hydrographic data. For example, Nitani (1970) used limited data to identify this eddy to be cold-core cyclonic and occurring in the summer. Xu et al. (1982) used historical (1921–1970) hydrographic data to identify this eddy to be cold-core cyclonic and occurring in the winter. Zhou et al. (1995) confirmed the occurrence of the northwestern Luzon cold-core cyclonic eddy in both winter and summer using the climatological monthly mean temperature and salin-

ity data. Recently, Li et al. (1998) analyzed the hydrographic data collected during a major expedition of the Northeastern South China Sea Circulation Cooperative Study in August–September 1994 and identified the northwestern Luzon eddy to be warm-core anticyclonic. All of these observational studies are based on the level-of-no-motion assumption. For example, Xu et al. (1982) and Li et al. (1998) assumed 1,200 and 1,000 db as the level-of-no-motion, respectively.

11.10.2 Observations

To remove the level-of-no-motion assumption, Chu et al. (1998d) (see Sect. 11.9) used the P-vector inverse method to identify the northwestern cold-core cyclonic eddy from an extensive AXBT survey conducted in May 1995 and historical salinity data. A weakness of the study (Chu et al. 1998d) is the use of the synoptic temperature data and the climatological salinity data. The incompatible T , S data may lead to some error in the inversion of absolute velocity.

One objective of SCSMEX is to detect the South China Sea eddy features. During the intensive observational period of the SCSMEX in July 1998, the US Naval Oceanographic Office conducted an intensive airborne expendable hydrographic survey of the northeast South China Sea on July 8–26, 1998. The Chinese Academy of Sciences conducted the ADCP measurements on R/V Shiyang3. The airborne hydrographic survey includes 307 AXBT stations and 9 AXCTD stations, uniformly distributed in the region ($114^{\circ}30'–121^{\circ}30'E$, $17–22^{\circ}N$) that is shown in Fig. 11.68 as the shaded box. Due to Navy regulations, it is unable to present the T , S station distribution. The maximum depth of the observations is 400 m. This data set provides something close to a “snapshot” of the temperature and salinity in the upper ocean in the northeast South China Sea in July 1998. With synoptic T , S data, we may obtain a more accurate estimation of the northwestern Luzon eddy using the P-vector inverse method. The 307 AXBTs and 9 AXCTDs were deployed over a period of July 8–26, 1998. The majority of the AXBTs/AXCTDs were nominally capable of reaching a depth of 400 m. The vertical resolution of the measurements is 1 m. The T – S diagram of the AXCTD data (Fig. 11.70) shows the typical northeast South China Sea water depicted by Li et al. (1998): The salinity maxima are less than 34.7 ppt and the salinity minima are larger than 34.40 ppt.

The in situ density with 1 m vertical resolution is computed from the 9 AXCTD stations. Horizontal average of 316 temperature stations, nine salinity stations, and nine in situ density profiles at each depth leads to the vertical mean profiles of temperature $\bar{T}(z)$, salinity $\bar{S}(z)$, and density $\bar{\rho}(z)$. From the mean density profile, the buoyancy frequency is computed,

$$N = \sqrt{-\frac{g}{\rho_0} \frac{d\bar{\rho}(z)}{dz}}. \quad (11.4)$$

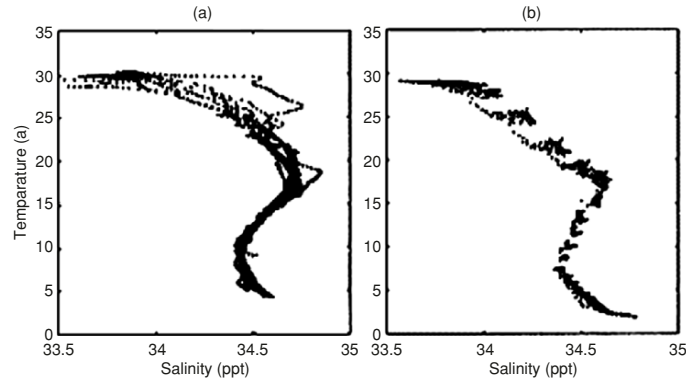


Fig. 11.70. (a) T - S diagram constructed from the AXCTD data, and (b) \hat{T} - \hat{S} diagram constructed from the interpolated data (from Chu and Fan 2001, *Journal of Oceanography*)

The mean temperature profile shows a very shallow mixed layer with the depth less than 20 m (Fig. 11.71a). Below the mixed layer, the mean temperature reduces rapidly with depth from 29.5°C at the base of the mixed layer (20 m) to 20°C at the 100 m depth, and then reduces slowly with depth from 20°C at the 100 m depth to 10°C at the 400 m depth.

The mean salinity profile (Fig. 11.71b) shows the existence of salinity maxima (34.63 ppt) located at the 125–175 m depths and of salinity minima (34.43 ppt) located at the 400 m depth. The mean density profile (Fig. 11.71c) shows that the vertical variability of $\bar{\rho}(z)$ follows the vertical variability of $\bar{T}(z)$. The buoyancy frequency (Fig. 11.71d) increases with depth from 0 at the surface to a maximum value (0.026 s^{-1}) at the 45 m depth and then tends to reduce with depth to a minimum value (0.007 s^{-1}) at the 400 m depth.

The same as in Sect. 11.9, the AXBT/AXCTD observations were mapped at each depth using a two-scale OI scheme (Gandin 1965; Lozano et al. 1996). The large-scale OI was used to estimate the background mean with a decorrelation scale of 450 km. The mesoscale OI was used to map the observational anomaly from the background mean field into a regular grid with a spatial decorrelation scale of 75 km and a temporal decorrelation scale of 10 days.

The spatial and temporal decorrelation scales associated to the mean field were estimated from the covariance matrix obtained from the MOODS for the South China Sea (Chu et al. 1997c). The large-scale mean was computed using the temperature and salinity profiles. The large-scale pattern for the surface (not shown) resembles the pattern previously estimated by Chu et al. (1997c). The decorrelation length scale for the fluctuations from the mean was estimated from the AXBT data. The results shown below are relatively insensitive to the length scale in the range of 60–90 km. The decorrelation timescale was selected to ensure synopticity. The SST horizontal scales seem rather larger than temperatures in the seasonal thermocline. In this study, we choose

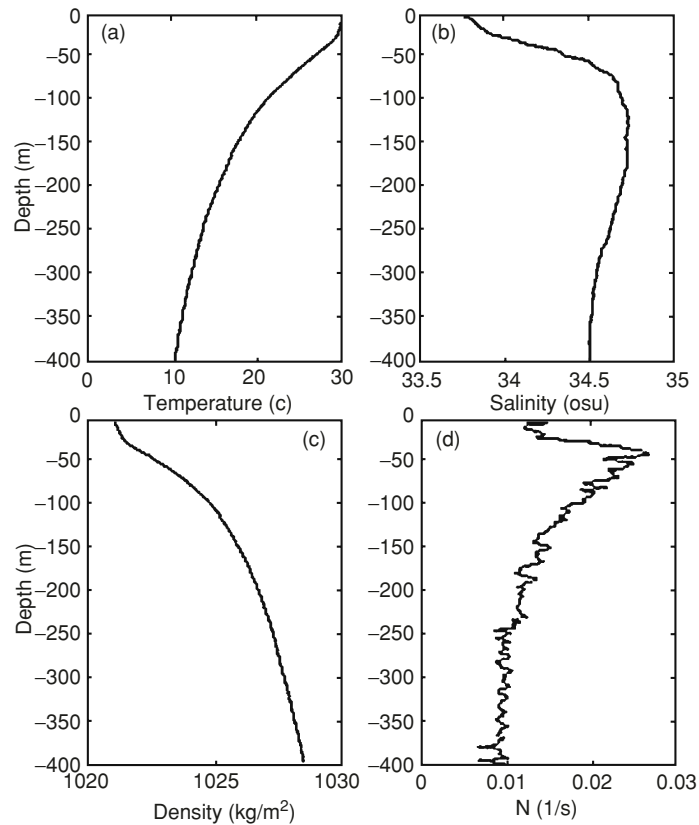


Fig. 11.71. Mean vertical profiles of (a) temperature, (b) salinity, (c) density, and (d) buoyancy frequency (from Chu and Fan 2001, *Journal of Oceanography*)

horizontal scales to be uniform in the vertical for convenience and for lack of sufficient data to discriminate these differences properly.

The current observations were made from R/V *Shiyan3* on 16–21 July 1998. That vessel was equipped with an ADCP and a global position system (GPS) receiver. This system measured currents underway from depths of about 10–250 m in 4 m depth bins. Five minute averages were recorded.

11.10.3 Temperature

Horizontal Structure

Figure 11.72 shows the horizontal depictions of temperature at nine different depths from the surface to the 400 m depth, with 50 m interval. A cold-core ring is located northwest of Luzon Island ($116\text{--}119^\circ\text{E}$, $19\text{--}21.5^\circ\text{N}$) with surrounding warmer water. The cold-core was evident at all levels, $1\text{--}2^\circ\text{C}$ cooler

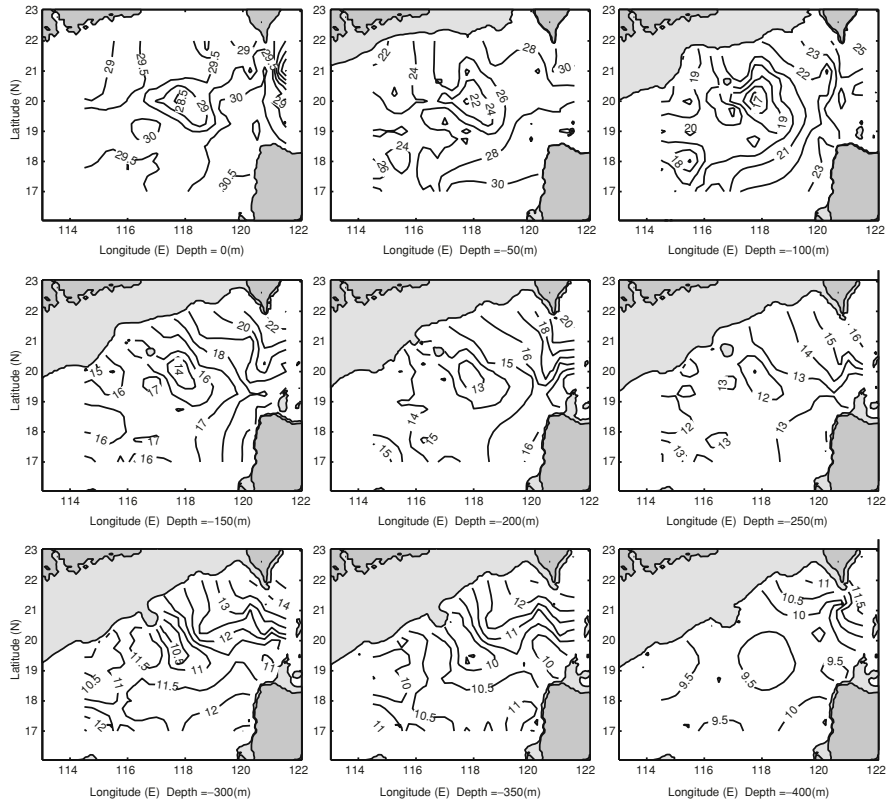


Fig. 11.72. Horizontal temperature fields at nine different depths from the surface to 400 m at 50 m intervals. Cooler water is situated northwest of Luzon Island (116–119°E, 19–21.5°N), surrounded by warmer water (from Chu and Fan 2001, *Journal of Oceanography*)

inside than outside of the eddy. The location and thermal features of the northwestern Luzon cold-core eddy are listed in Table 11.3.

Vertical Structure

Six zonal cross sections, from 17 to 22°N, of temperature (Fig. 11.73) show the vertical layered structure (mixed layer, thermocline, and layer below the thermocline). A cold-core can be identified by the uplifting (ridge) of isotherms and a warm-core can be identified from the downward bending (trough) of the isotherms.

The mixed layer is not evident at 22°N cross section but becomes evident as latitude decreases. From 21 to 17°N cross sections, the mixed layer shallows toward the west. A shallow layer (< 50 m depth) of warm water with temperature higher than 30°C occurs in Luzon Strait (120–120.7°E) at 20°N

Table 11.3. Location, typical temperature, salinity, and tangential velocity of the northwestern Luzon low salinity cool-core cyclonic eddy (from Chu 2001, Journal of Oceanography)

Depth (m)	location	T ($^{\circ}\text{C}$)	S (ppt)	Max tangential velocity (m s^{-1})
0	19–21 $^{\circ}$ N; 116.5–119 $^{\circ}$ E	28.5	33.60	0.50
50	18.8–21.5 $^{\circ}$ N; 116.5–119 $^{\circ}$ E	22.0	34.40	0.45
100	18.8–21.5 $^{\circ}$ N; 116.75–119 $^{\circ}$ E	17.0	34.52	0.20
150	19–20.8 $^{\circ}$ N; 116.5–119 $^{\circ}$ E	14.0	34.64	0.12
200	18.5–21 $^{\circ}$ N; 117–119 $^{\circ}$ E	13.0	34.56	0.06
250	19–21 $^{\circ}$ N; 116.5–119 $^{\circ}$ E	12.0	34.50	0.06
300	18.8–20.8 $^{\circ}$ N; 117–119 $^{\circ}$ E	10.5	34.46	0.05

cross section. This warm water westward extends as the latitude decreases. At 17 $^{\circ}$ N cross section, the warm water ($T > 30^{\circ}\text{C}$) reaches 117 $^{\circ}$ E.

The cross sections from 21 to 19 $^{\circ}$ N clearly show the existence of the northwestern Luzon cold-core near 117.5 $^{\circ}$ E from the uplifting (ridge) of isotherms. Taking 20 $^{\circ}$ N cross section as an example, the ridge is located at 117.8 $^{\circ}$ E from the surface to the 400 m depth. The longitudinal span of the northwestern Luzon cold eddy is around 300 km.

Six latitudinal cross sections from 116 to 121 $^{\circ}$ E of temperature (Fig. 11.74) show the same vertical layered structure (mixed layer, thermocline, and layer below the thermocline). The mixed layer shallows toward the north in the western cross sections (115–116.5 $^{\circ}$ E). A shallow layer (< 50 m depth) of warm water ($T > 30^{\circ}\text{C}$) occurs in the southern part of the Luzon Strait (south of 20.3 $^{\circ}$ N) at 120 $^{\circ}$ E cross section. This warm water retreats toward the south as the longitude decreases. At the 117 $^{\circ}$ E cross section, the warm water ($T > 30^{\circ}\text{C}$) disappears.

The cross sections from 117 to 119 $^{\circ}$ E show the existence of the northwestern Luzon cold-core eddy near 18–21 $^{\circ}$ N from the uplifting (ridge) of isotherms. Taking 118 $^{\circ}$ E cross section as an example, the ridge is located at 20 $^{\circ}$ N from the surface to the 400 m depth. The latitudinal span of the northwestern Luzon cold eddy is around 300 km.

11.10.4 Salinity

Horizontal Structures

Figure 11.75 shows the horizontal depictions of salinity at nine different depths from the surface to the 400 m depth with 50 m interval. In them, we see low salinity centers associated with the northwestern Luzon cold-core eddy at various depths: a low salinity center ($S < 33.60$ ppt) with the northwestern Luzon cold-core ($T < 29^{\circ}\text{C}$) at the surface, a low salinity tongue ($S < 34.64$ ppt) ($T < 14^{\circ}\text{C}$) at 150 m depth, and a low salinity center ($S < 34.45$ ppt) ($T < 9.5^{\circ}\text{C}$) at the 400 m depth.

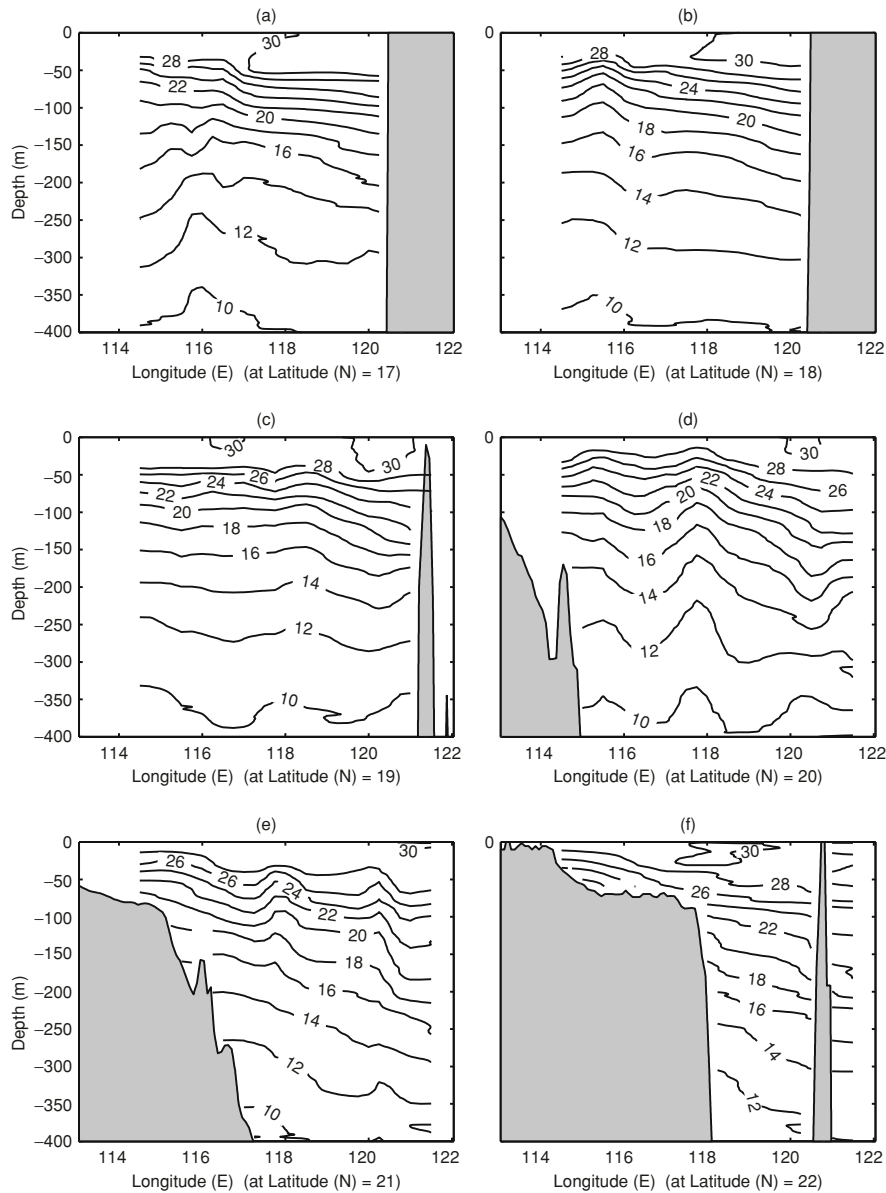


Fig. 11.73. Temperature distribution at several zonal cross sections: (a) 17°N, (b) 18°N, (c) 19°N, (d) 20°N, (e) 21°N, and (f) 22°N (from Chu and Fan 2001, *Journal of Oceanography*)

Vertical Structures

Six zonal cross sections, from 17 to 22°N, of salinity (Fig. 11.76) show a strong northward uplifting of halocline. The halocline occurs between 30 and 50 m depths north of 20°N and 40–75 m depths south of 20°N.

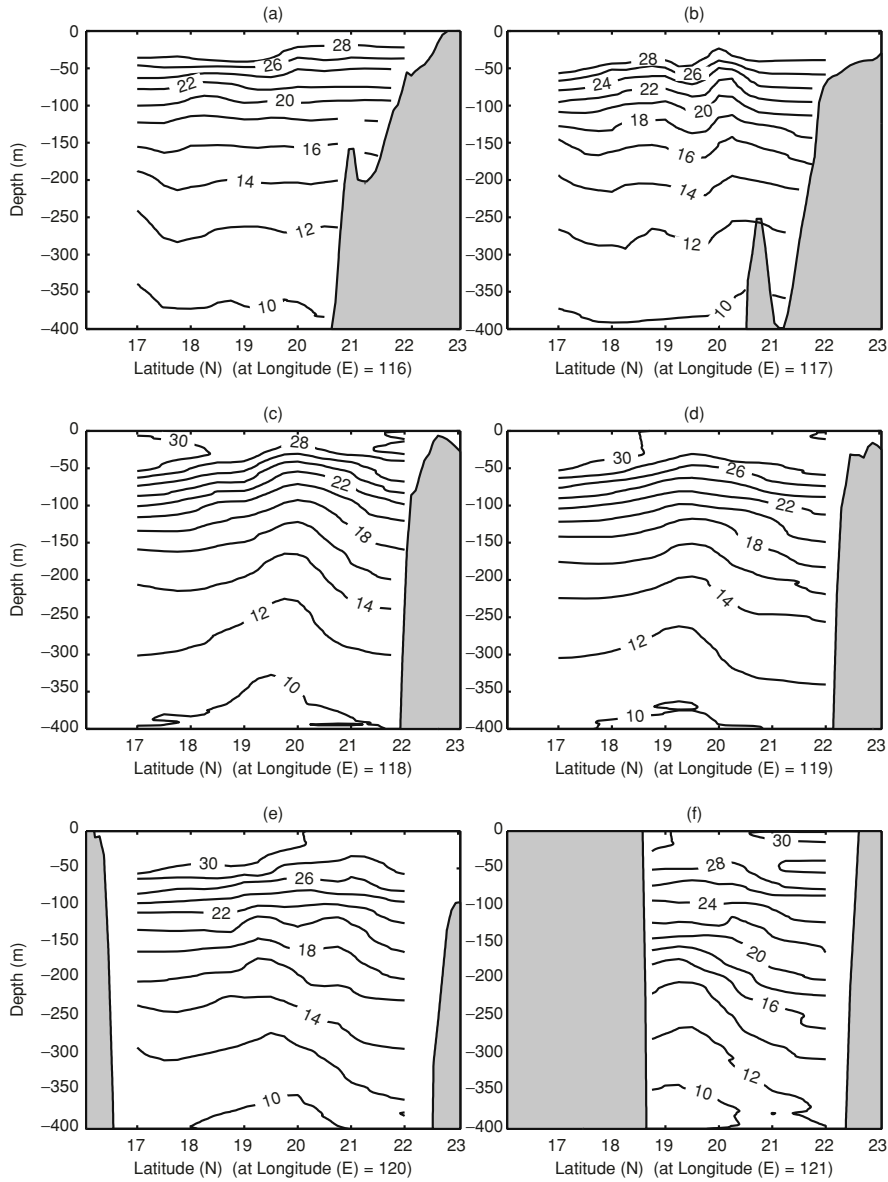


Fig. 11.74. Temperature distribution at several latitudinal cross sections: (a) 116°E, (b) 117°E, (c) 118°E, (d) 119°E, (e) 120°E, and (f) 121°E (from Chu and Fan 2001, *Journal of Oceanography*)

The strength of the halocline decreases toward south. The cross sections of 17°–18°N show an evident westward uplifting of the halocline. Below the halocline, salinity maxima (> 34.7 ppt) can be identified from all the cross

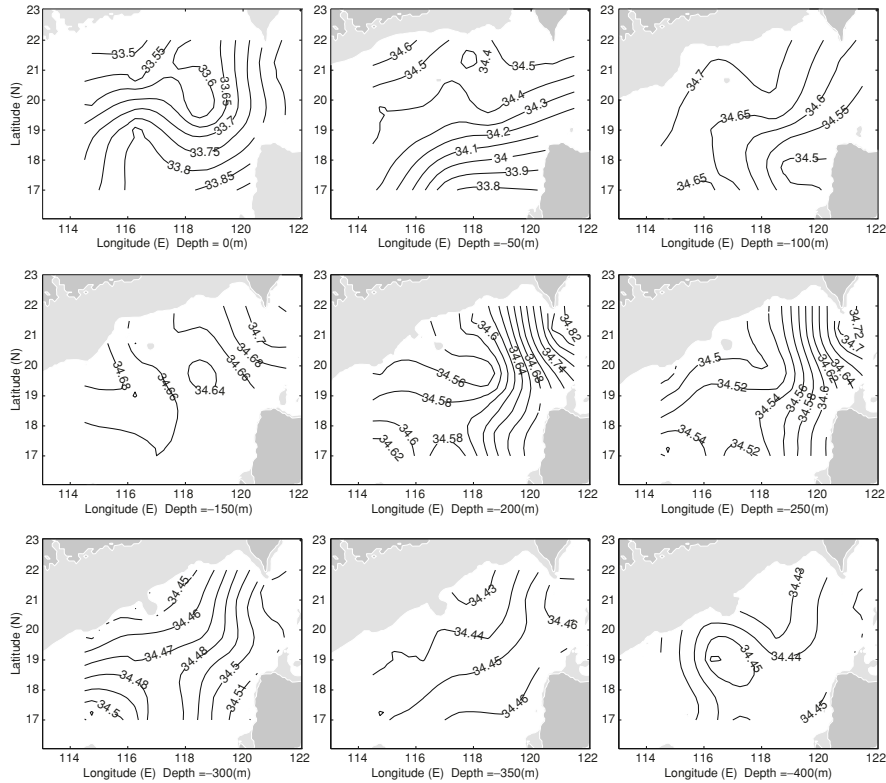


Fig. 11.75. Horizontal salinity fields at nine different depths from the surface to 400 m at 50 m intervals. Fresher water is situated northwest of Luzon Island, surrounded by saltier water (from Chu and Fan 2001, *Journal of Oceanography*)

sections with shallow depths (100–150 m) west of 119°E and with deep depths (150–250 m) east of 119°E . A low salinity-core can be identified by the uplifting of the isohalines or by sandwiching between the two salinity maxima. Looking at 20°N cross section, the western salinity maxima occurs west of 119°E between 100 and 150 m depths, and the eastern salinity maxima occurs east of 120°E between 150 and 250 m depths. Between the two salinity maxima, there exists a low salinity area, which is colocated with the northwestern Luzon cold-core eddy.

Six latitudinal cross sections, from 115 to 121°E , of salinity (Fig. 11.77) show the same features as Fig. 11.76 with the strong halocline occurring at all the cross sections. The halocline has a clear northward uplifting.

The bottom of the halocline is located at around 75 m depth at 17°N and at near 50 m depth at 22°N . The strength of the halocline on the latitudinal cross sections decreases eastward. Below the halocline, two salinity maxima (north and south) can be identified from several cross sections with a salinity

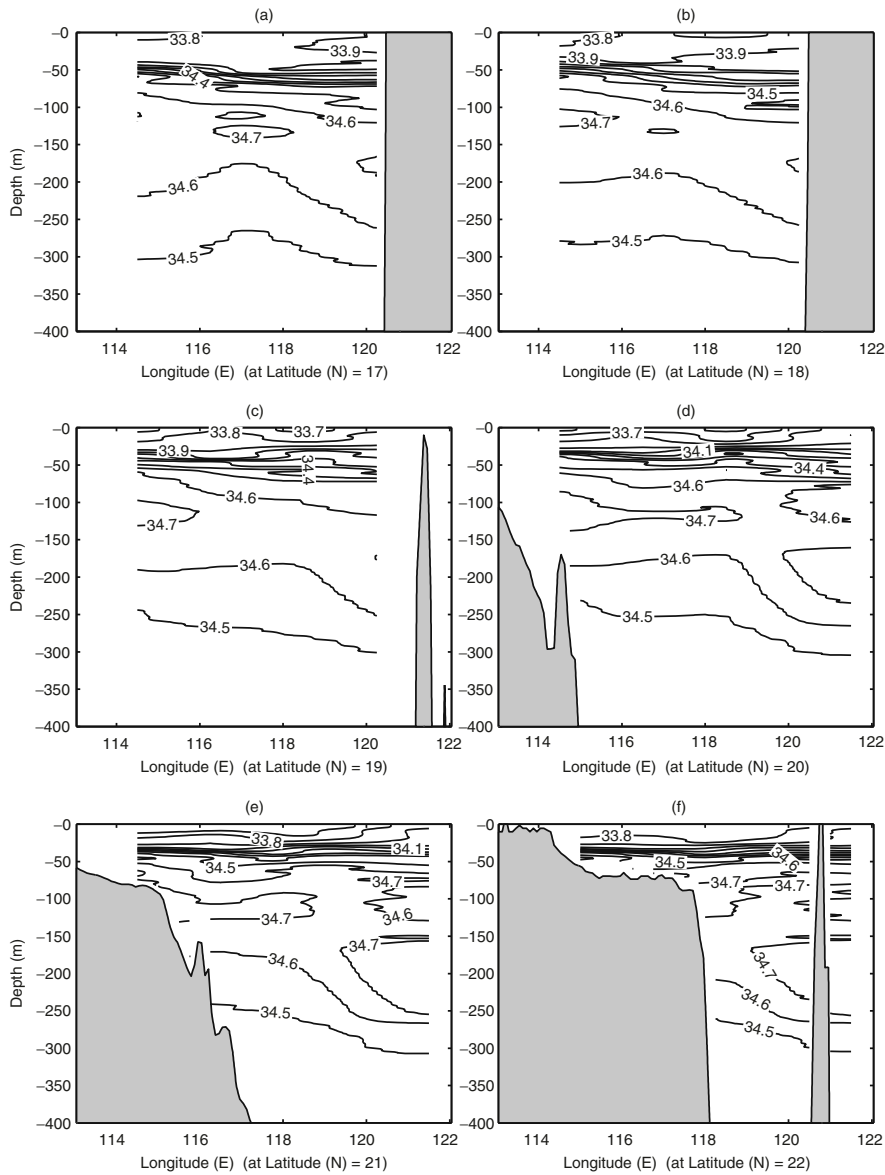


Fig. 11.76. Salinity distribution at several zonal cross sections: (a) 17°N, (b) 18°N, (c) 19°N, (d) 20°N, (e) 21°N, and (f) 22°N (from Chu and Fan 2001, *Journal of Oceanography*)

minimum in between them. Looking at the 117°E cross section, the southern salinity maximum (> 34.7 ppt) occurs south of 18.2°N between 120 and 150 m depths, and the northern salinity maximum (> 34.7 ppt) occurs north of 19.5°N between 75 and 125 m depths. Between the two salinity maxima,

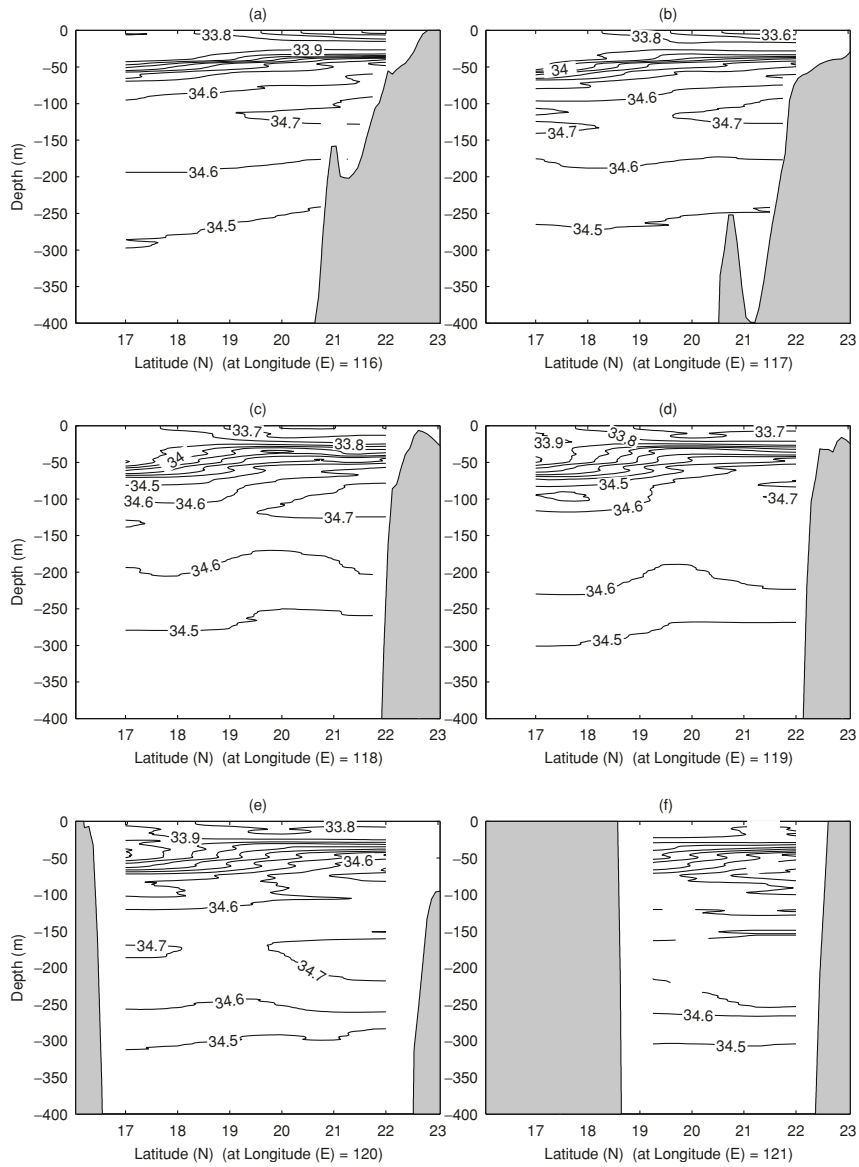


Fig. 11.77. Salinity distribution at several meridional cross sections: (a) 116°E, (b) 117°E, (c) 118°E, (d) 119°E, (e) 120°E, and (f) 121°E (from Chu and Fan 2001, *Journal of Oceanography*)

there exists a low salinity area, which is collocated with the northwestern Luzon cold-core eddy. Thus, the salinity is usually lower inside than outside of the northwestern Luzon cold-core eddy.

11.10.5 Velocity

Horizontal Structure

The inverted velocity vectors near Luzon Strait (Fig. 11.78) clearly show a pattern of upper layer (above 200 m depth) apparent Kuroshio intrusion and lower layer (below 200 m depth) weak outflow. The upper layer flow pattern is quite similar to the bifurcation pattern depicted in Fig. 11.69a. In this figure the upper layer intruded Kuroshio water bifurcated into northward and northwestward branches west of the Balingtang Channel ($120^{\circ}20'E$, $19^{\circ}30'N$). The northwestward branch was circulating around the cold-core area ($116\text{--}119^{\circ}E$, $19\text{--}21.5^{\circ}N$) and formed a cyclonic eddy (i.e., upper part of the northwestern Luzon baroclinic eddy). The maximum tangential velocity of the eddy decreased with the depth from around 0.5 m s^{-1} at the surface to 0.06 m s^{-1} at 200 m depth. The radius of the eddy was around 150 km. There was a smaller and weaker anticyclonic eddy associated with the warm-core ring southwest of the northwestern Luzon eddy.

Comparing Fig. 11.78 with Figs. 11.72 and 11.75, we may find that the northwestern Luzon cyclonic eddy has lower temperature and salinity than the surroundings. The location and kinetic features of the northwestern Luzon eddy at different depths are listed in Table 10.1. Several weak and small eddies are also found west and southwest of the northwestern Luzon eddy.

The current vectors at 50 m as measured by the ADCP aboard R/V Shiyun3 are shown in Fig. 11.79. At this depth, a cyclonic eddy can be identified. It was centered at $118^{\circ}E$, $19.5^{\circ}N$ with the zonal span of around 300 km. The maximum velocity is 1 m s^{-1} , which is higher than the speed inverted from the hydrographic data.

Zonal Cross Sections of v Component

Six zonal cross sections, from 17 to $22^{\circ}N$, of v -velocity show the vertical structure of the northwestern Luzon eddy (Fig. 11.80). The positive values indicate northward velocity, and the negative values refer to the southward velocity. Between 116 and $119^{\circ}E$ (the zonal span of the northwestern Luzon eddy), the northwestern Luzon baroclinic eddy can be identified by alternate positive and negative areas at the zonal cross sections of $19^{\circ}N$, $20^{\circ}N$, and $21^{\circ}N$. At each zonal cross section, we found a cyclonic rotation in the upper layer (surface to 200 m depth) from a neighboring eastern positive/western negative pattern and an anticyclonic rotation in the lower layer (below the 200 m depth) from a neighboring eastern negative/western positive pattern. The upper layer cyclonic rotation was quite strong with the maximum v -velocity higher than 0.3 m s^{-1} . The lower layer anticyclonic rotation was weaker with the maximum v -velocity around 0.1 m s^{-1} .

The area with a southern cyclonic eddy in the upper layer (surface to the 200 m depth) coincides with the area of the uplifting isotherms (cold-core).

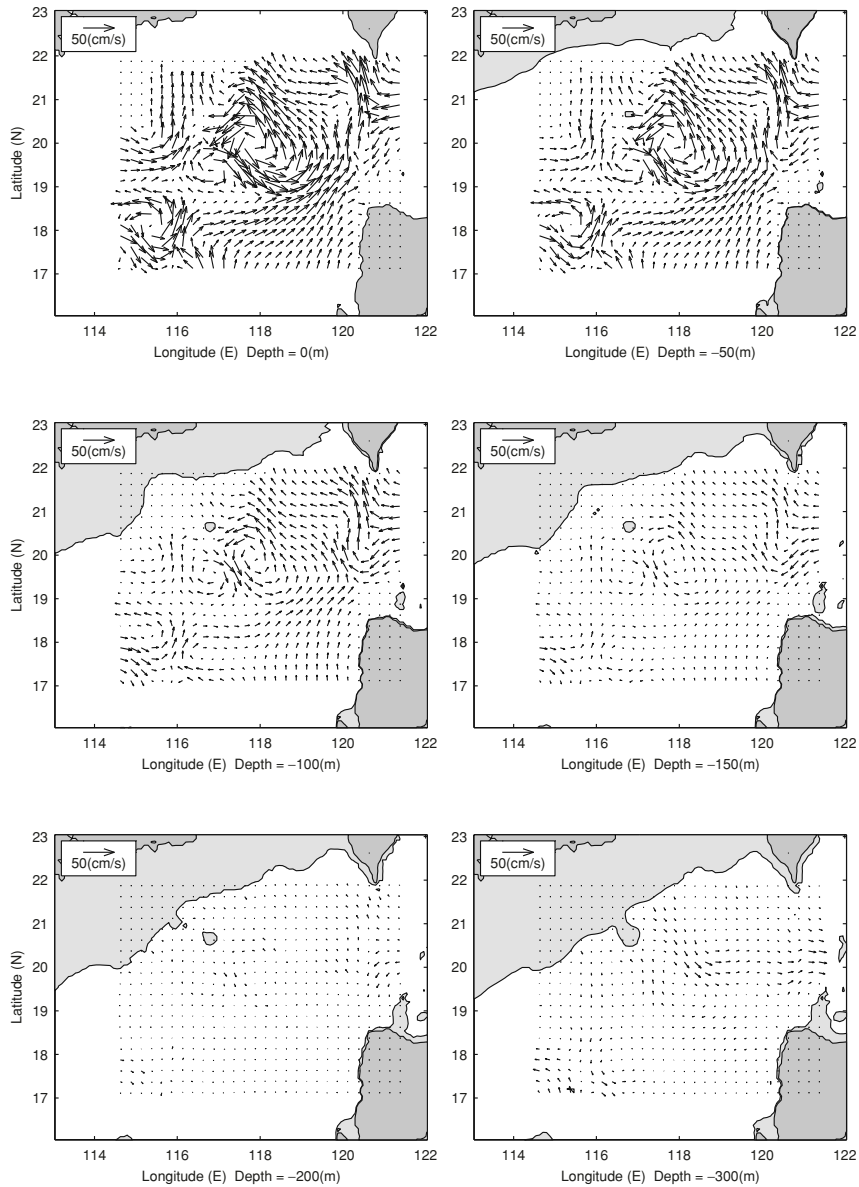


Fig. 11.78. Absolute velocity vectors at different depths: (a) 0 m, (b) 50 m, (c) 100 m, (d) 200 m, and (e) 300 m. The northwestern Luzon baroclinic eddy is cyclonic in the upper layer from the surface to 200 m depth and anticyclonic in the lower layer below 200 m depth (from Chu and Fan 2001, *Journal of Oceanography*)

At the 118°E cross section, the northwestern Luzon cold-core eddy is recognized by an isotherm ridge located at 19.5°N (Fig. 11.74). A strong cyclonic

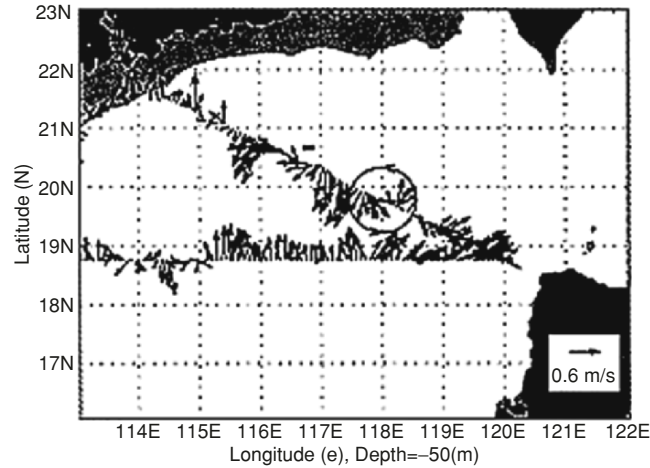


Fig. 11.79. ADCP velocity vectors (15 min averages) at 50 m depth measured during the SCSMEX on 16–21 July 1998 from R/V Shiyan3. Note the cyclonic circulation pattern centered 118°E, 19.5°N with the zonal span of around 300 km. The maximum velocity is 1 m s^{-1} (from Chu and Fan 2001, *Journal of Oceanography*)

eddy with the maximum speed of 0.5 m s^{-1} is identified by the southern positive/northern negative u pattern that is centered at 19.5°N in the upper layer (above the 250 m depth) and a weak anticyclonic eddy with the maximum speed of 0.1 m s^{-1} is identified by the southern negative/northern positive u pattern that is also centered at 19.5°N (Fig. 11.80) in the lower layer (below the 250 m depth).

11.10.6 Energy Budget of the Northwestern Luzon Eddy

Mean Kinetic Energy

The horizontal mean kinetic energy per unit mass is computed at each depth,

$$\bar{u}(z) = \frac{1}{M} \sum_i \sum_j u(x_i, y_j, z), \quad \bar{v}(z) = \frac{1}{M} \sum_i \sum_j v(x_i, y_j, z), \quad (11.5)$$

where M is the total number of the horizontal grid points. The mean kinetic energy \bar{K} is defined by

$$\bar{K}(z) = \frac{1}{2} [\bar{u}(z)^2 + \bar{v}(z)^2]. \quad (11.6)$$

Figure 11.81a shows the vertical profile of the mean kinetic energy. The mean kinetic energy, \bar{K} , has the maximum value of $3.5 \times 10^{-3} \text{ m}^2 \text{ s}^{-2}$ at the surface. It decreases with the depth from the surface maximum value to zero at the 200 m depth. Between 200 and 250 m, the mean kinetic energy is very small (near zero). Below the 250 m depth, the mean kinetic energy slightly increases with the depth.

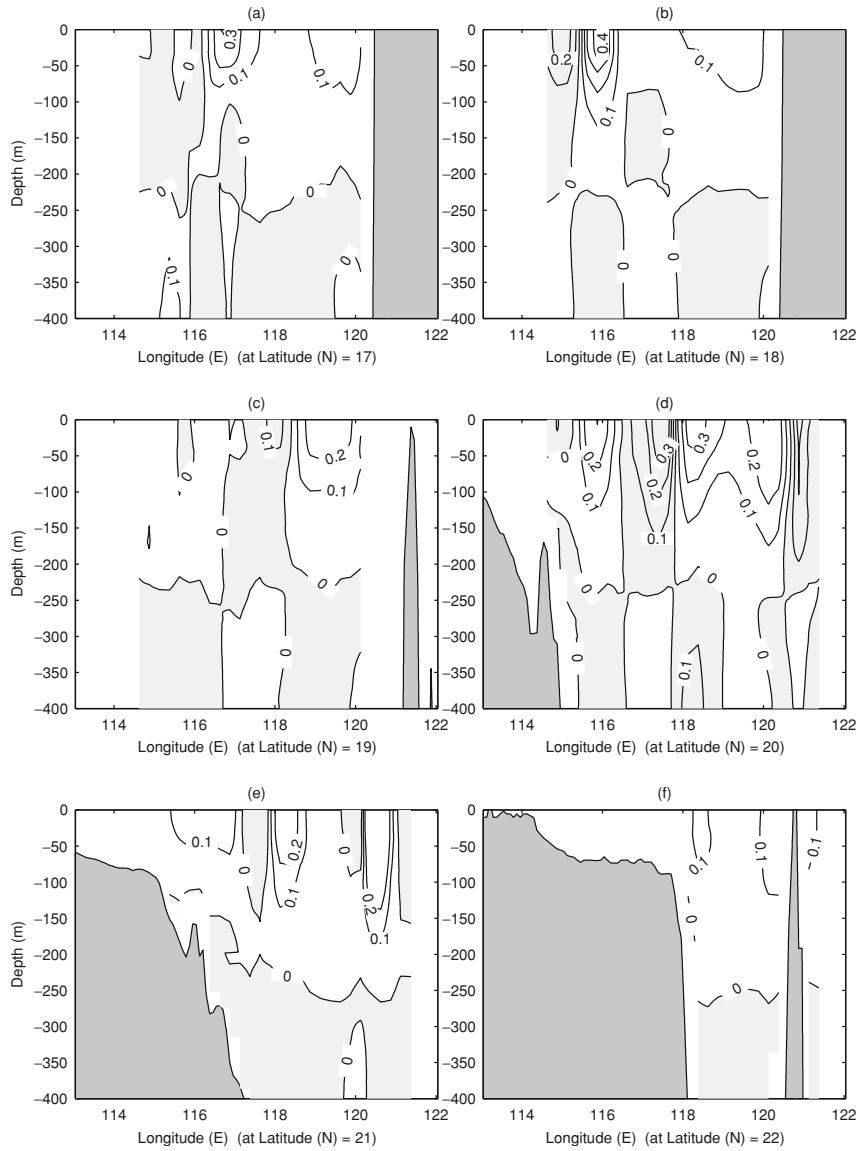


Fig. 11.80. Distribution of inverted velocity v component at several zonal cross sections: (a) 17°N, (b) 18°N, (c) 19°N, (d) 20°N, (e) 21°N, and (f) 22°N (from Chu and Fan 2001, *Journal of Oceanography*)

Eddy Kinetic Energy

The eddy kinetic energy can be computed by

$$K' = \frac{1}{2}(u'^2 + v'^2), \quad (11.7)$$

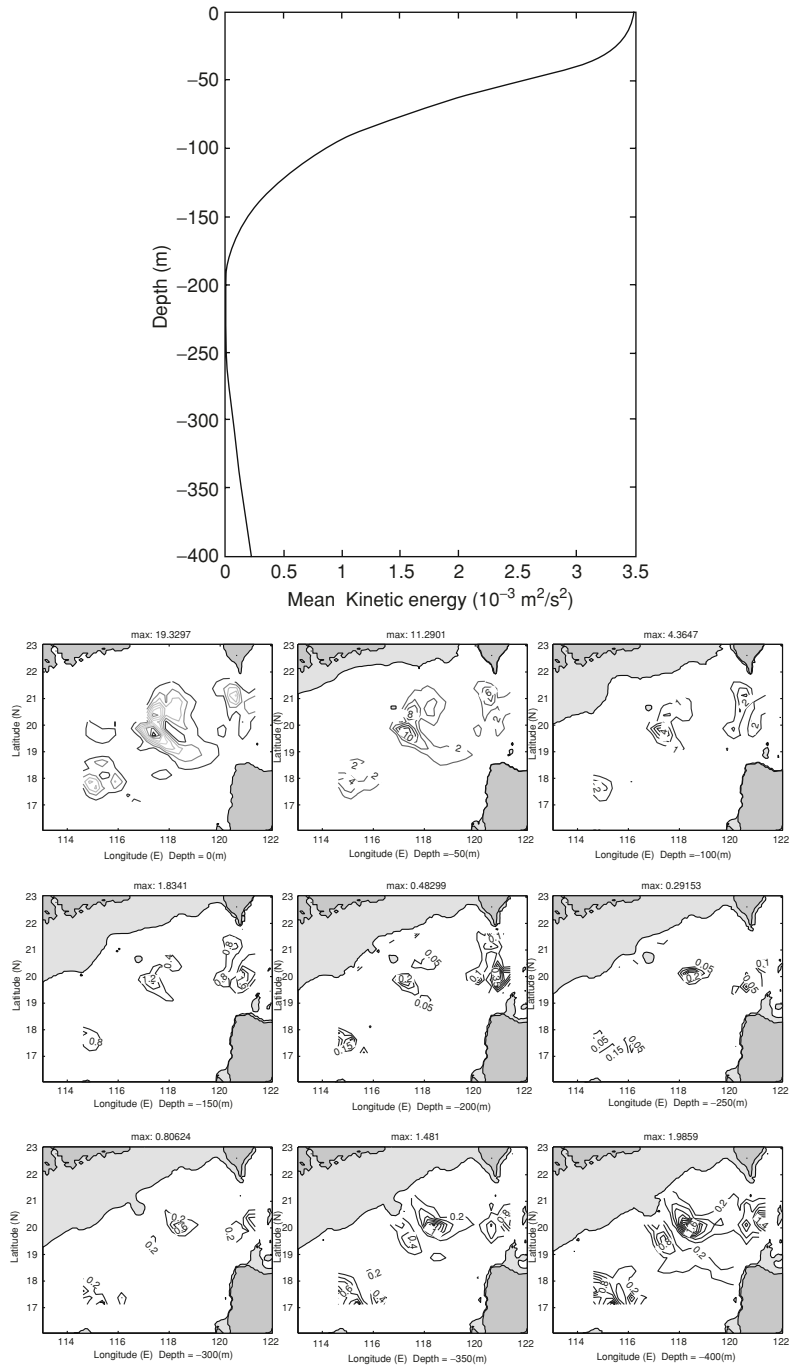


Fig. 11.81. (a) Vertical dependence of the mean kinetic energy per unit mass, \bar{K} (in: $10^{-3} \text{ m}^2 \text{ s}^{-2}$) (from Chu and Fan 2001, Journal of Oceanography). (b). Horizontal distribution of eddy kinetic energy per unit mass, K' (in $10^{-2} \text{ m}^2 \text{ s}^{-2}$), at nine different depths (from Chu and Fan 2001, Journal of Oceanography)

where

$$u'(x_i, y_j, z) = u(x_i, y_j, z) - \bar{u}(z), \quad v'(x_i, y_j, z) = v(x_i, y_j, z) - \bar{v}(z). \quad (11.8)$$

The horizontal distributions of K' at different depths (Fig. 11.81b) clearly show the isolated eddy structure such as the northwestern Luzon eddy in the middle of the region (18–22°N, 116.5–119°E). The eddy kinetic energy has the maximum value ($0.19 \text{ m}^2 \text{ s}^{-2}$) at the surface and decreases with the depth to $0.8 \times 10^{-2} \text{ m}^2 \text{ s}^{-2}$ at the 300 m depth. The maximum eddy kinetic energy is 1–2 orders of magnitude larger than the mean kinetic energy.

11.11 Japan/East Sea MultiEddy Structure Detected from AXBT Data

11.11.1 Background

In Sect. 6.5, the seasonal variability of the Japan/East Sea thermohaline structure and circulation is discussed. The Japan/East Sea has steep bottom topography (Fig. 6.11) that makes it a unique semienclosed ocean basin overlaid by a pronounced monsoon surface wind. It covers an area of 10^6 km^2 , has a maximum depth in excess of 3,700 m, and is isolated from open oceans except for small (narrow and shallow) straits which connect the Japan/East Sea to the Pacific Ocean. It contains three major basins called the Japan, Ulleung, and Yamato Basins, and a high central seamount called the Yamato Rise.

The Japan Sea experiences two monsoons, winter and summer, every year. During the winter monsoon season, a cold northwest wind blows over the Japan Sea as a result of the Siberian High Pressure System located over the East Asian continent. Radiative cooling and persistent cold air advection maintain cold air over the Japan Sea. The northwest–southeast oriented atmospheric Jet Stream is positioned at the Japan Sea. Such a typical winter monsoon pattern lasts nearly six months (November to April). During the summer monsoon, a warm and weaker southeast wind blows over the Japan Sea. Such a typical summer monsoon pattern lasts nearly four months (mid-May to mid-September).

May is the transition period between the two monsoons. Sudden change of the atmospheric forcing (transition from winter to summer monsoon) may vary the Japan Sea thermal structure and cause the formation of mesoscale eddies. Thus, detection of the Japan Sea thermal field during the monsoon reversal is important for the Japan Sea mesoscale dynamics. The Naval Oceanographic Office conducted an intensive AXBT survey during 1–8 May 1995, over the majority of the Japan Sea (Fig. 11.82). This temperature data set provides something close to a “snapshot” of the temperature in the upper ocean in the Japan/East Sea during the monsoon transition period. The density field during the survey period is estimated from the AXBT temperature field and

the climatological monthly mean salinity of May. The P-vector inverse method is used to obtain the absolute velocity field. Analysis on the temperature and velocity fields leads to a multieddy structure.

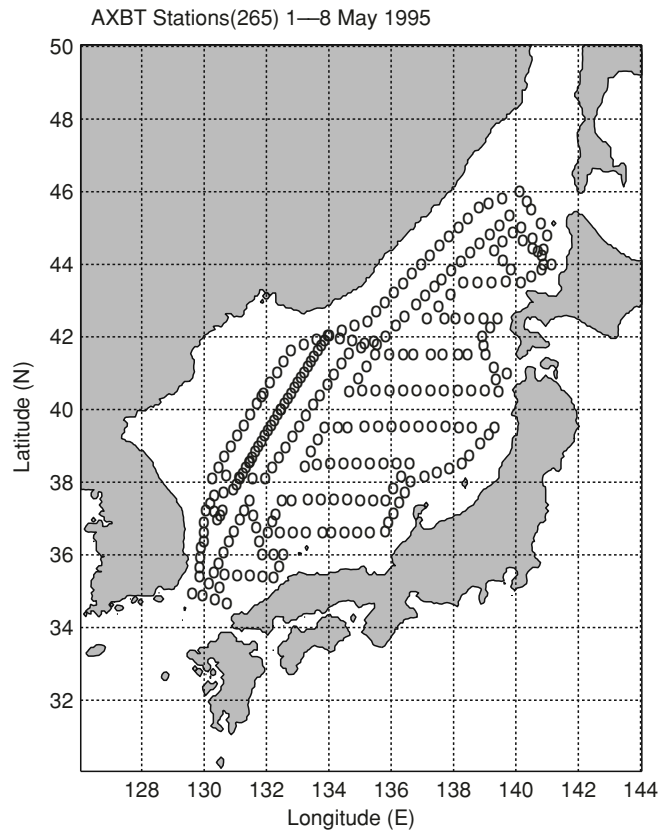


Fig. 11.82. Deployment pattern of AXBT survey during 1–8 May 1995.

11.11.2 AXBT Data

The total number of the AXBT stations is 265. The majority of the AXBTs were nominally capable of reaching a depth of 360–400 m. The vertical resolution of the AXBT data is 1 m. The ensemble of temperature profiles (Fig. 11.83a) and the mean profile with an envelope of a standard deviation (Fig. 11.83b) show the existence of a mixed layer with depths ranging from 20 to 200 m and a thermocline with a vertical temperature gradient varying from 5 to 12°C per 100 m below the mixed layer.

The same as in Sect. 11.9, the AXBT observations were mapped at each depth using a two-scale OI scheme (Gandin 1965; Lozano et al. 1996). The

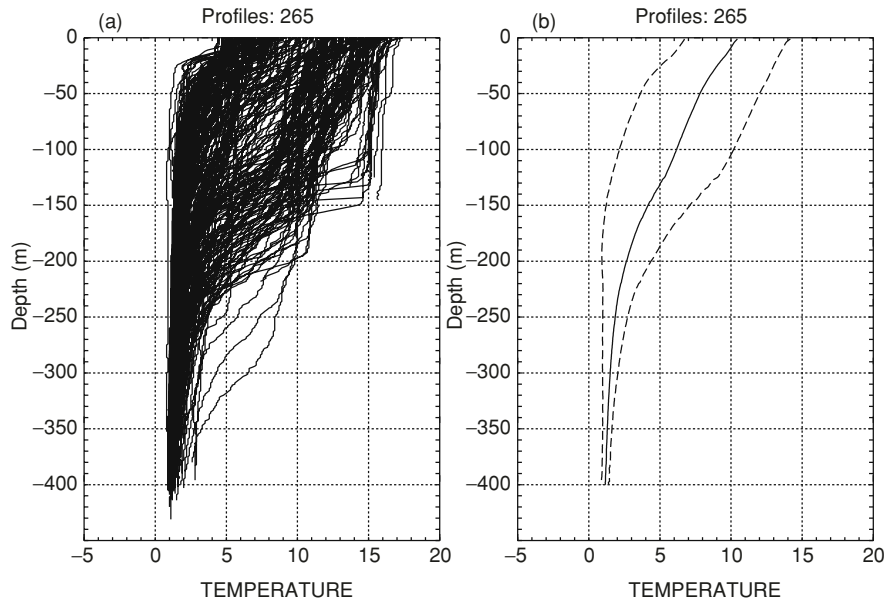


Fig. 11.83. Temperature profiles of AXBT survey during 1–8 May 1995: (a) ensemble of profiles, and (b) the mean profile with an envelope of a standard deviation

large-scale OI was used to estimate the background mean with a decorrelation scale of 450 km. The mesoscale OI was used to map the observational anomaly from the background mean field into a regular grid with spatial and temporal decorrelation scales of 150 km and 12 day. Since only temperature-measuring AXBTs were used, no salinity measurements were made at the same time. Three-dimensional velocity is inverted from this in situ temperature and climatological salinity fields in lieu of in situ salinity data.

11.11.3 Temperature

Horizontal Structures

Figure 11.84a–e shows horizontal depictions of temperature at 0-, 50-, 100-, 200-, and 300-m depths, respectively. The contour interval is 0.5°C . In them we see the Polar Front occurring near 40°N with meandering and stretching from the east Korean Bay to Tsugaru Kaikyo. Its strength increases from the surface (Fig. 11.84a) to 100 m depth (Fig. 11.84b, c) and then decreases below that depth.

The maximum horizontal temperature gradient of the Polar Front is around $8^{\circ}\text{C}/100\text{km}$, appearing near the East Korean Bay at 100 m depth (Fig. 6d). At 200 m (Fig. 11.84e) and 300 m (Fig. 11.84f) depths, the Polar Front is broken into several eddies. The Polar Front separates the cold water

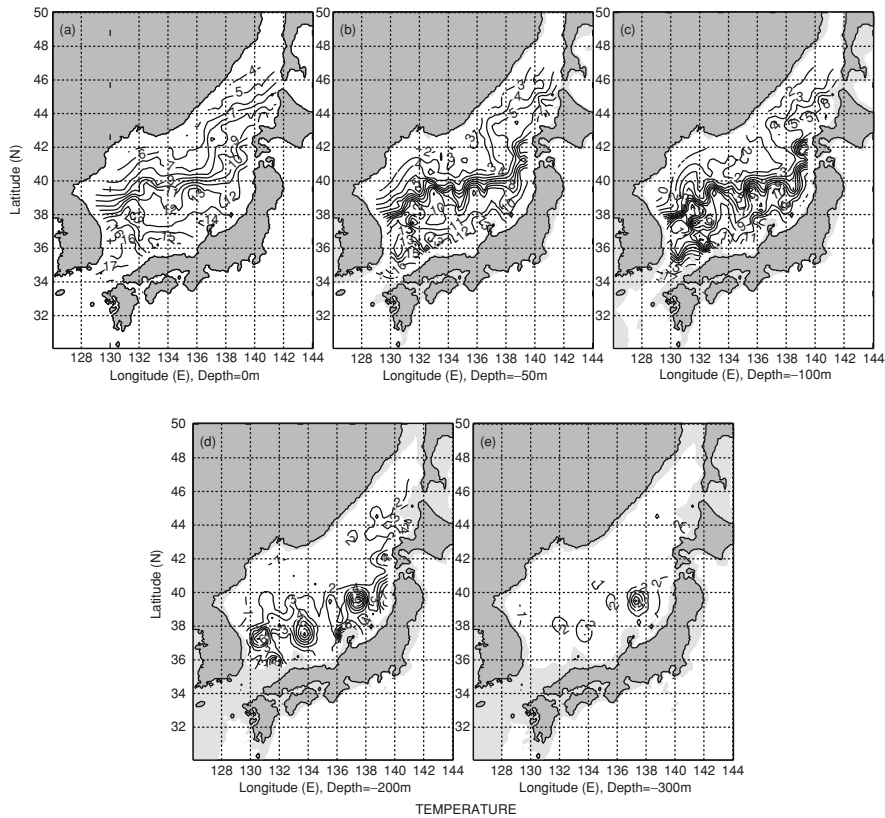


Fig. 11.84. Horizontal temperature fields at different depths: (a) 0-m, (b) 50-m, (c) 100-m, (d) 200-m, and (e) 300-m. The Polar Front with meandering and eddy shedding is clearly seen from the surface to 100 m depth

entering the Japan Sea from the north (Sea of Okhotsk) and the warm water entering the Japan Sea from the south (Yellow Sea) through the Korea Strait. The temperature has less variability in the north than in the south of the Polar Front. For example, at 50 m depth the temperature varies from 3 to 5°C in the north of the Polar Front and changes from 10 to 16°C in the south of the Polar Front. The meandering strengthens with depth from the surface to 100 m depth. The northward meandering of the Polar Front at 131°E, 134°E, and 138°E forms several warm-core eddies. The southward meandering of the Polar Front at 132°E forms a cold-core eddy. At 200 m depth, three warm-core eddies with temperature of 6°C are easily identified as the Ulleung eddy at 130°30'E, 37°N, the Oki Gunto eddy at 133°45'E, 37°30'N, and the Yamato eddy at 137°20'E, 39°30'N. Cold-core eddies are generally weaker than the warm-core eddies and are evident only in upper levels (0–100 m). An eddy is

Table 11.4. Locations, typical temperatures, and tangential velocities of major eddies in Japan Sea detected during May 1–8, 1995

Depth (m)	Ulleung (W)	Oki Gunto (W)	Yamato (W)	Tsushima (°C)
0	129–131°E	133–134°E	135–137°E	131–133°E
	35–37°N	36–39°N	38–40°N	36–38°N
	16°C, 0.1 m s ⁻¹	13°C, 0.06 m s ⁻¹	13°C, 0.1 m s ⁻¹	13°C, 0.06 m s ⁻¹
	anticyclonic	meandering	meandering	cyclonic
50	129–132°E	133–135°E	136–138°E	131–133°E
	36–38°N	36–39°N	38–40°N	36–38°N
	13°C, 0.08 m s ⁻¹	12°C, 0.08 m s ⁻¹	10°C, 0.08 m s ⁻¹	10°C, 0.06 m s ⁻¹
	anticyclonic	anticyclonic	anticyclonic	cyclonic
100	129–132°E	133–135°E	136–138°E	131–133°E
	36–38°N	36–39°N	38–40°N	36–38°N
	11°C, 0.05 m s ⁻¹	9°C, 0.05 m s ⁻¹	10°C, 0.05 m s ⁻¹	6°C, 0.05 m s ⁻¹
	anticyclonic	anticyclonic	anticyclonic	cyclonic
200	129–132°E	133–135°E	136–138°E	131–133°E
	36–38°N	36–39°N	38–40°N	36–38°N
	6°C, 0.03 m s ⁻¹	7°C, 0.02 m s ⁻¹	6°C, 0.02 m s ⁻¹	3°C, 0.02 m s ⁻¹
	cyclonic	cyclonic	cyclonic	cyclonic
300	129–132°E	133 – –135°E	136–138°E	131–133°E
	36–38°N	36–39°N	38–40°N	36–38°N
	2°C, 0.04 m s ⁻¹	2°C, 0.04 m s ⁻¹	4°C, 0.04 m s ⁻¹	2°C, 0.01 m s ⁻¹
	cyclonic	cyclonic	cyclonic	cyclonic

identified in the Tsushima Basin (131°–133°E, 36°–38°N) as the Tsushima cold-core eddy. The thermal features of these eddies are listed in Table 11.4.

Vertical Structures

Three zonal cross sections (43°N, 39°N, and 36°N) of temperature show the vertical structure of the mixed layer and the thermocline in the north of, along, and in the south of the Polar Front, respectively (Fig. 11.85). Below 300 m depth, the temperature is uniformly cold (2°C) at all three cross sections.

The cross section at 39°N clearly shows the existence of three warm-core eddies near 131°E, 133°E, and 137°30'E from the downward bending (trough) of isotherms. The longitudinal span of the three warm eddies (Ulleung, Oki Gunto, and Yamato eddies) is around 200 km. The 36°N cross section clearly shows the downward bending (trough) of isotherms between 130°30'E and 132°30'E, indicating the existence of a warm-core eddy. Both 39°N and 36°N cross sections clearly show the upward bending (ridge) of isotherms between 131 and 133°E, indicating the existence of a cold-core eddy, the Tsushima eddy.

Three latitudinal cross sections (131°E, 134°E, and 137°E) of temperature also show evident warm-core eddy structure (Fig. 11.86). The “trough” and “ridge” of the isotherms may be considered as centers of warm-core and cold-core eddies. The three cross sections indicate three shaded warm-core eddies

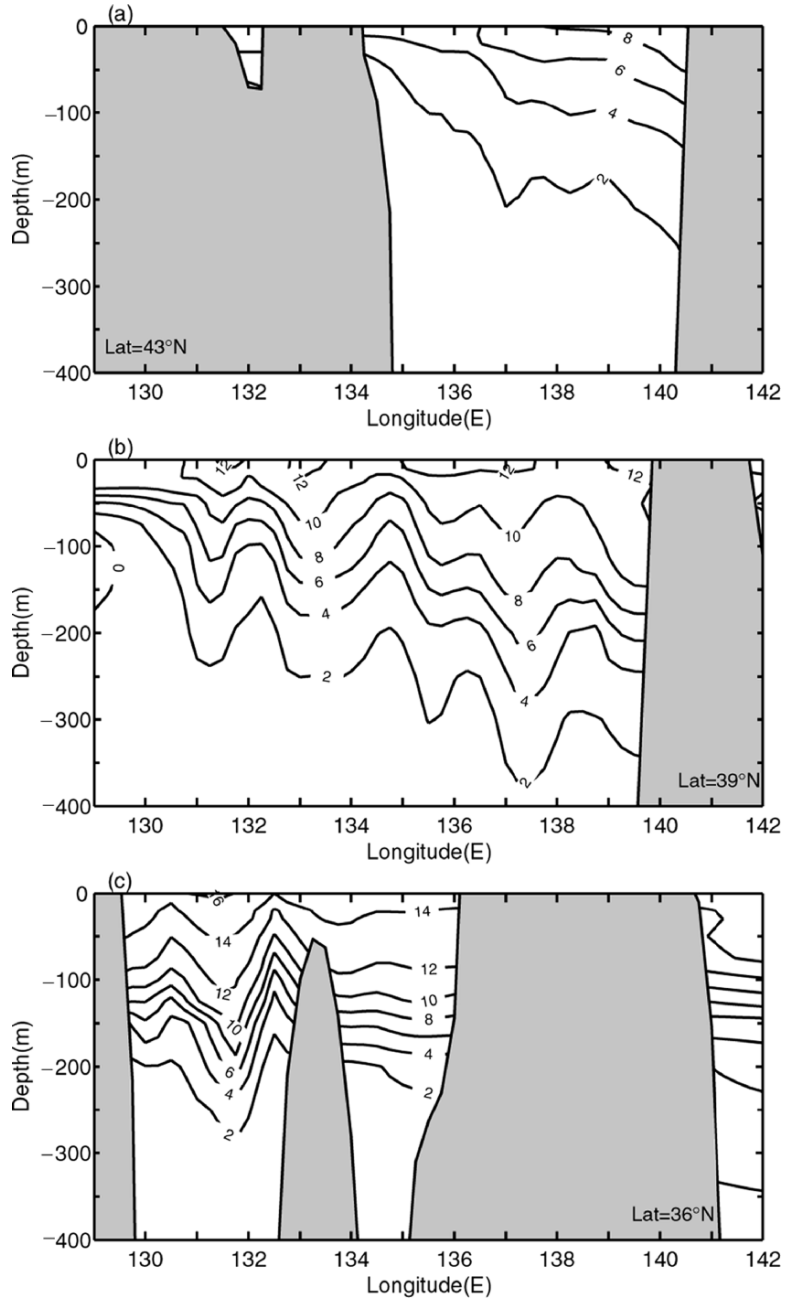


Fig. 11.85. Zonal cross sections of temperature: (a) 43°N, (b) 39°N, and (c) 36°N

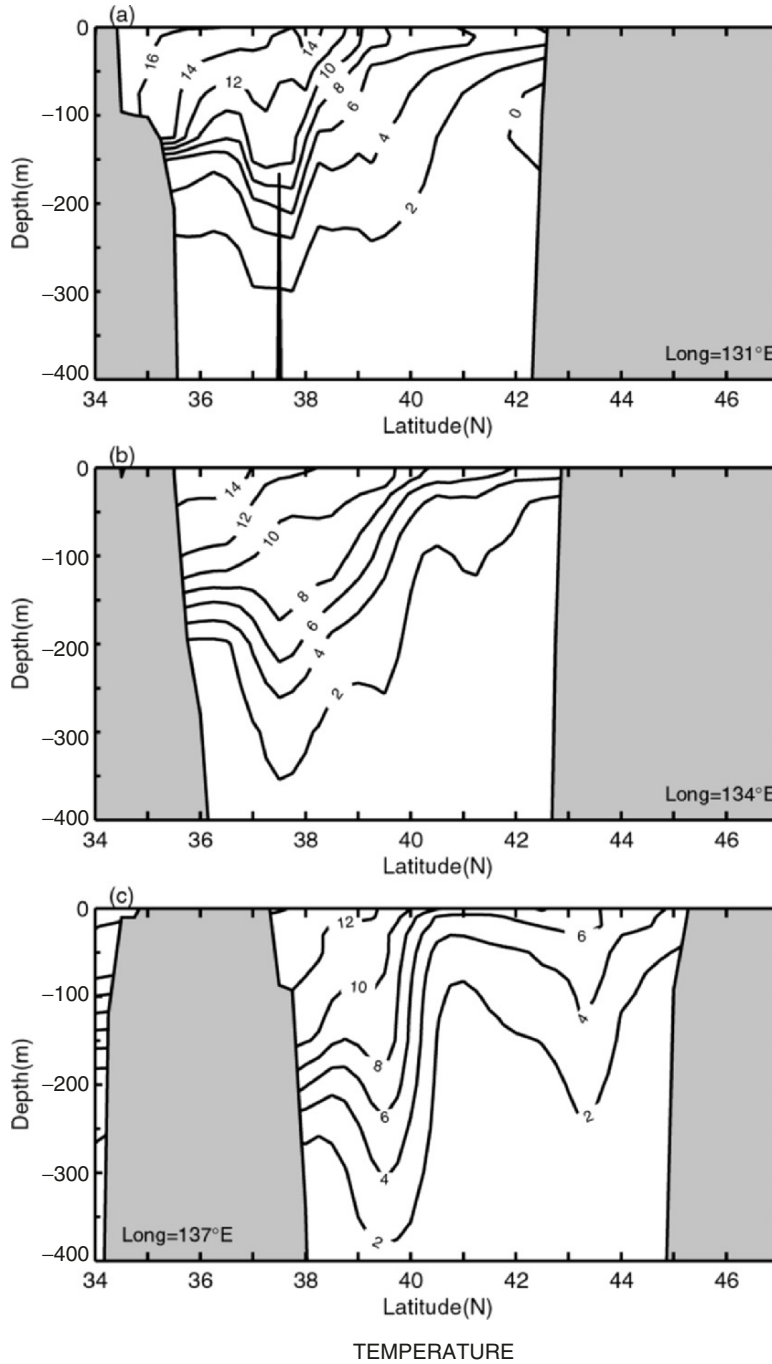


Fig. 11.86. Latitudinal cross sections of temperature: (a) 131°E, (b) 134°E, and (c) 137°E

from the downward bending (trough) of isotherms: 37°30'N at 131°E and 134°E, and 39°30'N at 137°E.

11.11.4 T - S and T - \bar{S} Relations

Since there were no salinity (S) observations in Japan/East Sea during 1–8 May 1995, May climatological salinity (Levitus et al. 1994) was interpolated to the AXBT stations and those salinity values (\bar{S}) were used for the P-vector computation. Figure 11.87a shows T - S diagram of 4,075 profiles from the MOODS in May during 1932–1994, and Fig. 10.86b shows T - \bar{S} diagram from 265 temperature (AXBT) and \bar{S} profiles. The spatial and temporal distributions of the MOODS data are illustrated in Fig. 11.88a, b. Comparison between the two diagrams shows that the T - S characteristics remain stable. However, we should be aware of the shortcomings in using climatological salinity values (\bar{S}). If the temperature field is relatively homogeneous in space, the density gradient depends mostly on the salinity gradient. Under that circumstance, the use of climatological salinity values may bring large errors in inverting the velocity field.

11.11.5 Velocity

The inverted horizontal velocity field (Fig. 11.89 indicates the evident Polar Front meandering and eddy shedding. It is easy to identify three warm-core (Fig. 11.84) baroclinic eddies: Ulleung eddy, Oki Gunto eddy, and Yamato

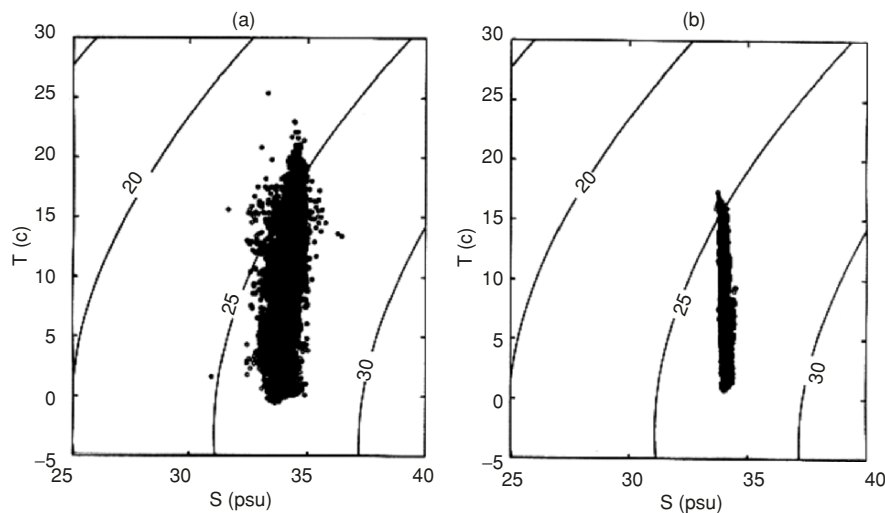


Fig. 11.87. T - S diagrams for: (a) the MOODS data set in May during 1933–1986, and (b) the AXBT temperature and May climatological salinity

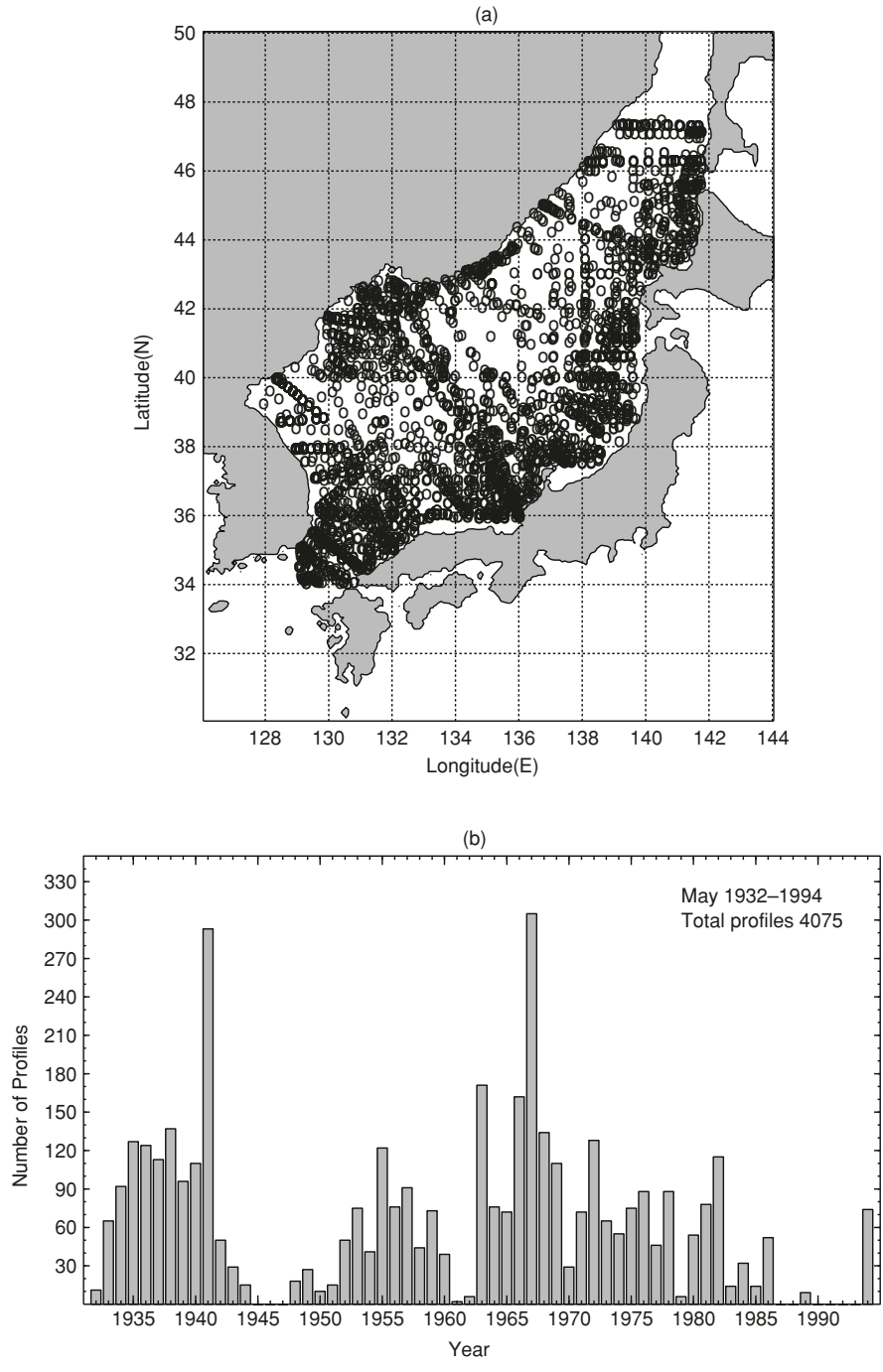


Fig. 11.88. The MOODS data distribution: (a) spatial, and (b) temporal

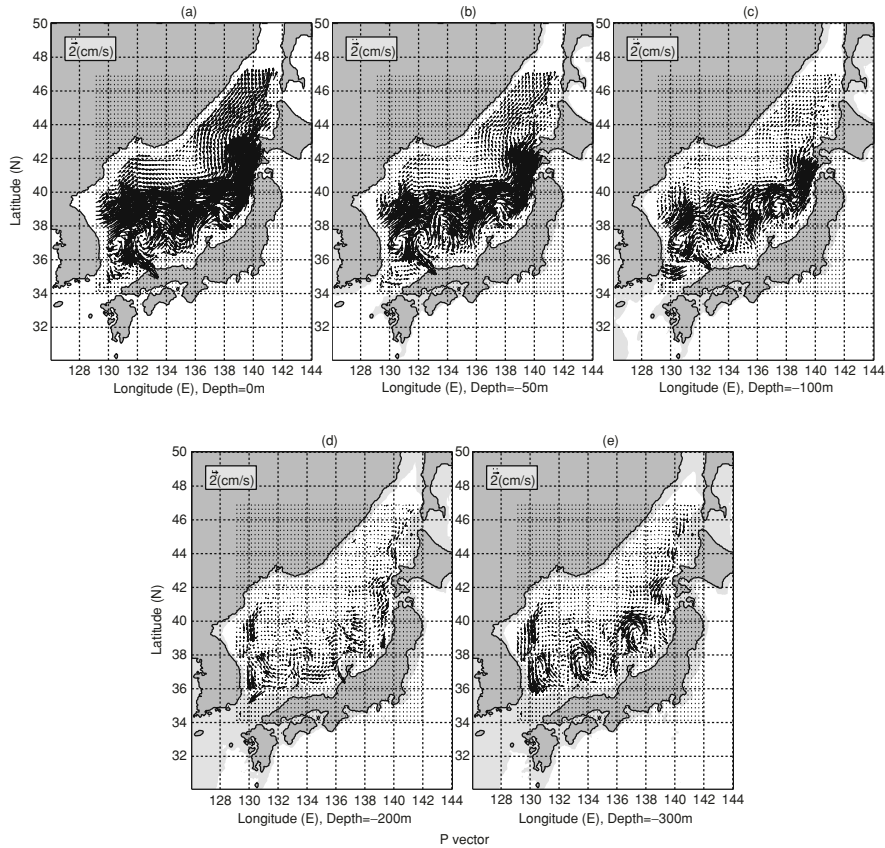


Fig. 11.89. Absolute velocity at different depths: (a) 0-m, (b) 50-m, (c) 100-m, (d) 200-m, and (e) 300-m

eddy. These eddies are anticyclonic at upper levels (0, 50, and 100 m), and cyclonic at lower level (300 m). It is easy to identify the Tshshima cold-core cyclonic eddy. The kinetic features of these eddies are listed in Table 11.4.

Zonal Cross Sections of *v*-Component

Three zonal cross sections (43°N, 39°N, and 36°N) of *v*-velocity show the vertical eddy structure (Fig. 11.90). The positive values indicate northward velocity, and the negative values refer to the southward velocity. Alternate positive and negative areas indicate the occurrence of cyclonic and anticyclonic eddies. At each zonal cross section, neighboring eastern negative and western positive patterns refer to an anticyclonic eddy. Neighboring western negative and eastern positive patterns refer to a cyclonic eddy. There is no evident eddy structure in 43°N cross section.

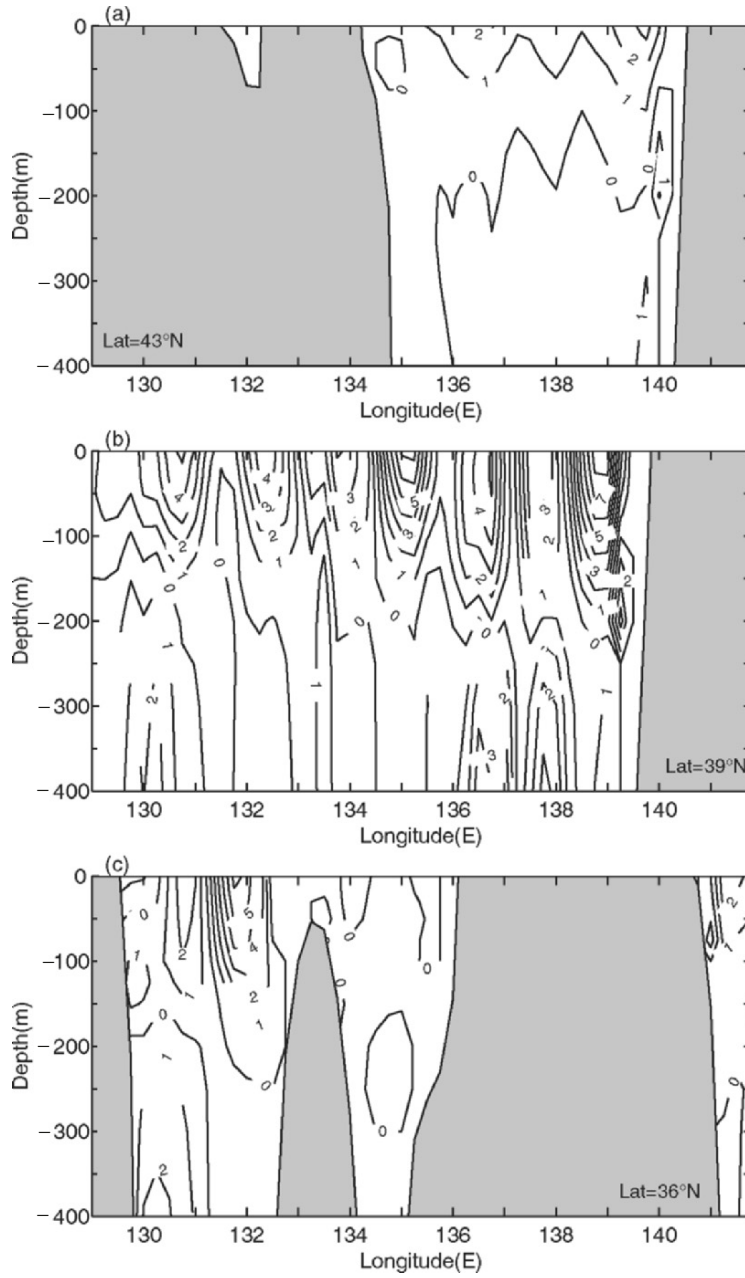


Fig. 11.90. Zonal cross sections of velocity v -component: (a) 43°N, (b) 39°N, and (c) 36°N

The cross section at 39°N clearly shows the existence of the Ulleung, Oki Gunto, and Yamato eddies with high baroclinicity: anticyclonic above 200 m depth and cyclonic below 200 m depth. The three eddies reveal a slightly asymmetric feature. The northward velocity in the western part is a little stronger than the southward velocity in the eastern part. For example, the Yamato warm-core eddy has a maximum northward speed of 0.09 m s^{-1} in the western part and a maximum southward speed of 0.04 m s^{-1} in the eastern part.

The cross section at 36°N clearly shows the coexistence of the Ulleung warm-core eddy and the Tsushima cold-core eddy sharing a wide southward branch between 130 and 132°E . The zonal span of both eddies is around 200 km. The depth of the Ulleung warm-core eddy is around 400 m with anticyclonic tangential velocity above 200 m depth and cyclonic below 200 m depth. The depth of the Tsushima cold-core eddy is quite shallow (above 200 m depth). Both eddies are quite asymmetric with a maximum tangential velocity of 0.05 m s^{-1} at the southward branch.

Latitudinal Cross Sections of u -Component

Three latitudinal cross sections (131°E , 134°E , and 137°E) of u -velocity also show the vertical eddy structure (Fig. 11.91). The positive values indicate eastward velocity, and the negative values refer to westward velocity. Alternate positive and negative areas indicate the occurrence of cyclonic and anticyclonic eddies. At each latitudinal cross section, neighboring southern negative and northern positive patterns refer to an anticyclonic eddy. However, neighboring northern negative and southern positive patterns refer to a cyclonic eddy.

The cross section at 131°E clearly shows the coexistence of the Ulleung warm-core eddy and the Tsushima cold-core eddy sharing an eastward branch near 36°N . Both 134°E and 137°E reveal baroclinic structure of the Oki Gunto and Yamato warm-core eddies, respectively. They have anticyclonic tangential velocities above 200 m depth, and cyclonic tangential velocities below 200 m depth.

11.12 Australian Mediterranean and South Australian Gyres

The inverted Ψ and (U, V) fields (Fig. 11.92) show the following features: the southward flowing East Australia Current is the western boundary current of the southern hemisphere. It is the weakest of all boundary currents, carrying only about 10 Sv. The current first follows the Australian coast, then separates from it somewhere around 34°S (the latitude of the northern end of New Zealand's North Island). This current recirculates (10 Sv) and forms an anticyclonic (anticlockwise) eddy. The path of the current from Australia to New Zealand is known as the Tasman Front, which makes the boundary of

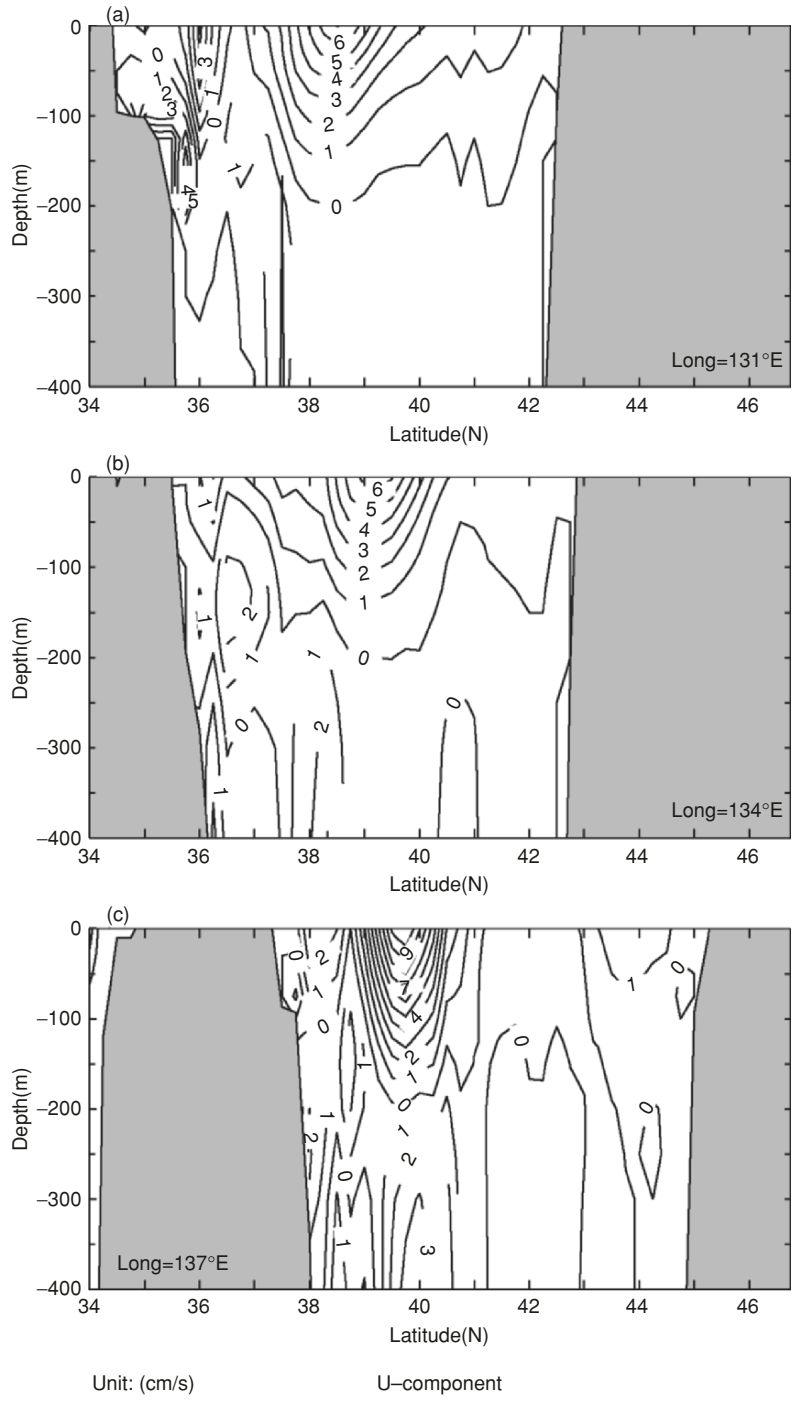


Fig. 11.91. Latitudinal cross sections of velocity u -component: (a) 131°E, (b) 134°E, and (c) 137°E

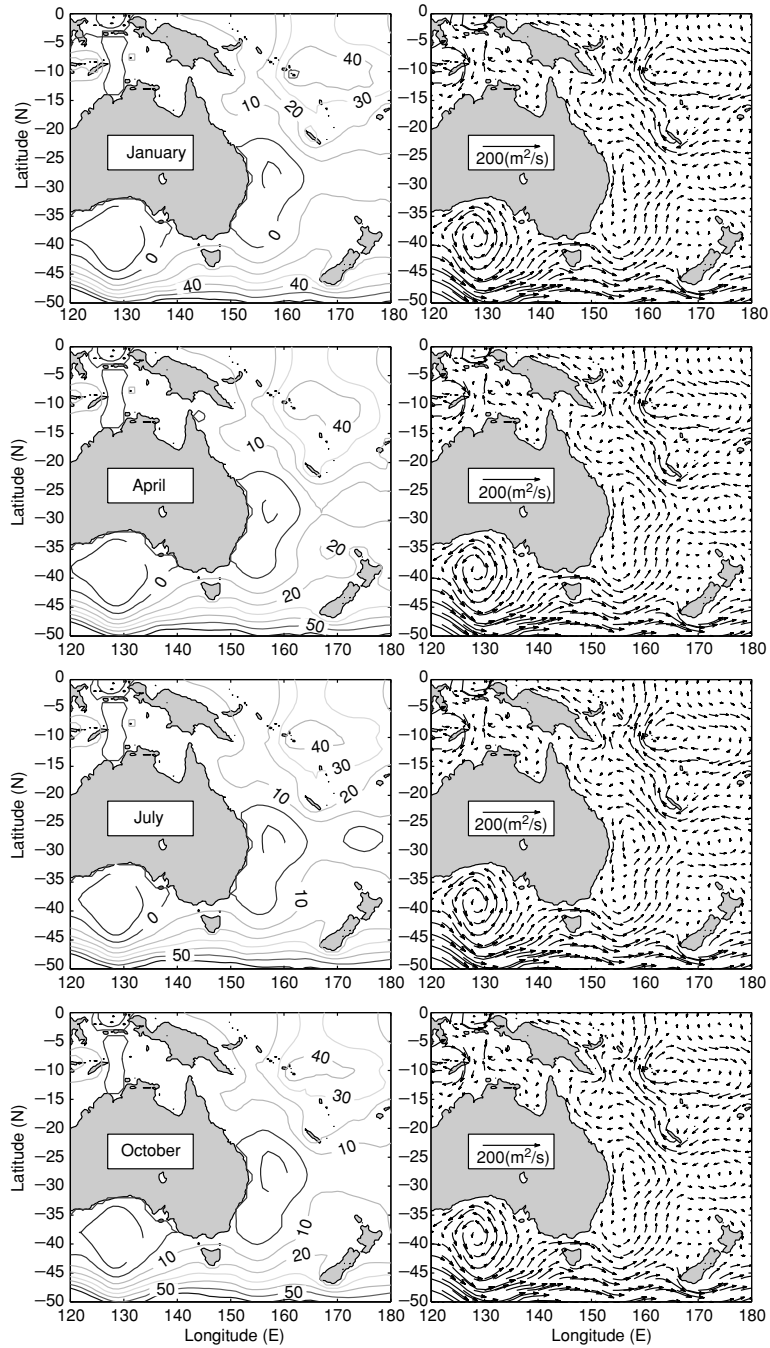


Fig. 11.92. Volume transport stream function (ψ) and vertically integrated velocity (U, V) for Australian Mediterranean and south Australian gyre

the warmer water of the Coral Sea and the colder water of the Tasman Sea. In the South Australian Basin, an anticyclonic eddy is identified and recirculates 10 Sv with a weak seasonal variation.

Questions and Exercises

- (1) Discuss the major features of the basin-scale circulations in the Pacific from Fig. 11.1. Compare inverted depth-integrated velocity vectors and stream function with the results obtained from widely used ocean general models.
- (2) Download the volume transport stream function from the enclosed DVD-ROM for the equatorial Pacific between 10°N and 10°S. Discuss the barotropic (depth-averaged) exchange between the Northern and Southern Hemispheres.
- (3) Use Fig. 11.2a, b or download the volume transport stream function from the enclosed DVD-ROM to discuss the seasonal variability of the volume transport in the Pacific basin.
- (4) Discuss the flow patterns in the Water Mass Crossroads. Figure 11.3 does not show evident seasonal variability. Do you think it is realistic? What is the flow pattern presented by other authors?
- (5) Identify the seasonal variation of the three major currents (Mindanao Current, New Guinea Coastal Undercurrent, and North Equatorial Counter Current) from Fig. 11.7. Which level and which month is the Mindanao Current strongest? Discuss the physical mechanism causing these Currents.
- (6) Search the velocity estimations of the three currents (Mindanao Current, New Guinea Coastal Undercurrent, and North Equatorial Counter Current) from the literature and compare them with the estimations using the P-vector method shown in Figs. 11.8, 11.9, and 11.10. Discuss the validity of using the P-vector method on isopycnal surface for the equatorial regions.
- (7) Identify the seasonal variability of Mindanao Eddy and Halmahera Eddy from Fig. 11.7. Discuss the physical mechanism causing the formation of these eddies.
- (8) What are the major features of the barotropic flow near Mindanao Island identified from Figs. 11.11 and 11.12? What is the physical mechanism causing the Mindanao Current to be weaker in July than in January?
- (9) Discuss the volume transport (Sv) between the Celebes Sea and Pacific Ocean including total volume transport and volume transport between two isopycnal levels.
- (10) Discuss the volume transport (Sv) between the Halmahera Sea and Pacific Ocean including total volume transport and volume transport between two isopycnal levels.
- (11) Is the weak seasonal variability of the Indonesia Throughflow shown in Fig. 11.17 realistic? Compare the volume transport of the Indone-

sia Throughflow identified using the P-vector method with the results reported by other authors.

- (12) There are several estimations of the Kuroshio transport in the literature. Compare them with the volume transport identified from the volume transport stream function shown in Fig. 11.18. Why is the Kuroshio transport stronger in winter than in summer?
- (13) The Kuroshio Water is intruded in the South China Sea as shown in Fig. 11.19. Compare this to the Gulf of Mexico, where the water is also intruded from the southern strait. Why does the Gulf of Mexico often have the Loop-Current while the South China Sea does not?
- (14) What are the major features of the Subtropical Counter Current in the North Pacific? What are theories to explain the formation of the Subtropical Counter Current?
- (15) Identify strong vertical shear in the Subtropical Counter Current from Fig. 11.21a, b. Discuss the effect of the baroclinic instability on the Subtropical Counter Current.
- (16) What are the major characteristics of seasonal variation of the South China Sea (T, S) fields?
- (17) What are the major characteristics of seasonal variation of the South China Sea circulation? What are the major currents identified from Figs. 11.34 to 11.37? Are these currents baroclinically stable or unstable?
- (18) Figure 11.38 shows the existence of a thermal front in the central South China Sea. Discuss the mechanisms for the formation of this front.
- (19) What is the relationship between the cross-basin circulation and the thermohaline front in the South China Sea?
- (20) What is the change of $T-S$ relation across the thermohaline front in the central South China Sea?
- (21) Discuss the seasonal variability of the thermohaline front and associated cross-basin flow in the central South China Sea.
- (22) What are the major features of the multieddy structure in the South China Sea? Discuss the mechanisms for the formation of the multieddies.
- (23) Figure 11.69 shows two patterns of the Kuroshio intrusion into the South China Sea (bifurcation and loop) with less occurrence of the loop pattern. Can you explain why?
- (24) What are the major characteristics of the cool-core eddy occurring to the west of Luzon detected by using AXBT/AXCTD during July 8–26, 1998? What is the major mechanism for the generation of this eddy?
- (25) Figures 11.80 and 11.81 show that the maximum eddy kinetic energy of the observed cool-core eddy west of Luzon is 1–2 orders of magnitude larger than the mean kinetic energy. Can you explain why?
- (26) What are the major features of the multieddy structure in the Japan/East Sea? Discuss the mechanisms for the formation of multieddies.
- (27) Discuss the major features of the Australian Mediterranean Gyre and the South Australian Gyre.

Inverted Circulations in the Atlantic Basin

Setting aside the part of the Pacific, west of New Zealand and the Tonga–Kermadec Ridge, which has no counterpart in the Atlantic, there is some correspondence in the features. The general circulation of the Atlantic Basin is represented by vertically integrated velocity or volume transport stream function (barotropic) and three-dimensional absolute velocity (baroclinic). Figure 12.1 shows the volume transport stream function for the Atlantic Basin that is calculated by using the method depicted in Chap. 8. Comparing Figs. 12.1 to 11.1, we find that each basin (Atlantic and Pacific) has an anticyclonic subtropical gyre, which are the western and eastern boundary currents.

For the Atlantic Basin, there is some correspondence between the transports north and south of the equator along the side from the Caribbean and Gulf of Mexico, which has no counterpart in the South Atlantic. The midlatitude anticyclonic gyres in the North Atlantic and the South Atlantic have a comparable strength (50 Sv). We may also identify the following major features from Fig. 12.1: the Gulf Stream, the Labrador Basin cyclonic gyre, and the Brazil–Malvinas confluence zone.

12.1 North Atlantic Ocean Circulation

12.1.1 General Description

Physical oceanographers have been estimating the North Atlantic Ocean circulation for relatively long period. Most estimation was on the basis of geostrophic calculation and inverse (e.g., box, β -spiral, P-vector) methods using hydrographic data. Fuglister (1960, 1963) published the seminal collection of hydrographic data in the Atlantic for the early post-World War II era. Wright and Worthington (1970) and Worthington and Wright (1970) produced hydrographic and water mass atlases. The atlases by Fuglister, Worthington, and Wright are useful. Dietrich's (1969) atlas of the northern North

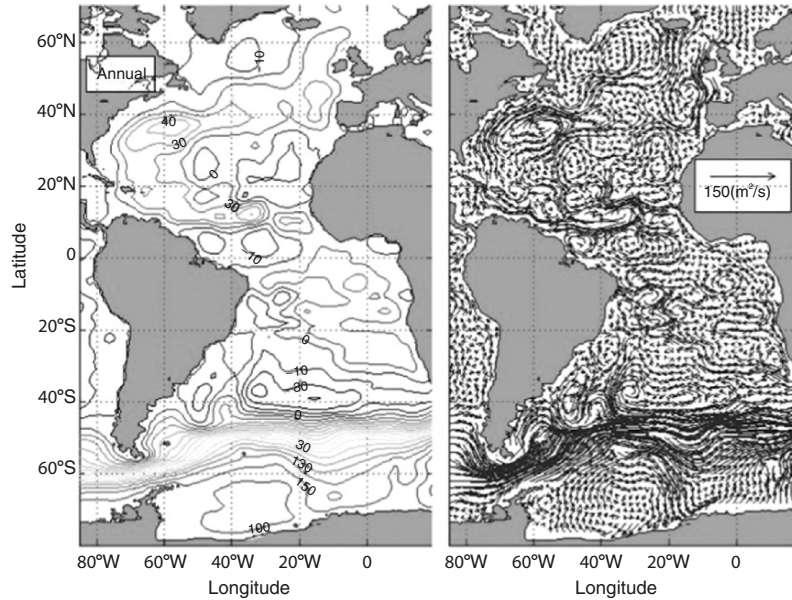


Fig. 12.1. Annual mean volume transport streamfunction (Ψ) and vertically integrated velocity (U, V) for the Atlantic Ocean (from Chu and Fan 2006, *Journal of Marine Systems*)

Atlantic contains a wealth of important information. More recent atlases of hydrographic data for the Atlantic have been published by Teague et al. (1990), Lozier et al. (1994, 1995), Levitus and Boyer (1994), and Levitus et al. (1994).

Using limited data, Iselin (1936) produced a map of the general circulation of the western North Atlantic Ocean. Later on, Sverdrup et al. (1942) generated a more detailed map of the upper layer transports for the North Atlantic circulation including northern and southern recirculation of the Gulf Stream, crossequatorial flow, Labrador and Irminger Currents, and a subpolar gyre. Stommel (1957) presented two-layer circulation for the entire Atlantic Ocean, contained in the similar, but observationally based, maps of Worthington (1976), Wunsch (1978, 1996), Wunsch and Grant (1982), Schmitz and McCartney (1993), Schmitz (1996a), and Olbers et al. (1985).

Worthington (1976) constructed the volume transport streamlines for the North Atlantic Circulation. In his calculation, the intergyre and interbasin exchanges are found overly restrictive within the North Atlantic and between the South and North Atlantic Ocean (Clark et al. 1980; Schmitz and Richardson 1991; Schmitz 1996a). Schmitz and McCartney (1993) presented an updated version of a transport schematic representation for the upper larger general circulation of the North Atlantic Ocean (0–800 m in the subtropical gyre; temperature $>7^{\circ}\text{C}$ say) and for some selected deep currents ($\sim 2,000$ – $4,000$ m depth, say).

One feature of the “update” involves a modified path (Reid 1994; Tschlya 1989) for Mediterranean Water (~ 1 Sv at the source according to Bryden and Kinder 1980), which entrains at least 1 Sv from the ambient water present as it plunges down the slope so that the net circulation (Price and Baringer 1994) is at least 2 Sv. Chu and Fan (2006) calculated volume transport stream function for the global oceans (see Chap. 7) from surface wind and hydrographic data.

US Naval Oceanographic Office produced a composite smoothed speed contour and direction (arrow) plot of the surface currents in the North Atlantic, based on one particular set of ship drift data (Fig. 12.2). Major circulation features of the upper layer flow in the North Atlantic Ocean are represented in Fig. 12.2 such as a strong Gulf Stream, double gyre structure (subtropical and subpolar gyres), crossequatorial current, and North Atlantic Current with flow into the polar seas as is the upper layer transports for the North Atlantic circulation. However, several important characteristics of the upper layer circulation (basically those on smaller spatial scales) are not clearly present in Fig. 12.2. Examples would be the northern and southern recirculation gyres of the Gulf Stream, although there is an Antilles Current in Fig. 12.2.

The P-vector method is used (Chu 1995a) to calculate three-dimensional absolute velocity from NOAA’s climatological temperature and salinity data. Many of the major circulation features of the upper layer flow in the North Atlantic Ocean are contained in the inverted velocity field at 500 m depth (Fig. 11.3). The circulation pattern is dominated by a strong Gulf Stream

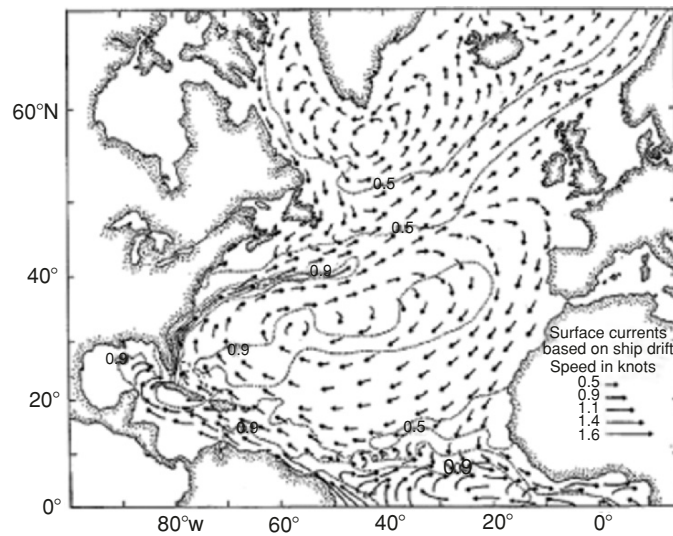


Fig. 12.2. A smoothed map of averaged surface currents for the North Atlantic Ocean based on ship drift data for the summer (Fig. 1.8, pp. 24 in US Naval Oceanographic Office Publ. 700, 1965). *Arrows* indicate flow directions; *contours* indicate current speed (magnitude, in knots)

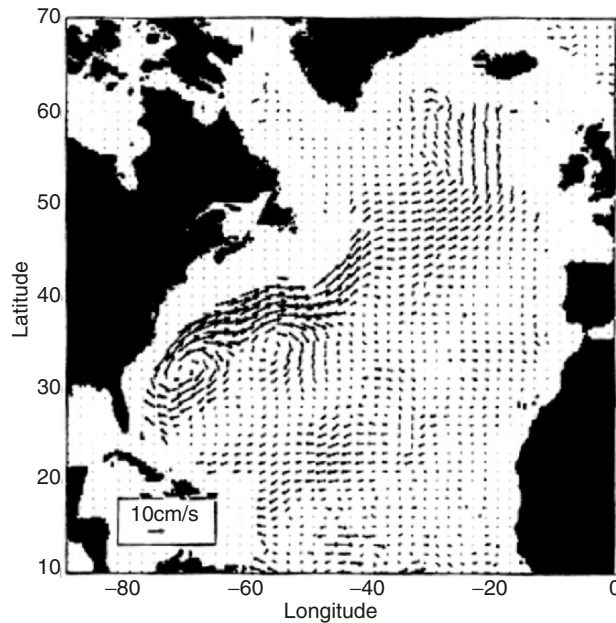


Fig. 12.3. Horizontal absolute velocity vector at 500 m depth calculated, using the P-vector method (after Chu 1995a, *Marine Technology Society Journal*)

leaving the North American coast at about 35°N , turning towards east at 38°N , 60°W to a branching point at about 40°N , 40°W , splitting into penetrating into the longitude of the Grand Banks, and some other features. The horizontal velocity field at 500 m depth (Fig. 12.3) displays a circulation pattern in the main thermocline very similar to that obtained by Olbers et al. (1985) using the β -spiral method. The circulation pattern is dominated by a strong Gulf Stream leaving the North American coast at about 35°N , turning towards the east at 38°N , 60°W to a branching point at about 40°N , 40°W , splitting into two branches. The northern branch moves the water in the northeastward direction until reaching 50°N and deflects towards north at 50°N , $15\text{--}30^{\circ}\text{W}$. The width of this branch increases to the northeastward from 700 km at 40°N , 50°W to nearly 1,500 km in the northeast Atlantic at $50\text{--}60^{\circ}\text{N}$, $15\text{--}30^{\circ}\text{W}$.

The southern branch moves the water to the southeastward direction between 30°N and 35°N toward Gibraltar, and feeds into the subtropical gyre. The velocity calculated using the P-vector method also shows a tight recirculation cell on the western side of the subtropical gyre which was depicted in earlier research (e.g., Stommel and Scott 1977; Olbers et al. 1985). Furthermore, a northern cyclonic gyre exists, but is much weaker than the subtropical gyre.

The vertical velocity is computed by

$$w = \gamma(x, y, z)P_z(x, y, z). \quad (12.1)$$

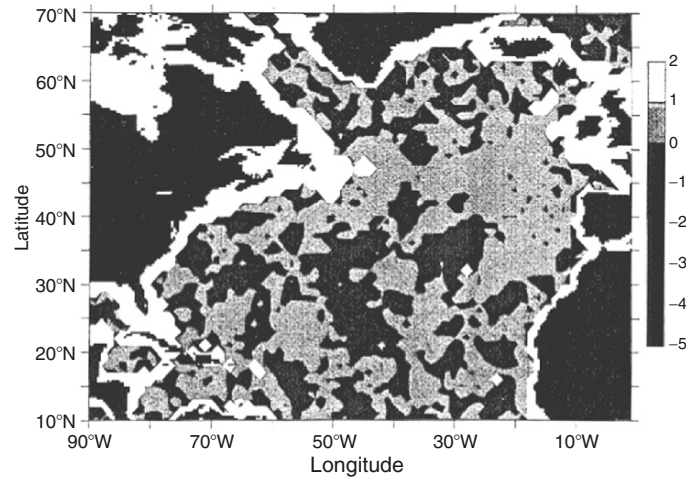


Fig. 12.4. Vertical velocity at 500 m depth calculated using the P-vector method (from Chu 1995a, Marine Technology Society Journal)

Figure 12.4 shows the w -field at 500 m depth. In the vast areas of the North Atlantic Ocean, the vertical velocity is quite weak (less than 1 m day^{-1}) and noisy except in a very small area south of Iceland, where a very strong downward velocity ($>4 \text{ m day}^{-1}$) is found. This coincides with the strong downward branch of the global conveyor belt (Broecker 1991). In the subtropical gyre, the water is usually downwelling. This indicates that the P-vector method has the capability to diagnose the vertical velocity.

12.1.2 Circulation at Different Depths

Figure 12.5 shows the absolute velocity vectors at different levels that is calculated by using the P-vector method. The flow pattern at 100 m level (Fig. 12.5a) is quite similar as that at 500 m level: the Gulf Stream, an anticyclonic subtropical gyre, a weak northern cyclonic gyre. A comparison between Figs. 12.3 and 12.5a leads to the fact that the subtropical gyre shrinks in its north-south extension with increasing depth, which agrees with Olbers et al.'s (1985) results. The flow pattern at deep oceans (2,500, 3,500, and 4,500 m levels) is shown in Fig. 12.5b-d. The dominant features at 2,500 m level (Fig. 12.5b) are the western boundary currents. After passing the Gibbs fracture zone at about 50°N , 40°W the current splits into two branches: a weak northern branch and strong southern branch. The southern branch flows in the southwestward direction, turns westward at 40°N 50°W , and then follows around the east coast of North America. As this branch enters the Sagasso Sea Trench, a noticeable cyclonic eddy appears at 4,500-m level (Fig. 12.5d) to conserve the potential vorticity as the ocean depth increase. The maximum swirl speed is 0.02 m s^{-1} . After passing 30°N , the mid-depth flow at the 2,500 m and 3,500 m (Fig. 12.5c) levels recirculates northeastward at 30°N , 70°W with

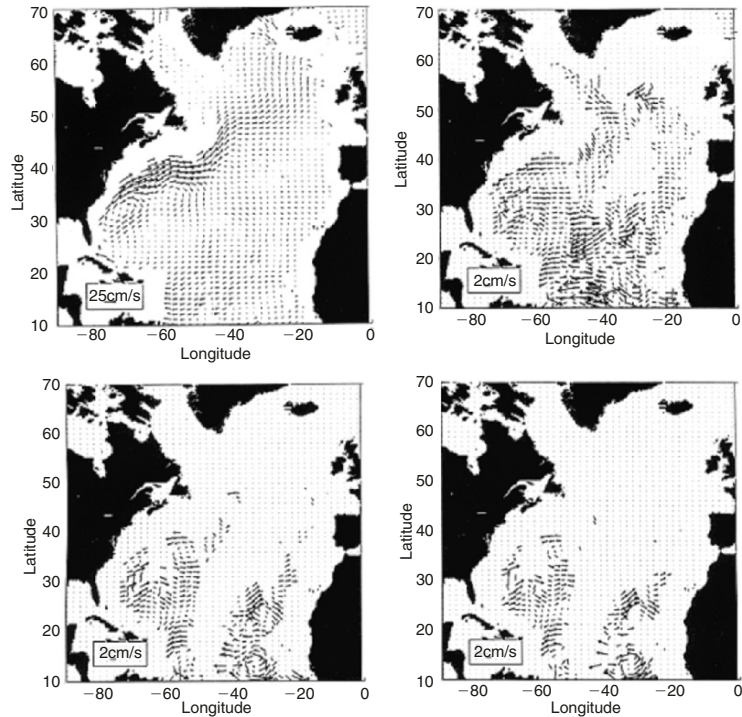


Fig. 12.5. Absolute velocity vectors at different levels calculated, using the P-vector method (from Chu 1995a, Marine Technology Society Journal)

a typical speed that is different from the β -spiral method. Our solution does not show a strong southeastward flow near Bahamas carrying water into the South Atlantic Ocean.

A cyclonic–anticyclonic pair is found in the deep water at the eastern ($20\text{--}40^\circ\text{W}$) tropical part ($10\text{--}30^\circ\text{N}$) of the North Atlantic Ocean. The cyclonic eddy is in the south, and the anticyclonic eddy is in the north. The maximum swirl speed is around 0.02 m s^{-1} . This feature is indeed, strikingly similar to the map (Defant 1941) of the absolute flow at 2,000 m. Furthermore, this dipole structure becomes more evident as the depth increases.

The absolute velocity computed by Olbers et al. (1985) has less noise at the deep level low latitudes than the P-vector method. This is partly because the turbulence fluxes and associated mixing are neglected in the P-vector computation.

12.1.3 Vertical Cross Sections

To compare the results from this method with the other inverse methods such as the box method (Wunsch 1978; Wunsch and Grant 1982) and the β -spiral

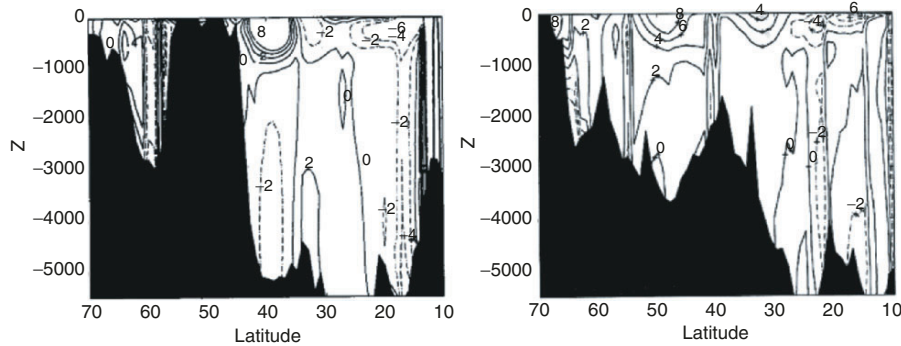


Fig. 12.6. Absolute u -velocity (unit: cm s^{-1}) along (a) 57°W , and (b) 30°W , calculated, using the P-vector method (from Chu 1995a, Marine Technology Society Journal)

method (Olbers et al. 1985), we display the longitudinal cross sections of u -velocity along 57 and 30°W (Fig. 12.6) and the latitudinal cross sections of v -velocity along 24°N (and 53°N and 59°N (Fig. 12.7).

The main features in the western (Fig. 12.6a) and eastern parts (Fig. 12.6b) of the subtropical gyre are (a) a strong upper ocean (above $1,000\text{ m}$ depth) eastward flow (the Gulf Stream) between 30 and 40°N with a maximum speed greater than 0.20 m s^{-1} , (b) a weak westward flow below the Gulf Stream (western boundary currents), (c) a near surface westward flow south of 30°N (southern branch of the subtropical gyre) with a maximum speed of 0.06 m s^{-1} , and (d) banded structure in the deep layers ($z < -1,500\text{ m}$), where the current direction alternates on a horizontal scale around $2,000\text{ km}$, which is wider than the Wunsch and Grant (1982) results.

Interesting features are found in the meridional flow at different latitudes (24°N , 36°N , 53°N , 59°N), which is summarized as follows. (a) In the upper ocean (above $1,000\text{ m}$), at 24°N (Fig. 12.7a) a narrow northward flow appears near the east coast of North America (the Gulf Stream) from 65 to 75°W , with the maximum speed around 0.05 m s^{-1} and the width near $1,000\text{ km}$, and a weaker returning southward flow occupies the rest of the region ($65 - 20^\circ\text{W}$).

At the latitude of 36°N (Fig. 12.7b), a narrow southward flow appears between 60 and 70°W and is sandwiched between two northward flows. This indicates the existence of a recirculation cell at that latitude (36°N). The core of the northward flow shifts towards east as the latitude increases (Fig. 12.7c, d): the maximum current speed appears between longitudes $20 - 30^\circ\text{W}$. (b) In the deeper layer (below $1,000\text{ m}$ depth), a banded structure reveals the alternating northward and southward flow with smaller current speed. The width of these alternating bands is around $1,000 - 2,000\text{ km}$, which is also wider than the results of Wunsch and Grant (1982).

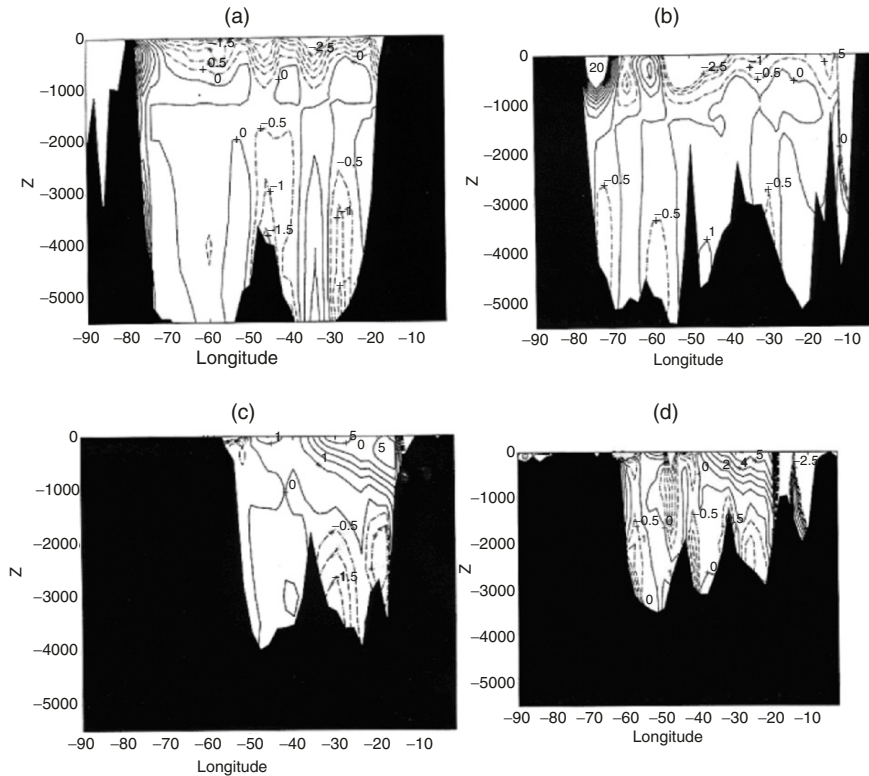


Fig. 12.7. Absolute v -velocity (unit: cm s^{-1}) along (a) 24°N, (b) 36°N, (c) 53°N, and (d) 59°N, calculated using the P-vector method (from Chu 1995a, Marine Technology Society Journal)

12.1.4 Gulf Stream Volume Transport

As the Florida Current leaves the Blake Plateau and becomes the Gulf Stream, this western boundary current turns from predominantly meridional to mostly zonal, near the Cape Hatteras and beyond. This separation of the Gulf Stream from the coast is a challenging problem.

The Gulf Stream volume transport has been estimated by many authors. The volume transport stream function (Ψ) can be calculated using the method described in Chap. 8. Difference of Ψ -value between the North Atlantic continent and at the center of the subtropical gyre is used to quantify the volume transport of the Gulf Stream. The monthly mean Gulf Stream transport is quite steady with a maximum transport of 62 Sv in October and a minimum of 52 Sv in March and April (Fig. 12.8). The calculated Gulf Stream volume transport (57 Sv) is weak compared to the value of 120 Sv found after detachment from Cape Hatteras when encompassing the Southern Recirculation gyre

transport (Hogg 1992). This is due to the smoothed nature of the climatological wind and hydrographic data used.

12.2 South Atlantic Ocean Circulation

From its littoral margin to the open ocean, the western South Atlantic is marked by the circulation patterns and exchange processes that are centrally important to the regional marine resources and local economics, and equally important to the global flux of heat and dissolved substances (Campos et al. 1995). The depth-integrated western boundary current (Brazil Current) originates from the South Equatorial Current (Fig. 12.1). A major change in the flow patterns along the western boundary occurs in the southern Brazil Basin. Among other important characteristics, the Southwest Atlantic is characterized by the presence of the Brazil Current (a warm western boundary current), Brazil–Malvinas confluence, subtropical gyre, and Benguela Current (an eastern boundary current).

The Brazil Current is a weak western boundary current (weaker than its counterpart in the North Atlantic – the Gulf Stream) carrying warm sub-

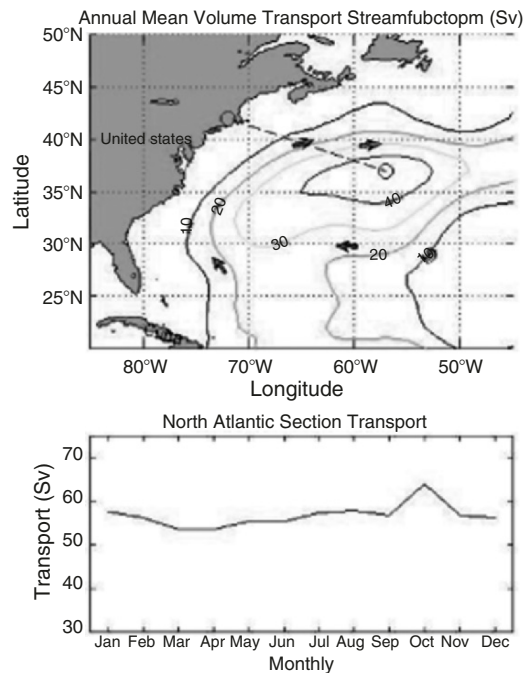


Fig. 12.8. The inverted monthly volume transport between the North American east coast and the center of the subtropical gyre representing the Gulf Stream transport (Chu and Fan 2006, *Journal of Marine Systems*)

tropical water, which runs south along the coast of Brazil from about 9°S to about 38°S and is generally confined to the upper 600 m of the water column. Its origin begins where the westward flowing trans-Atlantic South Equatorial Current bifurcates (or splits) as it approaches the continental shelf off the coast of Cabo de Sao Roque, Brazil (Stramma et al. 1990; Podesta et al. 1991). The South Equatorial Current water flowing north becomes the North Brazil Current, and the branch flowing south becomes the Brazil Current. The Brazil Current begins at about 10°S , separating slightly from the coast near 12°S where the continental shelf becomes wider (Stramma et al. 1990; Peterson and Stramma 1991). The Brazil Current continues to flow south off the Brazilian coast until it reaches about $33\text{--}38^{\circ}\text{S}$, where it collides with the north-flowing Malvinas (Falkland) Current. Gordon and Greengrove (1986) first defined this region the Brazil–Malvinas Confluence.

Olson et al. (1988) and Podesta et al. (1991) analyze satellite images (1984–1987) and show that the actual point at which the Brazil Current separates from the continental shelf varies anywhere between 33 and 38°S , with the average being about 36°S . The Brazil Current is then, in part, deflected to the east, off-shore of Rio de la Plata, a region known as the Brazil–Malvinas Confluence Zone – one of the most energetic regions in all the oceans (Sarçeno et al. 2004).

Comparing to its counterpart in the Northern Atlantic (i.e., the Gulf Stream), the transport of the Brazil Current is weak. In its northern part, this current is shallow and closely confined to the continental shelf. This causes difficulty in estimating the transport of the Brazil Current. Figure 11.9 shows the inverted monthly mean volume transport stream function Ψ , and vertically integrated velocity (U, V) (see Chap. 8) in the western side of South Atlantic Ocean. The volume transport of the Brazil Current is approximately 10 Sv.

The upper layer (500 m) transport is estimated to be 5 and 6.5 Sv around 20°S (Peterson and Stramma 1991; Stramma et al. 1990). At about 20.5°S , a cyclonic gyre seaward of the Brazil Current centered at about 17°S and 34°W has been observed, and attributed to the southernmost meanders of the South Equatorial Current that are reflected northward by this same seamount chain (Memery et al. 2000; Stramma et al. 1990). This pattern is also identified in the inverted global (Ψ, U, V) fields (Fig. 12.9). At about 20.5°S , near the seamount chain, the current velocity is estimated to be about $0.5\text{--}0.6\text{ m s}^{-1}$ by Evans et al. (1983).

As the Brazil Current flows south of 24°S , it intensifies by about 5% per 100 km, which is similar to the growth rate in the Gulf Stream, although transport values in the Brazil Current are considerably less (Peterson and Stramma 1991). Thus, at about 33°S the total transport (which includes a recirculation cell in the upper 1,400 m) is about 18 Sv, and reaches the values from 19 to 22 Sv at about 38°S , where it encounters the Malvinas (Falkland) Current (Olson et al. 1988; Peterson and Stramma 1991). The mean latitude of the Brazil Current’s separation from the shelf break is about $35.8^{\circ}\text{S} \pm 1.1^{\circ}$ and

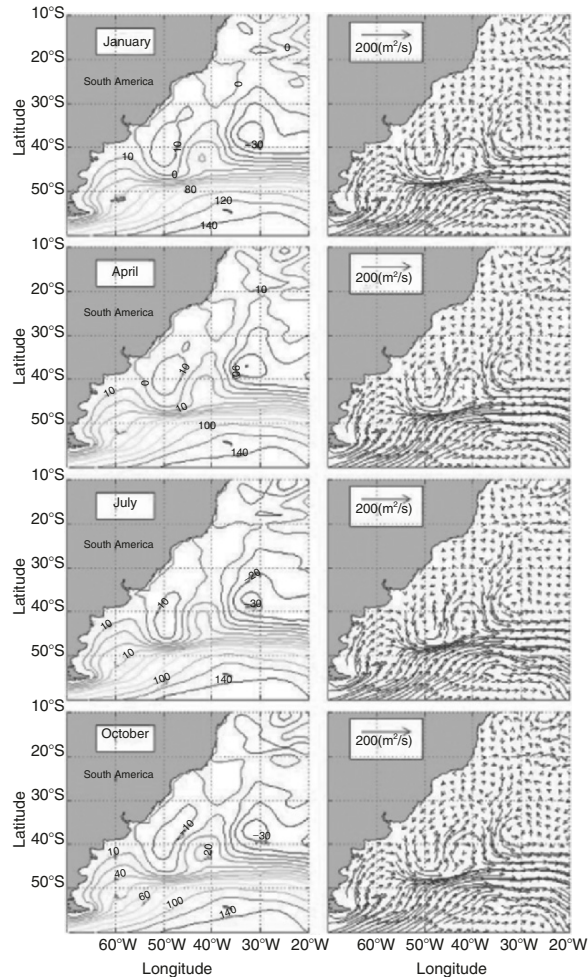


Fig. 12.9. The inverted monthly mean Ψ and (U, V) vector fields in the southwestern South Atlantic Ocean: (a) January, (b) April, (c) July, and (d) October (Chu and Fan 2006, *Journal of Marine Systems*)

for the Malvinas Current, the mean latitude of separation is $38.9^{\circ}\text{S} \pm 0.9^{\circ}$. The coastal ranges of the separation positions are at 950 and 850 km, respectively (Olson et al. 1988). These features are also identified from the global (Ψ, U, V) fields (Fig. 12.9).

12.3 Brazil–Malvinas Confluence

The combined flow of the two currents causes a strong thermohaline frontal region, called the Brazil–Malvinas Confluence in which the Brazil Current

breaks off into two branches, one turning to the north forming a recirculation cell, while the other continues southward and veers northeast at about 45°S , becoming the South Atlantic Current (Fig. 12.9). The mean transport in this region has been measured to be about 11 Sv (Garzoli and Bianchi 1987), which is very similar to the inverted value shown in Fig. 12.9.

Flow can increase up to 23 Sv at the Brazil–Malvinas Confluence (Garzoli and Bianchi 1987). The mean conditions of circulation vary significantly, and more recent evidence shows that they are more or less related to the meteorological anomalies (Assireu et al. 2003). Occasionally, when a meandering Brazil Current that has extended unusually far south retreats, it can shed a series of warm core eddies that migrate into the Antarctic Circumpolar Current (Partos and Piccolo 1988). The values also vary according to the measurement method and depth.

The range of the Brazil–Malvinas Confluence oscillate between 54 and 45°W , a total distance of about 770 km (at 38°S). The meanders appear to occur on a 12 month cycle and are likely to correlate to changes in the separation latitude of the Brazil Current (Boebel et al. 1999; Garzoli and Bianchi 1987; Goni and Wainer 2001; Maamaatuaiahutapu et al. 1999; Zavilov et al. 1999). The mean speed of the front is estimated to be about 0.14 m s^{-1} . The front oscillates around its mean seasonal position (farther north and east during austral winter and farther south and west during austral summer) within a period of about one month and amplitude that varies from 10 to 50 km day^{-1} . The mean velocity of the displacement of the front reaches values up to 10 km day^{-1} (Garzoli and Bianchi 1987). This area is also rich in eddies, more often called Brazil Current Rings, averaging to about 7–9 rings per year. These elliptical rings can vary in size from about 56 to 225 km along the semimajor axis, and 23–108 km for the semiminor axis. These anticyclones have a mean lifetime of about 35 days and translational speeds of anywhere between 4 and 27 km day^{-1} (Lentini et al. 2002). On an average, the temperature in the Brazil Current is about 18 – 28°C , with essentially three meridional zones that experience several degrees of distinctly different annual temperature fluctuations, which correspond to their proximity to the shore. The first zone is located over the shelf and experiences temperature variability of 7–10 degrees, which is controlled by both the winter invasions of sub-Antarctic water from the Malvinas Current and discharges from Rio de la Plata and Patos-Mirim. The second or central portion, closer to the eastern margin of the continental shelf, experiences a 5–7 degree variance. The third, on the seaward-most zone, shows little fluctuation up to the Confluence (Memery et al. 2000; Zavilov et al. 1999). Temperatures in the southern section of the current, near the Confluence, can change by 5–13 degrees, with the cooler temperatures occurring around August–September and the warmer values observed in February (Boebel et al. 1999; Podesta et al. 1991). Almost yearly temperature anomalies of warm and cold fronts occur that seem to be related to the El Niño–Southern Oscillation (ENSO) events. Anomalous cold water extensions to the north occur on the shelf generally 1 year after every

warm ENSO event, and anomalous warm water extensions occur generally 1 year after every cold ENSO (Lentini et al. 2001).

Surface salinities indicative of Brazil Current waters range from 35.1 to 36.2 ppt, with the maximum commonly found at around 20°S, where it can reach a salinity of 37.3 ppt (Memery et al. 2000; Wilson and Rees 2000). Although that is energetically comparable to its North Atlantic counterpart, particularly in the region of confluence with the northward-flowing Malvinas Current at approximately 38°S, while the salinity is weaker than the Gulf Stream in terms of the mass transport (Fig. 12.9). The western limb of the recirculation cell (anticyclonic) separates from the continental slope at about 38°S upon its confluence with the northward-flowing Malvinas Current, whereupon the bulk of the Malvinas retroflects cyclonically (clockwise) back towards the southeast while the lesser portions continue northeast along the coast. On the eastern side of the cyclonic trough is the combined southeastward flow of Malvinas and Brazil Current waters that extend to 45°S before the subtropical waters turn east and north to form the pole-ward limits of the subtropical gyre. The Malvinas waters continue south to the southern margin of the Argentine Basin (49°S) before turning east with the Antarctic Circumpolar Current regime. Our results are consistent with the earlier studies (e.g., Peterson and Whitworth 1989). The Brazil–Malvinas confluence occurs all year round with a very weak seasonal variability.

Questions and Exercises

- (1) What are the major characteristics of the North Atlantic Ocean circulations at various depths? Compare the inverted velocity fields to that calculated by other authors.
- (2) The monthly mean Gulf Stream volume transport is estimated from the WOA (T, S) data using the P-vector inverse method (Fig. 12.8) with weak seasonal variation (maximum value of 62 Sv in October and minimum value of 52 Sv in March and April). Is it realistic? Why?
- (3) Brazil–Malvinas Confluence is an important feature of the western boundary currents in the South Atlantic. Discuss the major characteristics of the Brazil–Malvinas Confluence and its impact on the global climatic systems.
- (4) Select an area with your interest. Download the P-vector inverse codes for calculating the absolute velocity at z - and isopycnal-coordinate systems from the DVD-ROM. Run these codes using the WOA or GDEM (T, S) data to get absolute velocity. Discuss the major characteristics of the circulation in the area including the seasonal variation, causes of these features, and the effect of the circulation on the global system.
- (5) Compare your computed absolute velocity with the absolute velocity data stored in the DVD-ROMs.

Inverted Circulations for the Southern Ocean

The Southern Ocean (Fig. 13.1) is bounded by the Antarctic continent to the south and the world ocean to the north; the Polar Front forms the boundary between the polar and subpolar water masses. The area of the Southern Ocean south of the Polar Front is about $3.8 \times 10^7 \text{ km}^2$. The ocean floor around Antarctica has four basins (the Weddell–Enderby, South Indian, Southwest Pacific, and Southeast Pacific basins) with depths exceeding 4,500 m, separated by broad submarine ridges and plateaus. The continental shelves surrounding the Southern Ocean are generally quite narrow; the exceptions being the two broad (about 400 km) and deep (about 400 m) shelves of the Weddell and Ross seas. Shelf regions are further characterized by irregular depressions and submarine canyons and by glacial ice shelves which extend seaward from the continent. The Antarctic shelf and bottom waters are cold, dense water masses which have relatively high concentrations of the gases that the ocean acquires from the atmosphere, such as oxygen. They form close to the sea surface near Antarctica, then flow away from their source and sink, and then they introduce water with near-surface characteristics while moving into the deep ocean. This process, usually called ventilation, is associated with important fluxes of heat, salt, nutrients, and gases.

The absolute currents are inverted from the (T, S) fields from WOA using the P-vector method. The general circulation in the Antarctic is characterized by the Antarctic Circumpolar Current, Antarctic Coastal Current, and Antarctic gyres.

13.1 Antarctic Circumpolar and Coastal Currents

Vertically integrated annual mean velocity is calculated from the WOA (T, S) fields using the P-vector method (Fig. 13.2). The water flows around Antarctica in a clockwise direction (the Antarctic Circumpolar Current) with gyres and eddies.

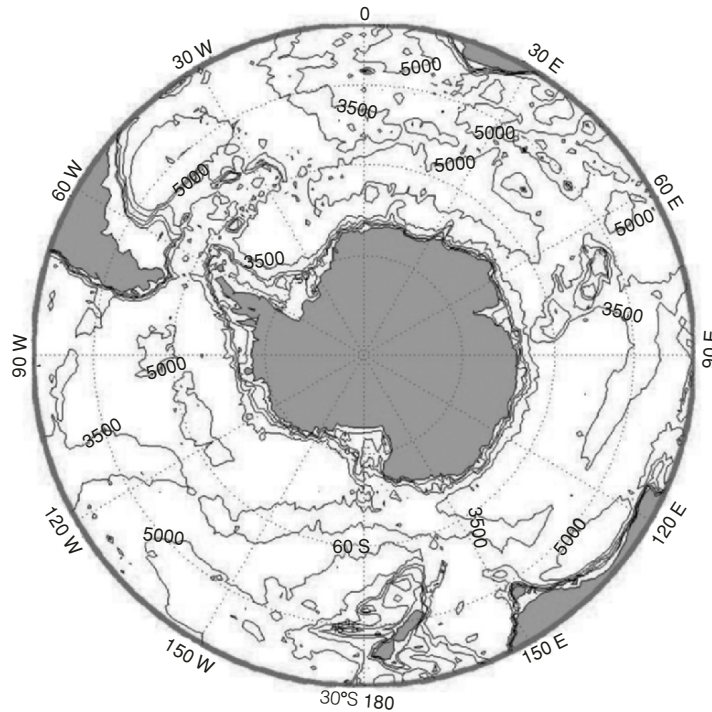


Fig. 13.1. Bathymetry of the Southern Ocean

The Antarctic Circumpolar Current is the most important current in the Southern Ocean, and the only current that flows completely around the globe. It encircles the Antarctic continent and flows eastward through the southern portions of the Atlantic, Indian, and Pacific Oceans. This current is arguably the “mightiest current in the oceans” (Pickard and Emery 1990). Despite its relatively slow eastward flow of less than 20 cm s^{-1} in regions between the fronts, it transports more water than any other current (Klinck and Nowland 2001). It extends from the sea surface to depths of 2,000–4,000 m and can be as wide as 2,000 km. This tremendous cross-sectional area allows for the current’s large volume transport. The Antarctic Circumpolar Current’s eastward flow is driven by strong westerly winds. The average wind speed between 40 and 60°S is $8\text{--}12 \text{ m s}^{-1}$ with strongest winds typically between 45 and 55°S. Historically, the Antarctic Circumpolar Current has been referred to as the ‘West Wind Drift’ because the prevailing westerly wind and current are both eastward.

The Antarctic Circumpolar Current is an intense flow around the Earth without interruption and displays little attenuation with depth. It is strong over the northern slope of the midocean ridge in the southwest Pacific, in

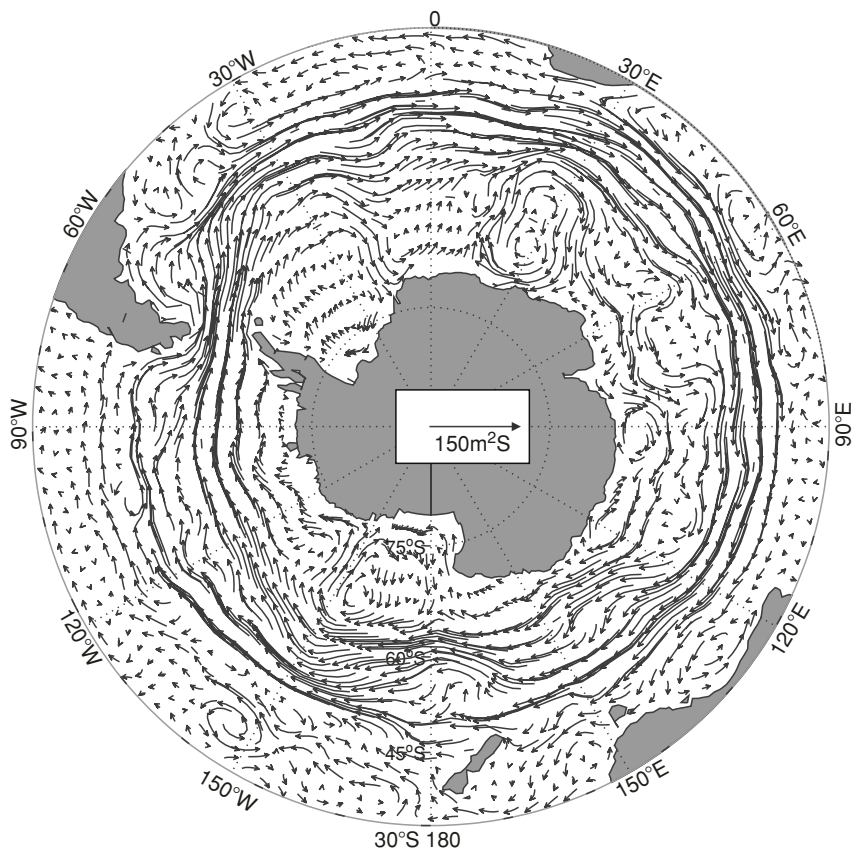


Fig. 13.2. Vertically integrated annual mean velocity is calculated from the WOA (T, S) fields using the P-vector method (from Chu and Fan 2006, *Journal of Marine System*)

Drake Passage, and the southwest Indian Ocean immediately below the Agulhas return current.

The computed monthly mean volume transport through the Drake Passage using the P-vector method is around 156 Sv with a small seasonal variation (Fig. 13.3), which compares well with recent year-long measurements of the transport of the Antarctic Circumpolar Current through Drake Passage (e.g., Nowlin et al. 1977; Bryden and Phillipsbury 1977; Fandry and Pillsbury 1979; Whitworth 1983; Whitworth and Peterson 1985). These observations indicate the mean annual transport to be 134 Sv with an uncertainty of about 10%; the instantaneous flow may vary from the mean by as much as 20% (Nowlin and Klinck 1986).

In a major review of the structure and dynamics of the Antarctic Circumpolar Current, Nowlin and Klinck (1986) note that the Antarctic Circumpolar

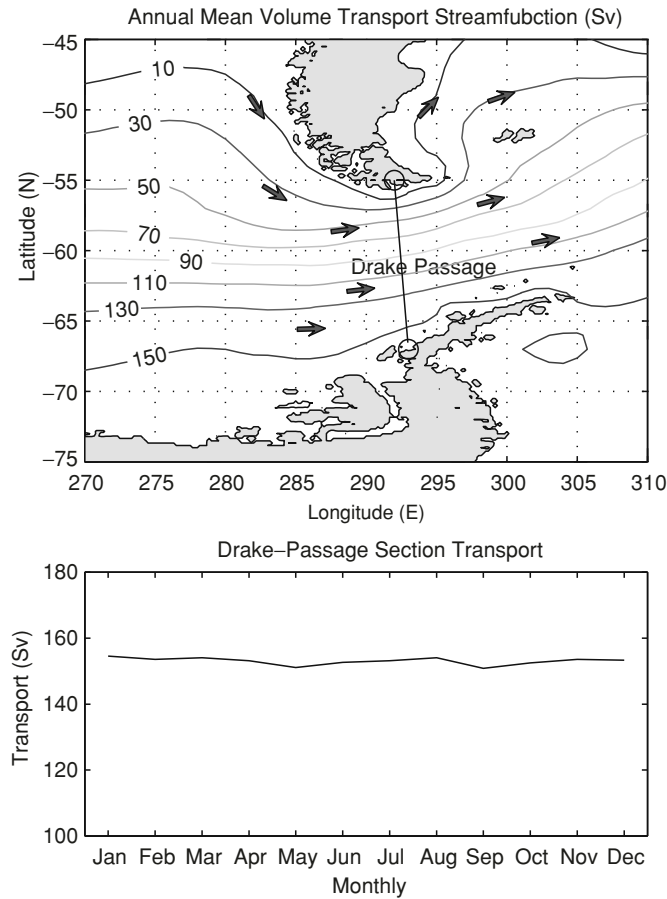


Fig. 13.3. The inverted (a) annual mean monthly volume transport stream function (unit: Sv) and (b) monthly mean volume transport through Drake Passage calculated from the WOA (T, S) fields using the P-vector method. Note that the seasonal variability is weak

Current exists as a banded structure, with multiple narrow jets associated with strong lateral density gradients at the sub-Antarctic and polar fronts. The position of these fronts is highly variable, and excursions of upto 100 km in 10 days have been observed. These meanders can lead to the formation of eddies and current rings (Joyce et al. 1981; Bryden 1983).

The Antarctic Coastal Current is the name commonly given to the narrow, westward-flowing current that tends to follow the continental margin (Sverdrup 1953). This flow lies south of the belt of low atmospheric pressure that extends around the continent at roughly 65°S . This current is not completely circumpolar, but instead becomes part of the clockwise gyres in the Weddell and Ross seas (see Fig. 13.2).

13.2 Cyclonic (Clockwise) Weddell Double Gyres

Figure 13.2 also shows the existence of several gyres in the western Weddell basin and north of the Ross Sea and south of the Antarctic Circumpolar Current. The horizontal structure and strength of the Weddell Gyre has been of interest to oceanographers for decades. Early estimates were based on (sparse) hydrographic data; which were used to conclude that there is a double-cell structure, at least in the baroclinic fields. However, this could not be confirmed by more recent measurements. Uncertainty also existed with respect to the magnitude of the mass transport in the Weddell Gyre, which was estimated to be between 30 and 70 Sv.

In the Weddell Sea, which probably contributes the most to the Bottom Water formation, the water flows westward under the influence of the Coriolis force as it sinks, forming a thin layer of extremely cold water above the continental slope. It mixes with the overlying water, which is recirculated with the large cyclonic eddy in the central Weddell Sea. The Weddell Sea is one of the few places in the world ocean where deep and bottom water masses are formed to participate in the global thermohaline circulation. The characteristics of exported water masses are the result of complex interactions among surface forcing, significantly modified by sea ice, ocean dynamics at the continental shelf break and slope (Foldvik et al. 1985; Muench and Gordon 1995), and subice shelf water mass transformation.

The inverted monthly (January, April, July, October) mean volume transport stream function Ψ and vertically integrated velocity (U, V) fields (Fig. 13.4) show a double-gyre structure of the Weddell Gyre as suggested by the hydrographic observations (Mosby 1934; Deacon 1979; Bagriantsev et al. 1989) and the numerical simulation of a regional coupled ice-ocean model (Beckmann et al. 1999). There is a western cell filling the western Weddell Basin, and another (even stronger) mostly confined to the deep basin northeast of Maud Rise. Both have a maxima that exceed 50 Sv in the annual mean.

Seasonal variability in (Ψ, U, V) is very weak. Maximum Ψ -value in the vicinity of the two cells is around 109 Sv. Minimum value of Ψ is around 55 Sv in the western Weddell Gyre and 39 Sv in the eastern Weddell Gyre. Thus, the volume transport is around 54 Sv associated with the western Weddell Gyre and 70 Sv associated with the eastern Weddell Gyre.

Quantitatively, the inverted transport compares well with calculations based upon observations along the Joinville Island-Kapp Norvegia section (30 ± 10 Sv) as well as more recent measurements along the Greenwich meridian (60 ± 10 Sv). The double cell structure persists throughout the year, but is most pronounced in austral winter. For example, this is consistent with earlier estimations such as 97 Sv by Carmack and Foster (1975) who utilized short-term current meter measurements and 76 Sv by Gordon et al. (1981) who computed the wind-driven transport of the Weddell Sea using Sverdrup dynamics, balanced by a western boundary current along the Antarctic Penin-



Fig. 13.4. Inverted monthly mean volume transport stream function and vertically integrated velocity vectors in the Weddell Sea (From Chu and Fan, 2006, *Journal of Marine Systems*)

sula. Deacon (1982) reviewed the physics of the Weddell Gyre in relation to ecological cycles and noted that southward flow along the eastern side of the Weddell Gyre appeared to be a critical factor determining krill cycles.

Figure 13.4 also shows the Weddell-Scotia Confluence in the northern end of the Weddell Gyre that lies to the northeastern side of the Antarctic Peninsula. It forms by the convergence of the Antarctic Circumpolar Current passing through Drake Passage and the recirculating flow of the Weddell Gyre (Gordon et al. 1977). This region is of considerable biological importance (Deacon and Foster 1977; Nelson et al. 1987). Foster and Middleton (1984) emphasized the eddy field lying downstream of the confluence.

13.3 Anticyclonic Ross Gyre

The inverted monthly (January, April, July, October) mean volume transport stream function Ψ and vertically integrated velocity (U, V) fields (Fig. 13.5) show a single gyre in the Ross Sea with the westward flow in the southern Ross Sea as pointed out by DeMaster et al. (1992) on the basis of moored current meter data. The anticyclonic (anticlockwise) Ross Gyre dominates the circulation in the Southeast Pacific Basin, between 160°E and 140°W .

The Ross Gyre extends from the surface to the deep ocean, and is approximately one-half to one-third as strong as the Weddell Gyre. Circumpolar Deep Water enters the Ross Gyre at its eastern end, and is ventilated by the shelf waters of the Ross Sea. Salinity and oxygen distributions show that the influence of shelf waters can be traced beyond the Ross Gyre into the mid-depth waters of the South Pacific Ocean.

Seasonal variability in (Ψ, U, V) is stronger in the Ross Sea (Fig. 13.5) than in the Weddell Sea (Fig. 13.4). The volume transport is around 80 Sv associated with the Ross Gyre. Such a strong cyclonic gyre represents important areas of biogenic production and potentially large sources of biogenic material to the water column and sediments. The inverted Ross Gyre is consistent with the current meter moorings (Pillsbury and Jacobs 1985), which show that the general circulation in the Ross Sea surface waters is cyclonic, with a slow southward flow in the central and eastern Ross Sea (the eastern part of the inverted Ross Gyre).

Questions and Exercises

- (1) The Antarctic Circumpolar Current is the most important source of current in the Southern Ocean, and the only current that flows completely around the globe. Figure 13.2 shows the Antarctic Circumpolar Current meandering and eddy generation. Discuss the mechanisms causing the eddy formation.
- (2) Discuss the effect of the Antarctic Circumpolar Current on the global climatic system.

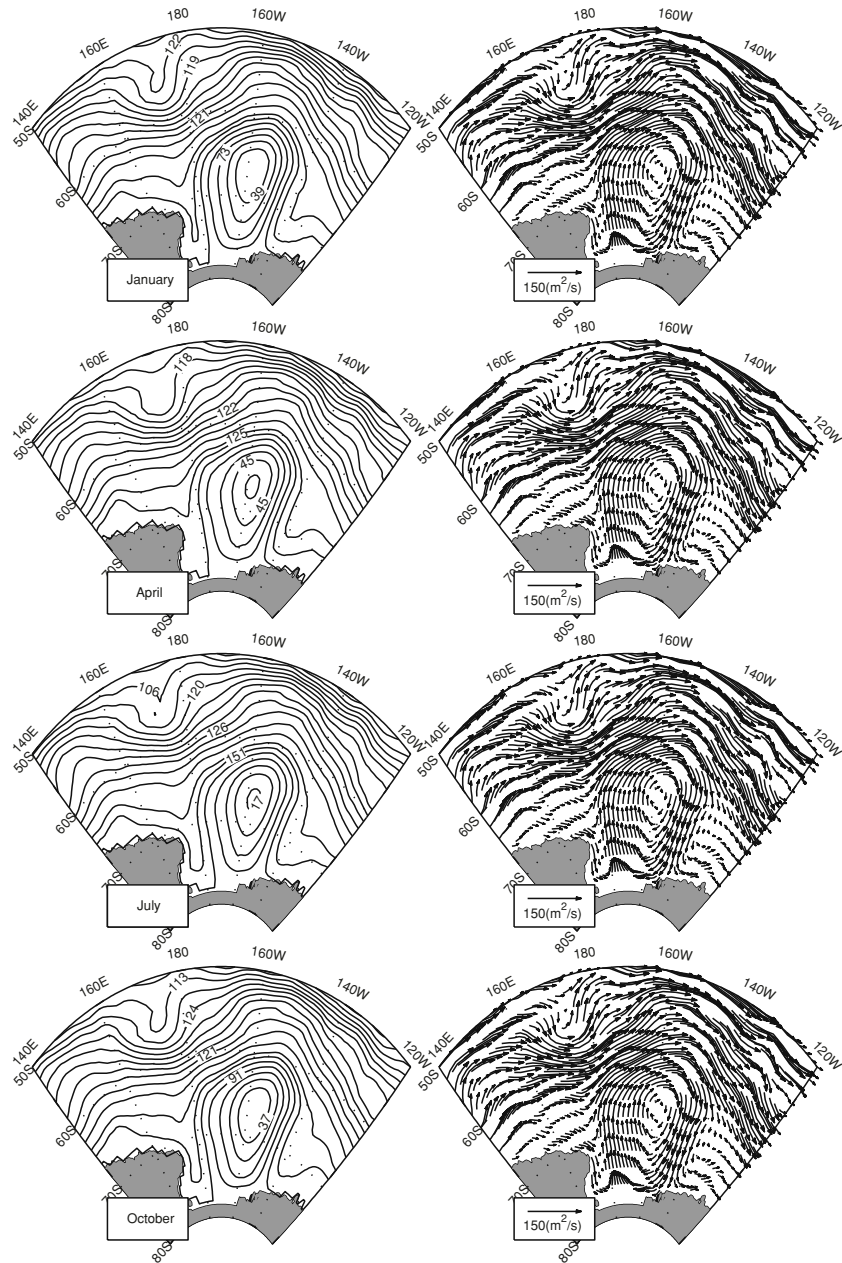


Fig. 13.5. Inverted monthly mean volume transport stream function and vertically integrated velocity vectors in the Ross Sea (From Chu and Fan, 2006, *Journal of Marine Systems*)

- (3) The volume transport across the Drake Passage is estimated as 156 Sv from WOA (T, S) data using the P-vector method. Compare this value with the estimations by other authors after searching the reference.
- (4) Figure 13.3 shows very weak seasonal variability. Is it realistic? What is the reason for that?
- (5) Compare between the bathymetry of the Southern Ocean (Fig. 13.1) and the volume transport stream function in the Weddell Sea (Fig. 13.4). Can you speculate the topographic effect on the formation of the Weddell Double Gyres?
- (6) What is the effect of the Weddell Double Gyres on the formation of the Weddell Polynya?
- (7) What are the major features of the Ross Gyre?
- (8) Find other gyres and their dynamic characteristics in the Southern Ocean using the inverted velocity data in the enclosed DVD-ROM.

Inverted Circulations in the Arctic Mediterranean Seas

The Arctic Mediterranean seas play an important role in global climate through its effects on the role of the ocean in the local radiation balance and water exchange with lower latitudes. To understand these effects, the large-scale circulation pattern and water mass distributions should be first studied.

14.1 Geographic Features

The Arctic Mediterranean seas, comprised of the basins lying north of the Greenland–Scotland Ridge, of about $9.5 \times 10^6 \text{ km}^2$, representing 2.6% of the total oceanic surface (Fig. 14.1). The two principal areas of this system are the Greenland–Iceland–Norwegian (GIN) Sea and the Arctic Ocean. They are connected by the Fram Strait, the wide (600 km), deep (sill depth about 2,600 m) passage between Greenland and Spitzbergen.

The Arctic Ocean is roughly divided into the Canadian basin (maximum depth about 3,800 m) and the Eurasian basin (maximum depth about 4,200 m) by the Lomonosov Ridge (sill depth about 1,400 m). The Canadian basin is further divided into the Canada and Makarov basins by the Alpha–Mendeleyev Ridge, and the Eurasian basin is divided into the Nansen and Amundsen basins by Nansen–Gakkel Ridge.

The continental shelf from Alaska to Greenland is relatively narrow, but from Spitzbergen eastward (the Barents, Kara, Laptev, East Siberian, and Chukchi seas) the shelf is broad, typically from 600 to 800 km. A number of submarine canyons indent the shelf, the largest being the Svataya Anna and Voronian canons in the Kara Sea.

The Arctic oceans have surface layers freshened by continental inputs (rivers and glacial melt water) and by sea ice melt water. Discussion on stream flow from major rivers entering the Arctic Ocean is given by a number of authors. The total annual stream flow into the Arctic, including the Arctic Archipelago, is about $3,500 \text{ km}^3 \text{ year}^{-1}$. An additional $1,500\text{--}2,000 \text{ km}^3 \text{ year}^{-1}$



Fig. 14.1. Bathymetry of the Arctic Ocean showing the Eurasian and Canadian basins separated by the Lomonosov ridge. The 200 m depth contour marks the edge of the continental shelf

enters as a freshwater fraction in the Bering Strait inflow (Coachman et al. 1975). Aagaard and Coachman (1975) compute the fresh-water residence time (defined as stored volume divided by inflow) to be roughly 10 years for the whole Arctic basin, with local values as low as 2 years applying to the southern Eurasian basin.

Significant annual and interannual variations occur in stream flow (Cattle 1985). The large Russian rivers Yenisei and Lena exhibit on average about a 40-fold change between low flows in winter and peak flows in June and July; seasonal variability for the Mackenzie River is much less, about fivefold. Interannual variability is from 5 to 20% of the mean annual flow, depending on the individual rivers.

Interannually, the total extent of sea ice in the Arctic varies by about 5° of latitude at all locations where the ice advance is not bounded by land (Walsh and Johnson 1979). At the winter maximum this amounts to about 30% variability for individual regions (Johnson 1980). On the other hand, Carsey (1982) examined ESMR data from the Arctic at the time of minimum ice extent and noted that while regional variations may be large, the total coverage varies interannually by about 2% only.

14.2 Thermohaline Features

Thermohaline features can be detected from the joint US-Russian EWG atlas (Arctic Climatology Project 1997, 1998). The EGW Atlas has gridded data distributed on local Cartesian coordinate. All the grid cells have the same size. This is different from the WOA dataset, which uses the spherical coordinate system. At the North Pole, the size of the grid cell is zero. Here, the (T, S) fields from the EGW Atlas at 50 m (subsurface level), 500 m (intermediate level), and 2,000 m (deep level) are presented to show the thermohaline characteristics.

14.2.1 Subsurface Level (50 m Depth)

Three main types of surface water are recognized from the EWG atlas. The first is Atlantic Water, which is carried into the system as a branch of the Norwegian—Atlantic Current. It can be defined as water with temperature (Fig. 14.2) above 3°C and salinity (Fig. 14.3) greater than 34.9 ppt. The second is the Polar Water, which is water that has been diluted by admixtures with fresh water; it is generally cold (temperatures below 0°C) and fresh (salinity below 34.4 ppt). It occupies the upper layers of the Arctic down to 200 m depth and makes up the surface outflow within the East Greenland Current and the Canadian Arctic Archipelago. The third is the Arctic Surface Water, which is found mainly in the gyres of the Greenland and Iceland seas. This water is warmer and more saline than Polar Water, but cooler ($0\text{--}3^{\circ}\text{C}$) and fresher (34.4–34.9 ppt) than Arctic Water. However, this water is notably denser than

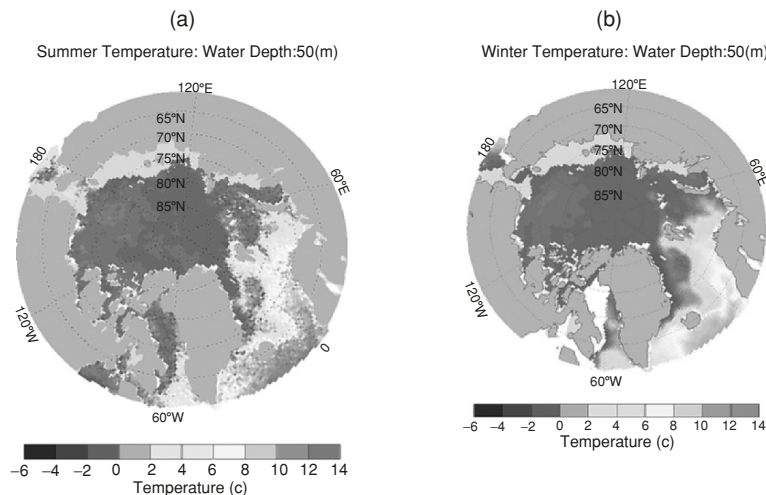


Fig. 14.2. Temperature of the Arctic Mediterranean Seas at 50 m depth from the Joint US-Russian EWG atlas: (a) summer, and (b) winter

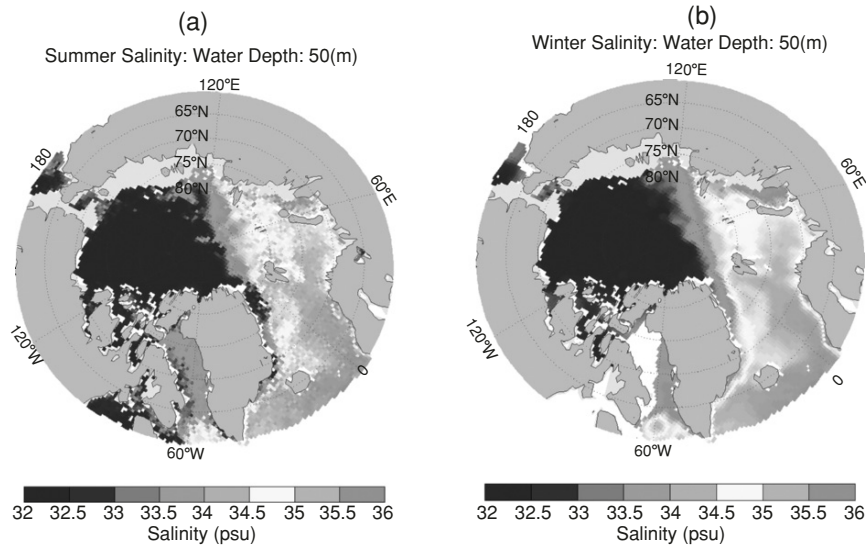


Fig. 14.3. Salinity of the Arctic Mediterranean Seas at 50 m depth from the Joint US-Russian EWG atlas: (a) summer, and (b) winter

either Polar Water or Arctic Water, indicating that it is not a simple mixture of the two and that large modifications due to air–sea exchanges occur locally.

In winter the surface layer tends to be uniform vertically in temperature and salinity. Ice melting in summer results in a pronounced salt stratification; however, this water remains near freezing except for areas that become completely ice free. The lower part of the surface layer contains the main halocline, the layer with low temperatures (less than -1°C) and salinities between about 30.4 and 34.4 ppt, which is arguably the most important feature of the Arctic Ocean. This cold, relatively saline layer is thought to be maintained by shelf drainage during winter (Aagaard et al. 1981; Melling and Lewis 1982). In the Eurasian basin the salinity increases rapidly with depth, reaching 34.9–35.0 ppt at about 200 m, while the temperature remains colder than -1.5°C to 150 m and then increases with depth. In the Canadian basin the halocline is deeper, and the salinity increases more slowly with depth. Here, the temperature shows two minima, near the depths with salinities of 31.6 and 33.1 ppt, and a maximum near 32.4 ppt. The minimum near 31.6 ppt is possibly a remnant of winter cooling. The maximum near 32.4 ppt and the minimum near 33.1 ppt possibly reflect the inflow from the Pacific through Bering Strait. Hence, the Arctic halocline is not a uniform structure nor is it likely composed of single water mass. It likely derives from more than one region and is formed by more than one ventilation mechanism (Jones and Anderson 1986).

Figures 14.2 and 14.3 show the existence of thermohaline fronts or frontal zones in the GIN Sea. They are oriented more or less meridionally. It separates the warm and salty Atlantic Water in the Norwegian and West Spitzbergen currents from the cooler and fresher water of the Arctic domain (Dietrich 1969). In the Greenland Sea it follows the mid-Atlantic Ridge (the Knipovich Ridge) and merges in the Fram Strait with the Polar front, owing to local recirculation. On the western side of the Arctic front a succession of cyclonic gyres in the Greenland Basin, the Boreas Basin, and the Fram Strait have been observed (Quadfasel et al. 1987; Quadfasel and Meincke 1987). In the transition different water masses interface and form frontal zones that not only separate water bodies with different hydrographic characteristics but also the regional biological systems. The GIN Sea is a key region in the advective–convective system that links the polar ice with the North Atlantic (van Aken et al. 1991).

The seas north of the Greenland–Scotland Ridge constitute a major heat sink in the global thermohaline circulation of the world ocean and therefore a crucial component of the earth climate (Aagaard et al. 1985). A large heat loss to the atmosphere, combined with sea ice production and melting, is responsible for the formation of deep and intermediate waters through winter convection, which, in some basins like the Greenland Sea, may reach down to the bottom.

The one-dimensional convection process is strongly affected by the horizontal dynamics of the convective basins including lateral exchanges of heat, salt, and ice at their boundaries. Concerning the Greenland Sea, important exchanges occur through its northern boundary, the Fram Strait, which is the only deep connection between the Arctic Ocean and the rest of the world ocean. A better knowledge of the dynamics of the strait is therefore crucial in the context of investigating the processes involved in the deep convection and their variability.

14.2.2 Intermediate Level (500 m Depth)

Three types of the Arctic intermediate water exist with different T/S characteristics (Swift and Aagaard 1981). The Arctic Surface Water usually lies above a temperature minimum at 75–150 m depth, a temperature maximum at 250 m, and a salinity maximum at about 400 m. To account for these features, the following distinction was made: lower Arctic Intermediate Water lies immediately above deep water, includes the temperature and salinity maxima, and has both temperature and salinity decreasing with depth; upper Arctic Intermediate Water lies in between the temperature minimum and the temperature maximum and has both temperature and salinity increasing with depth; and Polar Intermediate Water has to some extent lower salinities than the other two intermediate waters but is largely distinguished by its association with overlying Polar Surface Water.

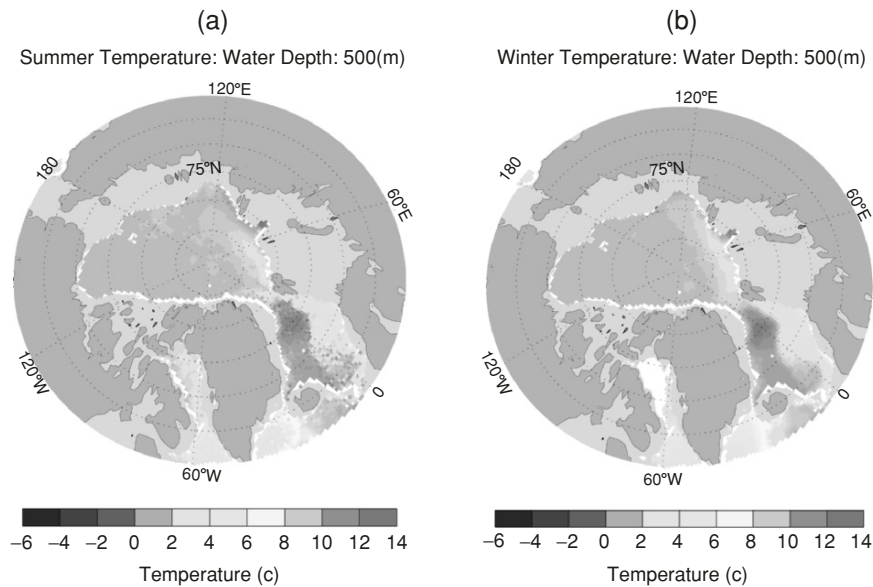


Fig. 14.4. Temperature of the Arctic Mediterranean Seas at 50 m depth from the Joint US-Russian EWG atlas: (a) summer, and (b) winter

Within the Arctic Ocean the surface layer overlies the relatively warm and saline water of Atlantic origin, carried into the Arctic through the Fram Strait by the West Spitzbergen Current. When this water enters the Arctic basin, the initially high temperature and salinity of the water (over 3°C and 35 ppt in the Fram Strait) rapidly decrease as it is cooled by the atmosphere and by mixing with local waters. When the current encounters the ice margin northwest of Spitzbergen, melting further cools and dilutes this water until its T/S properties approximate those of water found within the Atlantic layer throughout the Arctic (Perkin and Lewis 1984; Aagaard et al. 1987).

The ice breeze is generated near the marginal ice zone by the thermal inhomogeneity between the ice and water surfaces. Such a local circulation causes ice drift and in turn impacts on the oceanic motion and thermohaline structure (Chu 1986, 1987a, b, c). The Arctic Intermediate Water was discussed by Swift and Aagaard (1981) and Aagaard et al. (1985), whose core is identifiable over the entire basin at depths between 200 and 800 m by a temperature maximum (Fig. 14.4) and relatively high salinity (Fig. 14.5).

14.2.3 Deep Level (2,000 m Depth)

The lower portion of the water column is occupied by varieties of cold ($<0^{\circ}\text{C}$) deep water. Our basic understanding of the origin of the deep waters has undergone considerable revision in recent years (Aagaard 1982; Swift et al. 1983;

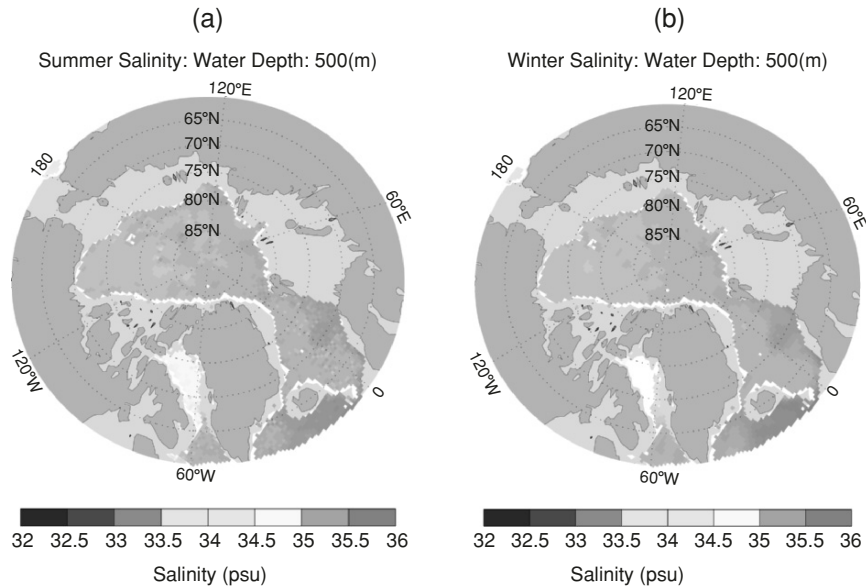


Fig. 14.5. Salinity of the Arctic Mediterranean Seas at 50 m depth from the Joint US-Russian EWG atlas: (a) summer and (b) winter

Aagaard et al. 1985; Rudels 1987; Swift and Koltermann 1988). Four basic varieties, each with distinctive T/S characteristics, are presently recognized. Greenland Sea Deep Water is the coldest (about -1.2°C) and freshest (<34.90 ppt) variety, and Canada Basin Deep Water is the warmest (about -0.5°C) and most saline (>34.95 ppt). In between are the Norwegian Sea Deep Water (-0.9°C , 34.92 ppt) and Eurasian Basin Deep Water (-0.7°C , 34.94 ppt) varieties.

14.3 Inverted Circulation in the Greenland–Iceland–Norwegian Sea

The different water masses encountered in the GIN Sea provide contrasting living conditions for zooplankton. The different faunas originating in the polar and Atlantic oceans are clearly distinguishable in the copepod population. Since the copepods cannot swim very well, their distribution primarily reflects the circulation pattern. From limited current meter observations and ecological measurements, general features of the GIN Sea circulation is presented in Fig. 14.6.

The GIN Sea is an important link between the Arctic Ocean and the North Atlantic, serving as a passageway for Atlantic waters streaming toward the Arctic waters, and Arctic waters passing in the East Greenland Current

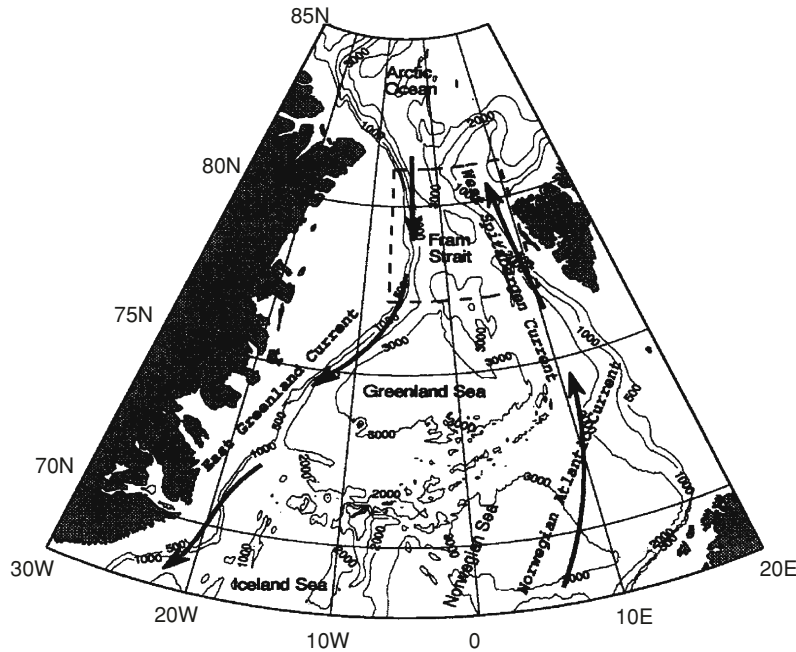


Fig. 14.6. Bathymetry of the GIN Sea and schematic circulation patterns

toward the Atlantic and the Labrador Sea. However, it also has its own important thermodynamic processes (particularly convection) that produce (or modify) deep waters that exit through the deeper parts of the Denmark Strait and the Faroe–Shetland Channel. To understand the role of the GIN Sea, the first step is to establish three-dimensional climatological velocity fields from the joint US-Russian EWG (T, S) data using the P-vector method.

With the (T, S) and corresponding velocity data, it is possible to estimate, through budget studies, the relative importance of the roles of the GIN Sea. In particular, a careful census is made of the different water masses entering and leaving, and their production in the basin due to interior mixing and atmospheric fluxes. The following subsections describe the major current characteristics inverted from the hydrographic data.

The seas north of the Greenland–Scotland Ridge constitute a major heat sink in the global thermohaline circulation of the world ocean and therefore a crucial component of the earth climate (Aagaard et al. 1985). A large heat loss to the atmosphere, combined with sea ice production and melting, is responsible for the formation of deep and intermediate waters through winter convection, which, in some basins like the Greenland Sea, may reach down to the bottom.

The one-dimensional convection process is strongly affected by the horizontal dynamics of the convective basins including lateral exchanges of heat,

salt, and ice at their boundaries. Concerning the Greenland Sea, important exchanges occur through its northern boundary, the Fram Strait, which is the only deep connection between the Arctic Ocean and the rest of the world ocean. A better knowledge of the dynamics of the strait is therefore crucial in the context of investigating the processes involved in the deep convection and their variability.

14.3.1 Circulation Patterns

The inverted subsurface (50 m) velocity field shows the following pattern. Gyres are formed over each of the sub-basins in the GIN Sea (Fig. 14.7). In the northward flowing Norwegian Atlantic Current north of about 66°N commonly two maximum salinity cores are observed (e.g., Dietrich 1969; Hopkins 1991). Hopkins (1991) assumed that this bifurcation is caused by the bathymetric control of the barotropic flow when the current passes the Voring Plateau. The western branch veers northeastward on encountering the Hohn Ridge, converging with the Jan Mayen Current until it rejoins the eastern branch of the Norwegian Atlantic Current and becomes the West Spitzbergen Current. On its way north the temperature and salinity of the Norwegian Atlantic Water decreases mainly as a result of air–sea interaction, not by mixing with the underlying cooler and fresher water (Hopkins 1991).

Upon entering the Arctic basin, the West Spitzbergen Current encounters the southward-moving pack ice carried by the Transpolar Drift. Here, sensible heat carried by the West Spitzbergen Current is used to melt the ice, resulting in a cooled and freshened upper layer (Quadfasel et al. 1987; Untersteiner 1988; Moore and Wallace 1988). This point of encounter is also a zone of maximum density at the surface. Before reaching this point, the surface cooling has increased the density of the surface layer; later, melting begins to decrease the surface density.

The southward flowing East Greenland Current extends to around 2,500 km along the Greenland coast. In addition to transporting surface, intermediate, and deep water, the East Greenland Current exports sea ice from the Arctic, removing between 4,000 and 5,000 km³ of ice each year, an amount approximately equal to the freshwater inflow (Wadhams 1983; Vinje and Finnekasa 1986). There are two branches off the mainstream of the EGC: a relatively minor one at about 77°N , which strikes southeast along the Greenland Fracture Zone, and a larger one called the Jan Mayen Current that branches eastward at about 73°N to form the southern margin of the Greenland Gyre (Fig. 14.7). This pattern is more evident in summer (Fig. 14.7a) than in winter (Fig. 14.7b).

Vertical cross sections of v -velocity (north–south) component along 75° , 70° , and 65°N for summer (Fig. 14.8) and winter (Fig. 14.9) clearly show the existence of the two basic currents with baroclinic characteristics: northward flowing Norwegian Atlantic Current (see 65°N cross section) and becoming the West Spitzbergen Current (see 70° , 75°N cross sections) in the eastern

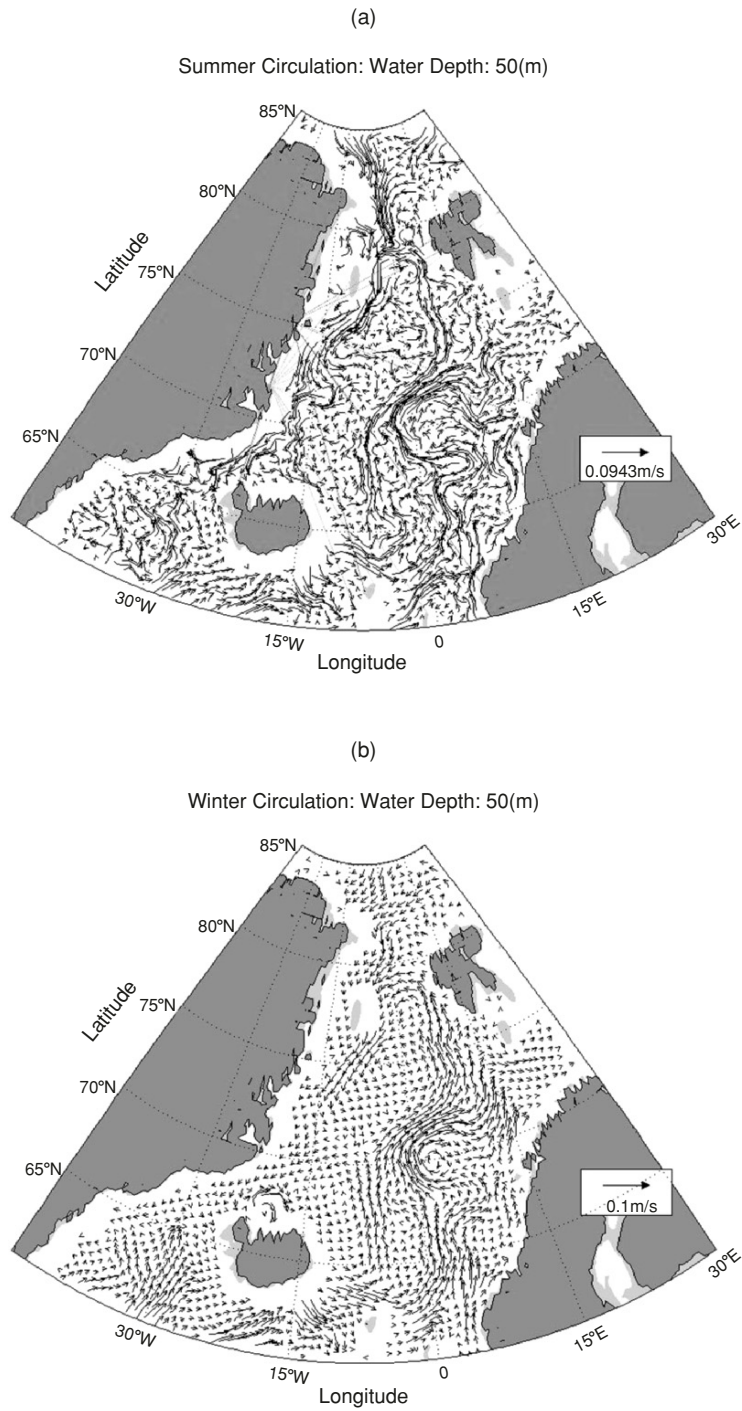


Fig. 14.7. Inverted subsurface (50 m depth) velocity vectors in the GIN Sea: (a) summer and (b) winter

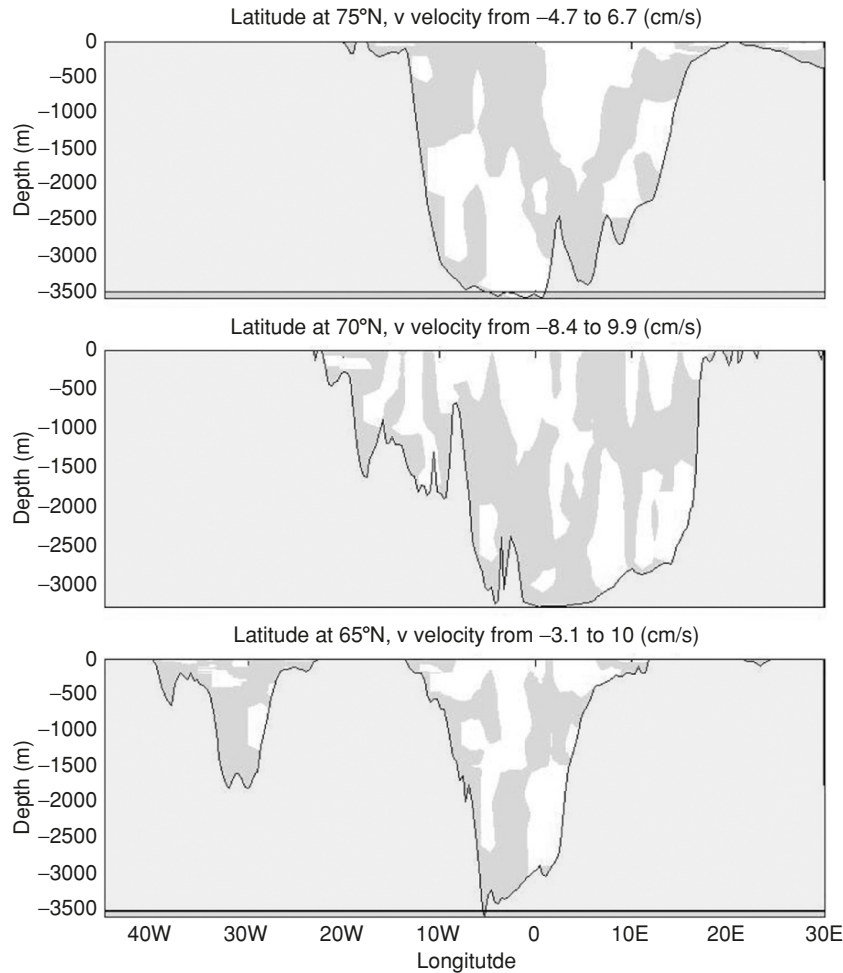


Fig. 14.8. Vertical cross sections of v -component (north–south) in summer along 75, 70, and 65°N. Here, *unshaded* areas refer to positive v (i.e., northward motion) and *shaded* areas refer to negative v (i.e., southward motion). The maximum value of the northward motion is 6.7 cm s^{-1} at 75°N, 9.9 cm s^{-1} at 70°N, and 10 cm s^{-1} at 65°N. The maximum value of the southward motion is 4.7 cm s^{-1} at 75°N, 8.4 cm s^{-1} at 70°N, and 3.1 cm s^{-1} at 65°N

GIN Sea and southward flowing East Greenland Current in the western GIN Sea.

The current systems are stronger in summer than in winter. For example, the maximum speeds of the northward flowing Norwegian Atlantic Current and West Spitzbergen Current vary from (6.7 cm s^{-1} at 75°N, 9.9 cm s^{-1} at 70°N, and 10 cm s^{-1} at 65°N) in summer to (4.8 cm s^{-1} at 75°N, 6.6 cm s^{-1}

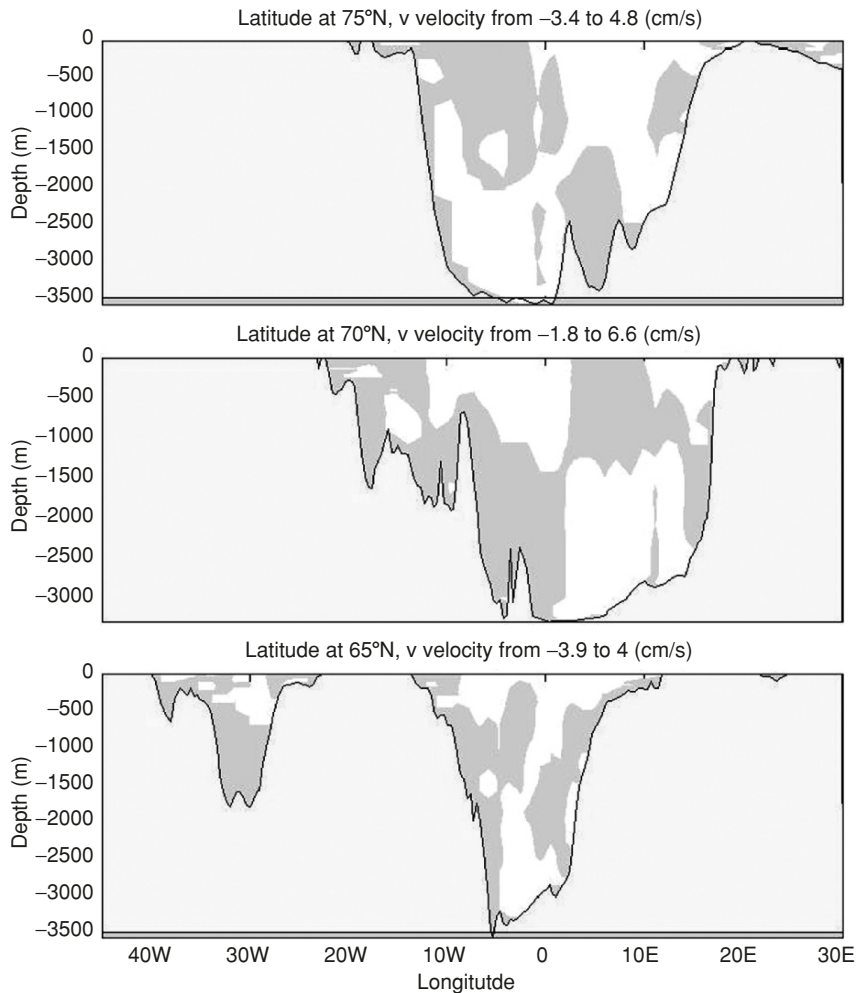


Fig. 14.9. Vertical cross sections of v -component (north–south) in winter along 75, 70, and 65°N. Here, *unshaded* areas refer to positive v (northward motion) and *shaded* areas refer to negative v (southward motion). The maximum value of the northward motion is 4.8 cm s^{-1} at 75°N, 6.6 cm s^{-1} at 70°N, and 4 cm s^{-1} at 65°N. The maximum value of the southward motion is 3.4 cm s^{-1} at 75°N, 1.8 cm s^{-1} at 70°N, and 3.9 cm s^{-1} at 65°N

at 70°N, and 4 cm s^{-1} at 65°N) in winter. The maximum speeds of the southward flowing East Greenland Current vary from (4.7 cm s^{-1} at 75°N, 8.4 cm s^{-1} at 70°N, and 3.1 cm s^{-1} at 65°N) in summer to (3.4 cm s^{-1} at 75°N, 1.8 cm s^{-1} at 70°N, and 3.9 cm s^{-1} at 65°N) in winter. Southward overflow in Denmark Strait is also identified from the vertical cross section of v -velocity along 65°N in summer (Fig. 14.8) and in winter (Fig. 14.9).

14.3.2 Fram Strait Exchange

The detailed flow pattern in the strait, however, is more complex and numerous recirculations with large spatial and temporal variability (Hopkins 1991) make reliable estimates of the transports through the strait more difficult.

Previous estimates of the transports through the Fram Strait based on hydrographic measurements mostly rely on the baroclinic component of the geostrophic currents (e.g., Timofeyev 1962). Direct current measurements are extremely sparse and contaminated by the mesoscale activity (Foldvik et al. 1988). Lagrangian observations can give insight into the circulation (Gascard et al. 1995) but are unable to provide transport estimates. Numerical models, which include the northern Greenland Sea, either have a highly coarse resolution in view of the complex bottom topography of the strait (e.g., Gerdes and Schauer 1997) or, considering a restricted domain, use the Fram Strait as an open boundary so that currents or transports cannot be reasonably predicted in the strait (e.g., Legutki 1991).

The P-vector inverse method combines hydrographic information with relevant constraints and offers an alternative approach. The inverted surface velocity shows the flow pattern through the Fram Strait. Two main currents exchange water between the Arctic and the world ocean (Fig. 14.10). On the eastern side of the strait, the northward West Spitzbergen Current carries relatively warm and salty waters of Atlantic origin above relatively cold and fresh deep waters that is formed in the Greenland and the Norwegian Seas. On the western side, sea ice and cold and fresh surface water are exported from the Arctic Ocean in the East Greenland Current above relatively warm and salty deep waters.

Recirculation of Atlantic water is also detected from the inverted velocity field (Fig. 14.10). Much of it joins the southward-moving East Greenland Current to flow back into the Greenland and Iceland seas. The continuation of the West Spitzbergen Current into the Arctic is also complex, as the current appears to split into two or more branches. This is consistent with earlier studies by Perkin and Lewis (1984), Aagaard et al. (1987), and Quadfasel et al. (1987).

Upon entering the Arctic basin, the West Spitzbergen Current encounters the southward-moving pack ice carried by the Transpolar Drift. Here, sensible heat carried by the West Spitzbergen Current is used to melt the ice, resulting in a cooled and freshened upper layer (Quadfasel et al. 1987; Untersteiner 1988; Moore and Wallace 1988). This point of encounter is also a zone of maximum density at the surface. Prior to reaching this point, surface cooling has increased the density of the surface layer; afterward, melting begins to decrease the surface density.

14.4 Inverted Circulation in the Arctic Ocean

The inverted annual mean surface velocity vector field in the Arctic Ocean shows two major characteristics (Fig. 14.11). The first is the Transpolar Drift,

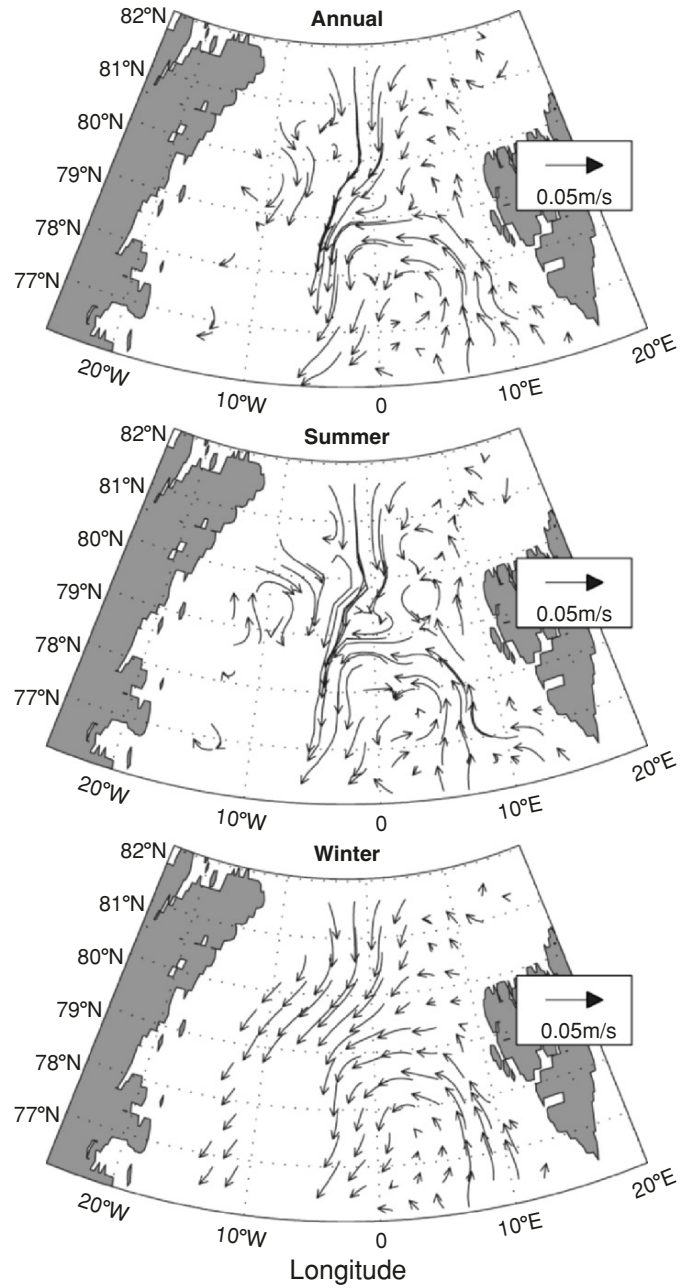


Fig. 14.10. Inverted surface velocity vectors in the Fram Strait from annual mean, summer, and winter EWG (T, S) data. Grid points without inverted velocity shows the necessary conditions for the P-vector method that are not satisfied. The recirculation of Atlantic Water through the West Spitzbergen Current is also identified

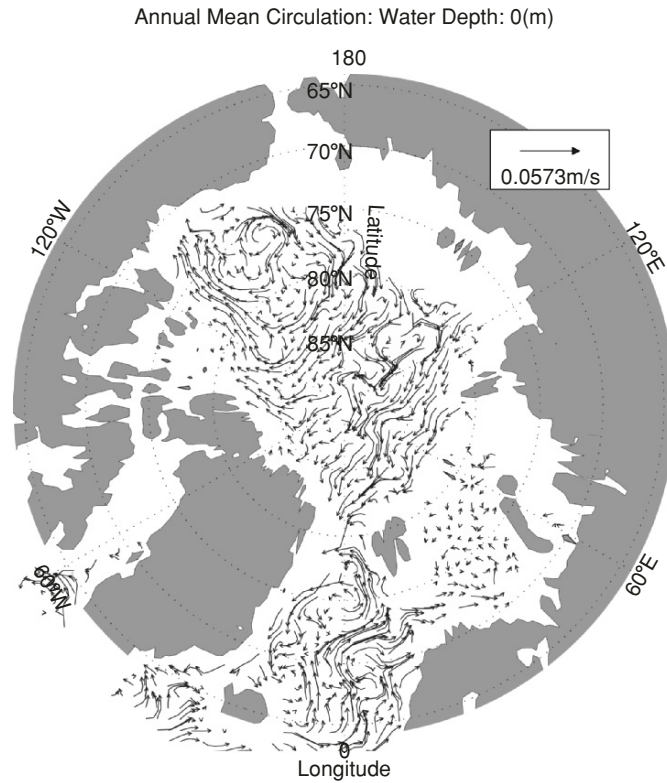


Fig. 14.11. Inverted surface velocity vectors in the Arctic Ocean from annual mean EWG (T, S) data. Grid points without inverted velocity shows the necessary conditions for the P-vector method that are not satisfied. The recirculation of Atlantic Water through the West Spitzbergen Current is also identified

in which the surface waters of Eurasian basin move across the basin toward the North Pole and then toward the Fram Strait; the second is the anticyclonic flow around the Beaufort Gyre in the Canadian basin. These two features are consistent with earlier studies (Coachman and Aagaard 1974; Gorschkov 1983). The maximum current speed is around 5 cm s^{-1} . Mean current speeds are slow in the central ocean, about 2 cm s^{-1} , but increase as water exits the basin as part of the East Greenland Current, which is consistent with Wadhams et al. (1979) as well as Vinje and Finnekasa (1986).

As the West Spitzbergen Current passes through the Fram Strait and subsides, it appears to branch. North of 79°N , where the 200-m and deeper isobaths diverge, the current splits into two main cores. The western or off-shore branch follows the western flank of the Yermak Plateau. North of 80°N a portion of this flow again splits off to contribute to the recirculation within the East Greenland Current. The eastern or in-shore branch of the West Spitzber-

gen Current follows the shelf break around Spitzbergen and into the Arctic Ocean. During its transit it is cooled and freshened by mixing with overlying waters, transforming the original Atlantic water into Arctic intermediate water. The inverted velocity is smaller (Fig. 14.12, 14.13) than the directly measured value by Aagaard (1989), who noted eastward flow that increased with depth to typical speeds of $0.2\text{--}0.3\text{ m s}^{-1}$.

Although the southern Beaufort Sea is generally thought of as an area of westward (clockwise) water and ice motion (Fig. 14.11), the average subsurface motion above the continental slope is in the opposite direction (Fig. 14.13). Aagaard (1984) called this flow the Beaufort Undercurrent. The presence of the undercurrent is indicated by a subsurface maximum in temperature caused by the eastward flow of water originating in the Bering Sea. Aagaard (1984) described the Beaufort Undercurrent as being a topographically steered eastward flow extending seaward of the 50 m isobath out to the base of the continental slope. Speeds are of the order 0.1 m s^{-1} and increase with depth down

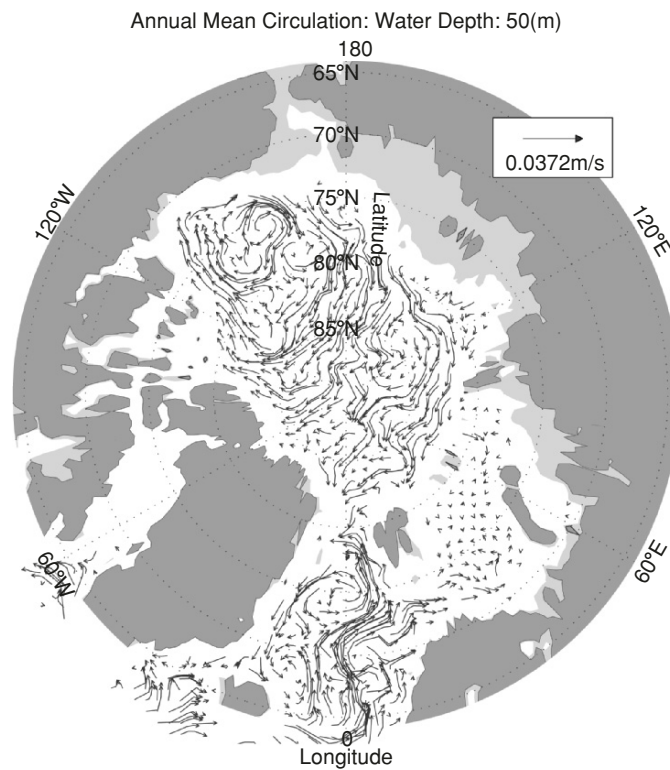


Fig. 14.12. Inverted velocity vectors at 50 m depth in the Arctic Ocean from annual mean EWG (T, S) data. Grid points without inverted velocity shows the necessary conditions for the P-vector method that are not satisfied. The recirculation of Atlantic Water through the West Spitzbergen Current is also identified

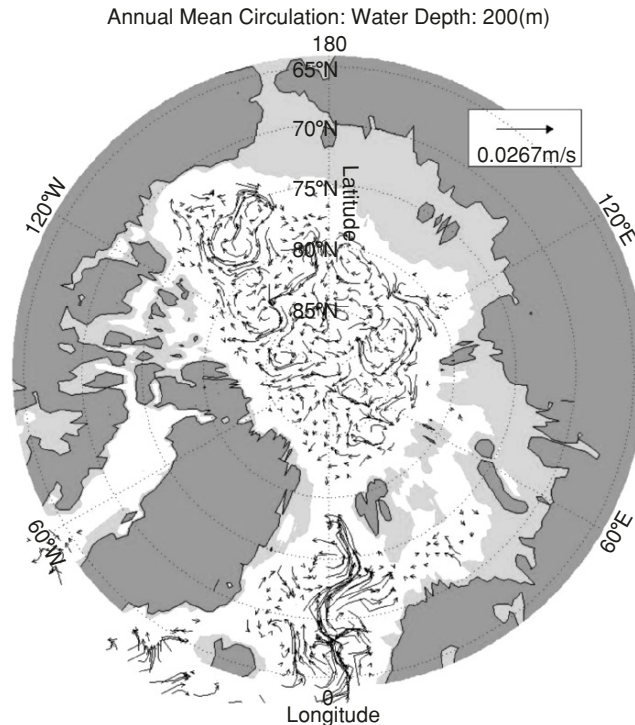


Fig. 14.13. Inverted velocity vectors at 200m depth in the Arctic Ocean from annual mean EWG (T, S) data. Grid points without inverted velocity shows the necessary conditions for the P-vector method that are not satisfied. The recirculation of Atlantic Water through the West Spits Bergen Current is also identified

to about 150 m. Transports are of the order 1 Sv. The current is probably part of the large-scale circulation of the Canada basin and thus not locally driven.

A possible forcing mechanism for undercurrents in the Arctic has been discussed by Holloway (1987). He argues that the interaction of eddies with along-shore variations in topography, together with coastally trapped planetary wave propagation, result in a systematic forcing that acts on the mean flow. Applied to the Arctic, this mechanism predicts an eastward (cyclonic) flow following the basin margins of similar magnitude to the Beaufort Undercurrent.

Questions and Exercises

- (1) Why is the GIN Sea circulation important for the climatic and ecological systems?
- (2) Download the US-Russian EWG and WOA (T, S) data for the Arctic Ocean. Compare the differences between the two datasets.

- (3) The WOA dataset uses the spherical coordinate system. Do you think it is good for the Arctic Ocean? Why?
- (4) What coordinate system does the US-Russian EWG dataset use for the Arctic Ocean?
- (5) What are the major characteristics of the GIN Sea thermohaline structures?
- (6) What are the major features of the northward flowing West Spitzbergen Current and southward flowing East Greenland Current? What are the roles of these currents in global ocean circulation and in turn in the climatic system?
- (7) What are the major features of the Fram Strait recirculation? Discuss its effect on the Arctic circulation.
- (8) What are the major features (including seasonal variation) of the Arctic circulation?
- (9) Select an area with your interest. Download the data of the volume transport stream function, absolute velocity at z -coordinate, and absolute velocity at isopycnal coordinate from the DVD-ROM. Discuss the major characteristics of the circulation in the area including the seasonal variation, causes of these features, and the effect of the circulation on the global system.

Applications to Data Assimilation

Ocean data assimilation is an important component in ocean modeling. For practical application, near-real-time, global ocean data assimilation that provides, regular, complete descriptions of the temperature, salinity and velocity structures of the ocean are important in support of operational oceanography, seasonal-to-decadal climate forecasts and analyses, and oceanographic research. Usually, observational (T, S) data are assimilated into models using various techniques such as nudging, optimal interpolation, variational (VAR) methods (3D VAR, 4D VAR), and Kalman filter. The velocity data are not used due to lack of observations. Since ocean models usually have (T, S, \mathbf{V}) as the dependent variables, assimilation with (T, S) data only may be called unbalanced data assimilation. Ideal approach is to assimilate the (T, S) along with the corresponding balanced \mathbf{V} data. This is called the balanced data assimilation.

In this chapter, a simple assimilation method (nudging) is used as an example showing the weakness of the unbalanced data assimilation and the strength of the balanced data assimilation. With the (T, S) data, the absolute velocity field (\mathbf{V}) can be calculated using the P-vector inverse method and therefore, using (T, S, \mathbf{V}) is the balanced data assimilation.

15.1 Data Nudging

Ocean data assimilation is a procedure that combines observational data from satellite or from ships and buoys (more direct measurements) with information from dynamical models to give the best possible estimate or analysis of the ocean state at a given time. This estimate can be used to initialize climate prediction models or to study ocean phenomena. The forecast skill of climate prediction models is sensitive to their initialization. Ideally, improvements in ocean data assimilation are reflected in improved forecasts.

In ocean data assimilation, observations are combined with information from predictive models in a manner that depends on statistical representations

of the observational and model errors. By including more dynamical information in the model error representation, observations are used primarily to correct large-scale errors.

Nudging is a simple and popular data assimilation scheme. For example, the GFDL/NOAA global data assimilation system uses the Newtonian nudging to assimilate the observational temperature data (Rosati et al. 1996),

$$\frac{\partial T}{\partial t} + \dots = -\gamma_N(T - T_{\text{obs}})\mathbb{S}, \quad (15.1)$$

where γ_N is the Newtonian damping coefficient and T_{obs} is the observed temperature. The nudging term [in right-hand of (17.1)] is to force T toward T_{obs} . For sufficiently long time period,

$$\lim_{t \rightarrow \infty} (T) = T_{\text{obs}}. \quad (15.2)$$

Burgers et al. (2002) used a shallow water model with data nudging to investigate the difference between balanced and unbalanced data assimilation for seasonal forecast of equatorial oceans. They found that the unbalanced data assimilation (updating the density field only) leads to distortion of the zonal velocity field around the equator.

15.2 Linear Shallow Water Model

Similar to Burgers (2002), a shallow-water model is used to illustrate the weakness of the unbalanced data assimilation. A linearized shallow water model on an f -plane is given by

$$\frac{\partial u}{\partial t} - f_0 v + \frac{\partial \Phi}{\partial x} = 0, \quad (15.3)$$

$$\frac{\partial v}{\partial t} + f_0 u + \frac{\partial \Phi}{\partial y} = 0, \quad (15.4)$$

$$\frac{\partial \Phi}{\partial t} + \bar{\Phi} \left(\frac{\partial u}{\partial x} + \frac{\partial v}{\partial y} \right) = 0, \quad (15.5)$$

where the Coriolis parameter is taken as a constant f_0 (the midlatitude f -plane assumption); $\bar{\Phi} = g\bar{h}$ and $\Phi = gh'$ is the deviation from $\bar{\Phi}$; and $h = \bar{h} + h'$ is the height of the free surface. Using Helmholtz's theorem, the velocity can be represented by a stream function ψ and a velocity potential (χ),

$$u = -\frac{\partial \psi}{\partial y} + \frac{\partial \chi}{\partial x}, \quad v = -\frac{\partial \psi}{\partial x} + \frac{\partial \chi}{\partial y}. \quad (15.6)$$

Because of the f -plane assumption, the Coriolis parameter passes through any differentiation. Thus, differentiating (15.3) with respect to y and (15.4) with respect to x and subtracting the first equation from the second equation yields the vorticity equation,

$$\frac{\partial}{\partial t} \nabla_h^2 \psi + f_0 \nabla_h^2 \chi = 0. \quad (15.7)$$

Differentiating (15.3) with respect to x and (15.4) with respect to y and adding the two equations yields the divergence equation,

$$\frac{\partial}{\partial t} \nabla_h^2 \chi - f_0 \nabla_h^2 \psi + \nabla_h^2 \Phi = 0. \quad (15.8)$$

Substituting (15.6) in (15.5) yields

$$\frac{\partial \Phi}{\partial t} + \bar{\Phi} \nabla_h^2 \chi = 0. \quad (15.9)$$

Consider a periodic domain with dimensions $2\pi a$ in each of the x and y directions. The solutions (ψ, χ, Φ) have the form,

$$\begin{bmatrix} \psi(x, y, t) \\ \chi(x, y, t) \\ \Phi(x, y, t) \end{bmatrix} = \sum_n \sum_m \begin{bmatrix} \hat{\psi}^{mn}(t) \\ i\hat{\chi}^{mn}(t) \\ f_0 \sqrt{K} \hat{\Phi}^{mn}(t) \end{bmatrix} \exp \left[\frac{i(mx + ny)}{a} \right], \quad (15.10)$$

where

$$K = \frac{(m^2 + n^2) \bar{\Phi}}{a^2 f_0^2}. \quad (15.11)$$

Substituting (15.10) in (15.7)–(15.9) yields

$$\frac{d\hat{\psi}^{mn}}{dt} + i f_0 \hat{\chi}^{mn} = 0, \quad (15.12)$$

$$i \frac{d\hat{\chi}^{mn}}{dt} - f_0 \hat{\psi}^{mn} + f_0 \sqrt{K} \hat{\Phi}^{mn} = 0, \quad (15.13)$$

$$\frac{d\hat{\Phi}^{mn}}{dt} - i f_0 \sqrt{K} \hat{\chi}^{mn} = 0. \quad (15.14)$$

The solutions of (15.12)–(15.14) are given by

$$\begin{bmatrix} \hat{\psi}(t) \\ \hat{\chi}(t) \\ \hat{\Phi}(t) \end{bmatrix} = \begin{bmatrix} A_\psi^{mn} \\ A_\chi^{mn} \\ A_\Phi^{mn} \end{bmatrix} \exp(-i f_0 \sigma t), \quad (15.15)$$

where $(A_\psi^{mn}, A_\chi^{mn}, A_\Phi^{mn})$ are the amplitudes for component (m, n) , σ satisfies the following algebraic equation,

$$\sigma^3 - \sigma(K + 1) = 0, \quad (15.16)$$

which has three roots

$$\sigma^{(1)} = 0, \quad \sigma^{(2)} = \sqrt{K+1}, \quad \sigma^{(3)} = -\sqrt{K+1}. \quad (15.17)$$

The three roots represent two dynamical modes: $\sigma^{(1)}$ for the geostrophic mode (or the Rossby mode), and $(\sigma^{(2)}, \sigma^{(3)})$ for the inertial-gravity mode. For each mode, the linear shallow water model has the solutions,

$$\begin{bmatrix} \psi(x, y, t) \\ \chi(x, y, t) \\ \Phi(x, y, t) \end{bmatrix} = \sum_n \sum_m \begin{bmatrix} A_\psi^{mn} \\ iA_\chi^{mn} \\ f_0\sqrt{K}A_\Phi^{mn} \end{bmatrix} \exp\left[\frac{i(mx+ny)}{a}\right] \exp[-if_0\sigma(t-t_0)], \quad (15.18)$$

with the initial conditions (without data assimilation),

$$\begin{bmatrix} \psi(x, y, t_0) \\ \chi(x, y, t_0) \\ \Phi(x, y, t_0) \end{bmatrix} = \sum_n \sum_m \begin{bmatrix} A_\psi^{mn} \\ iA_\chi^{mn} \\ f_0\sqrt{K}A_\Phi^{mn} \end{bmatrix} \exp\left[\frac{i(mx+ny)}{a}\right]. \quad (15.19)$$

When Newtonian nudging (15.1) is used to assimilate the observational data, (15.7)–(15.9) are changed into

$$\frac{\partial}{\partial t} \nabla_h^2 \tilde{\psi} + f_0 \nabla_h^2 \tilde{\chi} = -\gamma_N \nabla_h^2 (\tilde{\psi} - \psi_{\text{obs}}), \quad (15.20)$$

$$\frac{\partial}{\partial t} \nabla_h^2 \tilde{\chi} - f_0 \nabla_h^2 \tilde{\psi} + \nabla_h^2 \tilde{\Phi} = -\gamma_N \nabla_h^2 (\tilde{\chi} - \chi_{\text{obs}}), \quad (15.21)$$

$$\frac{\partial \tilde{\Phi}}{\partial t} + \tilde{\Phi} \nabla_h^2 \tilde{\chi} = -\gamma_N (\tilde{\Phi} - \Phi_{\text{obs}}). \quad (15.22)$$

The ocean model is integrated between the two consecutive time instances, say from $t = t_0$ to $t = t_1$, the observational data $(\Phi_{\text{obs}}, \psi_{\text{obs}}, \chi_{\text{obs}})$ are treated as time-independent during that period ($t_0 < t < t_1$). Equations (15.20)–(15.22) constitute a set of coupled linear partial differential equations with time-independent forcing terms: $\gamma_N \nabla_h^2 \psi_{\text{obs}}$, $\gamma_N \nabla_h^2 \chi_{\text{obs}}$, $\gamma_N \Phi_{\text{obs}}$.

15.3 Balanced Data Assimilation

The balanced data assimilation is to use the observational data $(\Phi_{\text{obs}}, \psi_{\text{obs}}, \chi_{\text{obs}})$ which are in geostrophic balance,

$$f_0 \psi_{\text{obs}} = \Phi_{\text{obs}}, \quad (15.23)$$

$$\nabla_h^2 \chi_{\text{obs}} = 0. \quad (15.24)$$

Equations (15.20)–(15.22) can be transformed into homogeneous equations,

$$\frac{\partial}{\partial t} \nabla_h^2 \psi + f_0 \nabla_h^2 \chi + \gamma_N \nabla_h^2 \psi = 0, \quad (15.25)$$

$$\frac{\partial}{\partial t} \nabla_h^2 \chi - f_0 \nabla_h^2 \psi + \nabla_h^2 \Phi + \gamma_N \nabla_h^2 \chi = 0, \quad (15.26)$$

$$\frac{\partial \Phi}{\partial t} + \bar{\Phi} \nabla_h^2 \chi + \gamma_N \Phi = 0, \quad (15.27)$$

where

$$\begin{aligned} \tilde{\psi}(x, y, t) &= \psi(x, y, t) + \psi_{\text{obs}}(x, y, t), \\ \tilde{\chi}(x, y, t) &= \chi(x, y, t) + \chi_{\text{obs}}(x, y, t), \\ \tilde{\Phi}(x, y, t) &= \Phi(x, y, t) + \Phi_{\text{obs}}(x, y, t). \end{aligned} \quad (15.28)$$

The solutions of homogeneous linear equations (15.25)–(15.27) are given by

$$\begin{bmatrix} \psi(x, y, t) \\ \chi(x, y, t) \\ \Phi(x, y, t) \end{bmatrix} = \sum_n \sum_m \begin{bmatrix} A_\psi^{mn} \\ iA_\chi^{mn} \\ f_0 \sqrt{K} A_\Phi^{mn} \end{bmatrix} \exp \left[\frac{i(mx + ny)}{a} \right] \exp[-if_0 \hat{\sigma}(t - t_0)], \quad (15.29)$$

where $(\pi A_\psi^{mn}, A_\chi^{mn}, A_\Phi^{mn})$ are the initial ($t = t_0$) amplitudes for the component (m, n) and $\hat{\sigma}$ satisfies the algebraic equation,

$$\left(\hat{\sigma} + \frac{i\gamma_N}{f_0} \right)^3 - \left(\hat{\sigma} + \frac{i\gamma_N}{f_0} \right) (K + 1) = 0, \quad (15.30)$$

where

$$\hat{\sigma} = -\frac{i\gamma_N}{f_0} + \sigma. \quad (15.31)$$

The solutions of (15.20)–(15.22) are given by

$$\begin{bmatrix} \tilde{\psi}(x, y, t) \\ \tilde{\chi}(x, y, t) \\ \tilde{\Phi}(x, y, t) \end{bmatrix} = \begin{bmatrix} \psi_{\text{obs}}(x, y, t) \\ \chi_{\text{obs}}(x, y, t) \\ \Phi_{\text{obs}}(x, y, t) \end{bmatrix} + \sum_n \sum_m \begin{bmatrix} A_\psi^{mn} \\ iA_\chi^{mn} \\ f_0 \sqrt{K} A_\Phi^{mn} \end{bmatrix} \exp \left[\frac{i(mx + ny)}{a} \right] \exp[-if_0 \sigma(t - t_0)] \exp(-\gamma_N t). \quad (15.32)$$

Since σ has three real values $(0, \sqrt{K+1}, -\sqrt{K+1})$ [see (15.17)], the first term in the right-hand side of (15.32) tends to 0 as $t \rightarrow \infty$. This means that the solutions are nudging to the observational values [second term in the right-hand side of (15.32)] as $t \rightarrow \infty$,

$$\begin{bmatrix} \tilde{\psi}(x, y, t) \\ \tilde{\chi}(x, y, t) \\ \tilde{\Phi}(x, y, t) \end{bmatrix} \rightarrow \begin{bmatrix} \psi_{\text{obs}}(x, y, t) \\ \chi_{\text{obs}}(x, y, t) \\ \Phi_{\text{obs}}(x, y, t) \end{bmatrix}, \quad (15.33)$$

which satisfies the nudging condition (15.2). If we continue to integrate the model, there are no spurious solutions to be generated since the observational data are geostrophically balanced.

15.4 Unbalanced Data Assimilation

The unbalanced data assimilation is to use the observational data $(\Phi_{\text{obs}}, \psi_{\text{obs}}, \chi_{\text{obs}})$ which are not in geostrophic balance. For example, ocean data assimilation is usually using (T, S) , but not (u, v) data. For the shallow water model, it is equivalent to assimilate Φ_{obs} , but not $(\psi_{\text{obs}}, \chi_{\text{obs}})$. The shallow water equations with the Newtonian nudging are given by

$$\frac{\partial}{\partial t} \nabla_h^2 \tilde{\psi} + f_0 \nabla_h^2 \tilde{\chi} = 0, \quad (15.34)$$

$$\frac{\partial}{\partial t} \nabla_h^2 \tilde{\chi} - f_0 \nabla_h^2 \tilde{\psi} + \nabla_h^2 \tilde{\Phi} = 0, \quad (15.35)$$

$$\frac{\partial \tilde{\Phi}}{\partial t} + \tilde{\Phi} \nabla_h^2 \tilde{\chi} = -\gamma_N (\tilde{\Phi} - \Phi_{\text{obs}}). \quad (15.36)$$

Since the variable $\tilde{\Phi}$ occurs in (15.30) and (15.31), it is hard to transform (15.29)–(15.31) into homogeneous equations directly [unlike (15.20–15.22)]. The dependent variables are decomposed into Fourier components

$$\begin{bmatrix} \tilde{\psi}(x, y, t) \\ \tilde{\chi}(x, y, t) \\ \tilde{\Phi}(x, y, t) \end{bmatrix} = \sum_n \sum_m \begin{bmatrix} \hat{\psi}^{mn}(t) \\ i\hat{\chi}^{mn}(t) \\ f_0 \sqrt{K} \hat{\Phi}^{mn}(t) \end{bmatrix} \exp \left[\frac{i(mx + ny)}{a} \right]. \quad (15.37)$$

Substituting (15.37) in (15.34)–(15.36) yields

$$\frac{d}{dt} \begin{bmatrix} \hat{\psi}^{mn} \\ \hat{\chi}^{mn} \\ \hat{\Phi}^{mn} \end{bmatrix} = \begin{bmatrix} 0 & -if_0 & 0 \\ -if_0 & 0 & if_0 \sqrt{K} \\ 0 & if_0 \sqrt{K} & -\gamma_N \end{bmatrix} \begin{bmatrix} \hat{\psi}^{mn} \\ \hat{\chi}^{mn} \\ \hat{\Phi}^{mn} \end{bmatrix} + \begin{bmatrix} 0 \\ 0 \\ \gamma_N \Phi_{\text{obs}}^{mn}(t) \end{bmatrix}, \quad (15.38)$$

which can be written in the matrix form,

$$\frac{d\mathbf{X}}{dt} = \mathbf{A}\mathbf{X} + \mathbf{F}, \quad (15.39)$$

with

$$\mathbf{X}(t) = \begin{bmatrix} \hat{\psi}^{mn}(t) \\ \hat{\chi}^{mn}(t) \\ \hat{\Phi}^{mn}(t) \end{bmatrix}, \quad \mathbf{A} = \begin{bmatrix} 0 & -if_0 & 0 \\ -if_0 & 0 & if_0\sqrt{K} \\ 0 & if_0\sqrt{K} & -\gamma_N \end{bmatrix}, \quad \mathbf{F}(t) = \begin{bmatrix} 0 \\ 0 \\ \gamma_N\Phi_{\text{obs}}^{mn}(t) \end{bmatrix}. \quad (15.40)$$

Integrating (15.39) from t_0 to t gives

$$\mathbf{X}(t) = \mathbf{T}(t, t_0)\mathbf{X}(t_0) + \int_{t_0}^t \mathbf{T}(t, s)\mathbf{F}(s)ds, \quad (15.41)$$

where

$$\frac{d}{dt}\mathbf{T}(t, s) = \mathbf{A}\mathbf{T}(t, s), \quad (15.42)$$

and $\mathbf{T}(T, S)$ is the transition matrix. Since the solution $\mathbf{X}(t)$ depends on \mathbf{F} not only at time instance t but during the time period $[t_0, t]$, the solutions of (15.34)–(15.36) are not likely nudging to the observational data at certain time instance. Therefore, unbalanced data assimilation should be avoided. Weakness of unbalanced data assimilation needs further investigation theoretically and numerically.

MODAS is the US Navy's ocean operational system to assimilate a wide range of ocean observations into twice daily global three-dimensional (T, S) fields with various horizontal resolutions (see Sect. 3.2.1). MODAS (T, S) fields are regarded as pseudo-“observational” data set and used for ocean model assimilation and acoustic calculation.

If only the MODAS (T, S) data are assimilated into ocean models, it is the unbalanced data assimilation. To avoid this, three-dimensional absolute velocity field (\mathbf{V}) should be calculated from the MODAS gridded (T, S) fields using the P-vector inverse method.

Questions and Exercises

- (1) Discuss the major differences between balanced and unbalanced data assimilations.
- (2) Mathematical difference between balanced and unbalanced data assimilations is in the eigenvalue equation. The eigenvalue equation for the balanced data assimilation is written by

$$\left(\hat{\sigma} + \frac{i\gamma_N}{f_0}\right)^3 - \left(\hat{\sigma} + \frac{i\gamma_N}{f_0}\right)(K + 1) = 0, \quad (\text{E15.1})$$

which is similar to the dynamical system without data assimilation,

$$\sigma^3 - \sigma(K + 1) = 0. \quad (\text{E15.2})$$

The eigenvalue equation for the unbalanced data assimilation does not have such a form. Why the balanced data assimilation will provide more realistic solutions?

- (3) Select a region and a numerical ocean model of your interest. The monthly WOA (T, S) data are used. The corresponding absolute velocity (\mathbf{V}) data are downloaded from the enclosed DVD-ROM. The balanced data assimilation is to use (T, S, \mathbf{V}) data. The unbalanced data assimilation is to use (T, S) data. Run the numerical model with the two types of data assimilation for several years. Analyze the difference between the two model runs, and discuss the results.

Applications in Numerical Modeling and Simulation

Chu et al. (1999a, b) investigates two kinds of predictability in the Lorenz system: uncertain initial condition (first kind) and uncertain external forcing (second kind). Similarly, the first kind ocean model predictability is due to uncertain initial condition, and the second kind ocean model predictability is due to uncertain lateral boundary condition and atmospheric forcing. Since the P-vector inverse method computes absolute velocity from (T, S) data, it can be used to overcome difficulties such as uncertain initial velocity field and open boundary condition. Besides, it can also be incorporated with (T, S) data assimilation system such as MODAS to establish a quick ocean environmental assessment system.

16.1 Velocity Initialization

Ocean modeling aims to integrate hydrodynamic and thermodynamic equations numerically with boundary conditions (lateral and vertical) from initial states of temperature (T), salinity (S), and velocity. Initial T, S fields are relatively easy to obtain, such as using climatological such as (WOA, GDEM) or synoptic data set such as MODAS (T_c, S_c). However, the initial velocity field is usually not available due to insufficient number of velocity observations. Thus, initialization of the velocity field becomes an important procedure for ocean modeling.

Diagnostic initialization is widely used. It integrates the model from known temperature (T_c) and salinity (S_c) and zero velocity fields while holding (T_c, S_c) unchanged. After a period (around 30 days) of the diagnostic run, the velocity field (\mathbf{V}_c) is established, and (T_c, S_c, \mathbf{V}_c) fields are then treated as the initial conditions for the prognostic numerical modeling. Chu and Wang (2003) show that during the diagnostic initialization period, the heat and salt “source/sink” terms are generated at each time step, and therefore it is not suitable for ocean modeling.

16.1.1 Initial Condition for Velocity in Ocean Models

Let (\mathbf{V}_h, w) be the horizontal and vertical velocity components, and ∇ the horizontal gradient operator. Ocean numerical models are based on the momentum equation

$$\frac{\partial \mathbf{V}_h}{\partial t} = -\mathbf{V}_h \cdot \nabla \mathbf{V}_h - w \frac{\partial \mathbf{V}_h}{\partial z} - \mathbf{k} \times f \mathbf{V}_h - \frac{1}{\rho} \nabla p + \frac{\partial}{\partial z} \left(K_M \frac{\partial \mathbf{V}_h}{\partial z} \right) + \mathbf{H}_V, \quad (16.1a)$$

and the temperature and salinity equations,

$$\frac{\partial T}{\partial t} = -\mathbf{V}_h \cdot \nabla T - w \frac{\partial T}{\partial z} + \frac{\partial}{\partial z} \left(K_H \frac{\partial T}{\partial z} \right) + H_T, \quad (16.1b)$$

$$\frac{\partial S}{\partial t} = -\mathbf{V}_h \cdot \nabla S - w \frac{\partial S}{\partial z} + \frac{\partial}{\partial z} \left(K_H \frac{\partial S}{\partial z} \right) + H_S, \quad (16.1c)$$

where (K_M, K_H) are the vertical eddy diffusivity for turbulent mixing of momentum, temperature, and salinity. The terms (\mathbf{H}_V, H_T, H_S) represent the subgrid processes causing the local time rate of change in (\mathbf{V}_h, T, S) .

In ocean modeling practice, climatological (T_c, S_c) data are usually taken as the initial (T, S) conditions. The climatological data may represent long term equilibrium state,

$$\frac{\partial T_c}{\partial t} \approx 0, \quad \frac{\partial S_c}{\partial t} \approx 0.$$

The vertical and horizontal diffusions are also small for the (T_c, S_c) fields. Thus, we have

$$\mathbf{V}_h \cdot \nabla T_c + w \frac{\partial T_c}{\partial z} = 0, \quad \mathbf{V}_h \cdot \nabla S_c + w \frac{\partial S_c}{\partial z} = 0, \quad (16.2)$$

which leads to

$$\mathbf{V} \cdot \nabla \rho = 0, \quad (16.3)$$

where $\mathbf{V} \equiv (\mathbf{V}_h, w)$ is the three-dimensional absolute velocity.

The inverted absolute velocity using the P-vector method has the property described by (16.3). This implies that when the absolute velocity calculated using the P-vector method $(\mathbf{V}^{(P)})$ is taken as the initial condition along with (T_c, S_c) , the heat and salt (16.1b, c) are generally satisfied at $t = 0$.

16.1.2 Weakness of the Diagnostic Initialization

The widely used model initialization is the diagnostic mode, which integrates the model from known T, S data such as climatological (T_c, S_c) and zero velocity fields, while holding (T_c, S_c) unchanged. After a period (about 30 days) of the diagnostic run, the velocity field (\mathbf{V}_c, w_c) is established, and

$(T_c, S_c, \mathbf{V}_c, w_c)$ fields are treated as the initial conditions for numerical prognostic modeling. Since initial condition error drastically affects model predictability (Lorenz 1963; Chu 1999a, b), questions arise: Does the diagnostic mode provide ideal initialization? What is the physical process associated with the diagnostic run? Chu and Lan (2003) found extra large nonphysical source/sink terms generated using the diagnostic initialization.

The diagnostic initialization procedure integrates (16.1a, b, c) from

$$T = T_c, \quad S = S_c, \quad \mathbf{V} = 0, \quad \text{at } t = 0, \quad (16.4)$$

with T and S unchanged. This procedure is analogous to the process of adding heat and salt source/sink terms (F_T, F_S) in (16.2) and (16.3)

$$\frac{\partial T}{\partial t} = -\mathbf{V} \cdot \nabla T - w \frac{\partial T}{\partial z} + \frac{\partial}{\partial z} \left(K_H \frac{\partial T}{\partial z} \right) + H_T + F_T, \quad (16.5)$$

$$\frac{\partial S}{\partial t} = -\mathbf{V} \cdot \nabla S - w \frac{\partial S}{\partial z} + \frac{\partial}{\partial z} \left(K_H \frac{\partial S}{\partial z} \right) + H_S + F_S, \quad (16.6)$$

to keep

$$\frac{\partial T}{\partial t} = 0, \quad \frac{\partial S}{\partial t} = 0, \quad (16.7)$$

at the each time step (diagnostic initialization). Comparison of (16.7) with (16.5) and (16.6) yields

$$F_T \equiv \mathbf{V} \cdot \nabla T + w \frac{\partial T}{\partial z} - \frac{\partial}{\partial z} \left(K_H \frac{\partial T}{\partial z} \right) - H_T, \quad (16.8)$$

$$F_S \equiv \mathbf{V} \cdot \nabla S + w \frac{\partial S}{\partial z} - \frac{\partial}{\partial z} \left(K_H \frac{\partial S}{\partial z} \right) - H_S. \quad (16.9)$$

Usually, $F_T \neq 0, F_S \neq 0$, thus, the heat and salt “source/sink” terms are generated during the diagnostic initialization at each time step.

16.1.3 Measures of “Source/Sink” Strength

Most diagnostic initialization uses the climatologically monthly (or annual) mean data as the initial T, S conditions. The maximum variability of T, S is estimated by 35°C and 35 ppt. Thus, maximum time rates of absolute change of the monthly mean T, S data (usually taken as initial conditions) are estimated by

$$\left| \frac{\partial T}{\partial t} \right| \leq 35^\circ\text{C year}^{-1} \simeq 0.1^\circ\text{C day}^{-1}, \quad \left| \frac{\partial S}{\partial t} \right| \leq 35 \text{ ppt year}^{-1} \simeq 0.1 \text{ ppt day}^{-1}. \quad (16.10)$$

These values may represent standard measures for “sources/sinks”. Twenty-four times of the standard measures

$$\left| \frac{\partial T}{\partial t} \right|_{\text{Strong}} \simeq 0.1^\circ\text{C h}^{-1}, \quad \left| \frac{\partial S}{\partial t} \right|_{\text{Strong}} \simeq 0.1 \text{ ppt h}^{-1}, \quad (16.11)$$

represent strong “sources/sinks”. Ten times of the strong “sources/sinks” $|\partial T/\partial t|_{\text{Strong}}$ and $|\partial S/\partial t|_{\text{Strong}}$,

$$\left| \frac{\partial T}{\partial t} \right|_{\text{Extra Strong}} \simeq 1^\circ\text{C h}^{-1}, \quad \left| \frac{\partial S}{\partial t} \right|_{\text{Extra Strong}} \simeq 1 \text{ ppt h}^{-1}, \quad (16.12)$$

represent extremely strong “sources/sinks”.

Question arises: how large are these source/sink terms after the initialization? Are the false “sources/sinks” bearable for numerical modeling? The Princeton Ocean Model (POM) implemented for the Japan Sea is used to evaluate the magnitude of the source/sink terms after the diagnostic initialization.

16.1.4 POM for the Japan/East Sea

The POM for the Japan/East Sea is used to illustrate the generation of numerically generated (nonphysical) extremely strong thermohaline source/sink terms. Information about the Japan Sea geography and oceanography can be found in Sect. 6.5.1. The smoothed bathymetry is shown in Fig. 16.1.

The Japan/East Sea model contains 94×100 horizontally fixed grid points with horizontal spacing of $10'$ latitude and longitude (approximately 11.54–15.18 km in the zonal direction and 18.53 km in the latitudinal direction) and 15 vertical nonuniform sigma coordinate levels. The model domain is from 35.0 to 52°N , and from 127.0 to 142.5°E . The bottom topography is obtained from the smoothed Naval Oceanographic Office Digital Bathymetry Data Base 5 min resolution. The horizontal diffusivities are modeled using the Smagorinsky form with the coefficient chosen to be 0.2 for this application. No atmospheric forcing is applied to the model. Closed lateral boundaries, i.e., the modeled ocean bordered by land, were defined using a free-slip condition for velocity and a zero gradient condition for temperature and salinity. No advective or diffusive heat, salt or velocity fluxes occur through these boundaries. At open boundaries, we use the radiative boundary condition with zero volume transport.

For computational efficiency, the mode splitting technique (Blumberg and Mellor 1987) is applied with a barotropic time step of 24 s, based on the Courant-Friederichs-Levy (CFL) computational stability condition and the external wave speed; and a baroclinic time step of 720 s, based on the CFL condition and the internal wave speed.

The annual mean GDEM T , S data are used for the study. Here, the fields at the surface and 150 m depth are presented. The depth of 150 m corresponds

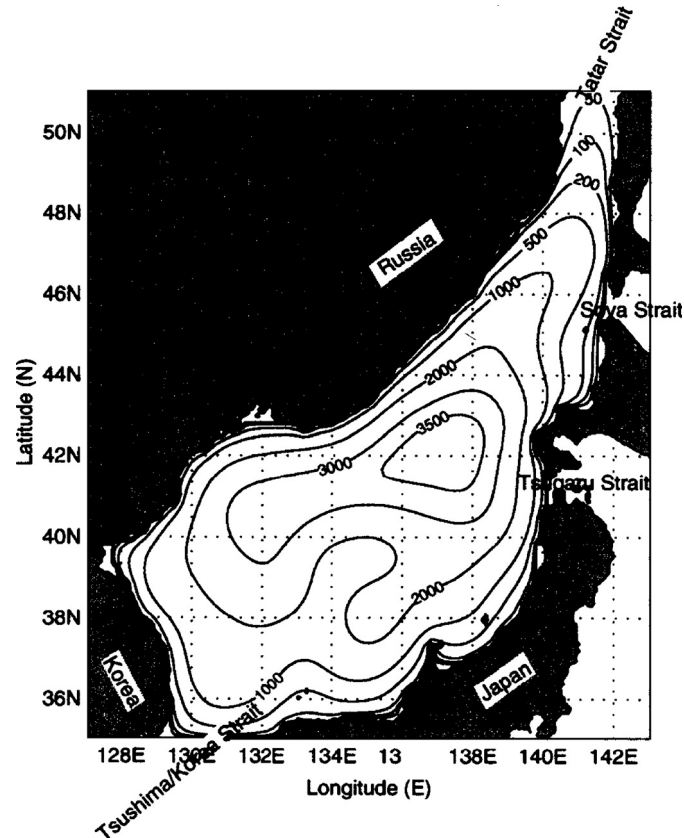


Fig. 16.1. Geography and isobaths showing the bottom topography of the Japan/East Sea model (from Chu and Wang 2003, *Geophysical Research Letters*)

to the permanent thermocline and the middle level of the Japan Sea Intermediate Water. Below the depth of 150 m, the water mass is quite uniform. Nonuniform heat/salt source and sink terms might cause abrupt thermohaline change.

The climatological mean temperature field at two depths (0, 150 m) clearly shows the existence of the Subpolar Front with the position around 38°N in the west and near 42°N in the east (Fig. 16.2a, b). The temperature is more than 6°C higher south of Subpolar Front than north of Subpolar Front at 0 and 150 m. The climatological mean salinity field at the surface (Fig. 16.2a) clearly shows that the saline Kuroshio water (>34.2 ppt) enters the Japan Sea from the Tsushima/Korean Strait into the Japan Sea and forms two permanent salty centers with the salinity higher than 34.0 ppt, located north of Subpolar Front (west of the Hokkaido Island) and south of Subpolar Front at 37–40°N, 132–136°E. Around the southern salty center, there are several fresh centers with the minimum salinity less than 33.9 ppt. The climatological

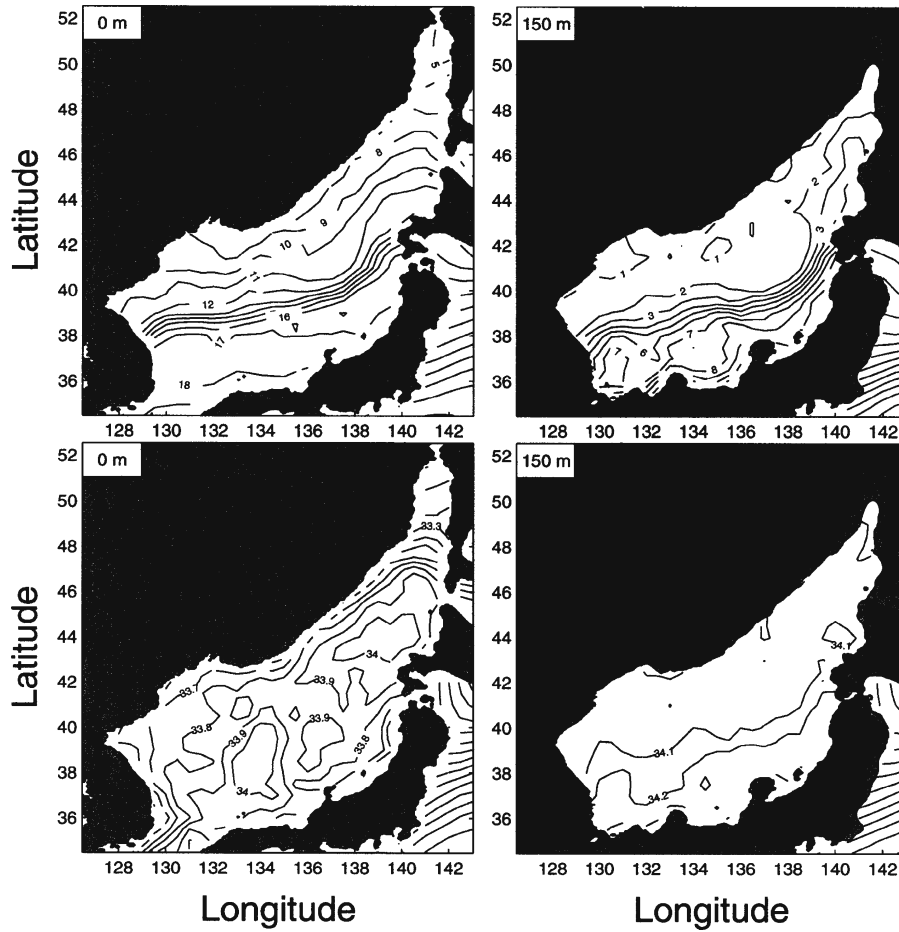


Fig. 16.2. GDEM annual mean (a) temperature and (b) salinity at various depths (from Chu and Wang 2003, *Geophysical Research Letters*)

mean salinity field at 150 m depth (Fig. 16.2b) clearly shows that the isohaline of 34.1 is collocated with the Subpolar Front (Fig. 16.2b) with the salinity above (below) 34.1 in the south (north) of the Subpolar Front. Salinity is more uniform north of than south of the Subpolar Front.

The POM was integrated in the diagnostic mode with all three components of velocity (u, v, w) initially set to zero, and with temperature and salinity specified by interpolating GDEM annual mean data to each model grid point.

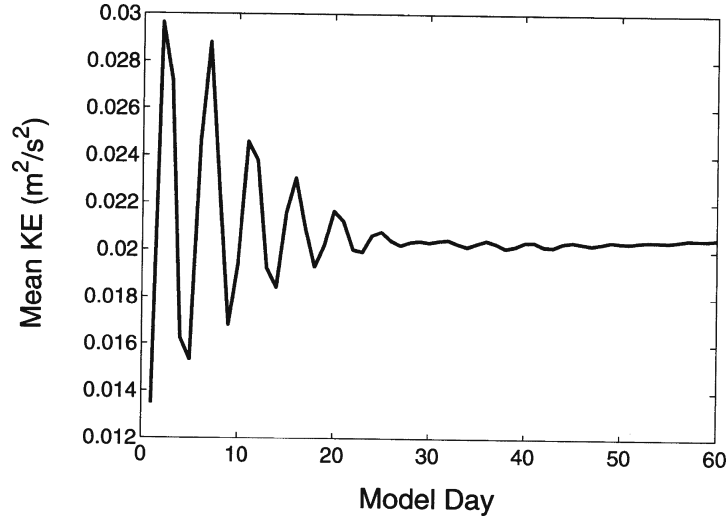


Fig. 16.3. Temporal variation of total kinetic energy. Note that the quasisteady state is reached after 30 day's integration (from Chu and Wang 2003, Geophysical Research Letters)

F_T and F_S are obtained at each time step. The diagnostic model was integrated for 60, 30 days were sufficient for the volume-mean model kinetic energy to reach quasisteady state under the imposed conditions (Fig. 16.3). The thermohaline source/sink terms (F_T , F_S) generated by the diagnostic initialization on day-30 and day-60 are used to identify their magnitudes and sensitivity to the integration period.

16.1.5 Extremely Strong Source/Sink Terms

Horizontal distributions of $\rho c_p F_T$ (unit: W m^{-3}) on day-30 (Fig. 16.4) at the four σ levels (0, -0.143 , -0.5 , and -0.929) show extremely strong heat sources/sinks generated by the diagnostic initialization. For $\rho c_p F_T = 1,000 \text{ W m}^{-3}$, the time rate of absolute temperature change $F_T = 0.84^\circ\text{C h}^{-1}$. The sources/sinks have various scales and strengths. They reveal small- to meso-scale patterns in most areas except a large-scale pattern near the bottom ($\sigma = -0.929$). The strength of the source/sink increases with depth from the surface to subsurface. The extremely strong source reaching $5,164 \text{ W m}^{-3}$ (corresponding to $F_T = 4.34^\circ\text{C h}^{-1}$) and the extremely strong sink reaching $-4,735 \text{ W m}^{-3}$ (corresponding to $F_T = -3.98^\circ\text{C h}^{-1}$), and decreases with depth below the subsurface. Near the bottom, the Japan/East Sea basin is dominated by cooling with the maximum sink strength $-1,557 \text{ W m}^{-3}$ (corresponding to $F_T = -1.31^\circ\text{C h}^{-1}$). From the subsurface to the bottom, the source/sink terms have some organized pattern near the Subpolar Front. At the subsurface, a dipole pattern occurs between 133 and 136°E with

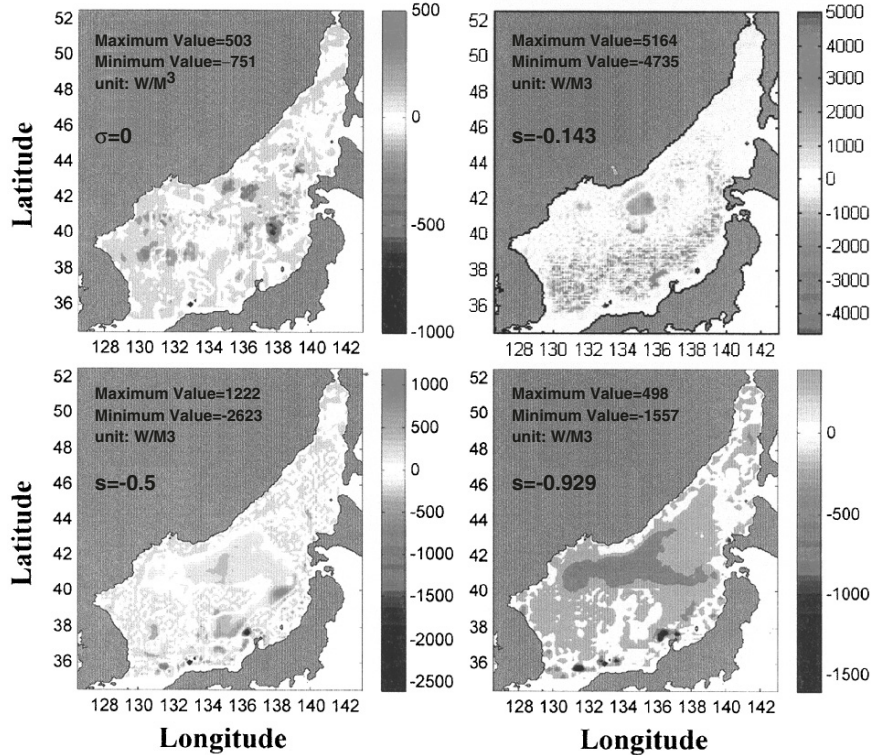


Fig. 16.4. Horizontal distribution of $\rho c_p F_T$ (unit: W m^{-3}) on day-30 at σ levels of: (a) 0, (b) -0.143 , (c) -0.5 , and (d) -0.929 (from Chu and Lan 2003, Geophysical Research Letters)

strong source strength approximate $2,000 \text{ W m}^{-3}$ (corresponding to $F_T = 1.68^\circ\text{C h}^{-1}$) north of the Subpolar Front and cooling rate ($\sim -2,000 \text{ W m}^{-3}$) south of the Subpolar Front. Near the bottom, a large cooling area with the cooling rate of 750 W m^{-3} occurs north of the Subpolar Front.

Horizontal distributions of F_S (unit: ppt m^{-3}) on day-30 (Fig. 16.5) at the four σ levels (0, -0.143 , -0.5 , and -0.929) show near-extremely strong salinity sources/sinks generated by the diagnostic initialization. These sources/sinks have various scales and strengths. They reveal small- to meso-scale patterns in most areas but a large-scale pattern in the southern Japan/East Sea near Tsushima/Korean Strait at the surface and north of the Subpolar Front at the midlevel and bottom. The strength of the source/sink increases with depth from the surface to the bottom. The maximum salinity source (sink) is found 0.80 ppt h^{-1} (-0.76 ppt h^{-1}) at $\sigma = -0.929$ ($\sigma = -0.5$).

When the prognostic integration starts, the source/sink terms F_T and F_S are removed from (16.5) and (16.6). Extremely strong and spatially nonuniform initial heating/cooling (salting/freshening) rates are introduced in the

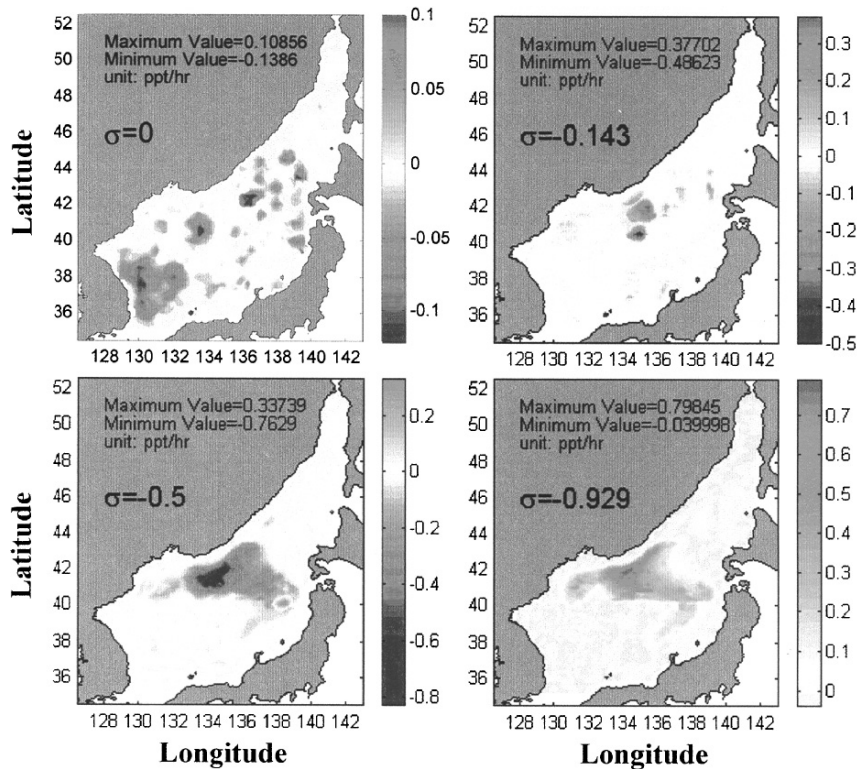


Fig. 16.5. Horizontal distribution of F_S (unit: ppts^{-1}) on day-30 at σ levels of: (a) 0, (b) -0.143 , (c) -0.5 , and (d) -0.929 (from Chu and Lan 2003, Geophysical Research Letters)

ocean models and cause drastic changes in thermohaline and velocity fields initially (after the diagnostic run) especially in the deep layer below the thermocline and halocline. Note that the problem is caused by the diagnostic initialization only, nothing to do with the ocean model itself.

In the diagnostic initialization, the source/sink terms drive the velocity through the pressure gradient force [see (16.1a)]. The pressure gradient error leads to errors in the initialized velocity field. Different models (z-level, σ -level, and s-level) have different pressure gradient errors, which in turns generate different initial velocity fields. Besides, the diagnostic process (spin up/down) largely depends on the diffusion. The spin down scale of 30 days is the state of balance between the pressure gradient force (not change with time) and other terms in (16.1a) such as the diffusion term that depends not only on the velocity field, but also on the model parameters. Thus, the diagnostic initialization depends on model type and model parameters.

If the diagnostic initialization continues to be used, it is urgent to study the following problems: does this artificial initial heating/cooling (salting/

freshening) induce false chaotic motion in ocean models? How long does the ocean model need to be adjusted? Does the spin-up of the prognostic run have the capability to diminish this initial effect?

If the monthly mean T_c, S_c data are used as the initial conditions, the initial heating (or cooling) and salting (or freshening) rates should not be greater than the standard measures (16.10) everywhere in the domain. If they reach the levels of strong “sources/sinks” ($|\partial T/\partial t|_{\text{Strong}}$ and $|\partial S/\partial t|_{\text{Strong}}$), the calculated $(T_c, S_c, \mathbf{V}_c, w_c)$ fields after diagnostic initialization are abnormal. If they reach the levels of extremely strong “sources/sinks” ($|\partial T/\partial t|_{\text{Extra Strong}}$ and $|\partial S/\partial t|_{\text{Extra Strong}}$), the calculated $(T_c, S_c, \mathbf{V}_c, w_c)$ fields cannot be used. Thus, development of a check-up algorithm on strength of the initial source and sink is urgent.

16.2 Uncertain Open Boundary Conditions

One difficult problem in shallow water modeling is the uncertainty of the open boundary condition. At open boundaries where the numerical grid ends, the fluid motion should be unrestricted since ideal open boundaries are transparent to motions. Two approaches, local-type and inverse-type, are available for determining open boundary condition. The local-type approach determines the open boundary condition from the solution of the governing equations near the boundary. The problem becomes selecting from a set of ad hoc open boundary conditions. Since any ad hoc open boundary condition will introduce noise into a numerical solution (Chapman 1985), it is important to choose the best one from ad hoc open boundary conditions for a particular ocean model. Without any ad hoc open boundary condition, the inverse-type approach can determine the open boundary condition from the “best” fit between model solutions and interior observations (Chu et al. 1997e). However, both methods bring considerable errors in open boundary conditions. In this section, the POM is used to illustrate the effect of uncertain open boundary condition on regional ocean prediction (Chu et al. 2005c).

16.2.1 Model Implementation

The model contains $181 \times 199 \times 23$ fixed grid points. The horizontal spacing is $5'$ latitude and longitude (approximately 5.77–7.59 km in the zonal direction and 9.265 km in the latitudinal direction) and there are 23 sigma levels in vertical coordinate. The model domain extends from 35.0 to 51.0°N, 127.0 to 142.0°E (Fig. 16.1). The horizontal friction and mixing are modeled using the Smagorinsky form with the coefficient chosen to be 0.2 for this application.

Tidal forcing was not included in this application of the model, since high frequency variability of the circulation is not considered. River outflow is also not included. However, the seasonal variation in sea surface height, temperature, salinity, circulation, and transport are represented by the model.

The atmospheric forcing includes mechanical and thermohaline forcing. The wind forcing is depicted by

$$\rho_0 K_M \left(\frac{\partial u}{\partial z}, \frac{\partial v}{\partial z} \right)_{z=0} = (\tau_x, \tau_y), \quad (16.13)$$

where K_M is the vertical mixing coefficient for momentum, (u, v) and (τ_x, τ_y) are the two components of the water velocity and surface wind stress vectors, respectively. The wind stress at each time step is interpolated from monthly mean climatological wind stress from COADS (1945–1989), with a resolution of $1^\circ \times 1^\circ$. The COADS wind stress was interpolated into the model grid with a resolution of $5'$. Surface thermohaline forcing is depicted by

$$K_H \frac{\partial \theta}{\partial z} = \alpha_1 \left(\frac{Q_H}{\rho C_p} \right) + \alpha_2 C (\theta_{\text{OBS}} - \theta), \quad (16.14)$$

$$K_S \frac{\partial S}{\partial z} = -\alpha_1 F S + \alpha_2 (S_{\text{OBS}} - S), \quad (16.15)$$

where K_H and K_S are the vertical mixing coefficients for heat and salt, (θ, S) and $(\theta_{\text{OBS}}, S_{\text{OBS}})$ are modeled and observed potential temperature and salinity, and c_p is the specific heat. (Q_H, F) are net heat and fresh water fluxes (downward positive). The parameters (α_1, α_2) are $(0, 1)$ switchers: $\alpha_1 = 0, \alpha_2 = 1$, would specify the restoring forcing; $\alpha_1 = 1, \alpha_2 = 0$, would specify the flux forcing. The relaxation coefficient C is the reciprocal of the restoring time period for a unit volume of water.

Boundary conditions for closed lateral boundaries, i.e., the modeled ocean bordered by land, were defined using a free-slip condition for velocity and a zero gradient condition for temperature and salinity. Thus, no advective or diffusive heat, salt or velocity fluxes occur through these boundaries. The radiation condition (local-type approach) is used to determine T, S at the open boundaries. When the water flows into the model domain, temperature and salinity at the open boundary are prescribed from observational data. When water flows out of the domain, the radiation condition,

$$\frac{\partial}{\partial t}(\theta, S) + U_n \frac{\partial}{\partial n}(\theta, S) = 0, \quad (16.16)$$

is applied. Here, the subscript n denotes the direction normal to the boundary. The temperature and salinity values at the open boundaries are obtained from monthly mean GDEM data.

For computational efficiency, the mode splitting technique (Blumberg and Mellor 1987) is applied with a barotropic time step of 25s, based on the CFL computational stability condition and the external wave speed; and a baroclinic time step of 900s, based on the CFL condition and the internal wave speed.

16.2.2 Two-Step Initialization

Two-steps are used to obtain “standard initial velocity field” for the study: presimulation and simulation. During the first step (presimulation run), POM is integrated for 2 years from zero velocity and climatological annual mean temperature and salinity fields with the monthly mean surface wind stress from the COADS data and restoring-type surface thermohaline forcing ($\alpha_1 = 0, \alpha_2 = 1$) which is relaxed to surface monthly mean values. The final states of the first step are taken as initial conditions for the second step (simulation run). During the simulation run, POM is integrated again for one and half years starting from Julian Day-1 to Julian Day-180 of the second year using the flux forcing ($\alpha_1 = 1, \alpha_2 = 0$) with monthly mean surface wind stress (τ_x, τ_y), net heat flux (Q_H), and net fresh-water flux (F) from the COADS data. The atmospheric forcing data are temporally interpolated into daily data. The final states of the simulation stage,

$$V_0 = V_{180}, \quad T_0 = T_{180}, \quad S_0 = S_{180}, \quad (16.17)$$

are taken as standard initial conditions for the numerical experiments.

16.2.3 Volume Transport at Open Boundaries

Volume transports at open boundaries are specified from historical data (Table 16.1). Positive (negative) values are referred to inflow (outflow). Warm water enters the Japan Sea through the Korea/Tsushima Strait with the Tsushima Warm Current from the East China Sea and exits the Japan Sea through the Tsugaru and Soya straits. There is no evident volume transport through the Tatar Strait (Martin and Kawase 1998), which is taken as 0. Recent estimate of the monthly mean volume transport, reported by Yi (1966), through the Korea/Tsushima Strait with the annual average of 1.3 Sv, a maximum of 2.2 Sv in October, and a minimum of 0.3 Sv in February. Bang et al. (1996) used the maximum inflow transport of about 3.5 Sv in August and minimum of 1.6 Sv in February, while Kim and Yoon (1999) used the mean value of 2.2 Sv with ± 0.35 Sv with the maximum in mid-September and the minimum in mid-March. The total inflow transport through Korea/Tsushima Straits should be the same as the total outflow transport through the Tsugaru and Soya Straits. We assume that 75% (80% in Bang et al. 1996) of the total inflow transport should flow out of the Japan/East Sea through the Tsugaru Strait, and 25% (20% in Bang et al. 1996) through the Soya Strait. This ratio is adopted from the maximum volume transport through the Tsugaru Strait estimated by Toba et al. (1982), and through the Soya Strait estimated by Preller and Hogan (1998). The monthly volume transports through open boundaries are listed in Table 16.1.

Table 16.1. Bimonthly variation of volume transport (unit: Sv)

month	Feb.	Apr.	Jun.	Aug.	Oct.	Dec.
Tatar strait (inflow)	0.05	0.05	0.05	0.05	0.05	0.05
Soya strait (outflow)	-0.1	-0.1	-0.4	-0.6	-0.7	-0.4
Tsugaru strait (outflow)	-0.25	-0.35	-0.85	-1.45	-1.55	-1.05
Tsushima strait (inflow)	0.3	0.4	1.2	2.0	2.2	1.4

16.2.4 Experimental Design

Evaluation Strategy

Ocean model output should be verified by the reality, which is represented approximately by observational (sampling) data with sufficient temporal and spatial coverage and resolution. Such a verification dataset is either not available or containing error. The initial and forcing data (wind and lateral transport) also contain error even the climatology. Difference between the model output and the observational data (if available) not only represents the model predictability but also the effect due to uncertain verification data.

In order to filter out the effect due to uncertain verification data and to quantify the uncertainty in initial and forcing data, a control run is designed with known initial condition, wind forcing, and lateral transport. The model input (initial and forcing) data are treated as “accurate.” The model output data are taken as the “reality” (i.e., the verification data without error).

Sensitivity runs are designed with quantified errors in initial condition (nonrandom error) or forcing data (random error). Comparison between the model output data and the “reality” (i.e., the output data from the control run) quantifies the two kinds of the model predictability.

Control Run

The control run is to integrate POM-Japan Sea from the standard initial conditions (16.17) for 180 days (to Julian Day-360) with the lateral transport shown in Table 16.1 (unperturbed) and the daily surface wind stress, net heat flux, and fresh-water flux interpolated from the COADS monthly mean data (unperturbed). Detailed information can be found in Chu et al. (2000c, 2001c, 2003c). The simulated surface velocity field coincides with earlier description of the Japan Sea circulation presented in Sect. 6.5.5.

Uncertain Lateral Transport

Two experiments are conducted to investigate the effect of lateral transport uncertainty. Everything keeps the same as the control run (run-0) except the bimonthly mean lateral boundary transport (see Table 16.1) where a Gaussian-type random variable is added with the zero mean and noise intensity being 5 and 10% of the transport (control run). The noise varies in two months.

Statistical Error Analysis

Difference between the horizontal velocity \mathbf{V} of control run and each sensitivity run at a σ -level,

$$\Delta \mathbf{V}(x, y, \sigma, t) = \mathbf{V}_c(x, y, \sigma, t) - \mathbf{V}_e(x, y, \sigma, t), \quad (16.18)$$

is defined as prediction error. Here, the subscripts (c, e) represent the control and sensitivity runs. Temporal evolution of the horizontal mean relative error is represented by the level dependent Relative Root Mean Square Error (RRMSE) between the control and sensitivity runs

$$R_1(\sigma, t) = \frac{\sqrt{\sum_{i=1}^{M_x} \sum_{j=1}^{M_y} \{[\Delta u(x_i, y_j, \sigma, t)]^2 + [\Delta v(x_i, y_j, \sigma, t)]^2\}}}{\sqrt{\sum_{i=1}^{M_x} \sum_{j=1}^{M_y} \{[u_c(x_i, y_j, \sigma, t)]^2 + [v_c(x_i, y_j, \sigma, t)]^2\}}}. \quad (16.19)$$

Temporal evolution of the volume mean relative error is represented by the level-independent RRMSE between the control and sensitivity runs,

$$R_2(t) = \frac{\sqrt{\sum_{i=1}^{M_x} \sum_{j=1}^{M_y} \sum_{k=1}^{M_z} \{[\Delta u(x_i, y_j, \sigma_k, t)]^2 + [\Delta v(x_i, y_j, \sigma_k, t)]^2\}}}{\sqrt{\sum_{i=1}^{M_x} \sum_{j=1}^{M_y} \sum_{k=1}^{M_z} \{[u_c(x_i, y_j, \sigma_k, t)]^2 + [v_c(x_i, y_j, \sigma_k, t)]^2\}}}. \quad (16.20)$$

16.2.5 Model Uncertainty

The level-dependent RRMSE, $R_1(\sigma, t)$, varies with time with smaller values on the fifth day (Fig. 16.6a) than on the 180th day (Fig. 16.6b). It increases with the noise intensity for the same (σ, t) , and increases from a minimum value at the surface (0.05 for 5% noise intensity and 0.08 for 10% noise intensity on the 5th day, and 0.10 for 5% noise intensity and 0.15 for 10% noise intensity on the 180th day) to a maximum value at the bottom (0.16 for 5% noise intensity and 0.23 for 10% noise intensity on the 5th day, and 0.18 for 5% noise intensity and 0.28 for 10% noise intensity on the 180th day). Level-independent RRMSE, $R_2(t)$, oscillates with time with smaller values (0.09–0.20) for 5% noise intensity and with larger values (0.17–0.34) for 10% noise intensity (Fig. 16.7).

Since the absolute velocity can be computed from (T, S) data using the P-vector inverse method, it is possible to incorporate the P-vector algorithm into the numerical model to compute the velocity from the (T, S) values at the open boundary. This will reduce the uncertainty in the lateral boundary transport and in turn reduce the model uncertainty.

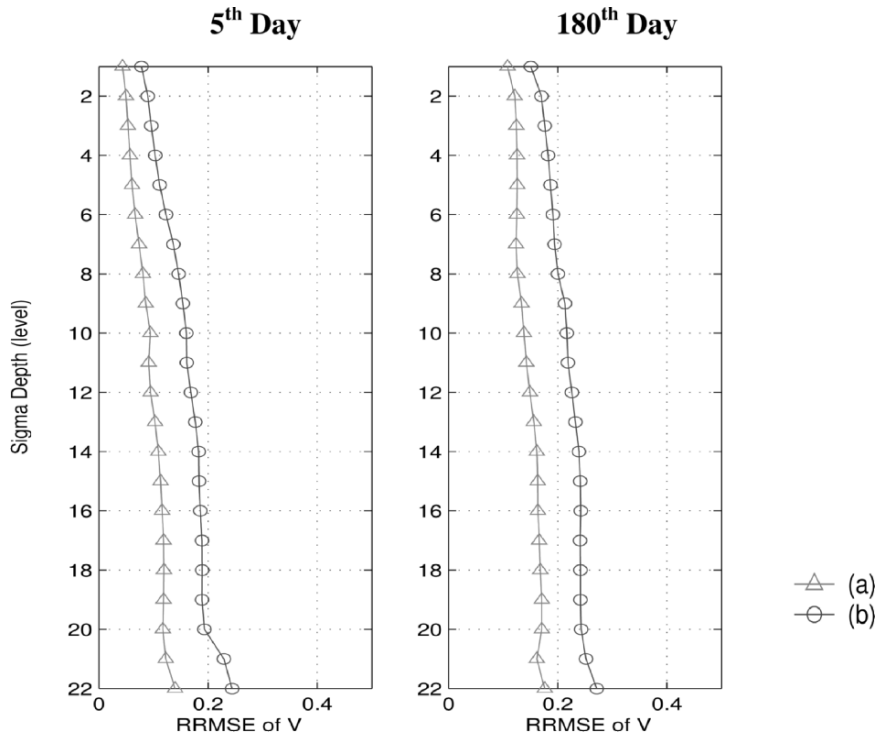


Fig. 16.6. Level dependent RRMSE due to uncertain lateral boundary transport with 5% noise intensity (represented by the symbol “ Δ ”) and 10% noise intensity (represented by the symbol “O”) on the (a) fifth day and (b) 180th day after the model integration (from Chu et al. 2005c, Continental Shelf Research)

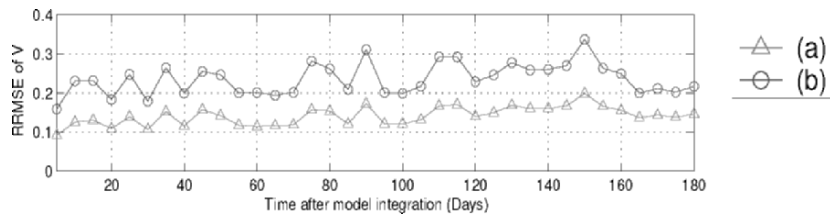


Fig. 16.7. Temporal evolution of level independent RRMSE due to uncertain lateral boundary transport with the symbol “ Δ ” denoting 5% noise intensity and the symbol “O” representing 10% noise intensity. Note that the error oscillates with no evident error growing trend (from Chu et al. 2005c, Continental Shelf Research)

Questions and Exercises

- (1) What is the major difficulty in ocean model initialization?
- (2) In ocean modeling practice, climatological (T_c, S_c) data are usually taken as the initial (T, S) conditions. Let the inverted absolute velocity from the (T_c, S_c) data be represented by $\mathbf{V}^{(p)}$. Why do the initial conditions $(T_c, S_c, \mathbf{V}^{(p)})$ satisfy the conservation of heat and salt?
- (3) For the same conditions as the previous question, why do the initial conditions $(T_c, S_c, 0)$ dissatisfy the conservation of heat and salt? How strong is the artificial source/sink added to the system?
- (4) Is diagnostic initialization (popularly used) feasible in ocean modeling practice? Why?
- (5) Figures 16.4 and 16.5 show large artificial heat and salt sources/sinks during the diagnostic initialization. Discuss the effect of this extra thermohaline forcing on the model results.
- (6) Discuss the two types of model predictability using the POM-Japan/East Sea model.
- (7) Select a region and a numerical ocean model of your interest. The annual mean WOA (T_c, S_c) data are used. The corresponding absolute velocity ($\mathbf{V}^{(p)}$) data are downloaded from the enclosed CD-ROM. Run the POM diagnostic mode with the fixed (T_c, S_c) fields for periods of time (30, 60, 90 days) to get velocity fields $(\mathbf{V}_{30}, \mathbf{V}_{60}, \mathbf{V}_{90})$. Analyze the difference between $\mathbf{V}^{(p)}$ and $(\mathbf{V}_{30}, \mathbf{V}_{60}, \mathbf{V}_{90})$.
- (8) Run the numerical model from the initial conditions $(T_c, S_c, \mathbf{V}^{(p)})$ for a year as the control case. Run the numerical model from the initial conditions $(T_c, S_c, \mathbf{V}_{30})$, $(T_c, S_c, \mathbf{V}_{60})$, and $(T_c, S_c, \mathbf{V}_{90})$ for a year as the sensitivity cases. Analyze the difference between the control and sensitivity cases. Report the results.

A

P-Vector Module for z -Coordinate

The P-Vector module for z -coordinate was developed to compute absolute velocity from hydrographic data. This package is stored in the enclosed DVD-Rom and includes the makefile, source codes, plotting files (using Matlab), and a sample case. The sample case is located at a subdirectory called sample.dir. The test data set is the WOA climatological (T, S) fields for the North Atlantic Ocean. The grid resolution is set to be $1^\circ \times 1^\circ$ with 50 vertical levels (i.e., $n_x = 360, n_y = 180, n_z = 50$). The users may change for their own sakes. Chenwu Fan and Carlos Lozano helped in developing these codes.

A.1 Makefile

```
*****
SRC = whoi.f pvector.f pv.f pvpar.f userinp.f setmask.f matopen.f
matclose.f mattotal.f matout.f

OBJS= $(SRC:.f=.o)
FFLAGS= -g

pvexe: $(OBJS)
       f77 $(FFLAGS) -o pvexe $(OBJS)
pvector.o: pstate.h pvector.f
          f77 $(FFLAGS) -c pvector.f
pv.o: pstate.h pv.f
      f77 $(FFLAGS) -c pv.f
userinp.o: pstate.h userinp.f
          f77 $(FFLAGS) -c userinp.f
whoi.o: whoi.f
        f77 -g -c whoi.f
pvpar.o: pstate.h pvpar.f
        f77 -g -c pvpar.f
setmask.o: setmask.f
```

```

f77 -g -c setmask.f matopen.o:  matopen.f
f77 -g -c matopen.f matclose.o: matclose.f
f77 -g -c matclose.f
mattotal.o:  mattotal.f
f77 -g -c mattotal.f
matout.o:  pstate.h matout.f
f77 $(FFLAGS) -c matout.f

```

A.2 Main Subdirectories

There are three major directories (*pvector*, *pvector_nc* and *pvector_rotation*) of the enclosed DVD-Rom for computing the absolute velocity in z -coordinate system. Among them, *pvector* and *pvector_nc* are used for (x, y) -axes aligning with (latitude, longitude); and *pvector_rotation* is used for (x, y) -axes not aligning with (latitude, longitude). The output of *pvector* is in the ASCII format. The output of *pvector_nc* is in the NetCDF format.

A.2.1 Subdirectory (*pvector*)

In this subdirectory, the input and output data are in the ASCII format. All the input and output files are arranged from west to east and north to south. A sample data set (North Atlantic) is located in `sample.dir`. The following procedures are taken for running the sample case. The commands are listed using *italics*. Since all the data files are in the ASCII format, running this program is slow and needs large disk space.

- (a) Create `pvexe` (executive file) in the `pvectorcode` director

```
< make
```

- (b) Go to `sample.dir` and run `pvexe`

```
../pvexe < pv.inp
```

for getting ASCII output data.

- (c) Use the following matlab files to plot the output data.

```

uvlev.m - plot vertical velocity at different levels
tsrlev.m - plot temp, salt and density at different levels.

```

- (d) Note that the input data order as:

West to east, top to bottom, north to south.

(e) Note that the output data order as:

Top to bottom, west to east, north to south.

A.2.2 Subdirectory (`pvector_nc`)

In this subdirectory, the input data are either in the ASCII or binary format, and the output in the NetCDF format. You must have NetCDF library in your system. If you do not have the NetCDF lib (library), you may download the netcdf library and the matlab-NetCDF interface from <http://www.unidata.ucar.edu/software/netcdf/>.

You may need to change the location of netcdf lib in the Makefile *mknc*. You can use *mknc* to compile the code in `code_nc` subdirectory. Two sample sets are located in the two subdirectories *Sample_NA_ASCII* and *Sample_NA_bin*. *Sample_NA_ASCII* contains input data in the ASCII format for the North Atlantic Ocean (similar to `pvector/sample.dir`) and one output file in the NetCDF format. *Sample_NA_bin* contains input data in the binary format for the North Atlantic Ocean and the output file in the NetCDF format. For the input file `pvnc.inp`, note that (a) `ts` (the first number on line 3): 1-ASCII data, 2-binary, (b) line 8: description of the netcdf file, and (c) line 9: the author.

A.2.3 Subdirectory (`pvector_rotation`)

When the horizontal coordinate system is not aligned with the longitude and latitude, you should use the subdirectory *pvector_rotation*. Different from *pvectorcode* and *pvector_nc*, use of *pvector_rotation* needs input of longitude and latitude data at each station. Line 2 of *pxy.inp* is used for naming the 2D longitude and latitude data file. A sample set (named `Sample_Arctic`) is taken as an example with *Arctic Ocean.inp* as the control data file. The second line in that file shows the latitude, longitude, *y*, *x*, and name of data file. The data file can be either binary or ASCII data. The first number of line 3, 'ts' is the key word of the input data type:

topography data always in ASCII format.

temperature and salinity data:

ts	temperature and salinity data type
1	ascii data with order (mx,mz,my)
-1	ascii data with order (mz,mx,my)
2	binary data with order (mx,mz,my)
-2	binary data with order (mz,mx,my)

latitude, longitude, *x*, and *y* data:

```

|ts|=1      ASCII data
|ts|=2      binary data
and with the order
            lat(mx, my)
            lon(mx, my)
            x(mx, my)
            y(mx, my)

```

It is noted that the output velocity (u, v) is in the directions of (x, y) axes not of longitude and latitude.

A.3 Major FORTRAN Programs

A.3.1 ASCII Format (pv.f)

This FORTRAN program is used for the coordinate system with the latitude as the x -axis and the longitude as the y -axis.

```

program pv

c
c — tempfile: temperature data file name
c — saltfile: salinity data file name
c — topofile: topography data file name
c   The Grid desired as:
c
c   (rhot,rho,q)      (rhot,rho,q)
c   o-----*-----o  —
c   |      ( U,V )    |  |
c   |                 |  |
c   |                 |  |
c   |                 |  |
c   |                 |  |
c   |*(w)             (w)*  Z
c   |                 |  |
c   |                 |  |
c   |                 |  |
c   |      ( U,V )    |  |
c   o-----*-----o  —
c   (rhot,rho,q)      (rhot,rho,q)
c   |-----X , Y-----|
c   |
c

```



```

c   lat0                [latitude (degree) at the NW corner]
c
c   lon0                [longitude (degree) at the NW corner]
c
c   ktop                [In the inversion procedure use
c                       only the levels [ktop:mz]]
c
c   ts                  read either TS or RHO RHOT
c       1                read temp & salt from ascii data files
c       2                read temp & salt from binary data files
c
c
c
c 2. Inputs:
c
c   stopog(mx,my)       topography for the subroutine read_topo
c                       see description in the subroutine header.
c
c   if(ts>=1):
c   temp(mx,my,mz)      temperature
c   salt(mx,my,mz)      salinity
c                       read in subroutine read_ts
c   if(ts==2):
c                       Temperature and salinity show non-number.
c                       The bottom topography is reset at the same
c                       depth with T and S taking non-numbers.
c                       Read in the subroutine read_ts.
c   if(ts=0):
c   rho(mx,my,mz)       density
c   rhot(mx,my,mz)      potential density
c
c 3. Outputs:
c
c   u(mx1,my1,mz),v(mx1,my1,mz) absolute horizontal velocity
c   (m/s)
c   px(mx1,my1,mz),py(mx1,my1,mz) P-vector
c   invmask(mx1,my1)
c
c                       =-1        for inverse not being accomplished
c                       =0         for land
c                       >0         for inverse being accomplished
c
c   [1:invmask(i,j)]
c                       levels at which the absolute horizontal
c                       velocity is estimated.
c
c

```

```

c-----
c
c - volume grid size (user defined) -----
c
c
c   include 'pstate.h'
c   common /maxval6/ veval,vmax,ii,jj
c   real veval(nz),vmax(6,nz)
c   integer ii(6,nz),jj(6,nz)
c-----
c   real temp(nx,2,nz),salt(nx,2,nz)
c   real tempgb(nx,nz),saltgb(nx,nz)
c-----
c
c   integer j,spherical
c   real lat0,lon0
c   integer ts,ktop,sect,sect1,sect2
c   real sims,pref,grid_size
c   real radius,omega
c   real f0
c   real deep(nz)
c   integer mx1,my1,stopog(nx,ny)
c   real latmin
c   integer iuvuni,iunpxy,iunrho,iuvunig,iunq
c   integer k,ll
c   character *30 topofile,tempfile,saltfile
c
c   iuvuni=15
c   iunpxy=26
c   iunrho=17
c   iuvunig=28
c   iunq=19
c
c   latmin=5.0
c   zero=0.0
c   one=1.0
c   pi = 3.1415926535
c   deg2rad = pi/180
c
c - cntrl parameters
c
c   call pvpar(deep,grid_size,lon0,lat0,ktop,pref,ts,spherical,
c   &      sims,topofile,tempfile,saltfile)
c   my1=my-1
c   mx1=mx-1
c   if(global) mx1=mx
c - physical and numerical constants
c   omega = 7.292e-5
c   radius = 6.371e6

```

```

c-----
c - grid spacing along latitude
c
  dy = grid_size*deg2rad*radius

  do j=1,my
    lat(j) = lat0 - (j-1)*grid_size
  enddo

c
c - grid spacing along longitude
c
  if (spherical.eq.0) then
    do j= 1, my
      dx(j) = dy
    enddo
  else

    do j= 1, my
      dx(j) = dy*cos(lat(j)*deg2rad)
    enddo
  endif

c
c - Coriolis (1/s)
c
  do j=1,my
    ff(j) = 2.*omega*sin(lat(j)*deg2rad)
    if(lat(j).lt.latmin .and. lat(j).ge.0.0)
&   ff(j)=2.*omega*sin(latmin*deg2rad)
    if(lat(j).gt.-latmin .and. lat(j).le.0.0)
&   ff(j)=-2.*omega*sin(latmin*deg2rad)
  enddo
  f0=0.5*(abs(ff(1))+abs(ff(my)))

  call read_topo(stopog,deep,ts,topofile,tempfile)

  call setmask(mx,my,istopog,rmask,invmask,global)

  do k=ktop,mz
    do ll=1,6
      vmax(i,k)=0.0
    enddo
    veval(k)=0.0
  enddo
  if(ts) then
    open(8,file=tempfile)
    open(9,file=saltfile)
  endif

```

```

call matopen(iuvuni,iunpxy,iunrho,iuvunig,iunq)
sect1=2
sect2=1
call userinp(stopog,deep,temp,salt,pref,ts,sect2,0)
call pvector(stopog,deep,ktop,sims,sect1,sect2,f0,0)

if(global) then
  do i=1,mx
    do k=1,mz
      tempgb(i,k)=temp(i,1,k)
      saltgb(i,k)=salt(i,1,k)
    enddo
  enddo
endif

do j=1,my1
  sect=sect2
  sect2=sect1
  sect1=sect
  call userinp(stopog,deep,temp,salt,pref,ts,sect2,j)
  call pvector(stopog,deep,ktop,sims,sect1,sect2,f0,j)
c
c - output
c
c
c - this output is designed for simple matlab inputs
c
  call matout(iuvuni,iunpxy,iunrho,iuvunig,iunq,
&          temp,salt,sect2,f0)

  enddo
  close(8)
  if(ts) close(9)
  call matclose(iuvuni,iunpxy,iunrho,iuvunig,iunq)
  do k=ktop,mz
    veval(k)=veval(k)/(mx1*my1)
    print 77,k,-deep(k),veval(k)*100.0,(vmax(i,k)*100.0,i=1,6)
    print 88,(ii(i,k),jj(i,k),i=1,6)
  enddo
77  format(/i4,f8.0,7f8.2)
88  format(20x,6(2x,2i3))
call mattotal(mx1,my1,mz,istopog,rmask,invmask,deep,
&          grid_size,lon0,lat0,ktop,pref,global)
stop
end

```



```

c
c ktop      [In the inversion procedure use
c           only the levels [ktop:mz]]
c
c ts        read either TS or RHO RHOT
c           1      read temp & salt from ascii data files
c           2      read temp & salt from binary data files
c
c
c 2. Inputs:
c
c stopog(mx,my)  read in subroutine read_topo
c                see description in subroutine header.
c
c if(ts=1):
c temp(mx,mz,my)  temperature
c salt(mx,mz,my)  salinity
c                 read in subroutine read_ts
c
c if(ts=0):
c rho(mx,mz,my)   density
c rhot(mx,mz,my)  potential density
c
c 3. Outputs: one NetCDF data format file
c
c-----
c
c The binary output data file is named as pvoutbin.dat.
c The structure of this file is given by
c mx1,my1,mz,grid_size,lat0,lon0,ktop,pref,global
c deep (mz)
c rho (j=my) (mx*mz)
c rhot (j=my) (mx*mz)
c stopog (j=my) (mx)
c istopog (j=my) (mx)
c *****
c (the follow is my1 crosssection from j=my1 to 1, each section as:)
c rmask (mx1)
c invmask (mx1)
c px (mx1*mz)
c py (mx1*mz)
c pz (mx1*mz)
c ug (mx1*mz)
c vg (mx1*mz)
c u (mx1*mz)

```

```

c   v                               (mx1*mz)
c   w                               (mx1*mz)
c   rho                             (mx*mz)
c   rhot                             (mx*mz)
c   stopog                           (mx)
c   istopog                           (mx)
c   *****
c
c   ----- volume grid size (user defined) -----
c   include 'pstate.h'
c   include 'netcdf.inc'
c
c   common /maxval6/ veval,vmax,ii,jj
c   real veval(nz),vmax(6,nz)
c   integer ii(6,nz),jj(6,nz)
c
c   -----
c   real temp(nx,nz),salt(nx,nz)
c
c   -----
c   real deg2rad,pi,one
c
c   -----
c   integer j,spherical,mx1,my1
c   integer my_handler
c   integer ts,ktop,sect,sect1,sect2
c   real sims,pref,grid_size,lat0,lon0
c   real radius,omega,f0
c   real deep(nz), r1d(nx+ny)
c   integer stopog(nx,ny), istw(3), ictw(3),
c   & dim2d(2), dim3d(3), ist2(2), ist3(3), ict2(2), ict3(3),
c   & dimr3d(3), ist3r(3), ict3r(3)
c   integer*2 i1d(nx*(ny+nz))
c   real latmin
c   character*30 topofile,tempfile,saltfile
c   character titl*80, author*30, created*9, ncflnm*30
c
c   real*8 facu, facut, facw, fact, ofstst, ofstr
c
c   data facu, facut, facw/1.0d-4,2.0d-2,1.0d-6/
c   data fact, ofstst, ofstr/1.0d-3, 1.5d1, 1.28d3/
c
c   data ist2,ist3,istw,ict2,ict3,ictw/16*1/
c   data ist3r, ict3r/6*1/
c
c   rlim=32760.0
c   latmin=5.0
c   zero=0.0

```

444 A P-Vector Module for z-Coordinate

```

    one=1.0
    pi = 3.1415926535
    deg2rad = pi/180
c
c - cntrl parameters
c
    call pvpar(deep,grid_size,lon0,lat0,ktop,pref,ts,spherical,
&    sims,topofile,tempfile,saltfile,titl,author,ncflnm)
    my1=my-1
    mx1=mx-1
    if(global) mx1=mx

c - physical and numerical constants
    omega = 7.292e-5
    radius = 6.371e6

c-----
c - gridspacing along latitude
c
    dy = grid_size*deg2rad*radius

    do j=1,my
        lat(j) = lat0 - (j-1)*grid_size
    enddo

c
c - grid spacing (m) along longitude
c
    if (spherical.eq.0) then
        do j= 1, my
            dx(j) = dy
        enddo
    else

        do j= 1, my
            dx(j) = dy*cos(lat(j)*deg2rad)
        enddo
    endif

c
c - Coriolis (1/s)
c
    do j=1,my
        ff(j) = 2.*omega*sin(lat(j)*deg2rad)
        if(lat(j).lt.latmin .and. lat(j).ge.0.0)
```

```

& ff(j)=2.*omega*sin(latmin*deg2rad)
  if(lat(j).gt.-latmin .and. lat(j).lt.0.0)
& ff(j)=-2.*omega*sin(latmin*deg2rad)
enddo
f0=0.5*(abs(ff(1))+abs(ff(my)))

call read_topo(stopog,deep,ts,topofile,tempfile,saltfile)

call setmask(mx,my,istopog,rmask,invmask,global)

do k=ktop,mz
  do ll=1,6
    vmax(i,k)=0.0
  enddo
  veval(k)=0.0
enddo

call date(created)

IRET = NF_CREATE(ncfnm,NF_CLOBBER,NCID)
CALL ERRCHECK(IRET)

IRET= F_PUT_ATT_TEXT(NCID,NF_GLOBAL,'title',80,titl)
CALL ERRCHECK(IRET)
IRET = NF_PUT_ATT_TEXT(NCID,NF_GLOBAL,'author',39,
&      author//created)
CALL ERRCHECK(IRET)
c
c  defind dimensions (lat, lon, lev)
c
IRET = NF_DEF_DIM(NCID,'lat',my,IDJDIM)
CALL ERRCHECK(IRET)
IRET = NF_DEF_DIM(NCID,'latuv',my1,IDJUVDIM)
CALL ERRCHECK(IRET)
IRET = NF_DEF_DIM(NCID,'latw',my1-1,IDIWDIM)
CALL ERRCHECK(IRET)
IRET = NF_DEF_DIM(NCID,'lon',mx,IDIIDIM)
CALL ERRCHECK(IRET)
IRET = NF_DEF_DIM(NCID,'lonuv',mx1,IDIUVDIM)
CALL ERRCHECK(IRET)
IRET = NF_DEF_DIM(NCID,'lonw',mx1-1,IDIWDIM)
CALL ERRCHECK(IRET)
IRET = NF_DEF_DIM(NCID,'lev',mz,IDKDIM)
CALL ERRCHECK(IRET)

```

```

c
c defined coordinate data (lat, lon, deep)
c
      IRET = NF_DEF_VAR(NCID,'lat',NF_float,1,
& IDJDIM,IDYCOORD)
      CALL ERRCHECK(IRET)
      IRET = NF_DEF_VAR(NCID,'latuv',NF_float,1,
& IDJUVDIM,IDYUVCOORD)
      CALL ERRCHECK(IRET)
      IRET = NF_DEF_VAR(NCID,'latw',NF_float,1,IDJWDIM,
& IDYWCOORD)
      CALL ERRCHECK(IRET)
      IRET = NF_DEF_VAR(NCID,'lon',NF_float,1,
& IDIDIM,IDXCOORD)
      CALL ERRCHECK(IRET)
      IRET = NF_DEF_VAR(NCID,'lonuv',NF_float,1,
& IDIUVDIM,IDXUVCOORD)
      CALL ERRCHECK(IRET)
      IRET = NF_DEF_VAR(NCID,'lonw',NF_float,1,
& IDIWDIM,IDXWCOORD)
      CALL ERRCHECK(IRET)
      IRET = NF_DEF_VAR(NCID,'depth',NF_float,1,
& IDKDIM,IDZCOORD)
      CALL ERRCHECK(IRET)
      IRET = NF_PUT_ATT_TEXT(NCID,
& IDZCOORD,'units',6,'meters')
      CALL ERRCHECK(IRET)
      IRET = NF_PUT_ATT_TEXT(NCID,
& IDYCOORD,'long_name',28,
& 'Latitudinal Position for rho')
      CALL ERRCHECK(IRET)
      IRET = NF_PUT_ATT_TEXT(NCID,IDYUVCOORD,
& 'long_name',28,'Latitudinal Position for u,v')
      CALL ERRCHECK(IRET)
      IRET = NF_PUT_ATT_TEXT(NCID,IDYWCOORD,
& 'long_name',26, 'Latitudinal Position for w')
      CALL ERRCHECK(IRET)
      IRET = NF_PUT_ATT_TEXT(NCID,IDXCOORD,
& 'long_name',29, 'Longitudinal Position for rho')
      CALL ERRCHECK(IRET)
      IRET = NF_PUT_ATT_TEXT(NCID,IDXUVCOORD,
& 'long_name',29, 'Longitudinal Position for u,v')
      CALL ERRCHECK(IRET)
      IRET = NF_PUT_ATT_TEXT(NCID,IDXWCOORD,
& 'long_name',27, 'Longitudinal Position for w')
      CALL ERRCHECK(IRET)
      IRET = NF_PUT_ATT_TEXT(NCID,IDZCOORD,
& 'long_name',27,'Vertical Position for u,v,w')
      CALL ERRCHECK(IRET)

```

```

dimr3d(1)=IDKDIM
dimr3d(2)=IDIDIM
dimr3d(3)=IDJDIM

dim3d(1)=IDKDIM
dim3d(2)=IDIUVDIM
dim3d(3)=IDJUVDIM

dim2d(1)=IDIUVDIM
dim2d(2)=IDJUVDIM

IRET = NF_DEF_VAR(NCID,'mask',NF_SHORT,2,
&      dim2d,IDMASK)
CALL ERRCHECK(IRET)
IRET = NF_DEF_VAR(NCID,'maskinv',NF_SHORT,2,
&      dim2d,IDMASKINV)
CALL ERRCHECK(IRET)

IRET = NF_DEF_VAR(NCID,'Temperature',NF_SHORT,3,
&      dimr3d,IDT)
CALL ERRCHECK(IRET)
IRET = NF_DEF_VAR(NCID,'Salinity',NF_SHORT,3,
&      dimr3d,IDS)
CALL ERRCHECK(IRET)
IRET = NF_DEF_VAR(NCID,'Density',NF_SHORT,3,
&      dimr3d,IDR)
CALL ERRCHECK(IRET)
IRET = NF_DEF_VAR(NCID,'Potential_Density',NF_SHORT,3,
&      dimr3d,IDRT)
CALL ERRCHECK(IRET)
IRET = NF_PUT_ATT_DOUBLE(NCID,IDT,'scale_factor',
&      NF_double,1,fact)
CALL ERRCHECK(IRET)
IRET = NF_PUT_ATT_DOUBLE(NCID,IDS,'scale_factor',
&      NF_double,1,fact)
CALL ERRCHECK(IRET)
IRET = NF_PUT_ATT_DOUBLE(NCID,IDR,'scale_factor',
&      NF_double,1,fact)
CALL ERRCHECK(IRET)
IRET = NF_PUT_ATT_DOUBLE(NCID,IDRT,'scale_factor',
&      NF_double,1,fact)
CALL ERRCHECK(IRET)
IRET = NF_PUT_ATT_DOUBLE(NCID,IDT,'add_offset',

```

```

&      NF_double,1,ofstst)
CALL ERRCHECK(IRET)
IRET = NF_PUT_ATT_DOUBLE(NCID,IDS,'add_offset',
&      NF_double,1,ofstst)
CALL ERRCHECK(IRET)
IRET = NF_PUT_ATT_DOUBLE(NCID,IDR,'add_offset',
&      NF_double,1,ofstr)
CALL ERRCHECK(IRET)
IRET = NF_PUT_ATT_DOUBLE(NCID,IDRT,'add_offset',
&      NF_double,1,ofstr)
CALL ERRCHECK(IRET)

IRET = NF_DEF_VAR(NCID,'u',NF_SHORT,3,dim3d,IDU)
CALL ERRCHECK(IRET)
IRET = NF_DEF_VAR(NCID,'v',NF_SHORT,3,dim3d,IDV)
CALL ERRCHECK(IRET)
dim3d(2)=IDIWDIM
dim3d(3)=IDJWDIM
IRET = NF_DEF_VAR(NCID,'w',NF_SHORT,3,dim3d,IDW)
CALL ERRCHECK(IRET)

dim2d(1)=IDIUVDIM
dim2d(2)=IDJUVDIM
IRET = NF_DEF_VAR(NCID,'utl',NF_SHORT,2,
&      dim2d,IDUTL)
CALL ERRCHECK(IRET)
IRET = NF_DEF_VAR(NCID,'vtl',NF_SHORT,2,dim2d,
&      IDVTL)
CALL ERRCHECK(IRET)

IRET = NF_PUT_ATT_TEXT(NCID,IDU,'long_name',14,
&      '3-D u-velocity')
CALL ERRCHECK(IRET)
IRET = NF_PUT_ATT_TEXT(NCID,IDU,'units',3,'m/s')
CALL ERRCHECK(IRET)
IRET = NF_PUT_ATT_DOUBLE(NCID,IDU,'scale_factor',
&      NF_double,1,facu)
CALL ERRCHECK(IRET)
IRET = NF_PUT_ATT_TEXT(NCID,IDV,'long_name',14,
&      '3-D v-velocity')
CALL ERRCHECK(IRET)

```

```

IRET = NF_PUT_ATT_TEXT(NCID,IDV,'units',3,'m/s')
CALL ERRCHECK(IRET)
IRET = NF_PUT_ATT_DOUBLE(NCID,IDV,'scale_factor',
&      NF_double,1,facu)
CALL ERRCHECK(IRET)
IRET = NF_PUT_ATT_TEXT(NCID,IDW,'long_name',14,
&      '3-D w-velocity')
CALL ERRCHECK(IRET)
IRET = NF_PUT_ATT_TEXT(NCID,IDW,'units',3,'m/s')
CALL ERRCHECK(IRET)
IRET = NF_PUT_ATT_DOUBLE(NCID,IDW,'scale_factor',
&      NF_double,1,facw)
CALL ERRCHECK(IRET)

IRET = NF_PUT_ATT_TEXT(NCID,IDUTL,'long_name',32,
&      'Vertically Integrated u-velocity')
CALL ERRCHECK(IRET)
IRET = NF_PUT_ATT_TEXT(NCID,IDUTL,'units',6,'m**2/s')
CALL ERRCHECK(IRET)
IRET = NF_PUT_ATT_DOUBLE(NCID,IDUTL,'scale_factor',
&      NF_double,1,facut)
CALL ERRCHECK(IRET)
IRET = NF_PUT_ATT_TEXT(NCID,IDVTL,'long_name',32,
&      'Vertically Integrated v-velocity')
CALL ERRCHECK(IRET)
IRET = NF_PUT_ATT_TEXT(NCID,IDVTL,'units',6,'m**2/s')
CALL ERRCHECK(IRET)
IRET = NF_PUT_ATT_DOUBLE(NCID,IDVTL,'scale_factor',
&      NF_double,1,facut)
CALL ERRCHECK(IRET)

IRET = NF_ENDDEF(NCID)
CALL ERRCHECK(IRET)

c
c  write coordinates
c
r1d(1)=lon0
do i=2,mx
  r1d(i)=r1d(i-1)+grid_size
enddo

```

```

IRET = NF_PUT_VAR_real(NCID,IDXCOORD,r1d)
CALL ERRRCHECK(IRET)
r1d(1)=lon0+0.5*grid_size
do i=2,mx1
  r1d(i)=r1d(i-1)+grid_size
enddo
IRET = NF_PUT_VAR_real(NCID,IDXUVCOORD,r1d)
CALL ERRRCHECK(IRET)
do i=1,mx1-1
  r1d(i)=(r1d(i)+r1d(i+1))/2.0
enddo
IRET = NF_PUT_VAR_real(NCID,IDXWCOORD,r1d)
CALL ERRRCHECK(IRET)
IRET = NF_PUT_VAR_real(NCID,IDYCOORD,lat)
CALL ERRRCHECK(IRET)
do j=1,my1
  r1d(j)=(lat(j)+lat(j+1))/2.0
enddo
IRET = NF_PUT_VAR_real(NCID,IDYUVCOORD,r1d)
CALL ERRRCHECK(IRET)
do j=1,my1-1
  r1d(j)=(r1d(j)+r1d(j+1))/2.0
enddo
IRET = NF_PUT_VAR_real(NCID,IDYWCOORD,r1d)
CALL ERRRCHECK(IRET)
IRET = NF_PUT_VAR_real(NCID,IDZCOORD,deep)
CALL ERRRCHECK(IRET)
do i=1,mx1
  do j=1,my1
    i1d(mx1*(j-1)+i)=rmask(i,j)
  enddo
enddo
IRET = NF_PUT_VAR_int2(NCID,IDMASK,i1d)
CALL ERRRCHECK(IRET)

if(ts.ge.2) then
  open(8,file=tempfile,access='direct',recl=mx*mz)
  open(9,file=saltfile,access='direct',recl=mx*mz)

```

```

elseif(ts.ge.1) then
  open(8,file=tempfile)
  open(9,file=saltfile)
endif
sect1=2
sect2=1

call userinp(stopog,deep,temp,salt,pref,ts,sect2,0)
call pvector(stopog,deep,ktop,sims,sect1,sect2,f0,0)
ist3r(3)=1
ict3r(1)=mz
ict3r(2)=mx

do i=1,mx
  do k=1,mz
    uuu=temp(i,k)/fact+0.5-ofstst
    uuu=max(-rlim,uuu)
    uuu=min(rlim,uuu)
    i1d(mz*(i-1)+k)=uuu
  enddo
enddo
IRET = NF_PUT_VARA_int2(NCID,IDT,ist3r,ict3r,i1d)
CALL ERRCHECK(IRET)
do i=1,mx
  do k=1,mz
    uuu=salt(i,k)/fact+0.5-ofstst
    uuu=max(-rlim,uuu)
    uuu=min(rlim,uuu)
    i1d(mz*(i-1)+k)=uuu
  enddo
enddo
IRET = NF_PUT_VARA_int2(NCID,IDS,ist3r,ict3r,i1d)
CALL ERRCHECK(IRET)
do i=1,mx
  do k=1,mz
    uuu=rho(i,sect2,k)/factr+0.5-ofstr
    uuu=max(-rlim,uuu)
    uuu=min(rlim,uuu)
    i1d(mz*(i-1)+k)=uuu
  enddo
enddo

```

```

IRET = NF_PUT_VARA_int2(NCID,IDR,ist3r,ict3r,i1d)
CALL ERRCHECK(IRET)
do i=1,mx
  do k=1,mz
    uuu=rhot(i,sect2,k)/factr+0.5-ofstr
    uuu=max(-rlim,uuu)
    uuu=min(rlim,uuu)
    i1d(mz*(i-1)+k)=uuu
  enddo
enddo
IRET = NF_PUT_VARA_int2(NCID,IDRT,ist3r,ict3r,i1d)
CALL ERRCHECK(IRET)

ict2(1)=mx1
ict2(2)=1
ict3(1)=mz
ict3(2)=mx1
ict3(3)=1
ictw(1)=mz
ictw(2)=mx1-1
ictw(3)=1
do j=1,my1
c      print *, ' j=' ,j
      sect=sect2
      sect2=sect1
      sect1=sect
      call userinp(stopog,deep,temp,salt,pref,ts,sect2,j)
      call pvector(stopog,deep,ktop,sims,sect1,sect2,f0,j)
c
c - output
c
      ist2(2)=j
      ist3(3)=j
      ist3r(3)=j+1
      istw(3)=j-1
      do i=1,mx
        do k=1,mz
          uuu=temp(i,k)/fact+0.5-ofstst
          uuu=max(-rlim,uuu)
          uuu=min(rlim,uuu)
          i1d(mz*(i-1)+k)=uuu
        enddo
      enddo
enddo

```

```

IRET = NF_PUT_VARA_int2(NCID,IDT,ist3r,ict3r,i1d)
CALL ERRCHECK(IRET)
do i=1,mx
  do k=1,mz
    uuu=salt(i,k)/fact+0.5-ofstst
    uuu=max(-rlim,uuu)
    uuu=min(rlim,uuu)
    i1d(mz*(i-1)+k)=uuu
  enddo
enddo
IRET = NF_PUT_VARA_int2(NCID,IDS,ist3r,ict3r,i1d)
CALL ERRCHECK(IRET)
do i=1,mx
  do k=1,mz
    uuu=rho(i,sect2,k)/factr+0.5-ofstr
    uuu=max(-rlim,uuu)
    uuu=min(rlim,uuu)
    i1d(mz*(i-1)+k)=uuu
  enddo
enddo
IRET = NF_PUT_VARA_int2(NCID,IDR,ist3r,ict3r,i1d)
CALL ERRCHECK(IRET)
do i=1,mx
  do k=1,mz
    uuu=rhot(i,sect2,k)/factr+0.5-ofstr
    uuu=max(-rlim,uuu)
    uuu=min(rlim,uuu)
    i1d(mz*(i-1)+k)=uuu
  enddo
enddo
IRET = NF_PUT_VARA_int2(NCID,IDRT,ist3r,ict3r,i1d)
CALL ERRCHECK(IRET)

do i=1,mx1
  i1d(i)=invmask(i,j)
enddo

IRET = NF_PUT_VARA_int2(NCID,IDMASKINV,ist2,
&    ict2,i1d)
CALL ERRCHECK(IRET)

```

```

do i=1,mx1
  do k=1,mz
    uuu=u(i,sect2,k)/facu+0.5
    uuu=max(-rlim,uuu)
    uuu=min(rlim,uuu)
    i1d(mz*(i-1)+k)=uuu
  enddo
enddo
IRET = NF_PUT_VARA_int2(NCID,IDU,ist3,ict3,i1d)
CALL ERRCHECK(IRET)
do i=1,mx1
  do k=1,mz
    uuu=v(i,sect2,k)/facu+0.5
    uuu=max(-rlim,uuu)
    uuu=min(rlim,uuu)
    i1d(mz*(i-1)+k)=uuu
  enddo
enddo
IRET = NF_PUT_VARA_int2(NCID,IDV,ist3,ict3,i1d)
CALL ERRCHECK(IRET)
if(j.gt.1) then
do i=1,mx1-1
  do k=1,mz
    uuu=w(i,k)/facw+0.5
    uuu=max(-rlim,uuu)
    uuu=min(rlim,uuu)
    i1d(mz*(i-1)+k)=uuu
  enddo
enddo
IRET = NF_PUT_VARA_int2(NCID,IDW,istw,ictw,i1d)
CALL ERRCHECK(IRET)
endif

do i=1,mx1
  utt=0.0
  do k=2,invmask(i,j)
    utt=utt+(deep(k-1)-deep(k))*

```

```

&          (u(i,sect2,k-1)+u(i,sect2,k))/2.0
      enddo
      utt=utt/facut+0.5
      utt=max(-rlim,utt)
      utt=min(rlim,utt)
      i1d(i)=utt
    enddo
    IRET = NF_PUT_VARA_int2(NCID,IDUTL,ist2,ict2,i1d)
    CALL ERRCHECK(IRET)
    do i=1,mx1
      utt=0.0
      do k=2,invmask(i,j)
        utt=utt+(deep(k-1)-deep(k))*
&          (v(i,sect2,k-1)+v(i,sect2,k))/2.0
      enddo
      utt=utt/facut+0.5
      utt=max(-rlim,utt)
      utt=min(rlim,utt)
      i1d(i)=utt
    enddo
    IRET = NF_PUT_VARA_int2(NCID,IDVTL,ist2,ict2,i1d)
    CALL ERRCHECK(IRET)

    enddo
    close(8)
    close(9)

    IRET = NF_CLOSE(NCID)

    do k=ktop,mz
      veval(k)=veval(k)/(mx*my)
      print 77,k,-deep(k),veval(k)*100.0,(vmax(i,k)*100.0,i=1,6)
      print 88,(ii(i,k),jj(i,k),i=1,6)
    enddo
77    format(/i4,f8.0,7f8.2)
88    format(20x,6(2x,2i3))

    end

```

```

C=====
C
C      SUBROUTINE ERRCHECK(IRET)
C*****
C
C      *ERRCHECK* ERROR HANDLER FOR GRAPHICAL
C      INTERFACE
C
C      AUTHOR - ROGER PROCTOR AND PATRICK LUYTEN
C
C      LAST UPDATE - 12 Jul 1999 @(COHERENS)netcdfint.f
C      8.4
C
C      DESCRIPTION - WRITE ERROR MESSAGE AND STOP
C      EXECUTION OF THE PROGRAM
C      IF AN ERROR OCCURS IN ONE OF THE netCDF
C      ROUTINES
C
C      REFERENCE -
C
C      CALLING PROGRAM - CDF2D, CDF3D
C
C      EXTERNALS - NF_STRERROR
C*****
C
C      INCLUDE 'netcdf.inc'
C
C
C      ARGUMENTS
C
C      INTEGER IRET
C
C      IF (IRET.NE.NF_NOERR) THEN
C        WRITE (0,*) NF_STRERROR(IRET)
C        STOP
C      ENDIF
C
C      RETURN
C      END

```



```

c   2. Inputs:
c
c   lat(mx,my), lon(mx,my) 2-D data
c
c   if(ts>0):
c   temp(mx,mz,my)    temperature
c   salt(mx,mz,my)    salinity
c   if(ts<0):
c   temp(mz,mx,my)    temperature
c   salt(mz,mx,my)    salinity
c
c   3. Outputs:  one Netcdf data format file
c
c-----
c
c----- volume grid size (user defined) -----
c   include 'pstate.h'
c   include 'netcdf.inc'
c
c   common /maxval6/ veval,vmax,ii,jj
c   real veval(nz),vmax(6,nz)
c   integer ii(6,nz),jj(6,nz)
c-----
c   real temp(nx,2,nz),salt(nx,2,nz)
c-----
c   real deg2rad,pi,one
c-----
c   integer j,mx1,my1
c   integer ts,ktop,sect,sect1,sect2
c   real sims,pref
c   real radius,omega,f0
c   real deep(nz), r1d(nx*ny)
c   integer ist3t(3), ict3t(3),
&   dim2d(2), dim3d(3), ist2(2), ist3(3), ict2(2), ict3(3)
c   integer*2 i1d(nx*(ny+nz))
c   real latmin
c   character*30 tempfile,saltfile,ltlnfile,pvoutfile
c   character titl*80, author*30, created*9
c
c   real*8 facu, facw, ofstu,
&   facr, ofstr, fact, ofstt, facts, ofsts
c
c   data facu, facw, ofstu/1.0d-4,1.0d-7,0.0d0/
c   data facr, ofstr/1.0d-3, 28.0d0/
c   data fact, ofstt/1.0d-3, 10.0d0/

```

```

data facts, ofsts/1.0d-3, 20.0d0/

data ist2,ist3,ist3t,ict2,ict3,ict3t/16*1/
c
  latmin=5.0
  zero=0.0
  one=1.0
  pi = 3.1415926535
  deg2rad = pi/180
c
c — cntrl parameters
c
  call pvpar(deep,ktop,pref,ts,sims,tempfile,saltfile,
&          ltlfile,pvoutfile,titl,author)
  my1=my-1
  mx1=mx-1

c — physical and numerical constants
  omega = 7.292e-5
  radius = 6.371e6

  deg2m=deg2rad*radius

c
c — read lat lon binary data
c
  if(abs(ts).eq.1) then
    open(18,file=ltlfile)
    read(18,*) ((lat(i,j),i=1,mx),j=1,my)
    read(18,*) ((lon(i,j),i=1,mx),j=1,my)
    read(18,*) ((y(i,j),i=1,mx),j=1,my)
    read(18,*) ((x(i,j),i=1,mx),j=1,my)
    close(18)
  else
    open(18,file=ltlfile,access='direct',recl=mx*my)
    read(18,rec=1) ((lat(i,j),i=1,mx),j=1,my)
    read(18,rec=2) ((lon(i,j),i=1,mx),j=1,my)
    read(18,rec=3) ((y(i,j),i=1,mx),j=1,my)
    read(18,rec=4) ((x(i,j),i=1,mx),j=1,my)
    close(18)
  endif
endif

```

```

c
c  convert units from km to m
c
do i=1,mx
  do j=1,my
    x(i,j)=x(i,j)*1000.0
    y(i,j)=y(i,j)*1000.0
  enddo
enddo

c-----
c - gridspaceing
c
do i=1,mx1
  i1=i+1
  do j=1,my1
    j1=j+1
    lonm(i,j)=(lon(i,j)+lon(i1,j)+lon(i,j1)+lon(i1,j1))/4.0
    latm(i,j)=(lat(i,j)+lat(i1,j)+lat(i,j1)+lat(i1,j1))/4.0
    dx(i,j)=(x(i1,j)+x(i1,j1)-x(i,j)-x(i,j1))/2.0
    dy(i,j)=(y(i,j1)+y(i1,j1)-y(i,j)-y(i1,j))/2.0
  enddo
enddo

66  continue
c
c - Coriolis (1/s) at the corner of the cell
c
do i=1,mx
  do j=1,my
    if(lat(i,j).lt.latmin .and. lat(i,j).ge.0.0) then
      ff(i,j)=2.*omega*sin(latmin*deg2rad)
    elseif(lat(i,j).gt.-latmin .and. lat(i,j).lt.0.0) then
      ff(i,j)=-2.*omega*sin(latmin*deg2rad)
    else
      ff(i,j)=2.*omega*sin(lat(i,j)*deg2rad)
    endif
  enddo
enddo

c
c - Coriolis (1/s) at the center of the cell
c

```

```

fmax=0.0
fmin=100.0
do i=1,mx1
  do j=1,my1
    if(latm(i,j).lt.latmin .and. latm(i,j).ge.0.0) then
      fm(i,j)=2.*omega*sin(latmin*deg2rad)
    elseif(latm(i,j).gt.-latmin .and. latm(i,j).lt.0.0) then
      fm(i,j)=-2.*omega*sin(latmin*deg2rad)
    else
      fm(i,j) = 2.*omega*sin(latm(i,j)*deg2rad)
    endif
    fmax=max(fmax,abs(fm(i,j)))
    fmin=min(fmin,abs(fm(i,j)))
  enddo
enddo
f0=0.5*(fmin,fmax)

call read_topo(ts,tempfile,saltfile)

call setmask(mx,my,istopog,rmask,invmask,global)

do k=ktop,mz
  do ll=1,6
    vmax(i,k)=0.0
  enddo
  veval(k)=0.0
enddo

call date(created)

print *,created
IRET = NF_CREATE(pvoutfile,NF_CLOBBER,NCID)
CALL ERRCHECK(IRET)
IRET = F_PUT_ATT_TEXT(NCID,NF_GLOBAL,'title',80,titl)
CALL ERRCHECK(IRET)
IRET = NF_PUT_ATT_TEXT(NCID,NF_GLOBAL,'author',39,
&          author//created)
CALL ERRCHECK(IRET)

c
c   defind dimensions (lat, lon, lev)
c

```

```

IRET = NF_DEF_DIM(NCID,'lat',my,IDJTDIM)
CALL ERRCHECK(IRET)
IRET = NF_DEF_DIM(NCID,'lon',mx,IDITDIM)
CALL ERRCHECK(IRET)
IRET = NF_DEF_DIM(NCID,'latuvw',my1,IDJDIM)
CALL ERRCHECK(IRET)
IRET = NF_DEF_DIM(NCID,'lonuvw',mx1,IDIDIM)
CALL ERRCHECK(IRET)
IRET = NF_DEF_DIM(NCID,'lev',mz,IDKDIM)
CALL ERRCHECK(IRET)
c
c   defined coordinate data (deep)
c

IRET = NF_DEF_VAR(NCID,'depth',NF_float,1,
&   IDKDIM,IDZCOORD)
CALL ERRCHECK(IRET)
IRET = NF_PUT_ATT_TEXT(NCID,IDZCOORD,
&   'units',6,'meters')
CALL ERRCHECK(IRET)
c
c   defined lon & lat as 2-D variables
c

dim2d(1)=IDITDIM
dim2d(2)=IDJTDIM
IRET = NF_DEF_VAR(NCID,'lat',NF_float,2,dim2d,IDTLAT)
CALL ERRCHECK(IRET)
IRET = NF_DEF_VAR(NCID,'lon',NF_float,2,dim2d,IDLON)
CALL ERRCHECK(IRET)
dim2d(1)=IDIDIM
dim2d(2)=IDJDIM
IRET = NF_DEF_VAR(NCID,'latuvw',NF_float,2,
&   dim2d,IDLAT)
CALL ERRCHECK(IRET)
IRET = NF_DEF_VAR(NCID,'lonuvw',NF_float,2,
&   dim2d,IDLON)
CALL ERRCHECK(IRET)
c
c   defined 2-D & 3-D variables
c

```

```

dim2d(1)=IDITDIM
dim2d(2)=IDJTDIM
IRET = NF_DEF_VAR(NCID,'itopo',NF_SHORT,2,
&      dim2d,IDITOPO)
CALL ERRCHECK(IRET)
dim3d(1)=IDKDIM
dim3d(2)=IDITDIM
dim3d(3)=IDJTDIM
IRET = NF_DEF_VAR(NCID,'temp',NF_SHORT,3,
&      dim3d,IDTEMP)
CALL ERRCHECK(IRET)
IRET = NF_PUT_ATT_TEXT(NCID,IDTEMP,'units',8,
&      'degree C')
CALL ERRCHECK(IRET)
IRET = NF_PUT_ATT_DOUBLE(NCID,IDTEMP,'scale_factor',
&      NF_double,1,fact)
CALL ERRCHECK(IRET)
IRET = NF_PUT_ATT_DOUBLE(NCID,IDTEMP,'add_offset',
&      NF_double,1,ofstt)
CALL ERRCHECK(IRET)
IRET = NF_DEF_VAR(NCID,'salt',NF_SHORT,3,
&      dim3d,IDSALT)
CALL ERRCHECK(IRET)
IRET = NF_PUT_ATT_TEXT(NCID,IDSALT,'units',3,'psu')
CALL ERRCHECK(IRET)
IRET = NF_PUT_ATT_DOUBLE(NCID,IDSALT,'scale_factor',
&      NF_double,1,facs)
CALL ERRCHECK(IRET)
IRET = NF_PUT_ATT_DOUBLE(NCID,IDSALT,'add_offset',
&      NF_double,1,ofsts)
CALL ERRCHECK(IRET)
IRET = NF_DEF_VAR(NCID,'rhot',NF_SHORT,3,dim3d,
&      IDRHOT)
CALL ERRCHECK(IRET)
IRET = F_PUT_ATT_TEXT(NCID,IDRHOT,'units',6,'kg/m^3')
CALL ERRCHECK(IRET)
IRET = F_PUT_ATT_DOUBLE(NCID,IDRHOT,'scale_factor',
&      NF_double,1,facr)
CALL ERRCHECK(IRET)
IRET = NF_PUT_ATT_DOUBLE(NCID,IDRHOT,'add_offset',
&      NF_double,1,ofstr)
CALL ERRCHECK(IRET)

```

```

dim3d(2)=IDIDIM
dim3d(3)=IDJDIM
dim2d(1)=IDIDIM
dim2d(2)=IDJDIM
IRET = NF_DEF_VAR(NCID,'mask',NF_SHORT,2,
&      dim2d,IDMASK)
CALL ERRCHECK(IRET)
IRET = NF_DEF_VAR(NCID,'maskinv',NF_SHORT,2,
&      dim2d,IDMASKINV)
CALL ERRCHECK(IRET)
IRET = NF_DEF_VAR(NCID,'u',NF_SHORT,3,dim3d,IDU)
CALL ERRCHECK(IRET)
IRET = NF_DEF_VAR(NCID,'v',NF_SHORT,3,dim3d,IDV)
CALL ERRCHECK(IRET)
IRET = NF_DEF_VAR(NCID,'w',NF_SHORT,3,dim3d,IDW)
CALL ERRCHECK(IRET)

dim2d(1)=IDIDIM
dim2d(2)=IDJDIM
IRET = NF_DEF_VAR(NCID,'utl',NF_FLOAT,2,dim2d,IDUTL)
CALL ERRCHECK(IRET)
IRET = NF_DEF_VAR(NCID,'vtl',NF_FLOAT,2,dim2d,IDVTL)
CALL ERRCHECK(IRET)

IRET = NF_PUT_ATT_TEXT(NCID,IDU,'long_name',14,
&      '3-D u-velocity')
CALL ERRCHECK(IRET)
IRET = NF_PUT_ATT_TEXT(NCID,IDU,'units',3,'m/s')
CALL ERRCHECK(IRET)
IRET = NF_PUT_ATT_DOUBLE(NCID,IDU,'scale_factor',
&      NF_double,1,faeu)
CALL ERRCHECK(IRET)
IRET = NF_PUT_ATT_TEXT(NCID,IDV,'long_name',14,
&      '3-D v-velocity')
CALL ERRCHECK(IRET)
IRET = NF_PUT_ATT_TEXT(NCID,IDV,'units',3,'m/s')
CALL ERRCHECK(IRET)
IRET = NF_PUT_ATT_DOUBLE(NCID,IDV,'scale_factor',
&      NF_double,1,faeu)
CALL ERRCHECK(IRET)
IRET = NF_PUT_ATT_TEXT(NCID,IDW,'long_name',14,
&      '3-D W-velocity')
CALL ERRCHECK(IRET)
IRET = NF_PUT_ATT_TEXT(NCID,IDW,'units',3,'m/s')

```

```

CALL ERRCHECK(IRET)
IRET = NF_PUT_ATT_DOUBLE(NCID,IDW,'scale_factor',
&      NF_double,1,fcw)
CALL ERRCHECK(IRET)

IRET = NF_PUT_ATT_TEXT(NCID,IDUTL,'long_name',29,
&      'Vertical Integrate u-velocity')
CALL ERRCHECK(IRET)
IRET = NF_PUT_ATT_TEXT(NCID,IDUTL,'units',6,'m**2/s')
CALL ERRCHECK(IRET)
IRET = NF_PUT_ATT_TEXT(NCID,IDVTL,'long_name',29,
&      'Vertical Integrate v-velocity')
CALL ERRCHECK(IRET)
IRET = NF_PUT_ATT_TEXT(NCID,IDVTL,'units',6,'m**2/s')
CALL ERRCHECK(IRET)

IRET = NF_ENDDEF(NCID)
CALL ERRCHECK(IRET)

```

c

c write lon lat & depth data

c

```

do j=1,my
  do i=1,mx
    r1d(i+mx*(j-1))=lon(i,j)
  enddo
enddo
IRET = NF_PUT_VAR_real(NCID,IDTLON,r1d)
CALL ERRCHECK(IRET)

do j=1,my
  do i=1,mx
    r1d(i+mx*(j-1))=lat(i,j)
  enddo
enddo
IRET = NF_PUT_VAR_real(NCID,IDTLAT,r1d)
CALL ERRCHECK(IRET)
do j=1,my
  do i=1,mx
    i1d(i+mx*(j-1))=istopog(i,j)
  enddo
enddo
IRET = NF_PUT_VAR_int2(NCID,IDITOPO,i1d)
CALL ERRCHECK(IRET)

```

```

do j=1,my1
  do i=1,mx1
    tt1=(lon(i,j)+lon(i+1,j))/2.0
    if(abs(tt1-lon(i,j)).gt.100.0) tt1=tt1+180.0
    tt2=(lon(i,j+1)+lon(i+1,j+1))/2.0
    if(abs(tt2-lon(i,j+1)).gt.100.0) tt2=tt2+180.0
    ttt=(tt1+tt2)/2.0
    if(abs(ttt-tt1).gt.100.0) ttt=ttt+180.0
    if(ttt.gt.180) ttt=ttt-360.0
    r1d(i+mx1*(j-1))=ttt
  enddo
enddo
IRET = NF_PUT_VAR_real(NCID,IDLON,r1d)
CALL ERRRCHECK(IRET)
do j=1,my1
  do i=1,mx1
    r1d(i+mx1*(j-1))=(lat(i,j)+lat(i,j+1)
* +lat(i+1,j)+lat(i+1,j+1))/4.0
  enddo
enddo
IRET = NF_PUT_VAR_real(NCID,IDLAT,r1d)
CALL ERRRCHECK(IRET)
IRET = NF_PUT_VAR_real(NCID,IDZCOORD,deep)
CALL ERRRCHECK(IRET)

do i=1,mx1
  do j=1,my1
    i1d(mx1*(j-1)+i)=rmask(i,j)
  enddo
enddo
IRET = NF_PUT_VAR_int2(NCID,IDMASK,i1d)
CALL ERRRCHECK(IRET)
if(abs(ts).eq.2) then
  open(8,file=tempfile,access='direct',recl=mx*mz)
  open(9,file=saltfile,access='direct',recl=mx*mz)
elseif(abs(ts).eq.1) then
  open(8,file=tempfile)
  open(9,file=saltfile)
else
  print *, ' Must input temp & salt (|ts|=1 or 2)!'
  stop
endif
sect1=2
sect2=1

```

```

call userinp(deep,temp,salt,pref,ts,sect2,0)
call pvector(deep,ktop,sims,sect1,sect2,f0,0)
ict3t(1)=mz
ict3t(2)=mx
ist3t(3)=1

do i=1,mx
  do k=1,mz
    r1d(mz*(i-1)+k)=temp(i,sect2,k)
  enddo
enddo
call real2int2(mx*mz,r1d,fact,ofstt,i1d)
IRET = NF_PUT_VARA_int2(NCID,IDTEMP,ist3t,ict3t,i1d)
CALL ERRCHECK(IRET)

do i=1,mx
  do k=1,mz
    r1d(mz*(i-1)+k)=salt(i,sect2,k)
  enddo
enddo
call real2int2(mx*mz,r1d,facs,ofsts,i1d)
IRET = NF_PUT_VARA_int2(NCID,IDSALT,ist3t,ict3t,i1d)
CALL ERRCHECK(IRET)

do i=1,mx
  do k=1,mz
    r1d(mz*(i-1)+k)=rhot(i,sect2,k)
  enddo
enddo
call real2int2(mx*mz,r1d,facr,ofstr,i1d)
IRET = NF_PUT_VARA_int2(NCID,IDRHOT,ist3t,ict3t,i1d)
CALL ERRCHECK(IRET)

ict2(1)=mx1
ict2(2)=1
ict3(1)=mz
ict3(2)=mx1
ict3(3)=1
do j=1,my1
c   print *, 'j=' , j
  sect=sect2
  sect2=sect1
  sect1=sect
  call userinp(deep,temp,salt,pref,ts,sect2,j)
  call pvector(deep,ktop,sims,sect1,sect2,f0,j)

```

```

c
c - output
c
  do i=1,mx1
    i1d(i)=invmask(i,j)
  enddo
  ist2(2)=j
  IRET = NF_PUT_VARA_int2(NCID,IDMASKINV,ist2,
&    ict2,i1d)
  CALL ERRCHECK(IRET)

  ist3t(3)=j+1
  do i=1,mx
    do k=1,mz
      r1d(mz*(i-1)+k)=temp(i,sect2,k)
    enddo
  enddo
  call real2int2(mx*mz,r1d,fact,ofstt,i1d)
  IRET = NF_PUT_VARA_int2(NCID,IDTEMP,ist3t,ict3t,i1d)
  CALL ERRCHECK(IRET)
  do i=1,mx
    do k=1,mz
      r1d(mz*(i-1)+k)=salt(i,sect2,k)
    enddo
  enddo
  call real2int2(mx*mz,r1d,facs,ofsts,i1d)
  IRET = NF_PUT_VARA_int2(NCID,IDSALT,ist3t,ict3t,i1d)
  CALL ERRCHECK(IRET)

  do i=1,mx
    do k=1,mz
      r1d(mz*(i-1)+k)=rhot(i,sect2,k)
    enddo
  enddo
  call real2int2(mx*mz,r1d,facr,ofstr,i1d)
  IRET = NF_PUT_VARA_int2(NCID,IDRHOT,ist3t,ict3t,i1d)
  CALL ERRCHECK(IRET)
  ist3(3)=j

  do i=1,mx1
    do k=1,mz
      r1d(mz*(i-1)+k)=u(i,k)
    enddo
  enddo

```

```

call real2int2(mx1*mz,r1d,facu,ofstu,i1d)
IRET = NF_PUT_VARA_int2(NCID,IDU,ist3,ict3,i1d)
CALL ERRRCHECK(IRET)

do i=1,mx1
  do k=1,mz
    r1d(mz*(i-1)+k)=v(i,k)
  enddo
enddo
call real2int2(mx1*mz,r1d,facu,ofstu,i1d)
IRET = NF_PUT_VARA_int2(NCID,IDV,ist3,ict3,i1d)
CALL ERRRCHECK(IRET)

do i=1,mx1
  do k=1,mz
    r1d(mz*(i-1)+k)=w(i,k)
  enddo
enddo
call real2int2(mx1*mz,r1d,facw,ofstu,i1d)
IRET = NF_PUT_VARA_int2(NCID,IDW,ist3,ict3,i1d)
CALL ERRRCHECK(IRET)
do i=1,mx1
  r1d(i)=0.0
  do k=2,invmask(i,j)
    r1d(i)=r1d(i)+(deep(k-1)-deep(k))*
&      (u(i,k-1)+u(i,k))/2.0
  enddo
enddo
IRET = NF_PUT_VARA_real(NCID,IDUTL,ist2,ict2,r1d)
CALL ERRRCHECK(IRET)
do i=1,mx1
  r1d(i)=0.0
  do k=2,invmask(i,j)
    r1d(i)=r1d(i)+(deep(k-1)-deep(k))*
&      (v(i,k-1)+v(i,k))/2.0
  enddo
enddo
IRET = NF_PUT_VARA_real(NCID,IDVTL,ist2,ict2,r1d)
CALL ERRRCHECK(IRET)

enddo
close(8)
close(9)

IRET = NF_CLOSE(NCID)

do k=ktop,mz
  veval(k)=veval(k)/(mx*my)

```

```

print 77,k,-deep(k),veval(k)*100.0,(vmax(i,k)*100.0,i=1,6)
print 88,(ii(i,k),jj(i,k),i=1,6)
enddo
77    format(/i4,f8.0,7f8.2)
88    format(20x,6(2x,2i3))
end

```

A.4 Include File (pstate.h)

```

c-----
integer nx,ny,nz
parameter (nx=360,ny=180,nz=50)
common /pstate/rho,rhot,
&      q,px,py,pz,qx,qy,qz,u,v,w,rhox,rhoy,
&      rhotx,rhoty,rhotz,ug,vg,fac_scale,power,
&      lat,ff,zero,one,pi,deg2rad,
&      dx,dy,
&      mx,my,mz,global,istopog,
&      qmask,rmask,invmask

real rho(nx,2,nz),rhot(nx,2,nz)
real q(nx,2,nz)
real px(nx,nz),py(nx,nz),pz(nx,nz)
real qx(nx,nz),qy(nx,nz),qz(nx,nz)
real u(nx,2,nz),v(nx,2,nz),w(nx,nz)
real fac_scale,power
real rhox(nx,nz),rhoy(nx,nz)
real rhotx(nx,nz),rhoty(nx,nz),rhotz(nx,nz)
real ug(nx,nz),vg(nx,nz)
real ff(ny),lat(ny)
real dx(ny),dy,one,zero,pi,deg2rad
integer mx,my,mz,global
integer istopog(nx,ny),rmask(nx,ny),invmask(nx,ny)

```

A.5 Data Input

The *subroutine userinp* is used to read (T , S , H) data into the P-vector inverse model. Here, H is the water depth.

```

*****
subroutine userinp(stopog,deep,temp,salt,pref,ts,sect,j)
include 'pstate.h'
integer i,j,k,ts,sect
real temp(nx,2,nz),salt(nx,2,nz),deep(nz),pref
real pressure,saltd,tempd,dum,svan,tempt,theta
integer stopog(nx,ny)

```

```

c
c — clear local array
c
  do i=1,mx
    do k=1,mz
      rho(i,sect,k)=0.0
      rhot(i,sect,k)=0.0
    enddo
  enddo
c — ts is a keyword, if ts=1 means input temp ans salt,
c otherwise input is rho
c
c ——— (User dependent inputs) ———
c
c
c — read stopog(mx,my)
c — stopog(i,j) is the last 'wet' level in the column (i,j)
c iunit=10
c call read_topo(stopog,deep,iunit)
c
c — read temperature and salinity
c
  read(8,*) ((temp(i,sect,k),i=1,mx),k=1,mz)
  read(9,*) ((salt(i,sect,k),i=1,mx),k=1,mz)
c ——— (end of user dependent inputs) ———
c
c — compute in situ density RHO and potential density RHOT
c
c Note: To minimize roundoff use sig=rho-1000.
c svan is UNESCO (Fofonoff) subroutine.

do i=1, mx
  do k=1, istopog(i,j+1)
    pressure= abs(deep(k))
    saltd=salt(i,sect,k)
    tempd=temp(i,sect,k)
    dum = svan(saltd,tempd,pressure,rho(i,sect,k) )
    if (pref .lt.0) then
      rhot(i,sect,k)=rho(i,sect,k)
    else
      tempt= theta(saltd,tempd,pressure,pref)
      dum = svan(saltd,tempt,pref,rhot(i,sect,k))
    end if
  end do
end do

```

```

        endif
    enddo
enddo
return
end

subroutine read_topo(stopog,deep,iunit,ts,topofile,
&                saltfile)
c -----
c   USER supplied subroutine to:
c
c   read stopog(1:mx,1:my) where
c   stopog(i,j) is the depth and
c   istopog(i,j) is the last wet point at (i,j);
c   that is, at (i,j) the levels istopog(i,j)+1,...,mz
c   if any, are land points.
c -----
    include 'pstate.h'
    integer iunit,i,j,k,ts
    integer stopog(nx,ny),minto
    real deep(nz)
    character*30 topofile,saltfile
c -----
    open(iunit,file=topofile,form='formatted')
    do j=1,my
        read(iunit,*) (stopog(i,j),i=1,mx)
    enddo
    close(iunit)
    minto=1000
    do i=1,mx
        do j=1,my
            minto=min(minto,stopog(i,j))
        enddo
    enddo
    if(minto.lt.-2) then
        do i=1,mx
            do j=1,my
                istopog(i,j)=0
                do k=1,mz
                    if(deep(k).ge.stopog(i,j)) istopog(i,j)=k
                enddo
            enddo
        enddo
    enddo
enddo
enddo

```

```

else
  do i=1,mx
    do j=1,my
      istopog(i,j)=stopog(i,j)
      stopog(i,j)=deep(istopog(i,j))
    enddo
  enddo
endif
if(ts.eq.2) then
  open(iunit,file=saltfile)
  do j=1,my
    read(iunit,*) ((w(i,k),i=1,mx),k=1,mz)
    do i=1,mx
      minto=0
      do k=1,mz
        if(w(i,k).gt.-80.0) minto=k
      enddo
      istopog(i,j)=min(istopog(i,j),minto)
    enddo
  enddo
  close(iunit)
endif

return
end

```

A.6 Equation of State (whoi.f)

The program *whoi.f* is used to calculate density from (T, S).

```

C Program whoi.f
C JUNE 24 1982
  REAL FUNCTION SVAN(S,T,P0,SIGMA)
C MODIFIED RCM
C *****
C SPECIFIC VOLUME ANOMALY (STERIC ANOMALY) BASED ON
  1980 EQUATION
C OF STATE FOR SEAWATER AND 1978 PRACTICAL SALINITY
  SCALE.
C REFERENCES
C MILLERO, ET AL (1980) DEEP-SEA RES.,27A,255-264
C MILLERO & POISSON 1981,DEEP-SEA RES.,28A PP 625-629.
C BOTH ABOVE REFERENCES ARE ALSO FOUND IN UNESCO
  REPORT 38 (1981)

```

```

C   UNITS:
C   PRESSURE  P0  DECIBARS
C   TEMPERATURE  T  DEG  CELSIUS (IPTS-68)
C   SALINITY  S  PSU  (IPSS-78)
C   SPEC. VOL. ANA. SVAN  M**3/KG *1.0E-8
C   DENSITY ANA.  SIGMA  KG/M**3
C   CHECK VALUE: SVAN = 981.30190 M**3/KG FOR S = 40 PSU,
C   T = 40 DEG C, P0= 10000 DECIBARS.
C *****
C *****
C CHECK VALUE: SIGMA = 59.82037 KG/M**3 FOR S = 40 PSU,
C T = 40 DEG C, P0= 10000 DECIBARS.
C *****
C *****
C   REAL P,T,S,SIG,SR,R1,R2,R3,R4
C   REAL A,B,C,D,E,A1,B1,AW,BW,K,K0,KW,K35
C EQUIV
C   EQUIVALENCE (E,D,B1),(BW,B,R3),(C,A1,R2)
C   EQUIVALENCE (AW,A,R1),(KW,K0,K)
C *****
C DATA
C   DATA R3500,R4/1028.1063,4.8314E-4/
C   DATA DR350/28.106331/
C   R4 IS REFERED TO AS C IN MILLERO & POISSON 1981
C CONVERT PRESSURE TO BARS AND TAKE SQUARE
C ROOT SALINITY.
C   P=P0/10.
C   SR = SQRT(ABS(S))
C *****
C PURE WATER DENSITY AT ATMOSPHERIC PRESSURE
C BIGG P.H.,(1967) BR. J. APPLIED PHYSICS 8 PP 521-537.
C
C   R1 = (((((6.536332E-9*T-1.120083E-6)*T+1.001685E-4)*T
C   X-9.095290E-3)*T+6.793952E-2)*T-28.263737
C SEAWATER DENSITY ATM PRESS.
C COEFFICIENTS INVOLVING SALINITY
C R2 = A IN NOTATION OF MILLERO & POISSON 1981
C   R2 = (((5.3875E-9*T-8.2467E-7)*T+7.6438E-5)*T-4.0899E-3)*T
C   X+8.24493E-1
C R3 = B IN NOTATION OF MILLERO & POISSON 1981
C   R3 = (-1.6546E-6*T+1.0227E-4)*T-5.72466E-3
C INTERNATIONAL ONE-ATMOSPHERE EQUATION OF STATE OF
C SEAWATER
C   SIG = (R4*S + R3*SR + R2)*S + R1
C SPECIFIC VOLUME AT ATMOSPHERIC PRESSURE
C   V350P = 1.0/R3500
C   SVA = -SIG*V350P/(R3500+SIG)
C   SIGMA=DR350-(SVA/(V350P*(V350P+SVA)))

```

```

C SCALE SPECIFIC VOL. ANAMOLY TO NORMALLY REPORTED
  UNITS
  SVAN=SVA*1.0E+8
  IF(P.EQ.0.0) RETURN
C *****
C ***** NEW HIGH PRESSURE EQUATION OF STATE FOR
  SEAWATER *****
C *****
C COMPUTE COMPRESSION TERMS
  E = (9.1697E-10*T+2.0816E-8)*T-9.9348E-7
  BW = (5.2787E-8*T-6.12293E-6)*T+3.47718E-5
  B = BW + E*S
C
  D = 1.91075E-4
  C = (-1.6078E-6*T-1.0981E-5)*T+2.2838E-3
  AW = ((-5.77905E-7*T+1.16092E-4)*T+1.43713E-3)*T
  X-0.1194975
  A = (D*SR + C)*S + AW
C
  B1 = (-5.3009E-4*T+1.6483E-2)*T+7.944E-2
  A1 = ((-6.1670E-5*T+1.09987E-2)*T-0.603459)*T+54.6746
  KW = (((-5.155288E-5*T+1.360477E-2)*T-2.327105)*T
  X+148.4206)*T-1930.06
  K0 = (B1*SR + A1)*S + KW
C EVALUATE PRESSURE POLYNOMIAL
C *****
C K EQUALS THE SECANT BULK MODULUS OF SEAWATER
C DK=K(S,T,P)-K(35,0,P)
C K35=K(35,0,P)
C *****
  DK = (B*P + A)*P + K0
  K35 = (5.03217E-5*P+3.359406)*P+21582.27
  GAM=P/K35
  PK = 1.0 - GAM
  SVA = SVA*PK + (V350P+SVA)*P*DK/(K35*(K35+DK))
C SCALE SPECIFIC VOL. ANAMOLY TO NORMALLY REPORTED UNITS
  SVAN=SVA*1.0E+8
  V350P = V350P*PK
C *****
C COMPUTE DENSITY ANAMOLY WITH RESPECT TO 1000.0 KG/M**3
C 1) DR350: DENSITY ANAMOLY AT 35 PSU 0 DEG. C & ATMOSPHERIC
  PRES.
C 2) DR35P: DENSITY ANAMOLY 35 PSU 0 DEG. C , WITH PRES.
  VARIATION

```

```

C 3) DVAN : DENSITY ANAMOLY VARIATIONS INVOLVING SPECIFIC
      VOL. ANAMOLY
C *****
C CHECK VALUE: SIGMA = 59.82037 KG/M**3 FOR S = 40 PSU,
C T = 40 DEG C, P0= 10000 DECIBARS.
C *****
      D350=GAM/PK
      DR35P=R3500*D350
      DVAN=SVA/(V350P*(V350P+SVA))
      SIGMA=DR350+DR35P-DVAN
      RETURN
      END
C SAL78 FCN ***** OCT 24 1979 *****
      REAL FUNCTION SAL78(CND,T,P,C1535,M)
C *****
C
C FUNCTION TO CONVERT CONDUCTIVITY TO SALINITY (M = 0)
      OR
C SALINITY TO CONDUCTIVITY (M = 1,CND = SAL)
C*****
C REFERENCES: ALSO LOCATED IN UNESCO REPORT # 37 1981
C PRACTICAL SALINITY SCALE 1978: E.L. LEWIS IEEE OCEAN
      ENG. JAN. 1980
C CONDUCTIVITY AT S=35.,T=15,P=0: CULKIN & SMITH IEEE
      OCEAN ENG. 1980.
C *****
C C1535 = 42.914 MMHO/CM ADOPTED VALUE OF ABSOLUTE
      CONDUCTIVITY AT
C SALINITY 35 PSU AND TEMPERATURE 15 DEG CELSIUS
      (IPSS-68) FOR
C ATMOSPHERIC (0 DECIBARS) PRESSURE
C SAL78: RETURNS ZERO FOR CONDUCTIVITY: < 0.0005 MMHO/CM.
C SAL78: RETURNS ZERO FOR SALINITY: < 0.02 PSU
C UNITS:
C PRESSURE P DECIBARS
C TEMPERATURE T DEG CELSIUS (IPSS-68)
C CONDUCTIVITY CND MMHO/CM.
C SALINITY SAL78 PSU (IPSS-78)
C CHECKVALUE: FOR C1535=42.914 MMHO/CM
C SAL78 = 81.02555 :S=40 PSU,T=40 DEG C,P=10000
      DECIBARS:M=0

```

```

C   SAL78 = 40.00000 FOR G = 81.02555,T=40 DEG C,P=10000
      DECIBARS:M=1
C N FOFONOFF, REVISED JUNE 8 1982
C C *****
C INTERNAL FUNCTIONS
C *****
C PRACTICAL SALINITY SCALE 1978 DEFINITION WITH
TEMPERATURE CORRECTION
C XT=T-15.0 : XR=SQRT(RT)
      SAL(XR,XT) = (((2.7081*XR-7.0261)*XR+14.0941)*XR+25.3851)*XR
      X-0.1692)* XR+0.0080
C TEMPERATURE CORRECTION TO 1978 PRACTICAL SALINITY
SCALE: (XT=T-15.0)
      X +(XT/(1.0+0.0162*XT))*(((((-0.0144*XR+
      X 0.0636)*XR-0.0375)*XR-0.0066)*XR-0.0056)*XR+0.0005)
C DSAL(XR,XT) EXPLICIT FUNCTION FOR DERIVATIVE
OF SAL(XR,XT)
C WITH RESPECT TO CONDUCTIVITY RATIO XR.
      DSAL(XR,XT) = (((13.5405*XR-28.1044)*XR+42.2823)*XR+50.7702)*XR
      X -0.1692)+(XT/(1.0+0.0162*XT))*(((((-0.0720*XR+0.2544)*XR
      X -0.1125)*XR-0.0132)*XR-0.0056)
C FUNCTION RT35 : CONDUCTIVITY RATIO C(35,T,0)/C(35,15,0)
VARIATION
C WITH TEMPERATURE.
      RT35(XT) = (((1.0031E-9*XT-6.9698E-7)*XT+1.104259E-4)*XT
      X + 2.00564E-2)*XT + 0.6766097
C POLYNOMIALS OF RP: CONDUCTIVITY RATIO C(S,T,P)/C(S,T,0)
PRESSURE
C VARIATION: COEFFICIENTS PRESSURE SET FOR UNITS OF
DECIBARS!!
C C(XP) POLYNOMIAL CORRESPONDS TO A1-A3 CONSTANTS:
LEWIS 1980
      C(XP) = ((3.989E-15*XP-6.370E-10)*XP+2.070E-5)*XP
      B(XT) = (4.464E-4*XT+3.426E-2)*XT + 1.0
C A(XT) POLYNOMIAL CORRESPONDS TO B3 & B4 CONSTANTS:
LEWIS 1980
      pcA(XT) = -3.107E-3*XT + 0.4215
C *****
C TEST FOR ZERO OR NEGATIVE ABSOLUTE CONDUCTIVITY
C SET DEFAULT CONDUCTIVITY VALUE AT S=35, T=15 &
ATMOSPHERIC PRES.
      IF(C1535.LE.0.0) C1535=42.914
C *****

```

```

C ZERO SALINITY/CONDUCTIVITY TRAP
  SAL78=0.0
  IF((M.EQ.0).AND.(CND.LE.5E-4)) RETURN
  IF((M.EQ.1).AND.(CND.LE.0.02)) RETURN
C *****
  DT = T - 15.0
C SELECT BRANCH FOR SALINITY (M=0) OR CONDUCTIVITY
  (M=1)
  IF(M.EQ.1) GO TO 10
C *****
C CONVERT CONDUCTIVITY TO SALINITY
  R = CND/C1535
  RT = R/(RT35(T)*(1.0 + C(P)/(B(T) + A(T)*R)))
  RT = SQRT(ABS(RT))
  SAL78 = SAL(RT,DT)
  RETURN
C ***** END OF CONDUCTIVITY TO SALINITY SECTION ***
C *****
C INVERT SALINITY TO CONDUCTIVITY BY THE
C NEWTON-RAPHSON ITERATIVE METHOD.
C *****
C FIRST APPROXIMATION
  RT = SQRT(CND/35.0)
  SI = SAL(RT,DT)
  N = 0
C
C ITERATION LOOP BEGINS HERE WITH A MAXIMUM OF
  10 CYCLES
C
  RT = RT + (CND - SI)/DSAL(RT,DT)
  SI = SAL(RT,DT)
  N = N + 1
  DELS = ABS(SI - CND)
  IF((DELS.GT.1.0E-4).AND.(N.LT.10))GO TO 15
C
C *****END OF ITERATION LOOP *****
C
C COMPUTE CONDUCTIVITY RATIO
  RTT = RT35(T)*RT*RT
  AT = A(T)
  BT = B(T)
  CP = C(P)
  CP = RTT*(CP + BT)
  BT = BT - RTT*AT

```

480 A P-Vector Module for z-Coordinate

```
C
C SOLVE QUADRATIC EQUATION FOR R: R=RT35*RT*(1+C/AR+B)
C
  R = SQRT(ABS(BT*BT + 4.0*AT*CP)) - BT
C CONDUCTIVITY RETURN
  SAL78 = 0.5*C1535*R/AT
  RETURN
  END
C DEPTH FCN ***** OCT 7 1980 *****
  REAL FUNCTION DEPTH(P0,LAT)
C *****
C DEPTH IN METERS FROM PRESSURE IN BARS USING
C SAUNDERS AND FOFONOFF'S METHOD.
C DEEP-SEA RES., 1976,23,109-111.
C FORMULA REFITTED FOR 1980 EQUATION OF STATE
C UNITS:
C   PRESSURE    P0    DECIBARS
C   DEPTH       DEPTH METERS
C CHECKVALUE: DEPTH = 9712.654 M FOR P=10000 DECIBARS,
  LATITUDE=30 DEG
C   ABOVE FOR STANDARD OCEAN: T=0 DEG. CELSUIS ; S=35 PSU
C
  REAL LAT
C
  X = SIN(LAT/57.29578)
C SCALE PRESSURE TO BARS
  P=P0/10.
C*****
  X = X*X
C GR= GRAVITY VARIATION WITH LATITUDE: ANON (1970)
  BULLETIN GEODESIQUE
  GR = 9.780318*(1.0+(5.2788E-3+2.36E-5*X)*X) + 1.092E-5*P
  DEPTH = (((-1.82E-11*P+2.279E-7)*P-2.2512E-3)*P+97.2659)*P
  DEPTH=DEPTH/GR
  RETURN
  END
C CPSW FCN *** OCT 3 1980 *****
  REAL FUNCTION CPSW(S,T,P0)
C *****
C SPECIFIC HEAT OF SEAWATER J/KG
C SALINITY PSU (IPSS-78), TEMPERATURE DEG. CELSIUS (IPSS-68),
C PRESSURE IN DECIBARS.
```

```

C REF: MILLERO ET AL,1973,JGR,78,4499-4507
C PRESSURE VARIATION FROM LEAST SQUARES POLYNOMIAL
C DEVELOPED BY FOFONOFF 1980.
C CHECK VALUE: CPSW = 3850.309 J/KG FOR S = 40 PSU,
C T = 40 DEG C, P0= 10000 DECIBARS
C SCALE PRESSURE TO BARS
  P=P0/10.
C*****
C SQRT SALINITY FOR FRACTIONAL TERMS
  SR = SQRT(ABS(S))
C SPECIFIC HEAT CP0 FOR P=0 (MILLERO ET AL 1973)
  A = (-1.3839E-3*T+0.107276)*T-7.6444
  B = (5.3539E-5*T-4.0772E-3)*T+0.17709
  C = (((2.093236E-5*T-2.654387E-3)*T+0.1412855)*T
  X  -3.720283)*T+4217.4
  CP0 = (B*SR + A)*S + C
C CP1 PRESSURE AND TEMPERATURE TERMS FOR S = 0
  A = (((1.7168E-8*T+2.0357E-6)*T-3.13885E-4)*T+1.45747E-2)*T
  X  -0.49592
  B = (((2.2956E-11*T-4.0027E-9)*T+2.87533E-7)*T-1.08645E-5)*T
  X  +2.4931E-4
  C = ((6.136E-13*T-6.5637E-11)*T+2.6380E-9)*T-5.422E-8
  CP1 = ((C*P+B)*P+A)*P
C CP2 PRESSURE AND TEMPERATURE TERMS FOR S > 0
  A = (((-2.9179E-10*T+2.5941E-8)*T+9.802E-7)*T-1.28315E-4)*T
  X  +4.9247E-3
  B = (3.122E-8*T-1.517E-6)*T-1.2331E-4
  A = (A+B*SR)*S
  B = ((1.8448E-11*T-2.3905E-9)*T+1.17054E-7)*T-2.9558E-6
  B = (B+9.971E-8*SR)*S
  C = (3.513E-13*T-1.7682E-11)*T+5.540E-10
  C = (C-1.4300E-12*T*SR)*S
  CP2 = ((C*P+B)*P+A)*P
C SPECIFIC HEAT RETURN
  CPSW = CP0 + CP1 + CP2
  RETURN
  END
C ATG FCN *** OCT 20 1980 ****
  REAL FUNCTION ATG(S,T,P0)
C *****
C ADIABATIC TEMPERATURE GRADIENT DEG C PER DECIBAR
C REF: BRYDEN,H.,1973,DEEP-SEA RES.,20,401-408
C UNITS:

```

482 A P-Vector Module for z-Coordinate

```
C PRESSURE P0 DECIBARS
C TEMPERATURE T DEG CELSIUS (IPTS-68)
C SALINITY S PSU (IPSS-78)
C ADIABATIC ATG DEG. C/DECIBAR
C CHECK: ATG=3.255976E-4 C/DBAR FOR S=40 PSU,T=40 DEG C,
P0=10000 DECIBAR
C SCALE PRESSURE TO BARS
P=P0/10.
C*****
DS = S - 35.0
ATG = (((-2.1687E-13*T+1.8676E-11)*T-4.6206E-10)*P
X+((2.7759E-10*T-1.1351E-8)*DS+((-5.4481E-12*T
X+8.733E-10)*T-6.7795E-8)*T+1.8741E-6))*P
X+(-4.2393E-7*T+1.8932E-5)*DS
X+((6.6228E-9*T-6.836E-7)*T+8.5258E-5)*T+3.5803E-4
C SCALE ATG TO PER DECIBAR
ATG=0.1*ATG
C*****
RETURN
END
C THETA FCN ***** OCT 20 1980 *****
REAL FUNCTION THETA(S,T0,P0,PR)
C *****
C TO COMPUTE LOCAL POTENTIAL TEMPERATURE AT PR
C USING BRYDEN 1973 POLYNOMIAL FOR ADIABATIC LAPSE
C RATE AND RUNGE-KUTTA 4-TH ORDER INTEGRATION
C ALGORITHM.
C REF: BRYDEN,H.,1973,DEEP-SEA RES.,20,401-408
C FOFONOFF,N.,1977,DEEP-SEA RES.,24,489-491
C UNITS:
C PRESSURE P0 DECIBARS
C TEMPERATURE T0 DEG CELSIUS (IPTS-68)
C SALINITY S PSU (IPSS-78)
C REFERENCE PRS PR DECIBARS
C POTENTIAL TMP. THETA DEG CELSIUS
C CHECKVALUE: THETA= 36.89072 C,S=40 PSU,T0=40 DEG C,
C P0=10000 DECIBARS,PRS=0 DECIBARS
C
C SET-UP INTERMEDIATE TEMPERATURE AND PRESSURE
VARIABLES
P=P0
T=T0
C*****
H = PR - P
XK = H*ATG(S,T,P)
```

```

T = T + 0.5*XK
Q = XK
P = P + 0.5*H
XK = H*ATG(S,T,P)
T = T + 0.29289322*(XK-Q)
Q = 0.58578644*XK + 0.121320344*Q
XK = H*ATG(S,T,P)
T = T + 1.707106781*(XK-Q)
Q = 3.414213562*XK - 4.121320344*Q
P = P + 0.5*H
XK = H*ATG(S,T,P)
THETA = T + (XK-2.0*Q)/6.0
RETURN
END
C SVEL FCN **** OCT 4 1980 *****
REAL FUNCTION SVEL(S,T,P0)
C *****
C SOUND SPEED SEAWATER CHEN & MILLERO 1977,JASA,62,
C 1129-1135 UNITS:
C PRESSURE P0 DECIBARS
C TEMPERATURE T DEG CELSIUS (IPSS-68)
C SALINITY S PSU (IPSS-78)
C SOUND SPEED SVEL METERS/SECOND
C CHECKVALUE: 1731.995 M/S FOR P0=10000 DECIBARS,
C T=40 DEG C, S=40 PSU
C
C EQUIVALENCE (A0,B0,C0),(A1,B1,C1),(A2,C2),(A3,C3)
C
C SCALE PRESSURE TO BARS
P=P0/10.
C*****
SR = SQRT(ABS(S))
C S**2 TERM
D = 1.727E-3 - 7.9836E-6*P
C S**3/2 TERM
B1 = 7.3637E-5 + 1.7945E-7*T
B0 = -1.922E-2 - 4.42E-5*T
B = B0 + B1*P
C S**1 TERM
A3 = (-3.389E-13*T+6.649E-12)*T+1.100E-10
A2 = ((7.988E-12*T-1.6002E-10)*T+9.1041E-9)*T-3.9064E-7
A1 = (((-2.0122E-10*T+1.0507E-8)*T-6.4885E-8)*T-1.2580E-5)*T
X +9.4742E-5

```

484 A P-Vector Module for z-Coordinate

```
A0 = (((-3.21E-8*T+2.006E-6)*T+7.164E-5)*T-1.262E-2)*T
X   +1.389
A = ((A3*P+A2)*P+A1)*P+A0
C S**0 TERM
C3 = (-2.3643E-12*T+3.8504E-10)*T-9.7729E-9
C2 = (((1.0405E-12*T-2.5335E-10)*T+2.5974E-8)*T-1.7107E-6)*T
X   +3.1260E-5
C1 = (((-6.1185E-10*T+1.3621E-7)*T-8.1788E-6)*T+6.8982E-4)*T
X   +0.153563
C0 = (((3.1464E-9*T-1.47800E-6)*T+3.3420E-4)*T-5.80852E-2)*T
X   +5.03711)*T+1402.388
C = ((C3*P+C2)*P+C1)*P+C0
C SOUND SPEED RETURN
SVEL = C + (A+B*SR+D*S)*S
RETURN
END
C
C BRVAL ***** BRUNT-VAISALA FREQ *****
C USES 1980 EQUATION OF STATE
FUNCTION BVFRQ(S,T,P,NOBS,PAV,E)
C *****
C UNITS:
C PRESSURE P0 DECIBARS
C TEMPERATURE T DEG CELSIUS (IPTS-68)
C SALINITY S PSU (IPSS-78)
C BOUYANCY FREQ BVFRQ CPH
C N**2 E RADIANS/SECOND
C CHECKVALUE: BVFRQ=14.57836 CPH E=6.4739928E-4 RAD/SEC.
C S(1)=35.0, T(1)=5.0, P(1)=1000.0
C S(2)=35.0, T(2)=4.0, P(2)=1002.0
C *****NOTE RESULT CENTERED AT PAV=1001.0 DBARS *****
C R MILLARD
C JULY 12 1982
C COMPUTES N IN CYCLES PER HOUR, & E=N**2 IN RAD/SEC**2
C AFTER FORMULATION OF BRECK OWEN'S
REAL*4 P(1),T(1),S(1)
E=0.0
BVFRQ=0.0
IF(NOBS.LT.2) RETURN
CXX=0.0
CX=0.0
```

```

CXY=0.0
CY=0.0
C COMPUTE LEAST SQUARES ESTIMATE OF SPECIFIC VOLUME
ANAMOLY GRADIENT
DO 20 K=1,NOBS
20 CX =CX+P(K)
PAV=CX/NOBS
DO 35 K=1,NOBS
DATA= SVAN(S(K),THETA(S(K),T(K),P(K),PAV),PAV,SIG)*1.0E-8
CXY=CXY+DATA*(P(K)-PAV)
CY =CY+DATA
CXX=CXX+(P(K)-PAV)**2
35 CONTINUE
IF(CXX.EQ.0.0) RETURN
A0=CXY/CXX
V350P=(1./(SIG+1000.))-DATA
VBAR=V350P+CY/NOBS
DVDP=A0
C
IF(VBAR.EQ.0.0) RETURN
E = -.96168423E-2*DVDP/(VBAR)**2
BVFRQ = 572.9578*SIGN(SQRT(ABS(E)),E)
RETURN
END

```

A.7 P-Vector Calculation

The subroutine *pvector* is used to compute the P-vector.

```

*****
subroutine pvector(stopog,deep,ktop,sims,sect1,sect2,f0,j)
include 'pstate.h'
common /maxval6/ veval,vmax,ii,jj
real veval(nz),vmax(6,nz)
integer ii(6,nz),jj(6,nz)
integer sect1,sect2

```

```

c-----
real aa,aa1,aa2,aa3,dr,dq,drdq
real fac
c-----
real dz,dz1,dz2
real zero,one,two,small,sims
real g,rho0
integer i,j,i1,j1,k,kk,kk1,kk2,kbot
integer mx1,mz1,kpv(nz),mkpv,ktop
integer stopog(nx,ny)
real uref,vref,deep(nz)
real minlat
c-----
real f0,small_rhotz
real a11,a12,a22,t11,t12,t22,ff1,ff2,wk,rxz,ryz
integer jms,jmn
c - physical constants
g=9.81
rho0=1028.0
c - numerical constants
zero=0.0
one=1.0
two=2.0
small=1.e-7
minlat=5.0
jms=1
jmn=0
mz1=mz-1
mx1=mx-1
if(global.gt.0) mx1=mx

small_rhotz=1.0e-20
c  f0=0.5*(abs(ff(1))+abs(ff(my)))
c
c - clear local array
c
do i=1,mx
do k=1,mz
rhop(i,k)=0.0
rhoy(i,k)=0.0
rhotx(i,k)=0.0
rhoty(i,k)=0.0
rhotz(i,k)=0.0
q(i,sect2,k)=0.0

```

```

qx(i,k)=0.0
qy(i,k)=0.0
qz(i,k)=0.0
px(i,k)=0.0
py(i,k)=0.0
pz(i,k)=0.0
ug(i,k)=0.0
vg(i,k)=0.0
u(i,sect2,k)=0.0
v(i,sect2,k)=0.0
w(i,k)=0.0
  enddo
  enddo

c
c – calculate potential velocity q= f drhot/dz:
c
do i=1,mx
  kbot=istopog(i,j+1)
  if(kbot.ge.2) then
    q(i,sect2,1)=ff(j+1)*(rhot(i,sect2,1)-rhot(i,sect2,2))/
&      (deep(1)-deep(2))/f0
    q(i,sect2,kbot)=ff(j+1)*(rhot(i,sect2,kbot-1)-
&      rhot(i,sect2,kbot))/(deep(kbot-1)-deep(kbot))/f0
    do k=2,kbot-1
      dz1=deep(k-1)-deep(k)
      dz2=deep(k)-deep(k+1)
      dz= dz1+dz2
      q(i,sect2,k)=ff(j+1)/f0*((rhot(i,sect2,k-1)-rhot(i,sect2,k))
&
&      *dz2/(dz1*dz)+(rhot(i,sect2,k)-
&      rhot(i,sect2,k+1))*dz1/(dz2*dz))
      enddo
    endif
  enddo
  if(j.eq.0) return

c
c –      rhotz=d rhot/dz and qz=dq/dz in the wet domain starting
from ktop
c      Not: rhotz and qz at the staged grid(B grid)
c

```

```

do i=1,mx1
  il=i+1
  if(il.gt.mx) il=i1-mx
  if(rmask(i,j).gt.1) then
kbot=rmask(i,j)
rhotz(i,1)=0.25*(rhot(i,sect1,1)+rhot(il,sect1,1)+
*       rhot(i,sect2,1)+rhot(il,sect2,1)-
*       rhot(i,sect1,2)-rhot(il,sect1,2)-
*       rhot(i,sect2,2)-rhot(il,sect2,2))/
*       (deep(1)-deep(2))
qz(i,1)=0.25*(q(i,sect1,1)+q(il,sect1,1)+
*       q(i,sect2,1)+q(il,sect2,1)-q(i,sect1,2)-
*       q(il,sect1,2)-q(i,sect2,2)-
*       q(il,sect2,2))/(deep(1)-deep(2))
rhotz(i,kbot)=(rhot(i,sect1,kbot-1)+
*       rhot(il,sect1,kbot-1)+
*       rhot(i,sect2,kbot-1)+rhot(il,sect2,kbot-1)-
*       rhot(i,sect1,kbot)-rhot(il,sect1,kbot)-
*       rhot(i,sect2,kbot)-rhot(il,sect2,kbot))/
*       (deep(kbot-1)-deep(kbot))/4.0
qz(i,kbot)=-1.0
do k=2,kbot-1
  pcdz1=deep(k-1)-deep(k)
  dz2=deep(k)-deep(k+1)
  dz= dz1+dz2
  aa1=rhot(i,sect1,k-1)+rhot(il,sect1,k-1)+
*     rhot(i,sect2,k-1)+rhot(il,sect2,k-1)
  aa2=rhot(i,sect1,k)+rhot(il,sect1,k)+
*     rhot(i,sect2,k)+rhot(il,sect2,k)
  aa3=rhot(i,sect1,k+1)+rhot(il,sect1,k+1)+
*     rhot(i,sect2,k+1)+rhot(il,sect2,k+1)
  rhotz(i,k)=0.25*((aa1-aa2)*dz2/(dz1*dz)+
*     (aa2-aa3)*dz1/(dz2*dz))
  aa1=q(i,sect1,k-1)+q(il,sect1,k-1)+q(i,sect2,k-1)
*     +q(il,sect2,k-1)
  aa2=q(i,sect1,k)+q(il,sect1,k)+q(i,sect2,k)
*     +q(il,sect2,k)
  aa3=q(i,sect1,k+1)+q(il,sect1,k+1)+q(i,sect2,k+1)
*     +q(il,sect2,k+1)
  qz(i,k)=0.25*((aa1-aa2)*dz2/(dz1*dz)+
*     (aa2-aa3)*dz1/(dz2*dz))
  enddo
endif
enddo

```

```

c
c - scale the d/dz
c
  do i=1,mx1
    do k=1,mz
      rhotz(i,k)=rhotz(i,k)*fac_scale
      qz(i,k)=qz(i,k)*fac_scale
    enddo
  enddo

c
c - calculate rhotx, rhoty, rhotz, rhox and rhoxy
c - rhox=d rho/dx; rhoxy= d rho/dy; etc.
c
  do i=1,mx1
    i1=i+1
    if(i1.gt.mx) i1=i1-mx
    kbot=rmask(i,j)
    if(kbot.ge.1) then
      do k=1,kbot
        rhox(i,k)=(rho(i1,sect1,k)+rho(i1,sect2,k)-
*         rho(i,sect1,k)-rho(i,sect2,k))/(dx(j)+dx(j+1))
        rhoxy(i,k)=-(rho(i,sect2,k)+rho(i1,sect2,k)-
*         rho(i,sect1,k)-rho(i1,sect1,k))/(2.0*dy)
        rhotx(i,k)=(rhot(i1,sect1,k)+rhot(i1,sect2,k)-
*         rhot(i,sect1,k)-rhot(i,sect2,k))/(dx(j)+dx(j+1))
        rhoty(i,k)=-(rhot(i,sect2,k)+rhot(i1,sect2,k)-
*         rhot(i,sect1,k)-rhot(i1,sect1,k))/(2.0*dy)
        qx(i,k)=(q(i1,sect1,k)+q(i1,sect2,k)-q(i,sect1,k)
*         -q(i,sect2,k))/(dx(j)+dx(j+1))
        qy(i,k)=-(q(i,sect2,k)+q(i1,sect2,k)-q(i,sect1,k)
*         -q(i1,sect1,k))/(2.0*dy)
      enddo
      qx(i,kbot)=(stopog(i1,j)+stopog(i1,j+1)-stopog(i,j)-
*         stopog(i,j+1))/(dx(j)+dx(j+1))
      qy(i,kbot)=-(stopog(i1,j+1)+stopog(i,j+1)-stopog(i1,j)-
*         stopog(i,j))/(2.0*dy)
    c - compute geostrophic shear (trapezoidal rule)
      fac=g/((ff(j)+ff(j+1))*rho0)
      ug(i,kbot)=0.0
      vg(i,kbot)=0.0
      do k=kbot,2,-1

```

```

        ug(i,k-1)=ug(i,k)+fac*(rhoy(i,k)+rhoy(i,k-1))
*           *(deep(k-1)-deep(k))
        vg(i,k-1)=vg(i,k)-fac*(rhex(i,k)+rhex(i,k-1))
*           *(deep(k-1)-deep(k))
        enddo
    endif
enddo
c
c - compute the p vector, pvec = (px, py, pz)
c
c
c set p-vector to zero first (for plotting purposes)
c
do i=1,mx1
    mkpv=0
    do k=ktop,rmask(i,j)-1
        aa1=1.0d10*(rhoty(i,k)*qz(i,k)-rhotz(i,k)*qy(i,k))
        aa2=1.0d10*(rhotz(i,k)*qx(i,k)-rhotx(i,k)*qz(i,k))
        aa3=1.0d10*(rhotx(i,k)*qy(i,k)-rhoty(i,k)*qx(i,k))
        aa=sqrt(aa1**2+aa2**2+aa3**2)
        dr=sqrt(rhotx(i,k)**2+rhoty(i,k)**2+rhotz(i,k)**2)
        dq=sqrt(qx(i,k)**2+qy(i,k)**2+qz(i,k)**2)
        drdq=aa/(1.0d10*dr*dq)
        if(drdq.ge.sims) then
            aa3=aa3*fac_scale
c         aa1=aa1/fac_scale
c         aa2=aa2/fac_scale
            aa=sqrt(aa1**2+aa2**2+aa3**2)
            px(i,k)=aa1/aa
            py(i,k)=aa2/aa
            pz(i,k)=aa3/aa
            mkpv=mkpv+1
            kpv(mkpv)=k
        endif
    enddo
enddo
c
c - optimization the uref and vref
c

if(mkpv.ge.3) then
    t11=0.0
    t12=0.0
    t22=0.0
    ff1=0.0
    ff2=0.0

```

```

do kk=1,mkpv
  k=kpv(kk)
  if(abs(rhotz(i,k)).gt.small_rhotz) then
    kk1=max(1,k-1)
    kk2=min(mz,k+1)
    wk=((deep(kk1)-deep(kk2))*1.0e-2)**power
    rxz=rhotx(i,k)/rhotz(i,k)
*      *fac_scale
    ryz=rhoty(i,k)/rhotz(i,k)
*      *fac_scale
    aa=1.0+rxz**2+ryz**2
    a11=wk*py(i,k)**2*aa
    a12=-wk*px(i,k)*py(i,k)*aa
    a22=wk*px(i,k)**2*aa
    t11=t11+a11
    t12=t12+a12
    t22=t22+a22
    ff1=ff1-a11*ug(i,k)-a12*vg(i,k)
    ff2=ff2-a12*ug(i,k)-a22*vg(i,k)
  endif
enddo
aa=t11*t22-t12**2
if(aa.ne.0.0) then
  uref=(ff1*t22-ff2*t12)/aa
  vref=(t11*ff2-t12*ff1)/aa
  invmask(i,j)=rmask(i,j)
  do k=1,rmask(i,j)
    u(i,sect2,k)=uref+ug(i,k)
    v(i,sect2,k)=vref+vg(i,k)
  enddo
  else
    invmask(i,j)=-1
  endif
  else
    invmask(i,j)=-1
  endif
  if(rmask(i,j).eq.0) invmask(i,j)=1
enddo
c
c - re-scale back
c

```

```

c
c - scale here before inversion, then re-scale back at the end
c
  do k=1,mz
    do i=1,mx1
      rhotz(i,k)=rhotz(i,k)/fac_scale
      qz(i,k)=qz(i,k)/fac_scale
    enddo
  enddo

c
c - compute vertical velocity
c
  if(j.gt.1) then
    do i=1,mx1
      i1=i-1
      if(i1.lt.1 .and. global.gt.0) i1=i1+mx
      if(i1.gt.0) then
        kbot=min(istopog(i,j),max(rmask(i,j),rmask(i1,j),
*          rmask(i,j-1),rmask(i1,j-1)))
        if(kbot.ge.2) then
          uref=0.0
          vref=0.0
          mkpv=0
          do k=i1,i,(i-i1)
            do j1=1,2
              if(u(k,j1,kbot).ne.0.0) then
                uref=uref+u(k,j1,kbot)
                vref=vref+v(k,j1,kbot)
                mkpv=mkpv+1
              endif
            enddo
          enddo
          if(mkpv.gt.0) then
            uref=uref/mkpv
            vref=vref/mkpv
            w(i,kbot)=(uref*(stopog(i+1,j)-stopog(i1,j))/dx(j)
*              +vref*(stopog(i,j-1)-stopog(i,j+1))/dy)/2.0
            do k=kbot-1,1,-1
              uref=(u(i,sect2,k)+u(i,sect2,k+1)+u(i,sect1,k)+
*                u(i,sect1,k+1)-u(i1,sect2,k)
*                -u(i1,sect2,k+1)-u(i1,sect1,k)-
*                u(i1,sect1,k+1))/(2.0*(dx(j)+dx(j+1)))
              vref=(v(i,sect1,k)+v(i,sect1,k+1)+v(i1,sect1,k)+
*                v(i1,sect1,k+1)-v(i,sect2,k)-v(i,sect2,k+1)-
*                v(i1,sect2,k)-v(i1,sect2,k+1))/(4.0*dy)
            w(i,k)=w(i,k+1)-(uref+vref)*(deep(k)-deep(k+1))

```

```

        enddo
      endif
    endif
  endif
enddo
endif

do k=ktop,mz
  do i=1,mx1
    aa=sqrt(u(i,sect2,k)**2+v(i,sect2,k)**2)
    call maxn(6,vmax,aa,ii,jj,i,j,k)
    veval(k)=veval(k)+aa
  enddo
enddo

return
end

subroutine maxn(n,v,a,ii,jj,i,j,kk)
parameter(nz=50)
integer i,j,k,kk,n,i,l,ii(n,nz),jj(n,nz)
real a,v(n,nz)
if(a.ge.v(1,kk)) then
  do k=n,2,-1
    v(k,kk)=v(k-1,kk)
    ii(k,kk)=ii(k-1,kk)
    jj(k,kk)=jj(k-1,kk)
  enddo
  v(1,kk)=a
  ii(1,kk)=i
  jj(1,kk)=j
else
  do k=2,n
    if(a.ge.v(k,kk) .and. a.lt.v(k-1,kk)) then
      do l=n,k+1,-1
        v(l,kk)=v(l-1,kk)
        ii(l,kk)=ii(l-1,kk)
        jj(l,kk)=jj(l-1,kk)
      enddo
      v(k,kk)=a
      ii(k,kk)=i
      jj(k,kk)=j
    endif
  enddo
endif

return
end

```

A.8 Avoiding P-Vector Calculation

The subroutine *setmask* is used to determine the area where the P-vector calculation is not valid (necessary conditions not being satisfied).

```

-----
*****
subroutine setmask(mx,my,istopog,rmask,invmask,global)
parameter(nx=360,ny=180)
integer istopog(nx,ny),rmask(nx,ny),invmask(nx,ny)
integer i,j,i1,i2,i3,j1,j2,j3,mx,my,mx1,my1
mx1=mx-1
if(global.eq.1) mx1=mx
my1=my-1
do j=1,my1
  do i=1,mx1
    rmask(i,j)=0
    invmask(i,j)=0
  enddo
enddo
c
c - calculate rmask
c
do i=1,mx-1
  do j=1,my1
    rmask(i,j)=min(istopog(i,j),istopog(i,j+1),istopog(i+1,j),
& istopog(i+1,j+1))
  enddo
enddo
if(global.eq.1) then
  do j=1,my1
    rmask(mx,j)=min(istopog(1,j),istopog(1,j+1),
& istopog(mx,j),istopog(mx,j+1))
  enddo
endif
c
c - re-calaulate rmask to void
c
do i=1,mx1
  do j=1,my1
    if(global.eq.1) then
      i1=i-1
      i2=i-2
      i3=i-3
      if(i1.lt.1) i1=i1+mx
      if(i2.lt.1) i2=i2+mx
    end if
  enddo
enddo

```

```

    if(i3.lt.1) i3=i3+mx
    j1=i+1
    j2=i+2
    j3=i+3
    if(j1.gt.mx) j1=j1-mx
    if(j2.gt.mx) j2=j2-mx
    if(j3.gt.mx) j3=j3-mx
    else
    i1=max(1,i-1)
    i2=max(1,i-2)
    i3=max(1,i-3)
    j1=min(mx1,i+1)
    j2=min(mx1,i+2)
    j3=min(mx1,i+3)
    endif
    kk1=max(min(rmask(i,j),rmask(i1,j),rmask(i2,j),rmask(i3,j)),
&      min(rmask(i,j),rmask(j1,j),rmask(j2,j),rmask(j3,j)))
    i1=max(1,j-1)
    i2=max(1,j-2)
    i3=max(1,j-3)
    j1=min(my1,j+1)
    j2=min(my1,j+2)
    j3=min(my1,j+3)
    kk2=max(min(rmask(i,j),rmask(i,i1),rmask(i,i2),rmask(i,i3)),
&      min(rmask(i,j),rmask(i,j1),rmask(i,j2),rmask(i,j3)))
    rmask(i,j)=min(kk1,kk2)
    enddo
enddo

return
end

```

A.9 Data Output

The following subroutines (*matopen*, *matout*, *matotal*, *matclose*) are used for the data output.

```

*****
*
  subroutine matopen(iuvuni,iunpxy,iunrho,iunuvg,iunq)
  integer iuvuni,iunpxy,iunrho,iunuvg,iunq
  open(iuvuni,file='puv.dat')
  open(iunpxy,file='pxyz.dat')
  open(iunrho,file='prho.dat')
  open(iunuvg,file='puvg.dat')
  open(iunq,file='pqxyz.dat')
  return
  end
*****

```

```

subroutine mattotal(mx1,my1,mz,istopog,rmask,invmask,deep,
&      grid_size,lon0,lat0,ktop,pref,global)
parameter(nx=360,ny=180,nz=50)
integer invmask(nx,ny),rmask(nx,ny),istopog(nx,ny)
integer i,j,k,mx1,my1,mz,ktop,iunit
real pref,deep(nz),grid_size,lon0,lat0
c - control
iunit=10
open(iunit,file='pctrl.dat',form='formatted')
write(iunit,102) mx1,my1,mz,grid_size,lat0,
$ lon0,ktop,pref,global
close(iunit)

c - masks
open(iunit,file='pmask.dat',form='formatted')
do i=1,mx1
  do j=1,my1
    write(iunit,103)
$    invmask(i,j),min(istopog(i,j),istopog(i,j+1)),
$    istopog(i+1,j),istopog(i+1,j+1)),rmask(i,j)
  enddo
enddo
close(iunit)

open(iunit,file='pdeep.dat',form='formatted')
do k=1,mz
  write(iunit,101) deep(k)
enddo
close(iunit)
101  format(1x,e18.7)
102  format(3i4,3(1x,e18.7),i4,1x,e16.7,2x,i3)
103  format(5i8)

return

end

*****
subroutine matout(iuvuni,iunpxy,iunrho,iunuvg,iunq,
&      temp,salt,sect,f0)
include 'pstate.h'
real temp(nx,2,nz),salt(nx,2,nz),s2day,f0

```

```

data s2day/86400.0/
integer iuvuni,iunpxy,iunrho,iunuvg,iunq
integer i,il,k,mx1,sect
mx1=mx-1

if(global) mx1=mx
c - primary fields
do i=1,mx1
  do k=1,mz
    write(iuvuni,100) u(i,sect,k),v(i,sect,k),s2day*w(i,k)
  enddo
enddo

do i=1,mx1
  do k=1,mz
    write(iunpxy,100) px(i,k),py(i,k),pz(i,k)
  enddo
enddo

do i=1,mx1
  il=i+1
  if(il.gt.mx) il=il-mx
  do k=1,mz
    write(iunrho,100)
    &      .25*(temp(i,1,k)+temp(i,2,k)+temp(il,1,k)+temp(il,2,k)),
    &      .25*(salt(i,1,k)+salt(i,2,k)+salt(il,1,k)+salt(il,2,k)),
    &      .25*(rho(i,1,k)+rho(i,2,k)+rho(il,1,k)+rho(il,2,k)),
    &      .25*(rhot(i,1,k)+rhot(i,2,k)+rhot(il,1,k)+rhot(il,2,k))
  enddo
enddo

do i=1,mx1
  do k=1,mz
    write(iunuvg,100) ug(i,k),vg(i,k)
  enddo
enddo

do i=1,mx1
  do k=1,mz
    write(iunq,100) (q(i,1,k)+q(i,2,k)+q(il,1,k)+q(il,2,k))
    &      *f0/4.0, qx(i,k), qy(i,k), qz(i,k)
  enddo
enddo

```

```

100  format(4(1x,e18.7))
101  format(1x,e18.7)
102  format(3i4,3(1x,e18.7),i4,1x,e16.7)
103  format(5i8)

      return
      end

*****
subroutine mattotal(mx1,my1,mz,istopog,rmask,invmask,deep,
&      grid_size,lon0,lat0,ktop,pref,global)
parameter(nx=360,ny=180,nz=50)
integer invmask(nx,ny),rmask(nx,ny),istopog(nx,ny)
integer i,j,k,mx1,my1,mz,ktop,iunit
real pref,deep(nz),grid_size,lon0,lat0
c - control
iunit=10
open(iunit,file='pctrl.dat',form='formatted')
write(iunit,102) mx1,my1,mz,grid_size,lat0,
$ lon0,ktop,pref,global
close(iunit)

c - masks
open(iunit,file='pmask.dat',form='formatted')
do i=1,mx1
  do j=1,my1
    write(iunit,103)
$   invmask(i,j),min(istopog(i,j),istopog(i,j+1)),
$   istopog(i+1,j),istopog(i+1,j+1)),rmask(i,j)
  enddo
enddo
close(iunit)

open(iunit,file='pdeep.dat',form='formatted')
do k=1,mz
  write(iunit,101) deep(k)
enddo
close(iunit)
101  format(1x,e18.7)
102  format(3i4,3(1x,e18.7),i4,1x,e16.7,2x,i3)
103  format(5i8)

      return
      end

```

```
*****  
*  
  subroutine matclose(iuvuni,iunpxy,iunrho,iunuvg,iunq)  
  integer iuvuni,iunpxy,iunrho,iunuvg,iunq  
  close(iuvuni)  
  close(iunpxy)  
  close(iunrho)  
  close(iunuvg)  
  close(iunq)  
  return  
  end
```

B

P-Vector Module for Isopycnal-Coordinate

Similar to Appendix A, the P-Vector module for isopycnal-coordinate is presented in Appendix B. This module is also stored in the enclosed DVD-Rom including the makefile, source codes, plotting files (using Matlab), and a sample case. Rongfeng Li and Chenwu Fan helped in developing these codes. Here, the code with the NetCDF output is listed for illustration.

B.1 Main Program

```
c   This program is calculating absolute current on isopycnals
c   at this subdirector program is running from south to north
c
c   sigmapvnc.f
c
c   to compile:
c       f77 -o sigmapvnc sigmapvnc.f -L/usr/local/netcdf-3.4/lib -
lnetcdf
c   Note: you may need to correct the netcdf lib path. If there is no
c       Netcdf lib support in your system, ask your system
c       administrator to download the netcdf lib.
c
c
c   include 'comblk.h'
c   include 'netcdf.inc'
c
c   real lon0, lat0, latmin, lonm0, latm0
c   integer data_type, dim3d(3), dim2d(2),
c   &   ist3(3),ict3(3),dimts3d(3), istts3(3), ictts3(3)
c   data_type 0-ASCII 1-binary
c   real*8 facu, fact, ofstst, ofstr, factpv
c   integer*2 i1d(im*(kl+jm)), i1s(im*kl), gb2
c   integer*1 i11d(im*kl)
c   character titl*80, author*20, created*9
```

```

data facu, factpv/1.0d-4,1.0d-2/
data fact, ofstst, ofstr/1.0d-3, 1.5d1, 30.0d0/
data pi/3.1415926535/
data radius/6.371e6/omega/7.292e-5/ g/9.806/
data rho0/1025./

data rlim/32767.0/
data gb2 /-32767/

data ist3,ict3/1,1,1,kl1,im1,1/
data istts3,ictts3/1,1,1,kl,im,1/
open(8,file='input.dat')
  read(8,*) lat0,lon0,y_gridsize,x_gridsize,data_type
  read(8,*) layers(1),drho, pref
  read(8,*) deep
  read(8,'(a20)') author
  read(8,'(a80)') titl
  read(8,*) kts,kpvect,kq
close(8)

do k=1,km1
  deepm(k)=(deep(k)+deep(k+1))/2.0
enddo

deg2rad=pi/180.
small=1.e-6

lonm0=lon0+x_gridsize/2.0
latm0=lat0+y_gridsize/2.0

latmin=5.
c ——— form depths spd (246) for interpolation ———
spd(1)=deep(1)
do kk=1,km-1
  dd=(deep(kk+1)-deep(kk))/nkp
  do k=nkp*(kk-1)+2,nkp*kk+1
    spd(k)=spd(k-1)+dd
  enddo
enddo

c – calculating lat(j) lon(i),ff(j) Change them when using another
c domain

do j=1,jm
  lat(j)=lat0+y_gridsize*(j-1)
enddo

```

```

ddx=x_gridsize*deg2rad*radius
dy=y_gridsize*deg2rad*radius

do j=1,jm
  dx(j)=ddx*cos(lat(j)*deg2rad)
  ff(j)=2.*omega*sin(lat(j)*deg2rad)
  if(lat(j).lt.latmin .and. lat(j) .ge.0.0) then
    ff(j)=2.*omega*sin(latmin*deg2rad)
  endif
  if(lat(j).gt.-latmin .and. lat(j) .le.0.0) then
    ff(j)=-2.*omega*sin(latmin*deg2rad)
  endif
enddo

c ----- for wnp pref=0.0 taking isopycnals as follow -----
do k=2,kl
  layers(k)=layers(1)+drho*(k-1)
  layerm(k-1)=0.5*(layers(k-1)+layers(k))
enddo

call date(created)

IRET = NF_CREATE('pvout.nc',NF_CLOBBER,NCID)
CALL ERRCHECK(IRET)
IRET = NF_PUT_ATT_TEXT(NCID,NF_GLOBAL,
&      'title',80,titl)
CALL ERRCHECK(IRET)
IRET = NF_PUT_ATT_TEXT(NCID,NF_GLOBAL,'author',29,
&      author//created)
CALL ERRCHECK(IRET)

c
c defind dimensions (lat, lon, lev)
c
IRET = NF_DEF_DIM(NCID,'lat',jm,IDJDIM)
CALL ERRCHECK(IRET)
IRET = NF_DEF_DIM(NCID,'lat_uv',jm1,IDJUVDIM)
CALL ERRCHECK(IRET)
IRET = NF_DEF_DIM(NCID,'lon',im,IDIDIM)
CALL ERRCHECK(IRET)
IRET = NF_DEF_DIM(NCID,'lon_uv',im1,IDIUVDIM)
CALL ERRCHECK(IRET)
IRET = NF_DEF_DIM(NCID,'zlev',km,IDKDIM)
CALL ERRCHECK(IRET)
IRET = NF_DEF_DIM(NCID,'sigma_level',kl,IDSIGDIM)
CALL ERRCHECK(IRET)
IRET = NF_DEF_DIM(NCID,'sigma_level_uv',kl1,IDSIGMDIM)
CALL ERRCHECK(IRET)

```

```

c   defined coordinate data (lat, lon, deep)
c
      IRET = NF_DEF_VAR(NCID,'lat',NF_float,1,IDJDIM,
&      IDYCOORD)
      CALL ERRCHECK(IRET)
      IRET = NF_DEF_VAR(NCID,'lat_uv',NF_float,1,IDJUVDIM,
&      IDYUVCOORD)
      CALL ERRCHECK(IRET)
      IRET = NF_DEF_VAR(NCID,'lon',NF_float,1,IDIDIM,
&      IDXCOORD)
      CALL ERRCHECK(IRET)
      IRET = NF_DEF_VAR(NCID,'lon_uv',NF_float,1,
&      IDIUVDIM,IDXUVCOORD)
      CALL ERRCHECK(IRET)
      IRET = NF_DEF_VAR(NCID,'depth',NF_float,1,
&      IDKDIM,IDZCOORD)
      CALL ERRCHECK(IRET)
      IRET = NF_PUT_ATT_TEXT(NCID,IDZCOORD,
&      'units',6,'meters')
      CALL ERRCHECK(IRET)
      IRET = NF_DEF_VAR(NCID,'sigma_level',NF_float,1,
&      IDsigDim,IDSig)
      CALL ERRCHECK(IRET)
      IRET = NF_PUT_ATT_TEXT(NCID,IDSig,'units',7,'kg/m**3')
      CALL ERRCHECK(IRET)
      IRET = NF_DEF_VAR(NCID,'sigma_level_uv',NF_float,1,
&      IDsigmDim,IDSigm)
      CALL ERRCHECK(IRET)
      IRET = NF_PUT_ATT_TEXT(NCID,IDSigm,'units',7,'kg/m**3')
      CALL ERRCHECK(IRET)

      IRET = NF_PUT_ATT_TEXT(NCID,IDYCOORD,'long_name',
&      30, 'Latitudinal Position for T,S,R')
      CALL ERRCHECK(IRET)
      IRET = NF_PUT_ATT_TEXT(NCID,IDYUVCOORD,
&      'long_name',28, 'Latitudinal Position for u,v')
      CALL ERRCHECK(IRET)
      IRET = NF_PUT_ATT_TEXT(NCID,IDXCOORD,
&      'long_name',31, 'Longitudinal Position for T,S,R')
      CALL ERRCHECK(IRET)
      IRET = NF_PUT_ATT_TEXT(NCID,IDXUVCOORD,
&      'long_name',29, 'Longitudinal Position for u,v')
      CALL ERRCHECK(IRET)
      IRET = NF_PUT_ATT_TEXT(NCID,IDZCOORD,
&      'long_name',27, 'Vertical Position for T,S,R')
      CALL ERRCHECK(IRET)

```

```

dim3d(1)=IDsigmDIM
dim3d(2)=IDIUVDIM
dim3d(3)=IDJUVDIM

dim2d(1)=IDIUVDIM
dim2d(2)=IDJUVDIM

dimts3d(1)=IDsigDim
dimts3d(2)=IDIDIM
dimts3d(3)=IDJDIM

IRET = NF_DEF_VAR(NCID,'ktop',NF_SHORT,2,
&      dim2d,IDKTOP)
CALL ERRCHECK(IRET)

IRET = NF_PUT_ATT_TEXT(NCID,IDKTOP,'long_name',21,
&      'Top Sigma Level Index')
CALL ERRCHECK(IRET)

IRET = NF_DEF_VAR(NCID,'kbot',NF_SHORT,2,dim2d,
&      IDKBOT)
CALL ERRCHECK(IRET)

IRET = NF_PUT_ATT_TEXT(NCID,IDKBOT,'long_name',24,
&      'Bottom Sigma Level Index')
CALL ERRCHECK(IRET)

if(kts.gt.0) then
IRET = NF_DEF_VAR(NCID,'temperature',NF_SHORT,3,
&      dimts3d,IDT)
CALL ERRCHECK(IRET)
IRET = NF_PUT_ATT_TEXT(NCID,IDT,'units',1,'C')
CALL ERRCHECK(IRET)
IRET = NF_PUT_ATT_DOUBLE(NCID,IDT,'scale_factor',
&      NF_double,1,fact)
CALL ERRCHECK(IRET)
IRET = NF_PUT_ATT_DOUBLE(NCID,IDT,'add_offset',
&      NF_double,1,ofstst)
CALL ERRCHECK(IRET)
IRET = NF_DEF_VAR(NCID,'salinity',NF_SHORT,3,
&      dimts3d,IDS)
CALL ERRCHECK(IRET)
IRET = NF_PUT_ATT_DOUBLE(NCID,IDS,'scale_factor',
&      NF_double,1,fact)
CALL ERRCHECK(IRET)
IRET = NF_PUT_ATT_DOUBLE(NCID,IDS,'add_offset',
&      NF_double,1,ofstst)
CALL ERRCHECK(IRET)
IRET = NF_PUT_ATT_TEXT(NCID,IDS,'units',3,'PSU')
CALL ERRCHECK(IRET)

```

```

IRET = NF_DEF_VAR(NCID,'sigma_depth',NF_float,3,
&      dimts3d, IDsdep)
CALL ERRCHECK(IRET)
IRET = NF_PUT_ATT_TEXT(NCID,IDsdep,'units',1,'m')
CALL ERRCHECK(IRET)
endif

if(kq.gt.0) then
IRET = NF_DEF_VAR(NCID,'q',NF_float,3,dim3d,IDQ)
CALL ERRCHECK(IRET)
IRET = NF_PUT_ATT_TEXT(NCID,IDQ,'long_name',19,
&      'Potential Vorticity')
CALL ERRCHECK(IRET)
IRET = NF_PUT_ATT_TEXT(NCID,IDQ,'units',3,'1/s')
CALL ERRCHECK(IRET)
endif

IRET = NF_DEF_VAR(NCID,'u',NF_SHORT,3,dim3d,IDU)
CALL ERRCHECK(IRET)
IRET = NF_PUT_ATT_TEXT(NCID,IDU,'long_name',14,
&      '3-D u-velocity')
CALL ERRCHECK(IRET)
IRET = NF_PUT_ATT_TEXT(NCID,IDU,'units',3,'m/s')
CALL ERRCHECK(IRET)
IRET = NF_PUT_ATT_DOUBLE(NCID,IDU,'scale_factor',
&      NF_double,1,facu)
CALL ERRCHECK(IRET)

IRET = NF_DEF_VAR(NCID,'v',NF_SHORT,3,dim3d,IDV)
CALL ERRCHECK(IRET)
IRET = NF_PUT_ATT_TEXT(NCID,IDV,'long_name',14,
&      '3-D v-velocity')
CALL ERRCHECK(IRET)
IRET = NF_PUT_ATT_TEXT(NCID,IDV,'units',3,'m/s')
CALL ERRCHECK(IRET)
IRET = NF_PUT_ATT_DOUBLE(NCID,IDV,'scale_factor',
&      NF_double,1,facu)
CALL ERRCHECK(IRET)

IRET = NF_DEF_VAR(NCID,'sigma_depth_uv',NF_float,3,
&      dim3d, IDsmdep)
CALL ERRCHECK(IRET)
IRET = NF_PUT_ATT_TEXT(NCID,IDsmdep,'units',1,'m')
CALL ERRCHECK(IRET)

```

```

    if(kpvect.gt.0) then
      IRET = NF_DEF_VAR(NCID,'pvector_x',NF_BYTE,3,
&      dim3d,IDPX)
      CALL ERRCHECK(IRET)
      IRET = NF_PUT_ATT_DOUBLE(NCID,IDPX,'scale_factor',
&      NF_double,1,factpv)
      CALL ERRCHECK(IRET)
      IRET = NF_DEF_VAR(NCID,'pvector_y',NF_BYTE,3,
&      dim3d,IDPY)
      CALL ERRCHECK(IRET)
      IRET = NF_PUT_ATT_DOUBLE(NCID,IDPY,'scale_factor',
&      NF_double,1,factpv)
      CALL ERRCHECK(IRET)
    endif

    IRET = NF_ENDDEF(NCID)
    CALL ERRCHECK(IRET)

c
c   write coordinate data
c
    r1d(1)=lon0
    do i=2,im
      r1d(i)=r1d(i-1)+x_gridsize
    enddo
    IRET = NF_PUT_VAR_real(NCID,IDXCOORD,r1d)
    CALL ERRCHECK(IRET)

    r1d(1)=lonm0
    do i=2,im1
      r1d(i)=r1d(i-1)+x_gridsize
    enddo
    IRET = NF_PUT_VAR_real(NCID,IDXUVCOORD,r1d)
    CALL ERRCHECK(IRET)

    IRET = NF_PUT_VAR_real(NCID,IDYCOORD,lat)
    CALL ERRCHECK(IRET)
    do j=1,jm1
      r1d(j)=(lat(j)+lat(j+1))/2.0
    enddo
    IRET = NF_PUT_VAR_real(NCID,IDYUVCOORD,r1d)
    CALL ERRCHECK(IRET)

    IRET = NF_PUT_VAR_real(NCID,IDZCOORD,deep)
    CALL ERRCHECK(IRET)

```

```
IRET = NF_PUT_VAR_real(NCID,IDSig,layers)
CALL ERRCHECK(IRET)
```

```
IRET = NF_PUT_VAR_real(NCID,IDSigm,layerm)
CALL ERRCHECK(IRET)
```

c

```
is1=2
is2=1

ifdt=18
ifds=19

if(data_type.eq.0) then
  open(ifdt,file='t.txt')
  open(ifds,file='s.txt')
else
  open(ifdt,file='t.bin',
&      form='unformatted',access='direct',recl=km*im)
  open(ifds,file='s.bin',
&      form='unformatted',access='direct',recl=km*im)
endif

j=0
j1=j+1
call qinput(ifdt,ifds,j1,data_type)

call qlyddz(drho,is2,j1)

istts3(3)=j1
if(kts.gt.0) then
  do i=1,im
    if(kb(i,j1).le.kt(i,j1)) then
      do k=1,kl
        i1d(kl*(i-1)+k)=gb2
        i1s(kl*(i-1)+k)=gb2
      enddo
    else
      do k=1,kt(i,j1)-1
        i1d(kl*(i-1)+k)=gb2
        i1s(kl*(i-1)+k)=gb2
      enddo
      k1=1
      k2=k1+1
      do k=kt(i,j1),kb(i,j1)
        do while(lyd(k,i,is2).gt.deep(k2))
          k1=k2
          k2=k1+1
        enddo
      enddo
    enddo
  enddo
enddo
```

```

        h1=(deep(k2)-lyd(k,i,is2))/(deep(k2)-deep(k1))
        h2=1.0-h1
        i1d(kl*(i-1)+k)=(tp(k1,i)*h1+tp(k2,i)*h2-ofstst)/fact+0.5
        i1s(kl*(i-1)+k)=(sp(k1,i)*h1+sp(k2,i)*h2-ofstst)/fact+0.5
    enddo
    do k=kb(i,j1)+1,kl
        i1d(kl*(i-1)+k)=gb2
        i1s(kl*(i-1)+k)=gb2
    enddo
endif
enddo

IRET = NF_PUT_VARA_int2(NCID,IDT,istts3,ictts3,i1d)
CALL ERRCHECK(IRET)

IRET = NF_PUT_VARA_int2(NCID,IDS,istts3,ictts3,i1s)
CALL ERRCHECK(IRET)

IRET = NF_PUT_VARA_real(NCID,IDSdep,istts3,ictts3,
&      lyd(1,1,is2))
CALL ERRCHECK(IRET)
endif

do 1000 j=1,jm1
    j1=j+1
    iiss=is1
    is1=is2
    is2=iiss

    print *, 'j=',j

    call qinput(ifdt,ifds,j+1,data_type)

    call qlyddz(drho,is2,j1)

    call fmask(is2,j1)

    call qcv(is1,is2,j)

    call caluv(drho,rho0,small,is1,is2,j)
c
c - output
c
    istts3(3)=j+1
    ist3(3)=j

    if(kts.gt.0) then
        do i=1,im
            if(kb(i,j1).le.kt(i,j1)) then

```

```

do k=1,kl
  i1d(kl*(i-1)+k)=gb2
  i1s(kl*(i-1)+k)=gb2
enddo
else
do k=1,kt(i,j1)-1
  i1d(kl*(i-1)+k)=gb2
  i1s(kl*(i-1)+k)=gb2
enddo
k1=1
k2=k1+1
do k=kt(i,j1),kb(i,j1)
  do while(lyd(k,i,is2).gt.deep(k2))
    k1=k2
    k2=k1+1
  enddo
  h1=(deep(k2)-lyd(k,i,is2))/(deep(k2)-deep(k1))
  h2=1.0-h1
  i1d(kl*(i-1)+k)=(tp(k1,i)*h1+tp(k2,i)*h2-ofstst)/fact+0.5
  i1s(kl*(i-1)+k)=(sp(k1,i)*h1+sp(k2,i)*h2-ofstst)/fact+0.5
enddo
do k=kb(i,j1)+1,kl
  i1d(kl*(i-1)+k)=gb2
  i1s(kl*(i-1)+k)=gb2
enddo
endif
enddo
IRET = NF_PUT_VARA_int2(NCID,IDT,istts3,ictts3,i1d)
CALL ERRCHECK(IRET)

IRET = NF_PUT_VARA_int2(NCID,IDS,istts3,ictts3,i1s)
CALL ERRCHECK(IRET)

IRET = NF_PUT_VARA_real(NCID,IDSdep,istts3,ictts3,
& lyd(1,1,is2))
CALL ERRCHECK(IRET)
endif
if(kq.gt.0) then
do i=1,im1
  if(maskb(i,j).le.maskt(i,j)) then
do k=1,kl1
  r1d(kl1*(i-1)+k)=0.0
enddo
else
do k=1,maskt(i,j)-1
  r1d(kl1*(i-1)+k)=0.0
enddo

```

```

do k=maskt(i,j),maskb(i,j)
  r1d(kl1*(i-1)+k)=0.25*(q(k,i,is1)+q(k,i,is2)+
&      q(k,i+1,is1)+q(k,i+1,is2))
  enddo
do k=maskb(i,j)+1,kl1
  r1d(kl1*(i-1)+k)=0.0
  enddo
endif
enddo
IRET = NF_PUT_VARA_real(NCID,IDQ,ist3,ict3,r1d)
CALL ERRCHECK(IRET)
endif

do i=1,im1
do k=1,kl1
  uuu=u(k,i)/facu+0.5
  uuu=max(-rlim,uuu)
  uuu=min(rlim,uuu)
  i1d(kl1*(i-1)+k)=uuu
enddo
enddo
IRET = NF_PUT_VARA_int2(NCID,IDU,ist3,ict3,i1d)
CALL ERRCHECK(IRET)

do i=1,im1
do k=1,kl1
  uuu=v(k,i)/facu+0.5
  uuu=max(-rlim,uuu)
  uuu=min(rlim,uuu)
  i1d(kl1*(i-1)+k)=uuu
enddo
enddo
IRET = NF_PUT_VARA_int2(NCID,IDV,ist3,ict3,i1d)
CALL ERRCHECK(IRET)

if(kpvect.gt.0) then
do i=1,im1
do k=1,kl1
  i11d(kl1*(i-1)+k)=px(k,i)/factpv
enddo
enddo
IRET = NF_PUT_VARA_int1(NCID,IDPX,ist3,ict3,i11d)
do i=1,im1
do k=1,kl1
  i11d(kl1*(i-1)+k)=py(k,i)/factpv
enddo
enddo
IRET = NF_PUT_VARA_int1(NCID,IDPY,ist3,ict3,i11d)
endif

```

512 B P-Vector Module for Isopycnal-Coordinate

```
IRET = NF_PUT_VARA_real(NCID,IDSmddep,ist3,ict3,lydm)
CALL ERRCHECK(IRET)
```

1000 continue

```
close(ifdt)
close(ifds)
```

```
do i=1,im1
  do j=1,jm1
    i1d(im1*(j-1)+i)=maskt(i,j)
  enddo
enddo
IRET = NF_PUT_VAR_int2(NCID,IDKTOP,i1d)
CALL ERRCHECK(IRET)
```

```
do i=1,im1
  do j=1,jm1
    i1d(im1*(j-1)+i)=maskb(i,j)
  enddo
enddo
IRET = NF_PUT_VAR_int2(NCID,IDKBOT,i1d)
CALL ERRCHECK(IRET)
```

```
IRET = NF_CLOSE(NCID)
```

```
stop
end
```

B.2 Graphic Interface

```
C
C SUBROUTINE ERRCHECK(IRET)
C*****
C
C *ERRCHECK* ERROR HANDLER FOR GRAPHICAL
C INTERFACE
C
C AUTHOR - ROGER PROCTOR AND PATRICK LUYTEN
C
C LAST UPDATE - 12 Jul 1999 @(COHERENS)netcdfint.f 8.4
C
C
C DESCRIPTION - WRITE ERROR MESSAGE AND STOP
C EXECUTION OF THE PROGRAM
```

```

C   IF AN ERROR OCCURS IN ONE OF THE netCDF
C   ROUTINES
C
C   REFERENCE -
C
C   CALLING PROGRAM - CDF2D, CDF3D
C
C   EXTERNALS - NF_STRERROR
C
C*****
C
C   INCLUDE 'netcdf.inc'
C
C
C*   ARGUMENTS
C
C   INTEGER IRET
C
C   IF (IRET.NE.NF_NOERR) THEN
C     WRITE (0,*) NF_STRERROR(IRET)
C     STOP
C   ENDIF
C
C   RETURN
C
C   END
c — This program is for inputing data of T and S and then
c   interpolating T,S from 56 levels into 246 levels
c
c   qinput.f cf77 qinput.f intpo.f intpo.f
c
c   subroutine qinput(ifdt,ifds,j,data_type)
c
c   include 'comblk.h'
c
c   real rhoz(kp)
c   integer data_type
c
c   ————— input tp(im,56) and sp(im,56) —————
c
c   if(data_type.eq.0) then
c     read(ifdt,*) tp
c     read(ifds,*) sp
c   else
c     read(ifdt,rec=j) tp
c     read(ifds,rec=j) sp
c   endif

```

```

do i=1,im
  itopo(i,j)=0
  do k=1,km
    if(tp(k,i).gt.-99.0 .and. sp(k,i).gt.-99.0) then
      itopo(i,j)=itopo(i,j)+1
    else
      goto 15
    endif
  enddo
15  continue
enddo

```

B.3 Transformation of (T , S) Data from z - to Isopycnal-Coordinate

The subroutines *qinput.f*, *interpo.f*, and *cub.f* are used to input and to transform (T , S) data from z -levels (e.g., 33 levels in WOA atlas) to n_σ isopycnal levels (e.g., 236 isopycnal levels in Sect 6.6).

```

*****
*
  subroutine qinput(ifdt,ifds,deep,tp,sp,spd,tpp,spp,is1,j)

  include 'comblk.h'

  real tp(mx,km,2),sp(mx,km,2)
  real tpp(mx,kp,2),spp(mx,kp,2)
  real deep(km),spd(kp)

  real rhoz(kp)
  dimension wk(mx,kp)
  dimension x(2,km),t(kp),a(km),b(km),s(kp)

c  ——— input tp(mx,33) and sp(mx,33) ———

*   read(ifdt,rec=my-j+1) ((tp(i,k,is1),k=1,km),i=1,mx)
*   read(ifds,rec=my-j+1) ((sp(i,k,is1),k=1,km),i=1,mx)
  read(ifdt,rec=my-j+1) ((tp(i,k,is1),i=1,mx),k=1,km)
  read(ifds,rec=my-j+1) ((sp(i,k,is1),i=1,mx),k=1,km)

c   print *, 'reading T and S j= ',j

  if(j .eq.99 ) then
    print *, ' tp(304,99,k)= '
    print 666,(tp(304,k,is1),k=1,km)
    print *, ' sp(304,99,k)= '
    print 666,(sp(304,k,is1),k=1,km)
  endif
666  format(5f12.4)

```

```

do 22 i=1,mx
  itopo(i,j)=0
  do k=1,km
    if(tp(i,k,is1).gt.-99.0 .and. sp(i,k,is1).gt.-99.0) then
      itopo(i,j)=itopo(i,j)+1
    endif
  enddo
22  continue

c ----- interpolate tp(mx,33) into tpp(mx,236) -----

  call intpo(tp,wk,deep,spd,x,t,a,b,s,is1,j)

  do 55 i=1,mx
  do 55 k=1,kp
55  tpp(i,k,is1)=wk(i,k)

c ----- interpolate sp(mx,my,56) into spp(mx,my,246) -----

  call intpo(sp,wk,deep,spd,x,t,a,b,s,is1,j)

  do 56 i=1,mx
  do 56 k=1,kp
56  spp(i,k,is1)=wk(i,k)

c ----- form index field itopp(i,j) according to tpp and spp -----
do 23 i=1,mx
  itopp(i,j)=0
  do k=1,kp
    if(tpp(i,k,is1).gt.-99. .and. spp(i,k,is1).gt.-99.) then
      itopp(i,j)=itopp(i,j)+1
    endif
  enddo
23  continue

c ----- calculating portential density rhot -----

  do 57 i=1,mx
  do 57 k=1,kp
    rho(i,k,is1)=0.0
    rhot(i,k,is1)=0.0
57  continue
  do 66 i=1,mx
    if(itopp(i,j) .eq. 0) go to 66
    do k=1,itopp(i,j)
      tempd=tpp(i,k,is1)
      saltd=spp(i,k,is1)
      pressure=spd(k)

```

```

        dum=svan(saltd,tempd,presure,rho(i,k,is1))
        tempt=theta(saltd,tempd,presure,pref)
        dumt=svan(saltd,tempt,pref,rhot(i,k,is1))
    enddo
66    continue

    if(j .eq.99 ) then
    print *, ' rhot(304,99,k)= '
    print 666,(rhot(304,k,is1),k=1,kp)
    print *, ' rhot(305,99,k)= '
    print 666,(rhot(305,k,is1),k=1,kp)
    endif

    return
    end

*****
    subroutine intpo(ts,wk,deep,spd,x,t,a,b,s,is1,j)
    include 'comblk.h'

    real ts(mx,km,2)
    real wk(mx,kp)
    real deep(km),spd(kp)

    dimension x(2,km),t(kp),a(km),b(km),s(kp)

c -----
    do 11 i=1,mx
    do 11 k=1,kp
11    wk(i,k)=-99.9999
c ----- interpolating ts(mx,km) to wk(mx,kp) -----

    do 100 i=1,mx
    kkb=itopo(i,j)
    if(itopo(i,j).le.1) go to 100
    q1=ts(i,1,is1)
    q2=ts(i,2,is1)
    y11=(q2-q1)/(deep(2)-deep(1))
    q3=ts(i,kkb-1,is1)
    q4=ts(i,kkb,is1)
    yn1=(q4-q3)/(deep(kkb)-deep(kkb-1))

    dd=deep(kkb)
    if(dd.gt.0.0.and.dd.le.1000.) then
        m=ifix(dd/10.+1.e-10)+1
    else if(dd.gt.1000.0 .and. dd .le.2500.) then
        m=ifix((dd-1000.)/20.+1.e-10)+101
    else if(dd.gt.2500.0.and.dd.le.5500.) then
        m=ifix((dd-2500.)/50.+1.e-10)+176
    endif

```

```

if(i.eq.304 .and. j.eq.99) then
  print *, ' for B point i=304, j=99 '
  print *, ' m= ',m, ' kb= ',kkb, ' deep(kkb)= ',deep(kkb)
endif

do k=1,kp
  t(k)=0.0
  s(k)=0.0
enddo
do kk=1,m
  t(kk)=spd(kk)
enddo

do k=1,km
  x(1,k)=deep(k)
  x(2,k)=ts(i,k,is1)
  a(k)=0.0
  b(k)=0.0
enddo

call cub(km,kkb,m,kp,x,t,a,b,s,y11,yn1)

do kk=1,m
  wk(i,kk)=s(kk)
enddo

100  continue

  return
  end

*****

subroutine cub(n,ns,m,mb,x,t,a,b,s,y11,yn1)
  dimension x(2,n),a(n),b(n),t(mb),s(mb)

  a(1)=0.0
  b(1)=y11
c   n1=n-1
  n1=ns-1
  do 1 j=2,n1
    h1=x(1,j)-x(1,j-1)
    h=x(1,j+1)-x(1,j)
    af=h1/(h+h1)
    bt=3.*((1.-af)*(x(2,j)-x(2,j-1))/h1+af*(x(2,j+1)-x(2,j))/h)
    a(j)=-af/(2.+(1.-af)*a(j-1))
1   b(j)=(bt-(1.-af)*b(j-1))/(2.+(1.-af)*a(j-1))
c   a(n)=yn1
    a(ns)=yn1
2   a(n1)=a(n1)*a(n1+1)+b(n1)
    n1=n1-1
    if(n1.gt.0) go to 2

```

518 B P-Vector Module for Isopycnal-Coordinate

```
      do 5 j=1,m
        i=1
3       if(t(j).le.x(1,i+1)) go to 4
        i=i+1
        go to 3
4       h=x(1,i+1)-x(1,i)
        h1=(x(1,i+1)-t(j))/h
        h2=(t(j)-x(1,i))/h
5       s(j)=(3.-2.*h1)*h1**2*x(2,i)+(3.-2.*h2)*h2**2*x(2,i+1)+
&         (1.-h1)*h1**2*h*a(i)-(1.-h2)*h2**2*h*a(i+1)

      return
      end
```

B.4 Calculation of Level Depth, Layer Thickness, and Potential Vorticity

The subroutine *qlyddz* is used to calculate the level depth (lyd), layer thickness (dz) and potential vorticity (q).

```
      subroutine qlyddz(drho, layers, spd, is1, j)

      include 'comblk.h'

      real layers(mz), spd(kp), rhoz(kp)

c ----- Calculate the level depth -----
      do 88 i=1, mx
        do 88 k=1, mz
88       lyd(i, k, is1) = 9999.9

        do 99 k=1, kp
99       rhoz(k) = 0.0
        do 11 i=1, mx
          mb = itopp(i, j)
          if (mb.le.1) goto 11
          do k=1, mb
            rhoz(k) = rhot(i, k, is1)
          enddo
          do k=1, mz
            rhof = layers(k)
            lyd(i, k, is1) = dpint(kp, mb, spd, rhoz, rhof, 1)
          enddo
11      continue
```

```

c ----- Calculate the layer thickness -----
  do 12 i=1,mx
  do 12 k=1,mz-1
    dd=lyd(i,k+1,is1)-lyd(i,k,is1)
    if (lyd(i,k,is1).ge.lyd(i,k+1,is1).or.
&      lyd(i,k+1,is1).ge.9999.9) then
      dz(i,k,is1)=0.0
    else
      dz(i,k,is1)=dd
    endif
12  continue

c ----- calculating q=drho/rhok*f/dz -----
  do 63 i=1,mx
  do 63 k=1,mz-1
63   q(i,k,is1)=9999.9

    do 64 i=1,mx
    do 64 k=2,mz-1
      if (dz(i,k-1,is1).gt.0.0 .and. dz(i,k,is1).gt.0.0) then
        rhok=1000.0+(layers(k)+0.5*drho)
        fact=drho/rhok
        q(i,k,is1)=fact*ff(j)/dz(i,k,is1)
      endif
64   continue

    if(j.eq.100) then
      print *, ' '
      print *, 'lyd(304,100,k)lyd(305,100,k)dz(304,100,k)dz(305,100,k)'
      print *, ' '
      do k=1,mz-1
        dd1=lyd(304,k,is1)
        dd2=lyd(305,k,is1)
        print 56,k,dd1,dd2,dz(304,k,is1),dz(305,k,is1)
      enddo
    endif
    if(j.eq.99) then
      print *, ' '
      print *, 'lyd(304,99,k)lyd(305,99,k)dz(304,99,k)dz(305,99,k)'
      print *, ' '
      do k=1,mz-1
        dd1=lyd(304,k,is1)
        dd2=lyd(305,k,is1)
        print 56,k,dd1,dd2,dz(304,k,is1),dz(305,k,is1)
      enddo
    endif
56   format(1x,i4,4f12.4)

  return
  end

```

B.5 Calculation of Absolute Velocity

The subroutine *caluvg* is used to calculate the absolute velocity.

```

subroutine caluvg(drho,rho0,small,is1,is2,j)

include 'comblk.h'

real hx(mx-1,mz-1),hy(mx-1,mz-1)
real dhx(mz-1),dhy(mz-1)
c real dumk(mz-1),dvmk(mz-1),hm(mz-1)
real hm(mz-1)
real pxm(mz-1),pym(mz-1)

c ----- calculate hx and hy from South to North -----
do 10 k=1,mz-1
do 10 i=1,mx-1
  hx(i,k)=0.0
  hy(i,k)=0.0
  u(i,k)=0.0
  v(i,k)=0.0
  ug(i,k)=0.0
  vg(i,k)=0.0
10 continue

do 21 i=1,mx-1
  ktop=maskt(i,j)
  kbot=maskb(i,j)
  if(ktop.gt.0 .and.ktop.lt.kbot) then
    do k=ktop,kbot
      q1=dz(i,k,is1)
      q2=dz(i+1,k,is1)
      q3=dz(i+1,k,is2)
      q4=dz(i,k,is2)
      if(q1 .gt.0.0 .and.q2 .gt.0.0 .and.
&      q3 .gt.0.0 .and.q4 .gt.0.0) then
        hx(i,k)=(q3+q2-q4-q1)/(dx(j+1)+dx(j))
        hy(i,k)=(q3+q4-q2-q1)/(2.*dy)
      endif
    enddo
  endif
21 continue

```

```

c ----- start to calculate current -----
  do 1000 i=1,mx-1
    invmask(i,j)=0
    do k=1,mz-1
      u(i,k)=0.0
      v(i,k)=0.0
    enddo
1000  continue

    do 2000 i=1,mx-1
      ktop=maskt(i,j)+5
      kbot=maskb(i,j)-1

      if(ktop.gt.0 .and. ktop.lt.kbot) then
        fuv=0.5*(ff(j)+ff(j+1))
        if (fuv.eq.0.0) goto 2000
        fac=g*drho/(fuv*rho0)

c - calculate d(Mk-Mkbot)/dy/fac, d(Mk-Mkbot)/dx/fac
        do k=1,mz-1
          dhx(k)=0.0
          dhy(k)=0.0
          hm(k)=0.0
          pxm(k)=0.0
          pym(k)=0.0
        enddo

        do k=ktop,kbot
          dhx(k)=hx(i,k)
          dhy(k)=hy(i,k)
          pxm(k)=px(i,k)
          pym(k)=py(i,k)
          hm(k)=0.25*(dz(i,k,is1)+dz(i+1,k,is1)+
&                dz(i+1,k,is2)+dz(i,k,is2))
          ug(i,k)=-pmkm(mz,k,kbot,dhy)*fac
          vg(i,k)=pmkm(mz,k,kbot,dhx)*fac
        enddo

c --- optmxization the uref and vref -----
        t11=0.0
        t12=0.0
        t22=0.0
        ff1=0.0
        ff2=0.0

```

```

do k=ktop,kbot
  wk=hm(k)**2
  a11=wk*pym(k)**2
  a12=-wk*pxm(k)*pym(k)
  a22=wk*pxm(k)**2
  t11=t11+a11
  t12=t12+a12
  t22=t22+a22
c   ff1=ff1-a11*dumk(k)-a12*dvmk(k)
c   ff2=ff2-a12*dumk(k)-a22*dvmk(k)
  ff1=ff1-a11*ug(i,k)-a12*vg(i,k)
  aff2=ff2-a12*ug(i,k)-a22*vg(i,k)
enddo
  aa=t11*t22-t12**2
  if(abs(aa).ge.1.e-10) then
    uref=(ff1*t22-ff2*t12)/aa
    vref=(t11*ff2-t12*ff1)/aa
    invmask(i,j)=0
  do k=ktop,kbot
c   u(i,k)=uref+dumk(k)
c   v(i,k)=vref+dvmk(k)
    u(i,k)=uref+ug(i,k)
    v(i,k)=vref+vg(i,k)
  enddo
  else
    invmask(i,j)=-1
  endif
endif
2000 continue

if(j.eq.99) then
  print *,', '
  print *, 'u(304,99,k) v(304,99,k) '
  print *,', '
  do k=1,mz-1
    print 56,k,u(304,k),v(304,k)
  enddo
endif
56 format(1x,i4,1x,2(1x,f9.6))

return
end

```

B.6 Functions

Several functions are defined for the computation.

```
*****
```

```
function dpint(n,mb,dep,r,rhof,key)
  dimension dep(n),r(n)
  data eps/1.e-20/

  do i=1,mb-1
    if((r(i)-rhof)*(r(i+1)-rhof).le.0.0) goto 10
  enddo
  dpint=9999.9
  return
```

```
10  continue
    if(key.eq.1) then
      i2=i+1
      x1=(rhof-r(i2))/(r(i)-r(i2)+eps)
      dpint=dep(i)*x1+dep(i2)*(1.0-x1)
      return
    elseif(key.eq.2) then
      if(i.eq.1) then
        i1=1
        i2=2
        i3=3
      elseif(i.eq.mb-1) then
        i1=i-1
        i2=i
        i3=mb
      elseif((rhof-r(i))/(r(i+1)-r(i)+eps).le.0.5) then
        i1=i-1
        i2=i
        i3=i+1
      else
        i1=i
        i2=i+1
        i3=i+2
      endif
      dpint=dep(i1)*(rhof-r(i2))*(rhof-r(i3))/
&      ((r(i1)-r(i2))*(r(i1)-r(i3))+eps)
&      + dep(i2)*(rhof-r(i1))*(rhof-r(i3))/
&      ((r(i2)-r(i1))*(r(i2)-r(i3))+eps)
&      + dep(i3)*(rhof-r(i1))*(rhof-r(i2))/
&      ((r(i3)-r(i1))*(r(i3)-r(i2))+eps)
      return
```

```

else
  if(i.eq.1) then
    i1=1
    i2=2
    i3=3
    i4=4
  elseif(i.eq.mb-1) then
    i1=mb-3
    i2=mb-2
    i3=mb-1
    i4=mb
  else
    i1=i-1
    i2=i
    i3=i+1
    i4=i+2
  endif
  dpint=dep(i1)*(rhof-r(i2))*(rhof-r(i3))*(rhof-r(i4))/
&      ((r(i1)-r(i2))*(r(i1)-r(i3))*(r(i1)-r(i4))+eps)
&      +dep(i2)*(rhof-r(i1))*(rhof-r(i3))*(rhof-r(i4))/
&      ((r(i2)-r(i1))*(r(i2)-r(i3))*(r(i2)-r(i4))+eps)
&      +dep(i3)*(rhof-r(i1))*(rhof-r(i2))*(rhof-r(i4))/
&      ((r(i3)-r(i1))*(r(i3)-r(i2))*(r(i3)-r(i4))+eps)
&      +dep(i4)*(rhof-r(i1))*(rhof-r(i2))*(rhof-r(i3))/
&      ((r(i4)-r(i1))*(r(i4)-r(i2))*(r(i4)-r(i3))+eps)
  return
endif

end

```

```

c
function pmkm(kl,kk,km,dh)
real dh(kl-1)

sumh=0.0
do k=1,kl-1
  sumh=sumh+dh(k)
enddo

sumrok=0.0
do j=1,kl-1-kk
  sumi=0.0
  do i=1,j
    sumi=sumi+dh(kl-i)
  enddo
  sumrok=sumrok+(sumh-sumi)
enddo

```

```

sumrom=0.0
do j=1,kl-1-km
  sumi=0.0
  do i=1,j
    sumi=sumi+dh(kl-i)
  enddo
  sumrom=sumrom+(sumh-sumi)
enddo

pmkm=(sumrok-sumrom)
end

```

B.7 Avoiding P-Vector Calculation

The subroutine *fmask* is used to determine the area where the P-vector calculation is not valid (necessary conditions not being satisfied).

```

*****
*
subroutine fmask(is1,j,key)

include 'comblk.h'

do 11 i=1,mx
  kt(i,j)=0
11  kb(i,j)=0
do 12 i=1,mx-1
  maskt(i,j)=0
12  maskb(i,j)=0
do 22 i=1,mx
  if(dz(i,1,is1).gt.0.1e-20) then
    kt(i,j)=1
  else
    do k=2,mz-1
      if(dz(i,k-1,is1).le.0.0.and.dz(i,k,is1).gt.0.1e-20) then
        kt(i,j)=k
        goto 22
      endif
    enddo
  endif
22 continue

```

```

do 23 i=1,mx
  kb(i,j)=kt(i,j)
  do k=kt(i,j)+1,mz-1
    if(dz(i,k,is1).gt.0.0) then
      kb(i,j)=kb(i,j)+1
    endif
  enddo
23  continue

if(key.eq.0) return

do 25 i=1,mx-1
  msmax=max(kt(i,j),kt(i+1,j),kt(i+1,j+1),kt(i,j+1))
  msmin=min(kb(i,j),kb(i+1,j),kb(i+1,j+1),kb(i,j+1))
  if(msmax.ge.msmin) then
    maskt(i,j)=0
    maskb(i,j)=0
    maskc(i,j)=0
  else
    maskt(i,j)=msmax
    maskb(i,j)=msmin
    maskc(i,j)=8
  endif
25  continue

if (j.eq.99 ) then
  print *, ' kt(304,99) kt(305,99) kt(305,100) kt(304,100)'
  print 55, kt(304,99),kt(305,99),kt(305,100),kt(304,100)
  print *, ' '
  print *, ' maskt(304,99)= ',maskt(304,99)
  print *, ' '
  print *, ' kb(304,99) kb(305,99) kb(305,100) kb(304,100)'
  print 55, kb(304,99),kb(305,99),kb(305,100),kb(304,100)
  print *, ' '
  print *, ' maskb(304,99)= ',maskb(304,99)
  print *, ' '
endif
55  format (1x,i5,5x,i5,5x,i5,5x,i5)

return
end

```

C

Thermohaline Parametric Model

The codes for calculating the autocorrelation function and decorrelation scale from observational (T , S) profiles were originally written by Steven D. Haeger in 1994, modified by Charles Fralick in 1995 and by Qianqian Wang in 1998.

C.1 Makefile

```
*****  
FFLAGS = -C # check array bounds (default f77 compiling.)  
GMODEL.OBJ = gmodel.o linr.o rms.o gfit.o grad3a.o grad3b.o dep1.o \  
             g3at.o grad1.o dep2.o dep3t.o grad2.o dep3.o bump.o inout4.o\  
             dep4.o dep4t.o grad4.o dep5.o dpall2.o  
gmodel: $(GMODEL.OBJ)  
        f77 -o $@ -n $(GMODEL.OBJ) -L/usr/local/disspla11/lib \  
        -l
```

C.2 Gradient Calculated from (T , S) Profiles

The program, *gradstat.f*, is use to calculate the vertical gradient from the (T , S) profile data, and to plot the gradient versus depth.

```
C *****  
C *                PROGRAM GRADSTAT                *  
C *****
```

```

C INPUT FILE: 3 (MASTER FILE - UNFORMATTED)
C
C *** DEFINITION OF TEMP AND DEPTH VARIABLES ***
C
C T: READ FROM MASTER FILE. PASSED TO LINR TO BE
C INTERPOLATED.
C T2: INTERPOLATED TEMP PASSED BACK FROM LINR AND
C PASSED TO TOP.
C GRAD: GRADIENT COMPUTED FROM T2
C D: READ FROM MASTER FILE AND PASS TO LINR.
C D2: DEPTH PASSED BACK FROM LINR.
C D3: DEPTHS FOR GRADIENT PLOT (2 LESS THAN D2)
C
CHARACTER IDENT*10,PARM*1,HEADER*60
DIMENSION IFLAG(8),T(2500),D(2500)
DIMENSION GRAD(201),D3(201)
DIMENSION T2(201),D2(201)
IU=3
IEND=0
ICNT=0
ICNT1=0
IERR0 = 0
  IERR1=0
  IERR2=0
  IERR3=0
  IERR4=0
N=0
IDAT=0
IFIRST=0
C
C M= NO OF SETS N= NO OF PTS EACH SET
C X ARRAY CONTAINS COMPUTED MODEL COEFFICIENTS-
C SEE COMMENTS IN TOP
C FOR DESCRIPTION
C
C
WRITE(6,*) ('WHAT IS MAX DEPTH OF GRAD MODEL? (M)')
READ(5,*) DMAX
WRITE(6,*) ('WHAT IS MIN DEPTH TO ACCEPT PROFILE? (M)')
READ(5,*) DMIN
WRITE(6,*) ('ENTER STARTING PROFILE')
READ(5,*) IFIRST
WRITE(6,*) ('HOW MANY PROFILES?')
READ(5,*) NUMPRO

```

```

C
C
C READ HEADER RECORD FROM MASTER FILE
C
  READ(3,ERR=9500) PARM,HEADER
  WRITE(6,600) PARM,HEADER
600 FORMAT(/,1X,'INPUT FILE DATA TYPE: ',A1,/, 1X,'HEADER:
',A60,/)
C
  WRITE(4,620) PARM,DMIN,DMAX
620 FORMAT(1X,A1,3X,F6.0,3X,F6.0)
C
C LOOP THROUGH UNWANTED PROFILES
C
  IF(IFIRST.NE.1) THEN
    DO 100 I=1,IFIRST-1
      READ(3,END=9000,ERR=9500)

      NPROF,(IFLAG(J),J=1,8),XLAT,XLON,
      *JPROF,ICLAS,IPAT,IMASS,IPOV,
      *WDEP1,WDEP2,IYEAR,IMON,IDAY,XHOUR,IDENT,ISOURC,NC
      *YC1,NCYC2,
      *EXTRA,IEXTRA,(D(J),T(J),J=1,NCYC1+NCYC2)
      ICNT = ICNT+1
100 CONTINUE
    END IF
C
C READ DESIRED PROFILES FROM MASTER FILE
C
  DO 12 I=1,NUMPRO
    READ(3,END=9001,ERR=9500) NPROF,(IFLAG(J),J=1,8),XLAT,XLON,
    *JPROF,ICLAS,IPAT,IMASS,IPOV,
    *WDEP1,WDEP2,IYEAR,IMON,IDAY,XHOUR,IDENT,ISOURC,NCYC1,
    *NCYC2,
    *EXTRA,IEXTRA,(D(J),T(J),J=1,NCYC1+NCYC2)
    NCYC=NCYC1+NCYC2
    ICNT1 = ICNT1+1
C
C PROFILE HAS BEEN READ - CHECK FLAG(1) FOR UNWANTED
C PROFILE
C
  IF(IFLAG(1).NE.0) THEN
    IERR0 = IERR0+1
    GO TO 12
  END IF

```

530 C Thermohaline Parametric Model

```
C
C CHECK TO SEE IF PROFILE EXTENDS TO DEPTH OF DMIN
C
    IF(D(NCYC).LT.DMIN) THEN
        IERR1 = IERR1+1
        GO TO 12
    END IF
    IKEEP = IKEEP+1
C
C INTERPOLATE PROFILE TO D(NCYC) OR DMAX, WHICHEVER
C WHICHEVER IS GREATER WITH LINR
C
    DELX = DMIN/50.
    IF(DELX.LT.2.) DELX = 2.
    BOT = DMAX
    IF(D(NCYC).LT.DMAX) BOT=D(NCYC)
    WRITE(6,*) ('DELX,BOT,D(NCYC) = '),DELX,BOT,D(NCYC)
    CALL LINR(DELX,NCYC,0.,BOT,ICT,D,T,D2,T2)
    WRITE(6,*) ('ICT = '),ICT
C
C CALCULATE GRADIENT
C
    GMAX = 0.
    GMIN = 999.
    DO 20 J=1,ICT-1
        GRAD(J) = (T2(J+1)-T2(J)) / DELX
        D3(J) = D2(J) + (DELX/2.)
        IF(GRAD(J).GT.GMAX) GMAX = GRAD(J)
        IF(GRAD(J).LT.GMIN) GMIN = GRAD(J)
20 CONTINUE
    WRITE(6,605) GMIN,GMAX
605 FORMAT(1X,',GMIN,GMAX = ',2F8.4)
C
C
C WRITE FILE TO PLOT GRADIENT
C
    XMIN = -.1
    XMAX = .1
    DO 21 L=1,10
        IF(GMIN.LT.XMIN) XMIN = XMIN - .1
        IF(GMAX.GT.XMAX) XMAX = XMAX + .1
21 CONTINUE
    WRITE(11,33) GMIN,GMAX,XMIN,XMAX,ICNT,DMIN,DMAX
```

```

C
  GO TO 9002
C
9000 WRITE(6,650) ICNT
  650 FORMAT(1X,'BEGINNING PROFILE NOT FOUND',/,
    *1X,'EOF ENCOUNTERED AFTER PROFILE',I5,'. END
    * PROGRAM.')
```

```

  GO TO 1000
C
9001 IEND = 1
9002 LAST = IFIRST+ICNT1-1
  WRITE(6,651) ICNT1,IFIRST,LAST
651  FORMAT(1X,I5,' PROFILES READ FROM MASTER FILE',/,
    *1X,'FIRST PROFILE:',I5,5X,'LAST PROFILE:',I5)
  GO TO 1000
C
9500 ITOT = ICNT+ICNT1
  WRITE(6,652) ITOT
652  FORMAT(1X,'READ ERROR AFTER RECORD NUMBER
    *(PROFILE)',I5,/,
    *1X,'*CHECK MASTER FILE* PROGRAM TERMINATED.')
```

```

C
1000 CONTINUE
  END
```

C.3 Main Program

The software, `gmodel.f`, is used to calculate the thermohaline parameters from observational (T , S) profiles for nonpolar region (see Sect. 2.4). User may use different numbers of (depth, gradient) parameters (called *coefficients* in the code).

```

C *****
C *
C *          PROGRAM GMODEL          *
C *
C *****
```

```
C
C
C VERSION FOR YELLOW SEA CALCULATION (Section 2.4)
C
C THIS PROGRAM READ PROFILES FROM THE MASTER FILE
C AND COMPUTES
C THE GRADIENT VS DEPTH.
C
C INPUT FILE: 3 (MASTER FILE - UNFORMATTED)
C
C *** DEFINITION OF TEMP AND DEPTH VARIABLES ***
C
C T: READ FROM MASTER FILE. PASSED TO LINR TO BE
C INTERPOLATED.
C T2: INTERPOLATED TEMP PASSED BACK FROM LINR AND
C PASSED TO TOP.
C TM: MODELED TEMPS COMPUTED FROM MODELED
C GRADIENTS
C GRAD: GRADIENT COMPUTED FROM T2
C XG: MODELED GRADIENT PASSED BACK FROM GFIT
C D: READ FROM MASTER FILE. PASSED TO LINR.
C D2: DEPTH PASSED BACK FROM LINR.
C D3: DEPTHS FOR GRADIENT PLOT (ONE LESS THAN D2)
C
C CHARACTER IDENT*10,PARM*1,HEADER*60,IOPT*1
C CHARACTER HD*60
C DIMENSION IFLAG(8),T(2500),D(2500)
C DIMENSION GRAD(400),D3(400),XG(400)
C DIMENSION T2(401),D2(401),TM(401)
C DIMENSION CD(7),CG(7),COEF(11),X2(12)
C IU=3
C IEND=0
C ICNT=0
C ICNT1=0
C IERR0 = 0
C IERR1=0
C IERR2=0
C IERR3=0
C IERR4=0
C N=0
C IDAT=0
C IFIRST=0
C
C WRITE(6,604)
```

```

604 FORMAT(//,1X,' — PROGRAM GMODEL —',/,
*1X,'RUN BATHTAG FIRST IF DMIN WILL BE LESS THAN
DMAX',/)
C
CALL INOUT4
99  FORMAT (A25)
OPEN (2,FILE='fguess.dat',FORM='FORMATTED',STATUS=
'OLD')
WRITE(6,*) ('WHAT IS MAX DEPTH OF GRAD MODEL? (M)')
READ(5,*) DMAX
WRITE(6,*) ('WHAT IS MIN DEPTH TO ACCEPT PROFILE?
(M)')
READ(5,*) DMIN
WRITE(6,*) ('ENTER STARTING PROFILE')
READ(5,*) IFIRST
WRITE(6,*) ('HOW MANY PROFILES?')
READ(5,*) NUMPRO
C
WRITE(6,*) ('DO YOU WANT TO WRITE OUT COEFS?
(Y OR N)')
READ(5,500) IOPT
500 FORMAT(A1)
C*****
C READ HEADER RECORD FROM MASTER FILE
C*****
READ(3,ERR=9500) PARM,HEADER
WRITE(6,600) PARM,HEADER
600 FORMAT(/,1X,'INPUT FILE DATA TYPE: ',A1,/,
*1X,'HEADER: ',A60,/)
HD=('REJECTED PROFILES FROM GMODEL')
WRITE(9) PARM,HD
WRITE(8) PARM,HEADER
C
WRITE(6,621) DMAX,DMIN
621 FORMAT(/,1X,'GRADIENT MODEL EXTENDS TO ',F6.0,' M',/,
*1X,'PROFILES AT LEAST ',F4.0,' M WILL BE ACCEPTED',/)
C*****
C COMPUTE DELZ AND WRITE HEADER TO OUTPUT FILE
C*****

```

534 C Thermohaline Parametric Model

```
      DELZ = DMAX/400.
      IF(DELZ.LT.0.5) DELZ = 0.5
C
      IF(IOPT.EQ.'Y') THEN
      WRITE(4,609) DELZ,DMIN,DMAX
      WRITE(7,609) DELZ,DMIN,DMAX
609  FORMAT(1X,3F8.2)
      END IF
C*****
C LOOP THROUGH UNWANTED PROFILES
C*****
      IF(IFIRST.NE.1) THEN
      DO 100 I=1,IFIRST-1
      READ(3,END=9000,ERR=9500)NPROF,(IFLAG(J),J=1,8),
      XLAT, XLON,
      *JPROF,ICLAS,IPAT,IMASS,IPOV,WDEP1,WDEP2,
      IYEAR,IMON,
      *IDAY,XHOUR,IDENT,ISOUC,NCYC1,NCYC2,
      *EXTRA,ICRUZ,(D(J),T(J),J=1,NCYC1+NCYC2)
      ICNT = ICNT+1
100  CONTINUE
      END IF
C*****
C READ DESIRED PROFILES FROM MASTER FILE
C*****
      DO 12 I=1,NUMPRO
      READ(3,END=9001,ERR=9500) NPROF,(IFLAG(J),J=1,8),XLAT,
      XLON,
      *JPROF,ICLAS,IPAT,IMASS,IPOV,
      *WDEP1,WDEP2,IYEAR,IMON,IDAY,XHOUR,IDENT,ISOUC,
      NCYC1,
      *NCYC2,EXTRA,ICRUZ,(D(J),T(J),J=1,NCYC1+NCYC2)
      NCYC=NCYC1+NCYC2
      ICNT1 = ICNT1+1
      WRITE(6,*) ('PROFILE '),I
C*****
C PROFILE HAS BEEN READ - CHECK FLAG(1) FOR UNWANTED
C PROFILE
C*****
```

```

      IF(NPROF.EQ.42.OR.NPROF.EQ.29.OR.NPROF.EQ.315.
*OR.NPROF.EQ.1234) THEN
        IERR0 = IERR0+1
        GO TO 12
      END IF
C*****
C CHECK TO SEE IF PROFILE EXTENDS TO DEPTH OF DMIN
C*****
      IF(D(NCYC).LT.DMIN) THEN
        IERR1 = IERR1+1
        GO TO 12
      END IF
      IKEEP = IKEEP+1
C*****
C INTERPOLATE PROFILE TO D(NCYC) OR DMAX, WHICHEVER
C WHICHEVER IS GREATEST.
C*****
      BOT = DMAX
      IF(D(NCYC).LT.DMAX) BOT=D(NCYC)
      CALL LINR(DELZ,NCYC,0.,BOT,ICT,D,T,D2,T2)
C*****
C CALCULATE GRADIENT
C*****
      GMAX = -999.
      GMIN = 999.
      DO 20 L=1,ICT-1
        GRAD(L) = (T2(L+1)-T2(L)) / DELZ
        D3(L) = D2(L) + (DELZ/2.)
        IF(GRAD(L).GT.GMAX) GMAX = GRAD(L)
        IF(GRAD( L).LT.GMIN) GMIN = GRAD(L)
      20 CONTINUE
C   WRITE(6,605) GMIN,GMAX
      605  FORMAT(/,1X,'GMIN,GMAX = ',2F8.4)
C*****
C CALL GRADFIT (GFIT) TO COMPUTE MODELED GRADIENT
C*****
      ICT2 = ICT-1
      CALL GFIT(DELZ,ICT2,D3,GRAD,XG,D2,T2,CD,CG)
C*****
C COMPUTE MODELED TEMPERATURE FROM MODELED
      GRADIENT
C*****

```

```

      TM(1) = T2(1)
      DO 30 L=2,ICT
30    TM(L) = XG(L-1) * (D2(L)-D2(L-1)) + TM(L-1)
C*****
C COMPUT FINAL RMS ERROR IN TEMPERATURE SPACE
C*****
      CALL RMS(TM,T2,ICT,R)
C*****
C FILL COEFFICIENT ARRAY (ORIGINAL COEFS: DEPTHS AND
C GRADIENTS)
C*****
C
      COEF(1) = T2(1)
      COEF(2) = CD(2)
      COEF(3) = CD(3)
      COEF(4) = CD(4)
      COEF(5) = CD(5)
      COEF(6) = CD(6)
      COEF(7) = CG(1)
      COEF(8) = CG(3)
      COEF(9) = CG(5)
      COEF(10) = CG(6)
      COEF(11) = CG(7)
C*****
C IF DESIRED, WRITE COEFFICIENTS TO UNIT 4
C*****
      IF(IOPT.EQ.'N') GO TO 24
      IF(R.GT.0.13) THEN
      GO TO 24
      END IF
      WRITE(4,610)NPROF,XLAT,XLON,WDEP2,(COEF(K),K=1,11),
      *NCYC1,IMASS
610  FORMAT(I5,2(F8.3,1X),F6.0,1X,F5.2,1X,5(F8.2,1X),5F8.4,I5,I4)
      WRITE(28,615) XLAT,XLON,COEF(1),COEF(2),COEF(3)
615  FORMAT(2(f8.3,2x),f5.2,2x,f8.2,2x,f8.2)
      24 CONTINUE
C
C*****
C COMPUTE TEMPS AT DEPTHS OF COARSE GRADIENTS:
  THESE WILL
C BE THE ACTUAL COEFFICIENTS FOR INTERPOLATION
C*****

```

```

X2(1) = T2(1)
CALL LINR(CD(2),ICT,CD(2),CD(2),ICT4,D2,TM,DOUT,TOUT)
X2(2) = TOUT
X2(8) = DOUT
CALL LINR(CD(3),ICT,CD(3),CD(3),ICT4,D2,TM,DOUT,TOUT)
X2(3) = TOUT
X2(9) = DOUT
CALL LINR(CD(4),ICT,CD(4),CD(4),ICT4,D2,TM,DOUT,TOUT)
X2(4) = TOUT
X2(10) = DOUT
CALL LINR(CD(5),ICT,CD(5),CD(5),ICT4,D2,TM,DOUT,TOUT)
X2(5) = TOUT
X2(11) = DOUT
CALL LINR(CD(6),ICT,CD(6),CD(6),ICT4,D2,TM,DOUT,TOUT)
X2(6) = TOUT
X2(12) = DOUT
X2(7) = TM(ICT)
C *****
C   IF DESIRED, WRITE INTERPOLATED COEFS TO UNIT 7 AND
C   MASTER FILE PROFILE TO UNIT 8 (TO USE FOR STD
C   DEPTH INTERP).
C   PROFILES NOT PASSING RMS TEST ARE WRITTEN TO
C   MASTER FILE C 9.
C *****
C   IF(IOPT.EQ.'N') GO TO 25
C   IF(R.GT.0.13) THEN
C     IRMS = IRMS+1
C     WRITE(9) NPROF,(IFLAG(J),J=1,8),XLAT,XLON,
C     * JPROF,ICLAS,IPAT,IMASS,IPOV,
C     * WDEP1,WDEP2,IYEAR,IMON,IDAY,XHOUR,IDENT,ISOURC,
C     * NCYC1,NCYC2,
C     * EXTRA,ICRUZ,(D(J),T(J),J=1,NCYC1+NCYC2)
C     GO TO 25
C   END IF
C
C   WRITE(7,611) NPROF,XLAT,XLON,WDEP2,(X2(K),K=1,12)
611 FORMAT(I5,2(F8.3,1X),F6.0,7F8.3,5F8.2)
C
C   WRITE(8) NPROF,(IFLAG(J),J=1,8),XLAT,XLON,
C   * JPROF,ICLAS,IPAT,IMASS,IPOV, WDEP1,WDEP2,IYEAR,
C   IMON,
C   * IDAY,XHOUR,IDENT,ISOURC,NCYC1,NCYC2,
C   * EXTRA,ICRUZ,(D(J),T(J),J=1,NCYC1+NCYC2)

```

```

25 CONTINUE
C
12 CONTINUE
GO TO 9002
C
9000 WRITE(6,650) ICNT
650 FORMAT(1X,'BEGINNING PROFILE NOT FOUND',/,
*1X,'EOF ENCOUNTERED AFTER PROFILE',I5,'.
END PROGRAM.')
GO TO 1000
C
9001 IEND = 1
9002 LAST = IFIRST+ICNT1-1
WRITE(6,651) ICNT1,IFIRST,LAST
651 FORMAT(1X,I5,' PROFILES READ FROM MASTER FILE',/,
*1X,'FIRST PROFILE:',I5,5X,'LAST PROFILE:',I5)
GO TO 1000
C
9500 ITOT = ICNT+ICNT1
WRITE(6,652) ITOT
652 FORMAT(1X,'READ ERROR AFTER RECORD NUMBER
*(PROFILE)',I5,/,
*1X,'*** CHECK MASTER FILE *** PROGRAM TERMINATED.')
```

```

C
1000 CONTINUE
C
WRITE(6,653) IERR1,IKEEP
653 FORMAT(/,1X,I5,' PROFILES NOT DEEP ENOUGH',/,
*1X,I5,' PROFILES KEPT FOR PROCESSING')
```

```

C
WRITE(6,654) IRMS
654 FORMAT(/,1X,I5,' PROFILE REJECTED FOR RMS GT 0.13 -
SEE UNIT
*9')
CALL DONEPL
END
```

C.4 Subroutines

C.4.1 Interpolation

The subroutine *LINR* is used for linear interpolation to fill the gaps in the input data.

```

*****
**
SUBROUTINE LINR(DELX,N,XBGN,XEND,ICT,X,Y,AX,AY)
C DELX=DESIRED INTERPOLATION INTERVAL, X AND Y
  ARE INPUT
C WITH X=INDEP.
C VARIABLE, AX AND AY ARE OUTPUT, N=LENGTH OF X,
  XBGN AND
C XEND=DESIRED
C BEGINNING AND ENDING VALUES OF AX,ICT=LENGTH OF AX
  DIMENSION X(*),Y(*),AX(*),AY(*)
  NN=N-1
  ICT=((XEND-XBGN)/DELX)+1.0001
  DO 1 J=1,ICT
    A=J-1
  1 AX(J)=A*DELX+XBGN
    KK=1
    DO 2 J=1,NN
      JJ=J+1
      SLOPE=(Y(JJ)-Y(J))/(X(JJ)-X(J))
      DO 3 K=KK,ICT
        I=K
        IF(AX(K).GT.X(JJ).AND.AX(K).LE.X(N)) GO TO 2
      3 AY(K)=SLOPE*(AX(K)-X(J))+Y(J)
        GO TO 4
      2 KK=I
    4 RETURN
  END

```

C.4.2 Iteration

As described in Sect. 2.4.3, the subroutine *BUMP* is used to perform an increment change in depth data; the subroutine *RMS* is used to compute the root mean square error; and the subroutine *DEPALL* is used to conduct the iteration.

```

*****
***
SUBROUTINE BUMP(CD,LEVEL,DINC,IB,ISIGN,IGO)
C
C *****
C *
C * SUBROUTINE BUMP
C *
C *****
C
C

```

```

C   *** PARAMETERS PASSED TO BUMP
C
C   CD: DEPTH ARRAY (7) FOR COARSE DEPTHS (GRADIENT
C   SPACE)
C   LEVEL: DEPTH BEING ADJUSTED IN CALLING PROGRAM
C   (2-6)
C   DINC: DEPTH INTERVAL (METERS) FOR ADJUSTMENTS
C   IB: FLAG TO INDICATE WHAT TYPE OF BUMP DESIRED -
C   IB = 0: DONT BUMP ANY DEPTH
C   IB = 1: BUMP ONLY DEPTHS ABOVE (IF ADJ UPWARD)
C   IB = 2: BUMP ONLY DEPTHS BELOW (IF ADJ DOWNWARD)
C   IB = 3: BUMP ANY DEPTH (DEPENDING IF GOING UP OR
C   DOWN)
C   ISIGN: FLAG TO INDICATE DIRCTION OF DEPTH ADJUSTMENT
C   (1 = ADDING DEPTHS, -1 = SUBTRACTING DEPTHS)
C
C   *** PARAMETERS PASSED BACK TO CALLING PROGRAM
C
C   CD: DEPTHS DEFINED ABOVE (BUT NOW USUALLY
C   DIFFERENT)
C   IGO: FLAG TO TELL WHERE TO GO IN CALLING PROGRAM
C   (0 = CONTINUE, 1 = GO TO END OF CALLING SUBROUTINE)
C
C
C   DIMENSION CD(7)
C
C   IGO = 0
C   L = LEVEL
C   F1 = CD(1)
C   F7 = CD(7)
C
C   IF(ISIGN.EQ.1) GO TO 10
C   IF(ISIGN.EQ.-1) GO TO 20
C
C   *****
C   CASE FOR ADDING DEPTHS IN CALLING SUBROUTINE
C   *****
C
C   DONT BUMP
C

```

```

10 CONTINUE
   IF(IB.EQ.0.OR.IB.EQ.1) THEN
   IF(CD(L).GE.CD(L+1)) THEN
   CD(L) = CD(L) - DINC
   IGO = 1
   END IF
   RETURN
   END IF
C
C BUMP DEPTHS BELOW
C
   IF(IB.EQ.2.OR.IB.EQ.3) THEN
   LL = L
   DO 15 K=1,7-LL
   IF(CD(L).GE.CD(L+1)) THEN
   CD(L+1) = CD(L+1) + DINC
   L = L+1
   END IF
15 CONTINUE
C
C IF BOTTOM DEPTH WAS BUMPED, MOVE ALL NECESSARY DEPTHS
C UP
C
   IF(CD(7).GT.F7) THEN
   L = 7
   DO 17 K=1,7-LL
   CD(L) = CD(L) - DINC
   L = L-1
17 CONTINUE
   IGO = 1
   END IF
   RETURN
   END IF
C
C *****
C CASE FOR SUBTRACTING DEPTHS IN CALLING SUBROUTINE
C *****
C

```

542 C Thermohaline Parametric Model

```
C DONT BUMP
C
20 CONTINUE
  IF(IB.EQ.0.OR.IB.EQ.2) THEN
  IF(CD(L).LE.CD(L-1)) THEN
  CD(L) = CD(L) + DINC
  IGO = 1
  END IF
  RETURN
  END IF
C
C BUMP DEPTHS ABOVE
C
  IF(IB.EQ.1.OR.IB.EQ.3) THEN
  LL = L
  DO 25 K=1,LL-1
  IF(CD(L).LE.CD(L-1)) THEN
  CD(L-1) = CD(L-1) - DINC
  pcL = L-1
  END IF
25 CONTINUE
C
C IF TOP DEPTH WAS BUMPED, MOVE ALL NECESSARY
  DEPTHS
C BACK DOWN
C
26 IF(CD(1).LT.F1) THEN
  L = 1
  DO 27 K=1,LL
  CD(L) = CD(L) + DINC
  L = L+1
27 CONTINUE
  IGO = 1
  GO TO 26
  END IF
  RETURN
  END IF
C
  END
*****
SUBROUTINE RMS(XG,GRAD,ICT2,R)
DIMENSION XG(*),GRAD(*)
R = 0
DO 10 J=1,ICT2
10 R = R + (XG(J)-GRAD(J))**2.
RT = XG(J)-GRAD(J)
R = (R/ICT2)**0.5
RETURN
END
```

```
*****
```

```

SUBROUTINE
*DEPALL(DELX,SUR,BOT,ICT2,CD,CG,D3,GRAD,R,TOL,NI)
C
C *****
C SUBROUTINE DEPALL
C MAKE INITIAL ADJUSTMENT OF D1,D2,D3,D4 (CD(2) - CD(5))
C ALSO ADJUST CD(6) AFTER ABOVE DEPTHS ARE ADJUSTED
C *****
C
C
C     DIMENSION D3(400),GRAD(400),CD(*),CG(*),XG(400)
C     DIMENSION RR(400)
C
C     IKEEP = 0
C     WRITE(6,606) (CD(J),J=1,7)
606 FORMAT(1X,'INITIAL CDS: ',7F6.1)
C
C CHECK FIRST TO SEE WHETHER TO ADD OR SUBTRACT
DEPTHS
C
C     ICNT = 0
C     RMIN = 999.
C     DINC = DELX
C     R1 = R
C
C COMPUTE DIFFERENCE BETWEEN CD(2) AND CD(1) AND
SUBTRACT
C THIS FROM CD(2) THROUGH CD(5) FOR STARTING DEPTHS
C
C     FIRST = CD(2)
C     DIFF = CD(2) - CD(1)
C     DO 5 K=2,5
5 CD(K) = CD(K) - DIFF + DINC
C
C FILL MODELED GRADIENT ARRAY WITH LINR USING NEW
DEPTHS
C
C     DO 80 M=1,ICT2
C     CALL LINR(DELX,7,SUR,BOT,ICT2,CD,CG,D3,XG)
C     CALL RMS(XG,GRAD,ICT2,R)
C     ICNT = ICNT+1
C
C     RR(ICNT) = R
C     IF(RR(M).LE.RMIN) THEN
C     IKEEP = ICNT
C     RMIN = RR(M)
C     END IF

```

544 C Thermohaline Parametric Model

```
C
  DO 6 K=2,5
  6 CD(K) = CD(K) + DINC
    IF(CD(5).GE.CD(6)) GO TO 85
  80 CONTINUE
C
C
  85 CONTINUE
    NEWCD2 = (IKEEP-1)*DINC
C
C ADJUST CD(2) THROUGH CD(5) TO OPTIMUM DEPTHS
C
  DIFF = CD(2) - NEWCD2
  DO 15 K=2,5
  15 CD(K) = CD(K) - DIFF + DINC
C
C COMPUTE INITIAL DEPTH FOR CD(6): 1/4 OF THE
C DISTANCE BETWEEN
C CD(5) AND CD(7).
C
  DIFF2 = CD(6) - CD(5)
  CD(6) = CD(5) + 0.25*DIFF2
  CALL LINR(DELX,7,SUR,BOT,ICT2,CD,CG,D3,XG)
  CALL RMS(XG,GRAD,ICT2,R)
C
C WRITE(6,604) (CD(J),J=1,7)
  604 FORMAT(1X,'NEW CDS: ',7F6.1)
  ADJ = FIRST - CD(2)
C WRITE(6,605) ICNT,ADJ,R
  605 FORMAT(1X,'DEPALL ITNS:',I3,4X,'ADJ: ',F6.0,3X,
    *'RMS = ',F7.4)
  RETURN
  END
```

C.4.3 Mixed Layer Depth

The subroutine *DEP1* is used to determine the mixed layer depth.

```
*****
  SUBROUTINE DEP1(DELX,SUR,BOT,ICT2,CD,CG,D3,
    *GRAD,R,TOL,NI,IB,IDUM)
C
C *****
C
C SUBROUTINE DEP1
C ADJUST D1 (CD(2)) - DEPTH OF MIXED LAYER
C
```

```

C *****
C
C     DIMENSION D3(400),GRAD(400),CD(*),CG(*),XG(400)
C
C     CHECK FIRST TO SEE WHETHER TO ADD OR
C     SUBTRACT
C     DEPTHS
C
C     ICNT = 0
C     FIRST = CD(2)
C     DINC = DELX
C     R1 = R
C     CD(2) = CD(2) + DINC
C     CALL BUMP(CD,2,DINC,IB,1,IGO)
C     IF(IGO.EQ.1) GO TO 199
C
C     FILL MODELED GRADIENT ARRAY WITH LINR USING
C     NEW DEPTHS
C
C     CALL LINR(DELX,7,SUR,BOT,ICT2,CD,CG,D3,XG)
C     CALL RMS(XG,GRAD,ICT2,R)
C     ICNT = ICNT+1
C
C     IF(ABS(R-R1).LT.TOL) GO TO 199
c
c     IF(R.LT.R1) GO TO 100   @ GOING RIGHT WAY
c     IF(R.GT.R1) THEN     @ GOING WRONG WAY
c
c     IF(R.LT.R1) GO TO 100
c     IF(R.GT.R1) THEN
c
c     CD(2) = CD(2) - DINC
c     R = R1
c     GO TO 150
c     END IF
C
C     ADJUST D1 BY ADDING DEPTHS
C
100 IF = 0
102 IF(ICNT.GT.NI) GO TO 199
    R1 = R
    CD(2) = CD(2) + DINC
    CALL BUMP(CD,2,DINC,IB,1,IGO)
    IF(IGO.EQ.1) GO TO 199
C
C     CALL LINR(DELX,7,SUR,BOT,ICT2,CD,CG,D3,XG)
C     CALL RMS(XG,GRAD,ICT2,R)
C     ICNT = ICNT+1

```

546 C Thermohaline Parametric Model

```
C
  IF(ABS(R-R1).LT.TOL) GO TO 199
  IF(R.LT.R1) GO TO 102
  IF(R.GT.R1.AND.IF.NE.4) THEN
  IF = IF+1
  CD(2) = CD(2) - DINC
  DINC = DINC/2.
  R = R1
  GO TO 102
  END IF

C
  GO TO 199

C
C  ADJUST D1 BY SUBTRACTING DEPTHS
C
150 IF = 0
152 IF(ICNT.GT.NI) GO TO 199
  R1 = R
  CD(2) = CD(2) - DINC
  CALL BUMP(CD,2,DINC,IB,-1,IGO)
  IF(IGO.EQ.1) GO TO 199

C
  CALL LINR(DELX,7,SUR,BOT,ICT2,CD,CG,D3,XG)
  CALL RMS(XG,GRAD,ICT2,R)
  ICNT = ICNT+1

C
  IF(ABS(R-R1).LT.TOL) GO TO 199
  IF(R.LT.R1) GO TO 152
  IF(R.GT.R1.AND.IF.NE.4) THEN
  IF = IF+1
  CD(2) = CD(2) + DINC
  DINC = DINC/2.
  R = R1
  GO TO 152
  END IF

C
  GO TO 199

C
199 CONTINUE

C
  ADJ = FIRST - CD(2)
C  WRITE(6,605) ICNT,ADJ,R
605 FORMAT(1X,'D1 ITERATIONS: ',I3,4X,'ADJ: ',F6.0,3X,
  *,'RMS = ',F7.4)

C
C
  RETURN
  END
```

C.4.4 Depth at the Top of Thermocline/Halocline

The subroutine DEP2 is used to determine the depth at the top of thermocline (or halocline).

```

*****
      SUBROUTINE DEP2(DELX,SUR,BOT,ICT2,CD,CG,D3,GRAD,R,
        TOL,NI,*IB,IF)
C
C *****
C SUBROUTINE DEP2 *
C ADJUST D2 (CD(3)) - DEPTH OF TOP OF THERMOCLINE *
C *****
C
C DIMENSION D3(400),GRAD(400),CD(*),CG(*),XG(400)
C
C CHECK FIRST TO SEE WHETHER TO ADD OR
C SUBTRACT DEPTHS
C
C ICNT = 0
C FIRST = CD(3)
C DINC = DELX
C R1 = R
C CD(3) = CD(3) + DINC
C CALL BUMP(CD,3,DINC,IB,1,IGO)
C IF(IGO.EQ.1) GO TO 199
C
C FILL MODELED GRADIENT ARRAY WITH LINR USING
C NEW DEPTHS
C
C CALL LINR(DELX,7,SUR,BOT,ICT2,CD,CG,D3,XG)
C CALL RMS(XG,GRAD,ICT2,R)
C ICNT = ICNT+1
C
C IF(ABS(R-R1).LT.TOL) GO TO 199
c
c IF(R.LT.R1) GO TO 100 @ GOING RIGHT WAY
c IF(R.GT.R1) THEN @ GOING WRONG WAY
C IF(R.LT.R1) GO TO 100
C IF(R.GT.R1) THEN
c
c CD(3) = CD(3) - DINC
C R = R1
C GO TO 150
C END IF

```

548 C Thermohaline Parametric Model

```
C
C ADJUST D2 BY ADDING DEPTHS
C
100 IF = 0
102 IF(ICNT.GT.NI) GO TO 199
    R1 = R
    CD(3) = CD(3) + DINC
    CALL BUMP(CD,3,DINC,IB,1,IGO)
    IF(IGO.EQ.1) GO TO 199
C
    CALL LINR(DELX,7,SUR,BOT,ICT2,CD,CG,D3,XG)
    CALL RMS(XG,GRAD,ICT2,R)
    ICNT = ICNT+1
C
    IF(ABS(R-R1).LT.TOL) GO TO 199
    IF(R.LT.R1) GO TO 102
    IF(R.GT.R1.AND.IF.NE.4) THEN
        IF = IF+1
        CD(3) = CD(3) - DINC
        DINC = DINC/2.
        R = R1
        GO TO 102
    END IF
C
    GO TO 199
C
C ADJUST D2 BY SUBSTRACTING DEPTHS
C
150 IF = 0
152 IF(ICNT.GT.NI) GO TO 199
    R1 = R
    CD(3) = CD(3) - DINC
    CALL BUMP(CD,3,DINC,IB,-1,IGO)
    IF(IGO.EQ.1) GO TO 199
C
    CALL LINR(DELX,7,SUR,BOT,ICT2,CD,CG,D3,XG)
    CALL RMS(XG,GRAD,ICT2,R)
    ICNT = ICNT+1
C
    IF(ABS(R-R1).LT.TOL) GO TO 199
    IF(R.LT.R1) GO TO 152
    IF(R.GT.R1.AND.IF.NE.4) THEN
```

```

      IF = IF+1
      CD(3) = CD(3) + DINC
      DINC = DINC/2.
      R = R1
      GO TO 152
      END IF
C
      GO TO 199
C
199 CONTINUE
C
      ADJ = FIRST - CD(3)
C      WRITE(6,605) ICNT,ADJ,R
605 FORMAT(1X,'D2 ITERATIONS: ',I3,4X,'ADJ: ',F6.0,3X,
          *'RMS = ',F7.4)
C
      RETURN
      END

```

C.4.5 Depth at the Bottom of Thermocline/Halocline

The subroutine DEP3 is used to determine the depth at the bottom of thermocline (or halocline).

```

*****
      SUBROUTINE DEP3(DELX,SUR,BOT,ICT2,CD,CG,D3,GRAD,R,
          TOL,NI,*IB,IF)
C
C *****
C SUBROUTINE DEP3 *
C ADJUST D3 (CD(4)) - DEPTH OF BOTTOM OF THERMOCLINE *
C OR HALOCLINE *
C *****
C
      DIMENSION D3(400),GRAD(400),CD(*),CG(*),XG(400)
C
C CHECK FIRST TO SEE WHETHER TO ADD OR SUBTRACT
      DEPTHS
C
      ICNT = 0
      FIRST = CD(4)
      DINC = DELX

```

```

550   C Thermohaline Parametric Model

      R1 = R
      CD(4) = CD(4) + DINC
      CALL BUMP(CD,4,DINC,IB,1,IGO)
      IF(IGO.EQ.1) GO TO 199

C
C   FILL MODELED GRADIENT ARRAY WITH LINR USING
NEW DEPTHS

C
      CALL LINR(DELX,7,SUR,BOT,ICT2,CD,CG,D3,XG)
      CALL RMS(XG,GRAD,ICT2,R)
      ICNT = ICNT+1

C
      IF(ABS(R-R1).LT.TOL) GO TO 199

c
c   IF(R.LT.R1) GO TO 100   @ GOING RIGHT WAY
c   IF(R.GT.R1) THEN     @ GOING WRONG WAY
      IF(R.LT.R1) GO TO 100
      IF(R.GT.R1) THEN

c
      CD(4) = CD(4) - DINC
      R = R1
      GO TO 150
      END IF

C
C   ADJUST D3 BY ADDING DEPTHS
C
100  IF = 0
102  IF(ICNT.GT.NI) GO TO 199
      R1 = R
      CD(4) = CD(4) + DINC
      CALL BUMP(CD,4,DINC,IB,1,IGO)
      IF(IGO.EQ.1) GO TO 199

C
      CALL LINR(DELX,7,SUR,BOT,ICT2,CD,CG,D3,XG)
      CALL RMS(XG,GRAD,ICT2,R)
      ICNT = ICNT+1

C
      IF(ABS(R-R1).LT.TOL) GO TO 199
      IF(R.LT.R1) GO TO 102
      IF(R.GT.R1.AND.IF.NE.10) THEN
          IF = IF+1
          CD(4) = CD(4) - DINC
          DINC = DINC/2.
          R = R1
          GO TO 102
      END IF

```

```

C
  GO TO 199
C
C ADJUST D3 BY SUBSTRACTING DEPTHS
C
  150 IF = 0
  152 IF(ICNT.GT.NI) GO TO 199
      R1 = R
      CD(4) = CD(4) - DINC
      CALL BUMP(CD,4,DINC,IB,-1,IGO)
      IF(IGO.EQ.1) GO TO 199
C
  CALL LINR(DELX,7,SUR,BOT,ICT2,CD,CG,D3,XG)
  CALL RMS(XG,GRAD,ICT2,R)
  ICNT = ICNT+1
C
  IF(ABS(R-R1).LT.TOL) GO TO 199
  IF(R.LT.R1) GO TO 152
  IF(R.GT.R1.AND.IF.NE.10) THEN
      IF = IF+1
      CD(4) = CD(4) + DINC
      DINC = DINC/2.
      R = R1
      GO TO 152
  END IF
C
  GO TO 199
C
  199 CONTINUE
C
      ADJ = FIRST - CD(4)
      WRITE(6,605) ICNT,ADJ,R
605 FORMAT(1X,'D3 INTERATIONS: ',I3,4X,'ADJ: ',F6.0,3X,
  *'RMS = ',F7.4)
C
  RETURN
  END

```

C.4.6 Depth at Top of Near-Zero Gradient Below Thermocline

```

      SUBROUTINE DEP4(DELX,SUR,BOT,ICT2,CD,CG,D3,GRAD,R,
  TOL,NI,*IB,IF,IR)
C
C *****

```

552 C Thermohaline Parametric Model

```
C
C VALUE OF IR DETERMINES INTERVAL OVER WHICH RMS IS
C COMPUTED.
C
C *****
C
C
C DIMENSION D3(400),GRAD(400),CD(*),CG(*),XG(400)
C KEEP = BOT
C
C IF(IR.EQ.1) THEN
C   BOT = CD(5)
C   CALL LINR(DELX,7,SUR,BOT,ICT2,CD,CG,D3,XG)
C   CALL RMS(XG,GRAD,ICT,R)
C END IF
C
C CHECK FIRST TO SEE WHETHER TO ADD OR SUBTRACT
C DEPTHS
C
C ICNT = 0
C FIRST = CD(5)
C DINC = DELX
C R1 = R
C CD(5) = CD(5) + DINC
C CALL BUMP(CD,5,DINC,IB,1,IGO)
C IF(IGO.EQ.1) GO TO 199
C
C FILL MODELED GRADIENT ARRAY WITH LINR USING
C NEW DEPTHS
C
C IF(IR.EQ.1) BOT = CD(5)
C CALL LINR(DELX,7,SUR,BOT,ICT2,CD,CG,D3,XG)
C CALL RMS(XG,GRAD,ICT2,R)
C ICNT = ICNT+1
C
C IF(ABS(R-R1).LT.TOL) GO TO 199
C
C IF(R.LT.R1) GO TO 100 @ GOING RIGHT WAY
C IF(R.GT.R1) GO TO 150 @ GOING WRONG WAY
C IF(R.LT.R1) GO TO 100
C IF(R.GT.R1) GO TO 150
C
C ADJUST D4 BY ADDING DEPTHS
C
100 IF = 0
102 IF(ICNT.GT.NI) GO TO 199
C R1 = R
C CD(5) = CD(5) + DINC
```

```

CALL BUMP(CD,5,DINC,IB,1,IGO)
IF(IGO.EQ.1) GO TO 199
C
IF(IR.EQ.1) BOT = CD(5)
CALL LINR(DELX,7,SUR,BOT,ICT2,CD,CG,D3,XG)
CALL RMS(XG,GRAD,ICT2,R)
ICNT = ICNT+1
C
IF(ABS(R-R1).LT.TOL) GO TO 199
IF(R.LT.R1) GO TO 102
IF(R.GT.R1.AND.IF.NE.4) THEN
  IF = IF+1
  CD(5) = CD(5) - DINC
  DINC = DINC/2.
  GO TO 102
END IF
C
GO TO 199
C
C ADJUST D4 BY SUBTRACTING DEPTHS
C
150 IF = 0
152 IF(ICNT.GT.NI) GO TO 199
  R1 = R
  CD(5) = CD(5) - DINC
  CALL BUMP(CD,5,DINC,IB,-1,IGO)
  IF(IGO.EQ.1) GO TO 199
C
IF(IR.EQ.1) BOT = CD(5)
CALL LINR(DELX,7,SUR,BOT,ICT2,CD,CG,D3,XG)
CALL RMS(XG,GRAD,ICT2,R)
ICNT = ICNT+1
C
IF(ABS(R-R1).LT.TOL) GO TO 199
IF(R.LT.R1) GO TO 152
IF(R.GT.R1.AND.IF.NE.4) THEN
  IF = IF+1
  CD(5) = CD(5) + DINC
  DINC = DINC/2.
  GO TO 152
END IF
C
GO TO 199
C
199 CONTINUE
C
ADJ = FIRST - CD(5)

```

554 C Thermohaline Parametric Model

```
C WRITE(6,605) ICNT,ADJ,R
605 FORMAT(1X,'D4 INTERATIONS: ',I3,4X,'ADJ: ',F6.0,3X,
*'RMS = ',F7.4)
C
C IF IR FLAG = 1, CALL LINR ONCE MORE WITH TRUE VALUE FOR
C BOTTOM
C
C IF(IR.EQ.1) THEN
C BOT = KEEP
C CALL LINR(DELX,7,SUR,BOT,ICT2,CD,CG,D3,XG)
C END IF
C
C RETURN
C END
```

```
SUBROUTINE DEP4T(DELX,SUR,BOT,ICT2,CD,CG,D3,GRAD,R,
*TOL3,NI,D2,T2)
```

```
C
C*****
C
C ADJUST D4 (CD(5)) - DEPTH OF TOP OF NEAR-ZERO
C GRADIENT BELOW THRMCLN
C USE TEMP FOR RMS
C
C*****
C
C
C DIMENSION D3(400),GRAD(400),CD(*),CG(*),XG(400),
C *D2(401),T2(401),TM(401)
C
C CALCULATE INITIAL RMS IN TEMP SPACE
C
C ICT = ICT2+1
C CALL LINR(DELX,7,SUR,BOT,ICT2,CD,CG,D3,XG)
C TM(1) = T2(1)
C DO 29 L=2,ICT
29 TM(L) = XG(L-1) * (D2(L) - D2(L-1)) + TM(L-1)
C CALL RMS(TM,T2,ICT,R)
C
C CHECK FIRST TO SEE WHETHER TO ADD OR SUBTRACT
C DEPTHS
C
```

```

ICNT = 0
FIRST = CD(5)
DINC = DELX
R1 = R
CD(5) = CD(5) + DINC
IF(CD(5).GE.CD(6)) THEN
CD(5) = CD(5) - DINC
GO TO 199
END IF
C
C FILL MODELED GRADIENT ARRAY WITH LINR USING
NEW DEPTHS
C
CALL LINR(DELX,7,SUR,BOT,ICT2,CD,CG,D3,XG)
TM(1) = T2(1)
DO 30 L=2,ICT
30 TM(L) = XG(L-1) * (D2(L) - D2(L-1)) + TM(L-1)
CALL RMS(TM,T2,ICT,R)
ICNT = ICNT+1
C
IF(ABS(R-R1).LT.TOL3) GO TO 199
C
C IF(R.LT.R1) GO TO 100 @ GOING RIGHT WAY
C IF(R.GT.R1) GO TO 150 @ GOING WRONG WAY
IF(R.LT.R1) GO TO 100
IF(R.GT.R1) GO TO 150
C
C ADJUST D4 BY ADDING DEPTHS
C
100 IF = 0
102 IF(ICNT.GT.NI) GO TO 199
R1 = R
CD(5) = CD(5) + DINC
IF(CD(5).GE.CD(6)) THEN
CD(5) = CD(5) - DINC
GO TO 199
END IF
C
CALL LINR(DELX,7,SUR,BOT,ICT2,CD,CG,D3,XG)
TM(1) = T2(1)
DO 31 L=2,ICT
31 TM(L) = XG(L-1) * (D2(L) - D2(L-1)) + TM(L-1)
CALL RMS(TM,T2,ICT,R)
ICNT = ICNT+1

```

```

C
  IF(ABS(R-R1).LT.TOL3) GO TO 199
  IF(R.LT.R1) GO TO 102
  IF(R.GT.R1.AND.IF.NE.4) THEN
    IF = IF+1
    CD(5) = CD(5) - DINC
    DINC = DINC/2.
    GO TO 102
  END IF
C
  GO TO 199
C
C ADJUST D4 BY SUBSTRACTING DEPTHS
C
  150 IF = 0
  152 IF(ICNT.GT.NI) GO TO 199
    R1 = R
    CD(5) = CD(5) - DINC
    IF(CD(5).LE.CD(4)) THEN
      CD(5) = CD(5) + DINC
    GO TO 199
  END IF
C
  CALL LINR(DELX,7,SUR,BOT,ICT2,CD,CG,D3,XG)
  TM(1) = T2(1)
  DO 32 L=2,ICT
32 TM(L) = XG(L-1) * (D2(L) - D2(L-1)) + TM(L-1)
  CALL RMS(TM,T2,ICT,R)
  ICNT = ICNT+1
C
  IF(ABS(R-R1).LT.TOL3) GO TO 199
  IF(R.LT.R1) GO TO 152
  IF(R.GT.R1.AND.IF.NE.4) THEN
    IF = IF+1
    CD(5) = CD(5) + DINC
    DINC = DINC/2.
    GO TO 152
  END IF
C
  GO TO 199
C
  199 CONTINUE
C
  ADJ = FIRST - CD(5)
C  WRITE(6,605) ICNT,ADJ,R
  605 FORMAT(1X,'D4T INTERATIONS: ',I3,4X,'ADJ: ',F6.0,3X,
    *'RMS = ',F7.4)
C
  RETURN
  END

```

C.4.7 Depth between Two Last Legs of Profile

```

      SUBROUTINE DEP5(DELX,SUR,BOT,ICT2,CD,CG,D3,GRAD,R,TOL,NI,
*IB,IF)
C
C *****
C
C ADJUST D5 (CD(6)) - DEPTH BETWEEN LAST TWO LEGS OF PROFILE
C *****
C
C
C
C DIMENSION D3(400),GRAD(400),CD(*),CG(*),XG(400)
C
C CHECK FIRST TO SEE WHETHER TO ADD OR SUBTRACT DEPTHS
C
C   ICNT = 0
C   FIRST = CD(6)
C   DINC = DELX
C   R1 = R
C   CD(6) = CD(6) + DINC
C   CALL BUMP(CD,6,DINC,IB,1,IGO)
C   IF(IGO.EQ.1) GO TO 199
C
C FILL MODELED GRADIENT ARRAY WITH LINR USING NEW DEPTHS
C
C   CALL LINR(DELX,7,SUR,BOT,ICT2,CD,CG,D3,XG)
C   CALL RMS(XG,GRAD,ICT2,R)
C   ICNT = ICNT+1
C
C   IF(ABS(R-R1).LT.TOL) GO TO 199
C
C   IF(R.LT.R1) GO TO 100 @ GOING RIGHT WAY
C   IF(R.GT.R1) THEN @ GOING WRONG WAY
C   IF(R.LT.R1) GO TO 100
C   IF(R.GT.R1) THEN
C
C   CD(6) = CD(6) - DINC
C   R = R1
C   GO TO 150
C   END IF
C
C ADJUST D4 BY ADDING DEPTHS
C
100 IF = 0

```

558 C Thermohaline Parametric Model

102 IF(ICNT.GT.NI) GO TO 199

R1 = R
CD(6) = CD(6) + DINC
CALL BUMP(CD,6,DINC,IB,1,IGO)
IF(IGO.EQ.1) GO TO 199

C

CALL LINR(DELX,7,SUR,BOT,ICT2,CD,CG,D3,XG)
CALL RMS(XG,GRAD,ICT2,R)
ICNT = ICNT+1

C

IF(ABS(R-R1).LT.TOL) GO TO 199
IF(R.LT.R1) GO TO 102
IF(R.GT.R1.AND.IF.NE.10) THEN
IF = IF+1
CD(6) = CD(6) - DINC
DINC = DINC/2.
R = R1
GO TO 102
END IF

C

GO TO 199

C

C ADJUST D4 BY SUBSTRACTING DEPTHS

C

150 IF = 0
152 IF(ICNT.GT.NI) GO TO 199

R1 = R
CD(6) = CD(6) - DINC
CALL BUMP(CD,6,DINC,IB,-1,IGO)
IF(IGO.EQ.1) GO TO 199

C

CALL LINR(DELX,7,SUR,BOT,ICT2,CD,CG,D3,XG)
CALL RMS(XG,GRAD,ICT2,R)
ICNT = ICNT+1

C

IF(ABS(R-R1).LT.TOL) GO TO 199
IF(R.LT.R1) GO TO 152
IF(R.GT.R1.AND.IF.NE.10) THEN
IF = IF+1
CD(6) = CD(6) + DINC
DINC = DINC/2.
R = R1
GO TO 152
END IF

```

C
  GO TO 199
C
199 CONTINUE
C
  ADJ = FIRST - CD(6)
C  WRITE(6,605) ICNT,ADJ,R
605  FORMAT(1X,'D4 INTERATIONS: ',I3,4X,'ADJ: ',F6.0,3X,
  *'RMS = ',F7.4)
C
  RETURN
  END

```

C.4.8 Adjustment of Bottom Gradient

```

SUBROUTINE
*GRAD3A(DELX,SUR,BOT,ICT2,CD,CG,D3,GRAD,R,TOL2,NI)
C
C *****
C
C SUBROUTINE GRAD3A
C ADJUST G3A - GRADIENT AT BOTTOM
C
C *****
C
  DIMENSION D3(400),GRAD(400),CD(*),CG(*),XG(400)
C
C CHECK FIRST TO SEE WHETHER TO ADD OR SUBTRACT
  GRADIENT
C
  FIRST = CG(5)
  GINC = FIRST/25.
  IF(GINC.LT.0.005) GINC = .005
  ICNT = 0
  R1 = R
  CG(5) = CG(5) + GINC
C
C FILL MODELED GRADIENT ARRAY WITH LINR USING NEW
C GRADIENT
C
  CALL LINR(DELX,7,SUR,BOT,ICT2,CD,CG,D3,XG)
  CALL RMS(XG,GRAD,ICT2,R)
  ICNT = ICNT+1
C
  IF(ABS(R-R1).LT.TOL2) GO TO 199

```

560 C Thermohaline Parametric Model

```
C
C IF(R.LT.R1) GO TO 100 @ GOING RIGHT WAY
C IF(R.GT.R1) THEN @ GOING WRONG WAY
  IF(R.LT.R1) GO TO 100
  IF(R.GT.R1) THEN
C
  CG(5) = CG(5) - GINC
  R = R1
  GO TO 150
  END IF

C
C ADJUST GRADIENT G3A BY ADDING
C
100 IF = 0
102 IF(ICNT.GT.NI) GO TO 199
  R1 = R
  CG(5) = CG(5) + GINC
C
  CALL LINR(DELX,7,SUR,BOT,ICT2,CD,CG,D3,XG)
  CALL RMS(XG,GRAD,ICT2,R)
  ICNT = ICNT+1
C
  IF(ABS(R-R1).LT.TOL2) GO TO 199
  IF(R.LT.R1) GO TO 102
  IF(R.GT.R1.AND.IF.NE.10) THEN
  IF = IF+1
  CG(5) = CG(5) - GINC
  GINC = GINC/2.
  R = R1
  GO TO 102
  END IF

C
C GO TO 199
C
C ADJUST GRADIENT G3A BY SUBTRACTING
C
150 IF = 0
152 IF(ICNT.GT.NI) GO TO 199
  R1 = R
  CG(5) = CG(5) - GINC
C
  CALL LINR(DELX,7,SUR,BOT,ICT2,CD,CG,D3,XG)
  CALL RMS(XG,GRAD,ICT2,R)
  ICNT = ICNT+1
```

```

C
  IF(ABS(R-R1).LT.TOL2) GO TO 199
  IF(R.LT.R1) GO TO 152
  IF(R.GT.R1.AND.IF.NE.10) THEN
    IF = IF+1
    CG(5) = CG(5) + GINC
    GINC = GINC/2.
    R = R1
    GO TO 152
  END IF
C
  GO TO 199
C
199 CONTINUE
C
  ADJ = FIRST - CG(5)
C  WRITE(6,605) ICNT,ADJ,R
605 FORMAT(1X,'GRAD3A ITERATIONS: ',I3,4X,'ADJ: ',F6.0,3X,
  *'RMS = ',F7.4)
C
  RETURN
  END

*****
SUBROUTINE
  *G3AT(DELX,SUR,BOT,ICT2,CD,CG,D3,GRAD,R,TOL3,NI,D2,T2)
C
C *****
C
C SUBROUTINE G3AT
C ADJUST G3A - GRADIENT AT BOTTOM
C DO RMS WITH TEMP INSTEAD OF GRADIENT
C
C *****
C
  DIMENSION D3(400),GRAD(400),CD(*),CG(*),XG(400),
  *D2(401),T2(401),TM(401)
C
C CHECK FIRST TO SEE WHETHER TO ADD OR SUBTRACT
  GRADIENT
C
  ICT = ICT2+1
  GINC = CG(5)/25.
  IF(GINC.LT.0.0005) GINC = .0005
  FIRST = CG(5)

```

```

      ICNT = 0
      CG(5) = CG(5) + GINC
C
C FILL MODELED GRADIENT ARRAY WITH LINR USING NEW
C GRADIENT
C
      CALL LINR(DELX,7,SUR,BOT,ICT2,CD,CG,D3,XG)
      TM(1) = T2(1)
      DO 30 L=2,ICT
30  TM(L) = XG(L-1) * (D2(L) - D2(L-1)) + TM(L-1)
      CALL RMS(TM,T2,ICT,R)
      ICNT = ICNT+1
      R1 = R
C
      IF(ABS(R-R1).LT.TOL3) GO TO 199
C
C   IF(R.LT.R1) GO TO 100 @ GOING RIGHT WAY
C   IF(R.GT.R1) THEN @ GOING WRONG WAY
      if(r.lt.r1) go to 100
      if(r.gt.r1) then
c
          CG(5) = CG(5) - GINC
          R = R1
          GO TO 150
      END IF
C
C ADJUST GRADIENT G3A BY ADDING
C
100 IF = 0
102 IF(ICNT.GT.NI) GO TO 199
      R1 = R
      CG(5) = CG(5) + GINC
C
      CALL LINR(DELX,7,SUR,BOT,ICT2,CD,CG,D3,XG)
      TM(1) = T2(1)
      DO 31 L=2,ICT
31  TM(L) = XG(L-1) * (D2(L) - D2(L-1)) + TM(L-1)
      CALL RMS(TM,T2,ICT,R)
      ICNT = ICNT+1
C
      IF(ABS(R-R1).LT.TOL3) GO TO 199
      IF(R.LT.R1) GO TO 102
      IF(R.GT.R1.AND.IF.NE.6) THEN
          IF = IF+1
          CG(5) = CG(5) - GINC
          GINC = GINC/2.

```

```

        R = R1
        GO TO 102
    END IF
C
    GO TO 199
C
C ADJUST GRADIENT G3A BY SUBTRACTING
C
    150 IF = 0
    152 IF(ICNT.GT.NI) GO TO 199
        R1 = R
        CG(5) = CG(5) - GINC
C
    CALL LINR(DELX,7,SUR,BOT,ICT2,CD,CG,D3,XG)
    TM(1) = T2(1)
    DO 32 L=2,ICT
    32 TM(L) = XG(L-1) * (D2(L) - D2(L-1)) + TM(L-1)
    CALL RMS(TM,T2,ICT,R)
    ICNT = ICNT+1
C
    IF(ABS(R-R1).LT.TOL3) GO TO 199
    IF(R.LT.R1) GO TO 152
    IF(R.GT.R1.AND.IF.NE.6) THEN
        IF = IF+1
        CG(5) = CG(5) + GINC
        GINC = GINC/2.
        R = R1
        GO TO 152
    END IF
C
    GO TO 199
C
    199 CONTINUE
C
    CALL LINR(DELX,7,SUR,BOT,ICT2,CD,CG,D3,XG)
    TM(1) = T2(1)
    DO 33 L=2,ICT
    33 TM(L) = XG(L-1) * (D2(L) - D2(L-1)) + TM(L-1)
    CALL RMS(TM,T2,ICT,R)
C
    ADJ = FIRST - CG(5)
C WRITE(6,605) ICNT,ADJ,R
    605 FORMAT(1X,'G3AT ITERATIONS: ',I3,4X,'ADJ: ',F6.4,3X,
        *'RMS = ',F7.4)
C
    RETURN
    END

```

C.4.9 Data Input/Output

```

SUBROUTINE INOUT4
CHARACTER*25 FOUT4,FOUT5,FOUT8,FOUT9,FIN3,allcoef
PRINT *, 'ENTER FILE NAME FOR COEF FILE (for unit 4)'
READ(5,99)FOUT4
print *, 'Enter file name for MATLAB use (unit 28)'
read(5,99)allcoef
PRINT *, 'ENTER FILE NAME FOR RECONSTRUCTED COEF
      (for unit 7)'
READ(5,99)FOUT5
PRINT *, 'ENTER FILE NAME FOR INPUT MASTER FILE'
READ(5,99) FIN3
PRINT *, 'ENTER FILE NAME FOR ACCEPTED PROFILES'
READ(5,99) FOUT8
PRINT *, 'ENTER FILE NAME FOR REJECT FILE'
READ(5,99) FOUT9
99 FORMAT(A25)
OPEN(4,FILE=FOUT4,FORM='FORMATTED',STATUS=
      'UNKNOWN')
OPEN(28,file=allcoef,form='formatted',status='unknown')
OPEN(7,FILE=FOUT5,FORM='FORMATTED',STATUS=
      'UNKNOWN')
OPEN(3,FILE=FIN3,FORM='UNFORMATTED',STATUS='OLD')
OPEN(8,FILE=FOUT8,FORM='UNFORMATTED',STATUS=
      'UNKNOWN')
OPEN(9,FILE=FOUT9,FORM='UNFORMATTED',STATUS=
      'UNKNOWN')
RETURN
END

```

D

Autocorrelation Matrix Calculated from (T, S) Profile Data

```
C PROGRAM corre.f (f77 corre.f -o corre; Running See corre.com)
C CALCULATE AUTOCORRELATION MATRICES FROM
  PROFILE DATA.
C JAPAN/EAST SEA EXAMPLE
C Longitude 127.5E-142E(mx=(142-127.5)/(15/60)+1= 59)
C Latitude 32.5N-50N(my=( 50- 32.5)/(15/60)+1= 71)
C*****
      parameter (maxpts =141330 , mx=59,my=71,Lv=28)
      real covar(64,64), var1(64,64), var2(64,64)
      integer num(64,64)
      real corr(64,64)
      character obsfile*80,infile*80,ofil1*80,ofil2*80,ofil3*80
      dimension itimlg(64), idstlg(64),tobs(200),tmean(mx,my,Lv)
      dimension anomly(maxpts,1) ,tlmean(mx,my)
      common /LL/dlat(my),dlon(mx),grid1
      common // zlat(maxpts,1), zlon(maxpts,1), time(maxpts,1),
1 lagdd(maxpts) , lagtt(maxpts),
2 zlati,zloni,timei,jpt,numpts(64),incdlg,inctlg,level
      crt=-50.0
      level = 1
      iloop = 0
C READ Parameter and FILE NAME
      print *, 'Enter Layer-num: nk(1 or 2...or 28)'
      read(*,*) nk
c   print *, 'obs.point filename'
      read(*,*)obsfile
c   print *, 'grad.point filename'
      read(*,*)infile
      read(*,*)ofil1
      read(*,*)ofil2
      read(*,*)ofil3
```

```

C OPEN THE INPUT FILE
  open(3,FILE=obsfile,form='formatted',STATUS='old')
  open(4,FILE=infile,form='formatted',STATUS='old')
  open(15,FILE='corrin.dat',form='formatted',STATUS='old')
C OPEN THE OUTPUT FILE.
  n=0
  open(16,FILE=ofil1,form='formatted', STATUS='unknown')
  open(17,file=ofil2,form='formatted', STATUS='unknown')
  open(18,file=ofil3,form='formatted', STATUS='unknown')
C READ IN THE MAXIMUM TIME(day)/DISTANCE(km)
LAGS AND THE LAG INCREMENT.
C READ IN THE LAT/LON BOUNDS OF THE AREA.
C   mxtlag- maximum TIME(days) difference allowed column
C   inctlg- time difference bin size
C   mxdlag- maximum DISTANCE(km) difference allowed rows
C   incdlg- distance difference bin size
  read(15,*) mxtlag,inctlg,mxdlag,incdlg,ntb,ndb
C   ex.input 25(day) 1(day) 250(km) 10(km) from file corrin.dat
  numtbn = mxtlag / inctlg + 1
  if ( numtbn .gt. ntb) stop ' more than ntb time bins'
  numdbn = mxdlag / incdlg + 1
  if ( numdbn .gt. ndb) stop ' more than ndb distance bins'
  write(16,'(6i6)') mxtlag,inctlg,mxdlag,incdlg,numtbn,numdbn
C READ IN TEMPERATURE PROFILE DATA FOR THE MEAN
  write(16,*)'input grad point filename',infile
  grid=15.0
  grid1=grid/60.
  do 100 j=1,my
  do 101 i=1,mx
    read(4,*) dlon(i),xla,(tmean(i,my-j+1,k),k=1,28)
  101 continue
    dlat(my-j+1)=xla
  100 continue
    write(16,120)dlon(1),dlon(mx),dlat(1),dlat(my),grid1,mx,my
    write(6,120)dlon(1),dlon(mx),dlat(1),dlat(my),grid1,mx,my
  120 format(' lonw lone lats latn grid mx my'/,5f7.2,2i4)
    Idepth = 1
C LOOP TO STORE TIME, PLACE, AND TEMPERATURE
ANOMALY
C VALUE.
C Reads in the data from tbin as formatted in it.
  write(16,*)' input obser. point filename',obsfile
C zero mean calc arrays
  do level=1,1
    numpts(level) = 0

```

```

do ix=1,mx
  do iy=1,my
    lmean(ix,iy)= tmean(ix,iy,nk)
  Enddo
Enddo
10 CALL READER(rlon,rlat,tobs,ILOOP,iyr,im,id,obsfile)
   if (iloop .eq. 0) go to 11
   CALL LMEAN(tm,rlon,rlat,tlmean,crt)
C   DETERMINE JULIAN DAY AND REAL-VALUED TIME
C   OF TEMPERATURE VALUE.
C   Type II = jday //// Type III = jday+(iyr*365)
   call juldat(iyr,im,id,jday)
   tmptim = jday
   write(16,165) rlon,rlat,tmptim
165   format(' rlon,rlat= ',2f9.3,' tmptim =',f12.2)
C   TAKE THE OBSERVED TEMPERATURE (tobs) AND
   SUBTRACT
C   THE MEAN
C   TEMPERATURE(tmean) OUT TO GET THE ANOMOLY
   (anomly)
C   STORE THE POSITION, TIME, AND VALUE.
   if( tobs(1) .lt. 900. .and. tm .gt. crt) then
   numpts(level) = numpts(level) + 1
     n = numpts(level)
     if ( n .gt. maxpts ) stop ' too many points to store!'
     zlat(n,level) = rlat
     zlon(n,level) = rlon
     time(n,level) = tmptim
     anomly(n,level) = tobs(1) - tm
     write(16,160) tm,iloop,tobs(1),anomly(n,level)
     endif
     go to 10
   enddo
11   continue
160   format('t local mean=',f8.3,' tobs',i7,'=',f8.3,' 2T.Diff=',f9.3)
   print *, 'level/n=',level,n,numpts(level)
     write(16,*) 'completed input from',obsfile
   print *, 'completed input from',obsfile
C   DETERMINE THE COVARIANCE, VARIANCE, AND
C   COUNTER ARRAYS.
C   ANY LAGS OUTSIDE THE BIN BOUNDARIES GO INTO
   A "SPARE"
C   ROW AND COLUMN
   do level =1,1,1

```

```

C INITIALIZE THE ARRAYS TO ZERO.
      ndbnp1 = numdbn + 1
      ptntbnp1 = numtbn + 1
      do lagt=1,ntbnp1
          do lagd=1,ndbnp1
              covar(lagd,lagt) = 0.
              var1(lagd,lagt) = 0.
              var2(lagd,lagt) = 0.
              num(lagd,lagt) = 0
          corr(lagd,lagt)= 0.
          end do
      end do
      numcmp = 0
do ipt=1,numpts(level)-1
      anom1 = anomly(ipt,level)
      zlati = zlat(ipt,level)
      zloni = zlon(ipt,level)
      timei = time(ipt,level)
      jpt = ipt + 1
      call tdsep
do jpt=ipt+1,numpts(level)
      numcmp = numcmp + 1
      lagd = min0 ( lagdd(jpt) , ndbnp1 )
      lagt = min0 ( lagtt(jpt) , ntbnp1 )
      anomj = anomly(jpt,level)
      covar(lagd,lagt) = covar(lagd,lagt) + anom1 * anomj
      var1(lagd,lagt) = var1(lagd,lagt) + anom1 * anom1
      var2(lagd,lagt) = var2(lagd,lagt) + anomj * anomj
      num(lagd,lagt) = num(lagd,lagt) + 1
end do
end do
C FOR EACH ELEMENT OF THE COVARIANCE AND
VARIANCE
C ARRAYS, DIVIDE THROUGH
C BY THE NUMBER OF VALUES USED IN THE
SUMMATIONS.
C THEN CALCULATE THE CORRELATION MATRIX.
      lagtmx = 0
      lagdmx = 0
      nmax = 0
      do lagt=1,numtbn
          itimlg(lagt) = ( lagt - 1 ) * inctlg

```

```

do lagd=1,numdbn
  n = num(lagd,lagt)
  if ( n .ne. 0 ) then
    covar(lagd,lagt) = covar(lagd,lagt) / n
    var1(lagd,lagt) = var1(lagd,lagt) / n
    var2(lagd,lagt) = var2(lagd,lagt) / n
    corr(lagd,lagt) = covar(lagd,lagt) /
*   ( sqrt ( var1(lagd,lagt) * var2(lagd,lagt) ) )
    endif
    idstlg(lagd) = ( lagd - 1 ) * incdlg
  end do
end do
C WRITE OUT THE CORRELATION MATRIX IN A MATRIX
  FORMAT.
  write(17,'(i4,35i6)') itimlg(1),(itimlg(i),i=1,numtbn)
  do lagd=1,numdbn
    write(17,'(i4,35f6.2)') idstlg(lagd),
*   (corr(lagd,lagt),lagt=1,numtbn)
  end do
  close(17)

C WRITE OUT THE MATRIX CONTAINING THE NUMBER OF
C PAIRS COMPARED IN
C EACH BIN. THE VALUES ARE SCALED TO 10.
  if ( nmax .lt. 9999 ) then
    scale = 1.
  else
    scale = 9999. / nmax
  endif
  do lagt=1,numtbn
    do lagd=1,numdbn
      num(lagd,lagt) = nint ( num(lagd,lagt) * scale )
    end do
  end do
  write(18,'(i4,35i6)') itimlg(1),(itimlg(i),i=1,numtbn)
  do lagd=1,numdbn
    write(18,'(i4,35i6)') idstlg(lagd),
*   (num(lagd,lagt),lagt=1,numtbn)
  end do
end do
1000 continue
  print *, 'n/nmax/scale=',n,nmax,scale
  close(18)
  stop ' normal end '
end

```

C

```

SUBROUTINE tdsep
  parameter ( maxpts =141330)
  common // zlat(maxpts,1), zlon(maxpts,1), time(maxpts,1),
1     lagdd(maxpts) , lagtt(maxpts),
2     xla1,xlo1,timei,jpt,numpts(64),incdlg,inctlg,level
  data pi/3.1415927/
  data rad/.0174533/
  data deg/57.29578/
data ert/6371.2/
A=XLA1*RAD
  COSA=COS(A)
  SINA=SIN(A)
do 10 kpt=jpt,numpts(level)
  B=zlat(kpt,level)*RAD
  CC=ABS(zlon(kpt,level)-XLO1)*RAD
  AMB=ABS(A-B)
  IF(AMB.GT.RAD.AND.CC.GT.RAD) GO TO 15
  XMLAT=(A+B)/2.
  DELY=AMB
  DELX=CC*COS(XMLAT)
  C=SQRT(DELX**2.+DELY**2.)
  GO TO 20
15  IF(CC.GT.PI) CC=2.*PI-CC
  COSB=COS(B)
  SINB=SIN(B)
  COSCC=COS(CC)
  COSC=sina*sinb+cosa*cosb*COSCC
  SINC=SQRT(1.-COSC**2.)
  C=ASIN(SINC)
  IF(COSC.LT.0.0) C=PI-C
20  CDEG=C*ert
  distnc=CDEG
  lagdd(kpt) = nint ( distnc / incdlg ) + 1
  lagtt(kpt) = nint(abs (timei - time(kpt,level)) /inctlg) +1
10  continue
  RETURN
  END

```

```

C*****
*
  SUBROUTINE LMEAN(tm,x,y,tlmean,crv)
  parameter(mx= 59,my=71)
c    tm =mean used for tobs
c    x = rlon y = rlat
    dimension tlmean(mx,my),ff(4),xx(4),yy(4)
    common /LL/dlat(my),dlon(mx),grid
c Find the mean temp value corresponding to x,y
  ii=(x-dlon(1))/grid+1
  jj=(y-dlat(1))/grid+1
  if(ii.gt.mx.or.jj.gt.my) then
    print*,'II,JJ EXCEED LIMIT!!! ===>RETURN'
    return
  endif
  xx(1)=dlon(ii)
  yy(1)=dlat(jj)
  ff(1)=tlmean(ii,jj)
  xx(2)=xx(1)
  yy(2)=dlat(jj+1)
  ff(2)=tlmean(ii,jj+1)
  xx(3)=dlon(ii+1)
  yy(3)=yy(2)
  ff(3)=tlmean(ii+1,jj+1)
  xx(4)=xx(3)
  yy(4)=yy(1)
  ff(4)=tlmean(ii+1,jj)
  call BLINT(xx,yy,ff,4,x,y,tm,crv)
  return
  end
C*****
  subroutine blint(xx,yy,ff,n,x,y,f,Z)
  dimension ff(n),xx(n),yy(n)
C Bilinear interpolation subroutine.
C (Xi,Yi,fi) = data grid & values surrounding model point (x,y)
C f = interpolated value at the model grid point.

```

```

if(ff(1).ge.Z.and.ff(2).ge.Z.and.ff(3).ge.Z.and.ff(4).ge.Z)then
  a1=xx(1)-xx(2)+xx(3)-xx(4)
  a2=-xx(1)+xx(4)
  a3=-xx(1)+xx(2)
  a4=xx(1)-x
  b1=yy(1)-yy(2)+yy(3)-yy(4)
  b2=-yy(1)+yy(4)
  b3=-yy(1)+yy(2)
  b4=yy(1)-y
  A=a3*b1-a1*b3
  B=b2*a3+b1*a4-a1*b4-a2*b3
  C=-a2*b4+a4*b2
  if(ABS(A*C).gt.0.002*B**2) then
    t=(-B-sqrt(B*B-4.*A*C))/(2.*A)
  else
    t=C/ABS(B)
  endif
10  continue
  A=a2*b1-a1*b2
  B=b3*a2+b1*a4-a1*b4-a3*b2
  C=-a3*b4+a4*b3
  if(ABS(A*C).gt.0.002*B**2) then
    s=(-B+sqrt(B*B-4.*A*C))/(2.*A)
  else
    s=-C/abs(B)
  endif
20  continue
  f=ff(1)*(1.-t)*(1.-s)+ff(2)*t*(1.-s)+ff(3)*s*t+ff(4)*(1.-t)*s
  else
  rmn=0.0
  fmn=0.0
  do i=1,n
    if(ff(i).ge.Z) then
      rrr=1./(1.0e-20+(x-xx(i))**2+(y-yy(i))**2)
      rmn=rmn+rrr
      fmn=fmn+ff(i)*rrr
    endif
  enddo
  if(rmn.gt.0.0) then
    f=fmn/rmn
  else
    f=-99.99
  endif
endif

```

```

C .....
  return
  end
C-----
  SUBROUTINE JULDAT(IYR,IMO,IDAY,JULD)
C SUBR TO CALCULATE THE JULIAN DATE
C ACCOUNTS FOR LEAP YEARS
C INPUTS: IYR - YEAR (INTEGER 0 TO 99)
C      IMO - MONTH (INTEGER 1 TO 12)
C      IDAY - DAY (INTEGER (1 TO LAST DAY OF MONTH)
C OUTPUTS: JULD - JULIAN DATE (1 TO 365/366 FOR LEAP
  YEAR)
C VARIABLES:
C      MON (12) - DAYS IN EACH MONTH
C.....
  DIMENSION MON(12)
  DATA MON /31,28,31,30,31,30,31,31,30,31,30,31/
  MON(2) = 28
C CHECK FOR LEAP YEAR
  IF (MOD(IYR,4) .EQ. 0 .AND. IYR .NE. 0) MON(2) = 29
  JULD = 0
  IF (IMO .EQ. 1) GOTO 120
  DO 100 K = 1, IMO-1
    JULD = JULD + MON(K)
100 CONTINUE
120 CONTINUE
  JULD = JULD + IDAY
  ym=iyr-1930
  ly=y/4.0
  ily=ifix(ly)
  juld=juld+ym*365+ily
  RETURN
  END
  SUBROUTINE READER(X,Y,TEMP,ILOOP,iy,im,id,INFILE)
C *****
C *          SUBROUTINE READER2          *
C *    READS TEMPS AT SPECIFIED PCT OF DBDB5 *
C *          FOR CHRTR          *
C *****

```

574 D Autocorrelation Matrix Calculated from (T, S) Profile Data

```
C INTERFACES TO CHRTR
C THIS SUBROUTINE READS TEMPERATURE (OR SALINITY)
C PROFILES.
C THE TEMP AT A USER SPECIFIED PCT DEPTH, AND PASSES
  THE
C LAT, LON, AND TEMP BACK TO PROGRAM CHRTR FOR
C SUBSEQUENT GRIDDING.
C VARIABLE WDEP2 IS DBDB5 DEPTH. XDEPTH IS DEPTH
  THAT TEMP
C IS PICKED OFF (VERTICALLY INTERPOLATED) FROM EACH
  MOODS
C PROFILE.
C XDEPTH WILL BE DIFFERENT FOR EACH PROFILE,
  DEPENDING ON
C WATER DEPTH (AS DETERMINED FROM DBDB5).
  NOTE THAT
C DBDB5 WAS NEVER MEANT TO BE USED IN
  SHALLOW WATER,
C THUS THE USER IS RESPONSIBLE TO UNDERSTAND ITS
  LIMITATIONS IN THE SPECIFIC ANALYSIS REGION.
C
  CHARACTER infile*80
  DIMENSION TEMP(200)
C FIRST TIME READER9 IS CALLED, SPECIFY AND OPEN
  INPUT FILE
  if(i loop.eq.0) then
    write(16,*)'opening ',infile
    close(3)
    open(3,FILE=infile,form='formatted',STATUS='old')
    read(3,*)lev
    write(6,600)lev
    write(16,600)lev
600 format(1x,'what level (depth of water column)?',i4)
    endif
    i loop = i loop+1
C READ PROFILE FROM MASTER FILE -
5 continue
  READ(3,*,END=99) XLAT,XLON,t,iy,im,id
  Y = XLAT
  X = XLON
  TEMP(1) = T
  RETURN
99 continue
  i loop = 0
  return
  END
```

```

SUBROUTINE LINR(DELX,N,XBGN,XEND,ICT,X,Y,AX,AY)
C  LINEAR INTERPOLATOR ROUTINE FOR USE WHEN SPLINE
C  IS NOT APPROPRIATE
C  IE.LARGE GAPS IN INPUT DATA NEAR SHARP CHANGES IN
C  GRADIENT WITH LOCALLY INADEQUATE SAMPLING.
C  DELX=DESIRED INTERPOLATION INTERVAL,X AND Y ARE
C  INPUT
C  WITH X=INDEP.
C  VARIABLE,AX AND AY ARE OUTPUT,N=LENGTH OF X,
C  XBGN AND
C  XEND=DESIRED
C  BEGINNING AND ENDING VALUES OF AX,ICT=LENGTH OF AX
C  DIMENSION X(*),Y(*),AX(*),AY(*)
  NN=N-1
  ICT=((XEND-XBGN)/DELX)+1.0001
  DO 1 J=1,ICT
    A=J-1
1  AX(J)=A*DELX+XBGN
    KK=1
    DO 2 J=1,NN
      JJ=J+1
      SLOPE=(Y(JJ)-Y(J))/(X(JJ)-X(J))
      DO 3 K=KK,ICT
        I=K
        IF(AX(K).GT.X(JJ).AND.AX(K).LE.X(N)) GO TO 2
3  AY(K)=SLOPE*(AX(K)-X(J))+Y(J)
        GO TO 4
2  KK=I
4  RETURN
  END

```

References

- Aagaard K (1989) A synthesis of the Arctic Ocean circulation. *Rapports. et Proces-verbaux des Réunion Conseil International pour. l'Exploration de la Mer*, 188, 11–22.
- Aagaard K, Coachman LK (1975) Toward an ice-free Arctic Ocean. *EOS Transaction, American Geophysical Union*, 56, 484–486.
- Aagaard K, Coachman LK, Carmack EC (1981) On the halocline of the Arctic Ocean. *Deep Sea Research*, 28, 529–545.
- Aagaard K, Swift JH, Carmack EC (1985) Thermohaline circulation in the Arctic Mediterranean seas. *Journal of Geophysical Research*, 90, 4833–4846.
- Aagaard K, Foldvik A, Hillman SR (1987) The West Spitzbergen Current: Disposition and water mass transformation. *Journal of Geophysical Research*, 92, 3778–3784.
- Arctic Climatology Project (1997) Environmental Working Group joint U.S.-Russian atlas of the Arctic Ocean – winter period, edited by L. Timokhov, F. Tanis. Environmental Research Institute of Michigan in association with the National Snow and Ice Data Center, Ann Arbor, MI. CD-ROM.
- Arctic Climatology Project (1998) Environmental Working Group joint U.S.-Russian atlas of the Arctic Ocean – summer period, edited by L. Timokhov, F. Tanis. Environmental Research Institute of Michigan in association with the National Snow and Ice Data Center, Ann Arbor, MI. CD-ROM.
- Arief D (1998) Outer southeast Asia: a region of deep straits, including the Benda Sea coastal segment (13, S). In: *The Sea*, Vol. 11, edited by Robinson and Brink, pp. 507–522.
- ARGO Science Team (2001) Argo: the global array of profiling floats. In: *Observing the Oceans in the 21st Century*, edited by CJ. Koblinsky, and NR. Smith, GODAE Project Office, Bureau of Meteorology, Melbourne, pp. 248–258.
- ASEAN Subcommittee on Climatology (1982) *The ASEAN Climatic Atlas*. Directorate of National Mapping. Malaysia, Kuala Lumpur, 104 pp.

- Assireu AT, Stevenson MR, Stech JL (2003) Surface circulation and kinetic energy in the SW Atlantic obtained by drifters. *Continental Shelf Research*, 23, 145–157.
- Bagriantsev NV, Gordon AL, Huber BA (1989) Weddell Gyre: Temperature and maximum stratum. *Journal of Geophysical Research*, 94, 8331–8334.
- Bang I, Choi JK, Kantha L, Horton C, Clifford M, Suk MS, Chang KI, Nam SY, Lie HJ (1996) A hindcast experiment in the East Sea (Sea of Japan), *La mer*, 34, 108–130.
- Bannon PR, Chu PC (1988) Anelastic semi-geostrophic flow over a mountain ridge. *Journal of the Atmospheric Sciences*, 45, 1025–1029.
- Bathen KH (1972) On the seasonal changes in the depth of the mixed layer in the North Pacific Ocean. *Journal of Geophysical Research*, 77, 7138–7150.
- Beckmann A, Hartmut H, Timmermann R (1999) A numerical model of the Weddell Sea: Large-scale circulation and water mass distribution. *Journal of Geophysical Research*, 104, 23375–23391.
- Behringer DW, Stommel H (1980) The beta spiral in the North Atlantic subtropical gyre. *Deep Sea Research*, 27A, 225–238.
- Bennett A (1992) *Inverse methods in physical oceanography*. Cambridge University Press, Cambridge, UK, 346 pp.
- Bingham FM, Lukas R (1994) The Southward intrusion of North Pacific Intermediate Water along the Mindanao coast. *Journal of Physical Oceanography*, 24, 141–154.
- Bingham, FM, Lukas R (1995) The distribution of intermediate water in the western equatorial Pacific during January–February 1986. *Deep Sea Research*, 42, 1545–1573.
- Bingham FM, Talley LD (1991) Estimates of Kuroshio transport using an inverse technique. *Deep Sea Research*, 38, S21–S43.
- Bleck R, Smith L (1990) A wind-driven isopycnal coordinate model of the north and equatorial Atlantic Ocean. I. Model development and supporting experiments. *Journal of Geophysical Research*, 95, 3273–3285.
- Blumberg A, Mellor G (1987) A description of a three dimensional coastal ocean circulation model, *Three-Dimensional Coastal Ocean Models*, edited by NS. Heaps, American Geophysics Union, Washington, DC, pp. 1–16.
- Boebel O, Schmid C, Podesta G, Zenk W (1999) Intermediate water in the Brazil–Malvinas Confluence Zone: A Lagrangian view. *Journal of Geophysical Research*, 104, 21063–21082.
- Bower AS, LeCann B, Rossby T, Zenk W, Gould J, Speer K, Richardson PL, Prater MD, Zhang HM (2002) Directly measured mid-depth circulation in the northeastern North Atlantic Ocean. *Nature*, 419, 603–607.
- Broecker WS (1991) The great ocean conveyor. *Oceanography*, 4, 79–89.
- Bryan K (1987) Parameter sensitivity of primitive equation ocean general circulation models. *Journal of Physical Oceanography*, 17, 970–985.
- Bryden HL (1983) The Southern Ocean. In: *Eddies in the Ocean*, edited by AR. Robinson, Springer, New York Berlin Heidelberg, 265–277.

- Bryden HL, Kinder TH (1980) Heat transport by currents across 25°N latitude in the Atlantic Ocean. *Science*, 207, 884–886.
- Bryden HL, Phillipsbury RD (1977) variability of deep flow in the Drake Passage from year-long current measurements. *Journal of Physical Oceanography*, 7, 803–810.
- Burgers G, Balmaseda MA, Vossepoel FC, van Oldenborgh GJ, van Leeuwen PJ (2002) Balanced ocean-data assimilation near the equator. *Journal of Physical Oceanography*, 32, 2509–2519.
- Campos EJD, Miller JL, Muller TJ, Peterson RG (1995) Physical oceanography of the Southwest Atlantic Ocean. *Oceanography*, 8, 87–91.
- Carmack EC, Foster TD (1975) Circulation and distribution of oceanographic properties near Filchner Ice Shelf. *Deep Sea Research*, 22, 77–90.
- Carsey FD (1982) Arctic sea ice distribution at the end of summer 1973–1976 from satellite microwave data. *Journal of Geophysical Research*, 87, 5809–5835.
- Cattle H (1985) Diverting Soviet rivers: Some possible repercussions for the Arctic Ocean. *Polar Record*, 22, 485–498.
- Chao SY, Shaw PT, Wang J (1996) Wind relaxation as a possible cause of the South China Sea Warm Current. *Journal of Oceanography*, 51, 111–132.
- Chapman D (1985) Numerical treatment of cross-shelf open boundaries in a barotropic ocean model. *Journal of Physical Oceanography*, 15, 1060–1075.
- Cheang BK (1980) Some aspects of winter monsoon and its characteristics in Malaysia. Research Publication, No. 2, Malaysian Meteorological Service, Kuala Lumpur.
- Chen CS, Beardsley RC, Limeburner R (1992) The structure of the Kuroshio southwest of Kyushu: Velocity, transport and potential vorticity fields. *Deep Sea Research*, 39, 245–268.
- Chen CS, Beardsley RC, Limeburner R, Kim K (1994) Comparison of winter and summer hydrographic observations in the Yellow and East China Seas and adjacent Kuroshio during 1986. *Continental Shelf Research*, 14, 909–929.
- Chu PC (1986) An instability theory of ice–air interaction for the migration of the marginal ice zone. *Geophysical Journal of Royal Astronomical Society*, 86, 863–883.
- Chu PC (1987a) Generation of unstable modes of the iceward attenuating swell by icebreeze. *Journal of Physical Oceanography*, 17, 828–832.
- Chu PC (1987b) An instability theory of ice–air interaction for the formation of ice-edge bands. *Journal of Geophysical Research*, 92, 6966–6970.
- Chu PC (1987c) An icebreeze mechanism for an ice divergence–convergence criterion in the marginal ice zone. *Journal of Physical Oceanography*, 17, 1627–1632.
- Chu PC (1988) An instability theory of air–sea interaction for coastal upwelling. *Advances in Atmospheric Sciences*, 5, 277–285

- Chu PC (1989) Relationship between sea surface temperature gradient and thermally forced planetary boundary layer air flow. *Pure and Applied Geophysics*, 130, 31–45.
- Chu PC (1993) Generation of low frequency unstable modes in a coupled equatorial troposphere and ocean mixed layer. *Journal of the Atmospheric Sciences*, 50, 731–749.
- Chu PC (1995a) P-vector method for determining absolute velocity from hydrographic data. *Marine Technological Society Journal*, 29(2), 3–14.
- Chu PC (1995b) A feature model for Arctic upper ocean thermal structure. *Proceedings on the Fourth Conference on Polar Meteorology and Oceanography*, American Meteorological Society, 224–227.
- Chu PC (1999a) Two kinds of predictability in Lorenz system, *Journal of the Atmospheric Sciences*, 56, 1427–1432.
- Chu PC (1999b) Fundamental circulation functions for the determination of open boundary conditions. *Proceedings on the Third Conference of Coastal Oceanic and Atmospheric Prediction*, American Meteorological Society, 389–394.
- Chu PC (2000) P-vector spirals and determination of absolute velocities. *Journal of Oceanography*, 56, 591–599.
- Chu PC (2002) C-vector for identification of oceanic secondary circulation across Arctic fronts in Fram Strait. *Geophysical Research Letters*, 29, 10.1029/2002GLO15978.
- Chu PC, Chang CP (1997) South China Sea warm pool. *Advances in Atmospheric Sciences*, 14, 195–206.
- Chu PC, Fan CW (2001) A low salinity cool-core cyclonic eddy detected northwest of Luzon during the South China Sea Monsoon Experiment (SC-SMEX) in July 1998. *Journal of Oceanography*, 57, 549–563.
- Chu PC, Fan CW (2006) An inverse model for calculation of global volume transport from wind and hydrographic data. *Journal of Marine Systems*, in press.
- Chu PC, Garwood RW Jr (1990) Thermodynamic feedback between cloud and ocean mixed layer. *Advances in Atmospheric Sciences*, 7, 1–10.
- Chu PC, Garwood RW Jr (1991) On the two – phase thermodynamics of the coupled cloud – ocean mixed layer. *Journal of Geophysical Research*, 96, 3425–3436.
- Chu PC, Lan J (2003) Extremely strong thermohaline source/sinks generated by diagnostic initialization. *Geophysical Research Letters*, 30(6), 10.1029/2002GL016525.
- Chu PC, Li RF (2000) South China Sea isopycnal surface circulations. *Journal of Physical Oceanography*, 30, 2419–2438.
- Chu PC, Liu H (1999) Seasonal and interannual variability of the world ocean thermal structure. *Proceedings on the 10th Symposium on Global Change Studies*, American Meteorological Society, 151–154.
- Chu PC, Wang GH (2003) Seasonal variability of thermohaline front in the central South China Sea. *Journal of Oceanography*, 59, 65–78.

- Chu PC, Garwood RW Jr, Muller P (1990) Unstable and damped modes in coupled ocean mixed layer and cloud models. *Journal of Marine Systems*, 1, 1–11, 1990.
- Chu PC, Wells SK, Haeger SD, Szczechowski C, Carron MJ (1997a) Temporal and spatial scales of the Yellow Sea thermal variability. *Journal of Geophysical Research*, 102, 5655–5668.
- Chu PC, Fralick CR, Haeger SD, Carron MJ (1997b) A parametric model for Yellow Sea thermal variability. *Journal of Geophysical Research*, 102, 10499–10508.
- Chu PC, Tseng HC, Chang CP, Chen JM (1997c) South China Sea warm pool detected from the Navy's Master Oceanographic Observational Data Set (MOODS). *Journal of Geophysical Research*, 102, 15761–15771.
- Chu PC, Lu SH, Chen YC (1997d) Temporal and spatial variabilities of the South China Sea surface temperature anomaly. *Journal of Geophysical Research*, 102, 20937–20955.
- Chu PC, Fan CW, Ehret LL (1997e) Determination of open boundary conditions from interior observational data. *Journal of Atmospheric and Oceanic Technology*, 14, 723–734.
- Chu PC, Fan CW, Cai WJ (1998a) Evaluation of P-vector method using modular ocean model (MOM). *Journal of Oceanography*, 54, 185–198.
- Chu PC, Chen YC, Lu SH (1998b) Temporal and spatial variabilities of Japan Sea surface temperature and atmospheric forcings. *Journal of Oceanography*, 54, 273–384.
- Chu PC, Lu SH, Chen YC (1998c) Wind-driven South China Sea deep basin warm-core/cool-core eddies. *Journal of Oceanography*, 54, 347–360.
- Chu PC, Fan CW, Lozano CJ, Kerling J (1998d) An airborne expandable bathythermograph (AXBT) survey of the South China Sea, May 1995. *Journal of Geophysical Research*, 103, 21637–21652.
- Chu PC, Wang QQ, Bourke RH (1999a) A geometric model for Beaufort/Chukchi Sea thermohaline structure. *Journal of Atmospheric and Oceanic Technology*, 16, 613–632.
- Chu PC, Lu SH, Liu WT (1999b) Uncertainty of the South China Sea prediction using NSCAT and NCEP winds during tropical storm Ernie 1996. *Journal of Geophysical Research*, 104, 11273–11289.
- Chu PC, Lu SH, Chen YC (1999c) A coastal atmosphere-ocean coupled system (CAOCS) evaluated by an airborne expandable bathythermograph survey in the South China Sea, May 1995. *Journal of Oceanography*, 55, 543–558.
- Chu PC, Edmons NL, Fan CW (1999d) Dynamical mechanisms for the South China Sea seasonal circulation and thermohaline variabilities. *Journal of Physical Oceanography*, 29, 2971–2989.
- Chu PC, Fan CW, Liu WT (2000a) Determination of sub-surface thermal structure from sea surface temperature. *Journal of Atmospheric and Oceanic Technology*, 17, 971–979.

- Chu PC, Veneziano JM, Fan CW (2000b) Response of the South China Sea to tropical cyclone Ernie 1996. *Journal of Geophysical Research*, 105, 13991–14009.
- Chu PC, Lan J, Strauhs H (2000c) A numerical simulation of the Japan/East Sea (JES) seasonal circulation. *Estuarine and Coastal Modeling*, 6, American Society of Civil Engineering, 94–113.
- Chu PC, Lan J, Fan CW (2001a) Japan Sea circulation and thermohaline structure. Part 1. Climatology. *Journal of Physical Oceanography*, 31, 244–271.
- Chu PC, Lan J, Fan CW (2001b) Japan Sea circulation and thermohaline structure. Part 2. A variational P-vector method. *Journal of Physical Oceanography*, 31, 2886–2902.
- Chu PC, Lu SH, Fan CW (2001c) An air-ocean coupled nowcast/forecast system for the east Asian marginal seas. *Advances in Mathematical Modeling of Atmosphere and Ocean Dynamics*, edited by PE. Hodnett, Kluwer Scientific Publishing Co., pp. 137–142.
- Chu PC, Liu QY, Jia YL, Fan CW (2001d) Evidence of barrier layer in the Sulu and Celebes Seas. *Journal of Physical Oceanography*, 32, 3596–3615.
- Chu PC, Li RF, You XB (2002a) Northwest Pacific subtropical countercurrent on isopycnal surface in Summer. *Geophysical Research Letters*, 29, 10.1029/2002GLO14831.
- Chu PC, Wang GH, Chen YC (2002b) Japan Sea circulation and thermohaline structure. Part 3. Autocorrelation Functions. *Journal of Physical Oceanography*, 32, 3596–3615.
- Chu PC, Ma BB, Chen YC (2002c) South China Sea thermohaline structure and circulation. *Acta Oceanologica Sinica*, 21, 227–261.
- Chu PC, Ivanov LM, Korzhova TP, Margolina TM, Melnichenko OM (2003a) Analysis of sparse and noisy ocean current data using flow decomposition. Part 1. Theory. *Journal of Atmospheric and Oceanic Technology*, 20, 478–491.
- Chu PC, Ivanov LM, Korzhova TP, Margolina TM, Melnichenko OM (2003b) Analysis of sparse and noisy ocean current data using flow decomposition. Part 2. Application to Eulerian and Lagrangian data. *Journal of Atmospheric and Oceanic Technology*, 20, 492–512.
- Chu PC, Lu SH, Fan CW, Kim CS (2003c) A numerical simulation of Japan/East Sea (JES) thermohaline structure and circulation. *Advances in Coastal Modeling*, edited by VC. Lakkhan, Elsevier Oceanographic Series, 67, 431–466.
- Chu PC, Li RF, Fan CW (2003d) Determination of the current system on isopycnal surface between Mindanao and New Guinea from GDEM. *Chinese Journal of Oceanology and Limnology*, 21, 193–213.
- Chu PC, Wang GH, Fan CW (2004a) Evaluation of US Navy's Modular Ocean Data Assimilation System Using SCSMEX data. *Journal of Oceanography*, 60, 1007–1021.

- Chu PC, Ivanov LM, Margolina TM (2004b) Rotation method for reconstructing process and field from imperfect data. *International Journal of Bifurcation and Chaos*, 14(8), 2991–2997.
- Chu PC, Ivanov LM, Margolina TM (2005a) Seasonal variability of the Black Sea chlorophyll-a concentration. *Journal of Marine Systems*, 56, 243–261.
- Chu PC, Ivanov LM, Melnichenko OM (2005b) Fall-winter current reversals on the Texas–Louisiana continental shelf. *Journal of Physical Oceanography*, 35, 902–910.
- Chu PC, Fang CL, Kim CS (2005c) Japan/East Sea model predictability. *Continental Shelf Research*, 25, 2107–2121.
- Chu PC, Chen YC, Kuminaka A (2005d) Seasonal variability of the East China/Yellow Sea surface buoyancy flux and thermohaline structure. *Advances in Atmospheric Sciences*, 22, 1–20.
- Chu PC, Ivanov LM, Melnichenko OM (2006) ARGO floats revealing bimodality of large-scale mid-depth circulation in the North Atlantic. *Journal of Oceanography*, submitted.
- Clancy RM, Pollak KD (1983) A real-time synoptic ocean thermal analysis/forecast system. *Progress in Oceanography*, 12, 383–424.
- Clark RA, Hill HW, Reiniger RF, Warren BA (1980) Current system south and east of the Grand Bank of Newfoundland. *Journal of Physical Oceanography*, 10, 25–65.
- Coachman LK, Aaggard K, Tripp RB (1975) *Bering Strait: the Regional Oceanography*. University of Washington Press, Seattle, 172 pp.
- Coats DA (1981) An estimate of absolute geostrophic velocity from the density field in the northeastern Pacific Ocean. *Journal of Geophysical Research*, 86, 8031–8036.
- Cox MD (1987): GFDL Ocean Model Circular No. 7. GFDL/Princeton University, Princeton, NJ, 1 pp.
- Cushman-Roisin B (1984) On the maintenance of the Subtropical Front and its associated countercurrent. *Journal of Physical Oceanography*, 14, 1179–1190.
- Dale WL (1956) Winds and drift currents in the South China Sea. *Malayan Journal of Tropical Geography*, 8, 1–31.
- Danilov AI, Ivanov LM, Kulakov MY, Margolina TM, Pavlov VK (1996) Modern radioactive climate of the Kara Sea. *Geophysical Report*, Russian Academy of Sciences, 346(4), 545–548 (in Russian).
- da Silva AM, Young CC, Levitus S (1994) *Atlas of Surface Marine Data 1994*. Technical Report of Geosciences, 94, University of Wisconsin-Milwaukee, 83 pp.
- Davis R (1978) On estimating velocity from hydrographic data. *Journal of Geophysical Research*, 83, 5507–5509.
- Deacon GER (1979) The Weddell gyre. *Deep Sea Research*, 26A, 981–995.
- Deacon GER (1982) Physical and biological zonation in the Southern Ocean. *Deep Sea Research*, 29, 1–16.

- Deacon GER, Foster TD (1977) The boundary region between the Weddell Sea and Drake Passage currents. *Deep Sea Research*, 24, 505–510.
- Defant A (1941) Quantitative Untersuchungen zur Statik und Dynamik des Atlantischen Ozeans. Die absolute Topographie des physikalischen Meeresspiegels und der Druckflächen sowie die Wasserbewegungen im Raum des Atlantischen Ozeans. In *Wissenschaftliche Ergebnisse der Deutschen Atlantischen Expedition auf dem Forschungs- und Vermessungsschiff "Meteor" 1925–27*, 6, Part 1, 191–260.
- Defant A (1961) *Physical Oceanography*, Vol 1, Pergamon, New York, 729 pp.
- DeMaster DJ, Dunbar RB, Gordon LI, Leventer AR, Morrison JM, Nelson DM, Nittrouer CA, Smith WO Jr (1992) Cycling and accumulation of biogenic and organic matter in high-latitude environments. *The Ross Sea, Oceanography*, 5, 146–153.
- Dietrich G (1969) *Atlas of the hydrography of the northern North Atlantic Ocean*. International Council for the Expedition of the Sea, Copenhagen, 140 pp.
- Egawa T, Nagata Y, Sato S (1993) Seasonal variation of the current in the Tsushima Strait deduced from ADCP data of Ship-of-Opportunity. *Journal of Oceanography*, 49, 39–50.
- Emery KO, Csanady GT (1973) Surface circulation of lakes and nearly landlocked seas. *Proceedings of National Academy of Sciences, USA*, 70, 93–97.
- Eremeev VN, Ivanov LM, Kirwan AD Jr, Melnichenko OV, Kochergin SV, Stanichnaya RR (1992) Reconstruction of oceanic flow characteristics from quasi-Lagrangian data. Part 2. Characteristics of the large-scale circulation in the Black Sea. *Journal of Geophysical Research*, 97, 9743–9753.
- Eremeev VN, Ivanov LM, Kirwan AD Jr, Margolina TM (1994) Amount of Cs-137 and Cs-134 radionuclides in the Black Sea produced by the Chernobyl disaster. *Journal of Environmental Radiology*, 26, 49–63.
- Eremeev VN, Ivanov LM, Kirwan AD Jr, Margolina TM (1995) Analysis of cesium pollution in the Black Sea by regularization method. *Marine Pollution Bulletin*, 30(7), 460–462.
- Evans DL, Signorini SS, Miranda LB (1983) A note on the transport of the Brazil Current. *Journal of Physical Oceanography*, 13, 1732–1738.
- Eykhoff P (1973) *System Identification: Parameter and State Estimation*. Elsevier, Amsterdam, 555 pp.
- Fahrbach E, Meincke J, Osterhus S, Rohardt G, Schauer U, Tverberg V, Verduin J (2001) Direct measurements of volume transports through Fram Strait. *Polar Research*, 20, 217–224.
- Fandry CG, Pillsbury RD (1979) On the estimation of absolute geostrophic volume transport applied to the Antarctic Circumpolar Current. *Journal of Physical Oceanography*, 9, 449–455.
- Ffield A, Gordon AL (1992) Vertical mixing in the Indonesian thermocline. *Journal of Physical Oceanography*, 22, 184–195.

- Fieux M, Andrieu C, Delecluse P, Ilahude AG, Kartavtseff A, Mantisi F, Molcard R, Swallow JC (1994) Measurements within the Pacific-Indian ocean throughflow region. *Deep Sea Research*, 41, 1091–1130.
- Fine RA, Lukas R, Bingham FM, Warner WJ, Gammon RH (1994) The western equatorial Pacific – a water mass crossroads. *Journal of Geophysical Research*, 99, 25063–25080.
- Foldvik A, Kvinge T, Torresen T (1985) Bottom currents near the continental shelf break in the Weddell Sea. *Antarctic Research Series*, 43, 21–34.
- Foldvik A, Aagaard K, Torresen T (1988) On the velocity field of the East Greenland Current. *Deep Sea Research*, 35, 1335–1354.
- Foster TD, Middleton JH (1979) Variability in the bottom water of the Weddell Sea. *Deep Sea Research*, 26, 743–762.
- Fox DN, Teague WJ, Barron CN, Carnes MR, Lee CM (2002) The modular ocean data assimilation system (MODAS). *Journal of Atmospheric and Oceanic Technology*, 19, 240–252.
- Fuglister FC (1960) *Atlantic Ocean Atlas of Temperature and Salinity Profiles and Data from the International Geophysical Year of 1957–1958*. Woods Hole Oceanographic Institution Atlas Series, 1, 209 pp.
- Fuglister FC (1963) Gulf Stream '60. *Progress in Oceanography*, 1, 265–373.
- Gandin LS (1965) *Objective Analysis of Meteorological Fields*. Israel Program for Scientific Translation, Jerusalem, 242 pp.
- Garzoli SL, Bianchi A (1987) Time-space variability of the local dynamics of the Malvinas–Brazil confluence as revealed by inverted echo sounders. *Journal of Geophysical Research*, 92, 1914–1922.
- Gascard JC, Kergomard C, Jeannin PF, Fily M (1988) Diagnostic study in Fram Strait marginal ice zone during summer from 1983 and 1984 marginal ice zone experiment Lagrangian observations. *Journal of Geophysical Research*, 93, 3613–3641.
- Gascard JC, Richez C, Rouault C (1995) New insights on large-scale oceanography in Fram strait: the West Spitzbergen Current. In *Arctic Oceanography: Marginal Ice Zones and Continental Shelves*. Coastal and Estuarine studies, 49, 131–182.
- Gerdes R, Schauer U (1997) Large-scale circulation and water mass distribution in the Arctic Ocean from model results and observations. *Journal of Geophysical Research*, 102, 8467–8484.
- Godfrey JS (1989) A Sverdrup model of the depth-integrated flow for the world ocean allowing for island circulations. *Geophysical and Astrophysical Fluid Dynamics*, 45, 89–112.
- Godfrey JS (1996) The effect of the Indonesian Throughflow on ocean circulation and heat exchange with the atmosphere: A review. *Journal of Geophysical Research*, 101, 12217–12237.
- Goni G, Wainer I (2001) Investigation of the Brazil Current front variability from altimeter data. *Journal of Geophysical Research*, 106, 31117–31128.
- Gordon AL, Greengrove CL (1986) Geostrophic circulation of the Brazil–Falkland Confluence. *Deep Sea Research*, 33, 573–585.

- Gordon AL, Georgi DT, Taylor WH (1977) Antarctic Polar Front zone in the western Scotia Sea, summer 1975. *Journal of Physical Oceanography*, 7, 309–328.
- Gordon AL, Martinson DG, Taylor WH (1981) The wind-driven circulation in the Weddell-Enderby basin. *Deep Sea Research*, 28, 151–163.
- Haney RL (1971) Surface boundary condition for ocean circulation models. *Journal of Physical Oceanography*, 1, 241–248.
- Hase H, Yoon JH, Koterayama, W (1999) The current structure of the Tsushima Warm Current along the Japanese Coast. *Journal of Oceanography*, 55, 217–235.
- Hidaka K (1940a) Absolute evaluation of ocean currents in dynamic calculations. *Proceedings of Imperial Academy of Tokyo*, 16, 391–393.
- Hidaka K (1940b) Practical evaluation of ocean currents. *Proceedings of Imperial Academy of Tokyo*, 16, 394–397.
- Hogg NG (1992) On the transport of the Gulf Stream between Cape Hatteras and the Grand Banks. *Deep Sea Research*, 39, 1231–1246.
- Holland WR (1973) Baroclinic and topographic influences on the transport in western boundary currents. *Geophysical Fluid Dynamics*, 4, 187–210.
- Hopkins TS (1991) The GIN Sea, Review of physical oceanography and literature from 1972. *Earth Science Review*, 30, 175–318.
- Hoskins BJ, Draghici L, Davies HC (1978) A new look at the ω -equation. *Quarterly Journal of Royal Meteorological Society*, 104, 31–38, 1978.
- Hu D, Cui M (1989) The western boundary current in the far-western Pacific Ocean. *Proceedings of the Western Pacific International Meeting and Workshop on TOGA COARE, ORSTOM, Noumea, New Caledonia*, 24–30 May, edited by J. Picaut, R. Lukas, T. Delcroix, pp. 135–143.
- Hu Y, Guan C, Gao H (1992) Water temperature and circulation structure in the upper ocean of the northern South China Sea. *Oceanography in China*, Vol. 6, Ocean Press, Beijing, pp. 60–69 (in Chinese with English abstract).
- Huang QZ, Wang WZ, Li YS, Li CW (1994) Current characteristics of the South China Sea. *Oceanology of China Seas*, Vol 1, edited by D. Zhou, YB. Liang, CK. Tseng, Kluwer Academic Press, Norwell, Massachusetts, pp. 113–122.
- Inoue N, Mitta T, Tawara S (1985) Tsushima Strait, II Physics. *Coastal Oceanography of Japanese Island*, Tokai University Press, pp. 914–933 (in Japanese).
- Iselin C (1936) A study of the circulation of the western North Atlantic. *Papers in Physical Oceanography and Meteorology*, 4(4), 101.
- Isobe A (1994) Seasonal variability of the barotropic and baroclinic motion in the Tsushima–Korea Strait. *Journal of Oceanography*, 50, 223–238.
- Isoda Y, Saitoh S (1988) Variability of the sea surface temperature obtained by the statistical analysis of AVHRR imagery – A case study of the south Japan Sea. *Journal of Oceanographic Society of Japan*, 44, 52–59.
- Isoda Y, Saitoh S (1993) The northward intruding eddy along the east coast of Korea. *Journal of Oceanography*, 49, 443–458.

- Ivanov LM, Kirwan AD Jr, Margolina TM (2001) Filtering noise from oceanographic data with some applications for the Kara and Black Seas. *Journal of Marine Systems*, 28(1–2), 113–139.
- Ivanov LM, Margolina TM, Danilov AI (2004) Application of inverse technique to study radioactive pollution and mixing processes in the Arctic Seas. *Journal of Marine Systems*, 48(1–4), 117–131.
- Johnson CM (1980) Wintertime sea-ice extremes and the simultaneous atmospheric circulation. *Monthly Weather Review*, 108, 1782–1791.
- Johnson GC, McPhaden MJ (1999) Interior pycnocline flow from the subtropical to the equatorial Pacific Ocean. *Journal of Physical Oceanography*, 29, 3073–3089.
- Jones EP, Anderson LG (1986) On the origin of the chemical properties of the Arctic Ocean halocline. *Journal of Geophysical Research*, 91, 10759–10767.
- Joyce TM, Patterson SL, Millard RC Jr (1981) Anatomy of a cyclonic ring in the Drake Passage. *Deep Sea Research*, 28, 1265–1287.
- Kajiura K, Tsuchiya M, Hidaka K (1958) The analysis of oceanographic condition in the Japan Sea. Report on Development of Fishery Resource in the Tsushima Warm Current, 1, 158–170 (in Japanese).
- Kano Y (1980) The annual variation of the temperature, salinity and oxygen contents in the Japan Sea. *The Oceanographic Magazine*, 31, 15–26.
- Kara AB, Rochford PA, Hurlburt HE (2000) Mixed layer depth variability and barrier layer formation over the North Pacific Ocean. *Journal of Geophysical Research*, 105, 16783–16801.
- Kashino Y, Aoyama M, Kawano T, Hendiarti N, Syaefudin Y, Anantasena Y, Muneyama K, Watanabe H (1996) The water masses between Mindanao and New Guinea. *Journal of Geophysical Research*, 101, 12391–12400.
- Kashino Y, Watanabe H, Herunadi B, Aoyama M, Hartoyo D (1999) Current variability at the Pacific entrance of the Indonesian Through flow. *Journal of Geophysical Research*, 104, 11021–11035.
- Kawabe M (1982a) Branching of the Tsushima Current in the Japan Sea. Part I. Data analysis. *Journal of Oceanographic Society of Japan*, 38, 95–107.
- Kawabe M (1982b) Branching of the Tsushima Current in the Japan Sea. Part II. Numerical experiment. *Journal of Oceanographic Society of Japan*, 38, 183–192.
- Keffer T (1985) The ventilation of the world's oceans: maps of the potential vorticity field. *Journal of Physical Oceanography*, 15, 509–523.
- Killworth P (1986) A Bernoulli inverse method for determining the ocean circulation. *Journal of Physical Oceanography*, 16, 2031–2051.
- Kim K, Chung JY (1984) On the salinity-minimum and dissolved oxygen-maximum layer in the East Sea (Sea of Japan). *Ocean Hydrodynamics of the Japan and East China Seas*, edited by T. Ichiye, Elsevier, Amsterdam, pp. 55–65.
- Kim YG, Kim K (1999) Intermediate Waters in the East/Japan Sea. *Journal of Oceanography*, 55, 123–132.

- Kim CH, Yoon JH (1996) Modeling of the wind-driven circulation in the Japan Sea using a reduced gravity model. *Journal of Oceanography*, 52, 359–373.
- Klinck JM, Nowland WD Jr (2001) Antarctic Circumpolar Current. *Encyclopedia of Ocean Science*, San Diego, 1st Edition, Academic Press, pp. 151–59.
- Kubokawa A (1997) A two-level model of subtropical gyre and subtropical countercurrent. *Journal of Oceanography*, 53, 231–244, 1997.
- Lavender KL, Davis RE, Owens WB (2000) Direct velocity measurements described a new circulation regime in the Labrador and Irminger seas. *Nature*, 407, 66–69.
- Lavender KL, Owens B, Davis RE (2005) Mid-depth circulation of the subpolar North Atlantic as measured by surface floats. *Deep Sea Research I*, 52, 767–785.
- Legutki S (1991) A numerical investigation of the circulation in the Greenland and Norwegian seas. *Journal of Physical Oceanography*, 21, 118–148.
- Lentini CAD, Podesta GG, Campos EJD, Olson DB (2001) Sea surface temperature anomalies on the Western South Atlantic from 1982–1994. *Continental Shelf Research*, 21, 89–112.
- Levitus S (1984) Annual cycle of temperature and heat storage in the world ocean. *Journal of Physical Oceanography*, 14, 727–746.
- Levitus S, Boyer T (1994) *World Ocean Atlas, Vol 4: Temperature*. NOAA Atlas NESDIS, 4, U.S. Government Printing Office, Washington, DC, 117 pp.
- Levitus S, Burgett R, Boyer T (1994) *World Ocean Atlas, Vol 3: Salinity*. NOAA Atlas NESDIS, 3, U.S. Government Printing Office, Washington, DC, 99 pp.
- Li H, Yuan Y (1992) On the formation and maintenance mechanisms of the cold water mass of the Yellow Sea. *Chinese Journal of Oceanology and Limnology*, 10(2) 97–106.
- Li L, Nowlin WD Jr, Su J (1998) Anticyclonic rings from the Kuroshio in the South China Sea. *Deep Sea Research*, 45, 1469–1482.
- Li R, Zeng Q, Ji Z, Gun D (1992) Numerical simulation for a northeastward flowing current from area off the eastern Hainan Island to Tsugaru/Soya Strait. *La Mer*, 30, 229–238.
- Li RF, You XB, Chu PC (2005) The eastward subtropical countercurrent on isopycnal surface in the Western North Pacific. *Science in China Ser D, Earth Sciences*, 48(7), 1065–1073.
- Lindstrom E, Lukas R, Fine R, Firing E, Godfrey S, Meyeyers G, Tsuchiya M (1987) The western Equatorial Pacific ocean circulation study. *Nature*, 330, 533–537.
- Liu Q, Jia Y, Liu P, Wang Q, Chu PC (2001) Seasonal and intraseasonal thermocline variability in the central South China Sea. *Geophysical Research Letters*, 28, 4467–4470.
- Lorenz EN (1963) Deterministic nonperiodic flow. *Journal of the Atmospheric Sciences*, 20, 130–141.

- Lozano CJ, Robinson AR, Arango HG, Gangopadhyay A, Sloan Q, Haley PJ, Anderson L, Leslie W (1996) An interdisciplinary ocean prediction system: assimilation strategies and structure data model. *Modern Approaches to Data Assimilation in Ocean Modeling*, edited by P. Malanotte-Rizzoli, Elsevier, Amsterdam, pp. 413–452.
- Lozier MS, McCartney MS, Owens WB (1994) Anomalous anomalies in averaged hydrographic data. *Journal of Physical Oceanography*, 24, 2624–2638.
- Lozier MS, Owens WB, Curry RG (1995) The climatology of the North Atlantic. *Progress in Oceanography*, 36, 1–44.
- Lukas R (1988) Interannual fluctuations of the Mindanao current inferred from sea-level. *Journal of Geophysical Research*, 93, 6744–6748.
- Lukas R, Lindstrom E (1991) The mixed layer of the western equatorial Pacific Ocean. *Journal of Geophysical Research*, 96, 3343–3357.
- Lukas R, Firing E, Hacker P, Richardson PL, Collins CA, Fine R, Gammon R (1991) Observations of the Mindanao current during the western equatorial Pacific-Ocean circulation study. *Journal of Geophysical Research*, 96, 7089–7104.
- Lukas R, Yamagata T, McCreary JP (1996) Pacific low-latitude western boundary currents and the Indonesian throughflow. *Journal of Geophysical Research*, 101, 12209–12216.
- Maamaatuaiahutapu K, Provost C, Andrie C, Vigan X (1999) Origin and ages of mode waters in the Brazil–Malvinas Confluence region during austral winter 1994. *Journal of Geophysical Research*, 104, 21051–21061.
- Maizuru Marine Observatory (1997) *Climate Chart of the Japan Sea*. Maizuru, Japan, 1 pp.
- Martin S, Kawase M (1998) The southern flux of sea ice in the Tatarskiy Strait, Japan Sea and the generation of the Liman Current. *Journal of Marine Research*, 56, 141–155.
- Masumoto Y, Yamagata T (1991) Response of the western tropical Pacific to the Asian winter monsoon – the generation of the Mindanao dome. *Journal of Physical Oceanography*, 21, 1386–1398.
- Masuzawa J (1969) The Mindanao Current. *Bulletin of Japanese Society of Fishery and Oceanography*, pp. 99–104.
- Maykut GA, McPhee MG (1995) Solar heating of the Arctic mixed layer. *Journal of Geophysical Research*, 100, 24691–24703.
- McCartney MS (1982) The subtropical recirculation of Mode Waters. *Journal of Marine Research*, 40(Suppl.), 427–464.
- McCreary JP, Anderson DLT (1984) A simple model of El Nino and the Southern Oscillation. *Monthly Weather Review*, 112, 934–946.
- McDougall TJ (1988) Neutral-surface potential vorticity. *Progress in Oceanography*, 20, 185–221.
- McWilliams JC (1977) A note on a consistent quasigeostrophic model in a multiply connected domain. *Dynamics of Atmosphere and Oceans*, 1, 427–441.

- Melling H, Lewis EL (1982) Shelf drainage flows in the Beaufort Sea and their effect on the Arctic Ocean pycnocline. *Deep Sea Research*, 29, 967–985.
- Mellor GL (2003) Users guide for a three-dimensional, primitive equation, numerical ocean model. Program in Atmospheric and Oceanic Sciences, Princeton University, 53 pp.
- Memery L, Arhan M, Alvarez-Salgado XA, Messias MJ, Mercier H, Castro CG, Rios AF (2000) The water masses along the western boundary of the south and equatorial Atlantic. *Progress in Oceanography*, 47, 69–98.
- Menke W (1984) *Geophysical Data Analysis: Discrete Inverse Theory*. Academic Press, San Diego, 451 pp.
- Metzger EJ, Hurlburt HE (1996) Coupled dynamics of the South China Sea, the Sulu Sea, and the Pacific Ocean. *Journal of Geophysical Research*, 101, 12331–12352.
- Miller JR (1976) The salinity effect in a mixed layer ocean model. *Journal of Physical Oceanography*, 6, 29–35.
- Mitta T, Ogawa Y (1984) Tsushima currents measured with current meters and drifters. In: *Ocean Hydrodynamics of the Japan and East China Seas*, edited by T. Ichiye, Elsevier Oceanography Series, 39, Amsterdam, pp. 67–76.
- Miyazaki M (1952) The heat budget of the Japan Sea. *Bulletin of Hokkaido Regional Fishery Research Laboratory*, 4, 1–54 (in Japanese with English abstract).
- Miyazaki M (1953) On the water masses of the Japan Sea. *Bulletin of Hokkaido Regional Fishery Research Laboratory*, 7, 1–65 (in Japanese with English abstract).
- Miyazaki M, Abe S (1960) On the water masses in the Tsushima Current area. *Journal of Oceanographic Society of Japan*, 16, 19–28 (in Japanese with English abstract).
- Monterey G, Levitus S (1997) Seasonal variability of mixed layer depth for the world ocean. NOAA Atlas NESDIS 14, U.S. Government Printing Office, Washington, DC, 100 pp.
- Moore RM, Wallace DWR (1988) A relationship between heat transfer to sea ice and temperature-salinity properties of Arctic Ocean waters. *Journal of Geophysical Research*, 93, 565–571.
- Morey SL, Shriver JF, O'Brien JJ (1999) The effects of Halmahera on the Indonesian throughflow. *Journal of Geophysical Research*, 104, 23281–23296.
- Moriyasu S (1972) The Tsushima current. In: *Kuroshio, Its Physical Aspects*, edited by Stommel, Yoshida, University of Tokyo Press, Tokyo, pp. 353–369.
- Mosby H (1934) The waters of the Atlantic Antarctic Ocean. *Scientific Results of the Norwegian Antarctic Expeditions, 1927–1928*, 11, Oslo, 1–131.
- Mountain DG, Coachman LK, Aagaard K (1976) On the flow through Barrow Canyon. *Journal of Physical Oceanography*, 6, 461–470.
- Muench RD, Gordon AL (1995) Circulation and transport of water along the western Weddell Sea margin. *Journal of Geophysical Research*, 100, 18503–18515.

- Munk WH (1950) On the wind-driven ocean circulation. *Journal of Meteorology*, 7, 79–93.
- Needler GT (1982) On determining the velocity from the density field including a closed form. *Ocean Modelling*, 46, unpublished manuscript.
- Nelson DM, Smith WO Jr, Gordon LI, Huber BA (1987) Spring distributions of density, nutrients and phytoplankton biomasses in the ice-edge zone of the Weddell/Scotia Sea. *Journal of Geophysical Research*, 92, 7181–7190.
- Nitani H (1970) Oceanographic conditions in the sea east of Philippines and Luzon Strait in summer of 1965 and 1966. In: *The Kuroshio-A Symposium on Japan Current*, edited by JD. Marr, East–West Press, Honolulu, Hawaii, pp. 213–232.
- Nowlin WD Jr, Klinck JM (1986) The physics of Circumpolar Current. *Reviews of Geophysics and Space Physics*, 24, 469–491.
- Nowlin WD Jr, Whitworth T, Pillsbury RD (1977) Structure and transport of the Antarctic Circumpolar Current at Drake Passage from short term measurements. *Journal of Physical Oceanography*, 7, 788–802.
- Ohlmann JC, Siegel DA, Gautier C (1996) Ocean mixed layer radiant heating and solar penetration: A global analysis. *Journal of Climate*, 9, 2265–2280.
- Olbers DJ, Wenzel M, Willbrand J (1985) The inference of North Atlantic circulation patterns from climatological hydrographic data. *Review of Geophysics*, 23, 313–356.
- Olson DB, Podesta GP, Evans RH, Brown OB (1988) Temporal variations in the separation of Brazil and Malvinas currents. *Deep Sea Research*, 35, 1971–1990.
- Oppenheim AV, Schafer RW (1975) *Digital Signal Processing*. Prentice-Hall, Englewood Cliffs, NJ, pp. 211–212.
- Ozsoy E, Hecht A, Unluata U (1989) Circulation and hydrology of the Levantine Basin. *Progress in Oceanography*, 22, 125–170.
- Pacanowski RC, Dixon KW, Rosati A (1991) *GFDL Modular Ocean Model, Users Guide Version 1.0*, GFDL Technical Report, 2, 46 pp.
- Park S, Chu PC (2006a) Interannual SST variability in the Japan/East Sea and relationship with environmental variables. *Journal of Oceanography*, 62(2), 115.
- Park S, Chu PC (2006b) Thermal and haline fronts in the Yellow/East China Sea: Surface and subsurface seasonality comparison. *Journal of Oceanography*, in press.
- Partos P, Piccolo MC (1988) Hydrography of the Argentine continental shelf between 38°S and 42°S. *Continental Shelf Research*, 8, 1043–1056.
- Pedlosky J (1986) Thermocline theories. In: *General Circulation of the Ocean*, edited by HDL. Abardanel, WR. Young, Springer, New York Berlin Heidelberg, 55–101.
- Pedlosky J (1987) *Geophysical Fluid Dynamics*. Springer, New York Berlin Heidelberg, 710 pp.
- Perkin RG, Lewis EL (1984) Mixing in the West Spitzbergen Current. *Journal of Physical Oceanography*, 14, 1315–1325.

- Peterson RG, Stramma L (1991) Upper-level circulation in the South Atlantic Ocean. *Progress in Oceanography*, 26, 1–73.
- Peterson RG, Whitworth T III (1989) The subantarctic and Polar Fronts in relation to deep water masses through the southwestern Atlantic. *Journal of Geophysical Research*, 94, 10817–10838.
- Phoebus PA (1988) Improvements to the data selection algorithms in the Optimum Thermal Interpolation System (OTIS). Naval Ocean Research and Development Activity Report, No. 239.
- Pickard GL, Emery WJ (1990) *Descriptive Physical Oceanography, An Introduction*, 5th Edition. Pergamon Press, Oxford, pp. 173–76.
- Pillsbury RD, Jacobs SS (1985) Preliminary observations from long-term current meter moorings near the Ross Ice Shelf. *Oceanography of the Antarctic Continental Shelf*, edited by SS. Jacobs, Antarctic Research Series, Vol. 43, American Geophysical Union Washington, DC, pp. 87–107.
- Podesta GP, Brown OB, Evans RH (1991) The annual cycle of satellite-derived sea surface temperature in the Southwestern Atlantic Ocean. *Journal of Climate*, 4, 457–467.
- Preller RH, Hogan PJ (1998) Oceanography of the Sea of Okhotsk and the Japan/East Seas. In: *The Sea*, Vol. 11, edited by AR. Robinson, KK. Brink, Wiley, New York, pp. 429–481.
- Press WH, Flannery BP, Teukolsky SA, Vetterling WT (1986) *Numerical Recipes – the Art of Scientific Computing*. Cambridge University Press, Cambridge, UK, pp. 660–667.
- Price JF, Baringer MO (1994) Outflows and deep water production by marginal seas. *Progress in Oceanography*, 33, 161–200.
- Price JF, Weller RA, Pinkel R (1986) Diurnal cycling: Observations and models of the upper ocean response to diurnal heating, cooling and wind mixing. *Journal of Geophysical Research*, 91, 8411–8427.
- Qiu B (1999) Seasonal eddy field modulation of the North Pacific Subtropical Countercurrent: TOPEX/Poseidon observations and theory. *Journal of Physical Oceanography*, 29, 2471–2486.
- Qiu DZ, Huang YT, Chen LM, Guo ZX (1985) Circulation structures in the studied waters. *Comprehensive Investigations and Studies of the South China Sea*, Vol. 2, Science Press, Beijing, pp. 204–230 (in Chinese).
- Qu TD (2000) Upper layer circulation in the South China Sea. *Journal of Physical Oceanography*, 30, 1450–1460.
- Qu TD, Mitsudera H, Yamagata T (2000) Intrusion of the North Pacific waters into the South China Sea. *Journal of Geophysical Research*, 105, 6415–6424.
- Quadfasel D, Meincke J (1987) Note on the thermal structure of the Greenland Sea gyres. *Deep Sea Research*, 35, 1143–1150.
- Quadfasel D, Ungewiß M (1988) MIZEX 87 – RV VALDIVIA cruise 54. CTD-observations in the Greenland Sea. Technical Reports, Institut für Meereskunde, Hamburg, Band-Nr. 88–5.

- Quadfasel D, Gascard JC, Koltermann KP (1987) Large-scale oceanography in Fram Strait during the 1984 marginal ice zone experiment. *Journal of Geophysical Research*, 92, 6719–6728.
- Reid JL (1989) On the total geostrophic circulation of the South Atlantic Ocean: flow patterns, tracers, and transports. *Progress in Oceanography*, 23, 149–244.
- Reid JL (1994) On the total geostrophic circulation of the North Atlantic Ocean: flow patterns, tracers, and transports. *Progress in Oceanography*, 33, 1–92.
- Reid JL (1997) On the total geostrophic circulation of the Pacific Ocean: flow patterns, tracers, and transports. *Progress in Oceanography*, 39, 263–352.
- Roden GL (1980) On the variability of surface temperature fronts in the western Pacific, as detected by satellite. *Journal of Geophysical Research*, 85, 2704–2710.
- Rosati A, Gudgel R, Miyakoda K (1996) Global ocean data assimilation system. *Modern Approaches to Data Assimilation in Ocean Modeling*, edited by P. Malanotte-Rizzoli, Elsevier, Amsterdam, pp. 181–203.
- Rudels B (1987) On the mass balance of the polar ocean with special emphasis on the Fram Strait. *Skr Nor Polarinst*, 188, 1–53.
- Saraceno M, Provost C, Piola AR, Bava J, Gagliardini A (2004) Brazil Malvinas Frontal System as seen from 9 years of advanced very high resolution radiometer data. *Journal of Geophysical Research*, 109, doi 10.1029/2003JC002122.
- Schmitz W Jr (1996a) On the world ocean circulation, Vol. 1, Some global features/North Atlantic circulation. Woods Hole Oceanographic Institution Technical Report, WHOI-96-03, 141 pp.
- Schmitz W Jr (1996b) On the world ocean circulation, Vol. 2, The Pacific and Indian Oceans/global update. Woods Hole Oceanographic Institution Technical Report, WHOI-96-08, 237 pp.
- Schmitz W Jr, McCartney MS (1993) On the North Atlantic circulation. *Review of Geophysics*, 31, 29–49.
- Schmitz W Jr, Richardson PL (1991) On the sources of the Florida Current. *Deep Sea Research*, 38(Suppl. 1), S389–S409.
- Schott F, Stommel H (1978) Beta spirals and absolute velocities in different oceans. *Deep Sea Research*, 25, 961–1010.
- SCSMEX Science Working Group (1995) The South China Sea Monsoon Experiment (SCSMEX) Science Plan. NASA/Goddard Space Flight Center, Greenbelt, Maryland, 65 pp.
- Sekine Y (1986) Wind-driven circulation in the Japan Sea and its influence on the branching of the Tsushima Current. *Progress in Oceanography*, 17, 297–312.
- Semtner AJ, Chervin RM (1992) Ocean general circulation from a global eddy-resolving model. *Journal of Geophysical Research*, 97, 5493–5550.

- Senjyu T (1999) The Japan Sea intermediate water: its characteristics and circulation. *Journal of Oceanography*, 55, 111–122.
- Seung YH (1992) A simple model for separation of East Korean Warm Current and formation of the North Korean Cold Current. *Journal of Oceanological Society of Korea*, 27, 189–196.
- Seung YH, Yoon JH (1995) Some features of winter convection in the Japan Sea. *Journal of Oceanography*, 51, 61–73.
- Shaw PT (1989) The intrusion of water masses into the sea southwest of Taiwan. *Journal of Geophysical Research*, 94, 18213–18226.
- Shaw PT (1991) The seasonal variation of the intrusion of the Philippine Sea water into the South China Sea. *Journal of Geophysical Research*, 96, 821–827.
- Shaw PT, Chao SY (1994) Surface circulation in the South China Sea. *Deep Sea Research, Part 1*, 41, 1663–1683.
- Shriver JF, Hurlburt HE (1997) The contribution of the global thermohaline circulation to the Pacific to Indian Ocean Throughflow via Indonesia. *Journal of Geophysical Research*, 102, 5491–5511.
- Soong YS, Hu JH, Ho CR, Niiler PP (1995) Cold-core eddy detected in South China Sea. *EOS Transaction, American Geophysical Union*, 76, 345–347.
- South China Sea Institute of Oceanology, 1985: Integrated Investigation Report on Sea Area of the South China Sea, Vol. 2, Science Press, Beijing, pp. 183–231 (in Chinese).
- Spall MA (1991) A diagnostic study of wind- and buoyancy-driven North Atlantic circulation. *Journal of Geophysical Research*, 96, 18509–18518.
- Sprintall J, Meyers G (1991) An optimal XBT sampling network for the eastern Pacific Ocean. *Journal of Geophysical Research*, 96, 10539–10552.
- Sprintall J, Tomczak M (1992) Evidence of barrier layer in the surface layer of tropics. *Journal of Geophysical Research*, 97, 7305–7316.
- Stommel H (1957) A survey of ocean current theory. *Deep Sea Research*, 4, 149–184.
- Stommel H, Schott F (1977) The beta spiral and the determination of the absolute velocity field from hydrographic station data. *Deep Sea Research*, 24, 325–329.
- Strakhov VN (1991) Method for filtration of the linear algebraic systems as basis for the solutions of linear problem in the gravimetry and magnetometry. *Dok Akad Nauk SSSR*, 320, 590–599 (in Russian).
- Stramma L, Ikeda Y, Peterson RG (1990) Geostrophic transport in the Brazil Current region north of 20°S. *Deep Sea Research*, 37, 1875–1886.
- Suda K, Hidaka K (1932) The results of the oceanographic observations on board R.M.S. ‘Syunpu Maru’ in the southern part of the Japan Sea in the summer of 1930. *Journal of Oceanography of Imperial Marine Observatory*, 4, 1–174 (in Japanese).
- Suda K, Hidaka K, Matsudaira Y, Kurashige E, Kawasaki H, Kubo T (1932) The results of the oceanographic observations on board R.M.S. ‘Syunpu Maru’ in the southern part of the Japan Sea in the summer of 1929, Part

1. *Journal of Oceanography of Imperial Marine Observatory*, 3, 291–375 (in Japanese).
- Sverdrup HU (1947) Wind driven currents in a baroclinic ocean with applications to the equatorial currents of the eastern Pacific. *Proceedings of National Academy of Sciences USA*, 33, 318–326.
- Sverdrup HU (1953) The currents of the coast of Queen Maud Land. *Norsk Geografisk Tidsskrift*, 14, 239–249.
- Sverdrup HU, Johnson MW, Fleming RH (1942) *The Oceans: Their Physics, Chemistry, and General Biology*, Prentice-Hall, Englewood, NJ, 1087 pp.
- Swenson MS, Hansen DV (1999) Tropical Pacific Ocean mixed layer heat budget: the Pacific cold tongue. *Journal of Physical Oceanography*, 29, 69–81.
- Swift JH, Aagaard K (1981) Seasonal transitions and water mass formation in the Iceland and Greenland seas. *Deep Sea Research*, 28, 1107–1129.
- Swift JH, Takahashi T, Livingston (1983) The contribution of the Greenland and Barents seas to the deep water of the Arctic Ocean. *Journal of Geophysical Research*, 88, 5981–5986.
- Talley LD (1988) Potential vorticity distribution in the North Pacific. *Journal of Physical Oceanography*, 18, 89–106.
- Talley LD (1993) Distribution and formation of North Pacific Intermediate Water. *Journal of Physical Oceanography*, 23, 517–537.
- Tao SY, Chen LX (1987) A review of recent research on the east Asian summer monsoon in China. In: *Monsoon Meteorology*, edited by C-P. Chang, TN. Krishnamurti, Oxford University Press, pp. 60–92.
- Teague WJ, Carron MJ, Hogan PJ (1990) A comparison between the Generalized Digital Environmental Model and Levitus climatology. *Journal of Geophysical Research*, 95, 7167–7183.
- Tikhonov AN, Arsenin VL (1979) *Methods for Solving Ill-posed Problems*. Nauka, Moscow, pp. 285.
- Tikhonov AN, Goncharsky AV, Stepanov VV, Yagola AG (1990) *Numerical Methods for Ill-Posed Problems*. Nauka, Moscow, 229 pp.
- Timofeyev VT (1962) The movement of Atlantic water and heat into the Arctic sea basin. *Deep Sea Research*, 9, 263–269.
- Toba Y, Tomizawa K, Kurasawa Y, Hanawa K (1982) Seasonal and year-to-year variability of the Tsushima–Tsugaru Warm Current system with its possible cause. *La Mer*, 20, 41–51.
- Toole JM (1987) WOCE, interbasin exchanges, and marginal sea overflows. *EOS Transactions, American Geophysical Union*, 68(1), 2–3, 11.
- Tschiya M (1989) Circulation of the Antarctic intermediate water in the North Atlantic Ocean. *Journal of Marine Research*, 47, 747–755.
- Tschiya M (1991) Flow path of the Antarctic intermediate water in the western equatorial south Pacific Ocean. *Deep Sea Research*, 38(Suppl. 1), S273–S279.
- Tully JP, Giovando LF (1963) Seasonal temperature structure in the eastern subarctic Pacific Ocean. In: *Marine Distributions*, edited by MJ. Dun-

- bar, Royal Society of Canadian Special Publications, No. 5, University of Toronto Press, Toronto, pp. 10–36.
- Uda M (1934) The results of simultaneous oceanographic investigations in the Japan Sea and its adjacent waters in May and June. *Journal of Imperial Fishery Experiment Stations*, 5, 57–190 (in Japanese).
- Uda M (1955) On the Subtropical Convergence and the currents in the North-western Pacific. *Records of Oceanographic Works in Japan*, 2, 141–150.
- Uda M, Hasunuma K (1969) The eastward Subtropical Countercurrent in the western North Pacific Ocean. *Journal of Oceanographic Society of Japan*, 25, 201–210.
- Uda M, Nakao T (1972) Water masses and currents in the South China Sea and their seasonal changes. Paper presented at the 3rd Cooperative Study of the Kuroshio and Adjacent Regions (CSK) Symposium, UNESCO, Bangkok, Thailand.
- Unidata (2004) NetCDF Documentation. This document can be downloaded from the website: <http://my.unidata.ucar.edu/content/software/netcdf/docs.html>.
- Untersteiner N (1988) On the ice and heat balance in Fram Strait. *Journal of Geophysical Research*, 92, 527–532.
- van Aken HM, Quadfasel D, Warpakowski A (1991) The Arctic front in the Greenland Sea during February 1989: hydrographic and biological observations. *Journal of Geophysical Research*, 96, 4739–4750.
- van Loon H (1984) Climates of the Oceans, *World Survey of Climatology*, 15, 453–458.
- Vapnik VN, Chervonenkis AY (1974a) On the method of ordered risk minimization, Part-1. *Avtomatika i Telemekhanika*, 8, 21–30, (in Russian).
- Vapnik VN, Chervonenkis AY (1974b) On the method of ordered risk minimization Part-2. *Avtomatika i Telemekhanika*, 9, 29–39 (in Russian).
- Vinje TK, Finnekasa O (1986) The ice transport through the Fram Strait. *Skr Nor Polarinst*, 186, 1–39.
- Wadhams P (1983) Sea-ice thickness distribution in Fram Strait. *Nature*, 305, 108–111.
- Wadhams P, Gill AE, Linden PF (1979) Transect by submarine of the East Greenland Polar Front. *Deep Sea Research*, 26, 1311–1327.
- Walsh JE, Johnson CM (1979) Interannual atmospheric variability and associated fluctuations in Arctic Sea ice extent. *Journal of geophysical Research*, 84, 6915–6928.
- Wang L, Koblinsky C, Howden S, Huang N (1999) Interannual variability in the South China Sea from expandable bathythermograph data. *Journal of Geophysical Research*, 104, 23509–23523.
- Wang GH, Su JL, Chu PC (2003) Mesoscale eddies in the South China Sea observed with altimeter data. *Geophysical Research Letters*, 30(21), doi: 10.1029/2003GL018532.

- White W, Hasunuma K, Solomon H (1978) Large-scale season and secular variability of the Subtropical Front in the western North Pacific from 1954 to 1974. *Journal of Geophysical Research*, 83, 4531–4544.
- White WB, Meyers G, Hasunuma K (1982) Space/time statistics of short-term climatic variability in the western North Pacific. *Journal of Geophysical Research*, 87, 1979–1989.
- Whitworth T III (1983) Monitoring the transport of the Antarctic Circumpolar Current at Drake Passage. *Journal of Physical Oceanography*, 13, 2045–2057.
- Whitworth T III, Peterson RG (1985) Volume transport of the Antarctic Circumpolar Current from bottom pressure measurements. *Journal of Physical Oceanography*, 15, 810–816.
- Wijffels SE, Firing E, Toole J (1995) The mean structure and variability of the Mindanao current at 8°N. *Journal of Geophysical Research*, 100, 18421–18435.
- Wilson HR, Rees NW (2000) Classification of mesoscale features in the Brazil–Falkland Current confluence zone. *Progress in Oceanography*, 45, 415–426.
- Worthington LV (1976) On the North Atlantic circulation. *The Johns Hopkins Oceanographic Studies*, 6, The Johns Hopkins University Press, 110 pp.
- Worthington LV, Wright WR (1970) North Atlantic Atlas of Potential Temperature and Salinity in the Deep Water, Including Temperature, Salinity, and Oxygen Profiles from Erika Dan Cruise of 1962. Woods Hole Oceanographic Institution Atlas Series 2, 58 plates.
- Wright WR, Worthington LV (1970) The water masses of the North Atlantic Ocean: a volumetric census of temperature and salinity. *Series Atlas in Marine Environment*, 19, 8 pp, 7 plates.
- Wunsch C (1978) The general circulation of the North Atlantic west of 50°W determined from inverse method. *Reviews of Geophysics*, 16, 583–620.
- Wunsch C (1996) *The ocean circulation inverse problem*. Cambridge University Press, Cambridge, UK, 442 pp.
- Wunsch C, Grant B (1982) Towards the general circulation of the North Atlantic Ocean. *Progress in Oceanography*, 11, 1–59.
- Wylie CR Jr (1975) *Advanced Engineering Mathematics*. McGraw-Hill, New York, 156–160.
- Wyrtki K (1961a) Scientific results of marine investigations of the South China Sea and Gulf of Thailand 1959–1961. *Naga Report*, 2, Scripps Institution of Oceanography, University of California, San Diego, pp. 164–169.
- Wyrtki K (1961b) Physical oceanography of the South east Asian Waters. *Naga Report*, 2, Scripps Institution of Oceanography, University of California, San Diego, pp. 195.
- Wyrtki K (1964) The thermal structure of the eastern Pacific Ocean. *Deutsche Hydrogr. Zeit., Suppl. Ser. A*, 8, 6–84.
- Xu Q (1992) Ageostrophic pseudovorticity and geostrophic c-vector forcing – a new look at the Q vector in three dimensions. *Journal of the Atmospheric Sciences*, 49, 981–990.

- Xu XZ, Qiu Z, Chen HC (1982) The general description of the horizontal circulation in the South China Sea. Proceedings of the Symposium of the Chinese Society of Marine Hydrology and Meteorology, Chinese Society of Oceanology and Limnology. Science Press, Beijing, pp. 119–127 (in Chinese with English abstract).
- Yi SU (1966) Seasonal and secular variations of the water volume transport across the Korea Strait. *Journal of Oceanological Society of Korea*, 1, 7–13.
- Yoon JH (1982) Numerical experiment on the circulation in the Japan Sea Part, III. Mechanism of the Nearshore Branch of the Tsushima Current. *Journal of Oceanographic Society of Japan*, 38, 125–130.
- Yoshida K, Kidokoro T (1967a) A subtropical countercurrent in the North Pacific – an eastward flow near the Subtropical Convergence. *Journal of Oceanographic Society of Japan*, 23, 88–91.
- Yoshida K, Kidokoro T (1967b) A subtropical countercurrent (II) – a prediction of eastward flows at lower subtropical latitudes. *Journal of Oceanographic Society of Japan*, 23, 231–246.
- You Y (1995) Salinity variability and its role in the barrier layer formation during TOGA-COARE. *Journal of Physical Oceanography*, 25, 2778–2807.
- You Y (1998) Rain-formed barrier layer of the western equatorial Pacific warm pool: A case study. *Journal of Geophysical Research*, 103, 5361–5378.
- Zavilov PO, Wainer I, Absy JM (1999) Sea surface temperature variability off southern Brazil and Uruguay as revealed from historical data since 1854. *Journal of Geophysical Research*, 105, 21021–21032.
- Zhou FX, Shen JJ, Berestov AL, Marushkevich AD (1995) Seasonal features of large-scale geostrophic circulations in the South China Sea. *Tropical Oceanology*, 14(4), 9–14 (in Chinese with English abstract).

Index

- advection type T profiles, 27, 28, 29, 30, 32, 75
- ageostrophic velocity, 229, 238
- Alaskan Coastal Water, 28
- Alpha-Mendeleyev Ridge, 389
- American Continent, 221
- Antarctic Circumpolar Current, 123, 124, 223, 376, 377, 379, 380, 381, 383, 385
- Antarctic Coastal Current, 379, 382
- Antarctic Intermediate Water, 255, 258, 260, 261
- Antarctic Peninsula, 385
- Antarctica, 208, 221, 379
- anticyclonic eddy, 191, 193, 215, 217, 255, 260, 278, 292, 294, 305, 326, 327, 328, 329, 343, 345, 357, 359, 362, 370
- Antilles Current, 123, 124, 367
- Arctic front, 232, 233, 238, 393
- Arctic Intermediate Water, 255, 258, 260, 261, 393, 394, 404
- Arctic Mediterranean seas, 389, 391, 392, 394, 395, 396, 397, 398, 399, 400, 401, 402, 403, 404
- Arctic Ocean, 77, 78, 232, 389, 390, 392, 393, 395, 397, 401, 403, 404, 405, 433
- Arctic Surface Water, 391, 393
- Arctic Water, 232, 376, 391, 392, 395
- Asian monsoon, 17, 83
- Atlantic Water, 78, 232, 391, 393, 395, 397, 401, 402, 403, 404, 405
- attribute, 242, 243, 244, 245, 374
- Australia, 83, 208, 221, 254, 273, 274, 359
- Australian Gyre, 359, 361, 363
- Australian Mediterranean, 359, 361
- autocorrelation function, 63, 64, 65, 66, 67, 68, 69, 76, 82, 527
- AXBT data, 316, 318, 319, 334, 348, 349
- AXCTD data, 13, 333, 334
- balanced data assimilation, 407, 410, 413, 414
- baroclinic instability, 279, 316, 363
- barrier layer, 40, 42, 43, 45, 46, 47, 48, 49, 50, 51
- basin-wide cyclonic gyre, 139, 140, 175, 176, 294
- basis functions, 88, 93, 100
- Beaufort Gyre, 403
- Beaufort Sea, 23, 25, 26, 28, 29, 404
- Beaufort Sea Deep Water, 30
- Beaufort Sea Shelf Water, 29
- Beaufort Undercurrent, 404, 405
- Bering Sea Water, 28, 29, 30
- Bering Strait, 28, 222, 390, 392
- Bernoulli method, 4
- beta-spiral method, 4, 7, 8, 109, 368, 370
- bi-modality, 107
- bin method, 63, 76
- Black Sea, 88, 92, 93, 95
- Borneo-Palawan islands, 287, 288

- bottom topography, 45, 54, 132, 141, 142, 165, 189, 203, 204, 255, 277, 281, 330, 348, 401, 418, 419, 436
- Boussinesq approximation, 1
- box model, 4, 5, 7, 8, 109, 187, 188
- Brazil Current, 373, 374, 375, 376, 377
- Brazil-Malvinas Confluence, 365, 373, 374, 375, 376, 377
- Brazil-Malvinas confluence zone, 365, 374
- Brunt-Vaisala frequency, 230
- buoyancy forcing, 237

- Celebes Sea, 43, 44, 45, 48, 49, 50, 261, 268, 269, 271, 272
- Chukchi Sea, 16, 23, 24, 25, 26, 389
- Circulation Research of the East Asian Marginal Seas, 153
- coefficient matrix, 89, 90, 92, 94, 107
- cold-core eddy, 167, 282, 316, 336, 337, 342, 344, 351, 352, 359
- complex empirical orthogonal function, 144
- composite analysis, 143, 167, 282, 284, 316
- Comprehensive Ocean-Atmosphere Data Set, 48, 204
- condition number, 89, 92, 94, 98
- continental shelf, 16, 17, 23, 56, 65, 289, 292, 374, 378, 383, 389, 390, 429
- continuity equation, 3, 110, 111, 114
- coordinate variables, 243, 244
- Coriolis force, 1, 2, 383
- Coriolis parameter, 2, 3, 204, 408, 409
- correlation coefficient, 58, 59, 62, 63
- cost function, 88, 107, 185, 188
- Cross-Basin Current, 291, 294, 301, 302, 305, 306, 316
- cubic spline, 113, 284
- curve-fitting model, 33, 35, 296
- C-vector, 229, 230, 231, 233, 235, 237
- cyclonic eddy, 143, 176, 178, 215, 217, 255, 260, 261, 267, 292, 295, 327, 329, 330, 332, 335, 343, 357, 359, 370, 383

- data assimilation, 81, 407, 408, 410, 412, 415
- data nudging, 407

- data variables, 243
- deep layer, 19, 21, 25, 52, 53, 58, 87, 181, 261, 265, 267, 271, 371, 423
- deep layer jet-core, 261
- deep sub model, 33, 35
- deep-mixing type T -profiles, 29
- deep-mixing type S -profiles, 28
- density jump, 44
- detrainment regime, 43, 44, 49, 50
- diagnostic initialization, 415, 416, 417, 418, 421, 423, 424
- difference criterion, 35, 76
- dimension ratio, 89, 94
- divergence equation, 409
- Drake Passage, 208, 381, 382, 385

- East Australia Current, 359
- East Greenland Current, 232, 391, 395, 397, 399, 400, 401, 403
- East Korean Bay, 143, 350
- East Korean Warm Current, 142, 143, 160, 189, 191
- eddy kinetic energy, 277, 346, 347, 348
- eigenfunctions, 88, 93, 107
- Ekman convergence, 278
- Ekman drift, 267
- Ekman flow, 6, 238
- Ekman Number, 2
- entrainment regime, 44, 49
- entrainment zone, 15, 19, 21, 26, 31, 52, 87, 230
- equatorial Rossby waves, 39
- Eurasian basin, 389, 390, 395, 403
- EWG atlas, 391, 392, 394, 395
- extraction, 245
- extra-equatorial region, 2, 3, 203, 204, 205
- extremely strong ‘sources/sinks’, 418, 421, 422

- first guess, 21, 22, 81, 82, 105, 211
- first necessary condition, 9, 119, 128, 136
- Fourier series, 87, 91, 93
- f -plane, 119, 408, 409
- Fram Strait, 232, 233, 234, 235, 389, 393, 394, 397, 401, 402, 403
- F-Test, 73

- Gaussian model, 71, 72, 73, 76
 Gaussian-type random variable, 223
 GDEM climatology, 144, 171
 GDEM data, 81, 83, 84, 153, 167, 246, 247, 296, 425
 geostrophic advection, 229
 geostrophic balance, 7, 109, 111, 114, 126, 201, 263, 410, 412
 geostrophic convergence, 278
 geostrophic forcing, 230, 233, 237, 239
 geostrophic shear, 3, 4, 127, 128, 332
 geostrophic velocity, 2, 3, 8, 81, 109, 174, 201, 277
 GIN Sea, 232, 389, 393, 395, 396, 397, 398, 399
 global conveyor belt, 369
 global heat storage, 102, 103, 104, 246
 gradient criterion, 35, 36
 gradient space, 19, 20, 540
 Greenland-Scotland Ridge, 389, 393, 396
 Greenland Fracture Zone, 397
 Gulf Stream, 36, 123, 124, 365, 366, 367, 368, 371, 372, 373, 377

 Hainan Island, 178, 331
 Halmahera Eddy, 249, 253, 255, 258, 260, 265, 267, 273, 362
 Halmahera Sea, 255, 256, 270, 273
 halocline, 15, 25, 26, 27, 29, 30, 31, 32, 87, 156, 157, 307, 338, 392, 547
 High Salinity Intermediate Water, 156, 157, 160
 histogram, 79, 86
 horizontal diffusivity, 2, 131
 horizontal Laplace operator, 88
 Hovgaard cell, 236
 Hovgaard Fracture Zone, 233, 234, 236
 hydrostatic balance, 1, 3, 7, 9, 109, 126, 229
 hydrostatic pressure, 113

 ice breeze, 394
 ice drift, 394
 ice freezing, 24, 25, 26
 ice melting, 25, 26, 392
 ill-posed algebraic equation, 98, 107
 Indian Ocean, 253, 261, 263, 271, 272, 381

 Indonesian Throughflow, 253, 271, 272
 inertial-gravity mode, 410
 isopycnal coordinate system, 109, 110, 111, 114, 119, 126, 127, 165, 173, 247
 isothermal/isohaline structure, 25
 iteration, 21, 23, 55, 82, 98, 99, 211, 212, 221, 479

 Jacobian, 117, 119, 123
 Japan Basin, 141, 142, 143, 154, 155, 156, 157, 160, 191, 193
 Japan Nearshore Branch, 143, 161, 162, 189, 191, 193
 Japan Sea Intermediate Water, 143, 156, 419
 Japan Sea Proper Water, 142, 143
 Japan/East Sea, 140, 141, 142, 144, 183, 193, 197, 198, 348, 355, 418, 419, 421, 426, 565

 Kara Sea, 389
 Kelvin waves, 39
 Knipovich cell, 235, 236
 Knipovich Ridge, 232, 234, 235, 236, 393
 Kuroshio Current, 249, 253, 278, 332
 Kuroshio intrusion, 166, 167, 172, 175, 178, 180, 181, 275, 285, 287, 289, 292, 294, 295, 343
 Kuroshio water, 17, 153, 169, 172, 175, 178, 181, 274, 293, 295, 331, 332, 343

 Labrador Basin cyclonic gyre, 365
 Labrador and Irminger Currents, 366
 Lagrangian parameter, 186, 198
 lateral boundary transport, 427, 428, 429
 lateral mixing, 112
 least square difference, 82, 88, 105
 least square error, 129
 level of no motion, 4, 9, 235, 326, 333
 Liyue Bank, 168, 171, 331
 Lomok Strait, 272
 Lomonosov Ridge, 389, 390
 Lorenz system, 94, 95, 98, 415

- Luzon Strait, 56, 165, 166, 167, 169, 172, 174, 175, 178, 180, 181, 182, 183, 274, 275, 284, 287, 289, 292, 293, 294, 295, 301, 332, 336, 337, 343
- Mackenzie Canyon, 23
- Mackenzie River, 390
- Madagascar, 221
- Malvinas Current, 375, 376, 377
- mass conservation, 3, 6, 7, 9, 109, 185, 186, 188
- MCSST data, 296
- mean kinetic energy, 345, 347, 348
- mid-depth of North Atlantic, 99
- middepth sub model, 33, 34, 35
- Mindanao Current, 253, 257, 258, 260, 261, 263, 265, 267, 269, 272
- Mindanao Eddy, 249, 253, 255, 258, 260, 261, 263, 267, 272, 273
- Mindanao Island, 255, 258, 260, 261, 262, 267
- mixed layer, 14, 15, 17, 19, 21, 24, 25, 26, 29, 30, 31, 32, 35, 39, 40, 43, 44, 52, 56, 58, 59, 65, 66, 73, 74, 81, 87, 149, 167, 230, 231, 238, 310, 318, 319, 321, 322, 334, 336, 337, 349, 352, 544
- mixed layer depth, 17, 21, 30, 35, 81, 149, 231, 544
- MODAS, 81, 82, 83, 84, 85, 86, 87, 106, 413, 415
- model uncertainty, 428
- modular ocean model, 131, 132, 133, 134, 135, 136, 137, 138, 139
- Molucca Sea, 269
- Montgomery potential, 109, 178
- MOODS data, 11, 24, 36, 43, 54, 55, 56, 60, 66, 144, 147, 167, 282, 283, 284, 323, 324, 355, 356
- multi-eddy structure, 191, 292, 305, 316, 318, 348, 349
- multi-layer structure, 19, 69, 70, 74
- multi-time scale, 59, 60, 62
- Nansen-Gakkel Ridge, 389
- NCEP data, 167, 287
- Needler's formula, 8, 9, 116, 120
- net fresh water flux, 48, 49, 426
- net heat flux, 48, 49, 50, 426, 427
- netCDF, vi, 241, 242, 243, 244, 245, 246, 432, 433, 440, 442
- Neumann boundary condition, 88
- neutral tangent plane, 112
- New Guinea, 221, 249, 253, 260
- New Guinea Coastal Current, 253, 255, 257, 272
- New Guinea Coastal Undercurrent, 253, 255, 257, 258, 260, 263, 265, 267
- New Zealand, 259, 365
- Newtonian nudging, 408, 410, 412
- noise level, 102, 217, 219, 220, 221
- noise-to-signal ratio, 89, 90, 94, 98, 101, 107
- North Atlantic Gyre, 123, 124
- North Atlantic Ocean, 36, 39, 116, 365, 366, 367, 369, 370, 377, 431, 433
- North Atlantic Water, 232
- North Equatorial Counter Current, 253, 255, 256, 257, 258, 260, 261, 263, 265, 266, 267, 268, 270, 272
- North Equatorial Current, 166, 249, 253, 272, 278, 280, 281, 301
- North Korean Cold Current, 143
- North Pacific Intermediate Water, 255, 258, 260
- North Pacific Tropical Water, 256
- Norwegian Atlantic Current, 233, 391, 397, 399
- null hypothesis, 33, 59, 73
- Oki Gunto eddy, 351, 355
- optimal interpolation, 37, 77, 81, 283, 407
- optimal mode truncation, 88
- optimal spectral decomposition, 77, 87, 88, 89, 90, 91, 92, 93, 94
- out-of-phase variation, 162, 191, 193, 265
- PacificOcean, 8, 36, 39, 42, 59, 78, 141, 142, 165, 208, 249, 251, 255, 259, 271, 272, 275, 281, 285, 295, 301, 348, 370, 385
- pair number, 6, 64, 66, 67
- parameter analysis, 15, 77

- parametric model, 16, 17, 19, 20, 21, 23, 25, 27, 29, 31, 32, 33, 35, 36, 52, 53, 54, 55, 80, 86, 527
- perfect vector, 115
- Perturbed Lorenz Attractor, 94
- Philippine Sea, 169, 172, 178, 180, 275, 295
- Philippines, 17, 165, 249, 253, 272, 273
- Point Barrow, 28
- Poisson equation, 213, 223
- Polar Front, 191, 350, 351, 352, 355, 379, 382, 393
- Polar Front Current, 181, 191, 193
- Polar Intermediate Water, 393
- Polar Water, 232, 391, 392
- potential density, 113, 116, 122, 123, 133, 134, 233, 234, 436, 442, 447, 472
- potential vorticity, 246, 247, 280, 281, 292, 369, 506, 518
- profile data analysis, 15
- pseudo potential vorticity, 112
- pseudovorticity, 229, 230, 234, 235, 236
- P**-spiral, 117, 118, 119, 120, 121, 123, 124, 128, 138
- P**-vector inverse method, 77, 116, 127, 137, 140, 165, 185, 201, 204, 291, 331, 333, 349, 401, 407, 413, 415, 428
- q-isoline, 119, 173, 175
- rain-formed mechanism, 44, 49, 50
- recirculation, 117, 143, 260, 267, 278, 280, 366, 367, 368, 371, 372, 374, 376, 377, 393, 401, 402, 403, 404, 405
- reconstruction, 91, 92, 93, 94, 99
- reference-level velocity, 3, 4, 5, 6, 7, 8
- regression model, 60, 62
- Reynolds stress, 1, 2, 204
- river run-off, 17, 26, 65, 285
- root mean square error, 215, 219, 428, 539
- Ross Gyre, 385
- Ross Sea, 379, 382, 383, 385, 386
- Rossby mode, 410
- rotation matrix method, 89, 90, 91, 92, 93, 94
- salinity maximum, 157, 160, 256, 306, 310, 341, 393
- salinity minimum, 143, 144, 157, 160
- satellite remote-sensing, 52
- Savu Sea, 272
- scatter diagrams, 47, 49, 51, 58, 84, 85
- SCSMEX, 82, 83, 84, 85, 333, 345
- seasonal adjustment, 26
- second necessary condition, 9, 119, 128, 137
- secondary circulation, 229, 236
- semi-isopycnal coordinate system, 109, 111
- sensibility matrix, 98
- shallow-mixing type, 26, 32
- signal to noise ratio, 64, 82
- significance level, 33, 59, 66
- source/sink terms, 3, 415, 417, 418, 420, 421, 422, 423
- South Atlantic Current, 376
- South Atlantic Ocean, 208, 370, 373, 374, 375
- South China Sea, 11, 12, 13, 14, 15, 16, 54, 55, 56, 57, 59, 60, 82, 83, 84, 165, 166, 167, 169, 170, 171, 172, 173, 174, 175, 178, 181, 247, 249, 253, 255, 272, 274, 275, 276, 281, 282, 284, 285, 287, 289, 291, 298, 301, 302, 305, 315, 316, 317, 319, 320, 321, 322, 323, 324, 325, 326, 327, 328, 329, 330, 331, 332, 333, 334
- South China Sea Deep Water, 84
- South China Sea Subsurface Water, 83
- South China Sea Surface Water, 83
- South Equatorial Current, 123, 124, 255, 373, 374
- South Pacific Tropical Water, 256, 257
- Southern Ocean, 379, 380, 385
- spatial decorrelation scale, 71, 72, 73, 74, 75, 283, 319, 334
- spectral coefficient, 88, 89, 100
- speed parameter, 116, 127, 128, 129, 130
- standard deviation, 14, 33, 36, 60, 62, 85, 140, 223, 226, 318, 319, 349, 350
- static instability, 78, 79, 131
- Stokes Theorem, 208

- stratification-formed mechanism, 44, 49
- strong ‘sources/sinks’, 418, 424
- Subpolar Front, 141, 144, 149, 153, 157, 160, 162, 419, 420, 421, 422
- Subtropical Countercurrent, 276–281, 363
- Sulu Sea, 47, 48, 49, 51, 54, 166, 255, 272
- summer monsoon, 19, 55, 56, 141, 142, 149, 152, 153, 157, 160, 162, 166, 167, 169, 175, 180, 193, 282, 292, 294, 296, 298, 316, 329, 330, 348
- surface cooling, 25, 26, 44, 48, 49, 397, 401
- surface salt flux, 25
- surface wind stress, 48, 49, 132, 202, 204, 223, 226, 230, 231, 238, 277, 302, 310, 329, 425, 426, 427
- Sverdrup transport, 277, 301
- Tasman Front, 359
- Tasman Sea, 362
- t*-distribution, 33, 59, 64, 256
- temporal decorrelation scale, 63, 72, 74, 82, 283, 319, 334, 350
- terrain-following coordinate, 66
- thermal expansion coefficient, 36, 43
- thermal structure, 13, 17, 19, 22, 52, 53, 62, 73, 348
- thermal wind relation, 3, 6, 7, 110, 120, 122, 127, 129, 189, 202, 229
- thermocline, 153, 318, 319, 321, 322, 334, 336, 337, 349, 352, 368, 419, 423, 547, 549, 551
- thermodynamic equation, 3, 415
- thermohaline circulation, 236, 261, 283, 293, 396
- thermohaline front, 296, 299, 301, 302, 305, 306, 307, 308, 309, 310, 311, 312, 313, 314, 315, 316, 317, 375, 393
- thermohaline variability, 63, 282, 305, 307, 310
- top shallow sub model, 34
- total kinetic energy, 132, 421
- trajectory, 119, 120, 122
- T-S* diagram, 83, 84, 306, 308, 309, 323, 324, 333, 334, 355
- Tsushima cold-core eddy, 352, 359
- Tsushima Strait, 142, 143, 426, 427
- Tsushima Warm Current, 143, 160, 162, 185, 189, 191, 193, 426
- t*-test, 32, 33
- two scalar functions, 236, 238
- two-step determination, 116
- Ulleung/Tsushima Basin, 143, 144, 157, 193
- Ulleung eddy, 351, 355
- unbalanced data assimilation, 407, 408, 412, 413
- unconstrained optimization, 186
- variational P-vector method, 185, 186, 187, 188, 189, 190, 191, 192, 193, 194, 195, 196, 197, 198
- velocity potential, 236, 237, 408
- vertical eddy diffusivity, 416
- Vietnamese Bight, 168, 169, 170, 171, 172, 320, 326, 331
- volume transport, 162, 163, 165, 166, 181, 183, 185, 187, 188, 201, 203, 204, 206, 207, 209, 211, 216, 221, 224, 226, 241, 243, 246, 247, 249, 250, 251, 253, 267, 268, 269, 270, 271, 272, 273, 274, 275, 276, 280, 361, 365, 366, 367, 372, 373, 374, 380, 381, 382, 383, 384, 385, 386, 418, 426, 427
- volume transport streamfunction, 274, 275, 276, 366
- volume transport vorticity, 203, 204, 205, 206, 207, 241
- vorticity equation, 3, 114, 203, 204, 409
- warm-core eddy, 167, 282, 316, 329, 330, 352, 359
- Weddell Gyre, 383, 385
- Weddell Sea, 383, 384, 385, 387
- Weddell-Scotia Confluence, 385
- West Spitzbergen cell, 236
- West Spitzbergen Current, 232, 233, 293, 394, 397, 399, 401, 402, 403, 404
- western boundary current, 133, 137, 139, 140, 166, 176, 177, 178, 253, 276, 277, 292, 301, 359, 369, 371, 372, 373, 383

- white noise, 90, 91, 92, 96, 97, 217, 221
- wind forcing, 26, 237, 425, 427
- wind-driven circulation, 236, 259, 301
- winter monsoon, 17, 141, 149, 153, 157,
160, 162, 166, 169, 175, 193, 292,
294, 295, 296, 348
- WOA dataset, 391
- WOCE, 256
- Yamato eddy, 351
- Yellow Sea, 16, 17, 18, 19, 22, 63, 65,
66, 68, 70, 73, 74, 75, 80, 351, 532
- z-level analysis, 15, 77, 78, 79, 104, 283,
296